D. C. Groeneveld
Chalk River Nuclear Laboratories,
Atomic Energy of Canada Ltd.,
Chalk River, Canada

Effect of a Heat Flux Spike on the Downstream Dryout Behavior

The effect of a short hot patch on the downstream dryout behavior was investigated in heated tubes cooled by Freon-12 at conditions equivalent (on the basis of liquid to vapor density ratio) to 69 bar in steam-water. The hot patch, located well upstream from the heated end, generated a heat flux spike which resulted in a local dry patch. Following an increase in downstream surface heat flux the dry patch would often spread in the downstream direction even though the heat flux was only a small fraction of the measured critical heat flux with uniform heating. A force balance on the dry patch boundary showed that, for certain conditions, spreading of the dry patch in the downstream direction is inevitable. This spreading however can be limited by interfacial instability, droplet-wall interaction and axial conduction.

Introduction

Neutron flux peaking may occur for a number of reasons in nuclear reactors, e.g., due to end-effects in short fuel bundles; use of control or booster rods, etc. If not adequately controlled, this could result in a considerable increase in local heat flux.

The simple case of a flux spike superimposed on a uniformly heated tube was investigated in a Freon-12 test facility. The flux spike profile was produced at selected locations by a hot patch clamp attached to the tube. The heat flux, mass velocity, and inlet quality were varied.

Freon-12 has been used successfully to model the CHF (critical heat flux) of steam-water mixtures in uniformly and nonuniformly heated channels (Groeneveld [1],[1] Ahmad [2]. It is suggested that the phenomena observed in this investigation could also occur in a Freon-equivalent water system.

Experimental Equipment

Freon-12 Loop. A schematic of the Freon test facility is shown in Fig. 1. The Freon flow enters the pump at approximately 15 deg C subcooling and 8.5 bar. The pump outlet pressure is reduced from 21 bar to 12 bar by a throttle valve located before the preheater of the test section. The test section outlet pressure is kept constant at 10.8 bar by maintaining the pressure in the jet condenser with a pressure controller which operates a three-way valve in the bypass.

Test Section. The test sections used had the following dimensions: inside diameter 0.780 cm and 1.095 cm; heated lengths 142.2–182.9 cm. Inconel-600 was selected as the tube material because of its low temperature coefficient of resistance. The test section tube was uniformly heated by a 50 v 1000 amp d-c power supply except at the hot patch clamp where the tube was short-circuited. The hot patch clamp was made of a 6.35 cm long, split copper cylinder silver-soldered to the tube to ensure good thermal contact. Six 0.95 cm OD cartridge heaters were placed in the holes provided (Fig. 2) and were connected in parallel to a 125 v 20 amp variable transformer. The hot patch clamp was equipped with two planes of two 0.050 cm OD metal sheathed thermocouples, located 1.5 cm from each end of the clamp. The location of the hot patch clamp was varied from 4 cm from the start of the heated section to 38 cm from the end.

Instrumentation. Downstream from the hot patch, 0.050 cm OD metal-sheathed thermocouples were attached to the test sec-

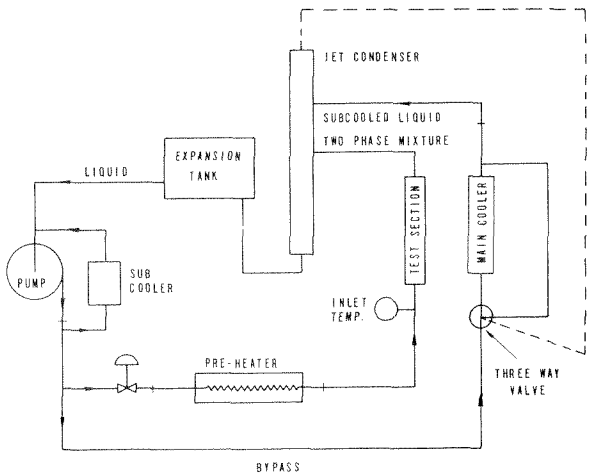

Fig. 1 Freon-12 loop schematic

[1] Numbers in brackets designate References at end of paper.

Contributed by the Heat Transfer Division of THE AMERICA SOCIETY OF MECHANICAL ENGINEERS and presented at the ASME-AIChE Heat Transfer Conference, Atlanta, Ga., August 5–8, 1973. Manuscript received by the Heat Transfer Division, August 28, 1973. Paper No. 73-HT-41.

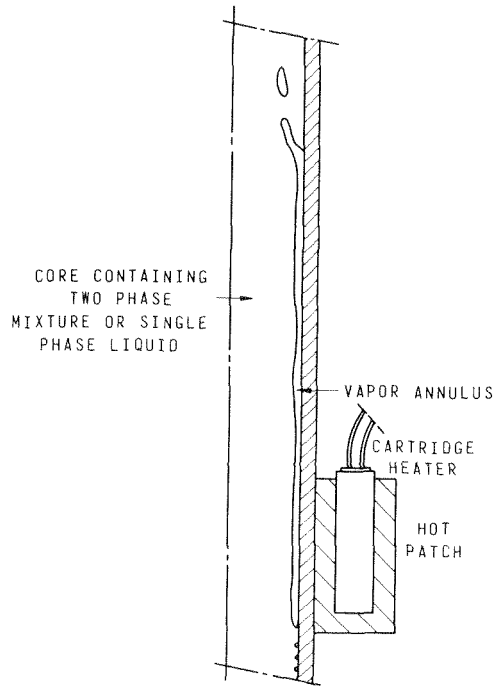

Fig. 2 Spreading of dry patch downstream of hot patch

tion. Flows through test section and bypass were measured by turbine flow meters. The outlet pressure was measured by a Heise Bourdon-tube pressure gauge and test section pressure drops were obtained from a strain-gauge type pressure transducer.

All measurements except the hot patch power were converted to mv signals, then fed to the on-line computer and printed out in engineering units. Most thermocouple outputs were also recorded on a Brush eight-channel recorder.

Experimental Results

In a previous experiment (Groeneveld [1, 3]), the CHF was measured using the same test sections but without the hot patch. The installation of the unheated hot patch clamp did not significantly change the CHF and post-dryout behavior for equal heated lengths; this was to be expected as it only added a short unheated length well upstream from the dryout location. However, when the hot patch power was raised such that dryout occurred first at the dry patch, the downstream dryout behavior was changed drastically.

Dryout at the hot patch was obtained by increasing the hot patch temperature to such a high level that the inside surface could no longer support liquid contact, and vapor blanketing occurred. The hot patch surface heat flux at which dryout occurred is roughly two to four times the measured CHF with uniform heating;[2] the hot patch power, however, was never more than one-tenth of the test section power. The high thermal inertia of the hot patch made it difficult to accurately measure the hot patch dryout heat flux. Dryout at the hot patch was detected when the temperature-time trace displayed a sudden change in slope;[3] for high mass flows this change in slope was less obvious. The corresponding hot patch temperature was between 100 and 130 deg C for all positive hot patch qualities and mass flows. The high thermal inertia of the hot patch clamp enabled the experimenter to limit the temperature rise at dryout by reducing the hot patch power. When steady film boiling temperatures were reached at the hot patch the test section power was raised slowly. At power levels well below the dryout power for uniform heating a phenomenon illustrated in Fig. 2 occurred: the dry patch started to spread from the hot patch in the downstream direction. During two runs drypatch spreading was observed visually using an infra-red camera focused on the bare test section tube; the hot region was seen to propagate slowly from the hot patch at an apparently constant rate.

It was attempted to stop this drypatch spreading by using a 6.3 cm long unheated section located 50 cm downstream from the hot patch; only at test section heat flux levels less than 50 per cent of the measured CHF with uniform heating did the unheated section prevent the dry patch from spreading across it.

Most measurements were obtained with the 0.78 cm ID test section having a total heated length of 142.2 cm and having the hot patch located 4 cm from the start of the heated section. Since a variation in heated length, diameter or hot patch location did not seem to affect the downstream dryout behavior, only the results obtained with this test section assembly will be discussed below.

The effect of a hot patch on the downstream thermal behavior of an otherwise uniformly heated tube is shown graphically in Figs. 3 to 7. The data on which these figures are based have been reported previously (Groeneveld [3]). The solid lines represent the boiling curves for uniform heating at constant inlet conditions while the broken lines illustrate the effect of an upstream hot patch in extending the film boiling temperature and heat flux range to lower values. Dryout at the hot patch does not seem to affect the film boiling temperatures as both symbols in Fig. 3 fall along a single curve. All figures show the occurrence of a decrease in wall temperature just before dryout. This decrease was found to be most pronounced at the lower mass flows, e.g., G = 135 g/cm^{2}s (Fig. 4). Similar temperature reductions were also observed in steam-water by Moeck [4] and Parsons [5]; they were attributed to the change in heat transfer mode just before dryout from forced convective evaporation to the more efficient nucleate boiling.

Discussion

Some previous investigators (e.g., Todreas [6], and DeBortoli [7] have also employed spiked heat flux profiles in their CHF studies; however they did not permit the hot patch to reach sta-

[2] Based on the same local quality.

[3] An example of the change in slope during rewetting of the hot patch is shown by the extreme left thermocouple trace of Fig. 9.

Nomenclature

C_P = specific heat of vapor
C_D = drag coefficient
k = thermal conductivity of vapor
l = stagnation length
m = wave number
P = pressure
Q = surface heat flux
$T(j)$ = temperature at location j
U = velocity
X = quality
y = distance from solid boundary
δ = film thickness
ΔH = subcooling of liquid
ΔT = wall temperature excess above saturation
θ = contact angle
ψ = angle as defined in Fig. 8
ρ = density
λ = latent heat
σ = surface tension
τ = shear stress

Subscripts

c = core flow
DO = dryout
i = inlet, interface
l = liquid
n = normal to interface
sat = saturated value
v = vapor
w = heated surface

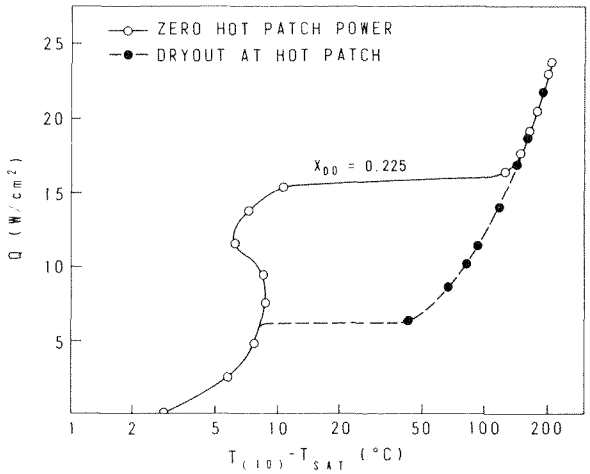

Fig. 3 Boiling curves measured 35 cm downstream of hot patch, run 624, G = 407.4 g/cm²s, P = 10.7 bar, X_i = 0.152

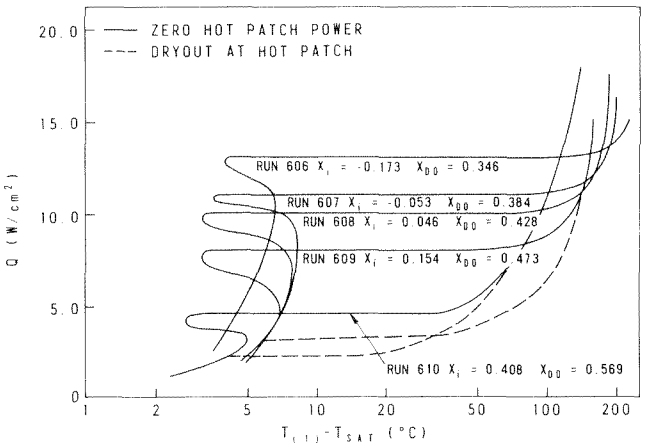

Fig. 4 Boiling curves measured 125 cm downstream of hot patch, G = 135 g/cm²s, P = 10.8 bar

ble film boiling and thus were not able to observe drypatch spreading.

Although downstream spreading of the dry patch at first may seem rather unusual there is a sound explanation for its occurrence. McPherson [8] has analyzed the force balance on the vertex (or axial boundary) of a dry patch in annular flow. He considered the following axial forces per unit of vortex width (Fig. 8(*a*)):

Stagnation force $$F_M = \int_0^\delta \rho_l U_l^2 dy$$

Vapor shear force $$F_S = \int_0^l (\tau_i - \tau_w) dl$$

Aerodynamic drag force $$F_D = \frac{C_D}{2} \int_0^\delta \rho_g U_g^2 dy$$

Surface tension force $$F_\sigma = \int_0^\theta \{\sigma \sin \psi - \cos \psi \frac{d\sigma}{d\psi}\} d\psi$$

Vapor thrust force $$F_T = \int_0^\delta \rho_g U_n^2 dy$$

(No gravity force is considered as this force is usually negligible at high mass flows.) The direction in which these forces act is shown in Fig. 8(*a*). McPherson evaluated these forces for 70 bar steam-water and concluded that the significant forces are the surface-tension force and the vapor shear force; for a stable dry patch, these forces are approximately equal but have opposite signs.

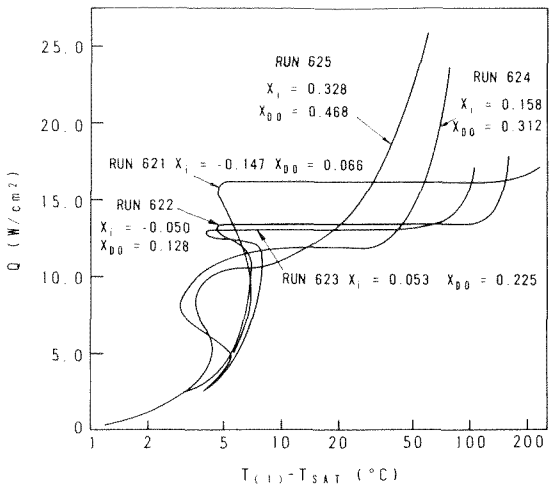

Fig. 5 Boiling curves measured 125 cm downstream of hot patch, G = 405 g/cm²s, P = 10.8 bar

For an upstream dryout (Fig. 8(*b*)), the aerodynamic drag force and the liquid stagnation force do not exist, but they may be replaced by a vapor stagnation force. In this case all forces act in the downstream direction; hence the vertex wants to move in this direction and only significant droplet-wall interaction can prevent the dry patch from spreading.

McPherson's drypatch force balance can obviously not be used at low void fractions. Here Tong's [9] bubbly layer model is more applicable in explaining drypatch spreading. The boundary layer coming from the upstream hot patch carries with it superheat and entrained bubbles when it contacts the downstream surface. This will impede the wall heat transfer with the subcooled or saturated core and thus encourages dryout to occur at heat flux levels well below those required for dryout in uniformly heated channels having the same cross-sectional average conditions.

An additional mechanism which could aid drypatch spreading can be deduced from the results of a previous experiment (Groeneveld [3]). Here the axial temperature distribution near a drypatch boundary was measured. The observed large temperature gradient resulted in significant axial conduction from the dry side to the wet side of the drypatch boundary thus increasing the wet side surface heat flux by as much as 50 per cent over the average value and encouraging the drypatch to spread.

At highly subcooled flows ($X < -0.15$) drypatch spreading did not occur; after dryout at the hot patch, an increase in test section

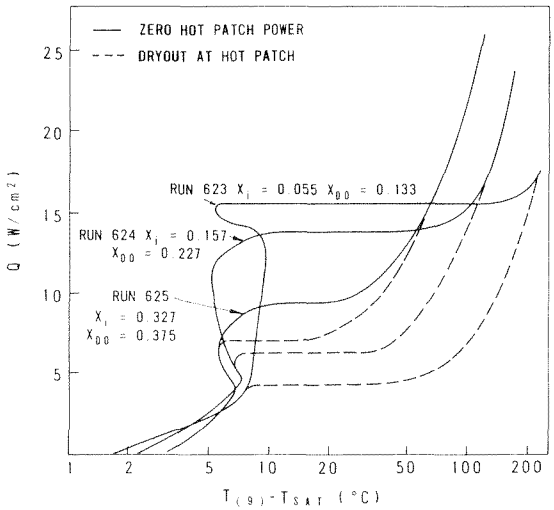

Fig. 6 Boiling curves measured 45 cm downstream of hot patch, G = 405 g/cm²s, P = 10.8 bar

power eventually led to dryout occurring at the downstream end of the heated section. This was to be expected, as under these conditions dryout is nucleation-induced and is virtually a local phenomenon since the void, generated at the hot patch will mostly condense as soon as the flow sees the reduced wall superheat downstream of the hot patch. The observed dryout behavior is in agreement with the flow memory effect (Tong [9]): for highly subcooled flow the local conditions are dominant in determining the CHF while in the net quality region, the upstream heat flux history must be considered.

Figs. 5 and 6 (G = 405 g/cm²s) show the boiling curves for two locations along the heated channel: $T(9)$ was measured 45 cm downstream from the hot patch while $T(1)$ was measured 80 cm downstream from $T(9)$. Following dryout at the hot patch the dry patch spread in the downstream direction past the location of $T(9)$, thus changing its boiling curve, but did not reach $T(1)$. The observed limited drypatch spreading frequently occurred at low void fractions and high mass flows. The following explanations are offered:

During film boiling at low void fractions the liquid is in the form of a continuous core which may contain entrained bubbles. The difference in axial velocity between vapor film and liquid core, $U_v - U_c$, gives rise to a wavy interface. The interface will be stable if (Lamb [10], and Birkhoff [11])

$$m\sigma(1/\rho_c + 1/\rho_v) > (U_v - U_c)^2 \tag{1}$$

Rankin [12] suggests that equation (1), which is based on surface wave propagation, is not applicable in film boiling, since here the interface waves experience a vapor thrust force during the dry wall collisions (collisions where a thin vapor layer will always be present between liquid and solid). By including the effect of such force Rankin derived the following criterion for a stable core flow during film boiling:

$$\left\{\frac{\sigma \cdot m}{\rho_c} + \frac{2k^2\Delta T^2}{m\rho_c\rho_v\lambda'\delta^3}\right\}\left\{1 + \frac{\rho_c}{\rho_v}m\delta\right\} > (U_v - U_c)^2 \tag{2}$$

where $\lambda' = \lambda(1 + 0.4\, C_p\, \Delta T/\lambda)^2$.

Both stability criteria depend on the wave number m which is unknown. If $U_v - U_c$ becomes very large the stability criteria will not be satisfied and small disturbances at the liquid core-vapor interface will amplify and grow. This phenomenon will give rise to an increased intensity of dry-wall collisions thus reducing the dry-wall temperature. A reduction in dry-wall temperature to below the Leidenfrost[4] temperature will result in rewetting of the heated surface.

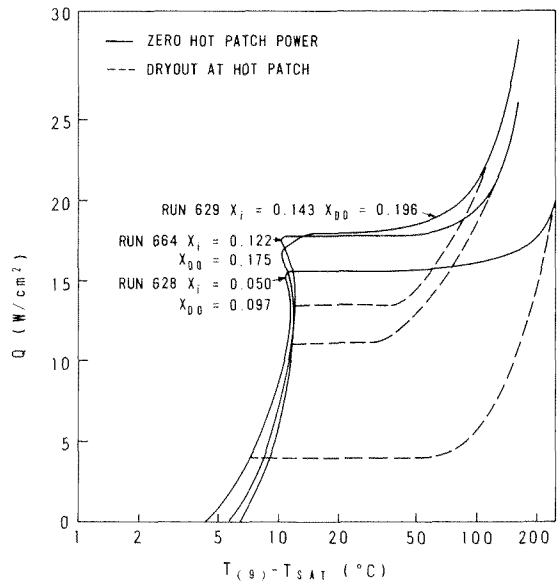

Fig. 7 Boiling curves measured 45 cm downstream of hot patch, G = 676 g/cm²s, P = 10.7 bar

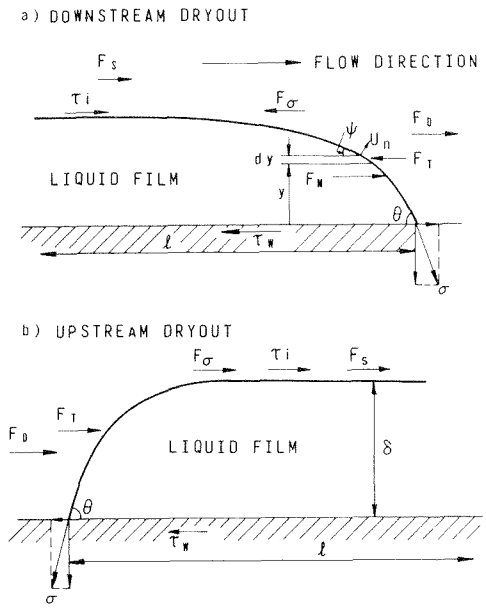

Fig. 8 Forces on vertex of dry patch

At low qualities, the post-dryout heat transfer coefficient increases approximately linearly with quality: the heat transfer coefficient approximately doubles by increasing quality from 10 to 20 per cent due to the corresponding increase in vapor velocity. Also, in the absence of a liquid film, droplet migration toward the heated surface will manifest itself in increased wall-droplet interaction. Both of these factors could reduce the surface temperature to below the Leidenfrost temperature. Once this occurs, droplets can wet the heated surface; if the local heat flux is also less than the heat flux required to evaporate all depositing droplets, a wet surface may be maintained.

After drypatch spreading had occurred, an 80 per cent reduction in hot patch power removed the heat flux spike and resulted in a complete rewetting of the heated channel wall, starting at the hot patch. This was accompanied by a large increase in total channel pressure drop (often more than 100 percent) which can be attributed to the large increase in fluid viscosity at the wall. In general, the occurrence of dryout will reduce the pressure drop, increase the mass flow and could initiate a flow oscillation, especially in parallel channels. To this author's knowledge, no investigator has ever studied the effect of dryout on flow stability.

An interesting phenomenon was observed at the high mass velocity, low quality runs. Limited drypatch spreading was observed downstream from the hot patch. When the hot patch power was switched off (the test section power remained unchanged) the vapor patch, instead of disappearing as was observed at higher qualities, persisted at the wall and started to move downstream. An example of this is given in Fig. 9 which shows the temperature history along the test section. A possible explanation of this behavior is offered: After rewetting of the hot patch, the upstream axial boundary of the vapor patch, which is no longer anchored to the hot patch, moves downstream at velocity U_1, limited by the high wall temperature which must first be reduced (by axial conduction, dry wall collisions and convection) to below the Leidenfrost temperature to permit rewetting. Meanwhile the downstream boundary of the vapor patch, whose location was fixed previously due to intense liquid-wall interaction,

[4] No single value can be assigned to the Leidenfrost temperature for our system since, besides the properties of the liquid and the surface, the Leidenfrost temperature also depends on the local hydrodynamic conditions (e.g., mass of liquid approaching heated surface, impact velocity, etc.)

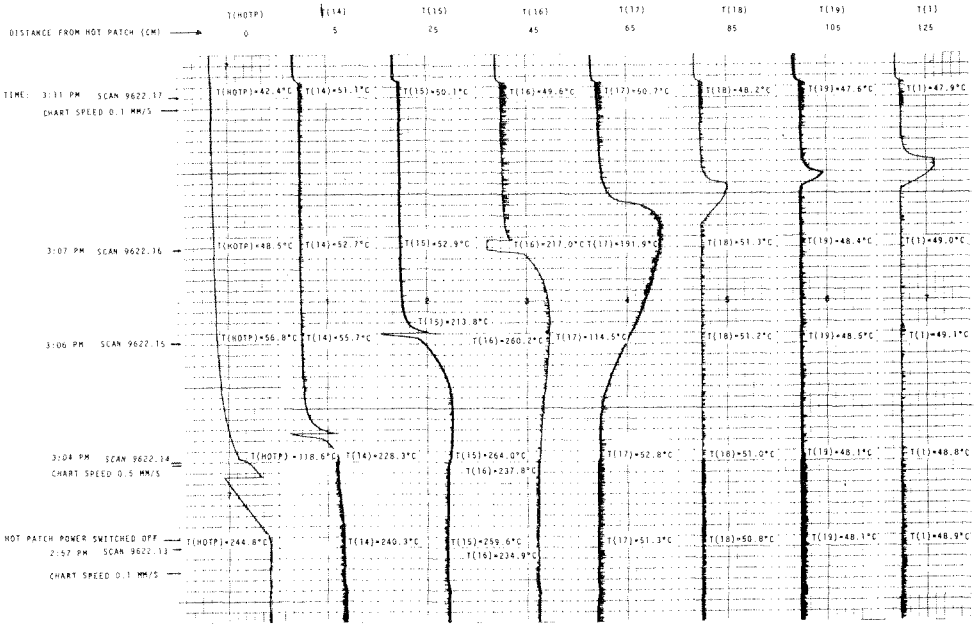

Fig. 9 Temperature history of run 9622 after hot patch rewetting, G = 406 g/cm^{2}s, X_i = −0.045, P = 10.8 bar, Q = 6.80 W/cm^2, CHF (uniform heating) = 13.26 W/cm^2

now sees a thicker and shorter vapor patch. This change in vapor patch size results in a decreased liquid-wall interaction and permits the vapor front to move downstream at velocity U_2, limited by the surface tension forces and the thermal inertia of the heated wall. If $U_2 \ll U_1$ the wall will rewet before the vapor patch reaches the end of the tube.

Duplication of this experiment in water at equivalent conditions is expected to be difficult as very high heat fluxes (typically fifteen times that of Freon-12) are required to create a drypatch. Drypatch spreading in a water system is expected to occur if the force balance or the bubble boundary layer model are the mechanisms controlling drypatch spreading. However, if axial conduction is the controlling mechanism, spreading probably will not occur, as the much higher heat fluxes in water result in a much smaller percentage increase in surface heat flux (due to wall conduction) at the wet side of a drypatch boundary.

In experiments designed to obtain film boiling data, the hot patch technique can be beneficial. It extends the film boiling temperature and heat flux range to values considerably below those obtained in uniformly heated channels without going to the expense of a temperature controlled system which usually requires a second circulation system. The minimum film boiling heat flux is in both cases well below the dryout heat flux. However the measured minimum film boiling temperature and heat flux do not represent absolute minima for those conditions since rewetting was caused by a propagating rewetting front which is always accompanied by significant axial conduction (Thompson [13], and Semeria [14]). If rewetting had been spontaneous, i.e., was not caused by a propagating rewetting front the wall temperature at rewetting would have been equal to the Leidenfrost temperature.

Conclusions

1 Flow boiling curves were constructed for a wide variety of mass flows and inlet qualities. They differ from the pool boiling curves in two aspects: (i) before dryout a reduction in surface temperature was usually observed, and (ii) the temperature excursion at dryout strongly depends on the mass flux and inlet quality and may disappear at high mass flows.

2. The employment of a so-called hot patch near the start of an otherwise uniformly heated channel can considerably extend the post-dryout temperature and film boiling heat flux range. If dryout is established at the hot patch the dry patch can spread in the downstream direction at heat flux values well below the CHF for uniform heating.

3 Drypatch spreading downstream of a hot patch can be limited by (i) interfacial instability, (ii) droplet-wall interaction, and (iii) improved post-dryout heat transfer.

References

1 Groeneveld, D. C., "Similarity of Water and Freon Dryout Data for Uniformly Heated Tubes," ASME Paper No. 70-HT-27, 1970.

2 Ahmad, S. Y., "Fluid to Fluid Modeling of Critical Heat Flux: A Compensated Distortion Model," AECL-3663, 1971.

3 Groeneveld, D. C., "The Thermal Behaviour of a Heated Surface at and Beyond Dryout," AECL-4309, 1972.

4 Moeck, E. O., "Annular-Dispersed Two-Phase Flow and Critical Heat Flux," PhD thesis, Department of Mechanical Engineering, McGill University, Montreal, Canada, 1970; also AECL-3656, 1970.

5 Parsons, C. B., "Experimental Investigation of the Physical Mechanisms of Dryout in a High Pressure Steam-Water System," PhD thesis, Department of Mechanical Engineering, University of Waterloo, Canada, 1971.

6 Todreas, N. E., and Rohsenow, W. M., "The Effect of Axial Heat Flux Distribution on Critical Heat Flux in Annular, Two-Phase Flow," *Proceedings of the Third International Heat Transfer Conference*, Chicago, Vol. III, 1966, pp. 78–85.

7 DeBortoli, R. A., et al., "Forced Convection Heat Transfer Burnout Studies for Water in Rectangular Channels and Round Tubes at Pressures Above 500 Psia," WAPD-188, 1958.

8 McPherson, G. D., "Axial Stability of the Dry Patch Formed in Dryout of a Two Phase Annular Flow," *International Journal of Heat and Mass Transfer*, Vol. 13, 1970, pp. 1133–1152.

9 Tong, L. S., *Boiling Heat Transfer and Two-Phase Flow*, Wiley, New York, 1965.

10 Lamb, H., *Hydrodynamics*, Sixth ed., Cambridge University Press, London, England, 1932, p. 370.

11 Birkoff, G., and Zarantonello, E. H., *Jets—Wakes and Cavities*, Academic Press, New York, 1957.

12 Rankin, S., "Forced Convection Film Boiling Inside of Vertical Pipes," PhD thesis, Department of Chemical Engineering, University of Delaware, 1961.

13 Thompson, T. S., "Liquid Film Breakdown and Dry-Patch Stability of Steam-Water Flows With Heat Transfer," PhD thesis, Queen Mary College, University of London, London, England, 1970.

14 Semeria, R., and Martinet, B., "Calefaction Spots on a Heating Wall; Temperature Distribution and Resorption," *Proceedings of the Institution of Mechanical Engineers*, Vol. 180, Part 3C, 1965–1966.

K. H. Sun
G. E. Dix

Nuclear Energy Division,
General Electric Co.,
San Jose, Calif.

C. L. Tien

Department of Mechanical Engineering,
University of California,
Berkeley, Calif.

Cooling of a Very Hot Vertical Surface by a Falling Liquid Film

The present study analyzes the cooling of a very hot vertical surface by a falling liquid film. An analytical model is developed to characterize this phenomenon in three distinctive regions: a dry region ahead of the wet front, a sputtering region immediately behind the wet front, and a continuous film region further upstream. The analysis leads to predictions of the wet front velocity, the sputtering length, and the temperature profiles with respect to the wet front. The heat transfer mechanisms are shown to be dependent upon two temperature parameters characterizing the initial wall temperature and the temperature range for sputtering, and two Biot numbers comparing the convective heat transfer in the liquid film region and the sputtering region with longitudinal heat conduction. The predictions are in good agreement with existing experimental results.

Introduction

A cold liquid film falling down a vertical solid surface has long been recognized and studied as a convenient and effective cooling mechanism for the hot solid surface [1].[1] However, the cooling mechanism, as well as the film wetting phenomenon, becomes quite different and considerably more complicated when the surface temperature is initially greater than the Leidenfrost temperature[2] of the coolant. This is indeed the case for the cooling of fuel rod bundles by spray water in the loss-of-coolant accident in water reactors [2], and it is also a common phenomenon for the cooling of surfaces at room temperature by cryogenic liquids. In such a case, there exists a finite liquid-sputtering region ahead of the continuous liquid film. Significant cooling effect is expected to occur in this sputtering region as a result of its highly turbulent nature and large boiling heat transfer coefficient.

An existing analytical model proposed by Yamanouchi [2] describes the phenomenon by one-dimensional quasi-steady heat conduction in a wall with two distinct regions. The region covered by the liquid film is characterized by a uniform surface heat transfer coefficient, while the bare region is assumed to be adiabatic. Recent experimental studies confirm qualitatively the description of this model [3]. The major drawback in the analytical description of this model is the total absence of the important sputtering region which is distinctly observable in experiments [3]. In addition, the value suggested by Yamanouchi for the wet front temperature, defined as the critical wall temperature at which liquid starts to adhere to the surface, is appreciably lower than those reported recently [3, 5]. As a result, Yamanouchi arrived at heat transfer coefficients on the order of 2×10^5 to 10^6 w/m^2 deg C ($4 \times 10^4 \sim 2 \times 10^5$ Btu/hr-ft^2-deg F) in order to predict velocities of the advancing liquid front comparable with the observed velocities. These values are unreasonably high for the continuous film region, and also an order of magnitude too high for the transition and nucleate boiling occurring in the sputtering region.

Recently, Thompson [6] considered the liquid film to be characterized by a temperature-dependent nucleate boiling heat transfer coefficient. He assumed that previous [7] experimental "sputtering temperatures" correspond to the initiation of film wetting and nucleate boiling. The transition boiling and bare regions downstream were assumed to be adiabatic. Using a two-dimensional heat conduction analysis (requiring numerical solution), the resultant heat transfer coefficient values obtained were more reasonable than those from a one-dimensional analysis. But, as in the Yamanouchi case, no effort was made to distinguish the two distinctively different regions: the sputtering region and the continuous film region.

The present study analyzes the cooling of a very hot vertical surface by a falling liquid film, with particular emphasis on the role of the sputtering region. A new analytical model, similar to but improved over the Yamanouchi model, has been developed to account for the sputtering region. Indeed, it will be shown that the heat transfer mechanism in the sputtering region plays the dominant role in the cooling process.

[1] Numbers in brackets designate References at end of paper.

[2] In a recent paper [4], Baumeister and Simon distinguished between the temperature corresponding to the minimum boiling heat flux and the Leidenfrost temperature. Strictly speaking, the Leidenfrost temperature applies to discrete liquid drops rather than to a liquid pool. However, in the present work, the term Leidenfrost temperature refers to the wet front temperature of the advancing liquid film.

Contributed by the Heat Transfer Division of THE AMERICAN SOCIETY OF MECHANICAL ENGINEERS and presented at the Winter Annual Meeting, Detroit, Mich., November 11-15, 1773. Manuscript received by the Heat Transfer Division. Paper No. 73-WA/HT-22.

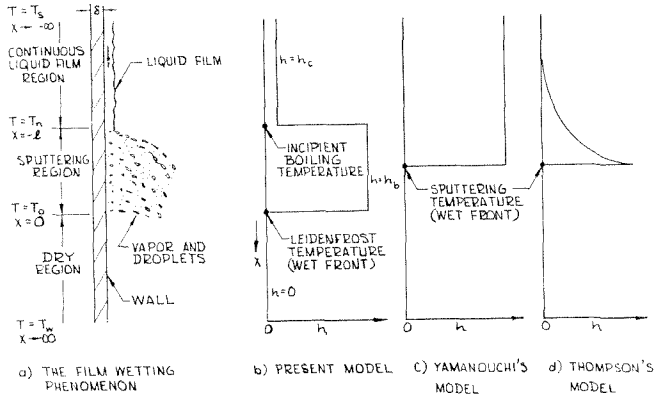

Fig. 1 The film wetting phenomenon, present model and comparison with existing models

Analysis

Physical Model. The physical system under consideration is a vertical surface with coolant supply from above. The liquid film progresses downward on the surface which is initially at a temperature higher than the Leidenfrost temperature of the liquid. As the liquid film advances, the surface is first cooled down to the Leidenfrost temperature at which the surface begins to wet (wet front). Behind the wet front, the surface temperature drops sharply due to direct contact with liquid. Transition boiling occurs immediately behind the wet front, followed by nucleate boiling as the surface temperature is further reduced. The boiling phenomenon ceases where the surface temperature drops below the temperature of incipient boiling, beyond which a continuous liquid film covers the surface. On the surface region bounded by the incipient boiling and the Leidenfrost temperatures, ebullition occurs as the result of bubble nucleation and violent vapor generation. This phenomenon is often termed as sputtering. In view of the differences in the thermal-hydraulic phenomena, the surface can be categorized into three regions: a dry region ahead of the wet front, a sputtering region right behind the wet front, and a region of continuous liquid film further upstream. A schematic diagram of the film wetting is shown in Fig. 1*(a)*.

To formulate the problem, it is first necessary to characterize the heat transfer mechanisms in the three distinct regions. The dry surface ahead of the wet front is cooled by the liquid particles expelled from the sputtering region. The particles flow downward in the form of a mist and large-size droplets. The effectiveness of heat removal by the mist is very small as compared with boiling in the sputtering region. Therefore, the dry surface can be treated as adiabatic [2]. The heat transfer coefficient in the sputtering region varies from transition boiling to nucleate boiling. However, since the length of the sputtering region is typically quite short (on the order of ten times the wall thickness [3], the boiling mechanisms of the sputtering region are characterized by a single average boiling heat transfer coefficient, h_b. Finally, the continuous film region where the surface is cooled by single-phase (liquid) convection, the heat transfer mechanism is characterized by a convection heat transfer coefficient h_c. Generally, h_c is much smaller than h_b. The current analysis assumes that all heat transfer coefficients are referenced to saturated vapor temperature.

In short, the present model divides the process into three regions, in contrast to the two-region models of Yamanouchi [2] and Thompson [3]. In addition, the Leidenfrost temperature is considered as the surface temperature at the wet front, instead of employing empirically determined sputtering temperatures. The differences among the models are illustrated in Figs. 1*(b)*, 1*(c)*, and 1*(d)*.

Mathematical Formulation. The formulation, in general, is a two-dimensional transient heat conduction equation with different boundary conditions prescribed on the surface of different regions. However, a numerical analysis is necessary to obtain the solution for this general case. To avoid the complexity of numerical calculation and the loss of physical interpretation of the pertinent parameters, a simplified one-dimensional analysis is used to show the validity of the present model.

For cases of the Biot numbers with respect to h_c and h_b less than one, the surface can be treated as a fin in which longitudinal heat conduction is the dominant heat transfer mode in determining the temperature profiles. By assuming the temperature profiles invariant with respect to the advancing wet front, simple heat balance consideration based on a differential element of the surface leads to the governing equation [2].

$$K\delta \frac{d^2T}{dx^2} + \rho c \delta u \frac{dT}{dx} = h(T - T_s). \tag{1}$$

By setting the wet front as the origin of the coordinate system given in Fig. 1, equation (1) can be transformed to appropriate dimensionless forms applying to different regions of the surface. For the continuous film region, $-\infty < x \leq -l$,

$$\theta''(\eta) + P\theta'(\eta) - B_c\theta(\eta) = 0 \tag{2}$$

where

$$\theta(\eta) \equiv \frac{T - T_s}{T_0 - T_s}, \quad \theta'(\eta) \equiv \frac{d\theta}{d\eta}, \quad \eta \equiv \frac{x}{\delta} \tag{3}$$

the dimensionless wet front velocity, P, in the form of the Peclet number, is defined as

$$P \equiv \frac{u\delta\rho c}{K} \tag{4}$$

and

Nomenclature

B_b = Biot number with respect to the average boiling heat transfer coefficient for the sputtering region, defined in equation (7)
B_c = Biot number with respect to the convective heat transfer coefficient for the continuous film region, defined in equation (5)
C = thermal capacitance, J/kg-deg C
h = surface heat transfer coefficient, W/m²-deg C
h_b = average boiling heat transfer coefficient for the sputtering region, W/m²-deg C
h_c = convective heat transfer coefficient for the continuous film region, W/m²-deg C
K = thermal conductivity, W/m-deg C
L = dimensionless length of the sputtering region, defined in equation (12)
l = length of the sputtering region, m
P = dimensionless wet front velocity, defined in equation (4)
T = temperature, deg C
T_0 = Leidenfrost temperature, deg C
T_n = incipient boiling temperature, deg C
T_s = saturation temperature, deg C
T_w = initial temperature of the dry surface, deg C
u = wet front velocity, m/hr
x = length coordinate, m
δ = wall thickness, m
η = dimensionless length coordinate, x/δ
θ = dimensionless temperature defined in equation (3)
θ_1 = dimensionless temperature parameter defined in equation (9)
θ_2 = dimensionless temperature parameter defined in equation (10)
ρ = density, kg/m³

Subscripts

$+$ = evaluated at an infinitesimal increment of distance
$-$ = evaluated at an infinitesimal decrement of distance

$$B_c \equiv \frac{h_c \delta}{K} \tag{5}$$

For the sputtering region, $-l \le x \le 0$,

$$\theta''(\eta) + P\theta'(\eta) - B_b\theta(\eta) = 0 \tag{6}$$

where

$$B_b \equiv \frac{h_b \delta}{K} \tag{7}$$

and for the dry region, $0 \le x < \infty$,

$$\theta''(\eta) + P\theta'(\eta) = 0 \tag{8}$$

Now, defining two dimensionless temperature parameters:

$$\theta_1 \equiv \frac{T_w - T_0}{T_0 - T_s} \tag{9}$$

and

$$\theta_2 \equiv \frac{T_n - T_s}{T_0 - T_s} \tag{10}$$

The boundary conditions can be expressed as

$$\theta(0) = 1,\ \theta(-\infty) = 0,\ \theta(\infty) = 1 + \theta_1,\ \text{and } \theta(-L) = \theta_2, \tag{11}$$

where L, the dimensionless sputtering length, is defined as

$$L \equiv l/\delta \tag{12}$$

Combining equations (9) to (12) with equations (2), (6), and (8), the solutions are:
for $-\infty < \eta \le -L$

$$\theta(\eta) = \theta_2 \text{ EXP } \{\frac{-P}{2}\gamma_1(\eta + L)\} \tag{13}$$

where

$$\gamma_1 = 1 - (1 + \frac{4B_c}{P^2})^{1/2}$$

for $-L \le \eta \le 0$

$$\theta(\eta) = \frac{1}{\alpha}\{[\text{EXP}(\frac{P\gamma_3 L}{2}) - \theta_2]\text{ EXP}(-\frac{P\gamma_2\eta}{2})\} + [\theta_2 - \text{EXP}(\frac{P\gamma_2 L}{2})]\text{ EXP}(-\frac{P\gamma_3\eta}{2})\} \tag{14}$$

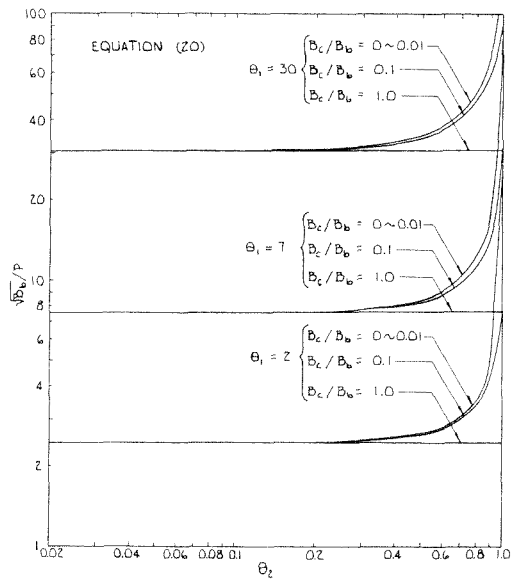

Fig. 2 The variation of $\sqrt{B_b}/P$ with θ_2

where

$$\alpha \equiv \text{EXP}(\frac{P\gamma_3 L}{2}) - \text{EXP}(\frac{P\gamma_2 L}{2})$$

$$\gamma_2 \equiv 1 - (1 + \frac{4B_b}{P^2})^{1/2},\ \gamma_3 \equiv 1 + (1 + \frac{4B_b}{P^2})^{1/2}$$

and for $0 \le \eta < \infty$

$$\theta(\eta) = 1 + \theta_1 - \theta_1 \text{ EXP } (-P\eta) \tag{15}$$

It is noted that the dimensionless wet front velocity, P, and the dimensionless sputtering length, L, are still unknown, yet to be determined by the continuity of heat fluxes which are

$$\theta'(0_+) = \theta'(0_-) \text{ and } \theta'(-L_+) = \theta'(-L_-) \tag{16}$$

Combining equations (13) to (15) with equation (16), P and L are determined by the simultaneous equations

$$-2\theta_1 = \frac{1}{\alpha}\{[\text{EXP}(\frac{P\gamma_3 L}{2}) - \theta_2]\gamma_2 + [\theta_2 - \text{EXP}(\frac{P\gamma_2 L}{2})]\gamma_3\} \tag{17}$$

and

$$\theta_2\gamma_1 = \frac{1}{\alpha}\{[\text{EXP}(\frac{P\gamma_3 L}{2}) - \theta_2]\gamma_2\text{ EXP}(\frac{P\gamma_2 L}{2}) + [\theta_2 - \text{EXP}(\frac{P\gamma_2 L}{2})]\gamma_3\text{ EXP}(\frac{P\gamma_3 L}{2})\} \tag{18}$$

Through simple algebraic manipulations equations (17) and (18) can be reduced to the forms

$$L = \frac{2}{P\gamma_2}\ln[\frac{\theta_2(\gamma_3 - \gamma_1)}{2\theta_1 + \gamma_3}] \tag{19}$$

and

$$\theta_1 = 0.5\{-\gamma_2 + \theta_2(\gamma_2 - \gamma_1)[\frac{2\theta_1 + \gamma_3}{\theta_2(\gamma_3 - \gamma_1)}]^{\frac{\gamma_3}{\gamma_2}}\} \tag{20}$$

It is noted that the L dependence has been eliminated from equation (20). Thus, P can be calculated with known values of B_c, B_b, θ_1, and θ_2 by the trial-and-error method. With P obtained, L can be calculated from equation (19). By inserting the values of P and L into equations (13) to (15), the temperature profile of the surface becomes known.

Examination of the solution equations (19) and (20) indicates that P and L can be identified explicitly in the form of $\sqrt{B_b}/P$ and $L\sqrt{B_b}$. Thus, for a fixed ratio of the Biot numbers (i.e., B_c/B_b constant), the wet front velocity varies directly with the root of the sputtering region heat transfer coefficient, while the sputtering length varies inversely with this root.

It is of interest to examine the solutions for the special case of $B_c = B_b$. This, of course, is equivalent to Yamanouchi's "two-region" model [2], since the sputtering region is not distinguishable. Indeed, the wet front velocity relation reduces to Yamanouchi's simple expression

$$\left.\frac{\sqrt{B_b}}{P}\right|_{(\frac{B_c}{B_b})=1} = [\theta_1(\theta_1 + 1)]^{1/2} \tag{21}$$

A comparable, though somewhat fictitious, sputtering length can also be defined for this case as:

$$\left.L\sqrt{B_b}\right|_{(\frac{B_c}{B_b})\to 1} = (\frac{1 + \theta_1}{\theta_1})^{1/2}\ln(\frac{1}{\theta_2}) \tag{22}$$

A further parameter of interest is the sputtering length for large values of θ_1. From equation (22), the limiting value is given by

$$\left.L\sqrt{B_b}\right|_{\substack{(\frac{B_c}{B_b})\to 1 \\ \theta_1\to\infty}} = \ln(\frac{1}{\theta_2})$$

Results and Discussions

Characteristics of Solutions. Based on the three-region model for the film wetting phenomenon, the present analysis predicts the wet front velocity, the length of the sputtering region, and the temperature profile of the surface with respect to the wet front. Four independent dimensionless parameters appear in the analysis: two temperature parameters, θ_1 and θ_2; and two Biot numbers, B_c and B_b.

The parameter θ_1 is a system parameter that characterizes the wall temperature in the dry region with respect to the Leidenfrost temperature. When θ_1 is close to zero, the film wetting phenomenon becomes increasingly hydrodynamic-dependent. The parameter θ_2 compares the superheat required for nucleation with that required for film wetting. At atmospheric conditions, θ_2 is on the order of 0.01 to 0.1 for water [8], 0.1 to 0.3 for liquid nitrogen and liquid hydrogen, and 0.1 to 0.5 for liquid helium [9]. Generally, θ_2 is smaller at higher pressures since the superheat required for nucleation decreases with pressure. It is also dependent on the surface condition since nucleation is highly dependent on the cavity size and population [10]. A rough surface on which there exists a large population of nucleation cavities results in less superheat for bubble generation and thus a smaller θ_2. In certain cases of boiling of organic liquids under vacuum [11], or boiling of alkali metals from smooth surfaces [12] when film boiling occurs directly after the single-phase convection regime, θ_2 becomes close to the limiting value of one.

The Biot Number, B_c, compares the convective cooling with longitudinal heat conduction in the continuous film region. Since the wall temperature is below the incipient boiling temperature, B_c characterizes the single-phase convective heat transfer by the falling liquid film. Typical values for this convective heat transfer coefficient, h_c, are $10^2 \sim 10^3$ w/m^2-deg C (10^2 Btu/hr-ft^2-deg F) for water and $10 \sim 10^2$ w/m^2-deg C (10 Btu/hr-ft^2-deg F) for liquid nitrogen [1]. The Biot number B_b compares the boiling heat transfer with longitudinal heat conduction in the sputtering region. Judging from the fact that transition and nucleate boiling occur in this region, an average boiling heat transfer coefficient associated with the transition and nucleate pool boiling would be representative in the sputtering region. Typical values of this average boiling heat transfer coefficient, h_b, are $10^3 \sim 10^4$ w/m^2-deg C (10^3 Btu/hr-ft^2-deg F) for water [8] and $10^2 \sim 10^3$ w/m^2-deg C (10^2 Btu/hr-ft^2-deg F) for liquid nitrogen [9].

Fig. 2 illustrates the relationship between wet front velocity and θ_2 for typical parametric values of θ_1 and B_c/B_b. For θ_2 close to one, the parameter $\sqrt{B_b}/P$ is strongly dependent on B_c/B_b. Thus, for cases where the incipient boiling temperature approaches the Leidenfrost temperature (i.e., small temperature range for sputtering), the rate of film wetting is dependent on the heat transfer in the continuous film region. However, for cases with θ_2 less than 0.2, the parameter $\sqrt{B_b}/P$ is virtually independent of θ_2 and B_c/B_b. Thus, with wide temperature ranges for sputtering, the heat transfer in the continuous film region and the temperature range of the sputtering region exert little influence on the rate of wetting; i.e., for $\theta_2 < 0.2$, $\sqrt{B_b}/P$ approaches the limiting case of $B_c/B_b = 1$. As previously indicated, the predictions for this limiting case correspond to the results from Yamanouchi's "two-region" model [2]. The effect of the sputtering region is further illustrated by Fig. 3 in which $\sqrt{B_b}/P$ is plotted against θ_1 for $\theta_2 = 0.7$, and for $\theta_2 \leq 0.2$. For a constant B_b, the rate of wetting is shown to be substantially lower when the temperature range for sputtering is small. However, for the cases of θ_1 close to zero (i.e., the initial dry wall temperature very close to the Leidenfrost temperature), the wet front velocity becomes independent of the temperature range for sputtering.

Fig. 4 shows the variation of $L\sqrt{B_b}$ with θ_2 for typical parametric values of θ_1 and B_c/B_b. It is shown that the length of the sputtering region, L, becomes longer when the temperature range for sputtering is wider. Of course, L drops to zero as θ_2 approaches one. The difference between the cases of $B_c/B_b = 0.01$ and $B_c/B_b = 1$ for a specific θ_1 shows that L is dependent on the heat transfer in the continuous film region. With greater cooling effectiveness in the continuous film region, B_c/B_b is closer to one and the sputtering length is shorter. The dependence of L on the wall temperature parameter θ_1 is manifest in Fig. 4 and is further depicted in Fig. 5. It is shown that $L\sqrt{B_b}$ decreases as θ_1 increases, but approaches a constant for large θ_1. For the special case of $B_c/B_b = 1$, this limiting value is defined by equation (23).

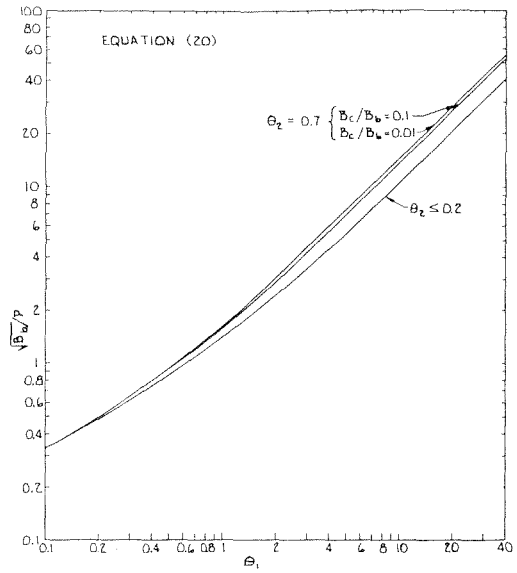

Fig. 3 The variation of $\sqrt{B_b}/P$ with θ_1

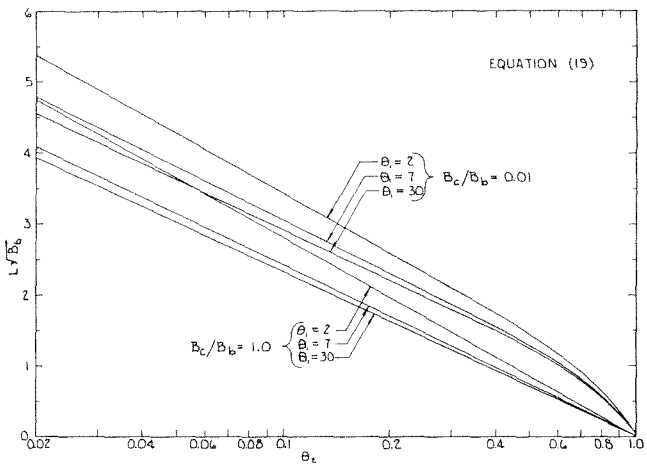

Fig. 4 The variation of $L\sqrt{B_b}$ with θ_2

It has been shown in Figs. 2 and 3 that for the cases of $\theta_2 > 0.2$, the heat transfer in the continuous film region cannot be neglected and the simple expression of equation (21) resulting from the two-region model becomes inapplicable. This is further illustrated in Fig. 6 which shows the temperature profiles in the vicinity of the wet front for a typical case of cryogenic coolants. The difference between the two curves of $B_c/B_b = 0.1$ (three-region model) and $B_c/B_b = 1$ (two-region model) clearly indicates that for a system with a small temperature range for sputtering, the two-region model predicts a wet front velocity too high and sputtering length too short.

Comparison With Experimental Results. While the present analysis is generally applicable to all coolants, reported experimental investigations are limited to a few cases using water. Among them, there is only one which measured sputtering length [3] while several [2, 3, 7, 13, 14] included measurements of wet front velocity. A direct comparison requires accurate data on the following variables: the properties of wall (K, ρ, C, and δ), the temperatures of incipient boiling (T_n) and initial dry wall (T_w), the Leidenfrost temperature (T_0), and the heat transfer coeffi-

cients for the continuous film region and the sputtering region (h_c and h_b, respectively). The precise values of some of these parameters are difficult to determine or to estimate, particularly the values of h_c, h_b, and T_0. These parameter requirements effectively limit comparisons to atmospheric water data.

In particular, the data of Shires, et al., [13] could not be meaningfully compared with the present analysis since the tests were conducted in an air environment rather than saturated vapor. Also, the data of Bennett, et al., [7] were not compared since consistent values for the Leidenfrost temperatures are not available for the high pressures of these tests.

To compare present predicted wet front velocities with experimental data, it is first necessary to specify the wet front temperature.[3] Yamanouchi [2] chose 150 C as the wet front temperature for water at atmospheric pressure. This value is very low as compared with the value of about 260 C [15, 16, 17] which was the surface temperature corresponding to the minimum heat flux in film boiling. This value is in good agreement with the value of 273 C reported [18] for the "maximum superheat temperature" and the value between 273 C and 328 C for the "maximum liquid temperature" [5], which were defined as the temperature limit beyond which nucleate and film boiling cannot be sustained. This value also compares favorably with the wet front temperatures between 207 C and 275 C (except for the cases of very large flow rates) reported by Duffey and Porthouse [3].

In a recent paper [4], the Leidenfrost temperature was shown to be dependent on the thermal properties of the solid as well as the surface energy of liquid and solid. However, data obtained for the temperature corresponding to the minimum heat flux from different surfaces [15, 16, 17] appear to be relatively independent of the surface conditions.

Assuming the wet front temperature to be 260 C, which is typical for water at atmospheric pressure, θ_1 is known. Since θ_2 is smaller than 0.2 in this case, the dependence on θ_2 and B_c/B_b drops out, and the relation for wet front velocity reduces to the simple expression of equation (21). Fig. 7 depicts the comparison of equation (21) with the experimental data of Duffey and Porthouse [3] and Yamanouchi [2]. It is shown that data taken in two

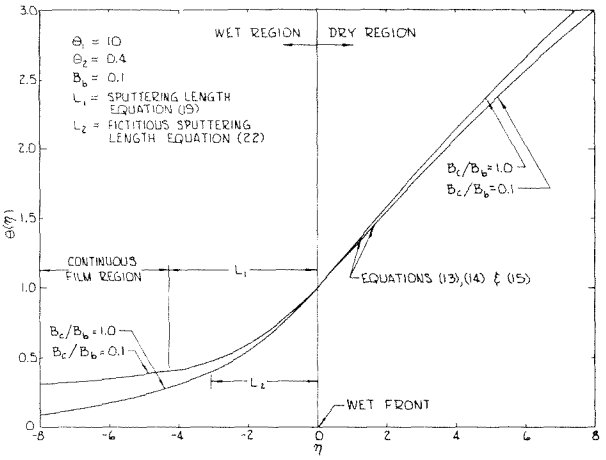

Fig. 6 Dimensionless temperature profiles in the vicinity of the wetting front (a typical case for cryogenic coolants)

different systems, with three different wall thicknesses and five different coolant flow rates, correlate very well under the dimensionless coordinates, with h_b chosen as 1.7×10^4 w/m^2-deg C (3.0×10^3 Btu/hr-ft^2-deg F). This value compares very well with the average boiling heat transfer coefficient associated with the transition and nucleate pool boiling. Corresponding to this value, the Biot number B_b lies in the range between 0.410 and 0.733. This confirms that the present one-dimensional analysis is justified for these data. At small θ_1, the trend of predicting high values of the wet front velocity indicates that the film wetting phenomenon becomes increasingly hydrodynamic dependent.

It should be noticed that data taken at very large flow rates are not well correlated with the present (constant h_b) prediction, and are not included in Fig. 7. For large flow rates, part of the coolant may flow as droplets which bounce between surfaces. The dry surface would thus be precooled ahead of the wet front, resulting in very large wetting rates as compared with the present analysis. Very recently, Duffey and Porthouse [19] suggested a two-dimensional analysis for the case of higher wetting rate. However, since the actual film flow rates were not directly determined [3], it is not possible to develop a meaningful relation for the heat transfer mechanisms at these large flow rates. It should also be cautioned that the present one-dimensional analysis is applicable only when the Biot number is less than one. For cases with thick walls, or high boiling heat transfer coefficients, i.e., pressures much higher than atmospheric, a two-dimensional analysis is necessary [6, 20].

The data of Duffey and Porthouse [3] also indicate an observed sputtering length of 0.5 cm. Since the present analysis predicts

[3] This is clearly distinguished from experimental "sputtering temperatures" which have been determined with some ambiguity. The sputtering temperature was first defined by Shires, et al., [13] by extrapolating linearly the wetting time-temperature relationship to determine the surface temperature at zero wetting time. Bennett, et al., [7] defined the sputtering temperature at the inverse wetting rate of 1.1 sec/ft for their high pressure (100 to 1000 psia) tests.

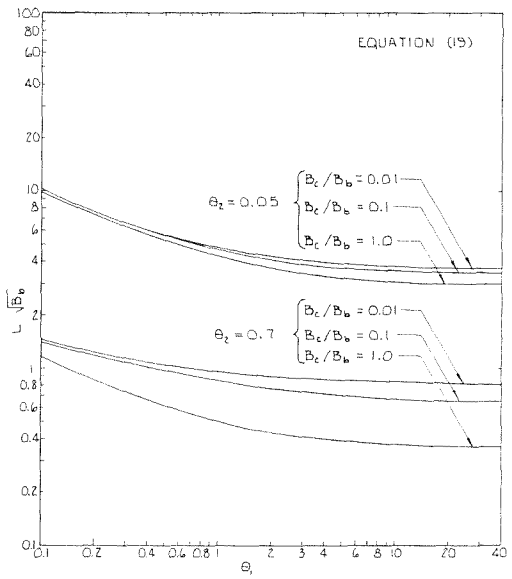

Fig. 5 The variation of $L\sqrt{B_b}$ with θ_1

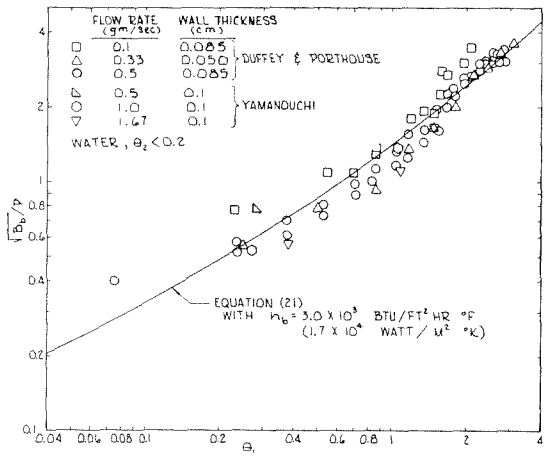

Fig. 7 Comparison of predicted wet front velocity with experimental results

the sputtering length for a known system, it is of interest to evaluate the sputtering region heat transfer coefficient, h_b, implied by this observed sputtering length. Unfortunately, the observed sputtering lengths were not recorded for each test condition. However, using the single 0.5-cm length with typical atmospheric water values of $\theta_2 = 0.05$ and $B_c/B_b = 0.1$ implies sputtering heat transfer coefficients ranging from 6.8×10^3 to 3.5×10^4 w/m^2-deg C ($1.2 \times 10^3 \sim 6.1 \times 10^3$ Btu/hr-ft^2-deg F) for the range of these tests. Thus, while more definitive sputtering length comparisons with the model are desirable, the current comparison magnitudes are entirely consistent with the film wetting velocity results.

Additional sources of data are the channel wetting rates measured by Rogers and Leonard [14] during the emergency cooling tests for water reactors. A procedure was developed based on the Yamanouchi model to correlate data with nonuniform initial wall temperatures. From the present study, it is apparent that the form of Yamanouchi's result does apply to these cases with water at atmospheric pressure ($\theta_2 < 0.2$). However, the use of the Leidenfrost temperature to characterize the wet front would result in more realistic values for the heat transfer coefficient in the resultant correlation.

Conclusions

1 When a surface initially at a temperature higher than the Leidenfrost temperature is cooled by a falling liquid film, sputtering occurs immediately behind the wet front. This phenomenon can be characterized by a three-region model: the dry region, the sputtering region, and the continuous film region.

2 The heat transfer mechanisms associated with the film wetting phenomenon are governed by four dimensionless parameters: two temperature parameters that characterize the wall temperature with respect to the Leidenfrost temperature and the temperature range for sputtering, and two Biot numbers that compare the convective cooling in the continuous film region and the boiling in the sputtering region with longitudinal heat conduction along the surface. A range is identified for one temperature parameter for which the heat transfer in the continuous film region exerts little influence on the wet front velocity. In this range, Yamanouchi's two-region model, despite its lack of physical reality, can be employed for predictions of the wet front velocity, provided that the correct Leidenfrost temperature is used.

3 The film wetting models are very sensitive to the wet front temperature. For a constant boiling heat transfer coefficient, the wet front velocity increases with this temperature. Thus, previous data correlations of wet front velocities using wet front temperatures considerably lower than the temperature corresponding to the minimum heat flux in pool boiling have led to unreasonably high heat transfer coefficients.

4 The heat transfer coefficient for the sputtering region can be determined either from observed sputtering lengths or measured wet front velocities. The comparison of the present model with atmospheric pressure water tests indicates very good predictions with a value of 1.7×10^4 w/m^2-deg C (3.0×10^3 Btu/hr-ft^2-deg F). This compares favorably with the average coefficient associated with the transition and nucleate pool boiling. This value also results in Biot number values less than unity, which justifies the one-dimensional conduction analysis for these tests.

References

1 Bird, R. B., Stewart, W. E., and Lightfoot, E. N., *Transport Phenomena* Wiley, New York, 1960, p. 349.

2 Yamanouchi, A., "Effect of Core Spray Cooling in Transient State After Loss-of-Coolant Accident," *Journal of Nuclear Science of Technology*, Vol. 5, 1968, p. 547.

3 Duffey, R. B., and Porthouse, D. T. C., "Experiments on the Cooling of High-Temperature Surfaces by Water Jets and Drops," Report No. RD/B/N2386, Berkeley Nuclear Laboratories, England, Aug. 1972.

4 Baumeister, K. J., and Simon, F. F., "Leidenfrost Temperature—Its Correlation for Liquid Metals, Cryogens, Hydrocarbons, and Water," JOURNAL OF HEAT TRANSFER, TRANS. ASME, Series C, Vol. 95, No. 2, May 1973, pp. 166–173.

5 Groeneveld, D. C., "The Thermal Behavior of a Heated Surface At and Beyond Dryout," PhD thesis, The University of Western Ontario, London, Canada, July 1972.

6 Thompson, T. S., "An Analysis of the Wet-Side Heat-Transfer Coefficient During Rewetting of a Hot Dry Patch," *Nuclear Engineering and Design*, Vol. 22, 1972, p. 212.

7 Bennett, A. W., Hewitt, G. F., Kearsey, H. A., and Keeys, R. K. F., "The Wetting of Hot Surfaces by Water in a Steam Environment at High Pressure," Report No. AERE-R5146, Atomic Energy Research Establishment, England, May 1966.

8 Kreith, F., *Principles of Heat Transfer*, 3rd ed., International Textbook Company, Scranton, Pa., 1973, p. 497.

9 Clark, J. A., "Cryogenic Heat Transfer," *Advances in Heat Transfer*, Vol. 5, T. F. Irvine, Jr., and J. P. Hartnett, eds., Academic Press, 1968, pp. 325–517.

10 Jordan, D. P., "Film and Transition Boiling," *Advances in Heat Transfer* Vol. 5, T. F. Irvine, Jr., and J. P. Hartnett, eds., Academic Press, 1968, pp. 55–128.

11 Lienhard, J. H., and Schrock, V. E., "The Effect of Pressure, Geometry and the Equation of State Upon the Peak and Minimum Boiling Heat Flux," JOURNAL OF HEAT TRANSFER, TRANS. ASME, Series C, Vol. 85, 1963, pp. 261–272.

12 Kutateladze, S. S., Moskvicheva, V. N., Bobrovich, G. I., Mamontova, N. N., and Avksentyuk, B. P., "Some Pecularities of Heat Transfer Crisis in Alkali Metals Boiling Under Free Convection," *International Journal of Heat and Mass Transfer*, Vol. 16, 1973, pp. 705–713.

13 Shires, G. L. Pickering, A. R., and Blacker, P. T., "Film Cooling of Vertical Fuel Rods," Report No. AEEW-R343, Atomic Energy Establishment, Winfrith, England, May 1964.

14 Rogers, A. E., and Leonard, J. E., "Analytical Model of the Transient Reactor Core Spray Cooling Process," *Chemical Engineering Progress Symposium*, Series 119, Vol. 67, 1971.

15 Cole, R., "Investigation of Transient Pool Boiling Due to Sudden Large Power Surge," Report NACA-TN-3885, 1956.

16 Hosle, E. R., and Westwater, J. W., "Film Boiling on a Horizontal Plate," *ARS Journal*, Vol. 32, No. 4, Apr. 1962, pp. 553–558.

17 Bradfield, W. S., "On the Effect of Subcooling on Wall Superheat in Pool Boiling," JOURNAL OF HEAT TRANSFER, TRANS. ASME, Series C, Vol. 89, No. 3, Aug. 1967, pp. 269–270.

18 Spiegler, P., Hopenfeld, J., Silberberg, M., Bumpus, C. F., Jr., and Norman, A., "Onset of Stable Film Boiling and the Foam Limit," *International Journal of Heat Mass Transfer*, shorter communications, Vol. 6, 1963, pp. 987–989.

19 Duffey, R. B., and Porthouse, D. T. C., "The Physics of Rewetting in Water Reactor Emergency Core Cooling," *Nuclear Engineering and Design*, Vol. 25, 1973, p. 379.

20 Thompson, T. S., "On the Process of Rewetting a Hot Surface By a Falling Liquid Film," Report AECL-4516, Chalk River Nuclear Lab., Chalk River, Ontario, Canada, June 1973.

J. P. Nail, Jr.
Engineer,
Chicago Bridge & Iron,
Birmingham, Ala.

R. I. Vachon
Professor.

J. Morehouse
Graduate Assistant.

Mechanical Engineering Department,
Auburn University,
Auburn, Ala.

An SEM Study of Nucleation Sites in Pool Boiling From 304 Stainless Steel

A Scanning Electron Microscope (SEM) was used to examine pool boiling nucleation sites on 304 stainless steel in contact with distilled, degassed water. Nucleation sites were located during the boiling process by noting the coordinates of the bubble locations on the surface. These locations were then magnified using the SEM and photographs made of the nucleation sites. The radii of the cavities varied from 14.8μ-in. to 180μ-in. and the widths of grooves varied from 75μ-in. to 154μ-in.

Introduction

The literature on boiling is extensive [1–14][1] with each study focusing on a particular variable or set of variables. Studies on surface conditions and their effects on boiling have been both rewarding and frustrating. The scanning electron microscope (SEM) has opened opportunities for examination of nucleation sites and the regions surrounding these sites. The objective of this study was to investigate, using a SEM, the surface locations of bubble formation on 304 stainless steel in contact with boiling water. The bubble formation sites were located during the boiling process by a measuring device that centered on the bubble on the surface and then related the location of the bubble center relative to a fixed point on the surface. The surface was then removed from the system and the bubble sites examined in the SEM. Heat flux versus superheat data were evaluated during the boiling process and correlated using the Rohsenow equation [36].

Related Studies

Sites. Bubbles in the boiling process are said to form at small nucleation sites such as pits, cavities, scratches, and grooves [18, 21]. The necessity for nucleation sites has been investigated experimentally by Hsu and Graham [7] and Otterman [8]. Westwater [9] has discussed "bumping" which occurs in liquids at the saturation temperature adjacent to surfaces without nucleation sites. Studies by Viskanta and Lottes [10] and Gordon, et al. [11], have shown that superheats initiating bubble formation on liquid mercury are considerably higher than the superheats required to cause bubble formation on solid surfaces. Bankoff's theoretical studies supplement the correlation of observation with theory [13].

Cavity Size. The size of a cavity must be within a given range if it is to be active during boiling. Hsu [14] has used a model [7] to predict the maximum and minimum size of effective cavities. The equations for maximum and minimum cavity size are

$$r_{max} = \frac{\delta}{2C_1}\left(1 - \frac{\theta_{sat}}{\theta_w} + \left[\left(1 - \frac{\theta_{sat}}{\theta_w}\right)^2 - \frac{4aC_3}{\delta\theta_w}\right]^{0.5}\right) \quad (1)$$

$$r_{min} = \frac{\delta}{2C_1}\left(1 - \frac{\theta_{sat}}{\theta_w} - \left[\left(1 - \frac{\theta_{sat}}{\theta_w}\right)^2 - \frac{4aC_3}{\delta\theta_w}\right]^{0.5}\right) \quad (2)$$

Although a necessary condition for a cavity to be active is that $r_{min} < r < r_{max}$, it is not a sufficient condition. In the event there are two cavities with similar geometry located very close to each other, the cavity with the shorter waiting period would be the preferred site. Further, the incipience of boiling can be predicted from the equation:

$$\theta_{w_0} = \theta_{sat} + \frac{2aC_3}{\delta} + \left[\left(2\theta_{sat} + \frac{2aC_3}{\delta}\right)\left(\frac{2aC_3}{\delta}\right)\right]^{0.5} \quad (3)$$

This equation applies to the case of constant wall temperature. The criterion for incipience of boiling for the constant heat flux case is:

$$q_0 = \frac{K}{\delta}\left(\theta_{sat} + \frac{2aC_3}{\delta} + \left[\left(2\theta_{sat} + \frac{2aC_3}{\delta}\right)\left(\frac{2aC_3}{\delta}\right)\right]^{0.5}\right) \quad (4)$$

Both these last equations show the effect of the "limiting thermal layer" (δ) and other variables on boiling and hence it should be realized that bubble formations are influenced by a number of variables in addition to the nucleation sites.

Site Population. Bubble populations have been studied by Gaertner and Westwater [15]; also, Gaertner [16] determined the spatial distributions of active nucleation sites for water containing dissolved nickel salts boiling from copper surfaces. Kurihara and Myers [17], who determined the active nucleation sites visually, reported that boiling sites increased with increasing sur-

[1] Numbers in brackets designate References at end of paper.

Contributed by the Heat Transfer Division for publication in the JOURNAL OF HEAT TRANSFER. Manuscript received by the Heat Transfer Division, March 5, 1974. Paper No. 74-HT-P.

face roughness and that boiling coefficients were proportional to the one-third power of the number of bubble columns rising from the heated surface. Heled and Orell [18] described an experimental technique facilitating the identification, location, and counting of nucleation sites. The technique is based on the observation of circular deposits formed on the heater surface from distilled water during the boiling process. The rings delineate nucleation regions within which nucleation sites should be expected. The size of the centrally located sites identified in [18] ranged from 590μ-in. to 2000μ-in. in diameter. Some 15,700 sites/ft^2 were counted. Theoretically determined diameters for these sites based on Hsu's model [14] were coincident with the experimentally determined diameters. No photographs of the surfaces were reported [18].

Photographic Studies. Porchey, et al. [19] used the scanning electron microscope to study pool boiling surfaces of gold plated copper, and silver and silver oxide. The main conclusion of the paper was that surfaces used in boiling heat transfer studies can differ physically and chemically from the surface one might expect as a result of surface preparation. Vachon, et al. [20] have also presented results of scanning electron microscope studies of surfaces used in boiling studies. The surfaces studied were etched, polished or Teflon coated. The character of the surfaces as a function of surface preparation was displayed vividly. Active nucleation sites have been identified by Clark, et al. [21] through photographic techniques. No active sites were found at grain boundaries. The sites identified ranged from 300μ-in. to 3300μ-in. in diameter for the pits and 500μ-in. in width for scratches. Patton and Hall [22] presented evidence showing the importance of nucleating cavity size in determining bubble emission frequency. The photographic studies by Kirby and Westwater [23] on boiling of methanol and carbon tetrachloride on ground-glass showed maximum bubble diameters to range from 17,000μ-in. to 9400μ-in. No surface studies are indicated. Strenge, et al. [24] photographed bubble growth rates for ether and pentane boiling on zinc and aluminum alloy. The photographs showed that bubbles formed at a given nucleation site under a constant superheat exhibited a pronounced variation in growth rates.

Surface Effects. Numerous studies exist on the effect of surface condition on boiling heat transfer [26-31]; analytical models of bubble evolution have been developed [25 and 26] and incipient boiling has been studied [32, 22, 23]. The occurrence of solid depositions on boiling surface as reported in [18] has been observed and studied by Pulling and Collier [35]. The deposits [35] were found to be 90 percent silica and occurred only where nucleate boiling had occurred. The Rohsenow correlation equation [36] has been examined in [39] and Nagarajan and Adelman [40] have shown the coefficient, C_{sf}, and exponent, r, in the Rohsenow correlation are functions of the liquid surface combination as well as grain structure.

All of the above studies, presented synoptically, serve as a background for the present study and form the basis for the conclusions drawn from the observations of this study.

Experimental Procedure and Apparatus

Four bright, cold rolled, 304 stainless steel test specimens (4.6 × 1.0 × 0.0351 in) were used in the tests. Each strip was placed in a pool boiler (Fig. 1) for a series of test runs. The test strips were electrically heated and thirty-gage iron-constantan thermocouples attached to the underside of each specimen as seen in Fig. 1 were used to monitor specimen surface temperature. The top surface temperature was determined by analysis of the conduction equation for the situation described.

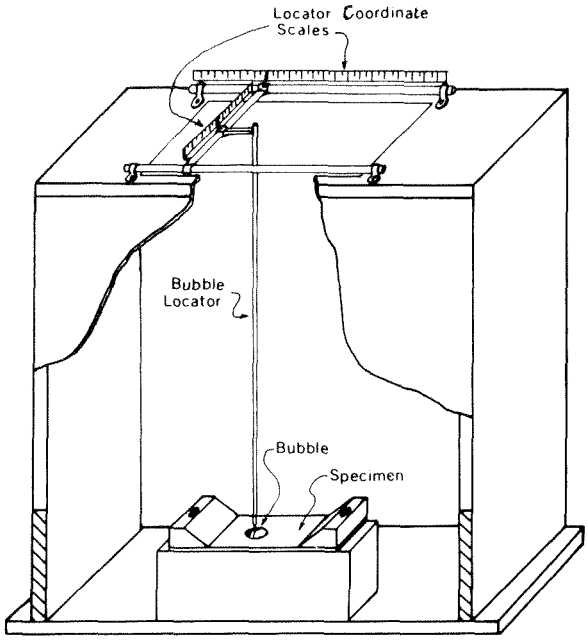

Fig. 1 Schematic of bubble locator

The entire system was cleaned and degassed before admitting distilled water to a level three in. above the specimen. The water was preheated to saturation conditions and test strip a-c power was initiated. Initial a-c power was controlled so that the first twelve to twenty bubbles formed on the surface remained on the surface sufficiently long to allow the bubble locator (Fig. 1) to be positioned over the center of selected bubbles. This procedure of reaching saturation and initiating test strip a-c power was repeated several times to determine the reproducibility of bubble locations. When reproducible bubble center locations were known relative to a fixed point on the surface, the surface was removed for study in the scanning electron microscope. It was assumed that the bubble site on the surface was directly in line with the center of the bubble under study.

Experimental Results

Examination of the 304 stainless steel test specimens revealed that a small spot or stain had formed at the location of the bubble source. The size of these stains was 25,000μ-in. to 30,000μ-in. in radius. These stains were thought to be due to silica in the distilled, degassed water as discussed by Heled and Orell [18] and Pulling and Collier [35].

The four stainless steel test specimens (numbered 2 through 5)

Nomenclature

a = parameter representing $2\sigma T_x/\Delta i\rho''$
C_1 = constant, $1 + \cos\psi/\sin\psi$
C_3 = constant, $1 + \cos\psi$
C_{sf} = coefficient in Rohsenow correlation
Δi = latent heat of vaporization, Btu/lbm
K = thermal conductivity, Btu/hr ft deg F
q_0 = heat flux at incipience of boiling, Btu/hr
r = exponent of the heat flux term in Rohsenow correlation
r_{max} = maximum cavity mouth radius, in.
r_{min} = minimum cavity mouth radius, in.
T_s, T_{sat} = saturation temperature, deg F
δ = limiting thermal-layer thickness, in.
σ = surface tension at liquid-vapor interface, lbf/ft
θ_{sat} = $T_{sat} - T_\infty$, deg
θ_w = $T - T_\infty$, deg
θ_{w0} = $T - T_\infty$ at incipience of boiling, deg
ρ = density of saturated liquid, lbm/ft^3
ψ = angle of bubble wall with respect to horizontal, deg

were examined on the Mark II Cambridge Scanning Electron Microscope at the NASA Marshall Space Flight Center. Photomicrographs were made from the oscilloscope display of the image.

Fig. 2(*a*) reveals an elliptically shaped cavity that served as a nucleation site. The size of this cavity is approximately 96μ-in. in radius. The photomicrograph shows the active cavity connected to several grooves in the surface. Also, after the first three or four bubbles formed on the surface and power was increased, the entire surface immediately began forming bubbles. This rapid spreading of bubbles occurred on all four specimens.

Fig. 2(*b*) reveals an almost circular nucleation site with a radius of approximately 55μ-in. Inspection of the photomicrograph indicates that this active site is interconnected to other sites by a network of grooves. The grooves in the surface are thought to be grain boundaries.

Fig. 3(*a*) shows a groove of approximately 75μ-in. in width and 450μ-in. in length. The white crusty material around the active site is thought to be silica as previously described. Fig. 3(*b*) gives a contrast between that part of the surface from which bubbles were originating and that part from which bubbles were not forming.

The cavity in Fig. 3(*c*) represents another active nucleation site on specimen 3. The radius of the cavity is approximately 38.5μ-in.

Figs. 4(*a*) and 4(*b*) represent the same active nucleation site at different magnifications. The radius of the cavity is approximately 37μ-in. A closer examination of the cavity in Fig. 4(*b*) seems to indicate another cavity within the cavity. This smaller cavity has a radius of 11μ-in.

Figs. 5*(a)* and 5*(b)* shows 1300 x and 13500 x magnifications of the same active nucleation center. The active nucleation center begins as a circular-type cavity and extends to a groove. The radius of the cavity is 115μ-in. and the groove has a width of 154μ-in.

Fig. 6(*a*) represents an active nucleation center that is a cavity-groove combination. The cavity has a radius of 30μ-in. and the groove has a width of approximately 38μ-in. This active center

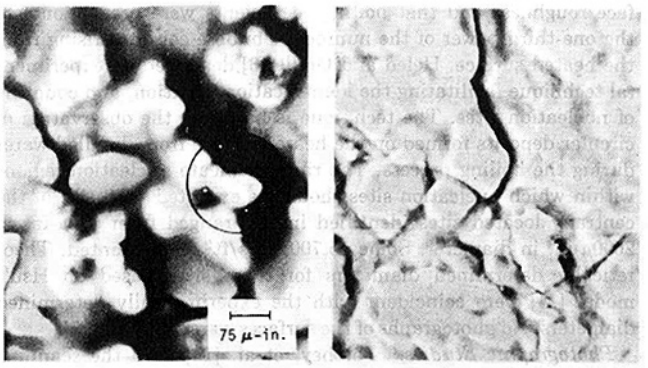

A. 2650 X Magnification B. 2650 X Magnification

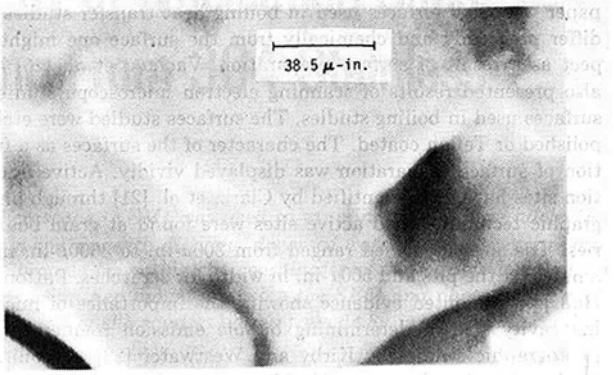

C. 13000 X Magnification

Fig. 3 Photomicrograph of specimen 3

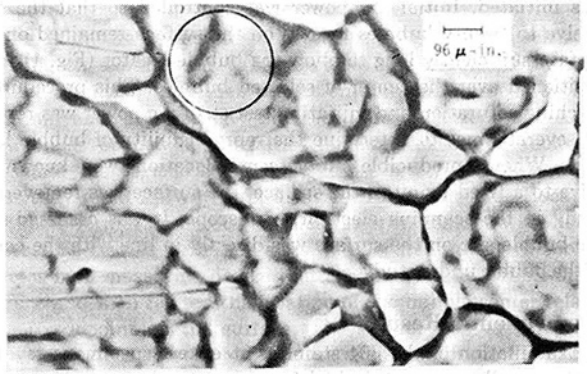

A. 2600 X Magnification

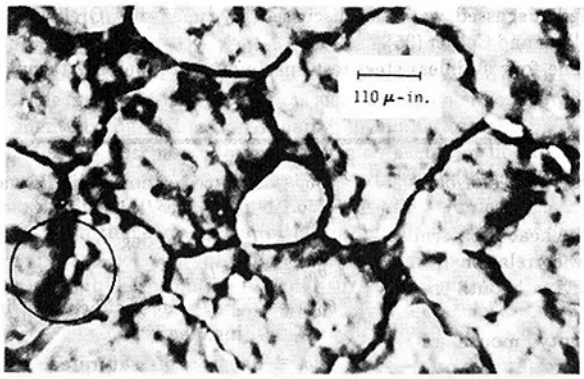

B. 2700 X Magnification

Fig. 2 Photomicrograph of specimen 2

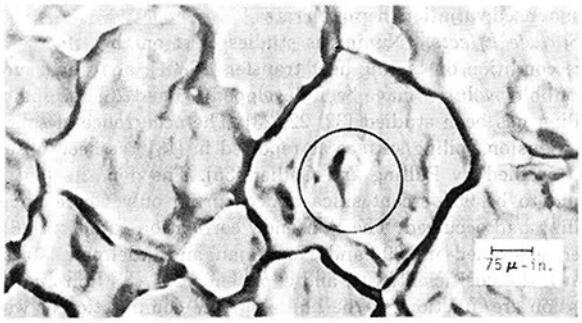

A. 2700 X Magnification

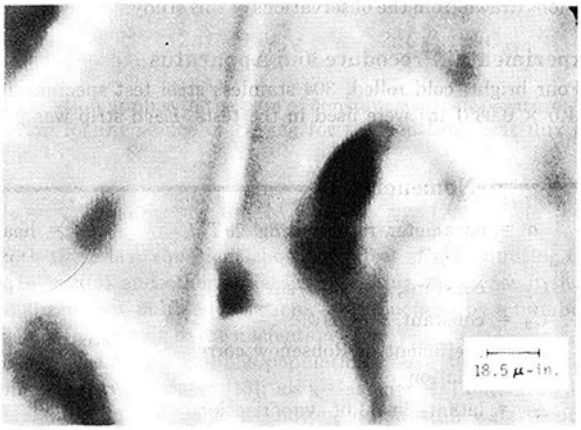

B. 13500 X Magnification

Fig. 4 Photomicrograph of specimen 4

A. 1300 X Magnification

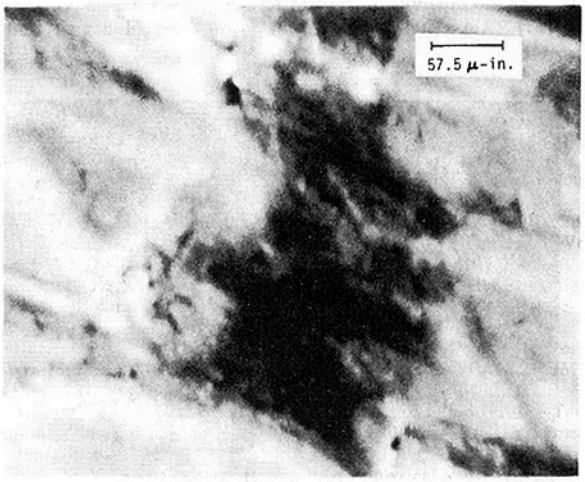

B. 13500 X Magnification

Fig. 5 Photomicrograph of specimen 4

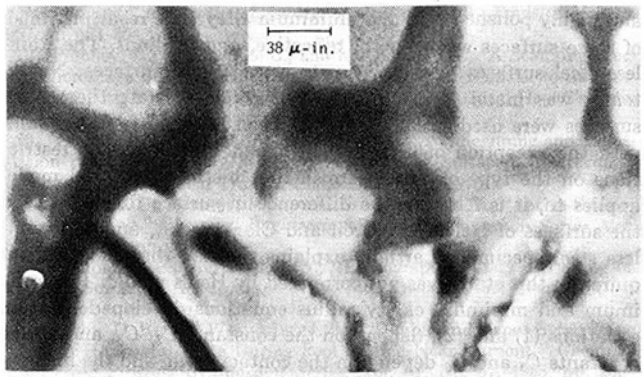

A. 6500 X Magnification

B. 6600 X Magnification

Fig. 6 Photomicrograph of specimen 4

seems to have formed in a grain boundary.

Fig. 6(b) illustrates a bubble site that begins as a void in the surface and leads to several grooves of different widths. This bubble site is most probably formed in a grain boundary also.

An elliptically shaped cavity with a radius of 180μ-in. is shown in the center of the spot of Fig. 7(*a*). Fig. 7(*b*) shows a 2700 *x* magnification of the white particles seen in Fig. 7(*a*). These particles are felt to be silica deposits previously discussed.

An elliptical cavity with an approximate radius of 18.5μ-in. is shown in Fig. 7(*c*).

An active site of specimen 5 is shown in Fig. 8(*a*) at a magnification of 2700. This site is enlarged to a magnification of 13,500 in Fig. 8(*b*). The radius of this cavity is approximately 14.8μ-in.

Discussion of Results

Heled and Orell [18] used the mathematical model of Hsu [14] for a temperature difference of 18 deg F and an assumed boundary layer thickness of 3000μ-in. and found a theoretical cavity radius range of 200μ-in. to 1300μ-in. Data by Clark, et al. [21] were correlated with the model of Hsu also, yielding a theoretical cavity radius range of 150 to 1500μ-in.

The radii of the active nucleation cavities found in the present study ranged from 14.8μ-in. to 180μ-in. The widths of the active grooves ranged from 75μ-in. to 154μ-in. Thus, the radii of the active nucleation sites did not fall into the range of radii predicted by Hsu's mathematical model. There seem to be several possible explanations to account for the discrepancies between the measured radii and those predicted by Hsu's Mathematical model. It is noted that data by Heled and Orell [18] and Clark, et al. [21] have been correlated successfully with the mathematical model of Hsu. The heat transfer surface used by Heled and Orell was highly polished brass. The brass was electroplated with either chrome or nickel. Extremely smooth and bright surfaces were exhibited. The heat transfer surfaces used by Clark, et al., were machined

A. 270 X Magnification

B. 2700 X Magnification

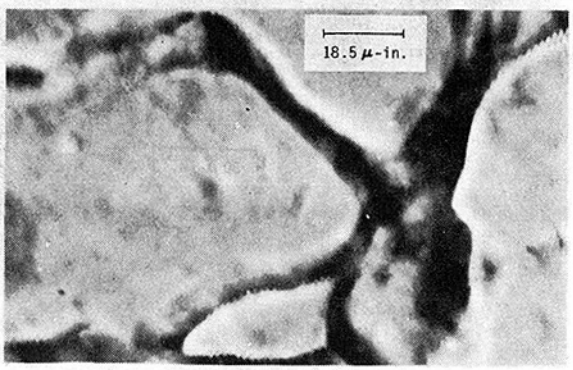

C.

Fig. 7 Photomicrograph of specimen 5

and highly polished zinc and aluminum alloy. The resulting finish of these surfaces was smooth, reflective, and brilliant. The stainless steel surfaces used in this study were mill surfaces. No attempt was made to machine, polish or electroplate them. The surfaces were used just as they had been received from the mill, with the exception of cleaning. Although Hsu places no restrictions on the type of surface finish that his mathematical model applies to, it is felt that the difference in surface finish between the surfaces of Heled and Orell and Clark, et al., and the stainless steel specimens partially explains the fact that the data acquired in this study was not correlated by Hsu's model. The maximum and minimum cavity radius equations developed by Hsu, equations (1) and (2), depend on the constants C_1, C_3, and δ. The constants C_1 and C_3 depend on the contact angle and the angle of the tangent to the cavity mouth with respect to the horizontal. Hsu did not measure these angles in order to calculate C_1 and C_3, but assumed values of C_1 and C_3 based on a very idealized cavity that had a bubble nucleus with a height equal to the bubble nucleus base radius. These types of bubbles were rarely encountered during observation in the laboratory. More accurate values of C_1 and C_3 should be determined for the case of water boiling on the mill-finish surface of stainless steel before an attempt is made to use Hsu's mathematical model to predict cavity radius. Furthermore, the value of δ = 0.003 in. was used in all calculations by Hsu. This value was chosen because it allowed successful correlation of the data. Hsu states that δ varies with each system and that δ for water may not always be the same for all cases. There seems to be a great loss of generality by using δ = 0.003 in. in all cases, especially when it is known that δ depends on turbulence, which is statistical in nature. It is also known that δ decreases in the vicinity of a bubble producing site. Hsu states that the higher the natural convective turbulence the smaller the value of δ. In general, a smaller δ means a narrower range of effective cavities. Thus a higher natural convective turbulence could result in smaller active cavities. The values of the constants C_1, C_3, and δ very possibly were not even in the range of the true values of C_1, C_3, and δ for water boiling on stainless steel. This further explains the fact that Hsu's mathematical model did not predict cavity radius as observed in this study.

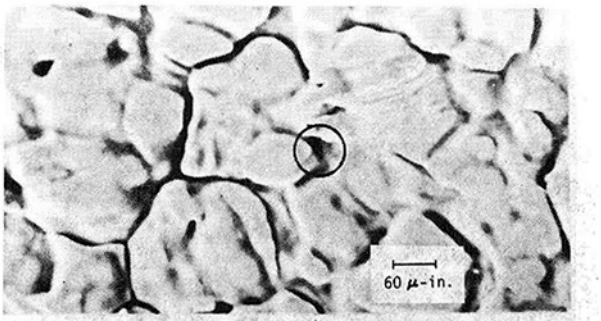

A. 2700 X Magnification

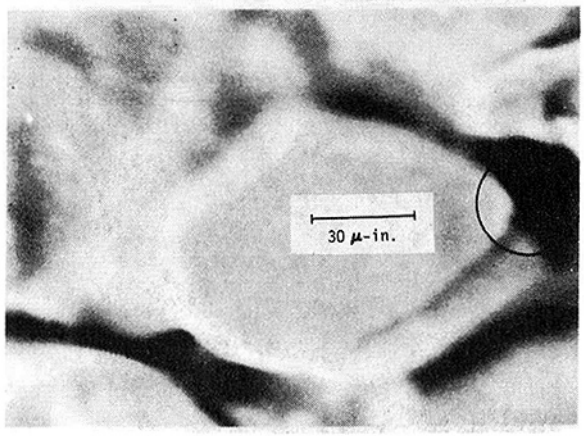

B. 13500 X Magnification

Fig. 8 Photomicrograph of specimen 5

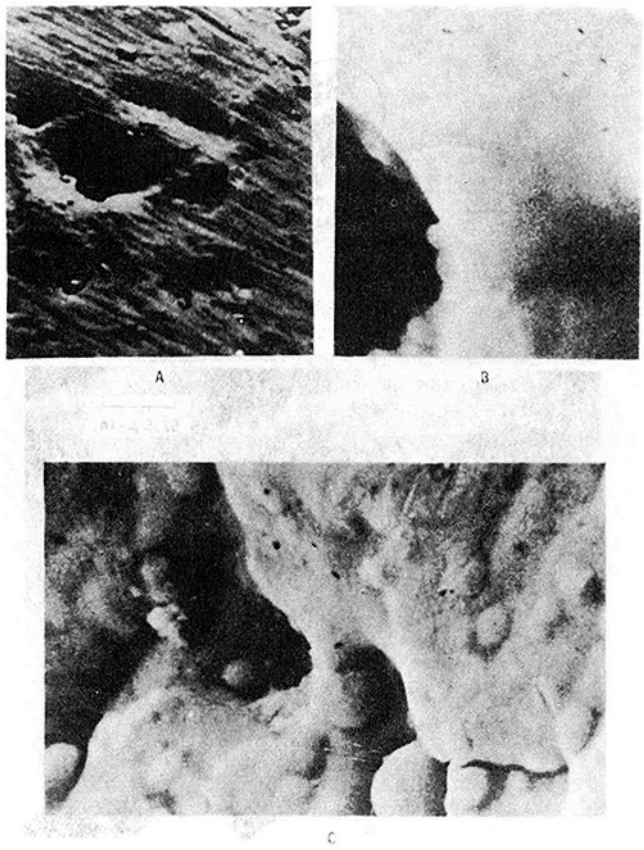

Fig. 9 Phomicrograph of gold-plated copper (reference [19])

The active nucleation sites shown in this study are not intuitively obvious as those illustrated by Porchey, et al. [19] and Clark, et al. [21]. This is seen by comparing Figs. 2 through 8 with Figs. 9(*a*), 9(*b*), and 9(*c*). The surfaces used by Porchey, et al., were gold plated copper and silver and silver oxide. The surfaces exhibited a smooth mirror finish. Clark, et al., used polished zinc and aluminum alloy surfaces. These surfaces exhibited a low density of nucleation sites. In contrast, the surfaces used in this study were mill rolled stainless steel specimens and were not polished. These surfaces did not exhibit a smooth mirror finish as those of Porchey, et al., and Clark, et al. This contrast of surfaces explains why those in this study did not have active nucleation sites that were easily discernible as in the investigations of Porchey, et al., and Clark, et al.

The grooves which were present at almost all nucleation sites could possibly have had an effect on the boiling. If the active site is interconnected to other active sites by these grooves, boiling could spread rapidly from one location to another along the grooves until the entire test specimen is active. Indeed, this rapid spreading was observed in the experiments. It is felt that this is due to the interconnected nucleation sites, as suggested by the photomicrographs.

Conclusions

The conclusions reached from the study are as follows:

1 The cavity radius prediction equations of Hsu do not generally apply to pool boiling of water on the surface of mill-finish stainless steel in the same manner as that previously employed by Hsu. These equations could be made to apply more generally to various systems by a thorough study of the variable δ and the constants C_1 and C_3 for different systems.

2 Photomicrographs indicate a possibility of grooves having the effect of instantaneously activating other sites. This phenomenon was witnessed during experimental runs.

3 Bubble sources were surrounded by white deposits. These white deposits were thought to be silica on the basis of work done by Pulling and Collier [35].

4 It was concluded that the grain boundaries had little effect on the boiling, except for their role in the inception of boiling.

The results of this study hopefully add another piece to the jigsaw puzzle of knowledge on boiling.

Acknowledgment

The authors are indebted to Messrs. R. Schwinghamer, R. A. Parr, and D. S. Kinkle, Jr. of the Materials Division of the NASA Marshall Space Flight Center for the use of the NASA-MSFC SEM.

References

1 Kreith, F., *Principles of Heat Transfer*, International Textbook Company, Scranton, Pa., 1969.

2 Madejski, J., "Theory of Nucleate Pool Boiling," *International Journal of Heat and Mass Transfer*, Vol. 8, 1965, pp. 155–171.

3 Rallis, C. J., Jawurek, H. H., "Latent Heat Transport in Saturated Nucleate Boiling," *International Journal of Heat and Mass Transfer*, Vol. 7, 1964, pp. 1051–1068.

4 Moissis, R., and Berenson, P. J., "On the Hydronamic Transitions in Nucleate Boiling," JOURNAL OF HEAT TRANSFER, TRANS. ASME, Series C, Vol. 85, No. 3, 1963, pp. 221–226.

5 Gaertner, R. F., "Photographic Study of Nucleate Pool Boiling on a Horizontal Surface," JOURNAL OF HEAT TRANSFER, TRANS. ASME, Series C, Vol. 87, No. 1, 1965, pp. 17–29

6 Moore, J. D., Mesler, R. B., "Measurements of Rapid Surface Temperature Fluctuations During Nucleate Boiling of Water," *AICHE Journal*, Vol. 7, 1961, pp. 620–624.

7 Hsu, Y. Y., and Graham, R. W., "An Analytical and Experimental Study of the Thermal Boundary Layer and the Ebullition Cycle in Nucleate Boiling," NASA TN-D-594, 1961.

8 Otterman, B., "A Photographic Study of Bubble Dimensions and Boiling Action on Mercury and Standard Engineering Surface," *Proceedings Heat Transfer and Fluid Mechanics Institute*, 1962, pp. 185–196.

9 Westwater, J. W., "Boiling Heat Transfer," *American Scientist*, Vol. 47, 1959, pp. 427–446.

10 Lottes, P. A., and Viskanta, R., "Nucleation and Boiling From a Liquid-Liquid Interface," *Proceedings Heat Transfer and Fluid Mechanics Institute*, 1962, pp. 171–184.

11 Gordon, F. K., Singh, T., and Weissman, E. Y., "Boiling Heat Transfer Between Immiscible Liquids," *International Journal of Heat and Mass Transfer*, Vol. 3, 1961, pp. 90–93.

12 Mead, B. R., Romie, F. E., and Guibert, A. G., "Liquid Superheat and Boiling Heat Transfer," *Proceedings Heat Transfer and Fluid Mechanics Institute*, 1951, pp. 209–216.

13 Bankoff, S. G., "Ebullition From Solid Surfaces in the Absence of a Pre-Existing Gaseous Phase," TRANS. ASME, Vol. 79, p. 735.

14 Hsu, Y. Y., "On the Size of Active Nucleation Cavities on a Heating Surface," JOURNAL OF HEAT TRANSFER, TRANS. ASME, Series C, Vol. 84, No. 3, 1962, pp. 207–216.

15 Gaertner, R. F., and Westwater, J. W., "Population of Active Sites in Nucleate Boiling Heat TRansfer," *Chemical Engineering Progress Symposium Series*, Vol. 56, No. 30, 1960, pp. 39–48.

16 Gaertner, R. F., "Distribution of Active Sites in the Nucleate Boiling of Liquids, "*Chemical Engineering Progress Symposium Series*, Vol. 59, No. 41, 1963, pp. 52–61.

17 Kurihara, H. M., and Myers, J. E., "The Effects of Superheat and Surface Roughness on Boiling Coefficients," *AICHE Journal*, Vol. 6, No. 1, 1960, pp. 83–86.

18 Heled, Y., and Orell, A., "Characteristics of Active Nucleation Sites in Pool Boiling," *International Journal of Heat and Mass Transfer*, Vol. 10, 1967, pp. 553–554.

19 Porchey, D. V., Park, E. L., and Mayhan, K. G., "A Scanning Electron Microscope Study of Nucleate Pool Boiling Heat Transfer to Saturated Liquid Nitrogen," AICHE Paper No. 3, Twelfth National Heat Transfer Conference, Aug. 1971.

20 Vachon, R. I., Nix, G. H., and Hall, D. M., "A Scanning and Transmission rence, Microscopy Study of Pool Boiling Surfaces," *Proceedings Fourth International Heat Transfer Conference, Sept. 1970.*

21 Clark, H. B., Strenge, P. S., and Westwater, J. W., "Active Sites of Nucleate Boiling," *Chemical Engineering Progress Symposium Series*, Vol. 55, No. 29, 1959, pp. 103–110.

22 Hatton, A. P., and Hall, I. S., "Photographic Study of Boiling on Prepared Surfaces," *Proceedings Third International Heat Transfer Conference*, Vol. 4, 1966, pp. 24–37.

23 Kirby, D. B., and Westwater, J. W., "Bubble and Vapor Behavior on a Heated Horizontal Plate During Pool Boiling Near Burnout," *Chemical Engineering Progress Symposium Series*, Vol. 61, No. 57, 1965, pp. 238–248.

24 Strenge, P. H., Orell, Aluf, and Westwater, J. W., "Microscopic Study of Bubble Growth During Nucleate Boiling, "*AICHE Journal*, Vol. 7, No. 4, 1961, pp. 578–583.

25 Corty, C., and Foust, A. S., "Surface Variables in Nucleate Boiling," *Chemical Engineering Progress Symposium Series*, Vol. 51, No. 17, 1955, pp. 1–12.

26 Griffith, P., and Wallis, J. D., "The Role of Surface Conditions in Nucleate Boiling," *Chemical Engineering Progress Symposium Series*, Vol. 56, No. 30, 1960, pp. 49–63.

27 Berenson, P. J., "Experiments on Pool Boiling Heat Transfer," *International Journal of Heat and Mass Transfer*, Vol. 5, 1962, pp. 985–999.

28 Bonilla, C. F., Grady, J. J., and Avery, G. W., "Pool Boiling Heat Transfer from Scored Surfaces," *Chemical Engineering Progress Symposium Series*, Vol. 61, No. 57, pp. 280–288.

29 Vachon, R. I., Tanger, G. E., Davis, D. L., and Nix, G. H., "Pool Boiling on Polished and Chemically Etched Stainless-Steel Surfaces," JOURNAL OF HEAT TRANSFER, TRANS. ASME, Series C, Vol. 90, No. 2, 1968, pp. 231–238.

30 Vachon, R. I., Nix, G. H , Tanger, G. E., and Cobb, R. O., "Pool Boiling Heat Transfer From Teflon-Coated Stainless Steel," ASME Paper No. 68-WA/HT-12.

31 Young, R. K., and Hummel, R. L., "Improved Nucleate Boiling Heat Transfer," *Chemical Engineering Progress Symposium Series*, Vol. 61, No. 59, pp. 264–270.

32 Coeling, K. J., and Merte, H., Jr., "Incipient and Nucleate Boiling of Liquid Hydrogen," *Journal of Engineering for Industry*, TRANS. ASME, May 1969, pp. 513–520.

33 Almgren, D. W., and Smith, J. S., Jr., "The Inception of Nucleate Boiling With Liquid Nitrogen," *Journal of Engineering for Industry*, TRANS. ASME, Nov. 1969, pp. 1210–1216.

34 Howell, J. R., and Siegel, R., "Incipience, Growth, and Detachment of Boiling Bubbles in Saturated Water From Artificial Nucleation Sites of Known Geometry and Size," *Proceedings Third International Heat Transfer Conference*, Vol. 4, 1961, pp. 24–37.

35 Pulling, D. J., and Collier, J. G., "The Deposition of Solids in a Vertical Tube Evaporator," *The Industrial Chemist*, Vol. 39, 1963, pp 129–133, 200–203.

36 Rohsenow, W. M., "A Method of Correlating Heat Transfer Data for Surface Boiling of Liquids," TRANS. ASME, Vol. 74, 1952, p. 969.

37 Fritz, W., "Berechnung des Maximal Volumens Von Dampfblasen," *Physik Z.*, Vol. 36, 1935, p. 379.

38 Jacob, M., *Heat Transfer*, Vol. 1, Wiley, New York, 1949, p. 614.

39 Vachon, R. I., Nix, G. H., and Tanger, G. E., "Evaluation of Constants for the Rohsenow Pool-Boiling Correlation," ASME Paper No. 67-HT-33.

40 Nagarajan, R., and Adelman, M., "An Experimental Investigation of the Influence of the Grain Size of the Metal Surface on Pool Boiling Heat Transfer," *Canadian Journal of Chemical Engineering*, Vol. 48, 1970, pp. 39–46.

41 Davis, D. L., "Effects of Mechanically Polished Surfaces on Multi-Phase Genesis," unpublished MS thesis, Auburn University, Auburn, Ala., May, 1965.

G. L. Wedekind
Assoc. Professor. Mem. ASME

B. T. Beck
Graduate Student.

Oakland University,
Rochester, Mich.

Theoretical Model of the Mixture-Vapor Transition Point Oscillations Associated With Two-Phase Evaporating Flow Instabilities

A horizontal tube evaporator in which complete vaporization takes place can be divided into three distinct regions—a subcooled, a two-phase, and a superheat region. The mixture-vapor transition point corresponds to the liquid film dryout point, and when entrainment is negligible, it represents the boundary between the two-phase and superheat regions. Experimental evidence indicates that during what is conventionally accepted as steady flow conditions, the motion of the mixture-vapor transition point is of an oscillatory nature. Furthermore, not only are the oscillations random, but their statistical characteristics can be represented by a modified Rayleigh distribution. This paper presents the formulation of a theoretical model which incorporates various deterministic mechanisms, while at the same time includes the existence of a random phenomenon. The model has the capability of predicting the influence of evaporator heat flux and inlet flow quality on the statistical characteristics of the transition point oscillations. Perhaps, the most significant potential of the proposed model is that it represents a first step toward the formulation of some of the fundamental mechanisms associated with two-phase evaporating flow instabilities on a statistical basis; a basis which appears to be consistent with many of the experimental observations currently available.

Introduction

Thermal-hydrodynamic instabilities encountered in two-phase evaporating flow have received considerable attention during the past decade. Bouré, Bergles, and Tong [1][1] recently reviewed the technical literature in this area in an effort to classify the various types of thermal-hydrodynamic flow instabilities, and to identify their causes and mechanisms.

Flow instabilities have been observed in vertical natural circulation evaporators, as well as vertical and horizontal forced circulation evaporators. In an experimental investigation of a horizontal-tube forced circulation evaporator in which complete vaporization takes place, Wedekind [2] observed an oscillatory phenomenon which appears to be related to the same mechanisms which cause density wave instabilities [3, 4], yet in its own unique way is different in its manifestations.

Mixture-Vapor Transition Point. The mixture-vapor transition point is experimentally observed by utilizing the light scattering properties of the two-phase mixture. The photographic technique which has been developed for a glass tube evaporator detects that position in the evaporator where the last of the liquid film is vaporized. This means that the tube wall is dry, and that no droplets of suspended liquid are visible. This does not rule out the possibility of there being some liquid in the form of microscopic droplets entrained as an invisible mist. In fact, when a small self-heating thermister probe is inserted into the flow stream immediately downstream of the visually detected transition point, the presence of some liquid droplets is evident.

However, for the range of experimental data under consideration, the effects of entrainment are believed to be negligible. This conclusion is supported by the fact that the dimensionless vapor velocity for all of the data is a factor of 1.8 below the critical value for the onset of entrainment is established by Steen and Wallis [9]. Furthermore, energy balances, assuming a quality of unity at the transition point, consistently predict the mean position of the transition point within the experimental accuracy of the instrumentation involved.

[1] Numbers in brackets designate References at end of paper.

Contributed by the Heat Transfer Division for publication in the JOURNAL OF HEAT TRANSFER. Manuscript received by the Heat Transfer Division, June 15, 1973. Paper No. 74-HT-T.

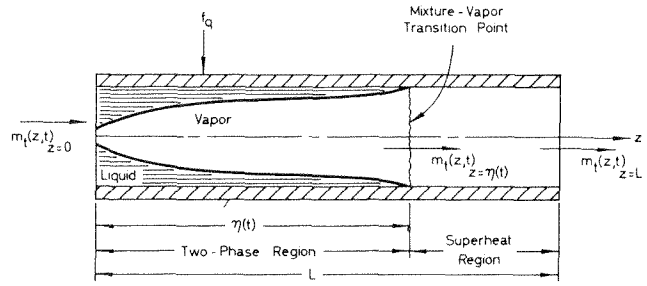

Fig. 1 Regions of a horizontal tube evaporator

If entrainment is negligible, the transition point represents the boundary between the two-phase region and the superheat region. In a horizontal tube evaporator, the transition point is sometimes tapered, due to the existence of a nonuniform film thickness in the liquid annulus. When a taper exists, the position of the transition point is defined as the taper midpoint. Much of the experimental data which will be referred to in this study was presented in an earlier paper [2]. Although it varied considerably, the average taper length for the aforementioned data was 4.0 in.

Experimental Observations. Experimental evidence [2] in the form of high speed motion pictures indicates that the transition point oscillates even for what is conventionally considered to be steady-state conditions. Furthermore, a study of the characteristics of these oscillations indicates that not only are the oscillations random, but that their statistical characteristics can be represented by a modified Rayleigh distribution. It is not uncommon for the peak-to-peak amplitude of the oscillations to be 10 percent of the transition point position.

As was pointed out in the aforementioned reference, the transition point oscillations appear to be a consequence of liquid waves which propagate along the liquid annulus in the annular flow regime. Those waves which reach the superheat region, "wash up on" and "recede from" the dry tube wall much like the surface waves on a lake interact with a beach. Visual observations indicate that the liquid waves which propagate within the annular flow regime are actually a continuation of waves or slug caused waves that form in the flow regimes existing in the early stages of the evaporation process.

In a very recent study [10], outlet flowrate oscillations have been observed to accompany oscillations in the mixture-vapor transition point, even under conditions conventionally accepted as steady-state. Theoretical and experimental evidence indicates a direct correlation between the two random phenomena. Again it was not uncommon to observe outlet flowrate oscillations with peak-to-peak amplitudes which were 10 percent of the mean flowrate; this taking place with an inlet flowrate which was invariant with time.

It would appear from the implications of some of the aforementioned observations, that the behavior of the mixture-vapor transition point is an important and necessary consideration in any attempt to analyze theoretically the overall dynamic characteristics of a tube-type evaporator in which complete vaporization takes place. Its behavior also has some interesting implications with respect to the statistical characteristics of some of the fundamental mechanisms associated with two-phase evaporating flow instabilities. The purpose of this study was to explore some of these implications.

Theoretical Model

The theoretical model which is presented represents an extension of an earlier model [5] which proved successful in predicting the transient response of the *mean* motion of the transition point due to a change in evaporator flowrate or heat flux. The model assumes entrainment to be negligible.

Fig. 1 schematically depicts an evaporator consisting of a two-phase and a superheat region. Although the schematic indicates an annular flow configuration in the entire two-phase region, this is for schematic simplicity only, and does not mean to imply in any way that an annular flow configuration always exists.

Conservation Analysis.

Continuity Equation. The conservation of mass principle, simultaneously applied to the liquid and vapor in the two-phase region, yields

$$\frac{d}{dt}\int_{z=0}^{\eta(t)}[\rho + (\rho' - \rho)\alpha]A_t dz = m_t(z,t)_{z=0} - m_t(z,t)_{z=\eta(t)} \quad (1)$$

Physically, the expression on the left-hand side of equation (1) represents the instantaneous time rate of change of the mass of liquid and vapor within the two-phase region. On the right-hand side, the first and second terms are the instantaneous rate at which fluid enters and leaves the region, respectively.

Energy Equation. The conservation of energy principle, simultaneously applied to the liquid and vapor in the two-phase region, yields

$$\frac{d}{dt}\int_{z=0}^{\eta(t)}[\rho h + (\rho' h' - \rho h)\alpha]A_t dz = \int_{z=0}^{\eta(t)} P f_q dz + \{[h + (h' - h)x]m_t(z,t)\}_{z=0} - \{h' m_t(z,t)\}_{z=\eta(t)} \quad (2)$$

The physical meaning of the various terms in equation (2) can be explained as follows: The left-hand side of the equation represents the instantaneous time rate of change of thermal energy within the two-phase region; the terms on the right-hand side

Nomenclature

a_0 = constant, in.
A_t = total cross-sectional area of tube, ft^2
$f(\ )$ = probability density function
$F(\ )$ = distribution function
f_q = evaporator heat flux, Btu/hr ft^2
h = specific enthalpy of saturated liquid, Btu/lb$_m$
$m_t(z,t)$ = local instantaneous total mass flow rate of fluid (liquid and vapor), lb$_m$/min
$m_{t,i}$ = total inlet mass flow rate to evaporator, lb$_m$/min
p = average evaporator pressure, lb$_f$/in.^{2}
P = inside circumference of evaporator tube, ft
t = independent variable, time, sec
t_0 = initial time, sec
t' = dummy variable, sec
$x(z,t)$ = local flow quality
$x_0(z,t)$ = nonoscillatory local flow quality
x_i = flow quality at evaporator inlet
$x_1(z,t)$ = local flow quality perturbation
$\bar{x}(t)$ = mean flow quality
$\bar{x}_0$ = mean nonoscillatory flow quality
$\bar{x}_1(t)$ = mean flow quality perturbation
z = independent variable, longitudinal position in evaporator, in
$\alpha(z,t)$ = local void fraction
$\alpha_0(z,t)$ = local nonoscillatory void fraction
$\alpha_1(z,t)$ = local void fraction perturbation
$\bar{\alpha}(t)$ = mean void fraction
α_i = void fraction at evaporator inlet
$\bar{\alpha}_0$ = mean nonoscillatory void fraction
$\bar{\alpha}_1(t)$ = mean void fraction perturbation
ζ = transformation constant
γ = principle characteristics parameter in the Rayleigh distribution
$\eta(t)$ = instantaneous position of the transition point, in.
$\bar{\eta}$ = mean value of the transition point, in.
$\xi(t)$ = oscillatory motion of transition point, in.
ρ = density of saturated liquid phase, lb$_m$/cu ft
σ_{x1} = standard deviation of mean flow quality perturbation
σ_η = standard deviation of the transition point, in.

Subscripts and Superscripts

Symbols of physical quantities and properties which do not possess a superscript generally refer to a saturated liquid. Primed (') symbols of quantities and properties refer to a saturated vapor.

represent, respectively, the instantaneous rate at which energy is being added to the two-phase region in the form of heat, and the instantaneous net rate at which thermal energy is being carried into the region by virtue of mass crossing its boundaries.

Combined Conservation Equation. At any given cross-sectional area of the two-phase region, the liquid and vapor pressures are assumed equal. Furthermore, the physical properties of the saturated liquid and vapor are assumed to be independent of both axial position and time. With these assumptions, equations (1) and (2) can be combined to yield the following conservation equation:

$$\rho A_t(h' - h)\left\{\frac{d\eta(t)}{dt} - \frac{d}{dt}\int_{z=0}^{\eta(t)} \alpha(z,t)dz\right\} + \int_{z=0}^{\eta(t)} Pf_q dz = (h' - h)(1 - x_i)m_t(z,t)_{z=0} \quad (3)$$

Perturbation Analysis.

Void Fraction Perturbations. The foregoing model is extended to include the oscillatory phenomenon by expressing the local void fraction, $\alpha(z,t)$, in terms of a nonoscillatory and a perturbation void fraction; thus

$$\alpha(z,t) = \alpha_0(z,t) + \alpha_1(z,t) \quad (4)$$

where $\alpha_0(z,t)$ represents the local void fraction distribution if there were no oscillations in the transition point, and $\alpha_1(z,t)$ represents the local void fraction perturbations directly associated with the random oscillations.

Within the two-phase region, a spatial mean void fraction, $\bar{\alpha}(t)$, can be approximated by

$$\bar{\alpha}(t) = \bar{\alpha}_0 + \bar{\alpha}_1(t) = \frac{1}{\bar{\eta}}\int_{z=0}^{\bar{\eta}} \alpha_0(z,t)dz + \frac{1}{\eta(t)}\int_{z=0}^{\eta(t)} \alpha_1(z,t)dz \quad (5)$$

where $\eta(t)$ is the actual position of the transition point, and $\bar{\eta}$ its mean position. In general, both could be functions of time, since, as was encountered in reference [5], the oscillations can be superimposed upon the mean transition point motion for both steady and transient flow conditions. However, this paper is primarily concerned with the mechanisms associated with the transition point oscillations. Therefore, what are conventionally accepted as steady-state conditions are assumed to exist; the evaporator inlet flow rate, $m_{t,i}$, inlet quality, x_i, and evaporator heat flux, f_q, are assumed to be constant. Under these conditions, the mean transition point position, $\bar{\eta}$, will be invariant with time, however, because of the random process involved, its instantaneous position, $\eta(t)$, will be time dependent.

Therefore, the mean nonoscillatory void fraction, $\bar{\alpha}_0$, is assumed to be invariant with time and is the same quantity described in reference [5]. However, because of its assumed relationship to the transition point oscillations, the mean void fraction perturbation, $\bar{\alpha}_1(t)$, will be time dependent.

Flow Quality Perturbations. Considering the void fraction to be a function of flow quality, the concept of a flow quality perturbation would be consistent with the foregoing; thus

$$x(z,t) = x_0(z,t) + x_1(z,t) \quad (6)$$

where $x_0(z,t)$ represents the local flow quality distribution if there were no oscillations in the transition point, and $x_1(z,t)$ represents the local flow quality perturbations directly associated with the random oscillations.

Since the flow quality and void fraction are directly related to each other, and since the mean void fraction, $\bar{\alpha}$, has already been defined as a spatial mean, the mean flow quality, $\bar{x}$, should be defined in a manner that is consistent with both interrelationships.

Such a definition for mean flow quality could be of the form:

$$\bar{x}(t) = \bar{x}_0 + \bar{x}_1(t) = \frac{1}{(1 - \alpha_i)}\int_{\alpha_0=\alpha_i}^{1.0} x_0(\alpha_0)d\alpha_0 + \frac{1}{(1 - \alpha_i)}\int_{\alpha=\alpha_i}^{1.0} x_1(\alpha,t)d\alpha \quad (7)$$

where α_i is the inlet void fraction corresponding to the inlet flow quality, x_i.

The first term on the right-hand side of the foregoing equation defines the nonoscillatory mean flow quality, $\bar{x}_0$, which is assumed to be invariant with time, and the second term defines what will be referred to as the mean flow quality perturbation, $\bar{x}_1$. Because of its relationship to the transition point oscillations, the mean flow quality perturbation will be time dependent.

Relationship Between the Nonoscillatory Mean Void Fraction and the Nonoscillatory Mean Flow Quality. Since for conventionally accepted steady-state conditions, $\alpha_0 = \alpha_0(x_0)$, a change of variables can be made to the appropriate term in equation (7) yielding

$$\bar{x}_0 \equiv \frac{1}{(1 - \alpha_i)}\int_{\alpha_0=\alpha_i}^{1.0} x_0(\alpha_0)d\alpha_0 = \frac{1}{(1 - \alpha_i)}\int_{x_0=x_i}^{1.0} x_0\frac{d\alpha_0}{dx_0}dx_0 \quad (8)$$

The foregoing expression can be evaluated by integrating by parts; yielding after rearrangement

$$\bar{x}_0 = \frac{1}{(1 - \alpha_i)}\left\{1 - (x_i\alpha_i) - \int_{x_0=x_i}^{1.0} \alpha_0(x_0)dx_0\right\} \quad (9)$$

Now, for a uniform heat flux, f_q, the nonoscillatory flow quality, x_0, can be expressed in terms of the axial position in the evaporator, z, as follows:

$$x_0(z) = x_i + \left\{\frac{Pf_q}{m_{t,i}(h' - h)}\right\}z \quad (10)$$

Because of the way in which the mean position of the transition point and the flow quality are defined, $x_0 = 1$ when $z = \bar{\eta}$, therefore equation (10) can be used to yield

$$(1 - x_i) = \left\{\frac{Pf_q}{m_{t,i}(h' - h)}\right\}\bar{\eta} \quad (11)$$

Using equations (10) and (11), and making a change of variables from axial position in the evaporator to the corresponding flow quality, the nonoscillatory mean void fraction, $\bar{\alpha}_0$, from equation (5) can be expressed as

$$\bar{\alpha}_0 = \frac{1}{(1 - x_i)}\int_{x_0=x_i}^{1.0} \alpha_0(x_0)dx_0 \quad (12)$$

The foregoing expression represents a means for calculating the nonoscillatory mean void fraction in conjunction with the availability of a relationship between void fraction and flow quality such as those suggested by Levy [6] and Fujie [7]. These relationships are shown [5] to be in reasonable agreement with Hufschmidt's [8] experimental data for Refrigerant-12 flowing in horizontal tubes over a wide range of flow qualities.

The combination of equations (9) and (12) yields the following relationship between the nonoscillatory mean void fraction and the corresponding mean flow quality:

$$\bar{\alpha}_0 = \frac{1}{(1 - x_i)}\left\{1 - (x_i\alpha_i) - (1 - \alpha_i)\bar{x}_0\right\} \quad (13)$$

It should be noted here that because of the way in which it is defined, $\bar{\alpha}_0 \neq \alpha_0(\bar{x}_0)$.

Relationship Between Mean Void Fraction Perturbations and Mean Flow Quality Perturbations. A relationship between the mean void fraction perturbation and mean flow quality perturbation, $\bar{\alpha}_1(t)$ and $\bar{x}_1(t)$, respectively, can be obtained by assuming that they are related in a manner similar to the way in which the nonoscillatory mean void fraction, $\bar{\alpha}_0$, is related to the nonoscillatory mean flow quality, $\bar{x}_0$; a concept consistent with perturbation theory. This idea can be expressed analytically by utilizing equation [13]; thus

$$\bar{\alpha}_1(t) = \frac{\partial\bar{\alpha}_0}{\partial\bar{x}_0}\bar{x}_1(t) = -\frac{(1 - \alpha_i)}{(1 - x_i)}\bar{x}_1(t) \quad (14)$$

Fig. 2 graphically depicts the various relationships between void fraction and flow quality that are presented in this section.

Relationship Between Transition Point Oscillations and Mean Flow Quality Perturbations. A relationship between the transition point oscillations and the mean flow quality perturbations is developed by introducing the void fraction perturbation into the

combined conservation equation.

Utilizing equations (5) and (11), for a uniform heat flux, equation (3) can be expressed in the form

$$\frac{d}{dt}\{\eta(t)[1-\bar{\alpha}_0-\bar{\alpha}_1(t)]\}=\frac{Pf_q}{\rho A_t(h'-h)}[\bar{\eta}-\eta(t)] \quad (15)$$

Separating the variables and integrating the foregoing differential equation from some initial time, t_0, to any arbitrary time, t; after rearrangement, yields the following expression for the mean void fraction perturbation, $\bar{\alpha}_1(t)$:

$$\bar{\alpha}_1(t)=\frac{1}{\eta(t)}\{(1-\bar{\alpha}_0)[\eta(t)-\bar{\eta}]+a_0+\frac{Pf_q}{\rho A_t(h'-h)}\int_{t'=t_0}^{t}[\eta(t')-\bar{\eta}]dt'\} \quad (16)$$

where the constant, a_0, is defined as

$$a_0\equiv\bar{\alpha}_1(t_0)\eta(t_0)-(1-\bar{\alpha}_0)[\eta(t_0)-\bar{\eta}] \quad (17)$$

Introduce the transition point oscillations, $\xi(t)$, defined as

$$\xi(t)\equiv\xi(t)-\bar{\eta} \quad (18)$$

Therefore:

$$\frac{1}{\eta(t)}=\frac{1}{\bar{\eta}+\xi(t)}=\frac{1}{\bar{\eta}}\left\{\frac{1}{1+\frac{\xi(t)}{\bar{\eta}}}\right\} \quad (19)$$

Since experimental data [2] indicates that, $\xi(t)/\bar{\eta}\leq 0.1$, the binomial expansion can be used and simplified to yield

$$\frac{1}{\eta(t)}\cong\frac{1}{\bar{\eta}}\left[1-\frac{\xi(t)}{\bar{\eta}}\right]\cong\frac{1}{\bar{\eta}} \quad (20)$$

Utilizing equations (18) and (20); equation (16), after rearrangement can be reduced to

$$\bar{\alpha}_1(t)=(1-\bar{\alpha}_0)\frac{\xi(t)}{\bar{\eta}}+\frac{a_0}{\bar{\eta}}+\frac{Pf_q}{\rho A_t(h'-h)\bar{\eta}}\int_{t'=t_0}^{t}\xi(t')dt' \quad (21)$$

A relationship between the mean flow quality perturbations, $\bar{x}_1(t)$, and the transition point oscillations, $\xi(t)$, can be obtained by introducing equation (14) into the foregoing expression; thus

$$\bar{x}_1(t)=-\frac{(1-x_i)}{(1-\alpha_i)}\left\{(1-\bar{\alpha}_0)\frac{\xi(t)}{\bar{\eta}}+\frac{a_0}{\bar{\eta}}+\frac{Pf_q}{\rho A_t(h'-h)\bar{\eta}}\int_{t'=t_0}^{t}\xi(t')dt'\right\} \quad (22)$$

Statistical Analysis.

Statistical Relationship Between Transition Point Oscillations and Mean Flow Quality Perturbations. In reference [2], it was shown that the motion of the mixture-vapor transition point, $\eta(t)$, could be treated as a random variable. Thus, because of its definition, the transition point oscillations, $\xi(t)$, will also be random. As a result of equation (22), this makes the mean flow quality perturbation, $\bar{x}_1(t)$, a random variable as well.

What is of primary interest in this section is the establishment of a relationship between the statistical characteristics of the transition point oscillations and the corresponding m characteristics of the mean flow quality perturbations. Since transition point oscillations, $\xi(t)$, have been measured and reported [2] for a variety of conditions, it is possible to use equation (22) to calculate the corresponding mean flow quality perturbations, $\bar{x}_1(t)$. This evaluation becomes somewhat cumbersome because of the need for the numerical integration of the integral term involved.

The contribution of the integral term has been investigated extensively in this study for the experimental data under consideration. Since $\xi(t)$ is an oscillatory function, a characteristic of the integral term is that its magnitude, for any value of time, is inversely proportional to the apparent frequency of the transition point oscillations. This fact can be readily demonstrated by considering the integral of any time dependent sinusoidal function. For the transition point oscillations under consideration, the frequencies range from 0.3 to 4.0 Hz. Therefore, for the experimental data under consideration, the contribution of the integral term to the statistical characteristics of the mean flow quality perturbation turns out to be small. It does contribute to its mean value, but not appreciably to its statistical distribution[2] about its mean, or its standard deviation. Therefore, because of the simplification obtained, the integral term will be neglected. Furthermore, the magnitude of the initial condition constant, a_0, is arbitrary, since it also does not influence either the statistical distribution or the standard deviation. Thus, it too will be set equal to zero.

Using the foregoing simplifications and equations (11) and (18), for the purposes of determining a correlation between the statistics involved, equation (22) can be expressed as the following simple relationship between the transition point oscillations and the mean flow quality perturbations:

$$\xi(t)=\eta(t)-\bar{\eta}=-\left\{\frac{(1-\alpha_i)}{(1-\bar{\alpha}_0)}\frac{m_{t,i}(h'-h)}{Pf_q}\right\}\bar{x}_1(t) \quad (23)$$

Applying the concepts of applied probability theory, the standard deviation of the transition point oscillations can be obtained by performing the appropriate operation on equation (23); thus yielding the following relationship between the standard deviation of the transition point oscillations, σ_η, and the standard deviation of the mean flow quality perturbations, $\sigma_{\bar{x}_1}$.

$$\sigma_\eta=\frac{(1-\alpha_i)}{(1-\bar{\alpha}_0)}\frac{m_{t,i}(h'-h)}{Pf_q}\sigma_{\bar{x}_1} \quad (24)$$

Statistical Characteristics of Mean Flow Quality Perturbations. In this section, experimental evidence will be presented which indicates that the statistical characteristics of the mean flow quality perturbations, $\bar{x}_1(t)$, are relatively independent of inlet flow quality and heat flux. Furthermore, it will be shown that these characteristics can be approximated by a transformed Rayleigh distribution. If the linear transformation $(\zeta+\bar{x}_1)$ is used as an argument, the density function for the mean flow quality perturbation becomes

$$f(\zeta+\bar{x}_1)=\frac{2}{\gamma}(\zeta+\bar{x}_1)\exp\{-(\zeta+\bar{x}_1)^2/\gamma\};\ (\zeta+\bar{x}_1)\geq 0 \quad (25)$$

where

$$\zeta=(1/2)(\pi\gamma)^{1/2} \quad (26)$$

and:

$$\gamma=\frac{4\sigma_{\bar{x}_1}^2}{(4-\pi)} \quad (27)$$

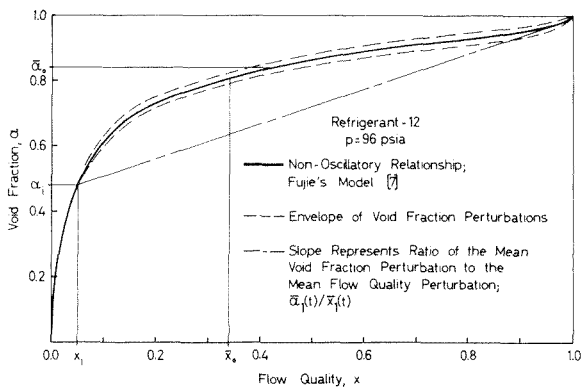

Fig. 2 Void fraction versus flow quality relationships

[2] The transition point oscillations under consideration have been shown [2] to have an assymetrical distribution. Physically, the transition point does not oscillate as far downstream of its mean as it does upstream. It is of interest to note that the contribution of the integral term in equation (22) attempts to make the mean flow quality perturbations more symmetric than that of the transition point; although for the data presently under consideration, this effect appears to be negligible. It is possible, however, that these effects cannot be neglected if the average heat flux in the domain of the transition point oscillations is high enough.

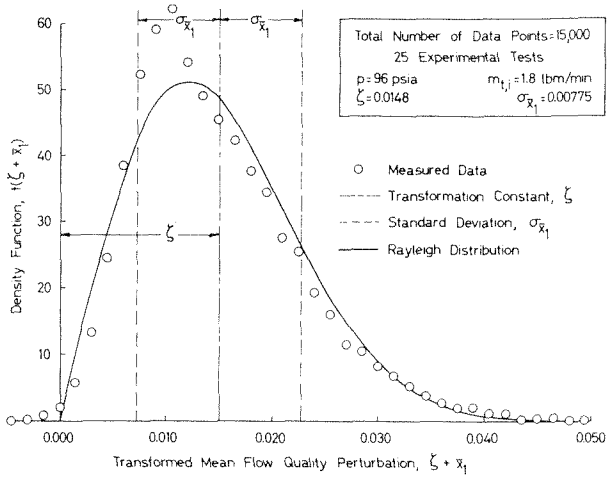

Fig. 3 Comparison of statistical characteristics with those predicted by a Rayleigh distribution

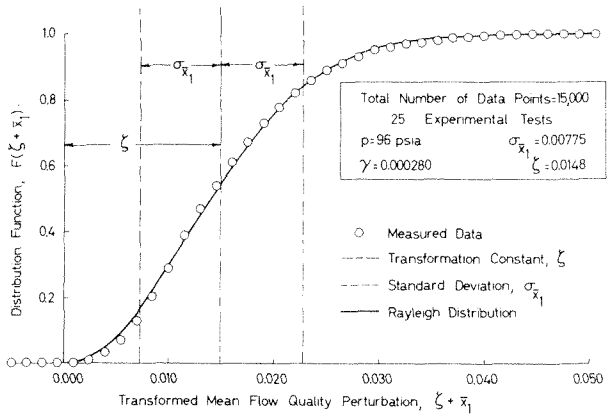

Fig. 4 Comparison of cumulative statistical characteristics with those of a Rayleigh distribution

An important implication of the ability of the transformed Rayleigh distribution to predict the statistical behavior of the mean flow quality perturbation, is that only one statistical parameter, $\sigma_{\bar{x}(1)}$, is needed to specify the distribution. Unbiased estimates of this parameter can be determined from experimental measurements of the mixture-vapor transition point oscillations during steady state conditions. Only two such measurements are needed, the mean value, $\bar{\eta}$, and the standard deviation of the transition point about its mean, σ_η.

With the foregoing density function, the distribution function for the mean flow quality perturbation can be expressed as:

$$F(\zeta + \bar{x}_1) = \int_{y=0}^{(\zeta+\bar{x}_1)} \frac{2}{\gamma} y \exp\{-y^2/\gamma\} dy$$

$$= 1 - \exp\{-(\zeta + \bar{x}_1)^2/\gamma\} \qquad (28)$$

Using the experimental data [2] on the transition point oscillations, it was possible, by using equation (23), to obtain approximately 15,000 values for the mean flow quality perturbation, $\bar{x}_1(t)$, for 25 different tests. These tests involved the same evaporator geometry, the same refrigerant and mass flow rate, but were for a variety of evaporator heat fluxes and inlet flow qualities. The evaporator geometry consisted of five 6 ft long, 0.292 inch ID glass tubes arranged in a serpentine configuration. Refrigerant-12 was used at a flowrate of 1.8 lb_m/min. Inlet flow qualities and heat fluxes ranged from 0–30 percent, and 3200–9100 Btu/hr-ft,^{2} respectively.

Consistent with the theoretical model, all of this experimental data were assumed to come from the same random sample. Therefore, such statistical parameters and characteristics as its standard deviation, frequency of occurrence, and cumulative frequency of occurrence could be determined. Fig. 3 depicts a comparison of the experimentally measured frequency of occurrence, with the density function as predicted with a modified Rayleigh distribution. There seems to be considerable agreement between the Rayleigh density function and the experimental data.

The experimentally measured cumulative frequency of occurrence is compared with the Rayleigh distribution function in Fig. 4. Excellent agreement is seen to exist. Therefore, since the 25 tests involved represented a variety of evaporator heat fluxes and inlet flow qualities, the independence of the mean flow quality perturbations from either of these parameters seems to be reasonably well supported.

Comparison of Theoretical Predictions With Experimental Observations

The complexity of the phenomenon under consideration has made it necessary to make a large number of approximating simplifications in an effort to formulate a theoretical model which has any analytical usefulness. Therefore, the success of the resulting model must be judged ultimately by its ability to predict the outcome of the phenomenon, and to provide insight into the effects of various physical parameters associated with the phenomenon.

Effects of Evaporator Heat Flux on Transition Point Oscillations. In the previous section, it was demonstrated that the mean flow quality perturbations are relatively invariant with evaporator heat flux. Therefore, the theoretical model developed earlier predicts that the amplitude of the transition point oscillations are inversely proportional to the evaporator heat flux. This is expressed statistically in terms of the standard deviation by equation (24); thus

$$\sigma_\eta = \left\{ \frac{(1 - \alpha_i)}{(1 - \bar{\alpha}_0)} \frac{m_{t,i}(h' - h)}{Pf_q} \right\} \sigma_{\bar{x}_1} \qquad (29)$$

The ability of this model to predict the influence of evaporator heat flux on the transition point oscillations is demonstrated in Fig. 5, where the predictions made by the foregoing model are compared to experimental data. In the theoretical curve presented, the mean flow quality perturbation statistics are based upon the average statistics of all of the accumulated experimental data. The agreement which exists between the analytical and experimental results seems to speak for itself; especially when consideration is given to the indirect experimental uncertainties which are possible; not uncertainties in measuring the transition point statistics, but in measuring parameters such as inlet flow quality, heat flux, flowrate, etc., used in the model.

Furthermore, it should be noted that the experimental statistical characteristics necessary to analytically predict the random characteristics of the mean flow quality perturbations for the

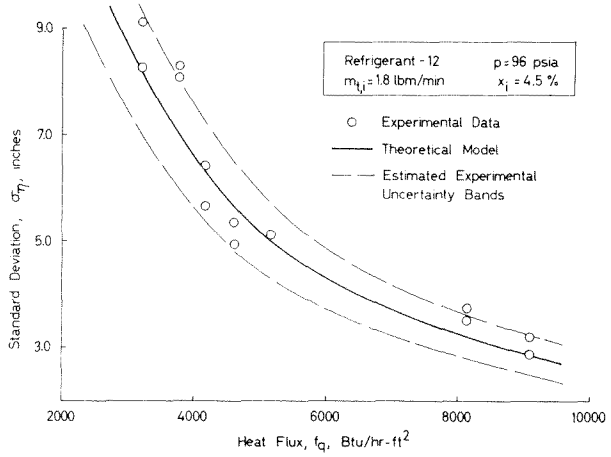

Fig. 5 Influence of heat flux on transition point oscillations

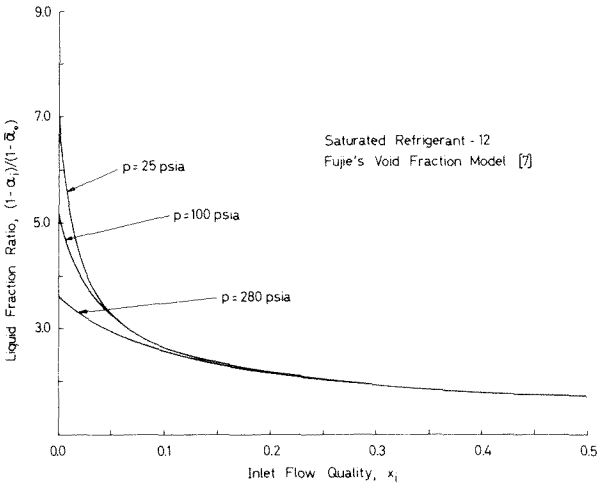

Fig. 6 Influence of inlet flow quality on liquid fraction ratio

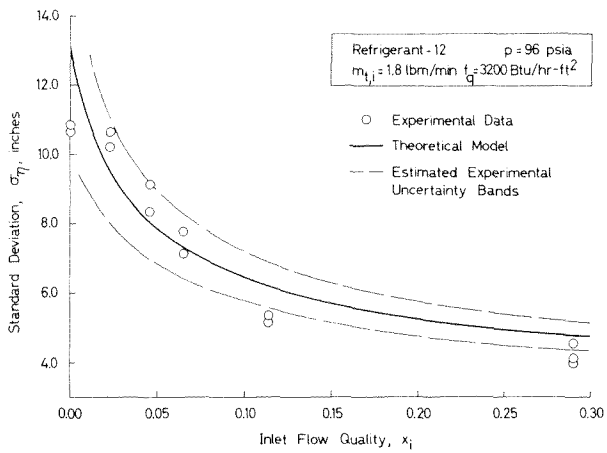

Fig. 7 Influence of inlet flow quality on transition point oscillations

range of heat fluxes shown could have been obtained from a single experimental test at one particular heat flux; thus emphasizing one of the primary utilities of the proposed theoretical model.

Effects of Inlet Flow Quality on Transition Point Oscillations. It is not immediately apparent from an examination of equation (29) just how the inlet flow quality affects the amplitude of the transition point oscillations, since both the inlet void fraction, α_i, and the nonoscillatory mean void fraction, $\bar{\alpha}_0$, are indirect functions of the inlet flow quality, x_i. The inlet void fraction, α_i, can be determined using Fujie's model [7], which relates the flow quality and void fraction.

$$x = \frac{\alpha\left[1 + \dfrac{\alpha^{1/4}\left(\dfrac{a}{p}\right)^{1/2}}{(1-\alpha^{1/2})}\right]}{\left\{(\rho/\rho')(1-\alpha) + \alpha\left[1 + \dfrac{\alpha^{1/4}\left(\dfrac{a}{p}\right)^{1/2}}{(1-\alpha^{1/2})}\right]\right\}} \tag{30}$$

The foregoing relationship is depicted graphically in Fig. 2, for refrigerant-12, where the parameter a = 10.0 psia; based upon Hufschmidt's [8] experimental data.

The nonoscillatory mean void fraction, $\bar{\alpha}_0$, can be determined utilizing equation (30), in conjunction with the numerical integration of equation (12). Therefore, the effect which the inlet flow quality has on the transition point oscillations can be seen by examining the liquid fraction ratio, $(1 - \alpha_i)/(1 - \bar{\alpha}_0)$, as a function of inlet quality. Fig. 6 displays a plot of this ratio as a function of inlet flow quality. Note the strong influence of evaporator pressure for inlet flow qualities of less than five percent.

The ability of the proposed theoretical model, expressed by equation (29), to predict the influence of inlet flow quality on the transition point oscillations is depicted in Fig. 7, where the predictions made by the model are compared to experimental data. The theoretical curve presented is based upon the accumulated experimental data associated with the mean flow quality perturbation statistics. The agreement which exists between the analytical predictions and experimental results seems to be quite good.

As with the influence of heat flux, the experimental data necessary to predict the random characteristics of the mean flow quality perturbations for the range of inlet flow qualities shown could have come from a single experimental test at one particular inlet flow quality. In fact, the same single test could have been used as was used for the heat flux data.

Conclusion

Normally, a prerequisite to the formulation of any theoretical model which describes a certain physical phenomenon, is an understanding of the various mechanisms involved. However, when a particular mechanism influencing a phenomenon is very complex or is not completely understood, it is sometimes possible to propose a simplified model of the phenomenon which lumps the mechanism's effects into a single, determinable parameter. Such simplifications usually render the model more amenable to analysis, although they often place definite restrictions on the results of such an analysis. The success of any theoretical model is judged ultimately by its ability to predict the outcome of a phenomenon, and to provide insight into the effects of various physical parameters associated with the phenomenon. This study has been approached with the foregoing perspective.

As was mentioned earlier, perhaps the most significant potential of the proposed theoretical model is that it represents a first step in the formulation of some of the fundamental mechanisms associated with two-phase evaporating flow instabilities on a statistical basis; a basis which appears to be consistent with many of the experimental observations currently available. Because the mean flow quality perturbations are relatively independent of evaporator heat flux and inlet flow quality, once the statistical characteristics of the transition point oscillations are known for a given evaporator at a particular heat flux and inlet quality, the proposed theoretical model has the capability of predicting the statistical characteristics of the oscillations over a range of heat fluxes and inlet flow qualities. Although the model considers the effects of various properties of the evaporating fluid, the accuracy of the model to predict the oscillatory behavior of the transition point for various evaporating fluids operating in the same evaporator geometry has not as yet been checked out experimentally.

However, the study is continuing in an effort to determine the influence of evaporator geometry and flowrate on the transition point statistics. Three different horizontal tube geometries have been studied thus far; a single tube 32 ft long, five 6 ft long tubes arranged in a serpentine configuration, and nine 3 ft long tubes arranged in a serpentine configuration. In each of these evaporator geometries, the transition point oscillations displayed similarly shaped statistical characteristics.

Although the experimental study is incomplete, preliminary evidence exists which suggests that the mean flow quality perturbations are not only relatively independent of inlet flow quality and heat flux, but are also independent of evaporator flowrate as well. If this preliminary conclusion is substantiated, then it would appear that for a given refrigerant, the mean flow quality perturbations associated with the transition point oscillations would be dependent only upon evaporator geometry. Therefore, from a design consideration, the potential exists for obtaining a single experimental measurement of the standard deviation of the mean flow quality perturbations for a particular evaporator geometry and set of operating conditions, and using the proposed model to predict the statistical behavior of the mixture-vapor transition point oscillations for a wide range of evaporator operating conditions.

Acknowledgments

The authors would like to acknowledge the National Science Foundation for its support of this research under Grant No. GK-35884.

References

1 Bouré, J. A., Bergles, A. E., and Tong, L. S., "Review of Two-Phase Flow Instability," ASME Paper No. 71-HT-42.

2 Wedekind, G. L., "An Experimental Investigation Into the Oscillatory Motion of the Mixture-Vapor Transition Point in Horizontal Evaporating Flow," JOURNAL OF HEAT TRANSFER, TRANS. ASME, Series A, Vol. 93, No. 1, 1971, pp. 47–54.

3 Wallis, G. B., and Heasley, J. H., "Oscillations in Two-Phase Flow Systems," JOURNAL OF HEAT TRANSFER, TRANS. ASME, Vol. 83, 1961, p. 363.

4 Stenning, A. H., "Instabilities in the Flow of a Boiling Liquid," *Journal of Basic Engineering*, Vol. 86, 1964, p. 213.

5 Wedekind, G. L., and Stoecker, W. F., "Theoretical Model for Predicting the Transient Response of the Mixture-Vapor Transition Point in Horizontal Evaporating Flow," JOURNAL OF HEAT TRANSFER, TRANS. ASME, Vol. 90, No. 1, 1968, pp. 165–174.

6 Levy, S., "Steam Slip-Theoretical Predicting From Momentum Model," JOURNAL OF HEAT TRANSFER, TRANS. ASME, Series C, Vol. 82, No. 2, 1960, pp. 113–124.

7 Fujie, H., "A Relation Between Steam Quality and Void Fraction in Two-Phase Flow," *AIChE Journal*, Vol. 10, No. 2, 1964, p. 227.

8 Hufschmidt, W., "Die Eigenschaften von Rippenrohrluftkuhlern im Arbeitsbereich der Klimaanlagen," *Forschungsberichte des Landes Nordrhein-Westfalen*, No. 889, 1960.

9 Steen, P. A., and Wallis, G. B., AEC Report NYO-3114-2, 1964.

10 Wedekind, G. L., and Beck, B. T., "Correlation Between Outlet Flowrate and Mixture-Vapor Transition Point Oscillations in Two-Phase Evaporating Flow," Accepted for possible presentation at the Fifth International Heat Transfer Conference, Tokyo, Japan, Sept. 1974.

ERRATA

An errata on S. Roy "Free Convection From a Vertical Cone at High Prandtl Numbers," published in the February, 1974, issue of the JOURNAL OF HEAT TRANSFER, pp. 115–117.

Footnote 1 line 1 should be Mechanical not Chemical.
Line 2 should be Jauhati not Delhi.
In equations (9) and (10) and last paragraph before the References section, line 4, all x's should be capitalized.
In equation (10) super 1's should be replaced by primes.

F. E. Megerlin
Werksgruppe Guldner,
Linde AG,
Aschaffenburg, West Germany

R. W. Murphy
Manager,
Advanced Thermodynamics Section,
Missile Systems Division,
Raytheon Co.,
Bedford, Mass.

A. E. Bergles
Professor and Chairman,
Department of Mechanical Engineering,
Iowa State University,
Ames, Iowa. MEM. ASME

Augmentation of Heat Transfer in Tubes by Use of Mesh and Brush Inserts

This paper summarizes the results of a study to determine the heat transfer and pressure drop characteristics of two types of tube inserts developed specifically for augmenting heat transfer and accommodating high heat fluxes. The best performing mesh-insert tubes exhibited heat transfer coefficients nine times the coefficients with empty tubes while brush-insert tubes had coefficients averaging five times the empty tube values, both comparisons being made at equal mass velocity. Both inserts produced very large pressure drops. Subcooled boiling curves and burnout points are presented; burnout heat fluxes are two to three times the empty tube values at equal mass velocity. For single-phase conditions and for burnout, the mesh and brush tubes have favorable performance characteristics, based on pumping power, which suggest use of these inserts in certain special cooling systems.

Introduction

The trend in heat exchanger design continues to be in the direction of higher heat transfer rates per unit volume. In the usual commercial fluid-to-fluid heat exchangers, there is an obvious economic incentive to reduce equipment size. This is accomplished by introduction of more surface area and/or augmenting heat transfer coefficients. Other devices, such as microwave power tubes, high field electromagnets, and electron accelerator targets, involve high heat generation rates which must be dissipated through relatively small surface areas. In these high heat flux systems, the surface-to-fluid temperature differences must be kept moderate to avoid melting or other structural failure of the heated surface. These situations have stimulated interest in development of techniques to augment or enhance heat transfer.

A variety of augmentative techniques (surface treatment, displaced promoters, vortex flow, surface vibration, fluid vibration, electrostatic fields, and additives) has been extensively investigated with single-phase flow in tubes, and to a lesser extent with boiling heat transfer [1].[1]

Two new schemes for augmenting heat transfer are the subject of this paper. The first method, originally conceived at Raytheon's Microwave and Power Tube Division, involves insertion of a porous wire matrix into cooling channels. Since the insert occupies the entire flow channel, the resulting assembly can be viewed as a variation of the packed tubes which have been used in the chemical industry. No data for high heat flux conditions have been reported for packed tubes of any kind. The second technique, developed at Raytheon's Missile Systems Division, uses metallic spiral brush inserts which create an improved packed tube by virtue of the swirl flow pattern.

The object of this study was to obtain the thermal and hydraulic characteristics of both types of packed tubes. Both single-phase and subcooled boiling conditions were considered.

Apparatus

Test Sections. Mesh and brush inserts were developed for testing in electrically heated, circular tube test sections. The tubes were 347 stainless steel, with 0.21 in. ID and 0.020 in. wall thickness. The mesh inserts were prepared from commercially available Feltmetal pads constructed of 430 stainless steel fibers, 0.004 in. in diameter. The pads were copper-plated, cut to fit the tube, and then inserted into the tube so that a porosity of about 80 percent was obtained. The operation was completed with furnace brazing of the mesh to the tube wall. The porosity of the 11 test tubes was 80 ± 3 percent; however, X-ray measurements indicated significantly nonuniform porosity distributions (Fig. 1). Efforts to fabricate an insert of higher porosity using individual fibers were unsuccessful as the fibers would compress under large pressure differentials. Inserts prepared from knitted wire mesh strips were also rejected, for reasons of large radial nonuniformity in porosity.

The brush inserts were fabricated using commercially available metallic spiral brushes made by Spiral Brush, Inc. Four twisted 20 ga 302 stainless steel wires constituted the stem while the bristles were formed from 0.003 in. dia 302 stainless steel wire. The

[1] Numbers in brackets designate References at end of paper.

Contributed by the Heat Transfer Division for publication in the JOURNAL OF HEAT TRANSFER. Manuscript received by the Heat Transfer Division, September 27, 1973.

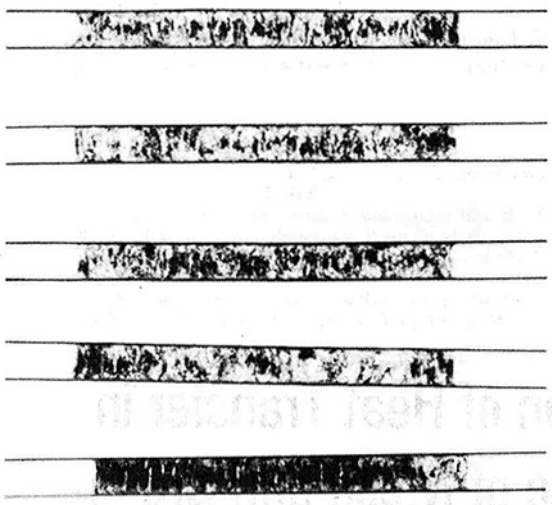

Fig. 1 X-ray of tubes with mesh inserts

Fig. 2 X-ray of tube with brush inserts

nominal outside diameter of the brush was 0.25 in. so that the insert was held firmly in place by friction alone (Fig. 2).

A schematic of the test-section assembly is presented in Fig. 1. After installation of the insert, copper power fittings and piping adapters were soldered to the tubing so that the heated length of the tube was 2.0 in. Pressure taps were drilled into the upstream and the downstream fittings. Thermocouples were spot-welded at ¼ or ⅜ in. from either end of the tube and at several intermediate points. Fiberglass insulation was provided for the entire assembly. The instrumented test section was installed into the flow loop by means of Victaulic couplings, which also provided for thermal expansion and electrical isolation.

The test section was supplied with a-c power transmitted through flexible water-cooled cables. One phase of the three-phase Laboratory service was fed through an ignitron controller and a 100 kw power transformer before being applied to the test section. The power was monitored by true rms, voltmeters, and ammeters.

Loop. The test loop utilized in this study was constructed in Raytheon's MSD Heat Transfer Laboratory. Distilled water was circulated in the closed system through a turbine pump which provided a maximum discharge pressure of 550 $lb_f/in.^2$ ga at 2 gal/min. In addition to the test-section and test-section bypass circuits, additional circuits were provided for degassing and demineralization. A high pressure filter with a pore size of 0.5 microns was installed upstream of the heated test section. Flow control and quick-acting isolation valves were provided at the test section.

Fluid temperatures and pressures were monitored at various points around the loop. The test circuit flow rate was determined by turbine flowmeters, with a digital indicator displaying the volume flow rate.

Procedure and Data Reduction

After installation of the first test section, the loop was filled and purged of air. The degassing circuit was then activated for a sufficient period to reduce dissolved air to a negligible value. The demineralizer was activated and kept operational throughout the testing so as to maintain the water resistivity above 1 megohm-cm.

After the flow rate, the system pressure, and the water inlet temperature were set, electrical power was applied to the test section. Testing started with moderate power inputs, and small increments were utilized so as to cover single-phase and boiling conditions up to burnout. Burnout conditions were defined as data recorded just prior to physical destruction of the test section. Isolation valves were closed to prevent excessive loss of coolant. New test sections could be installed without introducing appreciable air into the system.

The data reduction for this investigation was accomplished mainly by computer, using subroutines to generate accurate values for water properties. Test-section heat inputs computed by calorimetric and electrical methods generally agreed to within 5 percent.

With this type of experiment it was not obvious how the heat flux should be defined, as a portion of the power was dissipated in the mesh or brush inserts. Electrical resistance measurements made for all test sections established that less than 15 percent of the power was generated in the brush, whereas about 25 percent of the applied power was generated in the mesh. It was rather arbitrarily decided that the mesh heat transfer coefficients and boiling curve data would be computed by using the wall heat flux, and burnout heat flux would be based on total power and tube inside wall area. Because a relatively small fraction of the total power was generated in the brush, the brush data were all treated using total power and wall area.

The temperature of the inner tube wall was calculated using the measured outer wall temperature and an extended series solution to the nonlinear heat conduction equation involving temperature-dependent thermal conductivity and electrical resistivity. The mass velocity was based on the average unobstructed flow

Nomenclature

A_{fr} = cross-sectional area of empty tube
A_t = total mesh surface area
A_w = surface area based on tube inside diameter
C = constant in equation (1)
c = specific heat at constant pressure
D = tube diameter
d = wire diameter
F = fin-effect multiplier in equation (1)
f_b = Fanning friction factor for brush tubes, equation (4)
f_m = Fanning friction factor for mesh tubes, equation (2)
G = mass velocity
g = gravitational conversion factor
h = heat transfer coefficient
h_t = heat transfer coefficient based on q_t and A_w
h_w = heat transfer coefficient based on q_w and A_w
k = thermal conductivity of coolant
L = test section length—heated or pressure drop, as appropriate
P = pumping power
p = porosity
p = pressure
Δp = pressure drop
Pr = Prandtl number, $c\mu/k$
q_t = total heat transfer rate
q_w = heat transfer rate at tube wall
Re = Reynolds number, GD/μ
$\overline{T_b}$ = average bulk fluid temperature in test section
ΔT = wall-minus-fluid temperature difference
V = internal volume of heated portion of test section
y = tube diameters per 180 deg of brush or tape twist
$\alpha = \left(\frac{4y^2 + \pi^2}{4y^2}\right)^{1/2}$
β = bulk modulus of expansion
μ = dynamic viscosity
ρ = density

Subscripts

a = refers to augmented tube
i = based on inside tube diameter
h = based on tube hydraulic diameter
o = refers to empty tube
P = based on constant pumping power

area in the tubes.

Further details of the apparatus, operating procedure, and data reduction can be found in references [2 and 3].

Single-Phase Heat Transfer Data

Empty Tube Data. Heat transfer data for nonboiling conditions are presented in Fig. 2. These data represent average values for the short test sections; fluid properties were computed at the average bulk fluid temperature. Relative to the Dittus-Boelter and McAdams correlating equation, the present data are approximately 50 percent high. This trend is entirely expected due to the dominance of entrance effects in the short tube (L/D_i = 9.5). Other factors which could contribute to high heat transfer coefficients are radial property variation and free convection. In any event, these results serve as a proper reference for the test sections with mesh or brush inserts.

Mesh Tube Data. Single-phase heat transfer data for three mesh tubes are included in Fig. 2. The coordinates are based on nominal inside tube diameter in order to best show the improvement obtainable with mesh tubes over the comparable empty tube flow. Parameters were evaluated only for the exit location, approximately ⅜ in. from the downstream power bushing. Heat transfer coefficients were expected to be quite uniform over the test length due to the high degree of turbulence produced by the mesh.

A dramatic increase in heat transfer performance is certainly indicated by the mesh tubes. Test sections 14 and 15 yield heat transfer coefficients approximately nine times the coefficients obtained with the empty tubes at comparable Reynolds numbers. Heat transfer coefficients corresponding to the upper range of Nusselt numbers were in excess of 40,000 Btu/hr-ft²-deg F. The large enhancement in heat transfer can be attributed to the fin effect of the wires and the high degree of turbulence produced at the tube wall by the many irregular protuberances.

It is noted that the performance of test section 13 is considerably below that of the other two mesh tubes. This was attributed to locating the exit thermocouples in a zone of relatively high porosity where neither of the enhancement mechanisms was strongly active. These data confirm the importance of proper porosity control with mesh inserts, since extreme hot spots could develop in the more open regions.

Brush Tube Data. Fig. 3 presents the entire set of data for nonboiling heat transfer with brush tubes. The data primarily represent local measurements at ¼ in. from either end of each tube. The single test section that was instrumented at additional axial points did not yield any conclusive information about axial variation of heat transfer coefficients. In general, these tests indicate that brush tubes on the average have coefficients five times the empty tube values at comparable Reynolds numbers.

The scatter of about ±50 percent in these data can be explained from the fact that results from 25 test sections are included in the plot. The most probable reason for this behavior is the random location of the wall thermocouples relative to the brush helix. Wall temperatures near a point of brush contact with the wall can be expected to be lower (due to fin effects) than corresponding temperatures at positions distinctly removed from such contact points.

In order to gain insight into detailed wall temperature profiles, an infrared radiation measurement technique was utilized. An AGA Thermovision Camera with video display was used to record wall temperature isotherms during single-phase heat transfer operation. The IR display gave a clear indication of a spiral isothermal pattern; however, the apparent pitch of the pattern was greater than that of the brush insert. Although infrared scanning was not fully explored in the present study, it is felt that this technique is a valuable experimental tool for investigation of heat transfer in tubes with such complicated inserts.

Swirl Flow Model for Brush Tube Heat Transfer Data. The bush insert can be idealized as producing a four-start spiral flow if it is assumed that the bristles are packed tightly enough to prevent significant axial flow. A predominantly spiral flow was verified by using dye injection to visualize streamlines when the brush was inserted in a glass tube. An appropriate prediction equation is provided by the superposition model of Lopina and Bergles [4]. An augmented axial flow heat transfer coefficient, resulting from the increased path length (spiral convection), is added to a free convection term which arises from the large body force and a favorable temperature gradient (centrifugal convection). These two terms are modified by a fin-effect multiplier as indicated in equation (1).

$$\frac{hD_h}{k} = F\left\{C(\alpha \mathrm{Re}_h)^{0.8}\mathrm{Pr}^{0.4} + 0.193\left[\left(\frac{\mathrm{Re}_h}{y}\right)^2 \frac{D_h}{D_i}\beta\Delta T\ \mathrm{Pr}\right]^{1/3}\right\} \quad (1)$$

This equation has been shown to adequately correlate data for water flowing in tubes with twisted-tape inserts [4, 5].

The swirl flow model was applied without modification to the typical data for test section 4. These data are presented as length averages in Fig. 4. The predictions were computed from the forgoing equation using C = 0.023, F = 1.20, and representative values of the bulk temperature and temperature difference. The hydraulic diameter computed according to the usual definition was D_h = 0.12 in. The agreement between the prediction and the data is good enough to substantiate use of the model for swirl flow induced by brush inserts.

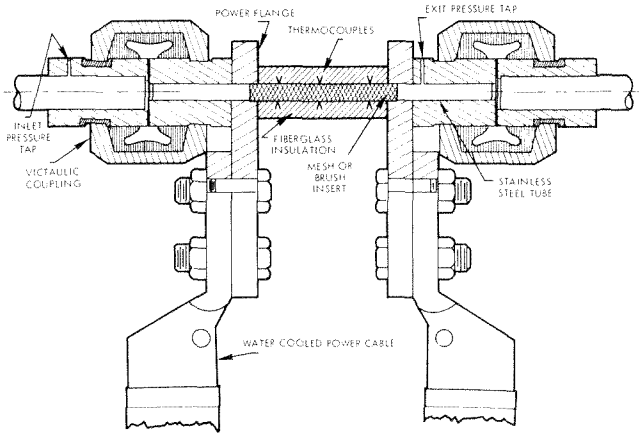

Fig. 3 Test-section assembly

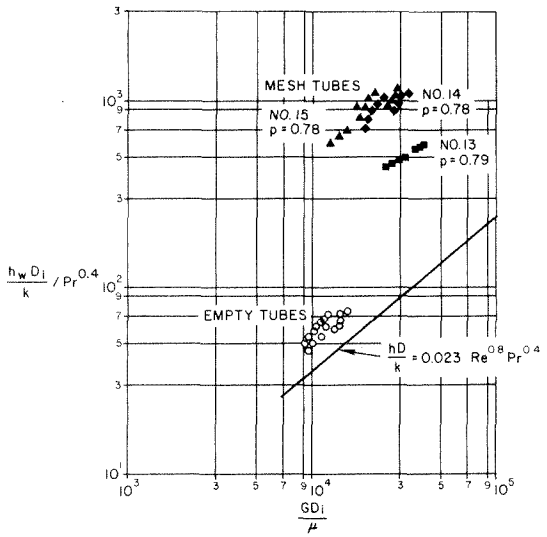

Fig. 4 Single-phase heat transfer results for empty and mesh-insert tubes

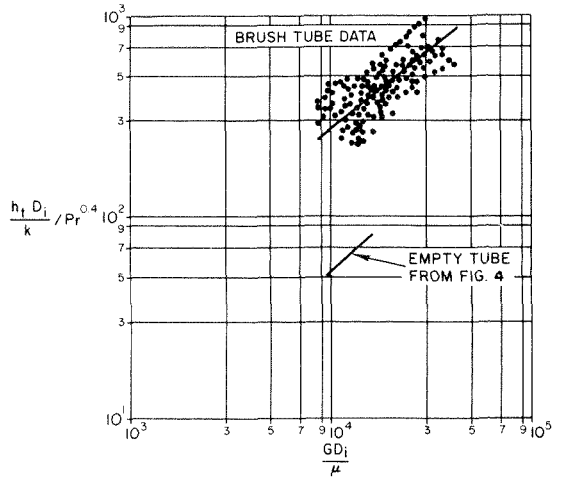

Fig. 5 Single-phase heat transfer results for brush-insert tubes

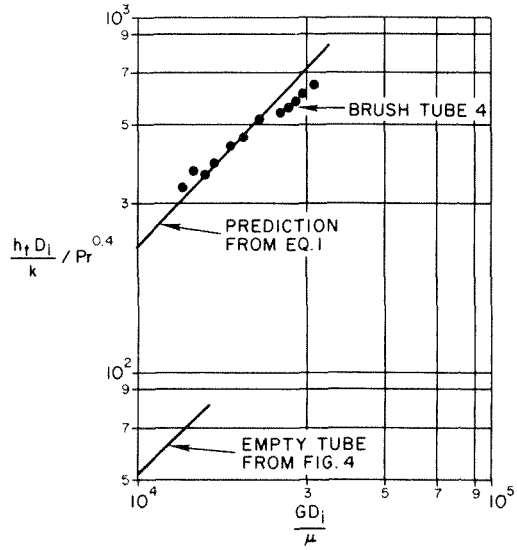

Fig. 6 Comparison of data for a typical brush-insert tube with predictions of swirl flow model

Pressure Drop Data

Pressure drop data in mesh tubes under single-phase conditions were reduced to friction factors based on hydraulic diameter:

$$f_m = \frac{\Delta p}{4(\frac{L}{D_h})(\frac{G^2}{2\rho g_0})} \tag{2}$$

where

$$D_h = \frac{4pA_{fr}L}{A_t} = \frac{pd}{1-p} \tag{3}$$

as adopted by Kays and London [6]. These data are presented in Fig. 5 along with the Kays and London correlating curves for woven-screen matrices. The present data are in reasonable agreement with the correlating curves; however, a stronger effect of porosity seems to be indicated.

For the test data indicated in Fig. 5, the pressure drop ranges from 100 to 380 $lb_f/in.^2$ across the 2.25 in-long mesh. The pressure drop is governed primarily by the form drag in the mesh, and the heat transfer regime has no effect on the pressure drop (or friction factor). As a result, the pressure drop versus heat flux curves are all straight horizontal lines for a particular mass velocity, spanning the isothermal, the forced-convection heating, and the subcooled boiling regimes.

The pressure drop data for brush tubes were reduced according to the spiral flow model mentioned in the forgoing. Correlating equations have been developed by modifying conventional friction factor relations by an empirical function of y [4, 7] or by using the conventional correlation with friction factor and Reynolds numbers defined in terms of swirl flow parameters [8]. The latter approach is chosen here for simplicity. Thus

$$f_b = \frac{\Delta p}{4(\frac{L}{D_h})(\frac{G^2}{2\rho g_0})} \tag{4}$$

and

$$\mathrm{Re} = \frac{GD_h\alpha}{\mu} \tag{5}$$

The data presentation is given in Fig. 6, and it is quite evident that the spiral flow model does not describe the data. Pressure drops of from 40 to 400 $lb_f/in.^2$ reduce to friction factors about 30 times the predicted values. This discrepancy is largely due to the very rough channel presented by the bristles and the core wires. As in the case of the mesh tubes, there was no noticeable change in pressure drop with heat flux, even up to the burnout condition.

Subcooled Boiling Data

Boiling Curves. Typical boiling curves are presented in Fig. 7 for empty tubes, mesh tubes, and brush tubes. As noted earlier, heat flux data for brush tubes are based on the total power, while

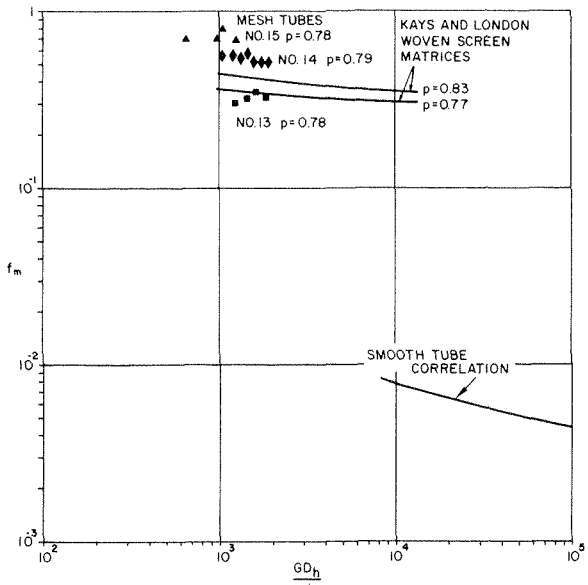

Fig. 7 Friction data for mesh-insert tubes compared with available correlations

boiling curve data for mesh tubes use wall heat flux only. The wall superheats are based on local wall temperatures and local saturation temperatures determined assuming a linear pressure gradient in the mesh region.

The empty tube data behave according to expectations; however, both the mesh tube and the brush tube data extend to much higher wall superheats than those generally reported for nucleate boiling. The behavior of these augmented data is actually more characteristic of single-phase flow since only a modest upswing is observed in the boiling curve before burnout.

Before attempting to describe a possible mechanism of boiling in the mesh and brush tubes, it should be noted that there is uncertainty in the derived wall temperatures. As pointed out earlier, the measured outer wall temperatures were corrected by the most accurate solution to the conduction equation which is currently available in order to obtain the tube inner wall temperatures. At the highest heat fluxes, this correction was found to be in excess of 500 deg F; hence, even modest errors in the computed correction translate to sizeable errors in the wall superheat. Uncertainties in wall thickness, electrical resistivity, thermal conductivity, and measured voltage drops could combine to produce these er-

rors. All factors were carefully examined, however, and it is felt that the uncertainty in computed wall temperature drops should be limited to ±10 percent. The high wall superheats are thus considered to be a real phenomenon.

While more detailed instrumentation of the augmented tubes would be required to confirm mechanism speculations, it seems that the data can be explained on the basis of partial film boiling. At the velocities and pressures of interest, bubble size is of the same order as the mesh or bristle spacing. It is probable, then, that bubble removal is inhibited at low nucleate-boiling heat fluxes. This could lead to local vapor blanketing; however, vapor patches would be expected to be quite unstable due to the high core turbulence. Furthermore, the mesh fibers and bristles act as fins and maintain a substantial portion of the tube wall in nucleate boiling. The probable result is a violent partial film boiling, with a heat transfer coefficient not too different from that for single-phase flow, rather than the efficient nucleate boiling process. The observed pressure effect for the mesh tubes is consistent with partial film boiling data.

Eventually, the heat flux is high enough to cause stable vapor blanketing, and the wall temperature undergoes an excursion to established film boiling. Burnout occurs during this excursion when the outside wall starts to melt. It is evident, of course, that wall temperatures are very high even at fluxes well below the burnout value; "glowing" tubes were observed several times.

Pressure Drop. As noted earlier, the pressure drop was essentially constant throughout all heat transfer regimes. This results from the pressure drop being controlled by the form drag in the core. The wall friction is affected by wall heat flux in both single-phase and boiling regimes; however, this friction is a small contributor to the total pressure drop.

The relative simplicity of the pressure drop behavior makes it a simple matter to design a pump for cooling systems utilizing mesh or brush inserts. However, some caution should be exercised in extrapolating these conclusions to lower velocities where the wall friction is likely to play a more important role.

Burnout Results. For the experimental data presented here, the upper operating limit is designated "burnout" because this term describes the physical destruction of the test section. The parameter values were actually recorded during operation at the settings immediately preceding those existing at the time of test section destruction. The inlet liquid temperature was maintained between 45 and 100 deg F for the 39 burnout runs. Exit pressures varied between 29 and 252 $lb_f/in.^2$ abs. This range of variables precludes a simple comparison on either a local or system parameter basis; however, the general trend of the data can be visualized on the latter basis as shown in Fig. 8. With this presentation, the burnout flux increases with increasing velocity for fixed geometry, inlet temperature, and pressure level.

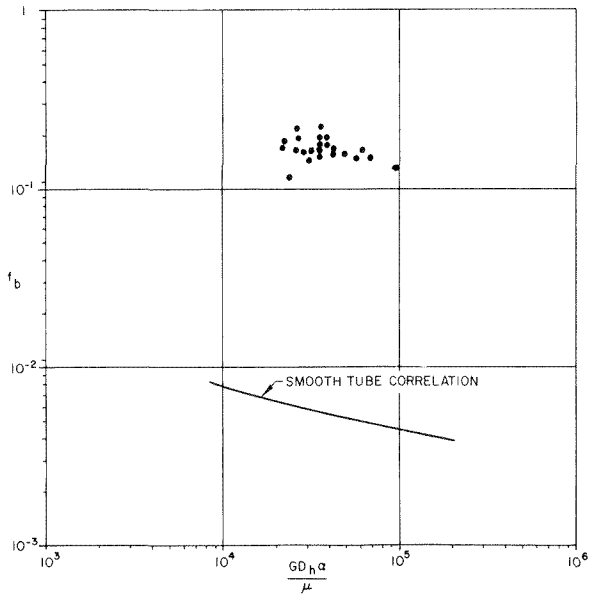

Fig. 8 Friction data for brush-insert tubes interpreted according to swirl flow model

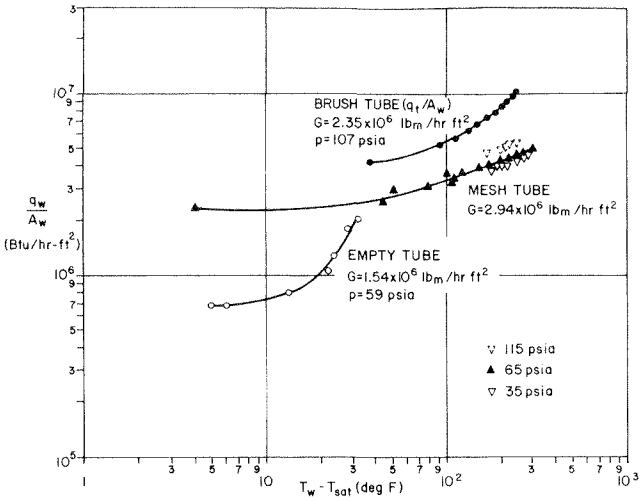

Fig. 9 Typical boiling curves for tubes used in this study

The empty tube data were found to be in good agreement with limited data available in the literature for similar geometrical and flow conditions [9]. No correlation is directly applicable since the test sections are so short. The mesh tubes burn out at fluxes more than twice the empty tube values while the brush tube burnout fluxes approach three times the empty tube values. Both the mesh tubes and the brush tubes follow the expected parametric trends with varying mass velocity, inlet subcooling, and pressure level.

It is possible to interpret the present data with the additive prediction method of Gambill [10] which involves a summation of the subcooled pool boiling burnout heat flux, and heat flux attributable to single-phase forced convection. As this model suggests, the high burnout fluxes result primarily from the very high heat transfer coefficients which exist prior to boiling. Once this single-phase coefficient is established, reasonable success at prediction of heat transfer is assured since the boiling contribution is relatively small.

Augmentation Evaluation

Single-Phase Flow. Up to this point, the evaluation of the relative performance of mesh and brush inserts has been based on equal-Reynolds-number comparisons. Judged on this criterion, both inserts were very effective in augmenting heat transfer performance to levels far above that realized with empty tubes. As pointed out in [11, 12], however, other performance evaluation criteria may be appropriate, depending on the design and economic constraints. For normal industrial heat exchanger evaluation, a particularly appropriate criterion is relative heat transfer coefficients for augmented and empty tubes at equal fluid pumping power. This can be expressed as the ratio:

$$\left(\frac{h_a}{h_0}\right)_{P,\ L,\ D_i,\ \bar{T}_b} \tag{6}$$

The present heat transfer and pressure drop data were combined to evaluate the foregoing ratio, with the results as shown in Fig. 9. Mesh tubes 14 and 15 are well above the "break even" point of $(h_a/h_0)_P = 1.0$. The performance ratios are approximately the same as those obtained with full-length twisted tapes [1]. Mesh tube 13 has quite inferior performance, an effect which seems to be related to an extreme sensitivity of the heat transfer coefficient to mesh porosity (Fig. 2). The brush tube performance averaged for all 25 test sections is only slightly above $(h_a/h_0)_P =$

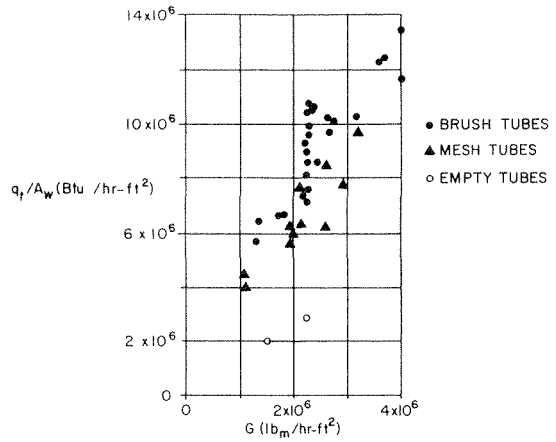

Fig. 10 Dependence of burnout heat flux on mass velocity

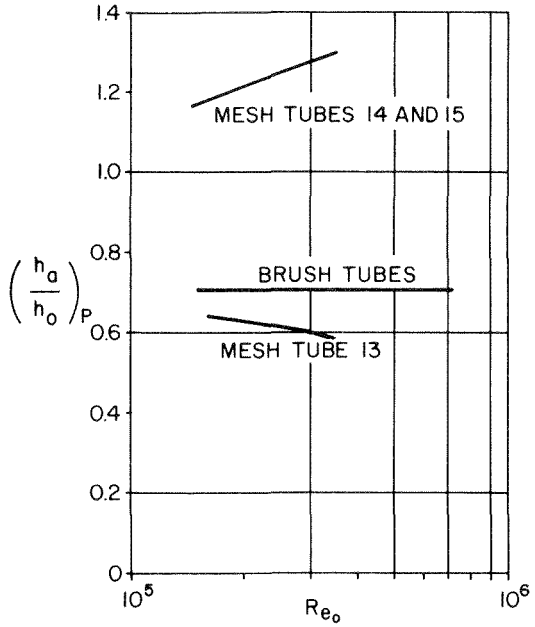

Fig. 11 Single-phase heat transfer performance of mesh and brush tubes according to constant pumping power criterion

0.7. This is a result of the high form drag. It is felt that some improvement may be possible by changing the brush geometry; however, the performance of smooth inserts is most likely unattainable. On the other hand, it should be pointed out that flow rates are greatly reduced with the present inserts. This can result in smaller pressure losses in the remainder of the circulating system, and could lead to overall reduction of pumping power and a less expensive pump. In addition, the mesh and brush inserts could present a significant advantage for cooling systems where coolant weight and supply is at a premium, as in some airborne applications.

Subcooled Burnout. At the present time there are no generally accepted performance criteria for boiling which consider both heat transfer and pressure drop. Gambill, et al. [7] ran a set of control experiments which indicated that twisted-tape inserts increased the burnout heat flux by about a factor of two over the empty tube value at equal pumping power. Geometry, inlet temperature, and outlet pressure were held approximately constant for these tests. In a later work, a burnout flux ratio of swirl-flow and empty tubes (at constant pumping power) was plotted versus fluid horsepower per square foot of surface area [11].

While these presentations do give an indication of the performance, they do not recognize that one of the concerns is designing high heat flux cooling systems is the volume occupied by the cooling channel. Accordingly, it seems appropriate to compare the present burnout data with data for cooling channels fitted with other augmentation devices, basing the heat transfer rate and pumping power on the internal tube volume ($\pi D_i^2 L/4$). This presentation is given in Fig. 10, where the extensive data for empty tubes and swirl flow devices are from studies by Gambill and coworkers.

The data presented in Fig. 10 exhibit considerable scatter, as might be expected since individual burnout fluxes are significantly altered by variations in tube diameter, tube length, exit pressure, and exit subcooling [9]. Ignoring these effects, it is seen that this presentation suggests an approximate relation between heat transfer and pumping power, both expressed on a volumetric basis. The collected data provide preliminary information for the design of high heat flux systems since the curves can be adjusted by an appropriate factor of safety.

On this particular basis the data suggest that the brush tubes are considerably more effective than the mesh tubes. The brush inserts perform better than the tangential slot or spiral ramp vortex generators but not quite as well as tubes having full-length twisted tape inserts. The mesh inserts and the spiral ramp generators do not perform quite as well as the empty tubes.

Concluding Remarks

This study has clarified the heat transfer and pressure drop characteristics of mesh and brush inserts developed specifically for accommodating high heat fluxes.

While some difficulty was encountered in achieving uniform porosity during mesh insert fabrication, extremely large heat transfer coefficients were obtained under single-phase conditions. The best performing tubes had coefficients about nine times the coefficients obtained with empty tubes at the same mass velocities. The friction factor data for these tests are in reasonable agreement with data reported in the literature for woven screen matrices.

Brush inserts are very inexpensive to fabricate and can be easily installed. The heat transfer coefficients average five times the empty tube values at equal mass velocity, and can be satisfactorily predicted by an available swirl flow model. The same model does not predict the pressure drop data due to excessive roughness of the flow channel away from the heated surface.

Boiling curves for both mesh and brush tubes extend to higher wall superheats than generally reported for nucleate boiling. It is hypothesized that this behavior is due to early occurrence of partial film boiling. The high wall superheats could be a problem in applications where temperature level must be restricted. Burnout heat fluxes are about two to three times the empty tube values at equal mass velocity.

From a performance standpoint, the best mesh tubes are effec-

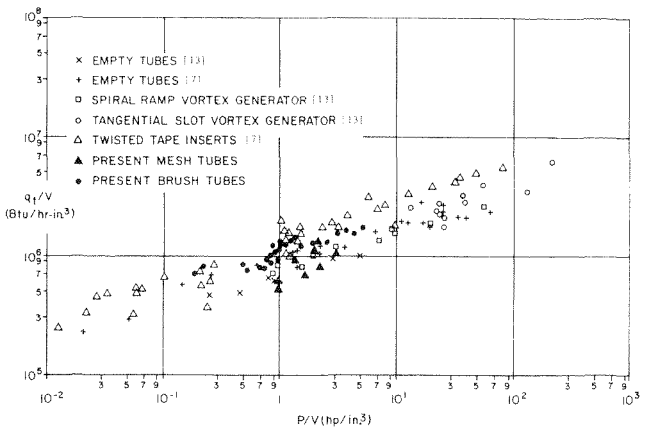

Fig. 12 Subcooled burnout performance of normal and augmented tubes with water coolant, on a volumetric basis

tive in single-phase flow, if the evaluation is based on constant pumping power for mesh and empty tubes. The brush tubes have considerably lower performance. The new performance evaluation developed for subcooled burnout suggests that brush tubes are more effective than the mesh tubes and several of the other vortex devices tested by Gambill and Greene [13]. Full-length twisted tapes seem to have the best performance of all.

The mesh and brush inserts achieve high heat transfer coefficients with low flow rates. This may be desirable in cooling systems where it is desirable to reduce pump or coolant reservoir capacity. The inserts seem to be particularly suited to very short channels or to portions of channels where the heat flux is excessive.

Acknowledgments

This study was funded by the Research Branch of the Naval Air Systems Command (NASC), Washington, D. C., and contracted to Raytheon Missile Systems Division by the Naval Air Development Center (NADC), Johnsville, Pennsylvania. Messrs. J. Willis (NASC), B. Plizak (NADC), and A. Saltzman (NADC) made many significant contributions to this effort. The research program was initiated at Raytheon under the direction of Mr. M. P. Bleday. Mr. P. Vingerhoet and Mr. S. Goldstein assisted with the experiments and data reduction.

References

1 Bergles, A. E., "Survey and Evaluation of Techniques to Augment Convective Heat Transfer," *Progress in Heat and Mass Transfer*, Pergamon Press, Vol. 1, 1961, pp. 331–424.

2 Megerlin, F. E., "The Experimental Determination of the Thermodynamic and Hydrodynamic Mechanism of Augmented Flow Boiling in Tubes," Final Report on Contract NADC N 62269-69-C-0162, Raytheon BR-5785, June 1970.

3 Murphy, R. W., and Megerlin, F. E., "The Augmentation of Flow Boiling Heat Transfer in Tubes (II), "Final Report on Contract NADC N 62269-70-C-0363, Raytheon BR-6518, June 1971.

4 Lopina, R. F., and Bergles, A. E., "Heat Transfer and Pressure Drop in Tape-Generated Swirl Flow of Single-Phase Water," JOURNAL OF HEAT TRANSFER, TRANS. ASME, Vol. 91, 1969, pp. 152–154.

5 Bergles, A. E., Lee, R. A., and Mikic, B. B., "Heat Transfer in Rough Tubes With Tape-Generated Swirl Flow," JOURNAL OF HEAT TRANSFER, TRANS. ASME, Vol. 91, 1969, pp. 443–445.

6 Kays, W. M., and London, A. L., *Compact Heat Exchangers*, Second ed., McGraw-Hill, 1964, p. 130.

7 Gambill, W. R., Bundy, R. D., and Wansbrough, R. W., "Heat Transfer, Burnout and Pressure Drop for Water in Swirl Flow Through Tubes With Internal Twisted Tapes," *Chemical Engineering Progress Symposium Series*, Vol. 57, No. 32, 1961, pp. 127–137.

8 Gutstein, M., Converse, G. L., and Peterson, J. R., "Augmentation of Single-Phase Heat Transfer in Tubes by Use of Helical Vane Inserts," Paper FC 4.7, Fourth International Heat Transfer Conference, Elsevier Publishing Company, Vol. II, 1970.

9 Bergles, A. E., "Subcooled Burnout in Tubes of Small Diameter," ASME Paper No. 63-WA-182, 1963.

10 Gambill, W. R., "Generalized Prediction of Burnout Heat Flux for Flowing, Subcooled Wetting Liquids," *Chemical Engineering Progress Symposium Series*, Vol. 59, No. 41, 1963, pp. 71–87.

11 Gambill, W. R., and Bundy, R. D., "An Evaluation of the Present Status of Swirl Flow Heat Transfer," ASME Paper No. 62-HT-42, 1962.

12 Bergles, A. E., Blumenkrantz, A. R., and Taborek, J., "Performance Evaluation Criteria for Enhanced Heat Transfer Surfaces," AIChE Paper 9 for 13th National Heat Transfer Conference, Denver, 1972.

13 Gambill, W. R., and Greene, N. D., "Boiling Burnout With Water in Vortex Flow," *Chemical Engineering Progress*, Vol. 54, No. 10, 1958, pp. 68–76.

H. O. Buhr
Assoc. Professor,
University of Cape Town,
South Africa

E. A. Horsten
Senior Lecturer,
University of Stellenbosch,
South Africa

A. D. Carr
Professor,
University of Cape Town,
South Africa

The Distortion of Turbulent Velocity and Temperature Profiles on Heating, for Mercury in a Vertical Pipe

Measurements were made in mercury, for turbulent flow and constant flux heating in a vertical pipe, in order to determine the extent to which the velocity and temperature distributions are affected by buoyancy forces. With increasing heat flux, velocity profiles at Reynolds numbers of 20,000 to 60,000 were found to be markedly distorted in comparison with the isothermal velocity profile. Even very low heat input caused significant distortion, while at high heat input a limiting profile shape was approached, with the center velocity well below the mean and the maximum occurring in the vicinity of the wall. Eddy diffusivities of heat and momentum calculated from the measured profiles exhibit a considerable variation with heat input, indicating that buoyancy forces not only change the radial shear stress distribution but also alter the nature of the turbulence in the pipe.

Introduction

In normal forced convection heat transfer, differential buoyancy forces will superimpose a free convection effect on the flow field. For the case of turbulent flow this effect has traditionally been ignored. Thus, Martinelli [1][1] and many subsequent workers have predicted temperature profiles in a pipe by using an isothermal turbulent velocity distribution and omitting buoyancy terms from the equation of motion. A numerical study by Ojalvo and Grosh [2] showed, however, that appreciable distortion of the velocity profile could occur in comparison with isothermal conditions, when allowance is made for buoyancy effects. Similarly, an investigation of the temperature distribution in liquid metals [3] produced evidence of likely distortion of the turbulent velocity profile. An experimental program was accordingly undertaken to characterize the distortion of velocity and temperature profiles with changing heat flux. Tests were conducted in mercury at Reynolds numbers of 2-, 3-, and 6×10^4. Constant-flux heating was used, with the fluid flowing vertically upwards in the test section. This physical configuration gives radial symmetry which facilitates profile measurements and simplifies the use of the equations of energy and motion.

Results show that the velocity profile distorts rapidly as heat flux is increased. At high heat flux a limiting profile shape is approached, with the center velocity well below the mean, but reverse flow, as predicted by Ojalvo and Grosh, is not observed. Calculated values of the eddy diffusivities of heat and momentum at a given Reynolds number are found to exhibit an appreciable variation with increasing heat flux.

[1] Numbers in brackets designate References at end of paper.

Contributed by the Heat Transfer Division of THE AMERICAN SOCIETY OF MECHANICAL ENGINEERS and presented at the AIChE-ASME *Heat Transfer Conference*, Denver, Colo., August 6-9, 1972. Manuscript received by the Heat Transfer Division, July 30, 1973. Paper No. 72-HT-21.

Equipment

The test loop [4], shown in Fig. 1, was constructed of seamless 316 stainless steel tubing, with a vertical test section 1.968 in. ID and 2.047 in. OD. A probing station, located 16 ft from the entrance to the test section, consisted of a nozzle carrying the probe traversing mechanism. The probe tip extended 2½ in. upstream from the nozzle, giving a thermodynamic calming length of 84 dia and a hydrodynamic calming length of 95 dia to the point of measurement.

Mercury was circulated by a 12 in. centrifugal pump which was belt driven at 70–300 rpm by a 3 hp electric motor. The test section was closely wound with 1 in. wide nichrome heating ribbon, applied over woven fiberglass tape and AC heating was supplied by a 160V/100A variable transformer. Heat losses were reduced to less than 2 percent by asbestos and polystyrene insulation. Inlet and outlet temperatures were measured at each end of the test section by iron-constantan thermocouples installed in mixing cups designed to provide two reversals of flow direction and symmetrical entry into the test section.

Preliminary velocity measurements showed that the use of a total head probe, together with a static pressure reading taken from a piezometer ring 9.5 in. downstream, gave unsatisfactory results. The differences in temperature, and hence density, between the height of mercury from the probe to the piezometer, inside the pipe, and the corresponding height of mercury in the pressure transmission leads, outside the pipe, caused significant

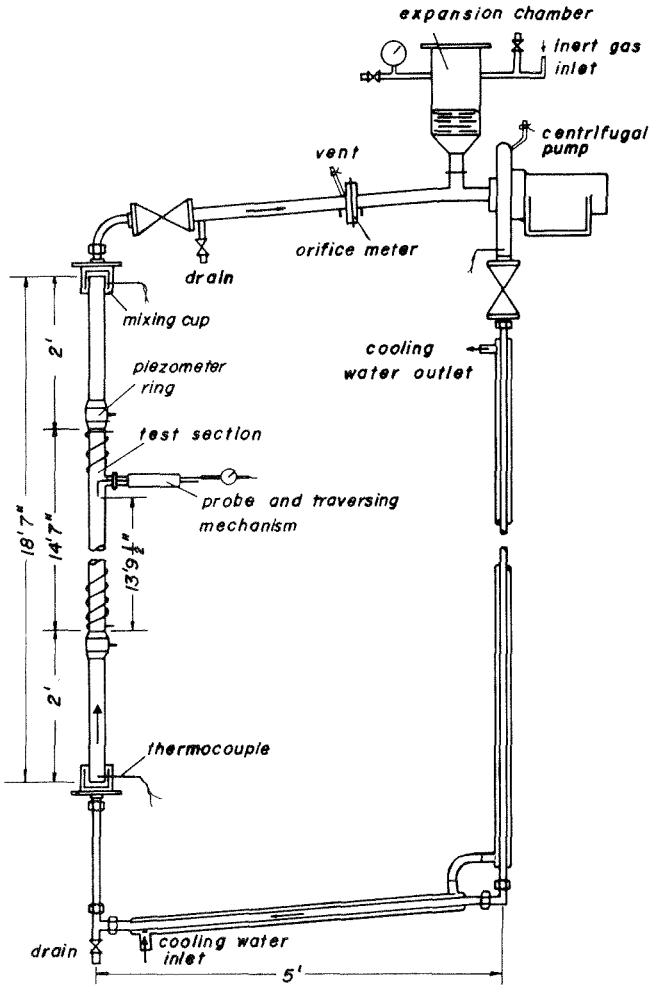

Fig. 1 Test loop—schematic arrangement

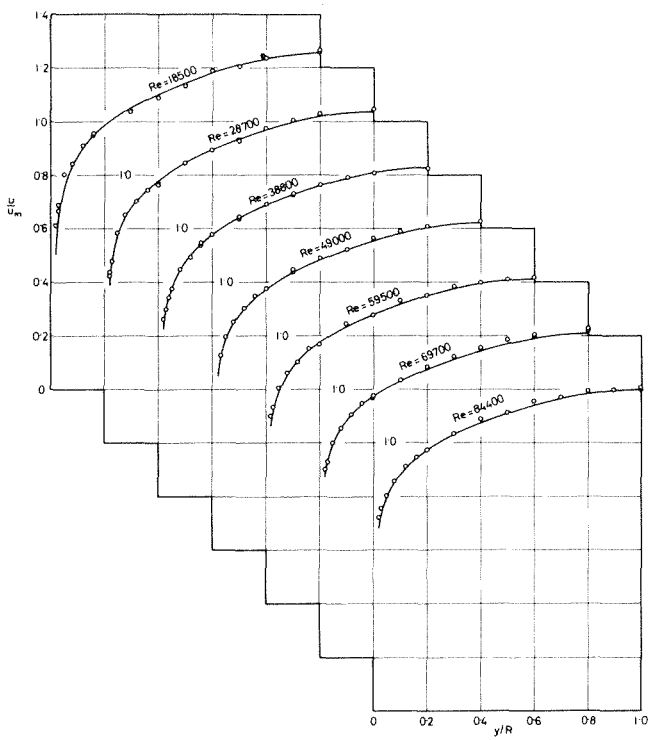

Fig. 2 Isothermal velocity profiles—Travis, et al. [5] correlation

offset in the low pressure differentials measured. A combined pitot-static probe was therefore constructed so that impact and static pressures could be taken from the same vertical location. This probe gave steady and reproducible results and was used to obtain the velocity data reported here. The impact tube of the probe had an ID of 0.010 in. and an OD of 0.015 in. at the tip, and static pressure holes drilled 1.3 in. from the tip in an outer tube of 0.128 in. OD. In view of the influence of the walls on the static holes, velocity readings were not taken for $y/R < 0.02$. Due to the same problem of temperature-related offset mentioned in the foregoing, it was not possible to make accurate axial pressure drop measurements for the purpose of evaluating the friction factor.

Differential pressures were measured using a strain-gage transducer with a range of 0–1 in. water gage, and in order to avoid contact of mercury with the sensitive transducer diaphragm, a change-over to water as the transmitting fluid was made using two 3 in. dia seal pots. The voltage signal from the transducer was passed through an electronic filter circuit to damp turbulent fluctuations, and recorded on a 10 in. recorder for approximately 10 min at each radial position.

After the series of velocity traverses had been completed, the velocity probe was removed and a temperature probe installed. Operating conditions for each velocity run were then reproduced to within 2 percent and the corresponding temperature profiles measured. The temperature probe had the same overall dimensions as the velocity probe and carried an iron-constantan thermocouple with a tip size of 0.018 in. The thermocouple signal was offset by a reference voltage, amplified and recorded through the same filter circuit as used for the velocity measurements.

Results

Profiles were measured over the tube radius furthest from the point of entry of the probe and were periodically checked for symmetry across the whole diameter. Heat flux was calculated from the electrical input. Mean velocities were determined by heat

Nomenclature

A = axial temperature gradient, dT/dz
C_p = specific heat at constant pressure
D = inside diameter of tube
f = Fanning friction factor
g = acceleration due to gravity
g_c = gravitational constant
h = heat transfer coefficient
k = thermal conductivity
Nu = Nusselt number, hD/k
p = pressure
Pe = Peclet number, Pe = Re × Pr
Pr = Prandtl number, $C_p\mu/k$
q = heat flux
R = tube radius
Ra = Rayleigh number, $(\beta g A D^4/\nu^2)$Pr
Re = Reynolds number, $u_m D/\nu$
r = radial distance from tube center
T = fluid temperature
T_m = mean cup temperature
T_{xm} = cross-sectional mean temperature
U = dimensionless velocity, u/u_m
u = axial fluid velocity
u_m = average fluid velocity
u^* = friction velocity, $u_m\sqrt{f/2}$
u^+ = dimensionless velocity, u/u^*
y = radial distance from tube wall
y^+ = dimensionless distance, yu^*/ν
α = thermal diffusivity, $k/\rho C_p$
β = coefficient of volume expansion
ϵ_H = eddy diffusivity of heat
ϵ_M = eddy diffusivity of momentum
η = dimensionless radius, r/R
μ = viscosity
ν = kinematic viscosity, μ/ρ
ρ = density
ρ_{xm} = density at T_{xm}
ϕ = dimensionless temperature difference, $k(T - T_{xm})/4\rho u_m C_p A D^2$

Subscripts

c = at the tube center
w = at the tube wall

Table 1 Operating conditions for nonisothermal profile measurements

V = Run carried out to measure velocity profile
T = Run carried out to measure temperature profile

Run No.	Re × 10^{-3}		Ra/Re		q_w Btu/hr ft²		Nu	T_m deg F	$T_w - T_c$ deg F
	V	T	V	T	V	T	T	T	T
1	21.5	19.6	4.90	5.38	1550	1570	11.2	103.6	6.81
2	19.6	19.4	2.83	2.86	837	842	9.9	93.4	4.47
3	20.5	19.3	1.82	1.91	568	572	9.4	78.0	3.23
4	19.8	19.0	1.20	1.26	363	364	8.0	79.5	2.60
5	19.3	19.0	0.75	0.80	228	233	7.1	76.5	1.91
6	19.3	18.8	0.56	0.58	167	165	7.4	75.1	1.34
7	18.2	18.9	0.49	0.47	138	137	7.2	73.8	1.15
8	18.7	19.0	0.34	0.35	102	103	7.3	73.4	.0.80
9	38.0	35.0	3.81	4.04	3590	3610	12.2	119.5	13.8
10	34.2	33.6	1.76	1.76	1550	1540	10.3	97.2	7.64
11	32.2	33.1	1.03	0.96	835	846	8.9	85.5	5.26
12	32.5	30.8	0.44	0.47	368	359	8.8	70.1	2.39
13	63.2	65.0	1.61	1.54	4860	4810	11.3	108.8	20.8
14	65.4	62.4	0.83	0.90	2580	2670	10.0	91.0	14.0
15	62.2	61.6	0.62	0.62	1840	1840	10.8	84.3	9.73
16	60.6	61.0	0.13	0.12	361	363	12.8	68.1	1.40
17	18.6	[a]	0.26	[a]	79	[a]	[a]	[a]	[a]
20	[a]	32.2	[a]	0.16	[a]	137	9.0	73.3	0.82

[a] Corresponding profile not measured.

balance, by integration of the velocity profile, and by using the orifice meter in the loop; the maximum variation between the three values was in the range 2–6 percent, except for Runs 1 and 9 (identified later) where the integrated velocity was found to be about 10 percent higher than the values obtained by the other two methods.

Isothermal Velocity Profiles. Velocity distributions under isothermal conditions were measured at Reynolds numbers from 18,500 to 84,400. Experimental results are given in Fig. 2, which shows that the data are in very good agreement with the correlation of Travis, et al. [5] for isothermal flow in pipes. Satisfactory operation of the experimental system is thus confirmed.

In this paper, isothermal velocity profiles used for comparative purposes are designated with a prefix *I*.

Nonisothermal Velocity and Temperature Profiles. Velocity and temperature distributions for Reynolds numbers of approximately 2-, 3-, and 6 × 10^4, under heated conditions, are shown in Fig. 3, and operating conditions are summarized in Table 1.

Velocity Profiles. It is clear that heat flux exerts a very strong influence on the shape of the velocity profile. Fig. 3 shows that, with increasing heat flux, the center velocity decreases and the position of maximum velocity switches from the center to the vicinity of the wall. As explained in the next section, the changes in shape are primarily attributable to the magnitude of the vertical buoyancy forces that are superimposed on the flow field by the radial temperature distribution.

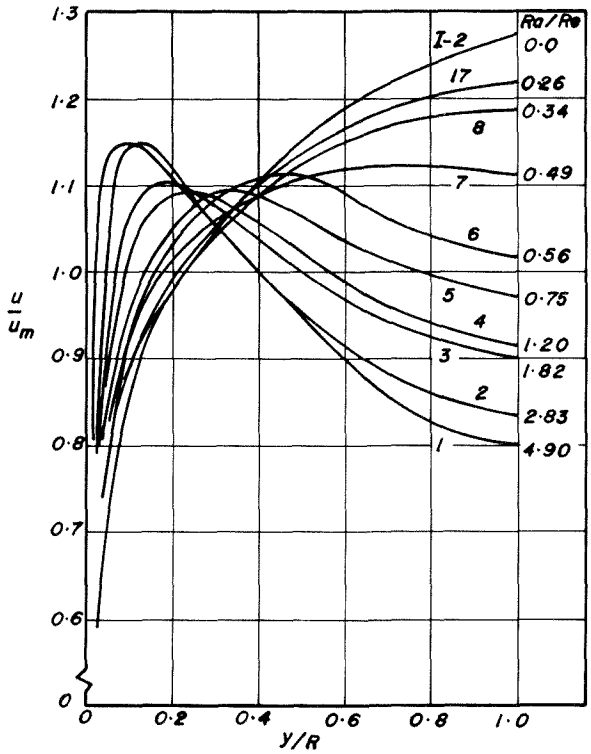

Fig. 3(*a*)

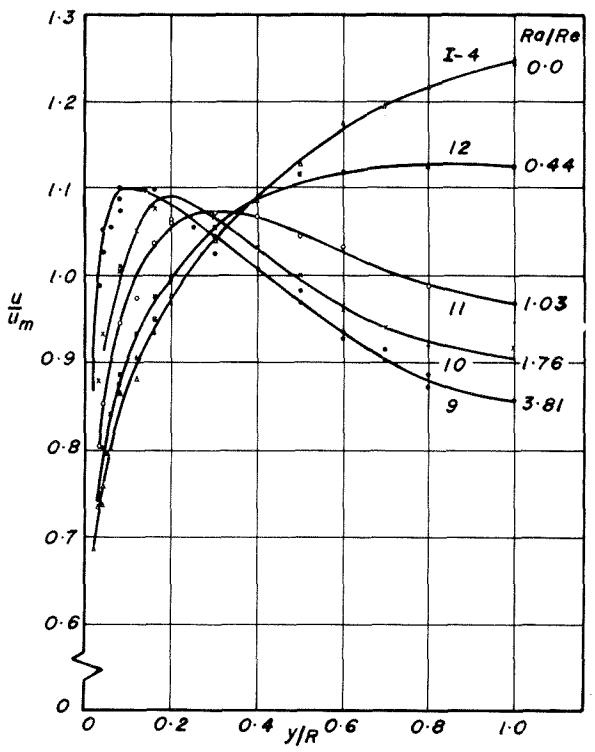

Fig. 3(*b*)

The effect of heat input on the velocity profile may be more clearly characterized by considering a particular radial position, such as the pipe center, and plotting the change in dimensionless velocity at that position versus a heat flux parameter. For this purpose, a suitable parameter was found to be the term Ra/Re, which allows data for different Reynolds numbers to be adequately combined on one plot. Fig. 4 thus shows the variation in dimensionless velocity versus Ra/Re, for a number of radial positions, and includes some further data taken by Louw [6] in the same apparatus. The curves shown indicate trends and permit the estimation of a velocity profile for a given heat flux condition over the range of Reynolds numbers investigated here.

Consideration of Figs. 3 and 4 shows that a rapid decrease in the center-line velocity occurs at low heat flux, and, over the relatively low Ra/Re range of 0 to 1, the profile switches from the isothermal shape to a condition where the maximum velocity occurs at 30 percent or less of the radial distance from the pipe wall. The exceptional sensitivity of the velocity profile to heat input is well illustrated by noting that, for the distortion exhibited by Run 5, Fig. 3, the radial temperature difference was only 1.9 deg F.

As heat flux is further increased, its influence on the velocity profile diminishes and it appears that a limiting profile shape is approached at high heat flux, with the center-line velocity about 80 percent of the mean, and the velocity maximum occurring at a radial position of about 10 percent from the wall. The approach to a limiting shape at high heat flux is confirmed by the flattening of the curves in Fig. 4.

Temperature Profiles. The measured radial temperature distributions are given in Fig. 3, while Fig. 5 shows the variation of the normalized temperature difference with Ra/Re for three radial positions. A similar general trend is evident at each position; the dimensionless temperature values, as plotted, initially decrease and then increase as heat flux is increased. The lowest profile occurs in the range Ra/Re = 0.4–0.6, the same range over which the velocity profile is found to undergo its sharpest change in shape.

It appears from Fig. 5 that normalized temperatures tend toward a constant value with increasing heat flux and that the temperature profile therefore also approaches a limiting shape at high heat flux.

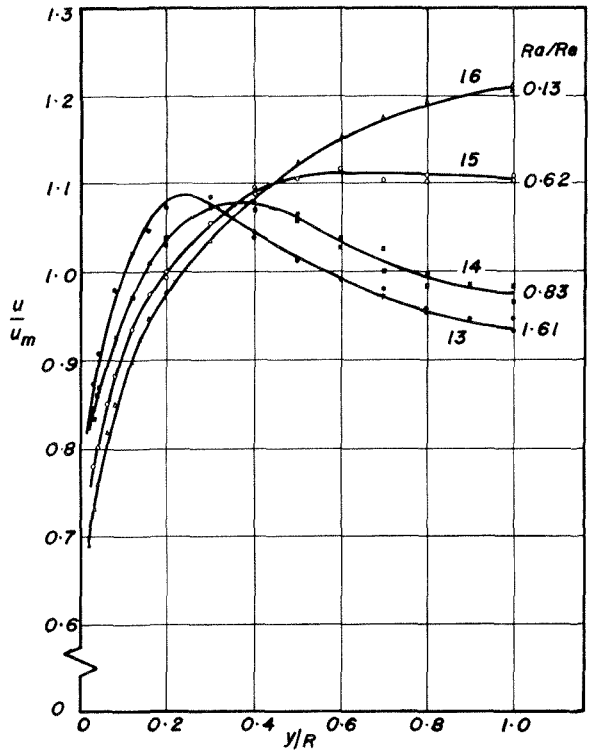

Fig. 3(c)

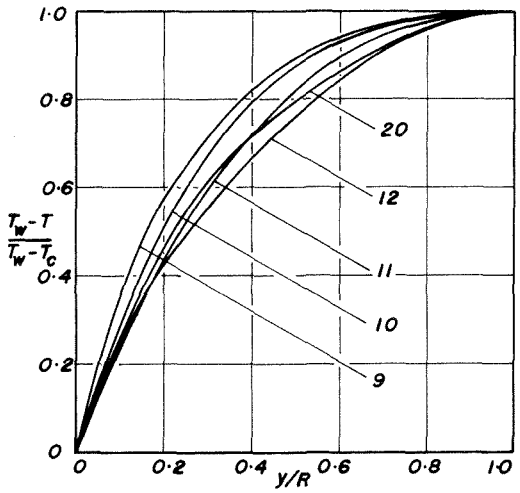

Fig. 3(e)

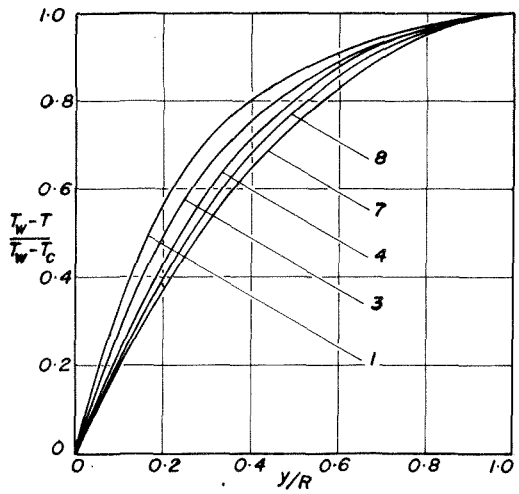

Fig. 3(d)

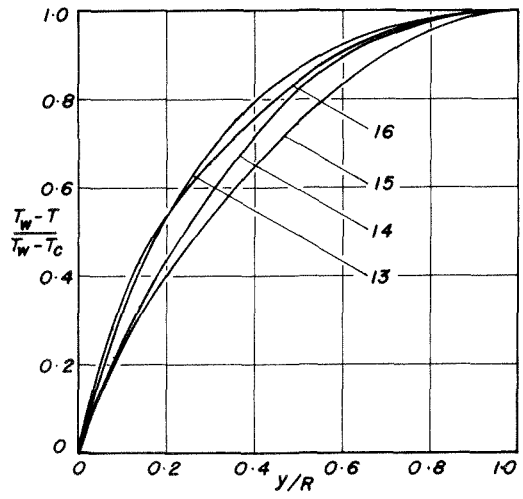

Fig. 3(f)

Fig. 3 Effect of heat flux on velocity and temperature distributions in mercury

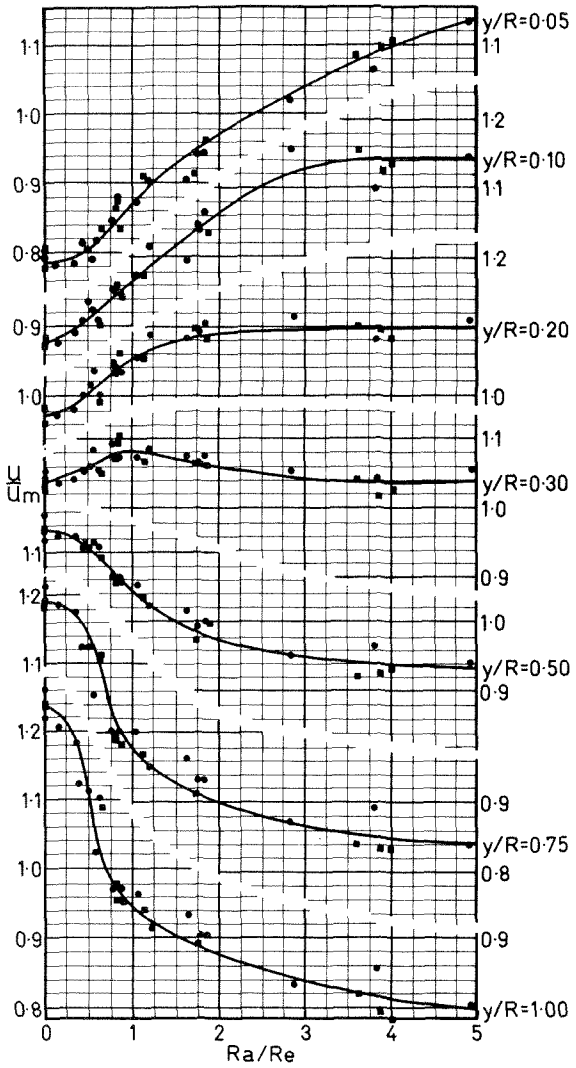

Fig. 4 Variation of velocity with heat flux, at a given radial position

● This work, Re = 20,000–60,000
■ Louw [6], Re = 30,000–55,000
— Mean curve through the data

Discussion

Buoyancy Effects in Turbulent Flow. In order to explain the observed distortion of velocity and temperature profiles with heat flux, the effect of a variation in physical properties on the equations of turbulent flow must be investigated.

The equation of motion for fully developed vertical upflow in a circular pipe, assuming incompressibility and radial symmetry, may be written as

$$\frac{1}{r}\frac{d}{dr}\left\{\mu r\left(1+\frac{\epsilon_M}{\nu}\right)\frac{du}{dr}\right\}=\frac{dp}{dz}g_c+\rho g \tag{1}$$

where ϵ_M, the eddy diffusivity of momentum, represents the turbulent contribution to momentum transfer. Preliminary computation showed that the effect of a variation in physical properties with temperature is significant only in respect to the density in the driving force term on the right in equation (1). Accordingly, mean physical properties, evaluated at the mean cup temperature, are used, while the temperature variation of the indicated density term is expressed as

$$\rho=\rho_{xm}\{1-\beta(T-T_{xm})\}. \tag{2}$$

The reference temperature, T_{xm}, is here chosen as the cross-sectional mean temperature,

$$T_{xm}=\frac{\int_0^R 2\pi rT\,dr}{\pi R^2} \tag{3}$$

in order that the reference density ρ_{xm} may also be used to describe the mean hydrostatic head in the pipe cross section. On substitution of (2), the right-hand side of equation (1) thus becomes

$$\frac{dp}{dz}g_c+\rho_{xm}g-\rho_{xm}g\beta(T-T_{xm}), \tag{4}$$

and, by a force balance over the pipe cross section, the first two terms may be written in terms of the standard friction factor relationship, as

$$\frac{dp}{dz}g_c+\rho_{xm}g=-\frac{2u_m\mu}{D^2}f\,\mathrm{Re}. \tag{5}$$

In terms of the dimensionless parameters defined in the Nomenclature, the equation of motion now becomes

$$\frac{1}{\eta}\frac{d}{d\eta}\left\{\eta\left(1+\frac{\epsilon_M}{\nu}\right)\frac{dU}{d\eta}\right\}=-0.5f\,\mathrm{Re}-\phi\,\mathrm{Ra}. \tag{6}$$

The energy equation, describing the distribution of heat in turbulent flow, may be written in a form corresponding to equation (1) as

$$\frac{1}{r}\frac{d}{dr}\left\{kr\left(1+\frac{\epsilon_H}{\alpha}\right)\frac{dT}{dr}\right\}=\rho C_p u\frac{dT}{dz} \tag{7}$$

and for constant heat flux, constant specific heat and a fully-developed temperature profile, it may be shown that

$$dT/dz=A,\ \text{a constant}. \tag{8}$$

In dimensionless terms, equation (7) becomes

$$\frac{1}{\eta}\frac{d}{d\eta}\left\{\eta\left(1+\frac{\epsilon_H}{\alpha}\right)\frac{d\phi}{d\eta}\right\}=\frac{U}{16}. \tag{9}$$

In their integrated form, equations (6) and (9) may be used to evaluate the eddy diffusivities ϵ_M and ϵ_H by

$$\frac{\epsilon_M}{\nu}+1=\frac{-0.25f\,\mathrm{Re}\,\eta-\dfrac{\mathrm{Ra}}{\eta}\displaystyle\int_0^\eta\phi\eta\,d\eta}{dU/d\eta} \tag{10}$$

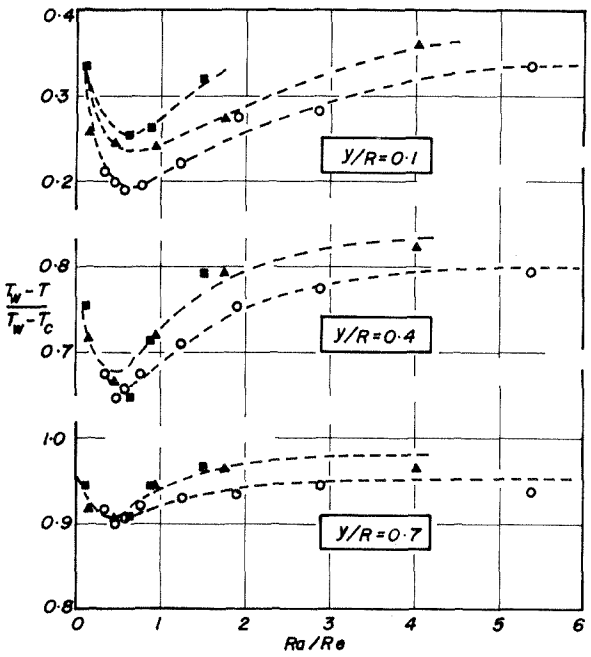

Fig. 5 Variation of dimensionless temperature with heat flux

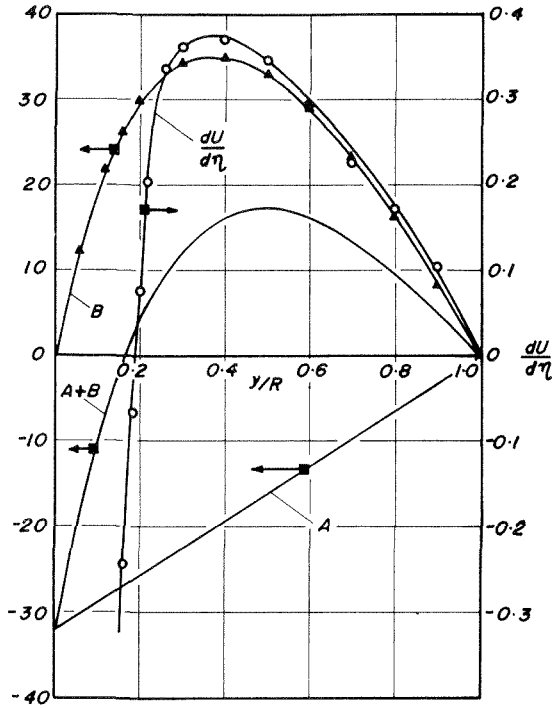

Fig. 6 Typical shear stress and velocity gradient distribution (Run 3): Re $\simeq$ 20,000; qw $\simeq$ 840 Btu/hr ft^2; *A*, *B* first and second terms in the numerator of equation (10)

and

$$\frac{\epsilon_H}{\alpha} + 1 = \frac{1}{16} \frac{\int_0^\eta U\eta \, d\eta}{\eta \, d\phi/d\eta} \cdot \tag{11}$$

Inspection of equation (10) shows that the two terms in the numerator represent the shear stress distribution in the flowing fluid, and it is instructive to consider the variation of these terms over the pipe cross section. Fig. 6 illustrates the relative magnitude of the two terms in a typical case, Run 3. The straight line A in the diagram represents the first term, which would be the normal linear shear stress distribution for an isothermal case. Curve *B* shows the additional stress contributed by the differential buoyancy forces as represented by the second term. Adding *A* and *B*, it is clear that the nonisothermal shear stress distribution, *A* + *B*, is greatly different from the isothermal, *A*, and it follows that an entirely different velocity distribution should be expected for nonisothermal, as compared to isothermal conditions.

While the linear shear stress, as shown, is always negative, it is seen that the nonisothermal curve becomes positive toward the tube center and passes through zero at some position intermediate between the center and the wall. At zero shear stress, a zero velocity gradient would be expected, and the $dU/d\eta$ curve given in Fig. 6 shows that such a condition is approximated fairly closely. In all runs the two zero points coincided to within a radial position of 2 percent. Since the $dU/d\eta$ curve is calculated from the experimental velocity profile, while the shear stress is based on the analysis presented here, the close agreement between the zero points of the two curves lends support to both the analysis and the experimental results.

It should be noted that the friction factor, *f*, used in equation (10) represented the wall shear stress under the actual (nonisothermal) conditions of operation, and could therefore be evaluated from the slope of the velocity profile at the wall. In these experiments, however, the use of a combined pitot-static tube did not allow readings to be taken in the immediate vicinity of the wall. Also, as mentioned previously, it was not possible to obtain accurate pressure drop measurements from which *f* could be evaluated. Hence, in these calculations, isothermal values of the friction factor were used. Such an approximation appears to be justified by the close agreement of the shear stress and velocity gradient zeroes discussed in the foregoing.

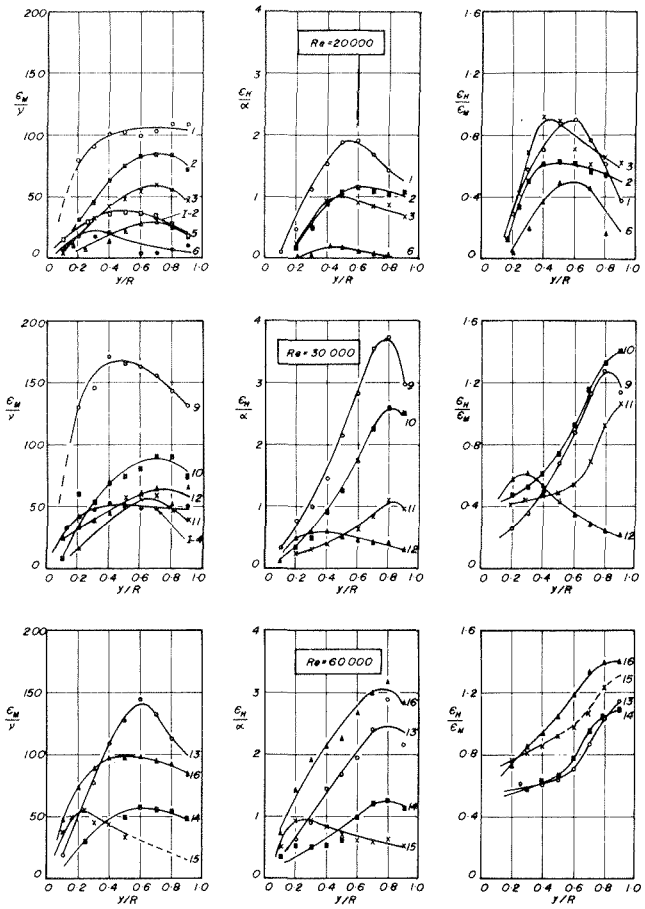

Fig. 7 Eddy diffusivities of heat and momentum numerals indicate Run numbers

It is clear that most of the data presented here lie in a region that might be described as a "mixed free- and forced convection" regime, and comparison with the well-known chart of Metais and Eckert [7] is of some interest. The present experimental results, however, are found to lie in the "forced convection" area, somewhat above the "mixed convection" regime. The Metais-Eckert chart, which was constructed for Pr $\geq$ 1, is thus not suitable for use with liquid metals.

Eddy Diffusivities. Values of the eddy diffusivities of heat and momentum, shown in Fig. 7, were calculated from equations (10) and (11), using isothermal values of the friction factor, as in the foregoing. Where required for integration or differentiation, second- or third-order polynomials were fitted to small groups of experimental data points at a time, and the required operation carried out over the center of the range. It may be observed that equation (10) will yield infinite values for ϵ_M/ν where $dU/d\eta$ is zero, if the numerator is not also identically zero at the same point. Since, in practice, the two points were close together, very large computed values in this region have been ignored. Also, for the low Re, low Ra runs, $(1 + \epsilon_H/\alpha)$ values are very close to unity, so that ϵ_H/α is subject to considerable uncertainty, and these values have not been included in Fig. 7.

The figure shows that the radial eddy diffusivity distribution is not a function of Reynolds number alone, but that it also exhibits a considerable variation with the Rayleigh number. After an initial decrease, the trend of eddy diffusivities is to increase with increasing Rayleigh number.

Fig. 7 also shows the ratio of eddy diffusivities, ϵ_H/ϵ_M. The variation with Rayleigh number is such that no clear impression regarding the relationship between heat and momentum transfer in turbulent flow emerges.

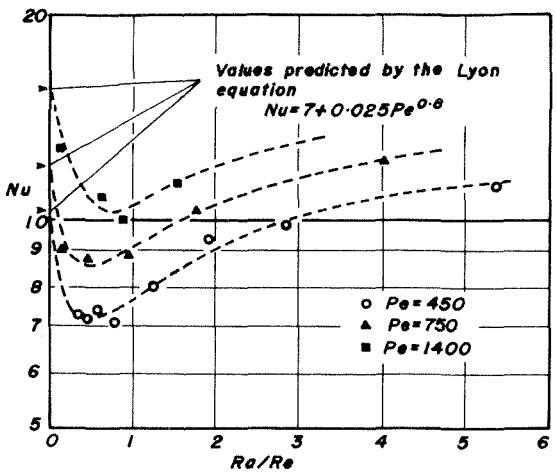

Fig. 8 Variation of Nusselt number with heat flux

Nusselt numbers. Since both velocity and temperature distributions are available for these experiments, the true mean cup temperature may be evaluated by integration, and hence local Nusselt numbers may be calculated. The variation of Nusselt number with increasing heat input is shown in Fig. 8. Nu values at low heat input are 25–30 percent below those predicted by the usual Lyon [8] equation and, in general, increase with increasing heat flux.

Conclusions

This paper presents a quantitative evaluation of the effect of heat input on the turbulent velocity and temperature distribution for mercury flowing vertically upwards in a circular pipe. A major conclusion reached from these measurements is that the shape of the velocity profile changes markedly with heat input. For high heat flux it appears that a limiting profile shape is approached. Corresponding changes also occur in the shape of the temperature profile. A consideration of the shear stress terms in the equation of motion confirms that velocity profile distortion is expected on heating, giving a maximum in the vicinity of the wall rather than in the tube center.

It has not been generally recognized that superimposed free convection effects distort the turbulent velocity profile, and many workers have assumed an isothermal velocity distribution in heat transfer calculations. Fig. 4 indicates, however, that such an assumption would only be valid for values of Ra/Re below about 0.1.

Because of the changes occurring in the velocity profile, it would be expected that the nature of the turbulence in the pipe would also change on heating. Such a change in the turbulence structure is indicated by the appreciable variation of eddy diffusivities with heat flux.

Acknowledgment

The authors wish to acknowledge financial support received from the S.A. Council for Scientific and Industrial Research, and from the S.A. Atomic Energy Board.

References

1 Martinelli, R. C., "Heat Transfer to Molten Metals," TRANS. ASME, Vol. 61, 1939, pp. 947–957.

2 Ojalvo, M. S., and Grosh, R. J., "Combined Free and Forced Turbulent Convection in a Vertical Tube," Argonne National Laboratory Report ANL-6528, 1962.

3 Buhr, H. O., Carr A. D., and Balzhiser, R. E., "Temperature Profiles in Liquid Metals and the Effect of Superimposed Free Convection in Turbulent Flow," *International Journal of Heat and Mass Transfer*, Vol. 11, 1968, pp. 641–654.

4 Horsten, E. A., "Combined Free and Forced Convection in Turbulent Flow of Mercury," PhD thesis, University of Cape Town, 1971.

5 Travis, J. R., Buhr, H. O., and Alexander Sesonske, "A Model for Velocity and Eddy Diffusivity Distributions in Fully Turbulent Pipe Flow," *Canadian Journal of Chemical Engineering*, Vol. 49, 1971, pp. 14–18.

6 Louw, R. A., "Velocity and Temperature Distributions for Mercury in Turbulent Flow," MSc thesis, University of Cape Town, 1971.

7 Metais, B., and Eckert, E. R. G., "Forced, Mixed, and Free Convection Regimes," JOURNAL OF HEAT TRANSFER, TRANS. ASME, Series C, Vol. 86C, 1964, pp. 295–296.

8 Lyon, R. N. "Liquid Metal Heat Transfer Coefficients," *Chemical Engineering Progress*, Vol. 47, 1951, pp. 75–79.

ERRATA

An errata on C. C. Gentry and D. E. Wollersheim, "Local Free Convection to Non-Newtonian Fluids From a Horizontal, Isothermal Cylinder," published in the February, 1974, issue of the JOURNAL OF HEAT TRANSFER, pp. 3-8.

Equation (4), term $\{\int_{\phi=0}^{\phi}(\sin\phi)^{\frac{1}{2n+1}}d\phi\}^{\frac{1}{3n+1}}$ should be $\{\int_{\phi=0}^{\phi}(\sin\phi)^{\frac{1}{2n+1}}d\phi\}^{\frac{n}{3n+1}}$

Equation (8) $G(n) = E(\frac{B}{C})^{\frac{n}{3n+1}}(\frac{D}{E})^{\frac{1}{3n+1}}$ should be $G(n) = E(\frac{B}{C})^{\frac{1}{3n+1}}(\frac{D}{E})^{\frac{n}{3n+1}}$

R. K. Shah
Research Engineer,
Harrison Radiator Division,
General Motors Corp.,
Lockport, N. Y. Mem. ASME

A. L. London
Professor,
Department of Mechanical Engineering,
Stanford University,
Stanford, Calif. Fellow ASME

Thermal Boundary Conditions and Some Solutions for Laminar Duct Flow Forced Convection

The importance of laminar flow forced convection theoretical solutions for the design of compact heat exchangers has been well realized. Many of these theoretical solutions published in the literature are difficult to interpret by a designer, because thermal boundary conditions used in the analysis are generally not defined clearly and consistently. The objective of this paper is to clarify this situation by a systemized presentation. Starting with a general classification, nine specific thermal boundary conditions are categorized for singly connected ducts. At the end, the most useful fully developed laminar flow solutions for some important duct geometries are summarized for the designer.

Introduction

The importance of forced convection theoretical solutions for the design of compact heat exchangers has been long realized. Many of these theoretical solutions published in the literature, using highly sophisticated mathematical and numerical techniques, are difficult to interpret by a designer. This is because thermal boundary conditions are generally not defined clearly and consistently. Thermal boundary conditions are the specifications of temperature and/or heat flux conditions at the wall of the duct. The objective of this paper is to clarify and systemize various thermal boundary conditions associated with duct flow forced convection heat transfer.

These heat transfer results are strongly dependent on the thermal boundary condition in the laminar flow regime, while very much less dependent in the turbulent flow regime for fluids with $Pr \geq 1$. Hence, the classification of the thermal boundary conditions made here is mainly useful for the laminar flow theory, even though the boundary conditions are applicable for both laminar and turbulent flows.

Laminar duct flow forced convection heat transfer solutions up to 1964 were compiled by Kays and London [1][1] for what is described here as (T) and (H1) boundary conditions. Based on a 1971 compilation [2], the present effort augments and extends the range of thermal boundary conditions to a wider range of heat exchanger applications.

Thermal boundary conditions are classified here only for singly connected ducts. Those for doubly and multiply connected ducts are summarized in [11].

[1] Numbers in brackets designate References at end of paper.

Contributed by the Heat Transfer Division of THE AMERICAN SOCIETY OF MECHANICAL ENGINEERS and presented at the Winter Annual Meeting, New York, N. Y., November 26-30, 1972. Revised manuscript received by the Heat Transfer Division, April 25, 1973. Paper No. 72-WA/HT-54.

Dimensionless groups associated with laminar duct flow analytical solutions should be defined in a uniform manner for ready interpretation by the designer. This aspect is discussed separately in [3].

Classification

A large variety of thermal boundary conditions can be specified for the constant cross-sectional duct of Fig. 1. These are categorized in three groups (horizontally) in Table 1: *(1)* specified axial wall temperature distribution t_w, *(2)* specified axial wall heat flux distribution q'', and *(3)* a specified combination of axial wall temperature and wall heat flux distributions. Around the periphery of the duct, Γ, any combination of t_w, q'' or $(q'' \propto t_w^n)$ may be specified. These boundary conditions may be applicable to either thermally developed or thermally developing flow, or both. A classification of these thermal boundary condition sets and their applications to the thermally developed or developing flows are outlined in Table 1.

It may be emphasized that the classification of thermal boundary conditions made here is applicable either to developing or fully developed velocity fields. If the velocity field is fully developed, the superposition methods mentioned below can be readily employed to derive solutions for arbitrary variations in t_w or q'' axially or peripherally. In contrast, if the velocity field is developing, a large number of thermal entrance solutions, with heating started at different locations in the hydrodynamic entry length, would be required for the superposition for a complete solution to arbitrary variations in t_w or q''. As a result, the superposition methods are less useful for simultaneously developing velocity and temperature fields.

For the case of specified arbitrary variations in wall temperature or wall heat flux, the solution to the energy equation may be obtained by superposition methods. Literature sources describing the superposition methods for arbitrary variations in t_w or q'' axially or peripherally are indicated in Table 1. Since so many

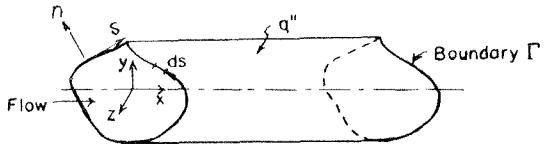

Fig. 1 A singly connected duct of constant cross-sectional area

boundary conditions can be generated by the superposition techniques, specific names are not recommended for axially variable thermal boundary conditions.

Boundary conditions, which include a combination of axial and peripheral heat conduction as well as thermal resistance in the wall, are difficult to analyze. One technique is to attempt to solve directly the so-called conjugated heat transfer problem. This type of problem is formulated for the entire solid body-fluid medium system, rather than using a priori specified boundary conditions of any kind. It involves the simultaneous solution of the energy equations for the solid and fluid media by considering temperatures and heat fluxes equal at the solid-fluid interface, as in equation (4). The velocity distribution for the fluid medium must first be found by solving the applicable continuity and momentum equations. Luikov, et al. [13, 14] solved the conjugated problem for the circular tube, while references [13, 14, 15, 16] solved the conjugated problem for the parallel plates. Luikov, et al. [13, 14] also formulated a criterion to solve the convection problem as a conjugated problem.

In the Russian literature [12, 13], conjugated problems and boundary conditions of four kinds are widely used for unsteady heat conduction problems. These are also applied to the duct flow forced convection heat transfer. In the most general form, these boundary conditions are

$$\text{First kind:} \quad t_w = t_w(x,y,z,\tau), \tag{1}$$

$$\text{Second kind:} \quad q_w'' = q_w''(x,y,z,\tau), \tag{2}$$

$$\text{Third kind:} \quad q_w'' = U_w(t_{w0} - t_w), \tag{3}$$

$$\text{Fourth kind:} \quad t_w(\tau) = [t_f(\tau)]_w \tag{4a}$$

$$q_w''(\tau) = [q_f''(\tau)]_w \tag{4b}$$

Boundary conditions of first, second and third kinds are, respectively, the Cases 1*d*, 2*d*, and the restricted 3*d* of Table 1 (corresponding to the linear functional relationship of equation (6*b*)), except that in steady laminar or quasi-steady turbulent flow, no time dependence is involved.

As the foregoing boundary conditions do not make any distinction between axial and peripheral conditions, and as solutions appear in the literature with this distinction, some specific thermal boundary conditions are proposed and systemized for *thermally developed and developing flows*. They are summarized in Table 2 and are described in the following section in further detail for the singly connected duct (Fig. 1) for negligible axial heat conduction in the fluid. From the solutions for these boundary conditions, a solution may be obtained for arbitrary variations in corresponding parameters by superposition methods. These basic boundary conditions are relatively simple for mathematical analysis, are

Nomenclature

A = heat transfer area
A_c = flow cross-sectional area
a' = duct wall thickness
c_p = specific heat of fluid at constant pressure
D_h = $4A_c/P$ = hydraulic diameter of the duct
(H1) = thermal boundary condition referring to constant axial wall heat flux with constant peripheral wall temperature
(H2) = thermal boundary condition referring to constant axial wall heat flux as well as constant peripheral wall heat flux
h = convective heat transfer coefficient
K_p = $k_w a'/kD_h$ = peripheral wall heat conduction parameter, dimensionless
k = thermal conductivity, for fluid if no subscript
m = exponent in equation (19*a*)
n, s = outer normal and tangential coordinates at a point on the duct periphery Γ
n^*, s^* = dimensionless coordinates n/D_h and s/D_h
p = fluid pressure
P = wetted perimeter of the duct (length of boundary Γ)
Pe = $u_m D_h/\alpha$ = Re Pr = Péclet number, dimensionless
Pr = $\mu c_p/k$ = fluid Prandtl number, dimensionless
q' = wall heat transfer rate per unit length of the duct; $q' = q''P$; it is assumed to be from wall-to-fluid for convenience
q'' = wall heat flux, heat transfer rate per unit area A of the duct; it is an average value with respect to perimeter, $q''P = \int q_p'' ds$; for fully developed flow, if neither x nor m appears as a subscript
q_p'' = peripheral local wall heat flux
Re = $\rho u_m D_h/\mu$ = Reynolds number, dimensionless
R_w = $k/U_w D_h$ = dimensionless wall thermal resistance
T = temperature of the fluid, on the absolute scale deg R or deg K
(T) = thermal boundary condition referring to constant wall temperature peripherally as well as axially
(T3) = thermal boundary condition referring to constant axial outside wall temperature with finite normal wall thermal resistance
(T4) = radiant-flux boundary condition
Δt = constant axial wall-to-fluid bulk temperature difference
t = temperature of the fluid to a specified arbitrary datum, deg F or deg C
t_m = $(1/u_m A_c) \int_{A_c} u\ t\ dA_c$ = fluid bulk mean temperature
t_w = wall or fluid temperature at the inside duct periphery Γ
t_{w0} = wall temperature at the outside duct periphery
$t_{w,m}$ = $(1/P)\int_\Gamma t_w ds$ = perimeter average wall temperature
U_w = wall thermal conductance, defined by equation (7)
u = fluid axial velocity, fluid velocity component in x direction
u_m = $(1/A_c) \int_{A_c} u\ dA_c$ = mean axial velocity
W = $\rho u_m A_c$ = fluid mass flow rate through the duct
x = cartesian coordinate along the flow direction
x^* = $x/(D_h \text{Pe})$ = dimensionless axial coordinate for thermal entrance region
y, z = cartesian coordinates across the flow cross section
α = $k/\rho c_p$ = fluid thermal diffusivity
Γ = inside periphery of the duct wall
γ = $\epsilon_w \sigma T_e^3 D_h/k$ = radiative wall heat-flux boundary condition parameter, dimensionless
ϵ_w = emissivity of the wall material
μ = fluid dynamic viscosity coefficient
ρ = fluid density
σ = Stefan-Boltzmann constant
τ = time

Subscripts

e = initial value at $x = 0$ (at entrance) or where the heat transfer starts
f = fluid
m = mean
p = pertaining to a local peripheral point on Γ
x = denoting arbitrary section along the duct length, a local value as opposed to a mean value
w = wall or fluid at the wall

Table 1 General classification of thermal boundary conditions

General Classification	Specified t_w, q' or q'' = $f(t_w)$ axially and/or peripherally, as noted in columns (a) through (d)			
	constant axially constant peripherally (a)	constant axially variable peripherally (b)	variable axially constant peripherally (c)	variable axially variable peripherally (d)
(1) Specified t_w axially	(T). Applicable to both thermally developed and developing flow.	Only (T3), (T4) analyzed Applicable to both thermally developed and developing flow.	Analyzed by superposition methods (4, 5, 6) from the solution of Case 1 (a); also (T4). Applicable to thermally developing flow only.	No known solution. Applicable to thermally developing flow only.
(2) Specified q'' axially	(H1), (H2). Applicable to both thermally developed and developing flow.	Analyzed by superposition methods (7, 8) from the solution of Case 2 (a); also (H3), (H4).	Analyzed by superposition methods (9, 10) from the solution of Case 2 (a). Applicable to thermally developing flow only. Also H2 analyzed for thermally developed flow only.	No known solution. Applicable to thermally developing flow only.
(3) Specified $q'' = f(t_w)$ axially	No known solution. Applicable to both thermally developed and developing flow.	No known solution. Applicable to both thermally developed and developing flow.	No known solution. Applicable to developing flow only.	No known solution. Applicable to thermally developing flow only.

Table 2 Thermal boundary conditions for developed and developing flow through singly connected ducts

Designation	Description	Equations	Applications
(T)	Constant wall temperature peripherally as well as axially	$t\|_\Gamma = t_w$ = constant, independent of (x,y,z)	condensers, evaporators, automotive radiators (at high flows), with negligible wall thermal resistance
(T3)	Constant axial wall temperature with finite normal wall thermal resistance	$t_w(x,y,z) = t_w(y,z)$, indep. of x; $\frac{\partial t}{\partial n^*}\|_\Gamma = \frac{1}{R_w}(t_w - t\|_\Gamma)$	same as those for (T) with finite wall thermal resistance
(T4)	Nonlinear radiant-flux boundary condition	$T_a(x,y,z) = T_a(y,z)$, indep. of x; $\frac{\partial T^*}{\partial n^*}\|_\Gamma = -\gamma\left[T^{*4}\|_\Gamma - T_a^{*4}\right]$	radiators in space power systems, high temperature liquid metal facilities, high temperature gas flow systems
(H1)	Constant axial wall heat flux with constant peripheral wall temperature	$q'(x)$ = constant, indep. of x; $t\|_\Gamma = t_w$ = constant, independent of (y,z)	same as those for (T4) for highly conductive materials
(H2)	Constant axial wall heat flux with uniform peripheral wall heat flux	$q'(x)$ = constant, indep. of x; $k\frac{\partial t}{\partial n^*}\|_\Gamma$ = constant, indep. of (y,z)	same as those for (T4) for very low conductive materials with the duct having uniform wall thickness
(H3)	Constant axial wall heat flux with finite normal wall thermal resistance	$q'(x)$ = constant, indep. of x; $\frac{\partial t}{\partial n^*}\|_\Gamma = \frac{1}{R_w}(t_w - t\|_\Gamma)$	same as those for (T4) with finite normal wall thermal resistance and negligible peripheral wall heat conduction
(H4)	Constant axial wall heat flux with finite peripheral wall heat conduction	$q'(x)$ = constant, indep. of x; $\frac{q''_p h}{k} - \frac{\partial t}{\partial n^*}\|_\Gamma + K_p\frac{\partial^2 t}{\partial s^{*2}}\|_\Gamma = 0$	electric resistance heating, nuclear heating, gas turbine regenerator, counterflow heat exchanger with $C_{min}/C_{max} \neq 1$, all with negligible normal wall thermal resistance
(H5)	Exponential axial wall heat flux	$q'_x = q'_e e^{mx^*}$; $t\|_\Gamma = t_w$ = constant, independent of (y,z)	parallel and counterflow heat exchangers with appropriate values of m
(ΔT)	Constant axial wall to fluid bulk temperature difference	$\Delta t(x) = t_{w,in} - t_{b,in}$ = constant, independent of x; $t\|_\Gamma = t_w$=constant, indep. of (y,z)	gas turbine regenerator

realized approximately in practical systems and have been analyzed to a varying degree for ducts of different cross section [2, 4]. Thermal boundary conditions which yield thermally fully developed flow for a long duct are limited in number. According to the authors' knowledge, Table 2 appears to be a complete list of such thermal boundary conditions.

The following nomenclature scheme is used for these boundary conditions. Generally two characters are enclosed in a circle; the first character T or H represents axially constant wall temperature or heat transfer rate, respectively; the second character, a numeral 1, 2, or 3 indicates respectively the foregoing boundary conditions of the first, second or third kind of the peripheral direction, in a restricted sense.[2] For example, (H1) represents constant axial heat transfer rate q' with constant peripheral surface temperature. The numerals 4 and 5 designate specialized axial or peripheral boundary conditions.

[2] For boundary conditions of the first, second and third kind, the constant temperature, constant heat flux, and a linear combination of heat flux and wall temperature are specified, respectively, peripherally around the duct boundary for the present classification scheme.

Constant Axial Wall Temperature, (T), (T3), and (T4). The thermal boundary conditions of approximately constant axial wall temperature is realized in many practical applications; for example, condensers, evaporators and automotive radiators at high liquid flows. If the wall temperature is also uniform peripherally, the boundary condition will be referred to as (T). According to the foregoing proposed scheme, it should have been designated as (T1); but as the wall temperature is the same everywhere, it is designated for convenience as (T). The peripheral constant wall heat flux case, (T2), is not realized in practical applications, and hence it is of less importance; moreover solutions are not available in the literature. The (T3) and (T4) have linear and nonlinear combinations of wall heat flux and temperature on the duct periphery as described in the following text.

(T) Boundary Condition. The wall temperature of the duct is constant, both axially and peripherally, for this boundary condition,

$$t|_\Gamma = t_w = \text{constant, independent of } (x,y,z). \qquad (5)$$

The constant wall temperature condition can be pictured in two ways: (i) With reference to Fig. 2, the thermal resistances of both the wall and the t_a fluid are zero, and t_a is constant. For this case the axial wall thermal conductivity can be arbitrary, but the normal (radial) thermal conductivity is implicitly assumed to be infinite. (ii) The wall thermal conductivity is idealized to be infinite in the axial and peripheral directions; therefore, the normal thermal conductivity or normal wall temperature profile is not involved in this analysis.

Some of the technical applications of (T) boundary condition

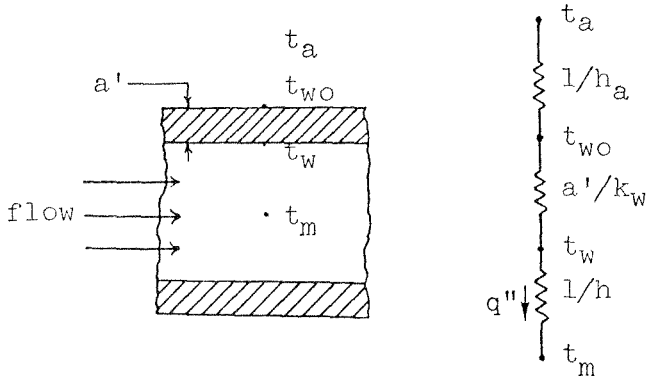

Fig. 2 Thermal circuit representation of the resistances

are indicated in Table 2. The (T) boundary condition has been analyzed for parallel plates, and circular, rectangular, isosceles triangular, sine, elliptical, and concentric annular ducts [2].

(T3) *Boundary Condition.* The outside wall temperature is constant axially, while the convected heat flux peripherally is linearly proportional to the wall temperature difference $(t_{w0} - t_w)$ of Fig 2.

$$t_{w0}(x,y,z) = t_{w0}(y,z), \text{ independent of } x, \tag{6a}$$

$$k \left.\frac{\partial t}{\partial n}\right|_\Gamma = U_w(t_{w0} - t|_\Gamma) . \tag{6b}$$

Note that the inside wall temperature $t_w = t|_\Gamma$ for this boundary condition is a function of (y, z) as well as x, unlike the outside wall temperature t_{w0} which does not depend on x.

The reciprocal of the proportionality constant in equation (6*b*), $1/U_w$, will be referred to as the wall thermal resistance. It is based on the inside duct wall area. For a straight, thin wall of uniform thickness a', it is

$$\frac{1}{U_w} = \frac{a'}{k_w} . \tag{7a}$$

For a circular tube of radius a and wall thickness a', it is

$$\frac{1}{U_w} = \frac{a \ln (1 + \frac{a'}{a})}{k_w} . \tag{7b}$$

If the outside wall to fluid thermal resistance is included in $1/U_w$, as is done sometimes in a condenser design,

$$\frac{1}{U_w} = \frac{a'}{k_w} + \frac{1}{h_a} . \tag{7c}$$

The corresponding wall heat flux of equation (6*b*) would be (from Fig. 2)

Insert ($$q'' = U_w(t_a - t|_\Gamma) . \tag{6c}$$

In the literature, t_a is generally considered as a constant. After dividing n by the characteristic dimension D_h, equation (6*b*) reduces to

$$\left.\frac{\partial t}{\partial n^*}\right|_\Gamma = \frac{1}{R_w}(t_{w0} - t|_\Gamma) , \tag{8}$$

where the dimensionless wall thermal resistance $R_w = k/U_w D_h$.

Implicit idealizations made for wall thermal conductivity for the (T3) boundary condition are described in Table 3. Two limiting cases of this boundary condition are (i) when the wall thermal resistance R_w approaches zero, (T3) reduces to the (T) boundary condition; (ii) when the wall thermal resistance R_w approaches infinity, $q'' = 0$ axially as well as peripherally, which is a special case of the (H2) boundary condition (q'' = constant everywhere). Thus when $R_w \to \infty$, the (T3) solution goes to (H2) .[3]

Some of the technical applications of the (T3) boundary condition are outlined in Table 2. The (T3) boundary condition has been analyzed for parallel plates and circular, elliptical, sine, and concentric annular ducts [2].

(T4) *Boundary Condition.* For this boundary condition, wall thermal resistance R_w is considered as zero so that $t_{w0} = t_w$ in Fig. 2. The outside fluid or the environment temperature T_a is now idealized as constant axially. Wall heat flux peripherally is nonlinearly proportional to wall temperature; a situation existing when the duct wall is radiating thermal energy to the environment.

[3] Nu_{H2} is higher than Nu_T for the circular tube, parallel plates and elliptical ducts, while Nu_{H2} is lower than Nu_T for sine ducts. Hence, with increasing value of R_w, Nu_{T3} will increase for the circular tube, parallel plates and elliptical ducts, while Nu_{T3} will decrease for the sine ducts. This is the reason for the apparently strange behavior of Nu_{T3} for sine ducts, not explained by [17].

Table 3 Idealizations of wall thermal conductivity implied for the thermal boundary conditions of Table 2

Thermal Boundary Condition	Axial k_w	Peripheral k_w	Normal k_w
(T)	arbitrary infinite	arbitrary infinite	infinite arbitrary
(T3)	zero	zero	finite
(T4)	zero	zero	infinite
(H1)	zero	infinite	infinite
(H2)	zero	zero	infinite
(H3)	zero	zero	finite
(H4)	zero	finite	infinite
(H5)	zero	infinite	infinite
(Δt)	zero	infinite	arbitrary

$$T_a(x,y,z) = T_a(y,z), \text{ independent of } x, \tag{9a}$$

$$-k \left.\frac{\partial T}{\partial n}\right|_\Gamma = \epsilon_w \sigma[T|_\Gamma{}^4 - T_a{}^4] , \tag{9b}$$

Here the equivalent temperature of the environment, T_a, is defined by

$$\alpha_w H = \epsilon_w \sigma T_a{}^4 . \tag{10}$$

where α_w is the absorptivity of wall material and H is the incident radiant energy. In the literature, T_a is usually taken as zero. $T_w = T|_\Gamma$ is a function of x for the (T4) boundary condition, as it is for the (T3) boundary condition.

Nondimensionalizing temperature and normal direction with T_e and D_h, respectively, and after some rearrangement, equation (9*b*) reduces to

$$\left.\frac{\partial T^*}{\partial n^*}\right|_\Gamma = -\gamma[T^*|_\Gamma{}^4 - T_a{}^{*4}] , \tag{11}$$

where the radiation parameter $\gamma = \epsilon_w \sigma T_e{}^3 D_h/k$.

Implicit idealizations made for the wall thermal conductivity for the (T4) boundary condition are described in Table 3. Two limiting cases of the (T4) boundary condition are: (i) when γ approaches ∞, (T4) reduces to the (T) boundary condition; (ii) when γ approaches 0, (T4) reduces to the (H2) boundary condition.

Some of the technical applications of the (T4) boundary condition are outlined in Table 2. The (T4) boundary condition has been analyzed only for the circular tube [2].

Constant Axial Wall Heat Flux, (H1) , (H2) , (H3) , and (H4) . The thermal boundary condition of approximately constant axial heat rate per unit duct length ($q' \simeq$ constant) is realized in many practical applications; for example, electric resistance heating, nuclear heating, counterflow heat exchanger with equal thermal capacity rates (Wc_p). This boundary condition will be referred to as (H) when there is no peripheral variation of wall temperature (or wall heat flux). This is the case for symmetrically heated straight ducts having constant peripheral curvature and no corners, e.g., circular duct, parallel plates, and concentric annular ducts. However, for symmetrically heated noncircular ducts (with corners or variable peripheral curvature), the peripheral wall temperature and/or heat flux are variable. Four simplified cases of these variations are: (i) the peripheral wall temperature constant, with the peripheral heat flux being variable, (ii) the peripheral wall heat flux constant, with the peripheral temperature

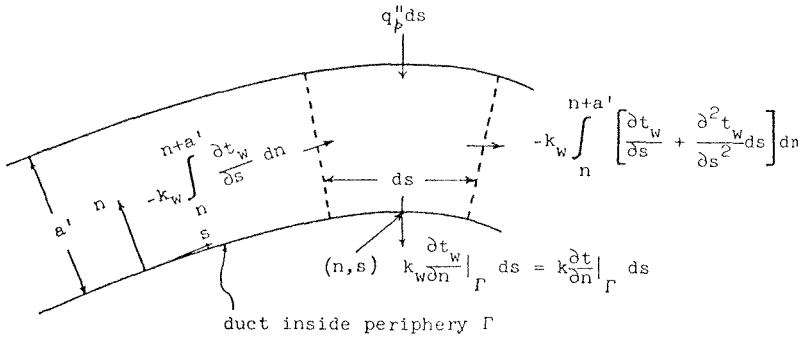

Fig. 3 Energy transfer terms in the duct wall cross section for finite peripheral conduction

being variable, (iii) the peripheral local heat flux linearly proportional to the wall temperature at that point, and (iv) finite peripheral heat conduction so that both the peripheral wall temperature and heat flux are varying. These four boundary conditions for noncircular ducts (e.g., rectangular, triangular, elliptical, etc.) will be referred to as (H1), (H2), (H3), and (H4), respectively. They are described below.

(H1) Boundary Condition. The wall heat transfer rate is constant in the axial direction, while the wall temperature at any cross section x is constant in the peripheral direction, for the (H1) boundary condition.

$$q'(x) = Wc_p\frac{dt_m}{dx} = \text{constant, independent of } x, \qquad (12a)$$

$$t|_\Gamma = t_w = \text{constant, independent of } (y,z)\,. \qquad (12b)$$

Implicit idealizations made for wall thermal conductivity for (H1) boundary condition are described in Table 3.

The (H1) boundary condition is a limiting case of a generalized boundary condition (H4) to be described. For a heat exchanger with highly conductive materials, the (H1) boundary condition may apply. In practice, it may be difficult to achieve this boundary condition for noncircular ducts [18]. However, as it is mathematically amenable, it is the most frequently investigated boundary condition in the literature and solutions are available for twenty duct geometries [2]. Nu_{H1} is always higher than Nu_T for a given duct geometry, as explained in [2, 4].

Note that q' is related to average and peripheral local wall heat fluxes q'' and q_p as

$$\frac{q'}{P} = q'' = \frac{1}{P}\int_\Gamma q_p''ds\,. \qquad (13)$$

(H2) Boundary Condition. The wall heat flux q'' is constant in the axial as well as the peripheral direction for this boundary condition.

$$q''P = q' = Wc_p\frac{dt_m}{dx} = \text{constant, independent of } x, \qquad (14a)$$

$$k\frac{\partial t}{\partial n}\Big|_\Gamma = q_p'' = \frac{q'}{P} = \text{constant, independent of } (y,z) \text{ as well as } x. \qquad (14b)$$

Implicit idealizations made for the wall thermal conductivity are described in Table 3.

For a heat exchanger with constant q' and low thermal conductivity materials, the (H2) boundary condition may be realized, if the wall thickness all around the duct periphery is uniform. This boundary condition, after (H1), is also easily amenable to analysis. Solutions have been obtained for rectangular, isosceles triangular, sine, circular segment, regular polygonal and cardioid ducts [2].

Nu_{H2} is lower than Nu_{H1} for noncircular ducts, due to corner or curvature effects, as explained in [2, 11]. The (H2) boundary condition is a limiting case of the (H4) boundary condition to be described.

(H3) Boundary Condition. The wall heat transfer rate is constant in the axial direction, the same as equation (12*a*), while the heat flux is linearly proportional to the wall temperature in the peripheral direction, the same as equations (6*b*) or (8). Thus

$$q'(x) = Wc_p\frac{dt_m}{dx} = \text{constant, independent of } x, \qquad (15a)$$

$$\frac{\partial t}{\partial n^*}\Big|_\Gamma = \frac{1}{R_w}(t_{w0} - t|_\Gamma)\,. \qquad (15b)$$

Implicit idealizations made for the wall thermal conductivity for the (H3) boundary condition are described in Table 3. Two limiting cases of the (H3) boundary condition are: (i) when the wall thermal resistance R_w approaches zero, (H3) reduces to (H1); (ii) when R_w approaches infinity, (H3) reduces to (H2).

This boundary condition appears to be of less practical importance and has not been analyzed for noncircular ducts.

(H4) Boundary Condition. Wall heat transfer rate q' is constant in the axial direction and finite wall heat conduction is specified in the peripheral direction for this boundary condition.

To derive the peripheral boundary condition, consider a steady-state energy balance on the wall element ds of unit depth in Fig. 3. The temperature distribution in the wall is related to the wall heat flux along the periphery as

$$q_p'' - k\frac{\partial t}{\partial n}\Big|_\Gamma + k_w\frac{\partial^2}{\partial s^2}\int_n^{n+a'} t_w\,dn = 0\,. \qquad (16)$$

The temperature across any cross section for a *thin wall* may be taken as uniform. This is equivalent to assuming zero wall thermal resistance in the normal direction. If the wall thickness a' is uniform, then

$$\int_n^{n+a'} t_w\,dn \simeq a't|_\Gamma\,. \qquad (17)$$

After dividing n and s by characteristic dimension D_h and some rearrangement, equation (16) reduces to

$$\frac{q_p''D_h}{k} - \frac{\partial t}{\partial n^*}\Big|_\Gamma + K_p\frac{\partial^2 t}{\partial s^{*2}}\Big|_\Gamma = 0\,, \qquad (18a)$$

where $K_p = k_w a'/kD_h$ is the peripheral heat conduction parameter. Additionally, along the axial direction,

$$q'(x) = Wc_p\frac{dt_m}{dx} = \text{constant, independent of } x. \qquad (18b)$$

The equation set (18*a*) and (18*b*) constitutes the (H4) boundary condition.

Implicit idealizations made for the wall thermal conductivity for the (H4) boundary condition are described in Table 3. The peripheral k_w is used in equation (16) and in the parameter K_p. The

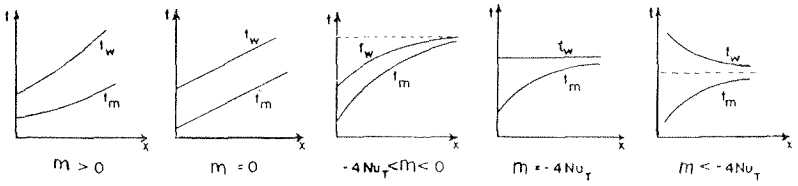

Fig. 4 (H5) temperature variations along the circular tube length

Table 4 Solutions for heat transfer and friction for fully developed laminar flow through specified ducts [2]

GEOMETRY ($L/D_h > 100$)	Nu_{H1}	Nu_{H2}	Nu_T	fRe
2b, 2a; $\frac{2b}{2a} = \frac{\sqrt{3}}{2}$	3.014	1.474	2.39*	12.630
2a, 60°, 2b; $\frac{2b}{2a} = \frac{\sqrt{3}}{2}$	3.111	1.892	2.47	13.333
2b, 2a; $\frac{2b}{2a} = 1$	3.608	3.091	2.976	14.227
	4.002	3.862	3.34*	15.054
2b, 2a; $\frac{2b}{2a} = \frac{1}{2}$	4.123	3.017	3.391	15.548
	4.364	4.364	3.657	16.000
2b, 2a; $\frac{2b}{2a} = .9$	5.099	4.35*	3.66	18.700
2b, 2a; $\frac{2b}{2a} = \frac{1}{4}$	5.331	2.930	4.439	18.233
2b, 2a; $\frac{2b}{2a} = \frac{1}{8}$	6.490	2.904	5.597	20.585
$\frac{2b}{2a} = 0$	8.235	8.235	7.541	24.000
$\frac{b}{a} = 0$, insulated	5.385	-	4.861	24.000

*interpolated values

special cases, $K_p = \infty$ and 0, yield the (H1) and (H2) boundary conditions, respectively, as is evident from Table 3.

Some of the many important technical applications of the (H4) boundary conditions are described in Table 2; but solutions are available only for a square duct [2, 19].

A more generalized boundary condition, which takes into account the wall heat conduction in the peripheral direction as well as a finite wall thermal resistance in the normal direction, has been discussed by Lyczkowski, et al. [19].

Exponential Axial Wall Heat Flux, (H5). The axial wall heat flux varies exponentially along the flow length, while the peripheral wall temperature is constant at a particular section x for this boundary condition.

$$q_x' = q_c' e^{mx^*}, \tag{19a}$$

$$t|_\Gamma = t_w = \text{constant, independent of } (y,z) \text{ but varies with } x. \tag{19b}$$

Implicit idealizations made for the wall thermal conductivity for the (H5) boundary condition are described in Table 3.

The wall and fluid bulk mean temperatures are shown in Fig. 4 for varying values of the exponent m for the circular tube. For $m = 0$, the (H5) boundary condition reduces to the (H1) boundary condition. For $m = -4Nu_T$, it reduces to the (T) boundary condition for the concentric annular duct family. The (H5) boundary condition with an appropriate value of m (Fig. 4) can be used to approximate either the parallel or counterflow heat exchanger for which the fluid bulk mean temperature varies exponentially along the duct. Solutions are available for circular tubes, parallel plates, concentric annular ducts, and longitudinal flow over parallel rods [2].

Constant Axial Wall-to-Fluid Temperature Difference, (Δt). The wall-to-fluid bulk mean temperature difference is constant in the axial direction, while the wall temperature at any cross section is uniform for the (Δt) boundary condition.

$$\Delta t(x) = t_w - t_m = \text{constant, independent of } x, \tag{20a}$$

$$t|_\Gamma = t_w = \text{constant, independent of } (y,z). \tag{20b}$$

It is implied that the wall thermal conductivity is zero in the axial direction, infinite in the peripheral direction, and arbitrary in the normal direction, Table 3.

Two limiting cases of the (Δt) boundary condition are: (i) when x approaches zero (i.e., in the thermal entrance region very close to the point of step change in wall temperature), then (Δt) approaches the (T) boundary condition; and (ii) when x approaches infinity (i.e., near the fully developed region), (Δt) approaches the (H1) boundary condition.

The (Δt) boundary condition has been analyzed only for the circular tube [20].

Laminar Flow Solutions

As shown in the description of the thermal boundary conditions, (T), (H1), and (H2) are limiting thermal boundary conditions of more generalized boundary conditions (T3), (T4), (H3), and (H4). The latter boundary conditions take into account the wall thermal resistance or wall heat conduction peripherally.

The magnitudes of Nu_T, Nu_{H1}, and Nu_{H2} for different duct geometries are useful for design purposes. To this end, the available literature information is summarized in [2]. These magnitudes for some of the practically more important duct geometries and fully developed laminar flow are condensed in Table 4, for the constant property Newtonian fluid. This table augments and corrects Fig. 6-1 of Kays and London [1]. Note that the following effects are excluded for the Nusselt numbers of Table 4: free convection, mass diffusion, chemical reaction, etc., as well as the axial heat conduction, viscous dissipation and thermal energy sources within the fluid.

Conclusions and Recommendations

Conclusions and recommendations derived from this work are summarized as follows.

1 Throughout the heat transfer literature, thermal boundary conditions associated with the duct flow forced convection problem are generally not defined in a consistent manner. These are defined and systemized in this paper for the interpretation of theoretical results by a designer.

2 Table 1 outlines the general classification of thermal boundary conditions. Table 2 presents specific thermal boundary conditions for singly connected ducts. Thermal boundary conditions for doubly and multiply connected ducts are described in [11].

3 Some of the more readily useful, fully developed laminar flow solutions are summarized in Table 4.

References

1 Kays, W. M., and London, A. L., *Compact Heat Exchangers*, Second ed., McGraw-Hill, New York, 1964.

2 Shah, R. K., and London, A. L., "Laminar Flow Forced Convection Heat Transfer and Flow Friction in Straight and Curved Ducts—A Summary of Analytical Solutions," TR No. 75, Department of Mechanical Engineering, Stanford University, Stanford, Calif., Nov. 1971.

3 Shah, R. K., and London, A. L., "Dimensionless Groups for Laminar Duct Flow Forced Convection Heat Transfer," presented at the 1972 ASME Winter Annual Meeting, New York, ASME Paper No. 72-WA/HT-53.

4 Kays, W. M., *Convective Heat and Mass Transfer*, McGraw-Hill, New York, 1966.

5 Sellers, J. R., Tribus, M., and Klein, J. S., "Heat Transfer to Laminar Flow in a Round Tube or Flat Conduit—the Graetz Problem Extended," TRANS. ASME, Vol. 78, 1956, pp. 441–448.

6 Mitchell, J. W., "An Expression for Internal Flow Heat Transfer for Polynomial Wall Temperature Distribution," JOURNAL OF HEAT TRANSFER, TRANS. ASME, Series C, Vol. 91, 1969, pp. 175–177.

7 Eckert, E. R. G., Irvine, T. F., Jr., and Yen, J. T., "Local Laminar Heat Transfer in Wedge-Shaped Passages," TRANS. ASME, Vol. 80, 1958, pp. 1433–1438.

8 Reynolds, W. C., "Effect of Wall Heat Conduction on Convection in a Circular Tube With Arbitrary Circumferential Heat Input," *International Journal of Heat and Mass Transfer*, Vol. 6, 1963, p. 925.

9 Siegel, R., Sparrow, E. M., and Hallman, T. M., "Steady Laminar Heat Transfer in a Circular Tube With Prescribed Wall Heat Flux," *Applied Scientific Research*, Vol. 7, Series A, 1958, pp. 386–392.

10 Noyes, R. N., "A Fully Integrated Solution of the Problem of Laminar or Turbulent Flow in a Tube With Arbitrary Wall Heat Flux," JOURNAL OF HEAT TRANSFER, TRANS. ASME, Vol. 83, Series C, 1971, pp. 96–98.

11 Shah, R. K., and London, A. L., "Thermal Boundary Conditions for Laminar Duct Flow Forced Convection Heat Transfer," presented at the 1972 ASME Winter Annual Meeting, New York, ASME Paper No. 72-WA/HT-54.

12 Zabrodskiy, S. S., "Several Specific Terms and Concepts in Russian Heat Transfer Notation," *Heat Transfer-Soviet Research*, Vol. 4, No. 2, 1972, pp. i–iv.

13 Luikov, A. V., *Heat and Mass Transfer* (in Russian), Energia Publishing House, Chapter IV, 1972.

14 Luikov, A. V., Aleksashenko, V. A., and Akeksashenko, A. A., "Analytical Methods of Solution of Conjugated Problems in Convective Heat Transfer," *Internaltional Journal of Heat and Mass Transfer*, Vol. 14, 1971, pp. 1047–1056.

15 Shelyag, V. R., "Calculation of the Temperature Field in Plane Slotted Channels With Laminar Gas Flow," *Journal of Engineering Physics*, Vol. 12, 1967, pp. 117–120.

16 Davis, E. J., and Gill, W. N., "The Effects of Axial Conduction in the Wall on Heat Transfer with Laminar Flow," *International Journal of Heat and Mass Transfer*, Vol. 13, 1970, pp. 459–470.

17 Shernoy, D. F., and Solbrig, C. W., "Analytical Investigation of Heat or Mass Transfer and Friction Factors in a Corrugated Duct Heat or Mass Exchanger," *International Journal of Heat and Mass Transfer*, Vol. 13, 1970, pp. 145–159.

18 Irvine, T. F., Jr., "Non-Circular Duct Convective Heat Transfer," in *Modern Developments in Heat Transfer*, W. Ibele, ed., Academic Press, New York, 1963, pp. 1–17.

19 Lyczkowski, R. W., Solbrig, C. W., and Gidaspow, D., "Forced Convection Heat Transfer in Rectangular Ducts—General Case of Wall Resistances and Peripheral Conduction," Institute of Gas Technology, Technical Information Center, File 3229, Chicago, Ill., 1969.

20 Kays, W. M., "Numerical Solutions for Laminar-Flow Heat Transfer in Circular Tubes," TRANS. ASME, Vol. 77, 1955, pp. 1265–1274.

C. Comstock
A. Zargary

LCDR, Imperial Iranian Navy.

J. E. Brock

Naval Postgraduate School, Monterey, Calif.

On the Delayed Hot Water Problem

A pipe with external insulation contains a flowing fluid at constant temperature. Suddenly there is a jump in inlet fluid temperature. The subsequent temperature distribution in the fluid and in the pipe is studied by means of perturbation expansions, one of which is singular. Simplifying assumptions are explicitly stated. Some extensions and unifications of previous work are found.

1 Introduction

The analysis herein is motivated by the following problem of practical importance. A uniform homogeneous fluid flows through a semi-infinite ($x \geq 0$) pipe of inside radius $r = a$ and outside radius $r = b$, the outside of which is perfectly insulated against heat flow. Initially all fluid and pipe in $x \geq 0$ is at a uniform temperature which may be taken as zero. Suddenly both the annular end face ($x = 0$) of the pipe and the fluid entering the pipe at $x = 0$ experience a common unit increase in temperature. It is desired to determine $\theta^*(r, x, t)$, the temperature in the fluid, and $T^*(r, x, t)$, the temperature in the pipe wall, as functions of position (r, x) and time (t). If one assumes that the material properties are uniform and do not depend on position or time and if one makes the assumption of plug or slug flow, i.e., that the fluid velocity is a constant V independent of position or time, the problem may be described mathematically as follows:

$$\alpha_1 \Delta^2 \theta^* - V \frac{\partial \theta^*}{\partial x} - \frac{\partial \theta^*}{\partial t} = 0; \quad \alpha_2 \Delta^2 T^* - \frac{\partial T^*}{\partial t} = 0;$$

$$\Delta^2 = \frac{\partial^2}{\partial x^2} + \frac{1}{x}\frac{\partial}{\partial r} + \frac{\partial^2}{\partial r^2}; \qquad \partial T^*/\partial r = 0 \text{ at } r = b;$$

$$k_1 \frac{\partial \theta^*}{\partial r} = k_2 \frac{\partial T^*}{\partial r} = h^*(T^* - \theta^*) \quad \text{on the interface} \quad r = a;$$

$$T^* = \theta^* = 1 \quad \text{for } x = 0, \ t > 0;$$

$$T^* = \theta^* = 0 \quad \text{for } t = 0 \tag{1}$$

Here k denotes thermal conductivity, α denotes diffusivity, and subscripts 1, 2 refer to the fluid, pipe, respectively; α_1 includes eddy diffusivity as well as thermal diffusivity. Note that this formulation includes the influence of a finite surface heat transfer coefficient (h^*) at the interface. It is also required, obviously, that all temperatures must remain finite.

The steady-state problem of determining the temperature field has been studied in a number of papers. The fundamental paper considering both the fluid and wall simultaneously was by Perelman [1][1] where the term "conjugated problem" was introduced. This work does not consider axial diffusion in the fluid. Similar problems have been considered by several authors [2, 3, 4], where the problem is solved by considering eigenfunctions and using Duhamel's theorem. The effect of axial conduction in the fluid, as well as the wall, in the steady-state problem, is considered by Taitel, et al. [5], among others.

The time dependent problem has not been as widely studied. The early studies make the assumption that the fluid and wall temperature are the same and ignore axial conduction. One of the simplest and earliest results is due to Monk [6], whose results will be discussed later. A time varying problem, ignoring axial conduction, is studied by Sparrow and De Farias [7], using sinusoidally varying conditions. A very theoretical investigation of the time varying problem, ignoring axial conduction, is contained in Perelman, et al. [8]. A different approach, partially reported in [10], has recently been employed by one of the authors [9]. These investigations reduce to the study of singular integral equations describing the fluid temperature at the wall interface.

It is the purpose of this report to study the time dependent problem, considering axial conduction in both the fluid and the wall. To do so we must simplify our basic equations, and we accomplish this by considering a radial average of the basic equations [$\theta^*(r, x, t) \to \theta(x, t)$; $T^*(r, x, t) \to T(x, t)$]. One independent variable is eliminated and the radial conductivity and surface film conductivity are combined into a modified surface coefficient h. Equally important is the fact that the coupling between the fluid and pipe wall temperatures is made to appear in the differential equations themselves rather than in the boundary conditions. An ordinary perturbation expansion of θ (fluid temperature) and T (pipe wall temperature) is developed in powers of $\epsilon^2 = V^{-2}$ and the first two terms for each are actually obtained explicitly. It may be seen that these solutions are valid only for $x < Vt$, delta function type singularities of increasing order occurring at the "wave front," $x = Vt$. Accordingly a singular perturbation expansion is then developed in the vicinity of the wave front. This is matched in an appropriate way to the ordinary expansion obtained earlier so as to result in a composite solution valid

Contributed by the Heat Transfer Division for publication in the JOURNAL OF HEAT TRANSFER. Manuscript received by the Heat Transfer Division, October 10, 1973. Paper No. 74-HT-U.

[1]Numbers in brackets designate References at end of paper.

Table 1 Significance of quantities p, A_1, and A_2

	Pipe	Parallel plates
p	$2\pi a$	1
A_1	πa^2	$^1/_2$ width of channel
A_2	$\pi(b^2 - a^2)$	thickness of duct wall

throughout the fluid and pipe.

Our results will be seen to describe a temperature front propagating at the fluid velocity V, and interestingly enough, a second "front" propagating at a retarded velocity originally found by Monk [6].

2 Radial Averaging of Temperatures

We define the average temperatures

$$\theta(x, t) = \int_o^a r\theta^*(r, x, t)dr / \int_o^a rdr \tag{2a}$$

$$T(x, t) = \int_a^b rT^*(r, x, t)dr / \int_a^b rdr \tag{2b}$$

and introduce the "equivalent" surface film coefficient, a constant,

$$h = -k_1(\frac{\partial\theta^*}{\partial r})_{r=a}/(\theta^* - T^*) = -k_2(\frac{\partial T^*}{\partial r})_{r=a}/(\theta^* - T^*) \tag{2a}$$

Then, by partial integration of the P.D.E.'s in (1) between appropriate radial limits and introduction of the average temperatures θ and T, we obtain the new P.D.E.'s

$$\alpha_1 \frac{\partial^2\theta}{\partial x^2} - V\frac{\partial\theta}{\partial x} = \frac{\partial\theta}{\partial t} + b_1(\theta - T);$$

$$\alpha_2 \frac{\partial^2 T}{\partial x^2} = \frac{\partial T}{\partial t} - b_2(\theta - T) \tag{3a, b}$$

where

$$b_1 = \alpha_i ph/A_i k_i \ (i = 1, 2) \tag{3c}$$

and the meanings of p and A_1, A_2 are given in Table 1, the second column of which pertains to the circular pipe geometry considered thus far. However, a plane parallel configuration leads to the same formulation, the third column of Table 1 pertaining to the case where flow takes place in the space between two identical, externally insulated, semi-infinite parallel plates. Details may be found in [9].

Equations (3a), (3b) must be solved subject to the conditions

$$\theta = T = 0 \quad \text{for} \quad x \geq 0, \ t > 0$$

$$\theta, T \to 0 \quad \text{for} \quad x \to \infty, \ t \geq 0 \tag{4}$$

$$\theta = T = 1 \quad \text{for} \quad x = 0, \ t > 0$$

It is convenient to normalize by introducing the new variable

$$\eta = x/V = \epsilon x \quad (\text{where } \epsilon = V^{-1}) \tag{5}$$

so that equations (3a), (3b) become

$$\alpha_1\epsilon^2 \frac{\partial^2\theta}{\partial\eta^2} - \frac{\partial\theta}{\partial\eta} = \frac{\partial\theta}{\partial t} + b_1(\theta - T); \ \alpha_2\epsilon^2 \frac{\partial^2 T}{\partial\eta^2} = \frac{\partial T}{\partial t} - b_2(\theta - T) \tag{6a, b}$$

Conditions (4) remain the same except for η appearing in place of x.

It may be remarked that this system has been treated previously. What appears to be the most successful prior treatment is that of Hiep [10] who analyzed some problems involving granular media; his equations appear to be more general but employment of fictitious material properties in the present analysis makes it equally general. Hiep employed Laplace transformation analysis but found it necessary to use strictly numerical procedures for dealing with the transformed system and for performing the inversion. Our own experiments with the numerical inversion procedure employed by Hiep have led us to question its accuracy in this application and to seek an alternate method of dealing with the problem.

3 Ordinary Perturbation Expansion

Accordingly we consider an expansion of the solution in powers of ϵ^2 and we expect useful results if $V = \epsilon^{-1}$ is "large." Note, however, that ϵ^2 is the coefficient of the highest order derivative present so that we expect eventually to be faced with a singular perturbation problem [11]. Thus, we look initially for an expansion

$$\theta(\eta, t;\epsilon^2) = \theta_0(\eta, t) + \epsilon^2\theta_2(\eta, t) + \epsilon^4\theta_4(\eta, t) + \ldots \tag{7a}$$

$$T(\eta, t;\epsilon^2) = T_0(\eta, t) + \epsilon^2 T_2(\eta, t) + \epsilon^4 T_4(\eta, t) + \ldots \tag{7b}$$

Substituting in (6a), (6b) and equating coefficients of like powers of ϵ^2, we obtain the following sequences of equations

$$\frac{\partial\theta_0}{\partial\eta} + \frac{\partial\theta_0}{\partial t} + b_1(\theta_0 - T_0) = 0; \quad \frac{\partial T_0}{\partial\eta} - b_2(\theta_0 - T_0) = 0 \tag{8a, b}$$

$$\frac{\partial\theta_i}{\partial\eta} + \frac{\partial\theta_i}{\partial t} + b_1(\theta_i - T_i) = \alpha_1 \frac{\partial^2\theta_{i-2}}{\partial\eta^2};$$

$$\frac{\partial T_i}{\partial\eta} - b_2(\theta_i - T_i) = \alpha_2 \frac{\partial^2 T_{i-2}}{\partial\eta^2}; \ (i = 2, 4, 6, \ldots) \tag{9a, b}$$

The boundary and initial conditions are

$$\theta_0(\eta, t) = T_0(\eta, t) = 1 \quad \text{for} \quad \eta = 0, \ t > 0$$

$$\theta_i(\eta, t) = T_i(\eta, t) = 0 \quad \text{for} \quad \eta = 0, \ t > 0; \ i = 2, 4, \ldots$$

$$\theta_i(\eta, t) = T_i(\eta, t) = 0 \quad \text{for} \quad \eta \geq 0, \ t = 0; \quad i = 0, 2, 4, \ldots \tag{10}$$

In equations (9), the second derivative of the previously determined function θ_{i-2} or T_{i-2} plays the role of a known excitation. Thus equations (8) and (9) are of first order in η and only one boundary condition can be applied. Consequently it cannot be expected that the solutions will be uniformly valid.

Starting with equations (8) we simply note that they are a specialization of equations treated by Arpaci (example 7-5 reference [12]) and write the solutions immediately as

$$\theta_0(\eta, t) = \begin{cases} & ; \ \tau < 0 \\ e^{-b_1\eta}e^{-b_2\tau}I_0(2\sqrt{\sigma\tau}) + b_2\int_0^\tau e^{-b_2 y} I_0(2\sqrt{\sigma y})dy & ; \ \tau \geq 0 \end{cases} \tag{11}$$

$$T_0(\eta, t) = \begin{cases} 0 & ; \ \tau < 0 \\ b_2 e^{-b_1\eta}\int_0^\tau e^{-b_2 y} I_0(2\sqrt{\sigma y})dy & ; \ \tau \geq 0 \end{cases} \tag{12}$$

where

$$\tau = t - \eta, \tag{13}$$

and

$$\sigma = b_1 b_2 \eta \tag{14}$$

It may easily be shown that θ_0 and T_0 both approach unity as $\tau \to \infty$.

These solutions have a wave-like character with no response at all ahead of the wave front, i.e., for $\tau < 0$, that is, for $t < \eta = x/V$. For fixed t there is no disturbance in the region $x > Vt$ and for fixed x no disturbance takes place until $t \geq x/V$. In what follows, the condition $\tau \equiv t - \eta = 0$ is referred to as the wave front. Observe that although the (zero order) pipe wall temperature T_0 is continuous at the wave front, it has a discontinuous slope. The (zero order) fluid temperature θ_0 is itself discontinuous at the wave front.

The first correction terms, $\theta_2(\eta, t)$ and $T_2(\eta, t)$ are governed by first order equations (9) with forcing terms involving second derivatives of θ_0 and T_0, respectively. These nonhomogeneous terms vanish ahead of the wave front so that, correspondingly no correction is expected ahead of the wave front. We actually obtain the results (see Appendix A),

$$\theta_2(\eta, t) = \begin{cases} 0 \text{ for } \tau < 0 \\ e^{-b_1\eta}e^{-b_2\tau}\alpha_1\eta\delta'(\tau) + \alpha_1\eta(2b_1 - b_2)\delta(\tau) \\ \quad + C_0I_0(2\sqrt{\sigma\tau}) + C_1I_1(2\sqrt{\sigma\tau}) \text{ for } \tau \geqq 0 \end{cases} \quad (15)$$

$$T_2(\eta, t) = \begin{cases} 0 \text{ for } \tau < 0 \\ e^{-b_1\eta}e^{-b_2\tau}\alpha_1\eta b_2\delta(\tau) + C_3I_0(2\sqrt{\sigma\tau}) + \\ \quad C_4I_1(2\sqrt{\sigma\tau}) \text{ for } \tau \geqq 0 \end{cases} \quad (16)$$

where C_0, C_1, C_3, C_4 are algebraic functions of η and t (see Appendix A). Also $\delta(\tau)$ denotes the (Dirac) delta function and $\delta'(\tau)$ denotes its derivative.

It is evident from the analysis in the Appendix not only that the labor of obtaining further corrections (i.e., θ_i and T_i for $i > 2$) would be formidable but also that such additional corrections would have a nature similar to those already obtained, namely, that they would exhibit discontinuous behavior at the wave front and would fail completely ahead of the wave front.

The nature of the failure of the original perturbation expansion is characteristic of singular perturbation problems [11] and we are therefore led to seek a singular perturbation expansion in order resolve the difficulties which have been encountered.

4 Singular Perturbation Analyses

We have seen that the ordinary perturbation solution represented by the series (7) involves no difficultjes, except those of analytical complexity, for any $\tau > 0$, that is, at any point behind the wave front. However, as we have also seen, this solution predicts identically zero response for points ahead of the wave front (thus failing to reflect the influence of diffusion through the wave front) and also exhibits discontinuities at the wave front, contrary to what is indicated by physical considerations. A mathematical indication of the difficulty may be seen from the fact that $\epsilon^2\theta_2$ is not small *at* the wave front and presumably the same thing could be shown for $\epsilon^4\theta_4$, etc. Accordingly, we now look for another solution which will be valid throughout the vicinity of the wave front. To do this it is convenient to introduce the new variable

$$\zeta = (\eta - t)/\epsilon = -\tau/\epsilon \quad (17)$$

(we note parenthetically that $\zeta = x - Vt$), and we now seek new solutions $\theta(\zeta, t)$, $T(\zeta, t)$ which will be valid in the vicinity of $\zeta = 0$.

Making the change of independent variable from (η, t) to (ζ, t) provides the differential equations

$$\alpha_1 \frac{\partial^2\theta}{\partial\zeta^2} = \frac{\partial\theta}{\partial t} + b_1(\theta - T) \; ; \quad \epsilon\alpha_2 \frac{\partial^2 T}{\partial\zeta^2} = -\frac{\partial T}{\partial\zeta} + \epsilon\frac{\partial T}{\partial t} - \epsilon b_2(\theta - T) \quad (18a, b)$$

In contradistinction to the situation dealt with previously, now ϵ (to the first power) appears in the governing equations. Accordingly, ϵ, not ϵ^2, is the natural parameter with respect to which we now construct a new perturbation expansion

$$\theta(\zeta, t) = \theta_0(\zeta, t) + \epsilon\theta_1(\zeta, t) + \epsilon^2\theta_2(\zeta, t) + \ldots \quad (19a)$$

$$T(\zeta, t) = T_0(\zeta, t) + \epsilon T_1(\zeta, t) + \epsilon^2 T_2(\zeta, t) + \ldots \quad (19b)$$

(Later, when we match these new solutions to the solutions obtained previously, we will add a tilde to distinguish these "boundary layer" solutions.) These new solutions must satisfy the conditions

$$\theta_i = T_i = 0 \text{ for } t = 0 \; ; \; \theta_i \; , T_i \to 0 \text{ for } \zeta \to \infty \; (i = 1, 2, \ldots) \quad (20)$$

and must also satisfy appropriate conditions to the left of the wave front. Substituting (19) into (18) and equating coefficients of like powers of ϵ, provides the following series of equations.

$$\alpha_1 \frac{\partial^2\theta_i}{\partial\zeta^2} = \frac{\partial\theta_i}{\partial t} + b_1(\theta_i - T_i) \quad (i = 0, 1, 2, \ldots) \quad (21)$$

$$\frac{\partial T_0}{\partial\zeta} = 0 \quad (22a)$$

$$\alpha_2 \frac{\partial^2 T_i}{\partial\zeta^2} = -\frac{\partial T_{i+1}}{\partial\zeta} + \frac{\partial T_i}{\partial t} - b_2(\theta_i - T_i) \; ; \quad (i = 0, 1, 2, \ldots) \quad (22b)$$

We immediately see, from (20) and (22a), that

$$T_0 \equiv 0 \quad (23)$$

so that there is no zero-order term in (19b) (we remember that T is continuous at $\tau = 0$). Putting this result in the first of (21) gives the classical diffusion equation, the solution of which, subject to (20), is

$$\theta_0(\zeta, t) = A_0e^{-b_1t} \operatorname{erfc}(\zeta/2\sqrt{\alpha_1 t}) \quad (24)$$

The constant A_0 is to be determined by matching with our previous solution to the left of the wave front. The next equation to be considered becomes

$$\frac{\partial T_1}{\partial\zeta} = -b_2\theta_0 \quad (25)$$

the solution of which, subject to (20), is

$$T_1(\zeta, t) = A_0b_2e^{-b_1t}M(\zeta, t) \quad (26)$$

$$M(\zeta, t) = \int_\zeta^\infty \operatorname{erfc}\left(\frac{\lambda}{2\sqrt{\alpha_1 t}}\right) d\lambda = 2\sqrt{\alpha_1 t/\pi}e^{-\zeta^2/4\alpha_1 t} - \zeta \operatorname{erfc}\left(\frac{\zeta}{2\sqrt{\alpha_1 t}}\right) \quad (27)$$

In contrast with the ordinary perturbation problem, there is no particular analytic difficulty in obtaining higher terms. For the next component, we have the equation

$$\alpha_1 \frac{\partial^2\theta_1}{\partial\zeta^2} = \frac{\partial\theta_1}{\partial\zeta} + b_1\theta_1 - b_1b_2A_0e^{-b_1t}M(\zeta, t) \quad (28)$$

and the solution, satisfying (20), is readily obtained (by Fourier transforms) as

$$\theta_1(\zeta, t) = A_1e^{-b_1t} \operatorname{erf} c(\zeta/2\sqrt{\alpha_1 t}) + A_0b_1b_2te^{-b_1t}M(\zeta, t) \quad (29)$$

Here A_1 is a second constant of integration.

In a similar fashion we could obtain additional terms in the expansion (19). However it appears to be of greater interest and value to turn immediately to the problem of matching the two solutions in an appropriate manner.

5 Matching of Solutions

We now employ a tilde to distinguish the solutions appearing in the "boundary layer" series (19) from those appearing in the outer series (7). There is a well developed theory of perturbation expansions of the kind encountered here [11] and we will develop only the details essential to our present purpose. According to this theory our ordinary (7) and singular (19) expansion (frequently called "outer" and "inner" expansions, respectively) are actually different asymptotic expansions of the same functions θ and T, representing different arrangements of terms to suit different purposes. If this is so, then in any region where both are valid, they must agree identically in x and t in that region, *provided* one employs the complete series. However, we have at most a few terms in each expansion and must, therefore, be adroit to observe the agreement. Cole [11] presents a formal procedure which minimizes the necessity for careful insight. However, here we can proceed simply as follows. For sufficiently small $\epsilon > 0$, we observe that $\zeta = -\tau/\epsilon = (x - Vt)/\epsilon$ becomes large even if τ is small. Accordingly, the outer (first) solution (7) for small values of $\tau > 0$ should match with the inner (second) solution (19) for large values of $\zeta < 0$, and we now proceed to do this, observing also that these results can also be obtained by using Cole's intermediate expansion method.

Using standard expansions of the Bessel functions and writing everything in terms of τ and t, we obtain (for small $\tau > 0$)

$$\theta_0(\tau, t) = e^{-b_1t}[1 + (1 + b_2t)b_1\tau + 0(\tau^2)] \quad (30)$$

$$T_0(\tau, t) = e^{-b_1 t} b_2 \tau + 0(\tau^2) \tag{31}$$

$$\theta_2(\tau, t) = \alpha_1 b_1 b_2 t e^{-b_1 t}\left[b_1/b_2 - 2 - \alpha_1/\alpha_2 + (2b_1 - b_2)t + \frac{3}{2} b_1 b_2 t^2 + 0(\tau)\right] \tag{32}$$

$$T_2(\tau, t) = e^{-b_1 t}\left[\alpha_2 b_2 + (2b_1 b_2 \alpha_1 - b_2^2 \alpha_1)t + \alpha_1 b_1 b_2^2 t^2 + 0(\tau)\right] \tag{33}$$

To match these, we consider $\tilde{\theta}_i$ and $\tilde{T}_i$ for large ζ. First we observe that for large positive ζ, corresponding to *negative* τ, the complementary error functions are exponentially small and thus do, indeed, match exponentially with the zero values of θ and T for $\tau < 0$. To determine the one unknown quantity in $\tilde{\theta}_0$, namely the constant A_0, we consider $\tilde{\theta}_0$ for large positive ζ. We easily show that

$$\tilde{\theta}_0(\zeta, t) \approx A_0 e^{-b_1 t}\left[2 - 0(e^{-\zeta^2/4\alpha_1 t})\right] \tag{34}$$

Comparing (30) and (34), we see that

$$A_0 = 1/2 \tag{35}$$

provides a match which gives an identity, to zeroth order, in t and τ. We also observe that $T_0 = 0(\tau)$ and thus matches $\tilde{T}_0 \equiv 0$ to zeroth order. These zeroth order solutions are indicated in Fig. 1.

Turning to the next corrections we note that there are no terms of order ϵ in the (outer) expansion (7), and also that θ_2 and T_2 are finite for small τ (except for the delta functions); this may be shown by taking a limit as $\tau \to 0^+$ in (15) and (16). Thus, $\tilde{\theta}_0 + \epsilon\tilde{\theta}_1$ must be matched by θ_0 and $\tilde{T}_0 + \epsilon\tilde{T}_1$ must be matched by T_0. Consider the latter comparison first.

$$\tilde{T}_0 + \epsilon\tilde{T}_1 = \epsilon A_0 b_2 e^{-b_1 t}\left[-\zeta \operatorname{erfc}\left(\frac{\zeta}{2\sqrt{\alpha_1 t/\pi}}\right) + 2\sqrt{\alpha_1 t/\pi}\, e^{-\zeta^2/4\alpha_1 t}\right] \tag{36}$$

We are interested in matching this to the solution T_0, given by (31) for small positive values of τ, matching for large negative values of ζ, for which $\operatorname{erfc}(\zeta/2\sqrt{\alpha_1 t})$ is asymptotically equal to 2. Thus

$$\tilde{T}_0 + \epsilon\tilde{T}_1 \approx \epsilon A_0 b_2 e^{-b_1 t}(-2\zeta) + 0\left[\exp(-\zeta^2/4\alpha_1 t)\right] = 2A_0 b_2 e^{-b_1 t}\tau + 0[\ldots] = b_2 e^{-b_1 t}\tau + 0[\ldots] \tag{37}$$

and the proper matching with T_0 (cf. equation (31) is in fact seen to be satisfied to first order in τ.

Next, turning to matching with θ_0 (cf. equation (30)) we have

$$\tilde{\theta}_0 + \epsilon\tilde{\theta}_1 = \frac{1}{2} e^{-b_1 t}\left\{(1 + \epsilon A_1/2 + \tau b_1 b_2 t) \operatorname{erfc}\left(\frac{\zeta}{2\sqrt{\alpha_1 t}}\right) + 0\left[\exp(-\zeta^2/4\alpha_1 t)\right]\right\} \tag{38}$$

which behaves like

$$\tilde{\theta}_0 + \epsilon\tilde{\theta}_1 = e^{-b_1 t}\left\{1 + \epsilon A_1/2 + \tau b_1 b_2 t + 0\left[\exp(-\zeta^2/4\alpha_1 t)\right]\right\} \tag{39}$$

for large negative ζ. Then by taking $A_1 = 0$, the match with (30) exists except for an unmatched term $b_1\tau \exp(-b_1 t)$ appearing in θ_0. The presence of such an unmatched term is a rather common feature in singular perturbation matching. This term actually matches with a term in $\tilde{\theta}_2$ but we will not bother to show this here.

We could continue by matching $\tilde{\theta}_0 + \epsilon\tilde{\theta}_1 + \epsilon^2\tilde{\theta}_2$ with $\theta_0 + \epsilon^2\theta_2$ and matching $\tilde{T}_0 + \epsilon\tilde{T}_1 + \epsilon^2\tilde{T}_2$ with $T_0 + \epsilon^2 T_2$ but this would be merely an exercise in manipulation which would not yield new insights and would require considerable effort. However, it is true that proceeding in this fashion would indeed yield better formulas for calculating the temperature profiles in the vicinity of the moving wave front, but in light of the approximations which go into our physical model, the value of such calculations is suspect.

6 Discussion and Comparision With Other Solutions

Our outer and inner solutions, properly matched, provide the complete solution to the problem initiallly proposed. Accordingly, this development represents a useful example of perturbation methods applied to an interesting physical problem. Moreover, it presents a unified picture of what had been revealed piece-meal in some previously known solutions and it provides higher order corrections capable of affording greater accuracy.

The lowest order terms of the outer expansion (equations (10) and (11)) are well known; e.g., cf., Arpaci [12]. The next terms in the outer expansion, given in the Appendix hereto, are new, and although they are too complicated to make any striking inferences, they are readily calculable and can provide additional accuracy if desired.

The lowest order terms of the inner expansion (equations (23) and (24)) represent simply the effect of diffusion in the fluid, a well known result. The next higher order terms of the inner expansion (equations (26) and (29)) appear to be new. (Recall, from the preceding section that matching of solutions gives $A_0 = 1/2$, $A_1 = 0$.)

Prior to discussing results and comparing with other solutions, it will be useful to discuss briefly some expected features of the physical phenomena and of how these features are revealed in the various solutions. From physical considerations we expect that the thermal capacity of the originally cold pipe wall causes the hot water faucet to continue to run cold for a while even after the originally cold contents of the pipe have run out. From a simple viewpoint, one may say that the "temperature front" advances at some velocity less than the velocity V of the fluid itself. Furthermore, because of thermal capacity and longitudinal diffusion in the fluid and in the pipe, the originally abrupt temperature front "softens" as it moves downstream.

Munk [6], studying a one dimensional initial value problem with the assumption that $\theta(x, t) \equiv T(x, t)$ and with no axial diffusion, found that temperature front travels with a retarded velocity V^*

$$V^* = V/(1 + b_1/b_2) \tag{40}$$

This result is widely believed to be realistic despite the approximations made. Including axial diffusion one obtains a softening of the front, but the same retarded velocity

$$\theta(x, t) \equiv T(x, t) = 1/2\left[\operatorname{erfc}\left(\frac{x - V^* t}{2\sqrt{\alpha^* t}}\right) + \exp\left(\frac{V^* x}{2\alpha^*}\right) \operatorname{erfc}\left(\frac{x + V^* t}{2\sqrt{\alpha^* t}}\right)\right] \tag{41}$$

(cf., Hiep [10] and Zargary [9]). Here α^* is an "effective" diffusivity.

$$\alpha^* = (1 + k_2 A_2/k_1 A_1)\alpha_1/(1 + b_1/b_2) \tag{42}$$

We have abandoned the assumption $\theta(x, t) \equiv T(x, t)$, and have found a front traveling at the fluid velocity V. We now show that Munk's retarded front is contained in our solution, and in fact it is contained in the first order outer terms θ_0 and T_0.

$$\theta_0(\tau, \eta) \sim 1 - e^{-b_1\eta} e^{-b_2\tau} e^{2\sqrt{\sigma\tau}} \sqrt[4]{\sigma}/2b_2\sqrt{\pi}\, \tau^{3/4} = 1 - \exp\left\{-(\sqrt{b_1\eta} - \sqrt{b_2\tau})^2\right\}/2\sqrt[4]{\pi^2 b_2^3 \tau^3/b_1\eta} \tag{43}$$

and similarly

$$T_0(\tau, \eta) \sim 1 - \exp\left\{-(\sqrt{b_1\eta} - \sqrt{b_2\tau})^2\right\}/2\sqrt[4]{\pi^2 b_1\eta b_2\tau} \tag{44}$$

(retaing only zero and first order terms). Observe that both these expressions show relative minima at

$$\tau \approx b_1\eta/b_2 \tag{45}$$

Recalling that $\tau = t - \eta$, $\eta = x/V$ we see that this occurs at

$$x = [V/(1 + b_1/b_2)]t = V^* t \tag{46}$$

Thus, this solution does indicate a temperature front moving with Munk's retarded velocity V^*. (The fact that the temperature ap-

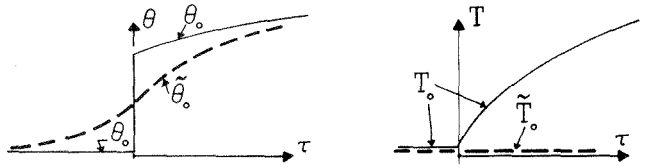

(a) Fluid Temperature (b) Pipe Wall Temperature

Fig. 1 Relation of zero-order solutions at the wave front

pears to rise again on the far side is due to our having taken only two terms.)

Softening of the temperature front results from a combination of diffusion (in each medium) and of thermal capacity. We can describe softening in terms of a characteristic length x_c (or a characteristic time $t_c = x_c/V$, say) in which there is attenuation of temperature by the factor e^{-1}. Since the function erfc is essentially like a negative exponential (for small argument), the estimate we get from equation (41) is

$$x_c = 2\sqrt{\alpha^* t} \tag{47}$$

or, expressed otherwise,

$$\frac{V^* t - x}{x_c} = 1. \tag{48}$$

Correspondingly, in equations (43) or (44) we set

$$1 = \sqrt{b_2 \tau} - \sqrt{b_1 \eta} \tag{49}$$

and by manipulation we can bring this to the form

$$\frac{V^* t - x}{\left(\frac{V}{b_1 + b_2}\right)\left(\sqrt{b_2 \tau} + \sqrt{b_1 \eta}\right)} = 1 \tag{50}$$

so that we identify the denominator on the left with the desired characteristic length, i.e.,

$$x_c = \frac{V}{b_1 + b_2}\left(\sqrt{b_2(t - \eta)} + \sqrt{b_1 \eta}\right) \tag{51}$$

To afford a comparison, we note that at the forward end of the temperature front, we have $x = V^* t$ so that (51) may be written as

$$x_c = \sqrt{Vt}\,\frac{\sqrt{b_1 V^*} + \sqrt{b_2(V - V^*)}}{b_1 + b_2}$$

$$= 2\sqrt{V}\sqrt{t\sqrt{b_1 b_2}/(b_1 + b_2)^2} \tag{52}$$

Both (47) and (52) indicate that the softening characteristic length increases as $t^{1/2}$ (thus, it also increases as $x^{1/2}$). However, from (47) and (42) we see no evidence of the influence of V whereas equation (52) indicates a linear dependence of V. This may be explained as follows. Equation (47) stems from (41) which is essentially a pure diffusion equation; the assumption $\theta(x, t) \equiv T(x, t)$ loses the effect of media at different temperatures moving relatively to one another. Thus, although the effect of thermal capacity is involved, it enters only in an idealized fashion. The linear dependence upon V, seen in equation (52), appears more reasonable from a physical viewpoint. Larger values of V imply more smearing out of the temperature front as warm fluid moves past cold pipe. Of course this linear dependence ceases to be valid as $V \to 0$ since diffusion still acts to soften the front. Our perturbation approach, in which we employ a series in terms of powers of $\epsilon = 1/V$ or of ϵ^2, makes it clear that unless V is "large" many terms of the series will be necessary. This is not evident in the previous developments which earlier led to the results given in equations (10) and (11).

Of course, actual softening is more complicated than what we have discussed so far. For example, equations (26) and (29) show a characteristic length for softening corresponding to

$$x_c = 2\sqrt{\alpha_1 t}$$

and this term, not vanishing with V, which shows the effect of longitudinal diffusion in the fluid, should be added to (or otherwise combined with) equation (52) so as to indicate a combined effect of thermal capacity and axial diffusion. However, because of the complicated nature of higher order terms, it does not seem profitable to attempt any further analytic exploration of softening or retardation.

Thus, our solution shows two fronts propagating down the pipe. The first propagates with the fluid velocity V. The inner solution (24) shows that its amplitude decays exponentially in time with a decay time of b_1^{-1}, so that after a short time this part is negligible. The second part is Munk's delayed solution, propagating with velocity V^*. Our analysis shows (equations (43) and (44)) that to first order this front decays only algebraically in time, so that for most systems, this is what one sees as he turns on the hot water faucet.

For completeness, we report an improvement, implicit in Hiep [10] and explicit in Zargary [9], over the results given in equations (10) and (11). This result, which incorporates axial conduction in the fluid, may be expressed as

$$\theta(x, t) = 1 - \frac{1}{\pi}\exp\,(Vx/2\alpha_1)\left\{\int_{\mu}^{b_2} G(\eta, t, x)\,d\eta + \int_{\lambda}^{\infty} G(\eta, t, x)\,d\eta\right\} \tag{53}$$

$$T(x, t) = b_2 \int_0^t e^{-b_2 \eta}\theta(x, t - \eta)\,d\eta \tag{54}$$

where

$$G(\eta, t, x) = \frac{1}{\eta}\,e^{-\eta t}\,\sin\left\{x\sqrt{\frac{(\eta - \mu)\,(\lambda - \eta)}{\alpha_1(b_2 - \eta)}}\right\} \tag{55}$$

$$\lambda, \mu = \frac{\omega}{2}\,(1 \pm \sqrt{1 - V^2 b_2/\alpha_1 \omega^2}) \tag{56}$$

and

$$\omega = b_2 + b_1\alpha_1 + V^2/4\alpha_1. \tag{57}$$

It may be shown that

$$\lambda > b_2 > \mu > 0. \tag{58}$$

References

1 Perelman, T. I., "On Conjugated Problems of Heat Transfer," *International Journal of Heat and Mass Transfer*, Vol. 3, 1962, p. 293.

2 Davis, E. J., and Gill, W. N., "The Effects of Axial Conduction in the Wall on Heat Transfer With Laminar Flow," *International Journal of Heat and Mass Transfer*, Vol. 13, 1970, pp. 459–470.

3 Gill, W. N., Porta, W. W., and Nunge, R. J., "Heat Transfer in Thermal Entrance Region of Cocurrent Flow Heat Exchangers With Fully Developed Laminar Flow," *International Journal of Heat and Mass Transfer*, Vol. 11, 1968, pp. 1408–1412.

4 Hsu, C-J., "Theoretical Solutions for Low-Peclet-Number Thermal-Entry-Region Heat Transfer in Laminar Flow Through Concentric Annuli," *International Journal of Heat Mass Transfer*, Vol. 13, 1973, p. 1907.

5 Taitel, Yehuda, Benturch, M., and Tamir, Abraham, "Effects of Upstream and Downstream Boundary Conditions on Heat (Mass) Transfer With Axial Diffusion," *International Journal of Heat and Mass Transfer*, Vol. 16, 1973, pp. 359–369.

6 Munk, Walter, "The Delayed Hot Water Problem," *Journal of Appl. Mech.*, Vol. 21, 1956, p. 193.

7 Sparrow, E. M., and DeFarias, F. N., "Unsteady Heat Transfer in Ducts With Time-Varying Inlet Temperature and Participating Walls," *International J. of Heat Mass Transfer*, Vol. 11, 1968, p. 837.

8 Perelman, T. L., Levitan, R. S., Gdalevich, L. B., and Khusid, B. M., "Unsteady-State Conjugated Heat Transfer Between a Semi-Infinite Surface and Incoming Flow of a Compressible Fluid—I. Reduction to the Integral Equation," *International Journal of Heat Mass Transfer*, Vol. 15, 1973, p. 2551.

9 Zargary, Abdollah, "Conjugated Transient Heat Transfer in Pipe Flow," thesis, Naval Postgraduate School, Monterey, Calif., 1972.

10 Hiep, D. D., "Heat Transfer in Porous Media," Thesis, Naval Postgraduate School, Monterey, Calif., 1965.

11 Cole, Julian, D., *Perturbation Methods in Applied Mathematics*, Blaisdel, 1968.

12 Arpaci, V. S., *Conduction Heat Transfer*, Addison-Wesley, 1966.

13 Zargary, Abdollah, and Brock, John, E., "An Integral Equation Describing Conjugate Transient Heat Transfer in Fluid Flowing Through Insulated Pipes," *International Journal of Heat and Mass Transfer*, Vol. 16, 1973, pp. 1325–1328.

APPENDIX A

Derivation of $\theta_2(\eta, t)$ and $T_2(\eta, t)$; Outer Expansion

Let

$$u_i(\eta, s) = \int_0^\infty e^{-st}\theta_i(\eta, t)\,dt;$$

$$v_i(\eta, s) = \int_0^\infty e^{-st} T_i(\eta, t)\,dt;\ i = 0, 2 \tag{A-1}$$

(i.e., Laplace transforms with respect to t). Operating on equa-

Table A-1 Coefficients m_n for u_2 (second column) and v_2 (third column) for use in equation (A-9).

	u_2	v_2
m_0	$\alpha_1\eta$	0
m_1	$2\alpha_1 b_1\eta$	$\alpha_1\eta b_2$
m_2	$b_1\eta(\alpha_1 b_1 + \alpha_2 b_2)$	$2\alpha_1 b_1 b_2\eta + \alpha_2 b_2$
m_3	$2\alpha_2 b_1^2 b_2\eta$	$b_1 b_2(\alpha_1\eta b_1 + 2\alpha_2 + \alpha_2 b_2\eta)$
m_4	$\alpha_2 b_1^3 b_2\eta$	$\alpha_2 b_1^2 b_2(1 + b_2\eta)$
m_5	0	$\alpha_2 b_1^3 b_2^2\eta$

tions (8), performing evident operations, and inverting leads to the solutions given in equations (11) and (12). In the process we obtain u_0 and v_0 prior to inversion, and can form the derivatives

$$\frac{\partial^2 u_0}{\partial\eta^2} = \frac{1}{s}p^2 e^{-\eta p};\ \frac{\partial^2 v_0}{\partial\eta^2} = \frac{b_2}{s(s+b_2)}p^2 e^{-\eta p} \quad \text{(A-2)}$$

where

$$p = s + b_1 - \frac{b_1 b_2}{s+b_2} = s\left(1 + \frac{b_1}{s+b_2}\right) \quad \text{(A-3)}$$

Taking Laplace transforms of equations (9), we find

$$\frac{\partial u_2}{\partial\eta} + (s+b_1)u_2 = b_1 v_2 + \alpha_1\frac{\partial^2 u_0}{\partial\eta^2};$$
$$(s+b_2)v_2 = b_2 u_2 + \alpha_2\frac{\partial^2 v_0}{\partial\eta^2} \quad \text{(A-4)}$$

Substituting the evaluations (A-2) and solving for v_2 in terms of u_2, we get

$$v_2 = \frac{b_2 u_2}{s+b_2} + \frac{\alpha_2 b_2}{s(s+b_2)^2}p^2 e^{-\eta p} \quad \text{(A-5)}$$

Substituting this in the first of (A-4), we obtain the first order linear equation

$$\frac{\partial u_2}{\partial\eta} + pu_2 = Ae^{-\eta p} \quad \text{(A-6)}$$

where

$$A = \left(\frac{1}{s}\right)\left[\alpha_1 + \frac{\alpha_2 b_1 b_2}{s(s+b_2)^2}\right]p^2 \quad \text{(A-7)}$$

The solution is

$$u_2 = (A\eta + B)e^{-\eta p} \quad \text{(A-8)}$$

where B is an arbitrary function of s which must be taken as zero in order to satisfy the second of equations (10). Substituting into (A-5), we get the solution for v_2

In order to invert these Laplace transforms, it is convenient first to exhibit them in the following compact form

$$u_2,\ v_2 = se^{-\eta p}\sum_{n=0}^{5} m_n(s+b_2)^{-n} \quad \text{(A-9)}$$

for which the coefficients m_n, as given in Table A-1, are independent of s

For the inversion we employ the formula

$$L^{-1}[s^{-n}e^{a/s}] = \left(\frac{t}{a}\right)^{(n-1)/2} I_{n-1}(2\sqrt{at}) \quad \text{(A-10)}$$

for integer $n \geq 1$. For $n = 0$, the formula is made valid by adding the Dirac delta function, $\delta(t)$, to the right side. (This inversion formula does not seem to appear in the literature but is not difficult to establish.)

Thus, the inverse of the function

$$f_1(\eta, s) = e^{a/s}\sum_{n=0}^{5} m_n s^{-n} \quad \text{(A-11)}$$

is

$$F_1(\eta, t) = m_0\delta(t) + \sum_{n=0}^{5} m_n(t/a)^{(n-1)/2} I_{n-1}(2\sqrt{at}) \quad \text{(A-12)}$$

and evidently the inverse of

$$f_2(\eta, s) = f_1(\eta, s + b_2) \quad \text{(A-13)}$$

is

$$F_2(\eta, t) = e^{-b_2 t}F_1(\eta, t) \quad \text{(A-14)}$$

Next, we define

$$f_3(\eta, s) = sf_2(\eta, s) \equiv [sf_2(\eta, s) - F_2(\eta, 0^+)] + F_2(\eta, 0^+)$$

the inverse of which is

$$F_3(\eta, t) = \frac{d}{dt}F_2(\eta, t) + F_2(\eta, 0^+)\delta(t) \quad \text{(A-15)}$$

$$= e^{-b_2 t}\{m_0\delta'(t) - b_2 m_0\delta(t) + \sum_{n=0}^{5} m_n\left(\frac{d}{dt} - b_2\right)$$
$$\left[\left(\frac{t}{a}\right)^{(n-1)/2} I_{n-1}(2\sqrt{at})\right]\} + m_6\delta(t) \quad \text{(A-16)}$$

where

$$m_6 = am_0 + m_1 = F_2(\eta, 0^+) = F_1(\eta, 0^+) \quad \text{(A-17)}$$

To simplify (A-16) we note first that

$$e^{-b_2 t}\{m_0\delta'(t) - b_2 m_0\delta(t)\} = m_0\delta'(t) \quad \text{(A-18)}$$

and we employ the formula

$$\left(\frac{d}{dt} - b_2\right)[(t/a)^{(n-1)/2} I_{n-1}(2\sqrt{at})] =$$
$$\left(\frac{t}{a}\right)^{(n-2)/2}\left[\left(\frac{n-1}{2}\right)\left(\frac{a}{t}\right)^{1/2} - (n-1) - b_2\left(\frac{t}{a}\right)^{1/2}\right]$$
$$I_{n-1}(2\sqrt{at}) + I_{n-2}(2\sqrt{at})\} \quad \text{(A-19)}$$

We also use the identity

$$I_{n+1}(x) = I_{n-1}(x) - (2n/x)I_n(x) \quad \text{(A-20)}$$

so as to reduce all such terms to forms containing only I_0 and I_1. Thus we arrive at the result

$$F_3(\eta, t) = m_6\delta(t) + m_0\delta'(t) + R_0(t)I_0(2\sqrt{at}) + R_1(t)I_1(2\sqrt{at}) \quad \text{(A-21)}$$

in which

$$R_0(t) = e^{-b_2 t}C_0(t),\ R_1(t) = e^{-b_2 t}C_1(t) \text{ for inverting } u_2 \quad \text{(A-22}b\text{)}$$

$$R_0(t) = e^{-b_2 t}C_2(t),\ R_1(t) = e^{-b_2 t}C_3(t) \text{ for inverting } v_2 \quad \text{(A-22}a\text{)}$$

and the functions $C_i(t)$ are

$$C_0(t) = [(b_1 b_2\eta^2\alpha_1)t^{-1} + b_1\eta\alpha_1(b_1 - 2b_2) + \alpha_1\alpha_2 b_1 b_2 + (\alpha_2 b_1)$$
$$(b_1 - 2b_2 + 2\eta^{-1})t] \quad \text{(A-23}a\text{)}$$

$$C_1(t) = (a/t)^{3/2}[-\alpha_1 b_1^{-1}b_2^{-1} + \alpha_1\eta(2b_1 - b_2)(t/a)$$
$$+ (2\alpha_2 b_1^2 b_2\eta - \alpha_2 b_1^2 - \alpha_2 b_1 b_2^2\eta - \alpha_1 b_1^2 b_2\eta$$
$$- 2\alpha_2 b_1\eta^{-1} + 2\alpha_2 b_1 b_2)(t/a)^2 - (\alpha_2 b_1^3 b_2^2\eta)(t/a)^3] \quad \text{(A-23}b\text{)}$$

$$C_2(t) = [(\alpha_2 b_2 + 2b_1 b_2\alpha_1\eta - \alpha_1 b_2^2\eta) +$$
$$(2b_1 b_2\eta + 5b_1 - b_2^2\eta + 2b_2 + 8\eta^{-1} -$$
$$b_1 b_2\eta\alpha_1\alpha_2^{-1})(\alpha_2 b_1 b_2)(t/a) - (\alpha_2 b_1^3 b_2^3\eta)(t/a)^2] \quad \text{(A-23}c\text{)}$$

$$C_3(t) = (a/t)^{1/2}[\alpha_1 b_2\eta + (\alpha_2)(b_1 b_2^2\eta - b_1\eta^{-1} - 6b_1 b_2\eta^{-1} -$$
$$2b_2\eta^{-1} - 8\eta^{-2} + 2b_1^2 b_2)(t/a)^{1/2} +$$
$$(\alpha_1 b_1 b_2\eta)(b_1 - 2b_2 + \eta^{-1})(t/a) +$$
$$(\alpha_2 b_1^2 b_2^2\eta)(b_1 - 2b_2 - 3\eta^{-1})(t/a)^2] \quad \text{(A-23}d\text{)}$$

Finally, by taking

$$a = b_1 b_2\eta \quad \text{(A-24)}$$

we see from (A-9) that

$$u_2,\ v_2 = e^{-(s+b_1)\eta}f_3(\eta, s) \quad \text{(A-25)}$$

whence, from (A-21) we have

$$\theta_2(\eta, t),\ T_2(\eta, t) = \begin{cases} 0 \text{ if } \tau = t - \eta < 0 \\ e^{-b_1\eta}F_3(\eta, \tau) \text{ if } \tau = t - \eta \geq 0 \end{cases} \quad \text{(A-26)}$$

These results appear as equations (15) and (16) in the body of the paper. Equations (A-18) indicate that a factor $e(-b_2 t)$ may be used to multiply $\delta(t)$ and $\delta'(t)$ as has been done in (15) and (16).

M. Roidt
Fellow Engineer,
Heat Transfer and Fluid
Dynamics Department,
Westinghouse Research Laboratories,
Pittsburgh, Pa.

M. J. Pechersky
Senior Engineer,

R. A. Markley
Manager,

LMFBR Thermal and Hydraulic Development,
Westinghouse Advanced Reactors Division,
Madison, Pa.

B. J. Vegter
Engineer,
Heat Transfer and Fluid Dynamics Dept.,
Westinghouse Research Laboratories,
Pittsburgh, Pa. Assoc Mem. ASME

Determination of Turbulent Exchange Coefficients in a Rod Bundle[1]

A tracer gas is injected into a single subchannel of a large air flow model of a reactor rod bundle. Axial variations in the tracer flux are determined by sampling at two downstream positions in both the injection subchannel and those adjacent to it. This information, with measured subchannel area changes, is used to calculate crossflows and the turbulent eddy diffusion coefficient. The latter number agrees with the results of other investigators in regular pipe flows. Also determined are distributional factors which would be required for modeling the transport equations, for this particular scalar distribution, with a typical lumped parameter computer code.

1 Introduction

A power reaction core is composed of a parallel array of cylindrical fuel rods through which the coolant flows axially. A typical cross section of such an arrangement is shown in Fig. 1. Molecular and turbulent transport of mass, momentum, and energy take place laterally through the clearance gaps, as well as in the axial direction, to result in transverse distributions of these quantities —distributions which are of considerable importance with respect to reactor design.

Due to the large numbers of fuel rods in power reactors the design computer codes treat the large interstices between the rods as differential elements or subchannels interconnected with adjacent subchannels through the clearance gaps. This reduction of the distributed transport system to a lumped parameter network introduces uncertainties which have only recently come under critical examination [1].[2] This, as well as a determination of the scalar turbulent diffusion coefficient, represents the purpose of this work.

2 The Computer Formulation of The Transport Equations

To represent the computer formulation of the transport equations pertinent to the calculation of reactor core energy distributions we will consider the well-known and often used COBRA code of Rowe [2, 3] who writes the enthalpy and mass balances for the ith subchannel, respectively, as:

$$\bar{m}_i \frac{d\bar{h}_i}{dx} + h_i \frac{d\bar{m}_i}{dx} = q_i' + \sum_{j=1}^{N} w_{ij}'(\bar{h}_j - \bar{h}_i) - \sum_{j=1}^{N} w_{ij} h^* \quad (1)$$

and

$$\frac{d\bar{m}_i}{dx} = -\sum_{j=1}^{N} w_{ij} \quad (2)$$

where

$$h^* = \begin{Bmatrix} \bar{h}_i; & w_{ij} \geq 0 \\ \bar{h}_j; & w_{ij} < 0 \end{Bmatrix}. \quad (3)$$

The subscript j refers to any of the N subchannels adjacent to the ith and the remaining symbols are defined in the Nomenclature. For our purposes, we may neglect molecular transport, internal heat generation and also, since equation (1) involves transport of a scalar quantity, the same equation may be written for tracer gas transport, which is more pertinent to the present investigation. Thus, we have:

$$\bar{m}_i \frac{d\bar{C}_i}{dx} = \sum_{j=1}^{N} w_{ij}'(\bar{C}_j - \bar{C}_i) - \sum_{j=1}^{N} \begin{Bmatrix} 0 & ; w_{ij} \geq 0 \\ w_{ij}(\bar{C}_j - \bar{C}_i); & w_{ij} < 0 \end{Bmatrix}. \quad (4)$$

In this expression w'_{ij} represents the turbulent exchange coefficient, usually taken as the turbulent mass flux exchanged between subchannel i and subchannel j per unit axial distance. The crossflow, w_{ij}, is simply the direct mass flow between the ith and jth subchannels, also per unit axial distance. Equation (4) is exact when the various subchannels have uniform tracer gas concentrations which then are discontinuous (step functions) at the

[1] This information was developed in work performed under AEC Contract AT(11-1)-3045.

[2] Numbers in brackets designate Reference at end of paper.

Contributed by the Heat Transfer Division and presented at the ASME-AIChE Heat Transfer Conference, Atlanta, Ga., August 5–8, 1973. Revised manuscript received by the Heat Transfer Division November 21, 1973. Paper No. 73-HT-51.

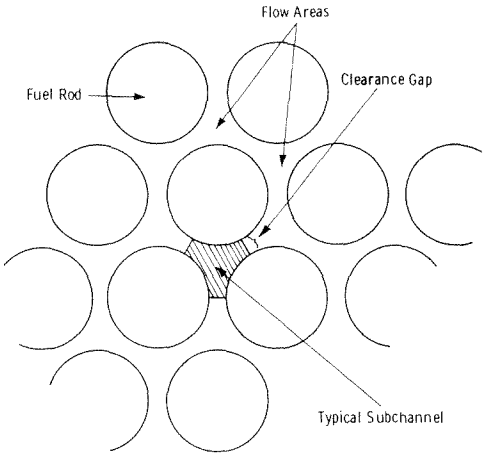

Fig. 1 Rod bundle cross section with triangular geometry

clearance gaps. It is in this context that w'_{ij} and w_{ij} may best be given physical meaning. For example, if there is an exchange of turbulent eddies between two adjacent subchannels such that $w'_{ij} = w'_{ji}$ and this exchange takes place across a step change in concentration from C_i to C_j, then there will be a net scalar flux into the ith subchannel of $w'_{ij}(C_j - C_i)$. The same reasoning holds for the cross-flow transport except when $w_{ij} \geq 0$, i.e., the cross-flow is from i to j. In this case, it simply cancels the second term on the left side of equation (1).

Rowe assumes

$$w_{ij}' = (1/2)\beta c_{ij}(\bar{m}_i/A_i + \bar{m}_j/A_j) \tag{5}$$

and empirically determines β to yield the best fit of the computer solution to experimental data. It may be noted that β represents the ratio of transverse turbulent eddy flow per unit area to the axial mass flow per unit area.

The foregoing procedure represents a method for calculating various distributions within experimentally tested reactor configurations but problems arise during preliminary design of untested rod assemblies since β must then be estimated based upon previous experience and judgment. Continuing efforts to develop more general formulations of w'_{ij} are reviewed by Rogers and Todreas [4] and Rogers and Rosehart [5]. Basically these efforts involve empirical relationships between the turbulent exchange coefficient, the cross-sectional geometry, and the turbulent scalar diffusion coefficient such as that proposed by Moyer [6], i.e.,

$$w_{ij}'(\bar{C}_j - \bar{C}_i) = \rho c_{ij}\bar{\epsilon}_{m\theta}\left(\frac{d\bar{C}}{dz}\right)_{ij} \approx \rho c_{ij}\bar{\epsilon}_{m\theta}\frac{(\bar{C}_j - \bar{C}_i)}{z_{ij}} \tag{6}$$

so that

$$w_{ij}' = \rho(c_{ij}/z_{ij})\bar{\epsilon}_{m\theta} \tag{7}$$

where c_{ij}/z_{ij} is sometimes known as the geometric factor. The turbulent eddy diffusion coefficient, $\bar{\epsilon}_{m\theta}$, is usually taken from temperature or tracer fluid studies in pipe flows and various formulas have been proposed for suitable values of z_{ij}, i.e., that distance which most closely satisfies the approximation,

$$d\bar{C}_i/dz \approx (\bar{C}_j - \bar{C}_i)/z_{ij} \tag{8}$$

3 Development of An "Integrated" Transport Equation and Comparison With The Computer Formulation

In a more exact analytical formulation of the transport associated with a (macroscopic) subchannel control volume we must consider the distributions of transport quantities over the various control volume surfaces. For example, in Fig. 2 the surface areas A_g correspond to clearance gaps and the molecular and turbulent transport per unit gap area may be written

$$-\rho(\alpha_m + \epsilon_{m\theta})_g(\partial C/\partial n)_g$$

where $(\partial C/\partial n)_g$ represents the local concentration gradient normal to the gap area. Since both $\epsilon_{m\theta}$ and $(\partial C/\partial n)$ are functions of position on A_g we must integrate over this surface and, summing over the N adjacent subchannels, we find the total flux to be

$$-\sum_{j=1}^{N}\int_{A_g}\int\rho(\alpha_m + \epsilon_{m\theta})_{gj}\left(\frac{\partial C}{\partial n}\right)_{gj} dA_{gj}$$

If we now take $dA_{gj} = dS_{gj}dx$, where dS_{gj} is a differential distance measured from the clearance gap center line toward the rods (spaced a distance c_{ij} apart), we have transport given by

$$-dx\sum_{j=1}^{N}\int_{-\frac{c_{ij}}{2}}^{\frac{c_{ij}}{2}}\rho(\alpha_m + \epsilon_{m\theta})_{gj}\left(\frac{\partial C}{\partial n}\right)_{gj} dS_{gj}$$

Considering the various fluxes through the other control surfaces as well as direct flow through the clearance gaps we find:

$$\frac{d}{dx}\left\{\int_{A_c}\int\rho uC dA_c\right\} = -\sum_{j=1}^{N}\int_{-\frac{c_{ij}}{2}}^{\frac{c_{ij}}{2}}(\rho vC)_{gj}dS_{gj} + \sum_{k=1}^{N}\int_{P_{rk}}Q_{rk}'dP_{rk} + \sum_{j=1}^{N}\int_{-\frac{c_{ij}}{2}}^{\frac{c_{ij}}{2}}\rho(\alpha_m + \epsilon_{m\theta})_{gj}\left(\frac{\partial C}{\partial n}\right)_{gj} dS_{gj} \tag{9}$$

Likewise, conservation of mass is written;

$$\frac{d}{dx}\left\{\int_{A_c}\int\rho u dA_c\right\} = -\sum_{j=1}^{N}\int_{-\frac{c_{ij}}{2}}^{\frac{c_{ij}}{2}}(\rho v)_{gj}dS_{gj} \tag{10}$$

Our apparatus can only measure values of $(C)_g$, and hence,

Nomenclature

A = subchannel cross-sectional area
C = tracer gas concentration
$(\partial C/\partial n)_g$ = tracer gas concentration gradient normal to and at the clearance gap
c_{ij} = clearance gap spacing between i and j subchannels
D = hydraulic diameter
$(F_d)_{ij}$ = crossflow distribution factor, equation (18)
h = enthalpy
$\dot{m}_1$ = axial mass flow rate through ith subchannel
P_r = circumferential distance along heated fuel rod surface wetted by subchannel control volume
Q_{rj}' = tracer gas injection flux per unit area model fuel rod
q_i' = total heat flux, per unit length into the ith subchannel
S = distance from the clearance gap center line toward the model fuel rod surfaces
$(T_d)_{ij}$ = turbulent exchange distribution factor, equation (17)
u = axial velocity
v = transverse velocity
v_{i0} = average crossflow velocity from subchannel (0) to subchannel (i)
w_{ij} = crossflow mass flux through clearance gap
w_{ij}' = turbulent exchange coefficient
x = axial distance
z = transverse distance in equation (6)
z_{ij} = empirical distance in equation (7)
α_m = molecular constant in equation (5)
ϵ = scalar turbulent eddy diffusivity
$(\epsilon_{m\theta})_g$ = average turbulent eddy diffusivity of mass parallel to the fuel rod surface at, and normal to, the clearance gap
ρ = density

$(\partial C/\partial n)_g$, but not values of $\epsilon_{m\theta}$ or v as functions of position in the clearance gap. Thus we may either assume spatial variations for the latter unknowns which would, say, let them become zero at the rod surface or we could treat the first and third integrals on the right of equation (9) as approximated by the product of mean values,i.e.,

$$\int_{-\frac{c_{ij}}{2}}^{\frac{c_{ij}}{2}} (\alpha_m + \epsilon_{m\theta})_{gj} \left(\frac{\partial C}{\partial n}\right)_{gj} dS_{gj} \approx c_{ij} \overline{(\alpha_m + \epsilon_{m\theta})_{gj}} \left(\overline{\frac{\partial C}{\partial n}}\right)_{gj} \quad (11)$$

and

$$\int_{-\frac{c_{ij}}{2}}^{\frac{c_{ij}}{2}} (vC)_{gj} dS_{gj} \approx c_{ij} \overline{(v)}_{gj} \overline{(C)}_{gj} \quad (12)$$

With respect to application to lumped parameter studies equations (11) and (12) appear acceptable. If we assume no tracer generation within the control volume and neglect molecular transport we have:

$$\frac{d}{dx} \overline{(uCA_c)}_i = \sum_{j=1}^{N} c_{ij} \overline{(\epsilon_{m\theta})}_{gj} \left(\overline{\frac{\partial C}{\partial n}}\right)_{gj} - \sum_{j=1}^{N} c_{ij} \overline{(v)}_{gj} \overline{(C)}_{gj} \quad (13)$$

and

$$\frac{d}{dx} \overline{(uA_c)}_i = - \sum_{j=1}^{N} c_{ij} \overline{(v)}_{gj} . \quad (14)$$

The foregoing equations are similar to the computer formulation presented in Section 2 but differ in that values of the concentration and gradients at the control volume boundaries are used as opposed to mean differences. Thus, if we compare the turbulent transport terms we have

$$w_{ij}'(\bar{C}_j - \bar{C}_i) = \rho c_{ij} \overline{(\epsilon_{m\theta})}_{gj} \overline{(\partial C/\partial n)}_{gj} \quad (15)$$

or

$$w_{ij}' = \rho \overline{(\epsilon_{m\theta})}_{gj} \{c_{ij} \overline{(\partial C/\partial n)}_{gj} / (\bar{C}_j - \bar{C}_i)\} \quad (16)$$

which is effectively identical with Moyer's equation (6). Besides determining whether or not $\epsilon_{m\theta}$ as determined from pipe flows is applicable to rod bundle work we would like to determine the range of the variable,

$$(T_d)_{ij} = c_{ij}/z_{ij} = c_{ij} \{\overline{(\partial C/\partial n)}_{gj} / (\bar{C}_j - \bar{C}_i)\} \quad (17)$$

for an experimental subchannel concentration distribution. If we make similar comparisons between the cross-flow terms of equations (1) and (13) we note that a more consistent form for C^* (corresponding to h^*) might be given by $C^* = (\bar{C}_j + \bar{C}_i)/2$. We could then write

$$w_{ij} = \rho c_{ij} \overline{(v)}_{gj} \{2\overline{(C)}_{gj} / (\bar{C}_j + \bar{C}_i)\} = \rho c_{ij} \overline{(v)}_{gi} (F_d)_{ij} . \quad (18)$$

If we call $(T_d)_{ij}$ and $(F_d)_{ij}$ the turbulent exchange and cross-flow distribution factors, respectively, we may note that for the former to remain constant the concentration gradient at the gap must always be proportional to the difference in mean subchannel concentrations and in the latter case, the gap concentration must be proportional to the average concentration in the two subchannels. Analytical studies of whether such conditions are met have been undertaken [1] but we know of no experimental work which has investigated these factors under flow conditions. The major point to be made here however is that the geometric factor c_{ij}/z_{ij}, for example, depends upon the distributions of the transferable quantities within the two interacting subchannels and hence, may vary from one experiment to another.

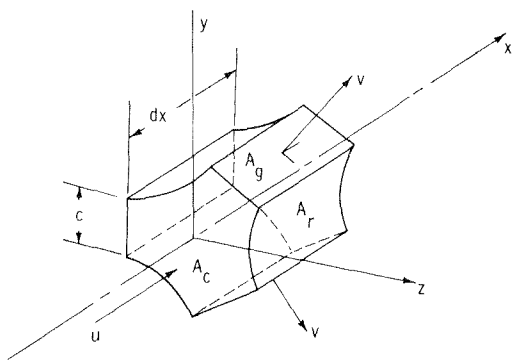

Fig. 2 Control volume for "integrated" transport equation formulation

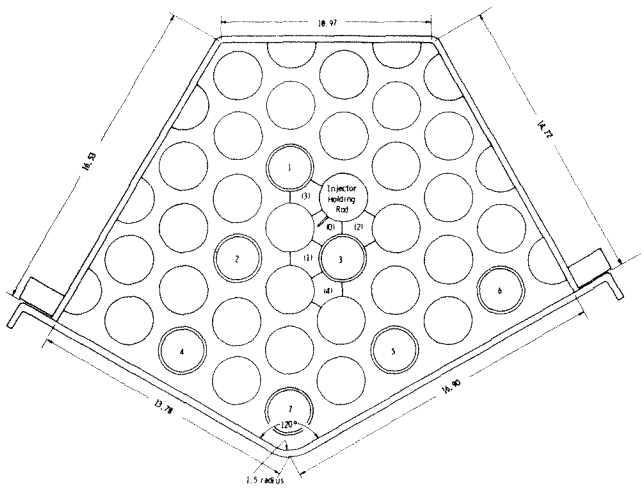

Fig. 3 Cross section of test section

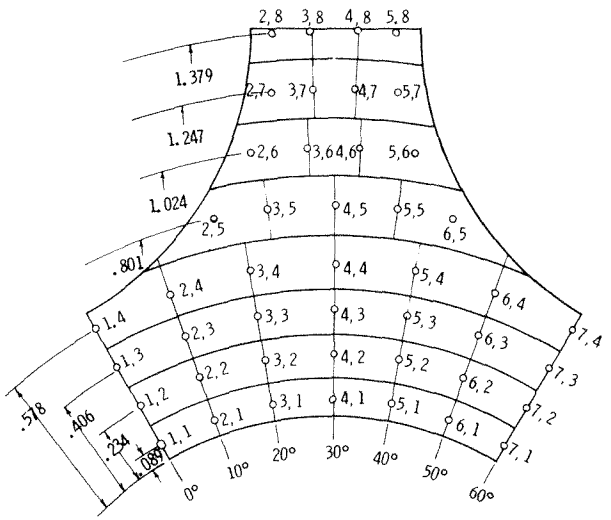

Fig. 4 Subchannel subdivisions for velocity and concentration readings

4 The Experimental Procedure

The experiment was performed on a large scale air-flow model of a liquid metal cooled fast breeder reactor rod bundle. A cross section of the facility is shown in Fig. 3. The 225 in. long test section contained 39 2.5 in. dia rods on triangular pitch at nominally 3.14 in. centers. The rods were held in place at the downstream end by two hexagonal grids and at the entrance section were spaced by 1.125 in. dia aluminum cylinders, having 0.035 in. wall thickness, placed in the subchannels. Air was drawn through the test section at velocities of up to 100 ft/sec to yield overall duct Reynolds numbers on the order of 70,000. The numbered rods in Fig. 3 could be slid in and out of the test section from the upstream end and each was equipped with a 0.0625 in. dia pitot-static probe which could be moved radially from the rod surface as well as rotated by turning the rod. Velocity readings were made over a subchannel mesh as shown in Fig. 4, to yield velocity distributions such as are indicated in Fig. 5. It was also determined that the mean velocity in any subchannel was a function (to within the experimental error) of only the local subchannel

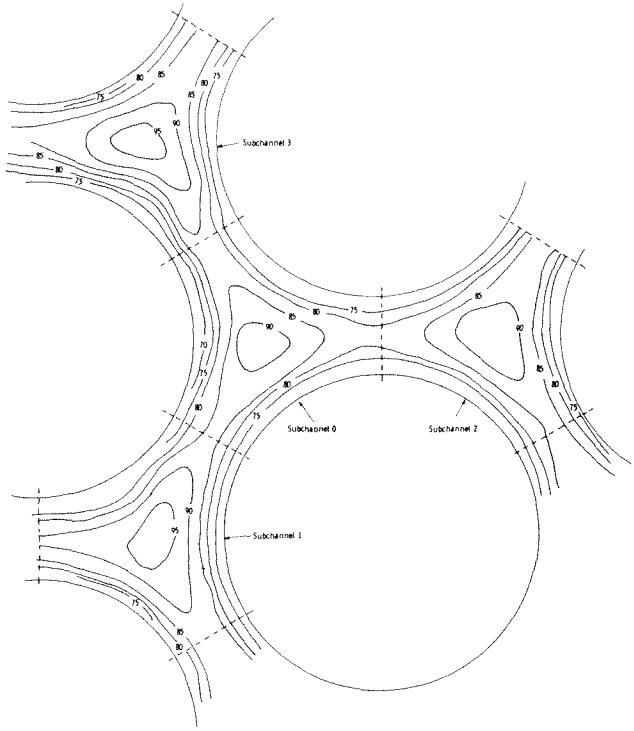

Fig. 5 Test subchannel velocities (in ft/sec)

hydraulic diameter, i.e.,

$$u_i/\bar{u} = (D_i/D_h)^{0.6284} \tag{19}$$

where $\bar{u}$ and $\bar{D}_h$ are the overall test section mean velocity and hydraulic diameter (D_h = 1.854 in.). These results are reported elsewhere [7].

The tracer gas used in the experiment was ethane (C_2H_6) with a molecular weight of 30.07 which is felt to be close enough to that of air so that buoyancy should be negligible. It was injected into the subchannel numbered (0) in Fig. 3 through an eight in. long, 0.0625 in. dia tube positioned axially 0.56 in. from the rod directly above number 3 rod in the same figure. The ethane samples were collected through the pitot-static probe dynamic head orifices at the same mesh positions as the velocity readings were taken, i.e., those indicated in Fig. 4. The concentrations were read from a MSA Type 300 LIRA infrared analyzer calibrated from zero to 2000 ppm ethane (on a volume basis). Due to the low pressure in the analyzer sample chamber somewhat higher concentrations in the test section could be accommodated through pressure corrections.

Tracer gas concentrations were to be read at an axial location where changes in velocity due to entrance effects would be minimal. This position was 60 hydraulic diameters into the duct (27 in. upstream from the support grid) where, over six in., no measurable velocity changes took place. Using a pitot-static probe as a sampler centered in subchannel (0) at this axial location, the axial location of the injector, its position within the subchannel (0) and the tracer gas flow rate were varied until a high concentration was obtained at the subchannel (0) center line with negligible concentrations at the "outside" clearance gaps of subchannels (1), (2), and (3). High concentrations and gradients were desirable at the clearance gaps between the (0) subchannel and those immediately adjacent to obtain more accurate concentration gradient measurements. The negligible concentrations at the outside clearance gaps meant that transport through these gaps could be neglected with considerable simplification of data reduction.

The final injector position was 68.3 in. upstream of the sampling probe with the injector position rotated approximately 15 deg clockwise from the subchannel (0) center line to the position

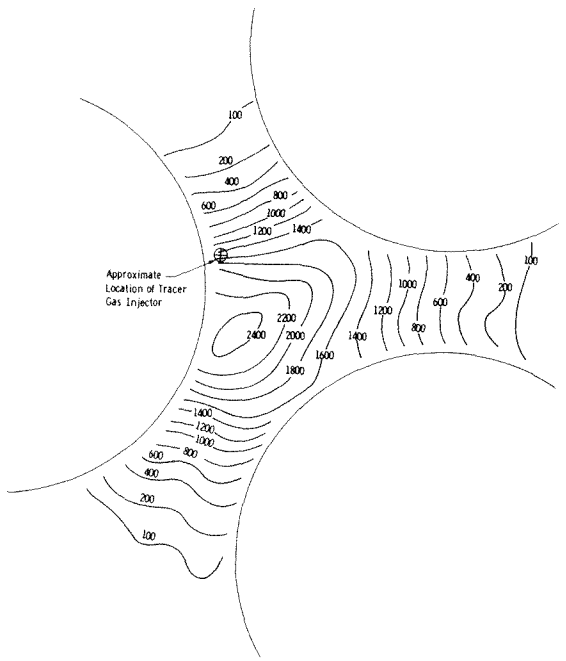

Fig. 6 Upstream ethane concentrations (in ppm)

shown in Fig. 6. A set of concentration readings were made with the results shown in Fig. 6 and it may be noted that the maximum concentration position has moved downward considerably from the injection point. In the following section, it is shown that this may be accounted for by crossflows. The concentration flux (uC values) plot is shown in Fig. 7. The average values of C, u, and (uC) at this axial station are given in Table 1 of Appendix A. These mean values were determined by averaging the readings within and on the boundaries of the areas shown in Fig. 4, summing over these incremental areas, and dividing by the sum of the increments.

To obtain the axial variation in the above mean values the sampling probes had to be moved downstream to a position where such a variation was detectable but where the values of both the

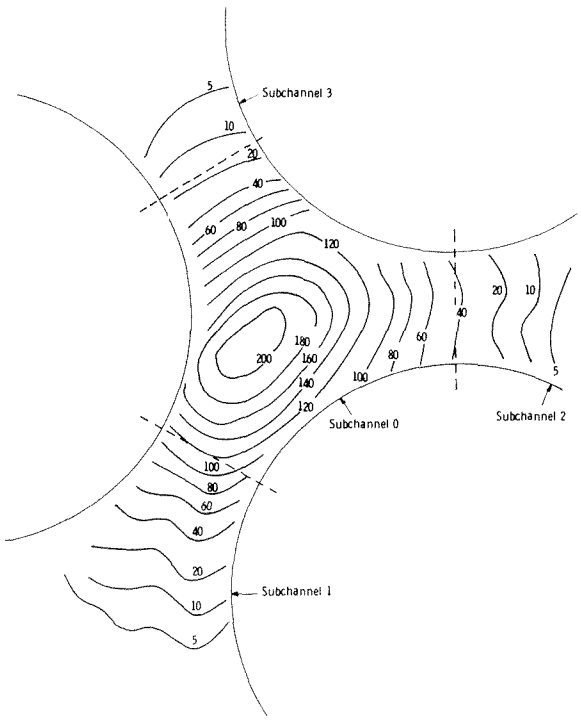

Fig. 7 Concentration flux distribution at upstream position, (ft/sec) ppm

Table 1 Experimental results at upstream position (27 in. upstream of grid)

Subchannel number	Average concentration (ppm)	Average velocity (ft/sec)	Area (in.^{2})	Average concentration flux $(\overline{uC})$, (ft/sec) ppm	Total flux $(uC)\,A$, (ft^3/sec) ppm
(0)	1409.9	78.39	1.6524	112474.9	1290.65
(1)	251.0	84.44	1.7861	19783.9	245.39
(2)	76.8	80.11	1.6783	5800.2	67.96
(3)	23.9	82.33	1.8043	1899.4	23.80
(4)	1.2	83.76	1.8244	89.7	1.14

Table 2 Experimental results at downstream position (21 in. upstream of grid)

Subchannel number	Average concentration (ppm)	Average[a] velocity (ft/sec)	Area[b] (in.^{2})	Average concentration flux[c] $(\overline{uC})$, (ft/sec) ppm	Total flux[d] $(\overline{uC})\,A$, (ft^3/sec) ppm
(0)	1347.3	79.33	1.6818	107574.2	1256.38
(1)	344.3	84.40	1.7849	27405.3	339.70
(2)	70.7	81.08	1.7085	5356.3	63.55
(3)	17.5	82.08	1.7964	1387.5	17.51
(4)	2.1	83.22	1.8074	165.7	2.08

[a] Velocity corrected from upstream reading with equation (21).
[b] Determined from second order curve fit described in Section 5.
[c] Flux determined by using upstream velocity over mesh in Fig. 5 and modified by factor to account for small velocity change.
[d] Note that the total flux downstream is 3 percent higher than that upstream.

concentration and the concentration gradients at the clearance gaps did not change sufficiently to prevent using mean values (the average of the upstream and downstream values) in equation (13). The distance to the downstream measuring plane, Δx, was taken as six in. where the readings were repeated to yield the results summarized in Table 2. The six in. distance was the smallest distance over which detectable flux changes could be measured and thus was felt to justify treatment of the data in the derivative form on the left side of equation (13).

5 Data Reduction

We may rewrite equation (13) for the subchannels (1), (2), and (3) to obtain:

$$\frac{d}{dx}\overline{(uCA_c)}_i = -c_{i0}\overline{(\epsilon_{m\theta})}_{gi0}\overline{\left(\frac{\partial C}{\partial n}\right)}_{i0} + c_{i0}\overline{(v)}_{i0}\overline{(C)}_{i0} \qquad (20)$$

where i = 1, 2 and 3 corresponding to the appropriate subchannels. The signs of the terms on the right have been changed so that the directions coincide with those appropriate for the (0) subchannel and the subscript $i0$ indicates evaluation of the quantity at the clearance gap between the ith and zeroth subchannel.

If we assume that $(\overline{\epsilon_{m\theta}})_g$ is the same for all clearance gaps expression (20) represents three equations in four unknowns, $(\overline{\epsilon_{m\theta}})_g$, $(\bar{v})_{10}$, $(\bar{v})_{20}$, and $(\bar{v})_{30}$, since rewriting it for the zeroth subchannel yields a linearly dependent equation. Since expression (20) represents the only independent equations associated with tracer gas transport the necessary fourth equation must be a relationship between the cross-flow terms arising from the conservation of mass, i.e., equation (14).

The clearance gap spacings were measured at the upstream experimental position and 24 in. on either side of this point during the assembly of the test section. Subchannel areas were calculated at these positions, and second order polynomials fitted to these data to obtain estimates of $A_i(x)$. These are the subchannel areas given in Tables 1 and 2. Differentiating equation (19) it may be noted that, for the area change in subchannel (0), velocity changes on the order of one percent should be anticipated over the six in. increment length. This is not within the accuracy capabilities of the pitot-static probes so that, as a best estimate of the volumetric flow rate change, equation (19) was used in conjunction with the measured areas to obtain;

$$\frac{d}{dx}(\bar{u}A)_0 = 0.0542\,\frac{\text{ft}^2}{\text{sec}} = -c_{10}\bar{v}_{10} - c_{20}\bar{v}_{20} - c_{30}\bar{v}_{30} \qquad (21)$$

Corrections for the area and velocity changes were also made for concentration flux data in Tables 1 and 2 since the data mesh of Fig. 4 did not expand or contract to coincide with the actual subchannel area but was simple superimposed on the subchannel for averaging purposes.

To determine concentrations and gradients at the clearance gaps, plots were made such as shown in Fig. 8 where R_1, R_2, R_3, and R_4 corresponds, respectively, to the arcs 0.089, 0.234, 0.406, and 0.578 inches above the rod surface in Fig. 4. The concentrations and gradients were weighted according to the clearance gap area subtended at each radius with the results shown in Table 3. No allowance was made for either v or $\epsilon_{m\theta}$ going to zero at the rod surface.

6 Experimental Results

Substituting the experimental values in Tables 1, 2, and 3 into equations (20) written for subchannels (1), (2), and (3) and using equation (21) for the total mass-flow variation we may solve for the eddy diffusion coefficient and cross-flow velocities. We find: $\bar{\epsilon}_{m\theta}$ = 0.0215 ft^2/sec, $\bar{v}_{10}$ = 2.346 ft/sec, $\bar{v}_{20}$ = −0.953 ft/sec, and $\bar{v}_{30}$ = −2.609 ft/sec. Thus, there is a considerable net crossflow from subchannel (3) to subchannel (1) which could account for the downward motion of the point of maximum concentration in subchannel (0).

If we make the usual dimensionless correlation on $\epsilon_{m\theta}$, we find $\epsilon_{m\theta}/\bar{u}D$ = 0.00193 at a Reynolds number of 67,900 based on the flow in subchannel (0). The foregoing result is consistent with the work of Quarmby and Anand [8] who find ϵ/uD = 0.00189 or Sheriff and O'Kane [9] who give ϵ/uD = 0.00244. It is somewhat lower than the earlier work of Towl and Sherwood [10], McCarter, Stutzman, and Koch [11], and Sherwood and Woertz [12] whose formula $\epsilon = 0.02\,uD\lambda$ would yield ϵ/uD = 0.00278 under our experimental conditions.

To determine the sensitivity of the calculations to the experimental accuracy, a set of calculations were performed after normalizing the downstream concentrations so that the upstream and downstream fluxes were identical (rather than having the 3 percent variation indicated in Table 2). The results of this calculations are: $\bar{\epsilon}_{m\theta}$ = 0.0173 ft^2/sec, $\bar{v}_{10}$ = 2.174 ft/sec, $\bar{v}_{20}$ = −0.967 ft/sec and $\bar{v}_{30}$ = −2.416 ft/sec. The 25 percent decrease in $\epsilon_{m\theta}$ does indeed imply considerable sensitivity. The crossflows are not affected to such an extent.

We also wish to evaluate the turbulent exchange and cross-flow distribution factors, $(T_d)_{ij}$ and $(F_d)_{ij}$ of Section 3. We note that these are not generally applicable but only pertain to the scalar distribution obtained in the present experiment. Also, no axial changes enter into the calculations, only the distributions at a particular cross section. The values of these factors, as determined from equations (17) and (18) are given in Table 4 and indicate a considerable range of variation.

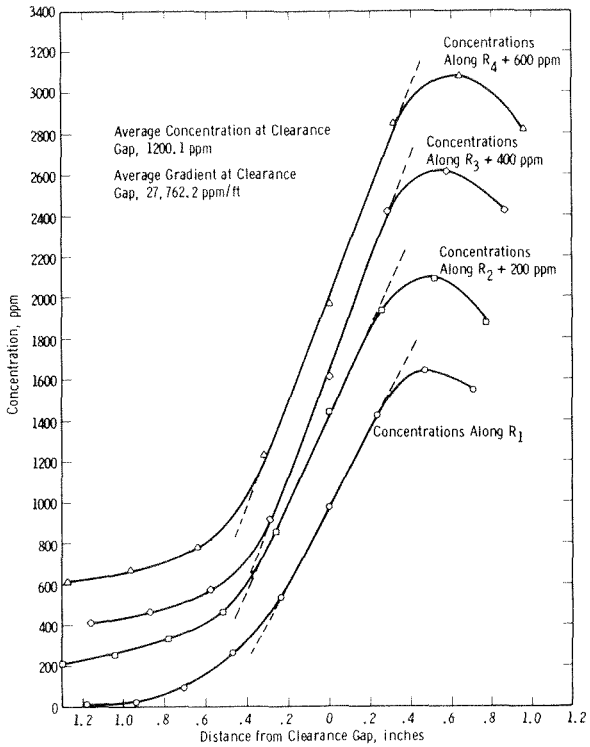

Fig. 8 Concentration gradients through upstream clearance gap 0-1 (ppm)

7 Conclusions

It has been shown that the mean eddy diffusivity at the clearance gaps in the model rod bundle under test (having a pitch to diameter ratio, $P/D = 1.25$) is close to that associated with experimental results in the central regions of tube flows. Since P/D was not varied no conclusions may be drawn for other values, although one would anticipate the same behavior for larger values of P/D.

The turbulent exchange coefficient varies by about ±50 percent from its mean value through the large variations in the turbulent exchange distribution factor, $(T_d)_{ij}$. The measurements of $(T_d)_{ij}$ indicate that the proportionality constant between the concentration gradient at the clearance gap and the difference in mean subchannel concentrations is not actually constant but varies considerably, at least for the distributions obtained in this work. It may be noted that with a symmetric tracer distribution within the subchannels one might be lead to assume a universally applicable transport distance, i.e., z_{ij} of equation (8). Such an assumption would not be correct.

The ratio of cross-flow transport to turbulent transport, i.e., $v_g C_g/((\epsilon_m)_g(\partial C/\partial n)_g)$, ranges from 1.5 to 5.5 for this experiment. Although some crossflows may be attributed to incomplete hydrodynamic inlet development we feel that their major cause in our experiment is the variation in subchannel areas over the test section. The mean subchannel velocities then vary according to equation (19) to obtain parallel channel equilibrium. Thus, area variations of a few percent imply average velocity changes of the same order of magnitude. These in turn yield values of crossflow, which, although small, are large relative to the turbulent transport terms.

Finally, while there appears to be a loose proportionality between $(T_d)_{ij}$ and $(F_d)_{ij}$ the latter exhibits a larger variation implying considerable caution is necessary if the clearance gap concentration is to be approximated as the average of the mean subchannel concentrations on either side.

Although the experimental procedure described in this work is not new [13], it is believed the interpretation of the data in terms applicable to computer reactor design studies is informative with respect to understanding both the capabilities and limitations of such efforts.

Table 3 Experimental results at clearance gaps

Gap number	Average concentration at the Gap (ppm)	Average concentration gradient at the gap (ppm/ft)
	Upstream	
0-1	1200.1	27763.2
0-2	664.2	18988.8
0-3	262.5	16347.6
	Downstream	
0-1	1547.0	26368.8
0-2	569.3	18072.0
0-3	218.2	16848.0
	Mean values over six in. section	
0-1	1373.5	27066.0
0-2	616.7	18530.4
0-3	240.3	16597.8

Clearance gap spacings (ft)

$C_{01} = 0.04958$
$C_{02} = 0.04642$
$C_{03} = 0.04842$

Table 4 Distribution factors, $(T_d)_{ij}$ and $(F_d)_{ij}$

Clearance gap number	w_{ij}' (lb/ft sec)	β	$(T_d)_{ij}$	$(F_d)_{ij}$
	Upstream			
0-1	0.00152	0.0051	1.188	1.445
0-2	0.000864	0.0031	0.661	0.893
0-3	0.000731	0.0026	0.571	0.366
	Downstream			
0-1	0.00167	0.0056	1.304	1.830
0-2	0.00084	0.0031	0.657	0.803
0-3	0.00078	0.0028	0.613	0.320

References

1 France, D. M., and Ginsberg, T., "Evaluation of Lumped-Parameter Heat Transfer Techniques for Nuclear Reactor Applications," *Nucl. Sci. and Engrg.*, Vol. 51, 1973.

2 Rowe, D. S., "COBRA-11: A Digital Computer Program for Thermal-Hydraulic Subchannel Analysis of Rod Bundle Nuclear Fuel Elements," BNWL-1229, UC-80, Battelle Memorial Institute, Richland, WA, Feb. 1970.

3 Rowe, D. S., "A Mathematical Model for Transient Subchannel Analysis of Rod-Bundle Nuclear Fuel Elements," JOURNAL OF HEAT TRANSFER, TRANS. ASME, Series, Vol. 95, No. 2, May 1973.

4 Rogers, J. T., and Todreas, N. E., "Coolant Interchannel Mixing in Reactor Fuel Rod Bundles—Single Phase Coolants," *Heat Transfer in Rod Bundles*, ASME Publication, 1968.

5 Rogers, J. T., and Rosehart, R. G., "Mixing by Turbulent Interchange in Fuel Bundles. Correlations and Inferences," ASME Paper No. 72-HT-53.

6 Moyer, C. B., "Coolant Mixing in Multi-Rod Fuel Bundles," Riso Report No. 125, July 1964 (issued 1966).

7 Pechersky, M. J., Roidt, R. M., Markley, R. A., and Vegter, B. J., "11:1 Scale Model Rod Bundle Air Flow Tests-Bare Rod Subchannel Flow Rate Studies," Presented at the 19th Annual Mtg., ANS, Chicago, IL, June 1973.

8 Quarmby, A., and Anand, R. E., "Axisymmetric Turbulent Mass Transfer in a Circular Tube," *Journal of Fluid Mechanics*, Vol. 38, Part 3, Sept. 1969.

9 Sheriff, N., and O'Kane, D. J., "Eddy Diffusivity of Mass Measurements for Air in a Circular Duct," *International Journal of Heat Mass Transfer*, Vol. 14, No. 5, 1971.

10 Towle, W. L., and Sherwood, T. K., "Eddy Diffusion-Mass Transfer in the Central Portion of a Turbulent Air Stream," *Ind. and Eng. Chem.*, Vol. 31, No. 4, 1939.

11 McCarter, R. J., Stutzman, L. F., and Koch, H. A., Jr., "Temperature Gradients and Eddy Diffusivities in Turbulent Fluid Flow," *Ind. and Eng. Chem.*, Vol. 41, No. 6, 1949.

12 Sherwood, T. K., and Woertz, B. B., "Mass Transfer Between Phases—Role of Eddy Diffusion," *Ind. and Eng. Chem.*, Vol. 31, No. 8, 1939.

13 Betts, C., Capewell, R. S., Winn, W. R., and Lunt, H. F., "DER 77-Pin Subassembly Flow Evaluation," TRG Report 644(R), UKAEA, Nov. 1963.

W. J. Minkowycz

Department of Energy Engineering,
University of Illinois at Chicago Circle,
Chicago, Ill.

E. M. Sparrow

Department of Mechanical Engineering,
University of Minnesota,
Minneapolis, Minn.

Local Nonsimilar Solutions for Natural Convection on a Vertical Cylinder

The local nonsimilarity solution method has been applied to solve for natural convection on a vertical cylinder for conditions where there are large deviations from the flat plate results. To assess and insure the accuracy of the results, solutions were obtained for three levels of truncation of the governing equations. The solutions were carried out for $Pr = 0.733$ and for a range of cases extending from small deviations from the flat plate to a factor-of-four deviation between the local heat fluxes for the cylinder and the flat plate. The results provided by the local similarity solutions were found to be highly accurate over this range. Comparisons were made with available results for the local and surface-integrated heat transfer, and solution methods were identified which appear promising for application beyond the range studied here. A presentation of representative temperature and velocity profiles showed only small deviations between the local similarity solutions and those for the third level of truncation.

Introduction

Natural convection about a vertical cylinder tends not to yield boundary layer similarity solutions owing to the curvature of the surface in planes transverse to the streamwise direction. Similarity solutions are possible only in the special case when the surface temperature linearly increases (or decreases) with the streamwise coordinate x and the surface and ambient temperatures are equal at the leading edge $x = 0$ [1, 2].[1] For other boundary conditions, the governing partial differential equations which describe momentum and energy conservation do not reduce to ordinary differential equations, thereby calling forth a variety of approximate analytical methods for obtaining heat transfer results.

The first prediction of heat transfer coefficients for vertical cylinders was given by Elenbaas [3], who dealt with the uniform wall temperature boundary condition. He employed Langmuir's stagnant film model to replace the natural convection problem by a heat conduction problem in an annulus of unmoving fluid surrounding the cylinder. The stagnant film model was also employed in [4], but with an alternate procedure for determining the thickness of the equivalent conducting annulus.

Also, in [4], the boundary layer equations were solved for the isothermal-walled cylinder by a series expansion wherein the first term corresponds to the flat plate and subsequent terms give corrections due to transverse curvature of the cylinder. More recently, series solutions were applied in studies dealing with nonisothermal vertical cylinders [5, 6]. Owing to their truncated nature and uncertain convergence characteristics, the series solutions are expected to be valid only for cylinders which do not deviate significantly from the flat plate.

Other approximate results have been obtained from the application of the Karman-Pohlhausen method [7, 8]. In [7], the solution was obtained by employing a truncated series expansion about the vertical plate, whereas in [8], the streamwise coordinate was arbitrarily multiplied by a constant to achieve a match with the plate solution and, in addition, inertia terms were neglected. In treating the case of uniform wall heat flux, Nagendra and coworkers [9] employed an unorthodox version of the method of local similarity, yielding results of uncertain accuracy.

The present investigation was undertaken to fulfill two complementary objectives. The first is to obtain highly accurate heat transfer results for isothermal vertical cylinders for conditions where there are large deviations from the results for the vertical plate. The solutions and results are to be obtained by applying the local nonsimilarity method that was introduced in [10] for nonsimilar velocity boundary layers and extended in [11] to nonsimilar thermal boundary layers. The present problem, in which there is mutual coupling between the velocity and thermal fields, is much more formidable than those of [10 and 11] where the velocity and temperature fields could be solved separately. Therefore, the second objective of the present investigation was to examine the applicability of the local nonsimilarity method to problems with mutually coupled velocity and temperature fields.

As a prelude to the analysis of the cylinder problem, a brief review of certain features of the local nonsimilarity solution method will be presented. One of the strengths of the method is that the solution at any streamwise location can be found without having to perform calculations at upstream locations. The governing equations encountered in the application of the method can be treated as ordinary differential equations and resemble those for similarity boundary layers, thereby facilitating their solution by

[1] Numbers in brackets designate References at end of paper.

Contributed by the Heat Transfer Division for publication in the JOURNAL OF HEAT TRANSFER. Manuscript received by the Heat Transfer Division, August 13, 1973. Paper No. 74-HT-Y.

established techniques. All of the nonsimilarity terms are retained in the momentum and energy equations; those approximations that are made are relegated to higher order equations. Finally, the method provides, within itself, a way of assessing the accuracy of the results.

Analysis

Consideration is given to an isothermal vertical cylinder of radius r_0 and wall temperature T_w situated in an otherwise quiescent environment having temperature T_∞. The radial and axial coordinates are r and x, with r measured from the axis of the cylinder and x measured vertically upward. The origin of x is the leading edge of the cylinder, where the boundary layer thickness is zero.

The natural convection boundary layer equations will be written using the Boussinesq model for the fluid properties, giving rise to a buoyancy term while otherwise neglecting the property variations. These equations are

$$\frac{\partial}{\partial x}(ru) + \frac{\partial}{\partial r}(rv) = 0 \tag{1}$$

$$u\frac{\partial u}{\partial x} + v\frac{\partial u}{\partial r} = g\beta(T - T_\infty) + \frac{\nu}{r}\frac{\partial}{\partial r}\left(r\frac{\partial u}{\partial r}\right) \tag{2}$$

$$u\frac{\partial T}{\partial x} + v\frac{\partial T}{\partial r} = \frac{\alpha}{r}\frac{\partial}{\partial r}\left(r\frac{\partial T}{\partial r}\right) \tag{3}$$

It has been established that these equations admit a similarity solution only when the wall temperature varies linearly with x [1]. For all other cases and, in particular, for uniform wall temperature, other types of solutions have to be sought. As already noted in the Introduction, the local nonsimilarity method will be employed here. Owing to the *mutual* coupling between the momentum and energy equations, the present problem is a much more demanding application of the method than were the problems treated in [10 and 11], which were all forced convection flows.

The pseudo-similarity variable η and the stretched x coordinate ξ are selected as

$$\eta = \left[\frac{g\beta(T_w - T_\infty)}{4\nu^2}\right]^{1/4}\frac{(r^2 - r_0^2)}{2r_0x^{1/4}} \tag{4}$$

$$\xi = \frac{2(x/r_0)^{1/4}}{\left[g\beta(T_w - T_\infty)r_0^3/4\nu^2\right]^{1/4}} \tag{5}$$

For very thin boundary layers, r does not differ appreciably from r_0, so that $(r^2 - r_0^2)/2r_0$ reduces to y (where $y = r - r_0$) and ξ reduces to the flat plate similarity variable. The magnitude of ξ is proportional to the ratio of the boundary layer thickness to the cylinder radius. Consequently, small values of ξ correspond to relatively thin boundary layers (compared with r_0) and to small deviations from the flat plate, whereas large values of ξ correspond to relatively thick boundary layers and large deviations from the flat plate. The constants appearing in equation (5) are historical [4], and no special significance need be attached to them.

Furthermore, the relationship between the stream function ψ and the transformed stream function F is taken to be

$$\psi = 4\nu r_0 x^{3/4}\left[\frac{g\beta(T_w - T_\infty)}{4\nu^2}\right]^{1/4}F(\xi,\eta) \tag{6}$$

which is identical to the flat plate relationship except that F is now a function of ξ and η rather than of η alone and the factor r_0 is included to give the proper dimensions for ψ. Finally, a dimensionless temperature θ may be defined as

$$\theta(\xi,\eta) = \frac{T - T_\infty}{T_w - T_\infty} \tag{7}$$

The mass conservation equation (1) is satisfied by introducing the stream function ψ as

$$ru = \frac{\partial\psi}{\partial r}, \qquad rv = -\frac{\partial\psi}{\partial x} \tag{8}$$

and subsequent transformation of equations (2) and (3) using the variables of (4) to (7) yields

$$\frac{\partial}{\partial\eta}\left[(1 + \xi\eta)\frac{\partial^2F}{\partial\eta^2}\right] + 3F\frac{\partial^2F}{\partial\eta^2} - 2\left(\frac{\partial F}{\partial\eta}\right)^2 + \theta = \xi\left[\frac{\partial F}{\partial\eta}\frac{\partial^2F}{\partial\xi\,\partial\eta} - \frac{\partial^2F}{\partial\eta^2}\frac{\partial F}{\partial\xi}\right] \tag{9}$$

$$\frac{1}{Pr}\frac{\partial}{\partial\eta}\left[(1 + \xi\eta)\frac{\partial\theta}{\partial\eta}\right] + 3F\frac{\partial\theta}{\partial\eta} = \xi\left[\frac{\partial F}{\partial\eta}\frac{\partial\theta}{\partial\xi} - \frac{\partial\theta}{\partial\eta}\frac{\partial F}{\partial\xi}\right] \tag{10}$$

Furthermore, the boundary conditions $u = v = 0$, $T = T_w$ at $r = r_0$ and $u = 0$, $T = T_\infty$ at $\eta = \infty$ become, after transformation,

$$F = \frac{\partial F}{\partial\eta} = 0, \quad \theta = 1 \text{ at } \eta = 0 \tag{11}$$

$$\frac{\partial F}{\partial\eta} = \theta = 0 \qquad \text{at } \eta = \infty \tag{12}$$

In accordance with the local nonsimilarity method, several sets of equations will be derived from equations (9) and (10), each set involving a different level of approximation. The first set of equations corresponds to local similarity and is obtained by deleting the right-hand sides of equations (9) and (10). The effect of this truncation is to eliminate all terms containing ξ derivatives from the transformed momentum and energy equations. The equations that remain after the truncation can, for computational purposes, be treated as ordinary differential equations at any streamwise location ξ, with ξ playing the role of a prescribable parameter. If $\partial/\partial\eta$ is denoted by a prime, the local similarity equations can be written as

$$(1 + \xi\eta)F''' + (\xi + 3F)F'' - 2(F')^2 + \theta = 0 \tag{13}$$

$$(1 + \xi\eta)\theta'' + (\xi + 3PrF)\theta' = 0 \tag{14}$$

with boundary conditions

$$F(\xi,0) = F'(\xi,0) = 0, \quad \theta(\xi,0) = 1, \quad F'(\xi,\infty) = \theta(\xi,\infty) = 0 \tag{15}$$

Equations (13) and (14) constitute a coupled pair of differential equations for the F and θ functions. These equations are not unlike those for conventional natural convection similarity boundary layers. They can be treated as ordinary differential equations at each given value of ξ, and solutions can be obtained by using the

Nomenclature

F = transformed stream function, equation (6)
G = auxiliary function, $\partial F/\partial\xi$
g = acceleration of gravity
H = auxiliary function, $\partial G/\partial\xi$
k = thermal conductivity
Nu_x = local Nusselt number, hx/k
$\overline{\mathrm{Nu}}_x$ = average Nusselt number, $\bar{h}x/k$
Pr = Prandtl number
Q = surface-integrated heat transfer rate
q = local heat transfer rate per unit area
r = radial coordinate
r_0 = radius of cylinder
T = temperature
T_w = wall temperature of cylinder
T_∞ = ambient temperature
u, v = velocity components
x = axial coordinate
y = reduced radial coordinate, $r - r_0$
α = thermal diffusivity
β = coefficient of thermal expansion
η = pseudo-similarity variable, equation (4)
θ = dimensionless temperature, equation (7)
ν = kinematic viscosity
ξ = stretched x coordinate, equation (5)
ϕ = auxiliary function, $\partial\theta/\partial\xi$
χ = auxiliary function, $\partial\phi/\partial\xi$
ψ = stream function

same numerical techniques as for similarity situations. The local similarity model will also be referred to later as the first level of truncation.

The set of equations corresponding to the second level of truncation will now be derived. As a first step, let

$$G = \partial F/\partial \xi, \quad \phi = \partial \theta/\partial \xi \tag{16}$$

so that the right-hand sides of equation (9) and (10) become

$$\xi(F'G' - F''G) \text{ and } \xi(F'\phi - \theta'G) \tag{17}$$

Then, after introduction of (17), equations (9) and (10) are differentiated with respect to ξ, with use being made of the definitions of G and ϕ from (16). The right-hand sides of the resulting equations, respectively, contain the terms

$$\frac{\partial}{\partial \xi}(F'G' - F''G) \text{ and } \frac{\partial}{\partial \xi}(F'\phi - \theta'G) \tag{18}$$

These terms are deleted in accordance with the local nonsimilarity method.

The equations of the second level of truncation include the *complete* transformed momentum and energy equations, (9) and (10), and the truncated equations described in the prior paragraph. Thus, the set of equations corresponding to the second level are

$$(1 + \xi\eta)F''' + (\xi + 3F)F'' - 2(F')^2 + \theta = \xi(F'G' - F''G) \tag{19}$$

$$(1 + \xi\eta)\theta'' + (\xi + 3\mathrm{Pr}F)\theta' = \mathrm{Pr}\ \xi(F'\phi - \theta'G) \tag{20}$$

$$(1 + \xi\eta)G''' + (\xi + 3F)G'' - 5F'G' + 4F''G + \eta F''' + F'' = 0 \tag{21}$$

$$(1 + \xi\eta)\phi'' + (\xi + 3\mathrm{Pr}F)\phi' - \mathrm{Pr}\ F'\phi + 4\mathrm{Pr}G\theta' + \eta\theta'' + \theta' = 0 \tag{22}$$

with boundary conditions

$$F(\xi,0) = F'(\xi,0) = G(\xi,0) = G'(\xi,0) = \phi(\xi,0) = 0, \quad \theta(\xi,0) = 1;\ F'(\xi,\infty) = G'(\xi,\infty) = \theta(\xi,\infty) = \phi(\xi,\infty) = 0 \tag{23}$$

It is seen that equations (19) to (22) constitute a coupled set of four equations for the functions F, G, θ, and ϕ. Inasmuch as ξ appears only as a parameter, these equations may be treated as a set of ordinary differential equations of the boundary layer type at any given ξ. The functions of primary interest are the F and θ functions, which correspond, respectively, to the velocity and temperature fields. However, owing to the coupling among the equations, F and θ cannot be solved for without also solving for G and ϕ.

A set of equations corresponding to a third level of truncation was also derived. In this set, the transformed momentum and energy equations are retained without approximation and, in addition, all terms are retained in the pair of equations generated by taking $\partial/\partial\xi$ of the momentum and energy equations. The truncation is performed in the equations generated by operating with $\partial^2/\partial\xi^2$, the deleted terms being

$$\frac{\partial^2}{\partial \xi^2}(F'G' - F''G) \text{ and } \frac{\partial^2}{\partial \xi^2}(F'\phi - \theta'G) \tag{24}$$

In stating the equations of the third level truncation, the already defined G and ϕ functions are used and, additionally,

$$H = \partial G/\partial \xi = \partial^2 F/\partial \xi^2, \quad \chi = \partial \phi/\partial \xi = \partial^2 \theta/\partial \xi^2 \tag{25}$$

In light of the foregoing paragraph, the equations of the third level truncation may be stated as

(a) equations (19) and (20);

(b) equations (21) and (22) with the following terms appended to the respective right-hand sides

$$\xi[F'H' + (G')^2 - F''H - G''G] \tag{26}$$

$$\mathrm{Pr}\ \xi[F'\chi + G'\phi - \theta'H - \phi'G] \tag{27}$$

(c) the truncated equations

$$(1 + \xi\eta)H''' + (\xi + 3F)H'' - 6F'H' + 5F''H - 6(G')^2 + (8G + 2)G'' + 2\eta G''' = 0 \tag{28}$$

$$(1 + \xi\eta)\chi'' + (\xi + 3\mathrm{Pr}\ F)\chi' - 2\mathrm{Pr}\ F'\chi - 2\mathrm{Pr}\phi G' + (8\ \mathrm{Pr}G + 2)\phi' + 2\eta\phi'' + 5\mathrm{Pr}\theta'H = 0 \tag{29}$$

The boundary conditions for this set may be written by appending to equation (23) the additional conditions

$$H(\xi,0) = H'(\xi,0) = \chi(\xi,0) = H'(\xi,\infty) = \chi(\xi,\infty) = 0 \tag{30}$$

The six coupled equations outlined in the preceding paragraph are to be solved simultaneously for the six unknown functions F, G, H, θ, ϕ, and χ. Of these, F and θ are directly relevant to the velocity and temperature problems. As was the case for the equations of the other levels of truncation, the current set can be treated as ordinary differential equations with ξ as a given parameter.

The logic of the local similarity method becomes apparent from a consideration of the operations used in deriving the various sets of equations. As one proceeds from the first level truncation to the second level truncation to the third level truncation, and so on, the place where the truncation is actually made becomes more and more remote from the momentum and energy equations. It is, therefore, expected that the higher the level of the truncation, the more accurate are the results. Furthermore, comparison of the results from the various levels of truncation enables an assessment of the accuracy of the results.

The numerical solutions of the various sets of equations were obtained by forward integration (Runge-Kutta), starting at $\eta = 0$ and integrating toward larger η. As is well known, the initiation of the forward integration requires N numerical values for the functions and their derivatives at $\eta = 0$, where N is the total order of the system of equations. Thus, for example, for the third level truncation, a total of fifteen function and derivative values are needed at $\eta = 0$, but only nine are available from equations (23) and (30). Therefore, it was necessary to determine simultaneously the six missing starting values. The missing values were successfully determined by the use of a shooting method. The authors are not aware of previously published boundary layer problems where it was necessary to deal with as many as six simultaneously unknown starting values.

For each one of the three levels of truncation, solutions were obtained for parametric values of ξ equal to 0, 0.1, 0.2, 0.5, 0.75, 1, 2, 5, 7.5, and 10. The Prandtl number was fixed at 0.733 for all of the solutions.

Results and Discussion

Attention is first turned to the results for the local heat transfer q. By application of Fourier's law at the surface of the cylinder and use of the transformed variables of equations (4) and (7), there follows

$$q_{\mathrm{cyl}} = k(T_w - T_\infty)\left[\frac{g\beta(T_w - T_\infty)}{4\chi\nu^2}\right]^{1/4}\left[-\theta'(\xi,0)\right]_{\mathrm{cyl}} \tag{31}$$

where the subscript cyl has been appended to make a clear distinction with the flat plate results that will be mentioned shortly. Numerical values of $[-\theta'(\xi,0)]_{\mathrm{cyl}}$ are listed in Table 1, but discussion of the significance of these results will be reserved for the upcoming graphical presentation.

It is of first importance to compare the local heat flux for the cylinder with that for the flat plate. The latter quantity is given by

$$q_{fp} = k(T_w - T_\infty)\left[\frac{g\beta(T_w - T_\infty)}{4\chi\nu^2}\right]^{1/4}\left[-\theta'(0)\right]_{fp} \tag{32}$$

so that

$$\frac{q_{\mathrm{cyl}}}{q_{fp}} = \frac{\left[-\theta'(\xi,0)\right]_{\mathrm{cyl}}}{\left[-\theta'(0)\right]_{fp}} \tag{33}$$

By evaluating equation (33), the ratio of local heat transfer rates for the cylinder and the flat plate have been plotted in Fig. 1 for all three levels of truncation. The abscissa variable ξ is a measure

Table 1 Values of θ' and F'' at $\eta = 0$ for the first, second, and third levels of truncation; Pr = 0.733

	$-\theta'$			F''		
ξ	First	Second	Third	First	Second	Third
0	0.5079	0.5079	0.5079	0.6741	0.6741	0.6741
0.1	0.5291	0.5302	0.5302	0.6802	0.6800	0.6800
0.2	0.5505	0.5525	0.5526	0.6865	0.6861	0.6861
0.5	0.6107	0.6154	0.6156	0.7051	0.7038	0.7037
0.75	0.6597	0.6655	0.6660	0.7194	0.7180	0.7178
1	0.7054	0.7125	0.7138	0.7336	0.7319	0.7316
2	0.8787	0.8884	0.8920	0.7868	0.7845	0.7840
5	1.330	1.349	1.354	0.9226	0.9202	0.9195
7.5	1.664	1.687	1.695	1.023	1.021	1.020
10	1.982	2.006	2.016	1.121	1.118	1.117

of the extent to which the boundary layer for a cylinder differs from that for a flat plate.

Since the ratio of local heat fluxes is equal to the ratio of local Nusselt numbers ($Nu_x = hx/k$ and $h = q/(T_w - T_\infty)$), the latter has also been indicated on the ordinate of the figure. Inspection of the ordinate affirms that the solutions were carried out for operating conditions where there are large deviations between the heat transfer results for the cylinder and the flat plate, with the maximum ratio being about four.

Perhaps the most noteworthy finding evidenced by the figure is the remarkably small spread between the results for the various levels of truncation. In particular, the greatest deviation between the results for the first level of truncation (local similarity) and the third level of truncation is about 1.8 percent. Between the second and third levels, the greatest deviation is only about 0.5 percent. Clearly, for the present problem, the results given by the local similarity model are sufficiently accurate for practical applications. This finding is, in itself, of considerable importance inasmuch as there are many problems where the local similarity model gives results that are substantially in error.

The near coincidence of the results from the second and third levels of truncation affirms the accuracy of the solutions.

The present results may be compared with heretofore published local heat transfer information. The series solution of [4] covered the limited ξ range between zero and one, with q_{cyl}/q_{fp} values of 1.209 and 1.392 at $\xi = 0.5$ and 1.0, respectively. The corresponding values from the third level of truncation solution are 1.212 and 1.405. The comparison indicates that the series solution is satisfactory in the range in which it was employed. The results of Hama and co-workers [8] are plotted in Fig. 1. They made use of the Karman-Pohlhausen integral method for their solution and made use of additional approximations as noted in the Introduction. Notwithstanding this, Hama's results show a maximum deviation of only 6.5 percent.

The surface-integrated heat transfer rate Q is also of interest. This quantity is evaluated as

$$Q = \int_A q dA \tag{34}$$

If s is the spanwise dimension ($s = 2\pi r_0$ for a cylinder), then for a length of cylinder or plate between $x = 0$ and $x = x$

$$Q = s\int_0^x q dx \tag{35}$$

Expressions for Q for the cylinder and the flat plate can be derived by substitution of equations (31) and (32) into (35). Then, upon forming the ratio, there follows

$$\frac{Q_{cyl}}{Q_{fp}} = \frac{3}{\xi^3}\int_0^\xi \frac{[-\theta'(\xi,0)]_{cyl}}{[-\theta'(0)]_{fp}}\,\xi^2 d\xi \tag{36}$$

The ratio of Q's is also equal to the ratio of the average Nusselt numbers (see Nomenclature for definition).

The ratio of the surface-integrated heat transfer rates is plotted in Fig. 2 as a function of ξ. The value of Q_{cyl}/Q_{fp} at any ξ is somewhat smaller than the corresponding value of q_{cyl}/q_{fp}, that is, the cylindrical geometry has a lesser effect on the surface-integrated heat transfer rate than on the local heat transfer rate. This is altogether reasonable inasmuch as the surface integration includes contributions from the upstream region where the cylindrical effects are minimal.

Prior analytical predictions for the surface-integrated heat transfer rate have been brought together in the figure. The Karman-Pohlhausen solution of [7] and the stagnant film model of [3] appear to be substantially in error and, interestingly enough, the results of these investigations respectively lie below and above those obtained here. On the other hand, the stagnant film model of [4] yields surprisingly good predictions (maximum deviation about 4 percent), especially in view of the simplicity of the model and its ease of evaluation. The series solution of [4] yields Q_{cyl}/Q_{fp} values of 1.158 and 1.302 at $\xi = 0.5$ and 1.0, which compare favorably with the corresponding values of 1.159 and 1.310 from the third level of truncation solution.

Figs. 1 and 2 not only convey the present highly accurate results for the range $\xi = 0$ to 10, but also indicate which of the available prediction methods appears to be suitable for applica-

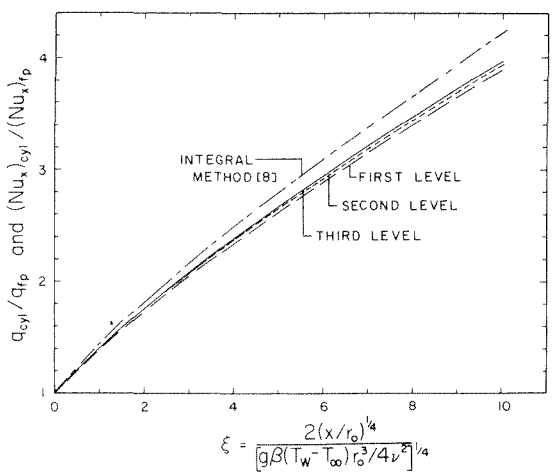

Fig. 1 Local heat transfer results

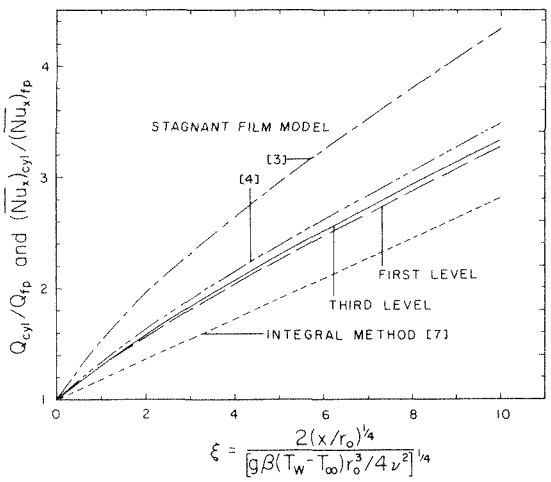

Fig. 2 Surface-integrated heat transfer results

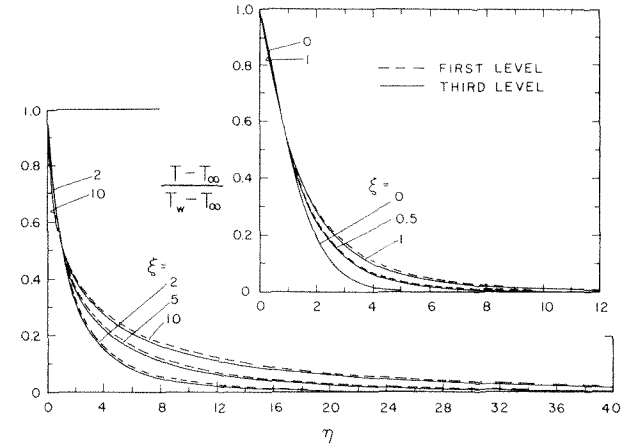

Fig. 3 Representative temperature profiles

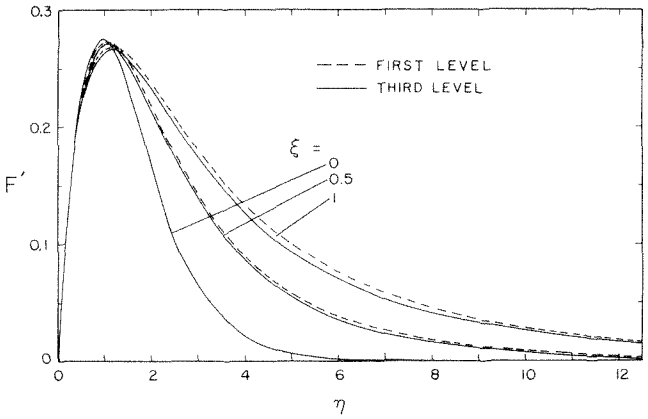

Fig. 4 Representative velocity profiles, ξ = 0, 0.5, and 1

tion outside of this range. Among these, the local similarity method seems to be most accurate. Among the others, Hama's local results and the surface-integrated results from the stagnant film theory of [4] may be of sufficient accuracy for most applications.

In addition to listing the $\theta'(\xi,0)$ values that are relevant to the heat transfer results, Table 1 also contains a listing of $F''(\xi,0)$ values that may be employed in evaluating the local wall shear stress.

Representative temperature and velocity profiles will now be presented and discussed. The temperature profiles are plotted in Fig. 3. The abscissa is the pseudo-similarity variable η defined by equation (4), while the curve parameter ξ (equation (5)) measures the importance of the cylindrical geometry. The figure contains two graphs, one for ξ = 0, 0.5, and 1, and the other for ξ = 2, 5, and 10. The solid and dashed lines, respectively, depict the results for the third level of truncation and for the first level of truncation (i.e., local similarity). The ξ = 0 curve represents the similarity solution for the flat plate.

The figure indicates that for any ξ, there are only small deviations between the temperature profiles from the first and third levels of truncation. At small and at large η values, the curves are coincident within the scale of the figure, and only at intermediate η values can distinct solid and dashed lines be drawn. In general, the local similarity curves lie above those from the third level of truncation.

The temperature profiles can be employed to estimate the radial extent of the boundary layer *relative* to the radius of the cylinder. From equations (4) and (5), it follows that

$$\frac{r}{r_0} = (1 + \xi\eta)^{1/2} \tag{37}$$

Let η_δ denote the value of η at the edge of the boundary layer and

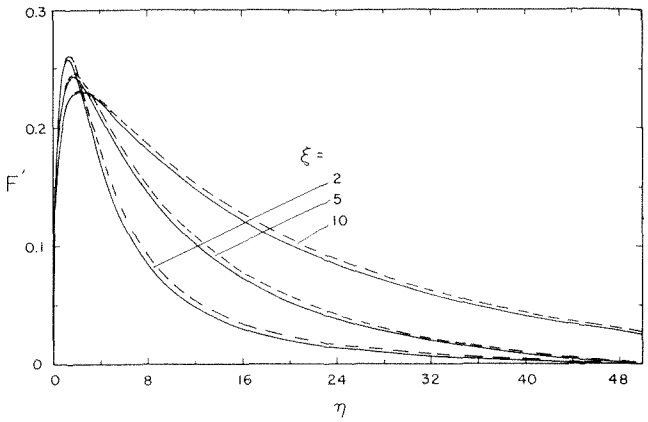

Fig. 5 Representative velocity profiles, ξ = 2, 5, and 10

r_δ the corresponding radial coordinate. With these, equation (37) becomes

$$\left(\frac{r}{r_0}\right)_\delta = (1 + \xi\eta_\delta)^{1/2} \tag{38}$$

For the present discussion, η_δ will be taken to correspond to θ = 0.02. Then, for example, $(r/r_0)_\delta$ = 2 for ξ = 0.5 and $(r/r_0)_\delta$ = 10.5 for ξ = 5. These results indicate that for larger values of ξ, the radial extent of the boundary layer is much, much greater than the radius of the cylinder.

From an initial inspection of the figure, it may appear that a large-ξ boundary layer on a cylinder is always thicker than a small-ξ boundary layer. Such a conclusion is tenuous, as will now be demonstrated. If y = $r - r_0$ is designated as the radial distance measured outward from the surface of the cylinder, then equation (4) becomes

$$\eta = \left[\frac{g\beta(T_w - T_\infty)}{4\nu^2}\right]^{1/4} \frac{y}{x^{1/4}} \left[\frac{1}{2}\left(1 + \frac{r}{r_0}\right)\right] \tag{39}$$

As noted in the foregoing, r/r_0 may be substantially in excess of one, especially at larger values of ξ. Therefore, the factor $\frac{1}{2}(1 + r/r_0)$ that appears in equation (39) acts to increase the range of η for $\xi > 0$, as is clearly in evidence in Fig. 3. However, as can be seen from equation (39), this increased range of η does not mean that the range of

$$\left[\frac{g\beta(T_w - T_\infty)}{4\nu^2}\right]^{1/4} \frac{y}{x^{1/4}} \tag{40}$$

has increased. Indeed, the range of this quantity could even decrease with increasing ξ and still not counteract the increased range of η caused by the factor $\frac{1}{2}(1 + r/r_0)$.

Velocity profiles are presented in Fig. 4 for ξ = 0, 0.5, 1 and for ξ = 2, 5, and 10 in Fig. 5. The ordinate variable F' is related to the streamwise velocity by

$$\frac{u}{[4\,g\beta(T_w - T_\infty)x]^{1/2}} = F'(\xi,\eta) \tag{41}$$

The velocity profiles show the characteristic shape for natural convection boundary layers, with a velocity maximum at a position somewhat displaced from the wall. The position of the maximum appears to move away from the wall as ξ increases. The factor $\frac{1}{2}(1 + r/r_0)$ is responsible for this apparent outward movement. In actuality, the quantity

$$\left[\frac{g\beta(T_w - T_\infty)}{4\nu^2}\right]^{1/4} \frac{y}{x^{1/4}} \tag{42}$$

diminishes slightly as ξ increases. By the same token, the apparent thickening of the profiles with increasing ξ is due to the factor $\frac{1}{2}(1 + r/r_0)$.

Another interesting result in evidence in Figs. 4 and 5 is that the magnitude of the maximum is not a very strong function of ξ. The deviations between the velocity profiles from the first and third levels of truncation are seen to be small, which is consistent with the behavior of the temperature profiles.

Acknowledgment

The authors wish to acknowledge Mr. Benjamin R. Strong, Jr., and Mr. Anupam Bagchi for their assistance in various aspects of the numerical computations.

References

1 Millsaps, K., and Pohlhausen, K., "The Laminar Free-Convection Heat Transfer From the Outer Surface of a Vertical Cylinder," *Journal of the Aeronautical Sciences*, Vol. 25, 1958, pp. 357–360.

2 Yang, K. T., "Possible Similarity Solutions for Laminar Free Convection on Vertical Plates and Cylinders," *Journal of Applied Mechanics*, Vol. 27, 1960, pp. 230–236.

3 Elenbaas, W., "The Dissipation of Heat by Free Convection From Vertical and Horizontal Cylinders," *Journal of Applied Physics*, Vol. 19, 1948, pp. 1148–1154.

4 Sparrow, E. M., and Gregg, J. L., "Laminar Free Convection Heat Transfer From the Outer Surface of a Vertical Circular Cylinder," TRANS. ASME, Vol. 78, 1956, pp. 1823–1829.

5 Kuiken, H. K., "Axisymmetric Free Convection Boundary Layer Flow Past Slender Bodies," *International Journal of Heat and Mass Transfer*, Vol. 11, 1968, pp. 1141–1153.

6 Fujii, T., and Uehara, H., "Laminar Natural Convective Heat Transfer From the Outer Surface of a Vertical Cylinder," *International Journal of Heat and Mass Transfer*, Vol. 13, 1970, pp. 607–615.

7 LeFevre, E. J., and Ede, A. J., "Laminar Free Convection From the Outer Surface of a Vertical Circular Cylinder," *Proceedings, 9th International Congress for Applied Mechanics*, Brussels, Vol. 4, 1956, pp. 175–183.

8 Hama, F. R., Recesso, J. V., and Christiaens, J., "The Axisymmetric Free Convection Temperature Field Along a Vertical Thin Cylinder," *Journal of the Aero*/Space Sciences, Vol. 26, 1959, pp. 335–342.

9 Nagendra, H. R., Tirunarayanan, M. A., and Ramachandran, A., "Laminar Free Convection From Vertical Cylinders with Uniform Heat Flux," Journal of Heat Transfer, Vol. 92, 1970, pp. 191–194.

10 Sparrow, E. M., Quack, H., and Boerner, C. J., "Local NonSimilarity Boundary-Layer Solutions," *AIAA Journal*, Vol. 8, 1970, pp. 1936–1942.

11 Sparrow, E. M., and Yu, H. S., "Local Nonsimilarity Thermal Boundary Layer Solutions," *Journal of Heat Transfer*, TRANS. ASME, Series C, Vol. 93, 1971, pp. 328–334.

M. Abrams
Sandia Laboratories,
Livermore, Calif.
Mem. ASME

R. Viskanta
Professor,
Purdue University,
Lafayette, Ind.
Mem. ASME

The Effects of Radiative Heat Transfer Upon the Melting and Solidification of Semitransparent Crystals[1]

Employing the assumptions of one-dimensional energy transfer, equilibrium phase change, and negligible convection in liquid regions, the time-dependent conservation of energy equation is formulated for the general situation of n semitransparent contiguous liquid and solid phases. The dimensionless parameters governing phase change are identified and the effects of their variation are ascertained by a finite difference solution of the rigorously formulated energy and radiative transfer equations. The chief conclusions of this investigation are that for the range of parameters encountered in the melting and solidification of many optical materials, radiant transfer has a significant effect, and that during solidification, radiation can force the temperature profile within the liquid phase to assume a shape which leads to unstable interfacial growth.

Introduction

The effects of heat transfer upon melting and solidification processes have been studied theoretically and experimentally for more than a century. Nearly all of these studies, however, have dealt with opaque materials and hence, the contribution of thermal radiation within the media has been justifiably ignored. The objective of the present work is to ascertain effects of thermal radiation in nonopaque materials during phase change where such effects have not yet been quantitatively established. To accomplish this end, the classical Stefan problem [1][2] is reformulated with the inclusion of radiative transfer, and numerical solutions are obtained.

Knowledge of the temperature gradients at a solid-liquid interface is of particular value in the analysis of interfacial stability during solidification [2]. An unstable interface is one where protrusions or dendrites grow into the liquid as the solidification progresses, whereas a stable interface is macroscopically a planar surface. Stable solidification is favored when temperature within the liquid increases with distance away from the solid-liquid interface, and vice versa. In the *steady-state* investigation of [3], in which S-shaped temperature profiles were obtained within the liquid, it was concluded that radiation enhances stable growth by increasing the temperature gradient within the liquid at the interface. The present investigation shows, however, that radiation can also cause temperature profiles to develop which promote unstable crystalline growth.

Apart from interfacial stability considerations, the present investigation sheds light on the obvious question in any phase change process, i.e., how much of each phase is present at an arbitrary time after the sudden application of a thermal driving force.

Except for Abrams [4] and Habib [5, 6] no prior treatment of the Stefan problem including combined radiative and conductive transfer has been reported, although the Stefan problem without radiation, and combined radiative and conductive transfer without phase change have, respectively, been thoroughly investigated. In references [5 and 6] a heat balance integral method was employed to approximate temperature profiles within the solid phase of planar and cylindrical media during solidification. It was assumed in these studies, however, that the temperature distribution within the liquid was uniform and therefore, no insight into interfacial stability could be gained.

Physical Assumptions Employed in Analysis. It is presumed that all solids are crystalline, and that liquids, upon solidification, assume the crystalline rather than the glassy state. Crystalline materials are characterized by discrete melting temperatures and latent heats, and hence, when such materials melt, there is a locatable interface between solid and liquid. Glasses, on the other hand, in a strict sense do not melt, but rather become progressively softer as temperature increases and there is no absorption of a latent heat. Thus, the problem under examination is fundamentally apart from the well-explored subject of the melting and solidification of glass.

Consideration is limited to one-dimensional radiative and conductive energy transfer in a region of finite thickness and of infi-

[1] This work was supported, in part, by the United States Atomic Energy Commission, Contract Number AT-(29-1)-789.

[2] Numbers in brackets designate References at end of paper.

Contributed by the Heat Transfer Division of THE AMERICAN SOCIETY OF MECHANICAL ENGINEERS and presented at the ASME-AIChE Heat Transfer Conference, Atlanta, Ga., August 5-8, 1973. Manuscript received by the Heat Transfer Division, October 4, 1973. Paper No. 73-HT-12.

nite lateral extent which consists of an arbitrary number of contiguous solid and liquid phases (Fig. 1(*a*)). The interfaces and boundaries are considered to be diffuse, parallel, and planar surfaces which are normal to the direction of energy transfer. Typically, Fig. 1(*a*) could represent a melting process, where phase 1 is a liquid which is being heated from the left and the other regions are the various solid phases. Natural convection is presumed absent in the liquid phases, which is a reasonable assumption if density gradients are normal to, or in the same direction as, the gravitational force, or if the Rayleigh number is less than the critical value [7].

The medium which undergoes the phase change is considered to be a pure substance whose phase transitions occur at fixed (equilibrium) temperatures. If a solute were present, the interfacial temperature would depend upon the concentration of solute at the interface and hence, the conservation of species equation would be required together with the energy equation in order to determine temperature distributions [8].

The solid phases are assumed to be isotropic so that at any location direction-independent thermophysical properties characterize the material. While only cubic crystals (NaCl, fluorite, etc.) are truly optically isotropic, the principal indices of refraction of many other crystals differ very little from one another. Such materials are presumed to be characterized by an average index of refraction and hence are treated in analysis as being isotropic. Born and Wolf [9] describe the propagation of electromagnetic waves in optically anisotropic absorbing media but do not account for thermal emission.

It is assumed that the index of refraction of each phase is uniform, a condition implicitly required by the classical equation of transfer employed in this investigation. If the index of refraction n_ν is variable, either through material inhomogeneity or dependency upon temperature, the path followed by a photon has a curvature which depends upon grad (log n_ν) [9, p 124]. However, since n_ν is relatively insensitive to temperature, its assumed uniformity is not expected to be a serious restriction even if large temperature gradients exist.

Finally, it is assumed that scattering is absent and that local thermodynamic equilibrium exists throughout the medium. The absence of scattering applies to physical situations in which the solid is either a single crystal or a composite of polycrystals which are small compared to the wavelengths of incident radiation. The scattering of thermal radiation in degassed liquids is negligible. In the absence of fluorescence or lasing, the assumption of local thermodynamic equilibrium in liquids and solids is excellent.

Mathematical Formulation

The Conservation of Energy Equation. The mathematical model of the phase change problem is shown in Fig. 1(*a*). Depicted are n regions each corresponding to a solid or liquid phase undergoing replenishment or depletion by material exchange with its neighbors. (It is convenient to regard the left and right-hand surroundings as fictitious phases having the indicies o and $n + 1$, respectively.) Although numerical results are obtained only for two-phase systems, the more general formulation for n phases is presented here.

Assuming that all phases have the same constant density[3] ρ, the conservation of energy equation becomes

$$\rho c_i \frac{\partial T_i}{\partial t} = -\frac{\partial}{\partial X}\left(k_i \frac{\partial T_i}{\partial X}\right) - \frac{\partial F_{r,i}}{\partial X}$$

$$i = 1, 2, \ldots n \tag{1}$$

where $X_{i-1}(t) < x < X_i(t)$, $t < 0$, and the radiative flux

$$F_{r,i}(x) = 2\int_0^\infty \{J^+_{\nu,i} E_3[\Upsilon_{\nu,i}(X_{i-1}, x)] - J^-_{\nu,i} E_3[\Upsilon_{\nu,i}(x, X_i)]\} d\nu \tag{2}$$

[3] In general, if the phases have differing densities, a different bulk velocity is imparted to each phase during the transient phase change process [4]. The neglect of such motion could be unrealistic in cylindrical or spherical media where the geometrical constraints could cause a physical separation of the phases.

Nomenclature

B_ν = Planck function $(2\pi h\nu^3/c^2) \times [\exp(h\nu/kT) - 1]^{-1}$
c = speed of light; also specific heat
$E_n(z)$ = exponential integral function defined as $\int_0^1 t^{n-2}\exp(-z/t)dt$
F_c = conductive flux
F_r = total radiative flux
$g_i(x)$ = initial temperature distribution on the region $X_{i-1}{}^0 < x < X_i{}^0$
$H^\pm$ = irradiation as defined by equations (10*a*) and (10*b*)
h = Planck's constant
I = intensity of radiation
J = radiosity (radiative flux leaving an interface); see Fig. 1(*b*)
k = Boltzmann's constant; also thermal conductivity
L = initial slab width
N = conduction-radiation interaction parameter $k_r/(4\sigma T_r{}^3 L)$
n = number of phases initially present; also index of refraction
T = absolute temperature
$T^E_{i,i+1}$ = equilibrium temperature at the interface between phases i and $i + 1$
t = time
$t_c{}^*$ = Fourier number
X_i = location of interface on the right-hand side of region i; see Fig. 1(*a*), $X_0 \equiv 0$
$X_i{}^0$ = initial location of ith interface
x = position
Y_i = quantity defined as $\Delta h_{i+1,i}/(c_r T_r)$
α = thermal diffusivity, $k/(\rho c)$
$\gamma_{\nu,i-1,i}$ = bidirectional transmittance function, in region $i - 1$, at the interface with region i
$\Delta h_{i+1,i}$ = enthalpy phase $i + 1$ minus enthalpy phase i evaluated at interfacial temperature between these phases
$\epsilon_{\nu,i,i+1}$ = hemispherical emittance of the surface of material i when it is in contact with material $i + 1$
ζ, ζ' = dummy position variables in the x direction
κ = absorption coefficient
μ = cosine of the angle between a given direction and the positive x direction
ν = frequency
ρ = density
$\rho_{\nu,i,i-1}$ = bidirectional reflectance function, in region i, at the interface with region $i - 1$
σ = Stefan-Boltzmann constant
$\Upsilon_{\nu,i}$ = transmission function for region i
$\Im_{\nu,i} = 2E_3[\Upsilon_{\nu,i}(X_{i-1}, X_i)]$
τ_ν = optical thickness of medium of width $L(=k_\nu L)$
$\Upsilon_\nu(a, b)$ = optical distance between planes $x = a$ and $x = b$ $\int_a{}^b \kappa_{\nu,i}(\zeta')d\zeta'$

Subscripts

i = pertains to the region i
k = pertains to the band k
r = reference condition or evaluated at reference conditions
ν = spectral quantity

Superscripts

$\cdot$ = differentiation with respect to time
$+$ = denotes the positive x direction (see Fig. 1(*b*))
$-$ = denotes the negative x direction (see Fig. 1(*b*))
$*$ = dimensionless quantity; see equations (9)
(k) = refers to kth band in the model of the absorption coefficient

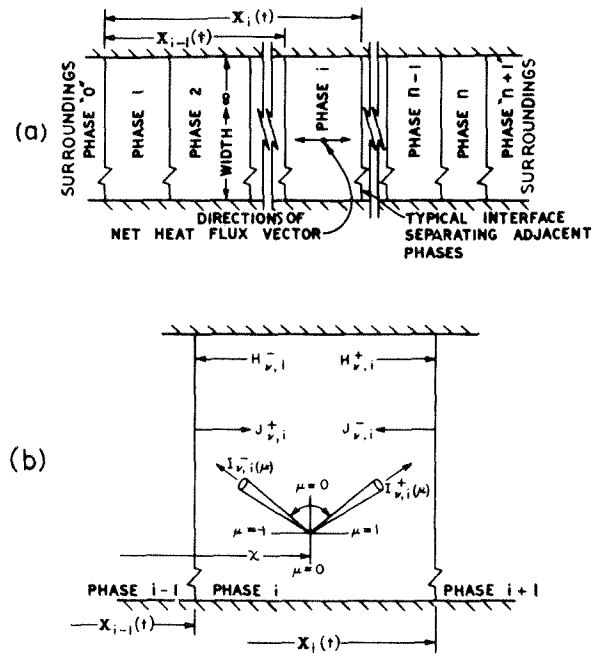

Fig. 1 One-dimensional idealization of the problem: (*a*) physical model of *n*-phase system; (*b*) detailed view of *i*th phase showing intensity and energy transfers

$$+ 2\pi \int_0^\infty n_{\nu,i}^2 \int_{X_{i-1}}^{X_i} \kappa_{\nu,i}(\zeta) B_{\nu,i}(\zeta)\ \text{sign}\ (x-\zeta)\ \cdot$$

$$E_2[|\Upsilon_{\nu,i}(\zeta,x)|]d\zeta d\nu \tag{2}$$

The details of the derivation of this equation are found in [4].

In order to evaluate the radiosities ($J\nu$) appearing in equation (2), a radiative flux balance is made at each interface and boundary. It can then be shown that the radiosities must satisfy the following set of $2n$ linear algebraic equations

$$-\gamma_{\nu,i-1,i}\tau_{\nu,i-1}J_{\nu,i-1}^{+} + J_{\nu,i}^{+} - \rho_{\nu,i,i-1}\tau_{\nu,i}J_{\nu,i}^{-} = \gamma_{\nu,i-1,i}H_{\nu,i-1}^{+} + \rho_{\nu,i,i-1}H_{\nu,i}^{-} \tag{3a}$$

$$-\rho_{\nu,i,i+1}\tau_{\nu,i}J_{\nu,i}^{+} + J_{\nu,i}^{-} - \gamma_{\nu,i+1,i}\tau_{\nu,i+1}J_{\nu,i+1}^{-} = \rho_{\nu,i,i+1}H_{\nu,i}^{+} + \gamma_{\nu,i+1,i}H_{\nu,i+1}^{-} \tag{3b}$$

where $i = 1, 2, \ldots n$ and where $J_{\nu,0}^{+}$ and $J_{\nu,n+1}^{-}$ are defined to be zero. The fluxes $H_{\nu,i}^{+}$ and $H_{\nu,i}^{-}$, respectively, denote the irradiations of the right and left-hand interfaces of the ith region due to emission within that region, and are given by

$$H_{\nu,i}^{+} = 2\pi n_{\nu}^2 \int_{X_{i-1}}^{X_i} \kappa_{\nu,i}(\zeta)\ \cdot$$

$$B_{\nu,i}(\zeta)E_2[\Upsilon_{\nu,i}(\zeta,X_i)]d\zeta \tag{4a}$$

$$H_{\nu,i}^{-} = 2\pi n_{\nu,i}^2 \int_{X_{i-1}}^{X_i} \kappa_{\nu,i}(\zeta)\ \cdot$$

$$B_{\nu,i}(\zeta)E_2[\Upsilon_{\nu,i}(X_{i-1},\zeta)]d\zeta \tag{4b}$$

for $i = 1, 2, \ldots n$. For transparent surroundings, $H_{\nu,0}^{+}$ and $H_{\nu,n+1}$ are, respectively, defined as the external radiation incident upon the left-hand and right-hand boundaries of the system.

If the region i ($i = 0, 1, 2, \ldots n, n+1$) is opaque at the frequency ν but has transparent neighbors, redefinition of the quantities $\Upsilon_{\nu,i}$, $H_{\nu,i}^{\pm}$, and $\gamma_{\nu,i,i\pm1}$ as follows

$$\tau_{\nu,i} = 0 \tag{5a}$$

$$H_{\nu,i}^{+} = n_{\nu,i+1}^2 \pi B_{\nu}(X_i) \tag{5b}$$

$$H_{\nu,i}^{-} = n_{\nu,i-1}^2 \pi B_{\nu}(X_{i-1}) \tag{5c}$$

$$\gamma_{\nu,i,i\pm1} = \epsilon_{\nu,i,i\pm1} \tag{5d}$$

enables computation of radiosities in the adjoining transparent region(s) with equations (3*a*) and (3*b*). The radiative flux $F_{r\nu,i}(x)$ is *a priori* taken to be zero if region i is opaque at the frequency ν.

Interfacial, Initial and Boundary Conditions. A mass and energy balance at each of the $n-1$ interfaces yields the relationship

$$\dot{\rho X}_i \Delta h_{i+1,i} - \left(k_i \frac{\partial T_i}{\partial X}\right)\Big|_{x=X_i} + \left(k_{i+1}\frac{\partial T_{i+1}}{\partial X}\right)\Big|_{x=X_i} + \int_0^\infty F_{r\nu,i}(X_i)d\nu - \int_0^\infty F_{r\nu,i+1}(X_i)d\nu = 0 \tag{6}$$

which, together with the assumption of equilibrium phase change, i.e.,

$$T_i(X_i,t) = T_{i+1}(X_i,t) = T_{i,i+1}^{E} \tag{7}$$

constitute the two necessary interfacial conditions of the problem. If the phases i and $i+1$ have identical opaque and transmitting bands, equation (14) becomes independent of the radiative flux at an interface, since in a transparent band $F_{r\nu,i}(X_i) = F_{r\nu,i+1}(X_i)$, and in an opaque band $F_{r\nu,i}(X_i) = F_{r\nu,i+1}(X_i) = 0$. The initial conditions of the problem are the temperature distributions and interfacial locations at $t = 0$ which, respectively, are

$$T_i(x,0) = g_i(x) \text{ for } X_{i-1} < x < X_i \tag{8a}$$

and

$$X_i(0) = X_i^0 \tag{8b}$$

Although a variety of radiation and temperature boundary conditions are possible, the present investigation considers only the situations in which the surroundings are opaque and the boundary temperatures or temperature gradients are prescribed. In the instance of opaque surroundings equations (5*b*) and (5*c*) are employed to determine the effective irradiations of the left and right-hand boundaries of the system. The more general situation of transparent and convective surroundings is presented in reference [4].

With the introduction of the dimensionless variables:

$$\begin{aligned}
x^* &= x/L;\\
t^* &= 4\sigma T_r^3 t/(\rho c_r L);\\
X_i^* &= X_i/L;\\
\nu^* &= h\nu/(kT_r);\\
\kappa_{\nu,i}^* &= \kappa_{\nu,i}/\kappa_r;\\
F_c^* &= F_c/\sigma T_r^4;\\
H_\nu^* &= H_\nu/[(h/k)\sigma T_r^3];\\
g_i^* &= g_i/T_r\\
T_i^* &= T/T_r\\
c_i^* &= c_i/c_r;\\
k_i^* &= k_i/k_r;\\
F_{r_\nu}^* &= F_{r_\nu}/[(h/k)\sigma T_r^3]\\
B_\nu^* &= B_\nu/[(h/k)\sigma T_r^3];\\
J_\nu^* &= J_\nu/[(h/k)\sigma T_r^3];\\
F_r^* &= F_r/\sigma T_r^4;
\end{aligned} \tag{9}$$

the energy equation (equation (1)) and the interfacial condition corresponding to equation (6), respectively, become

$$c_i^* \frac{\partial T_i^*}{\partial t^*} = N\frac{\partial}{\partial x^*}\left[k_i^*\frac{\partial T_i^*}{\partial x^*}\right] - \frac{1}{4}\frac{\partial F_{r,i}^*}{\partial x^*} \tag{10}$$

and

$$(Y_i/N)\frac{dX_i^*}{dt^*} + \left[\left(k_{i+1}^*\frac{\partial T_{i+1}^*}{\partial x^*}\right)\Big|_{x^*=X_i^*} - \left(k_i^*\frac{\partial T_i^*}{\partial x^*}\right)\Big|_{x^*=X_i^*}\right] + \frac{1}{4N}\left[\int_0^\infty F_{r\nu,i}^*(X_i^*)\,d\nu^* - \int_0^\infty F_{r\nu,i+1}^*(X_i^*)\,d\nu^*\right] = 0 \tag{11}$$

where the quantities N and Y_i are defined as

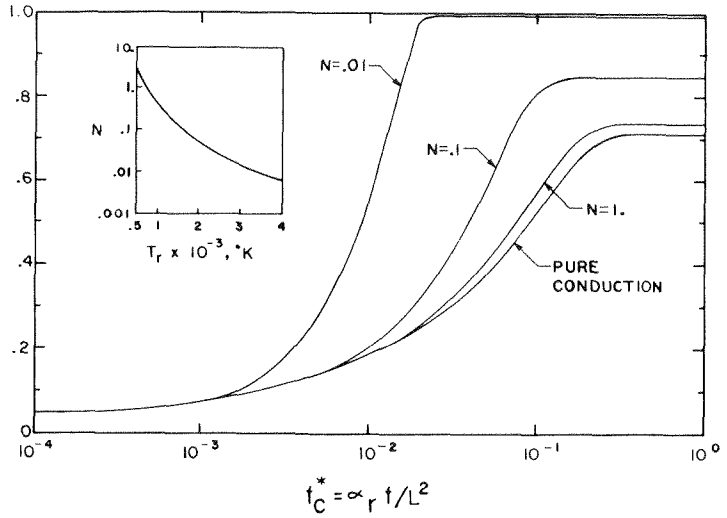

Fig. 2 Interfacial position versus dimensionless time during melting. For reference, the inset shows N versus T_r for a slab 10 cm thick having the flourite property $k_2 = 0.09$ w/cm-deg K.

$$N = k_r/(4\sigma T_r^3 L) \tag{12}$$

$$Y_i = \Delta h_{i+1,i}/(c_r T_r) \tag{13}$$

In general, a small value of N implies that radiation could significantly effect the temperature distribution in the ith region. However, this observation is not universally applicable as it is conceivable that the ith phase approaches being opaque or nonabsorbing over the effective width of the spectrum. In these cases radiation has no effect upon the temperature distribution regardless of the value of N. The quantity Y_i physically represents the ratio of latent to sensible heat at the ith interface, and has the form of a Jakob number.

Method of Solution. The details of the method of solution are given in reference [4]. Basically, equation (10) is recast in explicit finite difference form following the numerical scheme of Murray and Landis [10]. The radiative transfer integrals, which are all of the generic form

$$I(x) = \int^x f(\zeta) E_n[\tau(x-\zeta)]d\zeta, \tag{14}$$

are exactly evaluated after assuming that $f(\zeta)$ varies linearly between grid points. The error introduced by this process can be shown to be an order of magnitude less than the truncation error of the finite difference method. For the special case of steady combined radiation and conduction heat transfer (with no change of phase), the results of the finite difference solution are in excellent agreement with the exact results of Crosbie [11].

The stability criterion which places a limitation upon the maximum permissible time step is that given by Ames [12, p. 330] for parabolic partial differential equations. In conduction dominated problems ($N > 1$), the stability criterion is found to be less stringent if the Fourier number $t_c^* = \alpha_r t/L^2$ is employed as the dimensionless time variable instead of t^*. In any case, results based upon either dimensionless time can be related since

$$t_c^* = Nt^* \tag{15}$$

Results and Discussion

The results of this investigation are obtained by examining the effects of parameter variations upon the transient temperature distributions and interfacial motions during melting and solidification. Since prior work in this area is limited, the objective is to gain an understanding of the effects of radiative transfer upon the dynamics of the phase change process. Thermophysical properties are assumed to be independent of temperature, and for simplicity, only a single phase, either solid or liquid, is considered to be initially present. The melting example employs gray optical properties while a band model is employed in the solidification example.

The Melting of a Slab. The aims of this first study are to determine the significance of the conduction-radiation interaction parameter, N, and the error incurred by neglecting radiative transfer in an example representative of the melting of a large crystal in a furnace. The mathematical idealization is as follows. A slab of solid transparent material, initially at a uniform temperature, is suddenly brought into perfect contact with opaque regions at each boundary; see Fig. 1(*a*). The temperature of the region on the left is greater than the melting temperature of the slab and is held constant, while the region on the right is maintained at the slab's initial temperature. Both boundaries are assumed to have unit emissivities. The dimensionless input to the computations is the following:

Boundary, initial, and interfacial conditions:[4]

$$T^*(0, t^*) = 1 \text{ and } T^*(1, t^*) = 0.1 \text{ for } t^* > 0;$$

$$g_2^*(x^*) = 0.1 \text{ for } 0 < x^* < 1;$$

$$T_{1,2}^{E^*} = 0.5 \text{ and } X_1^{0^*} = 0$$

Parameters and properties:[4]

	Region 1 (liquid)	Region 2 (solid)
c_i^*	0.75	1
k_i^*	2	1
$\tau_{\nu,i}$	1	2
$n_{\nu,i}$	1.5	1.5

$Y_1 = -0.1$

$\rho_{\nu,1,2} = 0$

$\epsilon_{\nu,0,1} = \epsilon_{\nu,2,3} = 1$

$N = 0.01, 0.02, 0.05, 0.1, 1.$

Because of the general lack of property data for the liquid phase of high melting-temperature materials, it is impossible to determine input parameters and properties specifically for a given substance. The foregoing values of Y_1, k_i^*, and c_i^*, however, were selected to approximate the melting of fluorite (melting temperature 1700 deg K) with the temperature of the hot face at twice the melting temperature.

Fig. 2 depicts interfacial position as a function of the dimensionless time (Fourier number), t_c^*, for several values of the parameter N. For comparison, interfacial position in the corre-

[4] The effects of perturbations in these input quantities are examined in [4].

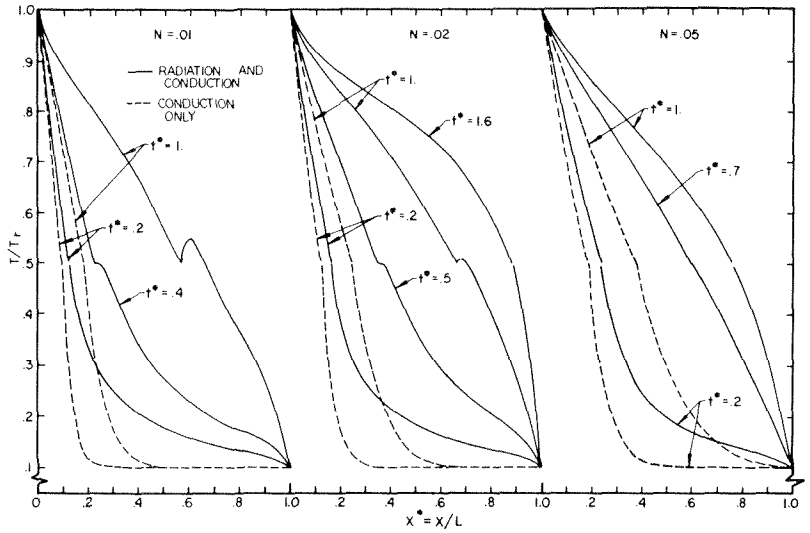

Fig. 3 Temperature distributions at various times during melting with N as a parameter

sponding pure conduction problem is also shown. It is found that the Fourier number is a more convenient time variable than t^* when comparing the effects of combined energy transfer to the effects of pure conductive heat transfer. For the purpose of reference, the inset in Fig. 2 gives N as a function of T_r for a slab 10 cm thick which has the fluorite property $k_2 = k_r = 0.09$ w/cm-deg K. Transient temperature distributions for several values of N are shown in Fig. 3.

It is seen in Fig. 2, that early in the transient, all curves coalesce into the pure conduction curve. This early time behavior is a consequence of the following physical conditions: *(a)* the regime $t^* = t_c/N \ll 1$ implies that the presence of radiation has not yet had sufficient time to appreciably affect the temperature distribution and hence interfacial movement; and *(b)* the infinite temperature gradient existing initially at the left-hand boundary exerts an overwhelming influence upon interfacial motion regardless of the magnitude of the radiative flux at the interface. From these physical considerations, it is concluded that conduction governs interfacial motion at early times, and hence, it is to be expected that interfacial motion would be similar to that for pure conduction. The pure conduction profiles of Fig. 3 indicate, however, that neglecting radiation, even at early times, leads to serious error in the temperature distribution.

In Fig. 3 it is noticed that, when N is relatively small, an anomalous bump begins to form within the temperature profile of the solid corresponding to the occurrence of superheat. In practice, superheat in a solid is an unlikely physical phenomenon, but, in the present study its occurrence is permitted in order to reveal the effects of radiative heat transfer. For N-values of 0.01 and 0.02 the maximum bump height occurs approximately at $t^* = 1$. For the conditions of this example, bumps are not observed to occur, at any time, for values of N equal to 0.05 and larger. The growth of these bumps stems from the fact that the interfacial temperature is forced to remain at the imposed constraint of $T_{1,2}{}^{E*} = 0.5$, while energy emitted by the hot liquid and left-hand boundary, after appropriate attenuation, enters the solid phase where it is partially absorbed. Recognizing that emission within the solid cannot be significant because of the relatively low temperature there, it is evident that the rate of absorption of radiant energy per unit of the volume exceeds the rate of emission. The occurrence of the bump in the present example, is analogous to the thermal trap effect described by Cobble [13]. In passing, it is noted that these peculiarities in the temperature distributions could have been missed if calculations were based upon methods which require assuming the functional form of the temperature distribution (e.g., heat balance integral methods).

The Solidification of a Slab—Gray Optical Properties. The purpose of this study is to determine the characteristics of solidification in the presence of combined radiative and conductive heat transfer. The physical situation under consideration is idealized as follows.

A liquid, at uniform temperature, bounded by two infinite parallel planes, is suddenly brought into perfect contact with opaque regions at each boundary. The region on the left (see Fig. 1(*a*)) is maintained at a constant temperature which is less than the freezing temperature of the liquid, while the right-hand boundary is maintained adiabatic. The left and right-hand boundaries are, respectively, assumed to be black and perfectly reflecting surfaces. In contrast to the interfacial motion of the previous study, the solid-liquid interface eventually reaches the right-hand boundary so that the region contained between the planar surfaces is entirely a single phase. Consideration is limited, however, to the period of time before complete solidification occurs. The data employed in this study are:

Boundary, initial and interfacial conditions:

$$T^*(0, t^*) = 0.1 \text{ and } \partial T^*(1, t^*)/\partial x^* = 0 \text{ for } t^* > 0;$$

$$g_2{}^*(x^*) = 1 \text{ for } 0 < x^* < 1;$$

$$T_{1,2}^{E*} = 0.5 \text{ and } X_1{}^0 = 0$$

Parameters and properties:

	Region 1 (solid)	Region 2 (liquid)
$c_i{}^*$	1	1
$k_i{}^*$	1	1
$\tau_{\nu,i}$ (Case 1)	1	10
$\tau_{\nu,i}$ (Case 2)	10	1
$n_{\nu,i}$	1.5	1.5

$Y_1 = 0.1$
$\rho_{\nu,1,2} = 0$
$\epsilon_{\nu,0,1} = 1$
$\epsilon_{\nu,2,3} = 0$
$N = 1, 0.1, 0.01$

Fig. 4 depicts the dimensionless interfacial position as a function of the dimensionless time (Fourier number) and the parameters N and $\tau_{\nu,i}$. Interchanging the optical thicknesses $\tau_{\nu,i}$ produce no discernible effect upon interfacial motion when $N = 0.1$ and 1, and hence only single curves appear for these values. Interfacial motion becomes more sensitive to changes in $\tau_{\nu,i}$, however, as radiative transfer becomes increasingly important, i.e., as N decreases. As with the melting process, it is seen that for a fixed $t_c{}^*$, a smaller N implies a greater interfacial motion, which is a consequence of the greater radiative cooling of the liquid. As shown, the degree of error introduced by neglecting radiation could be significant.

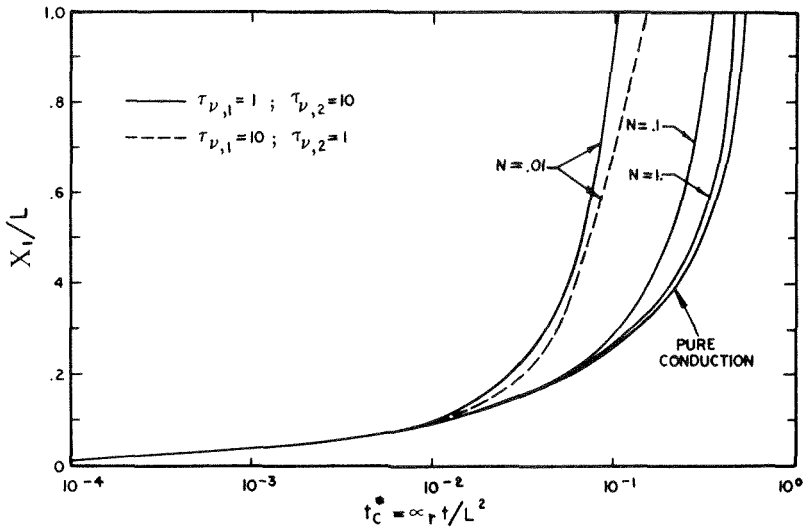

Fig. 4 Interfacial position versus dimensionless time during solidification

Transient temperature distributions, shown in Fig. 5 for N = 0.01, reveal a significant feature of the solidification process: the formation of a temperature depression within the liquid phase when the slab is about 50 percent solidified. From a crystal growth standpoint, such formation is undesirable because it increases the likelihood of dendritic growth. The temperature depression forms as temperature profiles within the liquid become relatively flat and it becomes difficult for conduction heat transfer to compensate for the radiant energy loss from the neighborhood of the interface.

The Solidification of a Slab With Absorption Coefficient Represented by Band Models. The physical situation under examination is described in the foregoing with the exception that the absorption coefficients of both solid and liquid are represented by the various band models of Fig. 6. For concreteness, it is also assumed that $\kappa_2 L = 1$ where κ_2 is the absorption coefficient of the second band. Wavelengths corresponding to the ν^* spectrum are shown for three values of the reference temperature on separate scales. It is seen that the three models characterize the behavior of many optical materials: high transparency in the visible part of the spectrum, an abrupt decrease in transparency in the ultra-violet, and a gradual decrease in transparency in the infrared. The f-scale of Fig. 6, which represents the fraction of energy emitted by a black body over the frequency range 0-ν^*, shows that only a negligible quantity of energy is emitted for $\nu^* > 20$. (The difference between two values on the f-scale represents the fraction of energy emitted by a black body over the dimensionless frequency range corresponding to the two f values.) Hence, for the three models shown, the precise ν^*—value of the ultraviolet cutoff is immaterial in the computations. Each band model represents a material having approximately the absorption characteristics of window glass [14]:

	$\lambda > 5\mu$:	opaque
Band 1	$5\mu > \lambda > 2.5\mu$	$\kappa_1 = 5\ \text{cm}^{-1}$
Band 2	$2.5\mu > \lambda > 1\mu$	$\kappa_2 = 0.1\ \text{cm}^{-1}$
Band 3	$1\mu > \lambda > 0.2\mu$	$\kappa_3 = 0.01\ \text{cm}^{-1}$
	$\lambda < 0.2\mu$	opaque

Fig. 7 depicts for N = 0.01 interfacial position as a function of the Fourier number for three spectral and three gray models of the absorption coefficient. Comparison of the gray and nongray results shows that interfacial motion cannot be described accurately over the entire solidification process by gray calculations which employ the optical properties of a particular band. Moreover, even if interfacial positions based, respectively, upon gray and nongray absorption coefficients are in agreement with one another, there is no assurance that the corresponding temperature profiles or energy fluxes would be in similar agreement [4].

Fig. 7 additionally indicates that the interfacial motion for $\tau_{\nu,i}$ = 1 is always greater than that for the other spectral models. This result is expected on the basis of steady-state and transient calculations [15] which have shown that the interaction between radiation and other modes of heat transfer should be greatest when the optical thickness of the medium is approximately unity. Therefore, on $X_1^* - t_c^*$ coordinates, for a fixed value of N, the curve for $\tau_{\nu,i} = 1$ represents an approximate upper bound, and

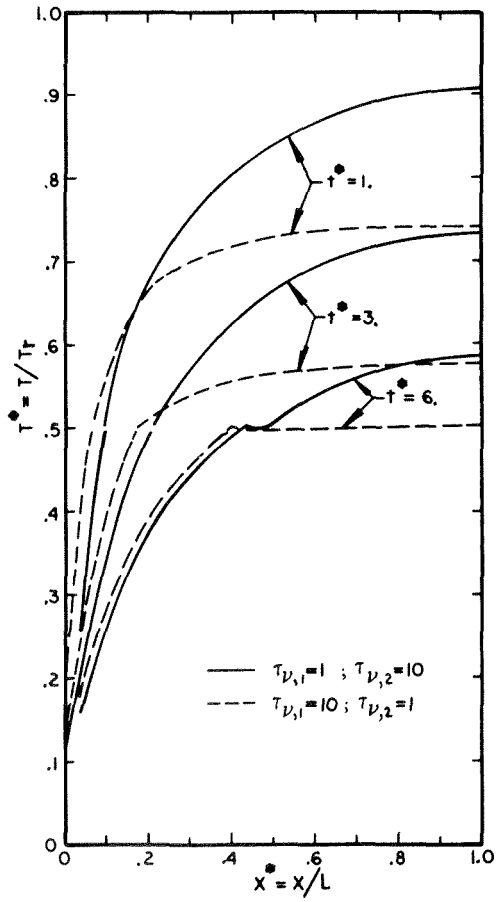

Fig. 5 Transient temperature distributions during solidification: N = 0.01

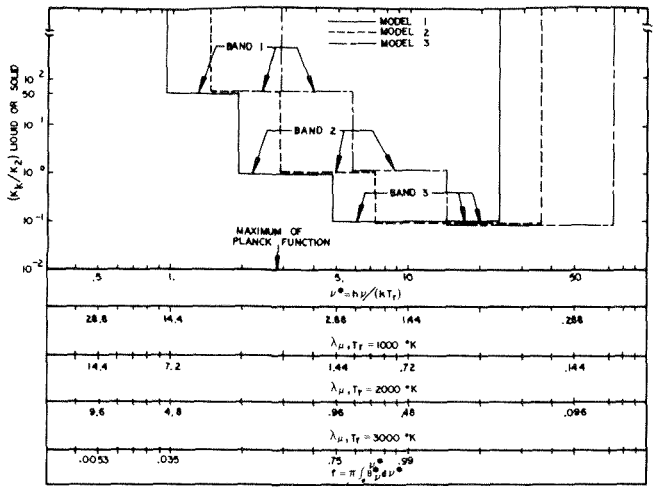

Fig. 6 Dimensionless absorption coefficient versus dimensionless frequency ν^*. The ordinate is the ratio: absorption coefficient of the kth band/absorption coefficient of the second band. The λ-scales represent wave lengths corresponding to the ν^* spectrum for the indicated values of the reference temperature. The f-scale is defined in text.

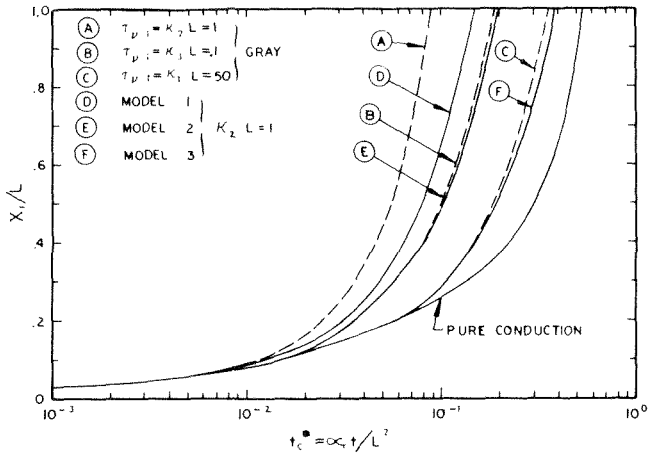

Fig. 7 Interfacial position versus time during solidification for various spectral and gray models of the absorption coefficient; $N = 0.01$

the pure conduction curve represents the lower bound to interfacial motion.

Conclusion

It has been determined that radiation can significantly affect the dynamics of the melting and solidification of many optical materials, and that *a priori* neglect of radiation can cause the temperature profile within the liquid to assume a shape which promotes unstable interfacial growth, a finding which is contrary to the idea that radiation always exerts a "stabilizing influence." Results have indicated that the dynamics of melting and solidification can qualitatively be predicted with the use of gray optical properties, but a quantitative description requires accounting for the spectral absorption characteristics.

In summary, the principal simplifying assumptions which have been employed are the following: 1 the absence of natural convection; 2 one-dimensional energy transfer; 3 the absence of scattering; and 4 the presence of isotropic media. Although the complexity of the calculations and computing time would greatly increase, there is no conceptual difficulty in relaxing assumptions 1-3 in order to obtain detailed numerical information about a specific system. The analysis of combined radiation, convection, and conduction is presently within the state of the art, and radiative heat transfer in several dimensions could be described by zonal (finite difference) methods. Similarly, the numerical techniques of handling scattering problems are also well known [16]. However, some fundamental theoretical and experimental studies have yet to be performed before the fourth assumption can be relaxed. As of the present time, there is no known formulation of the equation of transfer in anisotropic absorbing and emitting media, nor are there any experimental data.

References

1 Carslaw, H. S., and Jaeger, J. C., *Conduction of Heat in Solids*, Second ed., Oxford University Press, London, 1959.

2 Rutter, J. W., and Chalmers, B., "A Prismatic Substructure Formed During Solidification of Metals," *Can. J. Phys.*, Vol. 31, 1953, pp. 15–39.

3 O'Hara, S., Tarshis, L. A., and Viskanta, R., "Stability of the Solid/Liquid Interface of Semitransparent Materials," *J. Cryst. Growth*, Vol. 3, 4, 1968, pp. 583–593.

4 Abrams, M., "Energy Transfer During the Melting and Solidification of Semi-Transparent Crystals," PhD thesis, Purdue University, 1971.

5 Habib, I. S., "Solidification of Semi-Transparent Materials by Conduction and Radiation," *International Journal of Heat and Mass Transfer*, Vol. 14, 1971, pp. 2161–2164.

6 Habib, I. S., "Solidification of a Semi-Transparent Cylindrical Medium by Conduction and Radiation," JOURNAL OF HEAT TRANSFER, TRANS. ASME, Series C, Vol. 95, 1967, pp. 37–41.

7 Gille, J., and Goody, R., "Convection in a Radiating Gas," *J. Fluid Mech.*, Vol. 20, 1964, pp. 47–49.

8 Terwilliger, J. P., and Dizio, S. F., "Salt Rejection Phenomena in the Freezing of Saline Solutions," *Chem. Eng. Sci.*, Vol. 25, 1970, pp. 1331–1349.

9 Born, M., and Wolf, E., Principles of Optics, Pergamon Press, 3rd ed., Oxford, 1965.

10 Murray, W. D., and Landis, F., "Numerical and Machine Solutions of Transient Heat-Conduction Problems Involving Melting or Freezing," JOURNAL OF HEAT TRANSFER, TRANS. ASME, Ser. C, Vol. 81, 1959, pp. 106–112.

11 Crosbie, A. L., "Radiation Heat Transfer in a Nongray Planar Medium," PhD thesis, Purdue, University, 1969.

12 Ames, W. F., *Nonlinear Partial Differential Equations in Engineering*, Academic Press, New York, 1965.

13 Cobble, M. H, "Irradiation Into Transparent Solids and Thermal Trap Effect," *J. Franklin Inst.*, Vol. 278, 1964, pp. 383–393.

14 Neuroth, N., "Der Einfluss der Temperatur auf die spektrale Absorption von Glasern in Ultraroter, I," *Glastech Ber.*, Vol. 25, 1952, pp. 242–249.

15 Viskanta, R., "Radiation Heat Transfer and Interaction of Convection With Radiation Heat Transfer," in *Advances in Heat Transfer*, Vol. 3, pp. 175–251, Irvine, T. F., and Hartnett, J. P., eds., Academic Press, New York, 1966.

16 Love, T. J., *Radiative Heat Transfer*, Charles Merrill, Columbus, Ohio, 1968.

A. L. Crosbie
Assoc. Professor.
Assoc. Mem. ASME

T. R. Sawheny
Graduate Student.

Thermal Radiative Transfer Group,
Department of Mechanical and
Aerospace Engineering,
University of Missouri-Rolla,
Rolla, Mo.

Application of Ambarzumian's Method to Radiant Interchange in a Rectangular Cavity

Ambarzumian's method had been used for the first time to solve a radiant interchange problem. A rectangular cavity is defined by two semi-infinite parallel gray surfaces which are subject to an exponentially varying heat flux, i.e., $q = q_0 \exp(-mx)$. Instead of solving the integral equation for the radiosity for each value of m, solutions for all values of m are obtained simultaneously. Using Ambarzumian's method, the integral equation for the radiosity is first transformed into an integro-differential equation and then into a system of ordinary differential equations. Initial conditions required to solve the differential equations are the H functions which represent the radiosity at the edge of the cavity for various values of m. This H function is shown to satisfy a nonlinear integral equation which is easily solved by iteration. Numerical results for the H function and radiosity distribution within the cavity are presented for a wide range of m values.

Introduction

Radiant interchange between diffuse surfaces with nonuniform radiosity is one of the fundamental and important problems in the field of radiative heat transfer. Various configurations and thermal conditions have been studied [1-4].[1] The formulation of these problems results in a Fredholm integral equation. Only for a spherical cavity and a cylindrical arc cavity [2] have closed-form solutions been achieved. Some of the approximate analytical techniques employed are the zonal method, the variational method, the approximate kernel method, the least squares method, and Sokolov's method. The method of successive approximations is the most common numerical technique.

The approach taken in the present investigation has been used in gaseous radiation studies and is known as Ambarzumian's method [5, 6]. The method is applied for the first time to determine radiant interchange between surfaces. The integral equation for the radiosity is transformed into integro-differential equation which is then represented by a system of differential equations. The radiosity at the edge of the cavity is defined as the H function which represents the initial conditions for the integro-differential equation.

Physical Model

The present investigation deals with radiant interchange in a rectangular cavity formed by two semi-infinite, parallel, gray, diffuse surfaces. The surfaces of the cavity are separated by a distance h, and are subjected to nonuniform heat fluxes. The cavity is filled with a nonparticipating medium. The problem is made symmetrical by assuming the surface properties of the two surfaces are identical.

The radiosity can be expressed in general as

$$\tilde{B}(\bar{x}) = \tilde{q}(\bar{x}) + \tilde{G}(\bar{x}) \tag{1}$$

where $\tilde{q}(\bar{x})$ is the specified heat flux and $\tilde{G}(\bar{x})$ is irradiation from the other surface. Expressing the irradiation in terms of the radiosity yields the following linear integral equation

$$\tilde{B}(\bar{x}) = \tilde{q}(\bar{x}) + \frac{1}{2}\int_0^\infty \frac{h^2 \tilde{B}(\bar{y})\, d\bar{y}}{[(\bar{x}-\bar{y})^2 + h^2]^{3/2}} \tag{2}$$

Introducing $x = \bar{x}/h$, $y = \bar{y}/h$ and assuming the heat flux decays exponentially, $\tilde{q}(\bar{x}) = q_0 \exp(-m\bar{x}/h)$, integral equation (2) takes the form

$$B(x, m) = e^{-mx} + \frac{1}{2}\int_0^\infty K(|x-y|)B(y, m)dy \tag{3}$$

where $B(x,m) = \tilde{B}/q_0$ and the kernel is

$$K(x, y) = K(|x-y|) = 1/[(x-y)^2 + 1]^{3/2}\,. \tag{4}$$

The heat flux can be expressed in terms of the radiosity and emissive power as

$$q(x) = \frac{\epsilon}{\rho}[\sigma T^4(x) - q_0 B(x, m)]\,. \tag{5}$$

Solving equation (5) for the emissive power yields

$$\sigma T^4(x) = q_0\left[\frac{\rho}{\epsilon}e^{-mx} + B(x, m)\right]\,. \tag{6}$$

Thus, the emissive power can be determined from equation (6) once the radiosity is known.

[1] Numbers in brackets designate References at end of paper.

Contributed by the Heat Transfer Division for publication in the JOURNAL OF HEAT TRANSFER. Manuscript received by the Heat Transfer Division, September 11, 1973. Paper No. 74-HT-S.

Ambarzumian's Method

The equation (3) for the dimensionless radiosity $B(x,m)$ is classified as a linear Fredholm integral equation of second kind. $B(x,m)$ depends on the depth into the cavity x, and the heat flux distribution parameter m. In this section Ambarzumian's method [5, 6] transforms the integral equation into an integro-differential equation. The dimensionless radiosity $B(0,m)$ at the edge of the cavity, the H function, is the initial condition for the integro-differential equation. A nonlinear Fredholm integral equation for the H function is developed.

Integro-Differential Equation. The equation (3) for dimensionless radiosity $B(x,m)$ can be rewritten as follows

$$B(x, m) = e^{-mx} + \frac{1}{2}\int_0^x B(y, m)K(x - y)dy + \frac{1}{2}\int_x^\infty B(y, m)K(y - x)dy \quad (7)$$

Substituting $z = x - y$ in the first integral and $z = y - x$ in the second integral of the right-hand side of equation (7) yields

$$B(x, m) = e^{-mx} + \frac{1}{2}\int_0^x B(x - z, m)K(z)dz + \frac{1}{2}\int_0^\infty B(x + z, m)K(z)dz \quad (8)$$

Differentiating equation (8) with respect to x gives

$$\frac{\partial B(x, m)}{\partial x} = -me^{-mx} + \frac{1}{2}B(0, m)K(x) + \frac{1}{2}\int_0^x \frac{\partial B(x - z, m)}{\partial x}K(z)dz + \frac{1}{2}\int_0^\infty \frac{\partial B(x + z, m)}{\partial x}K(z)dz \quad (9)$$

Now substituting $y = x - z$ in the first integral and $y = x + z$ in the second integral of the right-hand side of equation (9) yields the following integral equation for the derivative of $B(x,m)$

$$\frac{\partial B(x, m)}{\partial x} = -me^{-mx} + \frac{1}{2}B(0, m)K(x) + \frac{1}{2}\int_0^\infty \frac{\partial B(y, m)}{\partial y}K(|x - y|)dy \quad (10)$$

The solution of equation (10) is determined by the superposition of solutions. Multiplying equation (3) by $mJ_1(m)dm/2$ and integrating from 0 to ∞ yields

$$\Phi(x) = \frac{1}{2}K(x) + \frac{1}{2}\int_0^\infty \Phi(y)K(|x - y|)dy \quad (11)$$

where

$$\Phi(x) = \frac{1}{2}\int_0^\infty mB(x, m)J_1(m)dm . \quad (12)$$

In obtaining equation (11) the following identity was employed

$$K(x) = \int_0^\infty me^{-xm}J_1(m)dm = 1/(x^2 + 1)^{3/2} . \quad (13)$$

Multiplying equation (3) by $-m$ and equation (11) by $B(0,m)$ and adding the two together yields an integral equation which is identical to integral equation (10). Thus, the integro-differential equation for $B(x,m)$ is given by

$$\frac{\partial B}{\partial x}(x, m) = -mB(x, m) + B(0, m)\Phi(x) = -mB(x, m) + \frac{1}{2}B(0, m)\int_0^\infty nB(x, n)J_1(n)dn \quad (14)$$

The initial condition $B(0,m)$ is needed before this equation can be solved.

***H* function.** In the physical sense, the H function is the radiosity at the edge of the cavity $B(0,m)$. The aim of this section is to achieve a nonlinear integral equation for the H function which is convenient for numerical solution. Evaluating equation (3) at $x = 0$ yields

$$B(0, m) = 1 + \frac{1}{2}\int_0^\infty B(y, m)K(y)dy \quad (15)$$

or

$$B(0, m) = 1 + \frac{1}{2}\int_0^\infty B(y, m)\int_0^\infty ne^{-yn}J_1(n)dn\,dy \quad (16)$$

By changing the order of integration, equation (16) can be written as

$$B(0, m) = 1 + \frac{1}{2}\int_0^\infty nJ_1(n)\bar{B}(n, m)dn \quad (17)$$

where $\bar{B}(n,m)$ is the Laplace transform of $B(y,m)$, i.e.,

$$\bar{B}(n, m) = L_n\{B(y, m)\} = \int_0^\infty B(y, m)e^{-ny}dy . \quad (18)$$

Thus $B(0,m)$ may be expressed in terms of Laplace transform of the dimensionless radiosity $B(y,m)$ and Bessel function of the first kind. $\bar{B}(s,m)$ can be expressed in terms of $B(0,m)$ by applying a Laplace transform to equation (14)

$$s\bar{B}(s, m) - B(0, m) = -m\bar{B}(s, m) + \frac{1}{2}B(0, m)\int_0^\infty \bar{B}(s, n)nJ_1(n)dn \quad (19)$$

or

$$(s + m)\bar{B}(s, m) = B(0, m)\left[1 + \frac{1}{2}\int_0^\infty n\bar{B}(s, n)J_1(n)dn\right] . \quad (20)$$

Comparison of equation (17) with the right-hand side of equation (20) reveals that in order to replace the term of equation (20) in brackets by $B(0,s)$, $\bar{B}(s,m)$ must be symmetric.

The first step in showing $\bar{B}(s,m)$ symmetric is to rewrite equation (3) as

$$B(x, s) = e^{-sx} + \frac{1}{2}\int_0^\infty B(y, s)K(|x - y|)dy \quad (21a)$$

and

$$B(x, m) = e^{-mx} + \frac{1}{2}\int_0^\infty B(y, m)K(|x - y|)dy . \quad (21b)$$

Multiplying equation (21a) and (21b), respectively, by $B(x,m)$ and

Nomenclature

$B(x, m)$ = dimensionless radiosity, $\tilde{B}(\tilde{x}, m)/q_0$
$\tilde{B}(\tilde{x}, m)$ = radiosity, radiant flux leaving the surface
$\bar{B}(x\ m)$ = Laplace transform of $B(x, m)$
$B_i(x)$ = $B(x, m_i)$
$G(x)$ = dimensionless irradiation, $\tilde{G}(\tilde{x})/q_0$
$\tilde{G}(\tilde{x})$ = irradiation, radiant flux incident on the surface
h = separation distance between surfaces
$H(m)$ = dimensionless radiosity at the edge of the cavity, $B(0, m)$
H_i = $H(m_i)$
$J_1(m)$ = Bessel function of first order
$K(x)$ = kernel of integral equation, equation (13)
m = decay parameter for heat flux
m_i, n_i = quadrature points for $i = 1, 2, \ldots N$, even values of m for $i = N + 1, \ldots, N + K$
N = total number of quadrature points
$q(x)$ = dimensionless surface heat flux
q_0 = magnitude of surface heat flux
$\tilde{q}(\tilde{x})$ = surface heat flux
r_i = real positive roots of $J_1(m)$
T = temperature
x, y = dimensionless depth into the cavity, $\tilde{x}/h, \tilde{y}/h$
$\tilde{x}, \tilde{y}$ = depth into the cavity
ϵ, ρ = emittance, reflectance
σ = Stefan-Boltzmann constant

$B(x,s)$ and integrating both with respect to x over the interval $(0,\infty)$ gives

$$\int_0^\infty B(x,s)B(x,m)dm = \int_0^\infty e^{-sx}B(x,m)dx \int_0^\infty B(x,m)\left[\frac{1}{2}\int_0^\infty B(y,s)K(|x-y|dy\right]dx \quad (22a)$$

and

$$\int_0^\infty B(x,m)B(x,s)dx = \int_0^\infty e^{-mx}B(x,s)dx + \int_0^\infty B(x,s)\left[\frac{1}{2}\int_0^\infty B(y,m)K(|x-y|)dy\right]dx. \quad (22b)$$

The left sides of the equations (22a) and (22b) are identical. Since the kernel $K(x,y)$ is symmetric, the first terms on the right side of the equations are identical. The last terms of (22a) and (22b) must therefore be equal, i.e.,

$$\int_0^\infty e^{-sx}B(x,m)dx = \int_0^\infty e^{-mx}B(x,s)dx . \quad (23)$$

Equation (23) can be rephrased as

$$\bar{B}(s,m) = \bar{B}(m,s) . \quad (24)$$

Therefore $\bar{B}(s,m)$ is symmetric.

Using equation (24), equation (17) can be written as

$$B(0,m) = 1 + \frac{1}{2}\int_0^\infty nJ_1(n)\bar{B}(m,n)dn . \quad (25)$$

Replacing m with s in equation (25) and substituting this equation into equation (20) yields

$$\bar{B}(s,m) = \frac{B(0,m)B(0,s)}{s+m} \quad (26)$$

Substitution of equation (26) into equation (25) gives

$$B(0,m) = 1 + \frac{1}{2}B(0,m)\int_0^\infty \frac{nJ_1(n)B(0,n)}{n+m}dn . \quad (27)$$

Utilizing the definition of the H function, i.e., $H(m) = B(0,m)$, equation (27) becomes

$$H(m) = 1 + \frac{1}{2}H(m)\int_0^\infty \frac{nJ_1(n)H(n)}{n+m}dn . \quad (28)$$

Since equation (28) would converge very slowly on application of an iterative technique, another form of the equation is needed. Using

$$\frac{n}{n+m} = 1 - \frac{m}{n+m} ,$$

equation (28) becomes

$$H(m) = 1 + \frac{\rho}{2}H(m)\int_0^\infty J_1(n)H(n)dn - \frac{1}{2}H(m)\int_0^\infty \frac{mJ_1(n)H(n)}{n+m}dn . \quad (29)$$

Dividing the equation (29) by $H(m)$ yields

$$\frac{1}{H(m)} = 1 - \frac{1}{2}\alpha_0 + \frac{1}{2}\int_0^\infty \frac{mJ_1(n)H(n)}{n+m}dn \quad (30)$$

where α_0 is the zeroth moment of the H function

$$\alpha_0 = \int_0^\infty H(n)J_1(n)dn . \quad (31)$$

α_0 can be determined by multiplying equation (28) by $J_1(m)dm$ and integrating over the interval $(0,\infty)$, thus

$$\alpha_0 = \int_0^\infty H(m)J_1(m)dm = \int_0^\infty J_1(m)dm + \frac{1}{2}\int_0^\infty\int_0^\infty \frac{nH(m)J_1(m)H(n)J_1(n)}{n+m}dndm . \quad (32)$$

Since m and n are dummy variables, in the second integral of the extreme right-hand side of equation (32) these variables may be interchanged yielding

$$\int_0^\infty H(m)J_1(m)dm = \int_0^\infty J_1(m)dm + \frac{1}{2}\int_0^\infty\int_0^\infty \frac{mH(n)J_1(n)H(m)J_1(m)}{m+n}dmdn . \quad (33)$$

The expression obtained by adding equation (32) and (33) is

$$2\int_0^\infty H(m)J_1(m)dm = 2\int_0^\infty J_1(m)dm + \frac{1}{2}\int_0^\infty\int_0^\infty H(m)J_1(m)H(n)J_1(n)dmdn . \quad (34)$$

Using the definition of α_0, equation (34) can be reduced to a quadratic equation of the form $\alpha_0^2 - 4\alpha_0 + 4 = 0$ or $\alpha_0 = 2$. Thus, equation (30) becomes

$$\frac{1}{H(m)} = \frac{1}{2}\int_0^\infty \frac{mJ_1(n)H(n)}{n+m}dn . \quad (35)$$

Numerical Procedure

Application of the method of successive approximations to equation (35) yields

$$H^{k+1}(m) = 2/\int_0^\infty \frac{mJ_1(n)H^k(n)}{n+m}dn .$$

$$k = 1, 2, 3\ldots \quad (36)$$

with initial approximation $H^1(m) = 1$. The most complex and critical part in each of the iterations is the computation of the integral term. Since $J_1(n)$ is contained in the integrand, i.e., $f(n) = mJ_1(n)H(n)/(n+m)$, the function $f(n)$ oscillates slowly about the abscissa. Consequently the integral term in equation (36) in each half cycle is smaller in absolute magnitude than, and opposite in sign to, that of the preceding half cycle. Using Longman's method [7] for computing infinite integrals of oscillatory functions with Euler's transformation, the present integration can be expressed as slowly convergent alternating series

$$\int_0^\infty f(n)dn \simeq \int_0^{r_1} f(n)dn - \left[V_0 - V_1 + V_2 - V_3 + \ldots + V_I\right] \quad (37)$$

where

$$V_0 = \int_{r_1}^{r_2}|f(n)|dn,\ V_1 = \int_{r_2}^{r_3}|f(n)|dn, \ldots, V_I = \int_{r_I+1}^{r_I+2}|f(n)|dn$$

and $r_1, r_2, \ldots$ are the roots of $J_1(n)$ and hence of $f(n)$.

Since the series (37) is slowly convergent and alternating, application of Euler's transformation gives

$$\sum_{i=0}^{\infty}(-1)^i V_i = \frac{1}{2}V_0 - \frac{1}{4}\Delta V_0 + \frac{1}{8}\Delta^2 V_0 - \ldots \quad (38)$$

where $\Delta V_i = V_{i+1} - V_i$ and $\Delta^{k+1}V_i = \Delta^k V_{i+1} - \Delta^k V_i$. The series on the right side of equation (38) can be shown convergent, whenever the original series is convergent. Equation (37) can be written as

$$\int_0^\infty f(n)dn \simeq \int_0^{r_1} f(n)dn - \frac{1}{2}V_0 + \frac{1}{4}\Delta V_0 - \frac{1}{8}\Delta^2 V_0 + \ldots \quad (39)$$

The H function is singular at $n = 0$ and decays rapidly in the interval, $0 \le n \le r_1$. Thus, the first integral term on the right side of equation (39) is broken into $M+1$ subdivisions

$$\int_0^{r_1} f(n)dn = \int_0^{c_1} f(n)dn + \int_{c_1}^{c_2} f(n)dn + \ldots + \int_{c_M}^{r_1} f(n)dn . \quad (40)$$

A Gaussian quadrature of order N_1 is used to evaluate the first

Table 1 Radiosity at the edge of cavity, $H(m)$ and functions $\Phi(x)$ and $\Psi(x)$

m	H(m)	x	2Φ(x)	Ψ(x)
0.03	24.4162	0.	2.04109	1.0000000
0.04	19.1331	0.005	2.04626	1.0051092
0.06	13.6663	0.010	2.05135	1.0102312
0.07	12.0557	0.020	2.06130	1.0205130
0.08	10.8284	0.030	2.07094	1.0308437
0.09	9.86035	0.040	2.08027	1.0412219
0.15	6.65388	0.050	2.08928	1.0516459
0.25	4.60464	0.060	2.09797	1.0621141
0.30	4.06738	0.070	2.10634	1.0726250
0.35	3.67480	0.080	2.11440	1.0831770
0.40	3.37452	0.090	2.12214	1.0937685
0.45	3.13691	0.100	2.12955	1.104398
0.60	2.64860	0.150	2.16191	1.158058
0.70	2.43276	0.200	2.18661	1.212430
0.80	2.26769	0.250	2.20412	1.267328
0.90	2.13715	0.300	2.21508	1.322581
1.50	1.70367	0.400	2.22046	1.433553
2.50	1.42887	0.500	2.20916	1.544349
3.00	1.35812	0.600	2.18716	1.654291
3.5	1.30709	0.700	2.15924	1.762968
4.0	1.26858	0.800	2.12877	1.870173
4.5	1.23850	0.900	2.09793	1.975839
6.0	1.17814	1.000	2.06799	2.07998
7.0	1.15224	1.500	1.94395	2.58055
8.0	1.13284	2.000	1.85716	3.05508
9.0	1.11778	2.500	1.79338	3.51103
15.0	1.06989	3.000	1.74395	3.95295
25.0	1.04155	4.000	1.67104	4.80557
30.0	1.03454	5.000	1.61867	5.62736
40.0	1.02581	6.000	1.57849	6.42625
150.0	1.00683	7.000	1.54624	7.20716
200.0	1.00512	8.000	1.51953	7.97341
250.0	1.00409	9.000	1.49687	8.72737
300.0	1.00341	10.000	1.47729	9.47080
400.0	1.00255	11.000	1.46011	10.2051
500.0	1.00204	12.000	1.44485	10.9312
600.0	1.00170	13.000	1.43117	11.6502
800.0	1.001277	14.000	1.41879	12.3626
1000.0	1.001021	15.000	1.40751	13.0691
2000.0	1.000511	16.000	1.39716	13.7703
4000.0	1.000255	17.000	1.38762	14.4664
6000.0	1.000170	18.000	1.37878	15.1580
8000.0	1.000128	19.000	1.37055	15.8453
10000.0	1.000102	20.000	1.36286	16.5287

subdivision integral, while a Gaussian quadrature of order N_2 is used to evaluate the other subdivision integrals and the integrals, V_0, V_1, V_2, ... Since the H function decays rapidly near $n = 0$, N_1 is larger than N_2.

Replacing the integral term by the foregoing quadrature of order $N = N_1 + (M + I - 1)N_2$, equation (36) takes the form

$$H^{k+1}(m) = 2/F(m, H_1^k, H_2^k, H_3^k, \ldots H_n^k) \tag{41}$$

where F represents the numerical quadrature with quadrature points n_1, n_2, n_3, ... n_N and $H_i^k = H^k(n_i)$. In the iterative technique the most recent values of $H^{k+1}(m)$ are preferred to those of $H^k(m)$ for use in the right side of equation (41). The iterative procedure is as follows:

$$\begin{aligned} H_1^{k+1} &= 2/F(m_1, H_1^k, H_2^k, H_3^k, \ldots H_N^k) \\ H_2^{k+1} &= 2/F(m_2, H_1^{k+1}, H_2^k, H_3^k, \ldots H_N^k) \\ H_3^{k+1} &= 2/F(m_3, H_1^{k+1}, H_2^{k+1}, H_3^k, \ldots H_N^k) \\ H_N^{k+1} &= 2/F(m_N, H_1^{k+1}, H_2^{k+1}, H_3^{k+1}, \ldots H_{N-1}^{k+1}, H_N^k) \end{aligned} \tag{42}$$

where m_1, m_2, m_3, ... m_N are the quadrature points. The iterative process is terminated when the required accuracy of $|H^{k+1}(m) - H^k(m)| < 0.5 \times 10^{-6}$ is obtained as all quadrature points. Using the final values of H_1, H_2, H_3, ... H_N, the H function is computed for even values of m from equation (36) as follows:

$$H(m) = 2/F(m, H_1, H_2, H_3, \ldots H_N) . \tag{43}$$

The H-function at even values of m is presented in Tables 1 to 3. These values were computed after fifteen iterations with the following parameters: $c_1 = 0.0001$, $c_2 = 0.0005$, $c_3 = 0.001$, $c_4 = 0.005$, $c_5 = 0.010$, $c_6 = 0.05$, $c_7 = 0.10$, $c_8 = 0.50$, $c_9 = 1.00$, $N_1 = 15$, $N_2 = 7$, $M = 9$, $I = 11$, and $N = 162$. This process required 0.4 minutes of CPU time on an IBM 370/165. The relative large number of subdivisions ($M = 9$) was required to maintain accuracy at small m values. The H-function decreases with m and approaches unity. Inspection of Table 1 reveals an asymptotic expression, i.e.,

$$H(m) = 1 + \frac{1.021}{m} \tag{44}$$

Integro-differential equation (14) can be expressed as a system of ordinary differential equations

$$\begin{aligned} \frac{dB_1(x)}{dx} &= -m_1 B_1(x) + H_1 \Phi(x) \\ \frac{dB_2(x)}{dx} &= -m_2 B_2(x) + H_2 \Phi(x) \\ &\vdots \\ \frac{dB_N(x)}{dx} &= -m_N B_N(x) + H_N \Phi(x) \end{aligned} \tag{45}$$

where $B_i(x) = B(x, m_i)$ and

$$\Phi(x) = S[B_1(x), B_2(x), \ldots B_N(x)] \tag{46}$$

with initial conditions

$$B_i(0) = H_i \tag{47}$$

The relation S represents a numerical quadrature similar to that used to evaluate the H function with N quadrature points: m_1, m_2 ... m_N. In order to obtain $B(x,m)$ at even values of m, additional differential equations must be solved. Evaluating equation (14) at $m_{N+1} = 0.001$, $m_{N+2} = 0.002$, ... $m_{N+K} = 100.0$ yields

$$\begin{aligned} \frac{dB_{N+1}(x)}{dx} &= -m_{N+1} B_{N+1}(x) + H_{N+1} \Phi(x) \\ \frac{dB_{N+2}(x)}{dx} &= -m_{N+2} B_{N+2}(x) + H_{N+2} \Phi(x) \\ &\vdots \\ \frac{dB_{N+K}(x)}{dx} &= -m_{N+K} B_{N+K}(x) + H_{N+K} \Phi(x) \end{aligned} \tag{48}$$

with initial conditions $B_{N+1}(0) = H_{N+1}$, $B_{N+2}(0) = H_{N+2}$, $B_{N+K}(0) = H_{N+K}$. Equations (45) and (48) represent a system of $N + K$ ordinary differential equations. These equations were solved numerically with a fourth order Runge-Kutta method using a step size of 0.00625 for $0 < x \leq 0.05$, 0.0125 for $0.05 < x \leq 1.0$, and 0.025 for $1.0 < x < 20.0$. This procedure required four minutes of CPU time on an IBM 370/165. This amount of computer time is quite reasonable, especially considering the number and range of m values.

The variation of the radiosity, $B(x,m)$, within the cavity is presented in Tables 2 and 3. The influence of the heat flux distribution on the radiosity is illustrated by presenting results for various values of m. In general, increasing m decreases the radiosity. The behavior at the edge of the cavity can be determined from evaluating equation (14) at $x = 0$, i.e.,

$$\left.\frac{\partial B(x,m)}{\partial x}\right|_{x=0} = H(m)[\Phi(0) - m] . \tag{49}$$

For $m < \Phi(0) = 1.02054$, the radiosity starts rising first at $x = 0$, then upon reaching a maximum, starts to decrease with depth into the cavity. For $m < 1.02054$, the radiosity starts decaying right from the edge of the cavity, and continues to decrease with depth into the cavity. However for very large m, i.e., $m = 100$, the radiosity rapidly decays near the edge, reaches a local minimum near $x = 0.1$, increases slowly to a local maximum near $x = 0.4$ and then continues to decrease with depth. For $m = 50$, the local minimum occurs near $x = 0.2$ and the local maximum occurs near $x = 0.4$.

When $\partial B(x,m)/\partial x$ can be neglected in equation (14) with respect to the other terms and the radiosity can be approximated by

$$B(x, m) \simeq H(m)\Phi(x)/m . \tag{50}$$

Table 2 Radiosity distribution $B(x,m)$

B(x,m)

x	m=0.001	m=0.002	m=0.005	m=0.010	m=0.02	m=0.05	m=0.10	m=0.20	m=0.50	m=1.00	m=2.00
0.	522.220	274.938	118.963	63.7895	34.6355	15.8807	9.07591	5.38909	2.94387	2.03119	1.53343
0.005	524.885	276.340	119.568	64.1123	34.8090	15.9579	9.11773	5.41123	2.95154	2.03141	1.52597
0.010	527.557	277.746	120.174	64.4358	34.9829	16.0352	9.15965	5.43341	2.95923	2.03166	1.51860
0.020	532.921	280.567	121.391	65.0852	35.3320	16.1905	9.24377	5.47791	2.97466	2.03222	1.50414
0.030	538.311	283.402	122.614	65.7376	35.6827	16.3464	9.32824	5.52258	2.99016	2.03288	1.49004
0.040	543.725	286.249	123.842	66.3930	36.0349	16.5030	9.41306	5.56742	3.00573	2.03363	1.47629
0.050	549.163	289.109	125.076	67.0513	36.3887	16.6602	9.49821	5.61241	3.02134	2.03446	1.46289
0.060	554.625	291.982	126.315	67.7123	36.7440	16.8181	9.58368	5.65756	3.03702	2.03537	1.44981
0.070	560.108	294.866	127.559	68.3760	37.1007	16.9766	9.66945	5.70284	3.05273	2.03636	1.43706
0.080	565.613	297.761	128.808	69.0422	37.4587	17.1356	9.75551	5.74826	3.06849	2.03743	1.42463
0.090	571.138	300.667	130.062	69.7109	37.8180	17.2952	9.84183	5.79379	3.08429	2.03856	1.41250
0.100	576.683	303.583	131.320	70.3820	38.1785	17.4553	9.92842	5.83944	3.10012	2.03976	1.40066
0.150	604.676	318.305	137.670	73.7689	39.9980	18.2629	10.3647	6.06908	3.17959	2.04660	1.34569
0.200	633.039	333.222	144.103	77.1995	41.8403	19.0797	10.8053	6.30025	3.25917	2.05452	1.29698
0.250	661.676	348.281	150.597	80.6620	43.6989	19.9028	11.2484	6.53194	3.33832	2.06309	1.25367
0.300	690.496	363.437	157.131	84.1453	45.5680	20.7294	11.6925	6.76323	3.41654	2.07194	1.21500
0.400	748.376	393.872	170.251	91.1365	49.3167	22.3839	12.5783	7.22141	3.56857	2.08927	1.14809
0.500	806.158	424.252	183.343	98.1096	53.0518	24.0274	13.4537	7.66957	3.71267	2.10461	1.09469
0.600	863.480	454.391	196.327	105.021	56.7499	25.6492	14.3127	8.10429	3.84728	2.11682	1.04903
0.700	920.153	484.177	209.154	111.845	60.3968	27.2428	15.1517	8.52366	3.97169	2.12542	1.00988
0.800	976.042	513.552	221.800	118.568	63.9855	28.8052	15.9690	8.92686	4.08581	2.13035	0.975782
0.900	1031.12	542.498	234.256	125.187	67.5138	30.3354	16.7644	9.31387	4.18994	2.13184	0.945724
1.000	1085.40	571.019	246.525	131.702	70.9823	31.8338	17.5380	9.68509	4.28462	2.13025	0.918098
1.50	1346.20	708.004	305.383	162.895	87.5261	38.8977	21.1139	11.3292	4.63003	2.09013	0.820840
2.00	1593.27	837.697	361.001	192.277	103.008	45.3790	24.2833	12.6838	4.84773	2.02479	0.760228
2.50	1830.52	962.154	414.273	220.329	117.696	51.4091	27.1348	13.8143	4.96217	1.95584	0.720370
3.00	2060.33	1082.63	465.745	247.350	131.755	57.0705	29.7233	14.7656	5.01497	1.89185	0.692399
4.00	2503.36	1314.65	564.597	299.004	158.381	67.4921	34.2561	16.2506	5.01346	1.78689	0.655227
5.00	2929.74	1537.74	659.298	348.188	183.424	76.9286	38.0920	17.3167	4.94211	1.70977	0.630800
6.00	3343.30	1754.09	750.810	395.429	207.186	85.5504	41.3655	18.0782	4.84636	1.65263	0.612021
7.00	3748.06	1965.08	839.732	441.060	229.861	93.4736	44.1726	18.6141	4.74702	1.60803	0.598092
8.00	4144.26	2171.61	926.471	485.305	251.584	100.783	46.5860	18.9815	4.65306	1.57432	0.587676
9.00	4533.66	2374.35	1011.32	528.331	272.456	107.546	48.6638	19.2225	4.56778	1.54602	0.578202
10.00	4917.16	2573.80	1094.49	570.260	292.554	113.817	50.4530	19.3684	4.49182	1.52225	0.570098
11.00	5295.50	2770.33	1176.17	611.190	311.939	119.639	51.9929	19.4432	4.42462	1.50186	0.563047
12.00	5669.24	2964.25	1256.47	651.199	330.663	125.052	53.3164	19.4650	4.36521	1.48407	0.556827
13.00	6038.83	3155.80	1335.52	690.352	348.769	130.090	54.4516	19.4477	4.31252	1.46834	0.551278
14.00	6404.66	3345.17	1413.40	728.702	366.293	134.780	55.4226	19.4017	4.26555	1.45426	0.546281
15.00	6767.04	3532.55	1490.19	766.296	383.268	139.151	56.2503	19.3353	4.22343	1.44156	0.541745
16.00	7126.24	3718.06	1565.96	803.173	399.721	143.225	56.9526	19.2546	4.18541	1.43000	0.537598
17.00	7482.48	3901.85	1640.76	839.368	415.678	147.023	57.5452	19.1643	4.15089	1.41941	0.533796
18.00	7835.97	4084.00	1714.64	874.911	431.162	150.565	58.0417	19.0679	4.11934	1.40965	0.530262
19.00	8186.89	4264.62	1787.65	909.830	446.193	153.868	58.4542	18.9682	4.09036	1.40062	0.526989
20.00	8535.38	4443.78	1859.82	944.149	460.790	156.949	58.7931	18.8672	4.06359	1.39222	0.523938

From Table 1 the function $\Phi(x)$ first increases, reaches a maximum at $x = 0.4$ and then slowly decreases with x. Physically, $\Phi(x)$ represents the dimensionless radiosity of a rectangular cavity subject to a nonuniform heat flux of the form $1/[2(x^2 + 1)^{3/2}]$. Inspection of Table 4 reveals that increasing m increases the range of x values for which this approximation is useful. In general the accuracy of this approximation increases with depth into the cavity. However for very large m, the percentage error first decreases, then becomes negative, increases and finally decreases with depth. This behavior is consistent with the behavior of $\partial B/\partial x$, as can be seen from Table 3.

When m is small, the term $mB(x,m)$ can be neglected in equation (14), i.e.,

$$\frac{\partial B(x,m)}{\partial x} = H(m)\Phi(x) \ . \tag{51}$$

The solution of this equation can be expressed as

$$B(x, m) = H(m)\Psi(x) \tag{52}$$

where the function

$$\Psi(x) = 1 + \int_0^x \Phi(x')dx' \tag{53}$$

is tabulated in Table 1. This function satisfies the following homogeneous integral equation:

$$\Psi(x) = \frac{1}{2}\int_0^\infty \Psi(y)K(|x - y|)dy \tag{54}$$

which corresponds to Milne's integral equation [6] in gaseous radiative transfer. Inspection of Table 5 reveals that the accuracy of approximation (52) decreases with m and x.

Discussion

Ambarzumian's method has been applied for the first time to solve a radiant interchange problem. A rectangular cavity subjected to an exponentially varying heat flux was analyzed, and numerical results were presented for a wide range of parameters. As a result of this investigation, the following comments are made concerning Ambarzumian's method:

1 An integro-differential equation (14) for the radiosity distri-

Table 3 Radiosity distribution $B(x,m)$ for $m = 5.00, 10.00, 20.00, 50.00$, and 100.00

B(x,m)

x	m=5.00	m=10.0	m=20.0	m=50.0	m=100.
0.	1.21438	1.10575	1.05213	1.02061	1.01026
0.005	1.19053	1.05734	0.957125	0.799463	0.616813
0.010	1.16727	1.01129	0.871171	0.627248	0.378189
0.020	1.12253	0.925875	0.723060	0.388705	0.145696
0.030	1.08002	0.848638	0.601844	0.244060	0.0601985
0.040	1.03964	0.778800	0.502645	0.156367	0.0287758
0.050	1.00128	0.715657	0.421472	0.103215	0.0172452
0.060	0.964848	0.658569	0.355055	0.0710120	0.0130316
0.070	0.930242	0.606958	0.300719	0.0515143	0.0115086
0.080	0.897373	0.560302	0.256271	0.0397212	0.0109744
0.090	0.866153	0.518128	0.219917	0.0326000	0.0108030
0.100	0.836501	0.480007	0.190190	0.0283112	0.0107641
0.150	0.709142	0.337861	0.105701	0.0224918	0.0108905
0.200	0.610716	0.252258	0.0750808	0.0222647	0.0110225
0.250	0.534623	0.200788	0.0641563	0.0224304	0.0111180
0.300	0.475739	0.169873	0.0603640	0.0225652	0.0111798
0.400	0.394610	0.140073	0.0586636	0.0226630	0.0112173
0.500	0.345202	0.128940	0.0582954	0.0225779	0.0111674
0.600	0.314397	0.124217	0.0578192	0.0223719	0.0110606
0.700	0.294492	0.121578	0.0571588	0.0220966	0.0109218
0.800	0.281008	0.119572	0.0563915	0.0217802	0.0107686
0.900	0.271358	0.117757	0.0555863	0.0214743	0.0106127
1.000	0.264051	0.116027	0.0547878	0.0211663	0.0104608
1.500	0.242288	0.108703	0.0514129	0.0198826	0.00982988
2.000	0.229668	0.103544	0.0490487	0.0189846	0.00938848
2.500	0.220821	0.0998002	0.0473218	0.0183262	0.00906449
3.000	0.214140	0.0969286	0.0459902	0.0178170	0.00881365
4.000	0.204511	0.0927348	0.0440350	0.0170672	0.00844395
5.000	0.197734	0.0897502	0.0426370	0.0165296	0.00817867
6.000	0.192597	0.0874728	0.0415670	0.0161175	0.00797519
7.000	0.188510	0.0856526	0.0407101	0.0157870	0.00777592
8.000	0.185145	0.0841492	0.0400013	0.0155135	0.00767683
9.000	0.182303	0.0828765	0.0394006	0.0152815	0.00756219
10.000	0.179856	0.0817783	0.0388819	0.0150810	0.00746313
11.000	0.177715	0.0808163	0.0384271	0.0149053	0.00737623
12.000	0.175818	0.0799631	0.0380235	0.0147492	0.00729908
13.000	0.174121	0.0791985	0.0376617	0.0146093	0.00722989
14.000	0.172587	0.0785074	0.0373345	0.0144827	0.00716730
15.000	0.171192	0.0778779	0.0370364	0.0143673	0.00711026
16.000	0.169914	0.0773011	0.0367631	0.0142615	0.00705795
17.000	0.168736	0.0767693	0.0365111	0.0141640	0.00700972
18.000	0.167646	0.0762768	0.0362777	0.0140736	0.00696502
19.000	0.166633	0.0758186	0.0360605	0.0139895	0.00692342
20.000	0.165686	0.0753907	0.0358576	0.0139109	0.00688456

Table 4 Percentage error in the approximation, $H(m)\Phi(x)/m$, to the radiosity

$\{[B(x,m) - H(m)\Phi(x)/m]/B(x,m)\} \times 100$

x	$m=2$	$m=5$	$m=10$	$m=20$	$m=50$	$m=100$
0.06	44.5	73.6	82.4	84.5	69.8	18.7
0.08	43.1	71.4	79.1	78.3	45.7	2.7
0.10	41.7	69.1	75.5	70.5	23.2	0.07
0.15	38.4	63.0	64.6	46.2	1.9	0.27
0.20	35.4	56.5	52.1	23.4	−0.23	−0.21
0.25	32.6	49.9	39.3	9.6	−0.29	−0.14
0.30	30.1	43.5	27.9	3.5	−0.19	−0.08
0.40	25.9	31.7	12.4	0.44	0.003	0.01
0.60	20.1	15.5	2.7	0.50	0.22	0.11
0.80	16.4	8.0	1.6	0.71	0.29	0.15
1.00	13.7	4.9	1.5	0.72	0.29	0.14
2.00	6.3	1.8	0.84	0.43	0.16	0.08
5.00	1.6	0.59	0.29	0.14	0.06	0.03
10.0	0.66	0.25	0.13	0.06	0.02	0.01
20.0	0.28	0.11	0.05	0.03	0.01	0.005

bution was developed. This equation was quite useful in analyzing special cases, i.e., m small or large.

2 The radiosity at the edge of the cavity was shown to satisfy a nonlinear integral equation which is readily solved by iteration. Thus, the radiosity at the cavity's edge was determined without determining the entire radiosity distribution.

3 Using a numerical quadrature, the integro-differential equation was converted into a system of ordinary differential equations of the initial-value type. Once the H function was determined, the numerical solution for the radiosity was direct not requiring an iterative approach.

4 Taking into account the number and range of m values considered, the computational time required was quite reasonable.

5 While the exponential varying heat flux was essential to the method, solutions can be found to other heat flux distributions which can be related to an exponential term, i.e., equation (13).

While Ambarzumian's method has been successfully applied to a rectangular cavity with a prescribed heat flux, the general applicability of the method to other physical situations must await further investigation. However, it should be pointed out that in gaseous radiative transfer studies Ambarzumian's approach has been successfully applied to many different situations. The authors are currently extending the method to other boundary conditions and geometries.

Table 5—Normalized radiosity, $B(x,m)/H(m)$

$B(x,m)/H(m)$

x	$m=0$	$m=0.001$	$m=0.010$	$m=0.05$	$m=0.10$
0	1.00000	1.00000	1.00000	1.00000	1.00000
0.005	1.00511	1.00510	1.00506	1.00486	1.00461
0.010	1.01023	1.01022	1.01013	1.00973	1.00923
0.050	1.05165	1.05159	1.05113	1.04908	1.04653
0.100	1.10440	1.10429	1.10335	1.09915	1.09393
0.500	1.54435	1.54371	1.53802	1.51299	1.48235
1.0	2.07998	2.07844	2.06463	2.00455	1.93237
5.0	5.62736	5.61017	5.45839	4.84414	4.19704
10.0	10.2051	9.41589	8.93971	7.16695	5.55900
15.0	13.0691	12.9582	12.0129	8.76225	6.19776
20.0	16.5287	16.3444	14.8010	9.88297	6.47793

References

1 Love, T. J., *Radiative Heat Transfer*, C. E. Merrill, Columbus, Ohio, 1968.

2 Sparrow, E. M., and Cess, R. D., *Radiation Heat Transfer*, Brooks/Cole, Belmont, Calif. 1967.

3 Siegel, R., and Howell, J. R., *Thermal Radiation Heat Transfer*, McGraw-Hill, New York, 1972.

4 Hottel, H. C., and Sarofim, A. F., *Radiative Transfer*, McGraw-Hill, New York, 1967.

5 Ambarzumian, V. A., "Diffusion of Light by Planetary Atmospheres," *Astronomicheskii Zhurnal* Vol. 19, 1942, pp. 30-41.

6 Kourganoff, V., *Basic Methods in Transfer Problems*, Dover Publications, New York, 1963.

7 Longman, I. M., "Note on a Method for Computing Infinite Integrals of Oscillatory Functions," *Cambridge Philos.* Vol. 52, 1956, pp. 764-768.

J. H. Lienhard
Professor. Mem. ASME

V. K. Dhir
Res. Assoc. Assoc. Mem. ASME

Mechanical Engineering Department,
University of Kentucky,
Lexington, Ky.

Laminar Film Condensation on Nonisothermal and Arbitrary-Heat-Flux Surfaces, and on Fins

The class of two-dimensional laminar film condensation problems with variable wall-subcooling, for which the full boundary layer equations admit similar solutions, is identified. The solutions of this problem reveal the limitations of the simple Nusselt-Rohsenow method when it is employed to deal with nonisothermal wall problems. The Nusselt-Rohsenow method is used to treat a wide spectrum of variable wall termpeature problems, and results are compared with the exact solutions. Problems in which the heat flux is arbitrarily specified are considered. Variable wall termperature problems involving axisymmetric bodies and arbitrary variations of gravity are also included. Finally, condensation on fins of various configurations is also treated.

Introduction

Considerable work has been done on laminar film condensation from isothermal surfaces since the earlier work of Nusselt [1][1] and Rohsenow [2]. The later work has amply documented the validity of neglecting inertia in condensation problems, and has thus supported the Nusselt-Rohsenow theory. Sparrow and Gregg's [3, 4] full solutions of the boundary layer equations verified it for the isothermal vertical wall and horizontal cylinder. Yang's [5] full solution verified our solution for the isothermal sphere [6] based on the Nusselt-Rohsenow theory. We provided both the simple [6] and the full [7] solution for the isothermal rotating plate.

In these cases, the simple theory generally proved accurate within about 2 percent or less, as long as the Prandtl number, Pr, was on the order of unity or greater, and [2] $c_p\Delta T/h_{fg}$ was less than unity. Almost all cases of practical interest which are excluded from the reach of the simple theory cannot be treated by the boundary layer theory either. When $\Pr \ll 1$, such problems as temperature discontinuities across the liquid-vapor interface arise. When $c_p\Delta T/h_{fg}$ is large, the film is more apt to become ripply or turbulent.

In discussing [4], Seban suggested that condensation on nonisothermal walls could be treated by the Nusselt-Rohsenow method if a weighted average were used for the temperature. Denny and Mills [8] pursued this idea in 1969. They integrated the full boundary layer equations numerically for power law variations of wall temperature, taking into account variable fluid properties and interfacial drag. They used these results to find an effective temperature at which fluid properties should be evaluated. This temperature, when used in the Nusselt-Rohsenow theory, gave heat transfer results within 2 percent of their numerical results for ΔT both increasing and decreasing with distance from the leading edge. This approach tended to average out deviations of the Nusselt-Rohsenow theory from the exact solutions, and it did not provide any bounds for the applicability of the Nusselt-Rohsenow theory to nonisothermal wall problems.

In 1966, Yang [9] also considered condensation on nonisothermal plates in a brief note. He developed a complex scheme for solving the boundary layer equations, but discusses numerical results only in qualitative terms indicating that some deviations from the Nusselt-Rohsenow results do occur.

The aim of this study is to find how well the simple Nusselt-Rohsenow theory applies to nonisothermal wall problems. We do this by solving the full equations for a class of variable wall temperature problems which admit similar solutions. This analysis will also help in identifying any distortions in the temperature profile caused by varying temperature.

Working within the range of applicability of the simple Nusselt-Rohsenow theory, we obtain a closed analytical solution for situations in which the heat flux at the wall is specified independently. We also do this for variable ΔT configurations in which the gravity, g, may depend on x, as well as axisymmetric bodies whose radius of curvature, R, depends upon x (see Fig. 1).

Finally we shall deal with fins heated by condensation. Fins present a special problem in that ΔT is not independently specifiable. Instead, ΔT is determined by the thermal properties and the configuration of the fin, and by the heat transfer coefficient, h, which itself depends upon ΔT. Fins would be very hard to deal with, were it not possible to use the simplified theory.

[1] Numbers in brackets designate References at end of paper.

[2] Symbols not explained in the text are ones in common use. They are defined in the Nomenclature section.

Contributed by the Heat Transfer Division for publication in the JOURNAL OF HEAT TRANSFER. Manuscript received by the Heat Transfer Division, June 28, 1973. Paper No. 74-HT-R.

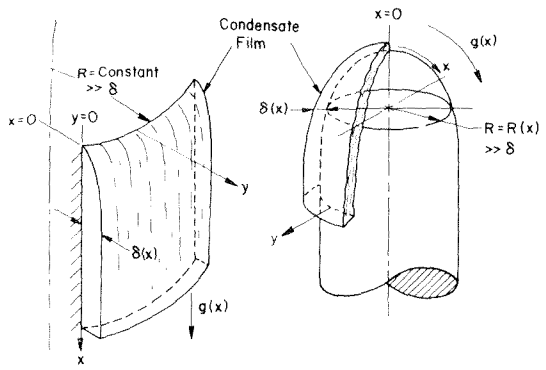

Fig. 1 Configurations considered in the arbitrary $\Delta T(x)$ and $q(x)$ analyses

Formulation of The Boundary Layer Equations For Condensation on a Vertical Plate With $\Delta T(x)$

The conventional equation of motion for condensation is expressed in terms of the stream function, ψ, as

$$\frac{\partial\psi}{\partial y}\frac{\partial^2\psi}{\partial x\partial y} - \frac{\partial\psi}{\partial x}\frac{\partial^2\psi}{\partial y^2} = \frac{g(x)(\rho_f - \rho_g)}{\rho_f} + \frac{\mu}{\rho_f}\frac{\partial^3\psi}{\partial y^3} \tag{1}$$

The flow configuration that this equation describes is shown in Fig. 1(*a*) (with a radius of curvature, R, approaching infinity). The boundary conditions are:

$$\frac{\partial\psi}{\partial y} = \frac{\partial\psi}{\partial x} = 0 \text{ at } y = 0\,;\ \frac{\partial^2\psi}{\partial y^2} = 0 \text{ at } y = \delta \tag{2}$$

where the last condition says that the motion of the condensate at the liquid-vapor interface induces no significant drag on the vapor. This assumption was proved to be reasonable by the work of Chen [10].

The energy equation can be written in boundary layer form as long as axial conduction is negligible. This will be the case since $\mathrm{Pr} \geq \mathrm{O}(1)$.

$$\frac{\partial\psi}{\partial y}\frac{\partial T}{\partial x} - \frac{\partial\psi}{\partial x}\frac{\partial T}{\partial y} = \alpha\frac{\partial^2 T}{\partial y^2} \tag{3}$$

The boundary conditions are

$$T = T_w(x) \text{ at } y = 0\,;\ T = T_{\mathrm{sat}} \text{ at } y = \delta \tag{4}$$

Sparrow and Gregg's similarity transformation

$$F(\eta) = \frac{\psi}{4\alpha c x^{3/4}}\,;\quad \eta = \frac{cy}{x^{1/4}}\,;\quad \theta(\eta) \equiv \frac{T_{\mathrm{sat}} - T}{\Delta T(x)} \tag{5}$$

where $c \equiv [g c_p(\rho_f - \rho_g)\rho_f/4\mu k]^{1/4}$ gives for the equation of motion

$$F''' + \frac{1}{Pr}[3F''F - 2F'^2] + 1 = 0 \tag{6}$$

with boundary conditions

$$F(0) = F'(0) = 0\,;\ F''(\eta_\delta) = 0 \tag{7}$$

where η_δ is η evaluated at $y = \delta$. Under this transformation, the energy equation becomes

$$-4\frac{d\ln\Delta T}{d\ln x}\theta F' + 3F\theta' + \theta'' = 0 \tag{8}$$

with boundary conditions

$$\theta(0) = 1\,;\ \theta(\eta_\delta) = 0 \tag{9}$$

It is interesting to note that arbitrary variations of gravity, $g(x)$ could easily be incorporated in this analysis. Just as this formulation is identical with that of Sparrow and Gregg [3] except for the added term $4(d\ln\Delta T/d\ln x)\theta F'$ in the energy equation; so too would the treatment for variable $g(x)$ and $\Delta T(x)$ be identical with our recent variable-gravity treatment [7] except for the addition of the same term in the energy equation.

Similar Solutions For The Vertical Plate With $\Delta T(x)$

The derivative, $d\ln\Delta T/d\ln x$, will be independent of x as long as $\Delta T \sim x^m$, where m is any constant. Accordingly similar solutions exist if

$$\frac{\Delta T}{\Delta T_0} = \left(\frac{x}{L}\right)^m \tag{10}$$

where ΔT_0 is a constant "characteristic" temperature difference and L is the length of the plate. In this case equation (8) becomes

Nomenclature

A = cross-sectional area of a fin
B = normalized Nusselt number, $\theta'(0)\sqrt[4]{c_p\Delta T(x)/h_{fg}}$
C = constant multiplier defined in the context of equation (33)
c = $[g\rho_f(\rho_f - \rho_g)c_p/4\mu k]^{1/4}$
c_p = specific heat of condensate
D = diameter of a horizontal cylindrical fin
E = constant defined by equation (35)
F = dimensionless stream function, $\psi/4\alpha c x^{3/4}$
$g, g(x)$ = gravitational acceleration, considered to be constant unless the x dependence is noted.
g_{eff} = an effective g for use in the Nusselt-Rohsenow approximations, defined by equation (28)
h = heat transfer coefficient
h_{fg} = latent heat of vaporization
h_{fg}' = h_{fg} corrected to include sensible heat of subcooling in the film; equal to $h_{fg} + 0.68\,c_p\Delta T$
k = thermal conductivity of condensate
k_s = thermal conductivity of fin material
L = length of condensing surface and/or length of fin
l = height of a horizontal blade-shaped fin
m = exponent of power-law temperature dependence
Nu_x = local Nusselt number, hx/k
P = perimeter of the cross section of a fin
Pr = Prandtl number of the condensate, $\mu/\rho_f\alpha$
q = heat flux from condensate to wall
R = radius of curvature of an axisymmetric body
$T, T_w, T_{\mathrm{sat}}, T_r$ = temperature; subscripts denote temperature of wall, saturated condensate, and root of a fin, respectively
x = distance along wall in the direction of condensate flow, measured from the leading edge
y = distance normal to wall measured from its surface
z = distance along the axis of a fin (equal to x in the case of a vertically oriented fin)
α = thermal diffusivity of condensate, $k/\rho_f c_p$
Γ_c = rate of mass flow of condensate per unit breadth
ΔT = difference between saturation temperature and wall temperature
ΔT_0 = a characteristic temperature difference (see equation (10))
ζ = z/L
η, η_δ = similarity variable, $cy/x^{1/4}$; subscript denotes $c\delta/x^{1/4}$
δ = condensate film thickness
θ = $(T_{\mathrm{sat}} - T)/(T_{\mathrm{sat}} - T_w)$, where T_w is replaced by T_r in the fin problem
μ = viscosity of condensate
ρ_f, ρ_g = densities of condensate and saturated vapor, respectively
ψ = stream function in condensate

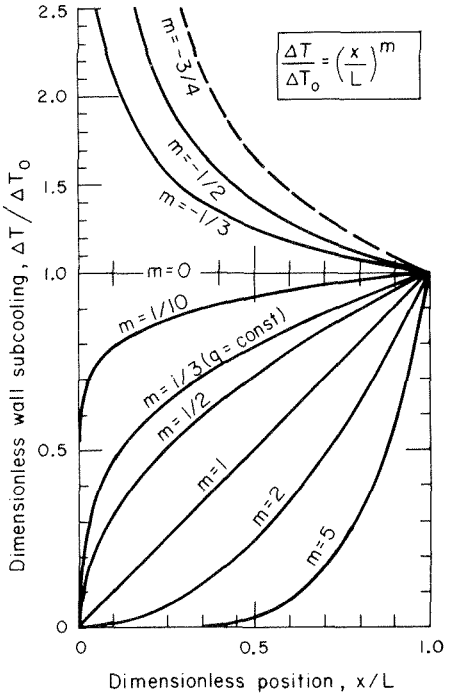

Fig. 2 Temperature variations for which similar solutions exist

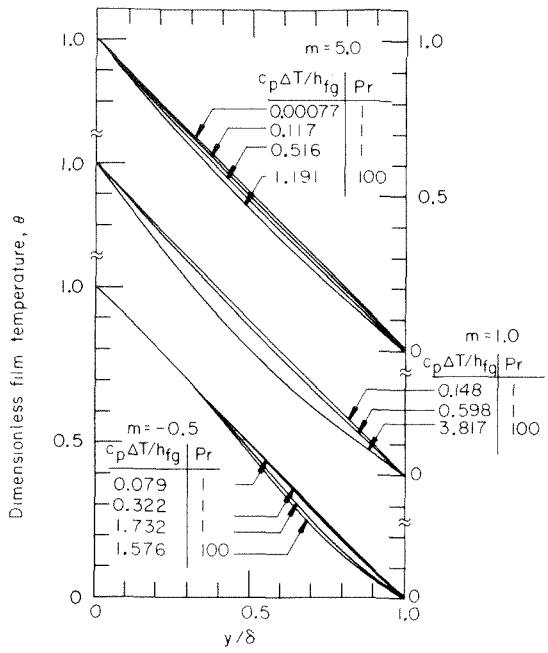

Fig. 3 Temperature distribution in the condensate film

$$-4m\theta F' + 3F\theta' + \theta'' = 0 \tag{11}$$

The boundary-layer formulation requires that $dT/dx \ll \Delta T/\delta$. In this case this requirement reduces to

$$m \ll \frac{x}{\delta} \simeq \mathrm{Nu}_x \tag{12}$$

Thus, the solutions (like any boundary layer results) will be invalid close to the leading edge. Equation (12) also poses a warning against applying the solution for very large values of m.

The dimensionless film thickness, η_δ, is obtained from an energy balance. Equating the heat transfer to the film with the energy carried out by the film, we get Sparrow and Gregg's expression

$$k\int_0^x \left.\frac{\partial T}{\partial y}\right|_{y=0} dx = \rho_f h_{fg}\int_0^\delta u dy + \rho_f c_p \int_0^\delta u(T_{\mathrm{sat}} - T)dy \tag{13}$$

Substituting dimensionless variables and using equation (11) we get from equation (13)

$$\frac{c_p\Delta T(x)}{h_{fg}} = \left[\frac{4m}{12m+9}\,\frac{\theta'(0)}{F(\eta_\delta)} - \frac{\theta'(\eta_\delta)}{3F(\eta_\delta)} + \frac{4m}{3F(\eta_\delta)}\int_0^{\eta_\delta}\theta F' d\eta\right]^{-1} \tag{14}$$

All of the preceding expressions reduce to those of Sparrow and Gregg for $m = 0$, the isothermal case.

The computational procedure is now as follows: Solve equation (6), using any Pr of interest, subject to boundary conditions (7) for an assumed value of η_δ. Use the resulting function, F, in the numerical evaluation of θ from equation (11), subject to boundary conditions (9). Then use the results of these calculations in the RHS of equation (14) and compute the value of $c_p\Delta T(x)/h_{fg}$ which corresponds to the assumed η_δ.

This procedure has been carried out for the temperature variations shown in Fig. 2. These include m's from $-3/4$ up to $+5$. Inspection of equation (14) reveals that when $m = -3/4$, $c_p\Delta T(x)/h_{fg}$ is infinite for any choice of η. For $m < -3/4$ it turns out that only negative values of $c_p\Delta T(x)/h_{fg}$ result. The reason is that $\Delta T(x)$ approaches infinity too rapidly as x approaches zero. Consequently the vapor film is required to acquire infinite thickness immediately. Therefore the present solutions are limited to $m > -3/4$.

Heat transfer results can be obtained easily once θ has been evaluated since

$$h = \frac{1}{\Delta T}\,k\left.\frac{\partial T}{\partial y}\right|_{y=0} = -k\left[\frac{\partial\theta}{\partial\eta}\,\frac{\partial\eta}{\partial y}\right]_{\eta=0} = -\frac{kc}{x^{1/4}}\theta'(0) \tag{15}$$

Using the definitions of c and of the local Nusselt number, $\mathrm{Nu}_x = hx/k$, in equation (15) we obtain

$$\mathrm{Nu}_x = -\theta'(0)\sqrt[4]{\frac{c_p\Delta T(x)}{h_{fg}}}\left[\frac{g\rho_f(\rho_f - \rho_g)h_{fg}x^3}{4\mu k\Delta T(x)}\right]^{1/4} \tag{16}$$

But the term in square brackets to the 1/4 power includes the solution for the isothermal plate with $c_p\Delta T_0/h_{fg}$ small, i.e., $(x/L)^{m/4}(\mathrm{Nu}_x)_{\Delta T = \Delta T_0}$. Thus

$$\frac{\mathrm{Nu}_x}{(x/L)^{m/4}(\mathrm{Nu}_x)_{\Delta T=\Delta T_0}} = -\theta'(0)\sqrt[4]{\frac{c_p\Delta T(x)}{h_{fg}}} \tag{16a}$$

Fig. 3 shows the calculated dimensionless temperature distributions for three values of m ($-1/2$, 1, and 5), two values of Pr (1 and 100), and wide variations of values of $c_p\Delta T(x)/h_{fg}$. We are fortunate to find that, as in the isothermal-wall configurations, there is little deviation from linearity for $c_p\Delta T(x)/h_{fg} \leq 0.1$. However, it should be noted that the curves do not asymptotically approach a linear profile. Rather, they retain a little curvature even at very small values of $c_p\Delta T/h_{fg}$. This will cause the limiting heat transfer coefficients to deviate slightly from those given by the Nusselt-Rohsenow theory, particularly for $m < 0$.

Fig. 4 shows the variation of the normalized local Nusselt number with[3] $c_p\Delta T(x)/h_{fg}$. This plot is awkward in one respect: for any arbitrary value of $c_p\Delta T_0/h_{fg}$, the curve gives different results at different positions, x/L, along the plate. However, as was true for the isothermal cases, the Nusselt number becomes virtually independent of $c_p\Delta T(x)/h_{fg}$ when $c_p\Delta T(x)h_{fg}$ is small. We see from the figure that "small" can generally be considered as less than 0.1 which is still substantial in terms of practical applications. Finally we define

$$\lim_{\frac{c_p\Delta T(x)}{h_{fg}} \to 0}\left[-\theta'(0)\sqrt[4]{\frac{c_p\Delta T(x)}{h_{fg}}}\right] \equiv \text{a constant, } B \tag{17}$$

This constant is plotted as a function of m in Fig. 5.

[3] $c_p\Delta T(x)/h_{fg}$ is plotted on a logarithmic abscissa only for convenience of presentation. No physical significance is implied for the nonlinear scale.

The Nusselt-Rohsenow Theory For General Nonisothermal and Arbitrary-Heat-Flux Surfaces

General Considerations. The heat flux, q, during condensation from any body can be expressed as $k\Delta T/\delta$ in accordance with Nusselt's assumption that T varies linearly with y. Whether or not ΔT varies with x, q can still be written as

$$q = k\frac{\Delta T}{\delta} = h_{fg}'\frac{d\Gamma_c}{dx} \tag{18}$$

The quantity h_{fg}' is Rohsenow's corrected latent heat and it is equal to $h_{fg}(1 + 0.68\, c_p\Delta T/h_{fg})$ where c_p is the specific heat of the condensate. And Γ_c is the mass flow rate per unit breadth. For Γ_c, the Nusselt-Rohsenow theory gives

$$\Gamma_c = \frac{g\rho_f(\rho_f - \rho_g)}{3\mu}\delta^3 \tag{19}$$

Substituting equation (19) in (18) and integrating the result we obtain

$$\delta = \left[\frac{4\mu k}{g\rho_f(\rho_f - \rho_g)h_{fg}}\int_0^x \frac{\Delta T}{1 + 0.68c_p\Delta T/h_{fg}}dx\right]^{1/4} \tag{20}$$

Since $0.68\, c_p\Delta T/h_{fg}$ is seldom large enough to be of importance, ΔT in the denominator of the integral can generally be approximated with an average value—say $(\int_0^x \Delta T dx)/x$ for example. Accordingly the denominator in the integral in equation (20) can usually be removed and h_{fg} replaced with an h_{fg}' based on the average ΔT. This approximation will be used in the following applications:

The Vertical Flat Plate With Arbitrary Wall-Temperature. In this case, δ is given by equation (20) which, if h_{fg}' is approximately constant, becomes

$$\delta = \left[\frac{4\mu k\int_0^x \Delta T dx}{g\rho_f(\rho_f - \rho_g)h_{fg}'}\right]^{1/4} \tag{21}$$

and, since the local Nusselt number, Nu_x, is equal to x/δ,

$$\mathrm{Nu}_x = \left[\frac{g\rho_f(\rho_f - \rho_g)h_{fg}'}{4\mu k(\frac{1}{x}\int_0^x \Delta T dx)}\right]^{1/4} \tag{22}$$

For $\Delta T = \Delta T_0(x/L)^m$ we obtain from equation (22)

$$\mathrm{Nu}_x = (m+1)^{1/4}\left[\frac{g\rho_f(\rho_f - \rho_g)h_{fg}'x^3}{4\mu k\Delta T(x)}\right]^{1/4} \tag{23}$$

This expression breaks down for $m \le -1$, just as the exact solution breaks down at $m = -3/4$, since the film becomes infinitely thick at the leading edge. For other values of m, we compare the approximate and exact expressions in Fig. 5 as follows:

$$\frac{(\mathrm{Nu}_x)_{\text{Nusselt}}}{(\mathrm{Nu}_x)_{\text{exact}}} = -\frac{(m+1)^{1/4}}{\theta'(0)\sqrt[4]{c_p\Delta T(x)/h_{fg}}} = \frac{(m+1)^{1/4}}{B} \tag{24}$$

Fig. 5 shows that for negative m's (i.e., for infinite ΔT at $x = 0$) the Nusselt-Rohsenow theory deteriorates. It is completely invalid for $m \le -3/4$, but for $m > -0.4$ it is accurate within ± 6 percent. The error increases slowly with increasing positive values of m. This observation is consistent with Denny and Mills [8] results.

Two cautions must be observed with regard to $c_p\Delta T/h_{fg}$ in using the simple theory. 1 Equation (24) is based on the use of h_{fg} in both Nusselt numbers. Actually $(\mathrm{Nu}_x)_{\text{Nusselt}}$ is based on h_{fg}' and will accordingly be slightly higher. Thus the simple theory will be a little more accurate than Fig. 5 suggests, when ΔT increases with x. 2 Equation (24) is valid for "small" $c_p\Delta T(x)/h_{fg}$. While "small" generally means less than about 0.1, the reader should look at Fig. 4 to see if a given $c_p\Delta T(x)/h_{fg}$ is in the asymptotic range for a given m.

Finally, we should note that the power-law axial variations of $\Delta T(x)$ generally pose a severe and a varied test of the simple theory. But the simple theory fails only as the film approaches infinite thickness at $x = 0$. We can thus proceed to apply the simple theory to other ΔT's for which similar solutions do not exist.

The Vertical Flat Plate With Constant Heat Flux. Here we wish to pick $\Delta T(x)$ so that $q = k\Delta T/\delta$ = constant. Using equation (21) it is easy to see that the correct variation is $\Delta T = \Delta T_0(x/L)^{1/3}$. Thus

$$\delta = \left[\frac{3\mu k\Delta T_0 x^{4/3}}{g\rho_f(\rho_f - \rho_g)h_{fg}'}\right]^{1/4} \tag{25}$$

and

$$\mathrm{Nu}_x = \left[\frac{g\rho_f(\rho_f - \rho_g)h_{fg}'x^{3/3}}{3\mu k\Delta T_0}\right]^{1/4} \tag{26}$$

The exact solution gives for the constant-heat-flux case.

$$(\mathrm{Nu}_x)_{\text{exact}} = 1.023\,(\mathrm{Nu}_x)_{\text{Nusselt}} \tag{27}$$

General Axisymmetric or Plane Body With Arbitrary Variations of Wall-Temperature, Gravity, and/or Curvature, R, With x. In 1971, we [6] showed how to generalize the Nusselt-Rohsenow problem for all the foregoing variations except wall-temperature. (Fig. 1 shows the configurations implied by these variations.) The inclusion of $\Delta T(x)$ in that formulation is straight

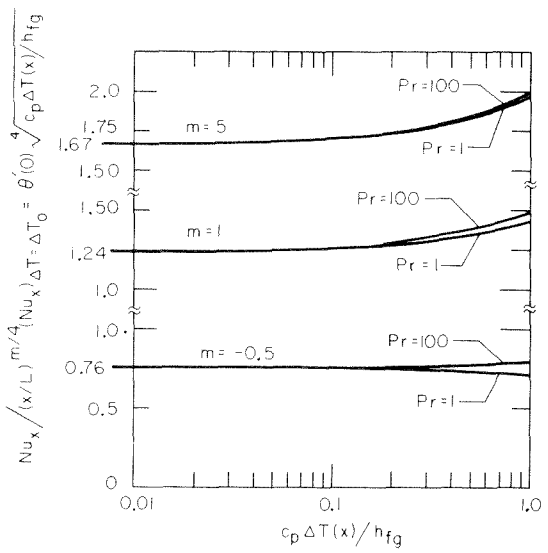

Fig. 4 Influence of Pr and film subcooling on heat transfer

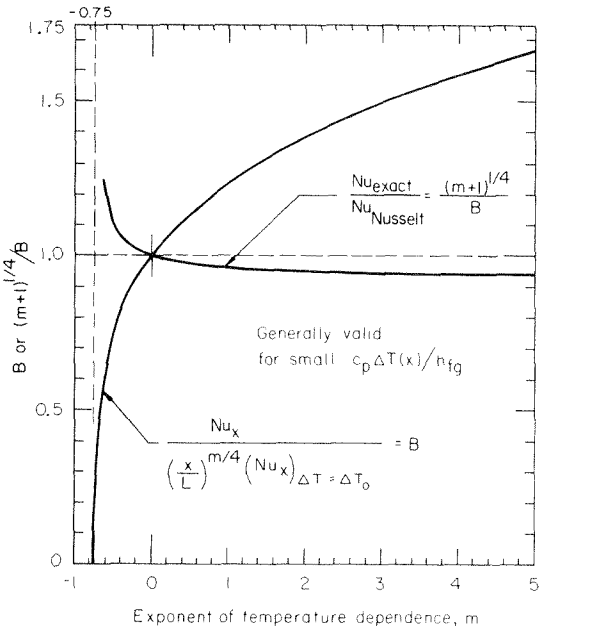

Fig. 5 Variation of local Nusselt number for the similar solutions, and test of the simple Nusselt-Rohsenow theory, as a function of m

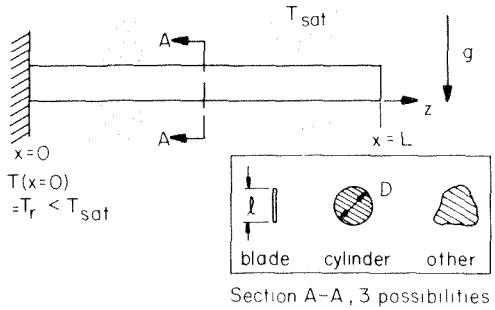

a.) horizontal fin configuration

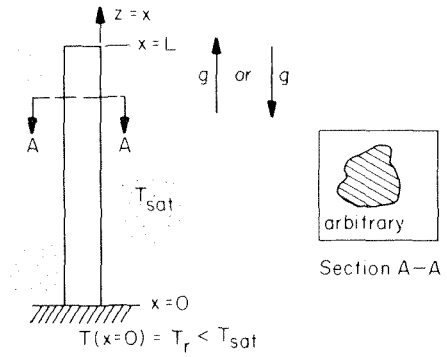

b.) vertical fin with root at the top or the bottom.

Fig. 6 Fin configurations in the present study

forward and it yields equations (21) and (22) except in that the gravity term $g/\int_0^x \Delta T dx$ must be written in terms of an effective gravity, g_{eff}, defined in such a way that

$$\frac{g_{eff}}{\int_0^x \Delta T dx} = \frac{(gR)^{4/3}}{\int_0^x \Delta T g^{1/3} R^{4/3} dx} \tag{28}$$

The Vertical Flat Plate With Arbitrary Heat Flux, $q(x)$. We integrate equation (18) again using equation (19) and obtain

$$\delta = \left[\frac{3\mu \int_0^x q dx}{g\rho_f(\rho_f - \rho_g) h_{fg}'} \right]^{1/3} \tag{29}$$

The resulting temperature difference can then be obtained immediately by using: $\Delta T(x) = (q/k)\delta$. Finally, the Nusselt number in this case is:

$$\mathrm{Nu}_x = \frac{x}{\delta} = \left[\frac{g\rho_f(\rho_f - \rho_g) h_{fg}' x^3}{3\mu \int_0^x q dx} \right]^{1/3} \tag{30}$$

These results are equivalent to equations (25) and (26) for constant q.

Fins Heated by Condensation

General Considerations. Much attention has been given to the design of fins cooled by boiling heat transfer. This work has been reviewed by Westwater [11]. Since the relation between q and ΔT is usually only known empirically that problem must be treated numerically.

Condensation, which yields h's comparable to those for nucleate boiling, can also be used very effectively to heat a fin. And since h's are known analytically, the analytical design of a fin is possible, albeit potentially difficult. However the fact that the Nusselt-Rohsenow analysis is valid for most $\Delta T(x)$, vastly simplifies the design.

We shall only consider fins of constant cross-sectional area, A, and perimeter, P, for which the fin equation is

$$\frac{d^2\theta}{d\zeta^2} = \frac{hPL^2}{k_s A}\theta \tag{31}$$

where $\theta \equiv (T_{sat} - T)/(T_{sat} - T_r)$, $\zeta \equiv z/L$, and L is the length of the fin. This expression is true when the Biot number, hl/k_s or $h(A/P)/k_s$, is small. We shall use two boundary conditions:

$$\theta(\zeta = 0) = 1 \; ; \; \theta'(\zeta = 1) = 0 \tag{32}$$

The latter condition is strictly correct for fins insulated at $\zeta = 1$. However, when it is used for fins that are uninsulated at $\zeta = 1$, it introduces less error than the approximation $\theta(1) = 0$.

Three fin orientations, shown in Fig. 6 will be treated. The first, the horizontal fin, is not a variable ΔT problem of the type we have been discussing, since ΔT is constant in the x direction. But the upward and downward pointing fins *do* involve ΔT variations in the x direction.

The Horizontal Fin. The average heat transfer coefficient for the horizontal fin is given by the Nusselt-Rohsenow theory as

$$h_{avg} = C\left[\frac{g\rho_f(\rho_f - \rho_g) h_{fg}' l^3}{4\mu k \Delta T(z)} \right]^{1/4} \left(\frac{k}{l}\right) \tag{33}$$

where C is a constant which depends upon cross section. For a blade-shaped section, it is 1.075. For a circular cross section C = 0.959 and the diameter, D, should replace l in the bracketed term. For any other cross section, C and the characteristic dimension will change.

Substituting equation (33) in equation (31) gives:

$$\frac{d^2\theta}{d\zeta^2} = E\theta^{3/4} \tag{34}$$

where

$$E \equiv C\frac{k}{k_s}\frac{PL^2}{lA}\left[\frac{g\rho_f(\rho_f - \rho_g) h_{fg}' l^3}{4\mu k (T_{sat} - T_r)} \right]^{1/4} \tag{35}$$

We have solved equation (34) numerically, subject to the boundary conditions (32). In each case value of $\theta'(0)$ was guessed and then iterated until the condition $\theta'(1) = 0$ was satisfied. The results are given in Fig. 7 for $5 \le E \le 100$. When $E < 10$, the condition $\theta'(1) = 0$ is no longer a good approximation unless the tip actually is insulated. However, such a fin is far too short to achieve much heating of the wall. When $E > 10$ there is less than 3 percent residual temperature at the tip and even if there is still a little heat flow into the tip, $\theta'(1)$ will be small. Furthermore, if $E \gg 10$ there will be a length of the fin, almost at T_{sat}, which serves no purpose.

Accordingly a good fin design is one for which $E = O(10)$. For steam at 1 atm condensing on a cylindrical copper fin, we obtain

$$E \simeq 50L^2/D^{5/4}(T_{sat} - T_r)^{1/4} = O(10)$$

where L and D are in feet and $(T_{sat} - T_r)$ is in deg F. For a 16 deg F temperature difference, a ⅛ in-dia fin would accordingly function

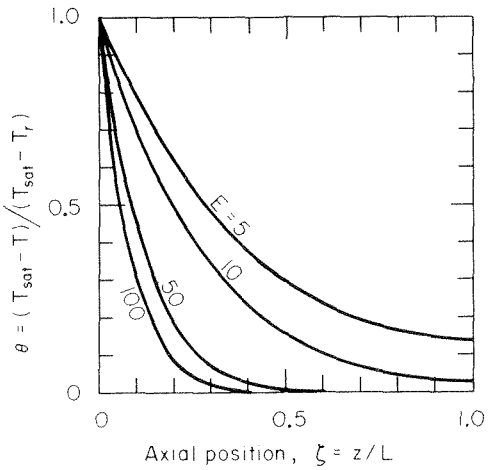

Fig. 7 Temperature distribution along the axis of a horizontal fin

best as a fin if it were only about 2/5 in. long.

The Vertical Fin. In this case the formulation is the same as for the horizontal fin except in that θ is introduced into the heat transfer coefficient as suggested by equation (22). Consequently we obtain the following differential equation in place of equation (35):

$$\frac{d^2\theta}{d\zeta^2} = \frac{E\theta}{\left[\int_0^\zeta \theta(\zeta)d\zeta\right]^{1/4}} \tag{36}$$

The boundary conditions on equation (36) are

$$\theta(0) = 1,\ \theta'(1) = 0 \quad \text{if the root is on top}$$

$$\theta(1) = 1,\ \theta'(0) = 0 \quad \text{if the root is on the bottom} \tag{37}$$

In this case the constant, C, which is contained in E, is always equal to unity, and the characteristic length l is replaced with L.

Equation (36) was again integrated and made, by trial and error, to fit both sets of boundary conditions (37). The results for both the upward and downward pointing fins are plotted in Fig. 8. As was also true for the horizontal fin, the vertical fins with practical utility are the ones for which $E = 0$ (10). The temperature profiles for upward and downward pointing fins differ only a little from each other and from those for horizontal fin.

Finally we note that the curves in Fig. 8 show temperature variations with z that are not unlike those in Fig. 2. They involve no pathological behavior—no discontinuities or locally infinite temperatures. Accordingly we do not expect more than 6 percent error in Fig. 9.

Fin Effectiveness. The overall heat transfer to a fin is given by

$$qA = \left|kA\left.\frac{dT}{dx}\right|_{\text{root}}\right| = \left|\frac{k_s}{L}A(T_{\text{sat}} - T_r)\theta'(\zeta = \text{root})\right| \tag{38}$$

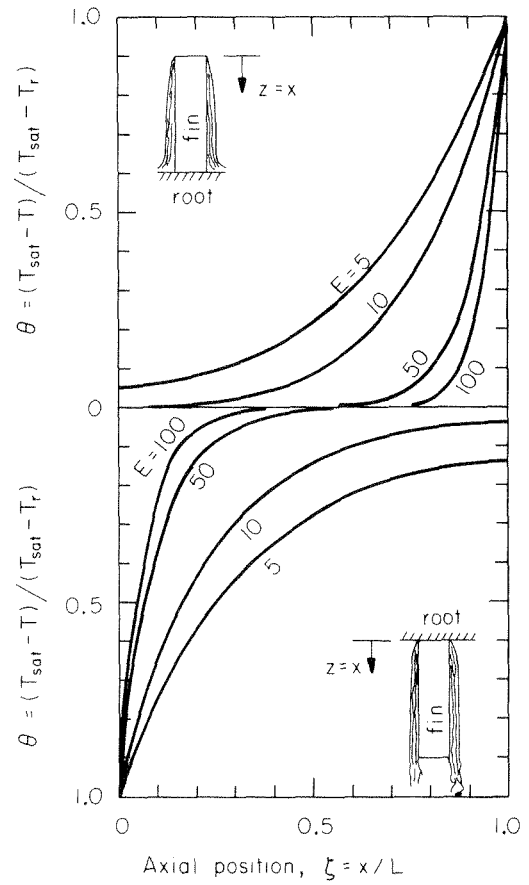

Fig. 8 Temperature distribution along the axis of upward and downward pointing vertical fins

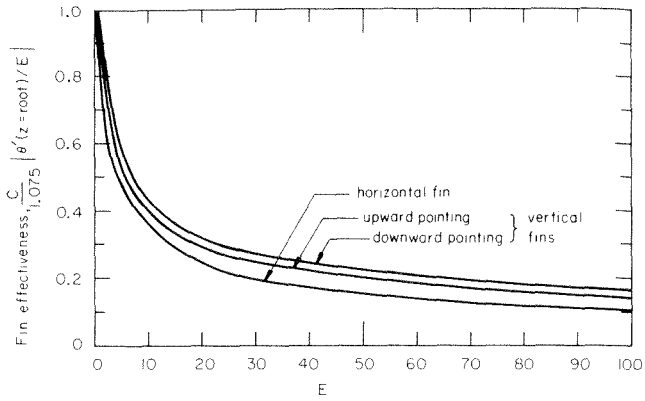

Fig. 9 The "effectiveness" for three condensing fin configurations

The overall heat transfer to the same fin, if it were maintained at a constant temperature, T_r, would be

$$h_{\text{avg}}(T_{\text{sat}} - T_r)(PL) = \frac{k_s}{L}A(T_{\text{sat}} - T_r)\frac{1.075}{C}E \tag{39}$$

Accordingly the "effectiveness' of the fin, defined as the ratio of these quantities, is

$$\text{effectiveness} = \frac{C}{1.075}\left|\theta'(\zeta = \text{root})/E\right| \tag{40}$$

The effectiveness of the present fins is plotted in Fig. 9. Here we see that the effectiveness falls off rapidly with E. It turns out that a well designed fin is about 40 or 50 percent effective. It is convenient to note that the heat flux from the wall at the base of a fin can be expressed as:

$$q_{\text{root}} = \frac{1.075}{C}E\frac{k_s(T_{\text{sat}} - T_r)}{L} \quad (\text{effectiveness}) \tag{41}$$

It should be recognized that we have only scratched the surface of the condensing fin problem. A vast number of important situations and problems remain to be done—fins of variable cross section, the problem of optimization, sloping fins, etc. The execution of such problems is, by and large, a matter of patience and available computing money, once it has been shown that the simple Nusselt-Rohsenow theory can be used. We have solved the three most obvious configurations to emphasize that, as a result of our similarity solution, the simple approximation is valid and that such fin problems therefore lie within easy grasp.

Conclusions

1 The boundary layer equations for condensing flow are formulated for vertical nonisothermal walls. These equations have similar solutions for $\Delta T = \Delta T_0(x/L)^m$ where $m > -3/4$. The comparable problem with variable g, and for axisymmetric bodies, is also briefly formulated.

2 The exact solution for the boundary layer equations gives

$$\text{Nu}_x = B\left[\frac{g\rho_f(\rho_f - \rho_g)h_{fg}'x^3}{4\mu k\Delta T_0}\right]^{1/4}$$

where B varies with m as shown in Fig. 5. If $c_p\Delta T(x)/h_{fg}$ is large, then B should be replaced with $-\theta'(0)\sqrt[4]{c_p\Delta T(x)/h_{fg}}$ as given by Fig. 4. This solution is restricted to $\text{Nu}_x \gg m$.

3 The Nusselt-Rohsenow theory is within 6 percent of the exact solution for $m > -0.4$, as long as $c_p\Delta T(x)/h_{fg}$ is not large, It should also apply to other variations of ΔT as long as they do not lead to $\delta = \infty$ anywhere. For the vertical wall the simple theory gives

$$\text{Nu}_x = \left[\frac{g\rho_f(\rho_f - \rho_g)h_{fg}'x^4}{4\mu k\int_0^x \Delta T dx}\right]^{1/4}$$

where h_{fg}' is based upon an appropriate average ΔT.

4 $\Delta T = \Delta T_0(x/L)^{1/3}$ yields a constant heat flux at the wall.

5 The Nusselt-Rohsenow vertical-wall result for $\Delta T(x)$ can be used with $g = g(x)$, and/or axisymmetric bodies with $R = R(x)$, by replacing g with

$$g_{eff} = \frac{(gR)^{4/3}\int_0^x \Delta T dx}{\int_0^x \Delta T^{1/3} R^{4/3} dx}$$

6 The Nusselt-Rohsenow vertical-wall result for arbitrary q is:

$$Nu_x = \left[\frac{g\rho_f(\rho_g - \rho_g)h_{fg}'x^3}{3\mu\int_0^x q dx}\right]^{1/3}$$

7 The present work simplifies the design of fins heated by condensation. Such design is illustrated in three examples. The effectiveness of such fins is inherently low.

References

1 Nusselt, W., "Die Oberflächenkondensation des Wasserdampfes," *Z. Ver. Deutsch. Ing.*, Vol. 60, 1916, pp. 541–546, 569–575.

2 Rohsenow, W. M., "Heat Transfer and Temperature Distribution in Laminar Film Condensation," TRANS. ASME, Vol. 78, 1956, pp. 1645–1648.

3 Sparrow, E. M., and Gregg, J. L., "A Boundary-Layer Treatment of Laminar-Film Condensation," JOURNAL OF HEAT TRANSFER, TRANS. ASME, Series C, Vol. 81, No. 1, Feb. 1959, pp. 13–18.

4 Sparrow, E. M., and Gregg, J. L., "Laminar Condensation Heat Transfer on a Horizontal Cylinder," JOURNAL OF HEAT TRANSFER, TRANS. ASME, Series C, Vol. 81, 1959, pp. 291–296.

5 Yang, J. W., "Laminar Film Condensation on a Sphere," JOURNAL OF HEAT TRANSFER, TRANS. ASME, Series C, Vol. 95, No. 2, May 1973, pp. 174–178.

6 Dhir, V. K., and Lienhard, J. H., "Laminar Film Condensation on Plane and Axisymmetric Bodies in Nonuniform Gravity," JOURNAL OF HEAT TRANSFER, TRANS. ASME, Series C, Vol. 93, No. 1, Feb. 1971, pp. 97–100.

7 Dhir, V. K., and Lienhard, J. H., "Similar Solutions for Film Condensation With Variable Gravity or Body Shape," JOURNAL OF HEAT TRANSFER, TRANS. ASME, Series C, Vol. 95, No. 4, Nov. 1973, pp. 483–486.

8 Denny, V. E., and Mills, A. F., "Nonsimilar Solutions for Laminar Film Condensation on a Vertical Surface," *International Journal of Heat and Mass Transfer*, Vol. 12, 1969, pp. 965–979.

9 Yang, K. T., "Laminar Film Condensation on a Vertical Nonisothermal Plate," *Journal of Applied Mechanics*, TRANS. ASME, Series E, Vol. 88, Mar. 1966, pp. 203–205.

10 Chen, M. M., "An Analytical Study of Laminar Film Condensation," Parts 1 and 2, JOURNAL OF HEAT TRANSFER, TRANS. ASME, Series C, Vol. 83, No. 1, Feb. 1961, pp. 48–60.

11 Westwater, J. W., "Development of Extended Surfaces for Use in Boiling Liquids," Max Jakob Memorial Award Lecture, 13th Natl Heat Trans. Conf., ASME-AICHE, Denver, Colo., Aug. 6–9, 1972.

M. L. Koosinlin
B. E. Launder
B. I. Sharma

Mechanical Engineering Department,
Imperial College,
London, S.W., England

Prediction of Momentum, Heat and Mass Transfer in Swirling, Turbulent Boundary Layers

The paper presents the outcome of finite-difference calculations of turbulent flow near spinning cones, disks, and cylinders. The turbulence model used is a version of the mixing-length hypothesis in which the mixing length which would prevail in the absence of swirl is made a linear function of the local "swirling flow" Richardson number. Agreement with available experimental data for these geometries is generally good. At high swirl rates, however, a few systematic differences between experiment and calculation become evident which are probably attributable to the nonisotropic nature of the effective viscosity in such complex strain fields.

Introduction

There are numerous practically important flows in the fields of turbomachinery and space projectiles where a fluid stream flows over a body rotating about its axis of symmetry. The rotating motion of the body generates shear stresses within the fluid imparting a swirl component of velocity in the flow. When, as is usually the case, the flow near the body is turbulent, appreciable augmentation of the turbulence energy may be caused by the interaction of the stress-strain fields arising from swirl. Sometimes, it is known [1][1] that the swirl will appreciably modify the length scale distribution, too.

How well do existing models of turbulent motion account for the observed behavior of turbulent flow past rotating surfaces? The question is large and one to which only a partial answer is attempted here.

Prandtl's [2] mixing length hypothesis (MLH) provides the simplest physical basis for turbulent flow computations. While it is now surpassed in generality by newer, more elaborate models which calculate the turbulence energy and dissipation rate throughout the flow [3], the MLH has proved to be extremely reliable for predicting boundary layer flows on stationary walls. Moreover, by virtue of its simplicity, its use in numerical solutions of the boundary layer equations is very economical of computer time.

The present contribution provides numerical predictions of surface friction and heat and mass transfer for several flows over spinning cones, disks, and cylinders, based on a version of the MLH which is known to provide accurate predictions of boundary layers on plane surfaces. Our aim has been to determine what level of predictive accuracy may be expected with the model and to discover in what aspects the model requires improvement (or replacement) to bring entirely satisfactory agreement.

The Mathematical Model

The streamwise and swirl momentum equations for a uniform property, axisymmetric turbulent flow may be written:

$$\rho U\frac{\partial U}{\partial x} + \rho V\frac{\partial U}{\partial y} = -\frac{\partial p}{\partial x} + \frac{1}{r}\frac{\partial}{\partial y}\left[r\mu_{\text{eff}}\frac{\partial U}{\partial y}\right] + \rho\frac{V_\theta^2}{r}\sin\alpha \quad (1)$$

$$\rho U\frac{\partial rV_\theta}{\partial x} + \rho V\frac{\partial rV_\theta}{\partial y} = \frac{1}{r}\frac{\partial}{\partial y}\left[r^3\mu_{\text{eff}}\frac{\partial V_\theta/r}{\partial y}\right] \quad (2)$$

where the notation is illustrated in Fig. 1. The presence of swirl causes the static pressure to vary across the boundary layer. Provided the variation with x of the radius of curvature of the body is small, radial equilibrium may be assumed and hence:

$$0 = -\frac{\partial p}{\partial y} + \rho\frac{V_\theta^2}{r}\cos\alpha \quad (3)$$

The effective viscosity of the fluid, μ_{eff}, is taken as the sum of the molecular and turbulent contributions, i.e., $\mu_{\text{eff}} = \mu + \mu_t$.

The turbulent viscosity is calculated from the following simple extension of Prandtl's original hypothesis to account for the additional effect of swirl on the level of μ_t:

$$\mu_t = \rho l^2\left[\left(\frac{\partial U}{\partial y}\right)^2 + \left(r\frac{\partial (V_\theta/r)}{\partial y}\right)^2\right]^{1/2} \quad (4)$$

Equation (4), proposed and used in [4], appeared superior to earlier proposals [5, 6] in which the turbulent transport coefficient for angular momentum was held to depend only on gradients in swirling velocities, not axial ones.

A two-part specification is adopted for the distribution of mixing length l based on practices used by numerous workers for predicting flows without swirl. In the region where the presence of the wall affects the turbulence structure it is assumed that

$$l = \kappa y(1 - \exp - D) \quad (5)$$

[1] Numbers in brackets designate References at end of paper.

Contributed by the Heat Transfer Division for Publication in the JOURNAL OF HEAT TRANSFER. Manuscript received by the Heat Transfer Division, October 9, 1973

where, following the recommendation of [7], the damping function D is taken as:

$$D = y_+ \tau_+^{3/2}/26 \tag{6}$$

When the variation of τ_+ across the viscous sublayer and "buffer" regions is negligible, equation (6) is identical to Van Driest's proposal for the damping of the mixing length at low Reynolds numbers. The inclusion of $\tau_+^{3/2}$ however is found to give better predictions when there is rapid change in τ with y, as occurs in transpired boundary layers and flows with severe streamwise pressure gradients.

In the outer region l is given by

$$l = \lambda\delta \tag{7}$$

δ being the effective thickness of the boundary layer. The constants κ and λ are given the values 0.42 and 0.085, respectively, for all test cases, a consensus of values currently in use for plane boundary layer flows. Equation (7) is used in place of (5) at all positions further from the spinning surface greater than that at which l given by (5) first exceeds the value given by (7).

The model as presented so far assumes that there is no direct influence of the swirl on the mixing length. Simple stability arguments suggest however, that swirl will act either to decrease or increase the level of l according to whether the fluid's rate of change of angular momentum with radius is positive or negative. By analogy with the effects of density stratification in atmospheric turbulence, therefore, Bradshaw [9] has proposed that the length scale in swirling flows be modified as follows:

$$l = l_0(1 - \beta \mathrm{Ri}) \tag{8}$$

where l_0 is the level of mixing length prescribed by equations (5 to 7) above, Ri is the swirl flow Richardson number:

$$\mathrm{Ri} = \frac{\frac{2V_\theta \cos\alpha}{r^2}\frac{\partial}{\partial y}(rV_\theta)}{(\frac{\partial U}{\partial y})^2 + (r\frac{\partial V_\theta/r}{\partial y})^2}$$

and β is a constant coefficient. Notice that cos α is zero for flow near a spinning disk. In all the flows considered here, rV_θ is a maximum at the spinning surface and decreases uniformly to the edge of the boundary layer. The Richardson number is always negative and hence for positive β, l is increased. Predictions of the test flows have been obtained for two values of β, 5, and zero. The latter corresponds with the "Standard"model for flows without swirl, the former is approximately that which gives the best overall level of agreement of predictions with measurement.

Heat and mass transfer rates from the surfaces are computed by solving the stagnation enthalpy or chemical-species equations as follows:

$$\rho U\frac{\partial \hat{h}}{\partial x} + \rho V\frac{\partial \hat{h}}{\partial y} = \frac{1}{r}\frac{\partial}{\partial y}\left[r\left(\frac{\mu_{\mathrm{eff}}}{\sigma_{\mathrm{eff}}}\frac{\partial \hat{h}}{\partial y} + U\tau_{x,y} + V_\theta\tau_{\theta,y}\right)\right] \tag{9}$$

$$\rho U\frac{\partial m}{\partial x} + \rho V\frac{\partial m}{\partial y} = \frac{1}{r}\frac{\partial}{\partial y}\left[r\frac{\mu_{\mathrm{eff}}}{\sigma_{\mathrm{eff}}}\frac{\partial m}{\partial y}\right] \tag{10}$$

In the foregoing, the effective Prandtl/Schmidt number σ_{eff}, is related to the molecular and turbulent values by:

$$\frac{\mu_{\mathrm{eff}}}{\sigma_{\mathrm{eff}}} = \frac{\mu}{\sigma} + \frac{\mu_t}{\sigma_t} \tag{11}$$

Equation (11) rests on the supposition that the effective transport coefficients for enthalpy and species are the sum of their molecular and turbulent values. For both the $\hat{h}$ and the m equations σ_t is given the value of 0.9.

Equations (1) to (3) and (9) to (10), together with the indicated auxiliary equations have been solved by means of an adapted version of GENMIX, the computer program based on the finite difference procedure of Patankar and Spalding [10]. Forty cross-stream grid nodes were used nearly half of which were concentrated in the sublayer and buffer regions where gradients of dependent variables were steepest. Computing time per run on a CDC 6600 was typically 10s.

Presentation and Discussion of Predictions

First the numerical accuracy of the finite difference procedure applied to swirling flows was tested. Fig. 2 compares the finite difference predictions of the *laminar* flow induced by a spinning infinite disk with the similar solutions of Cochran [11] for the velocity field and Sparrow and Gregg [12] for the thermal field. The thermal solution is for a uniform disk temperature with a fluid Prandtl number of 0.7. The finite difference predictions of the radial and tangential velocity profiles and of the temperature profile, are scarcely distinguishable from the "exact" similar solutions, the maximum discrepancy being less than 0.2 percent.

Nomenclature

$\bar{C}_M$ = $8\pi\int_0^\delta UV_\theta dy \sin\alpha/\omega^2 r^3$, average drag coefficient for disk and cone; $\int_0^\delta UV_\theta dy/\omega R^2\, U_\infty = \delta_{2\theta}/R$, average drag coefficient for cylinder;
D = damping function in mixing length formulas
$\hat{h}$ = stagnation enthalpy
l = mixing length
m = mass fraction of chemical species
$\overline{\mathrm{Nu}}$ = average Nusselt number
p = pressure
r = radial distance from axis of symmetry
R = radius of cylinder
Re = $\omega rx/\nu$, spin Reynolds number
Re_t = value of Re at which transition occurs
Re_∞ = $U_\infty \mathrm{R}/\nu$, free stream Reynolds number
Ri = $\dfrac{\frac{2V_\theta\cos\alpha}{r^2}\frac{\partial}{\partial y}(rV_\theta)}{\left(\frac{\partial U}{\partial y}\right)^2 + \left(r\frac{\partial V_\theta/r}{\partial y}\right)^2}$, local Richardson number
$\overline{\mathrm{Sh}}$ = average Sherwood number
U = velocity in the x direction
U_∞ = free stream velocity
V = velocity in the y direction
V_θ = velocity in the circumferential direction
x = coordinate measured along the surface
y = coordinate measured normal to the surface
α = angle made by x direction with symmetry axis
β = parameter in equation (8)
δ = boundary layer thickness where $\frac{U}{U_\infty} = 0.99$
δ_2 = $\frac{1}{(r\omega)^2}\int_0^\delta (r\omega - U)U dy$
δ_{2x} = $\int_0^\delta \frac{U}{U_\infty}\left(1 - \frac{U}{U_\infty}\right)dy$, momentum thickness in x direction
$\delta_{2\theta}$ = $\int_0^\delta UV_\theta/U_\infty\, \omega R dy$, swirl momentum thickness
θ = angle of revolution about symmetry axis
κ,λ = mixing length constants
μ = dynamic viscosity of fluid
ν = kinematic viscosity of fluid
ρ = density of fluid
σ = Prandtl or Schmidt number
τ = shear stress
ω = rotational speed
Ω = swirl velocity/free stream velocity

Subscripts

eff = effective value
∞ = free stream
t = turbulent value
x,y,θ = coordinate directions
+ = quantity nondimensioned by $(\tau_w/\rho)^{1/2}$ and ν
W = wall value

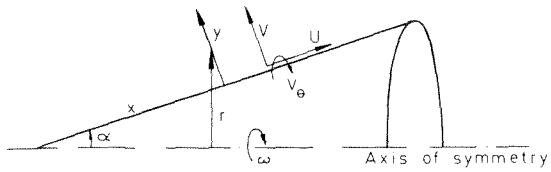

Fig. 1 Geometry and nomenclature for swirling flows

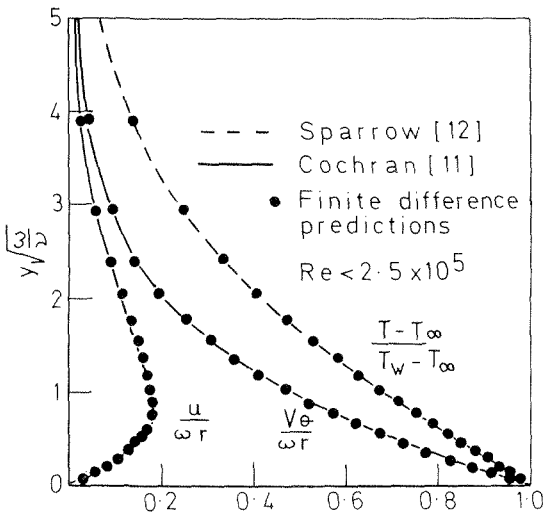

Fig. 2 Laminar flow near a swirling disk: velocity and temperature profiles

Calculations relating to turbulent flow near a spinning disk are presented in Figs. 3 to 5. Mean velocity profiles are shown in Fig. 3, the experimental data being those of Erian and Tong [13*a*] and Cham and Head [13*b*]. The shape of these profiles is distinctly different from those for laminar flow. As in nonswirling flows, very steep velocity gradients occur in the immediate neighborhood of a wall because stresses there are high but effective viscosities low. For both test conditions extremely close agreement is observed between measured and calculated components of swirl velocity. The axial velocity is well predicted for Cham and Head's test and for values of $y\sqrt{\omega/\nu}$ up to 20 in Erian and Tong's work. Thereafter, however, the predicted velocity falls to zero much more quickly than the measured. We are uncertain which of these experimental axial velocity profiles is the more correct. It should be noted, however, that in the region where there is disagreement between the predictions and Erian and Tong's data, the average velocity is only about 3 percent of the disk velocity. It would thus seem unlikely that failure to predict the mean velocity correctly would have noticeable effect on surface heat transfer coefficients.

To make accurate predictions of torque coefficient and Nusselt/Schmidt number, the Reynolds number at which the flow becomes turbulent must be prescribed. It may be expected that R_t will vary a little from one apparatus to another because of detailed differences in apparatus design. Our practice has therefore been to choose the value of R_t which seemed most consistent with

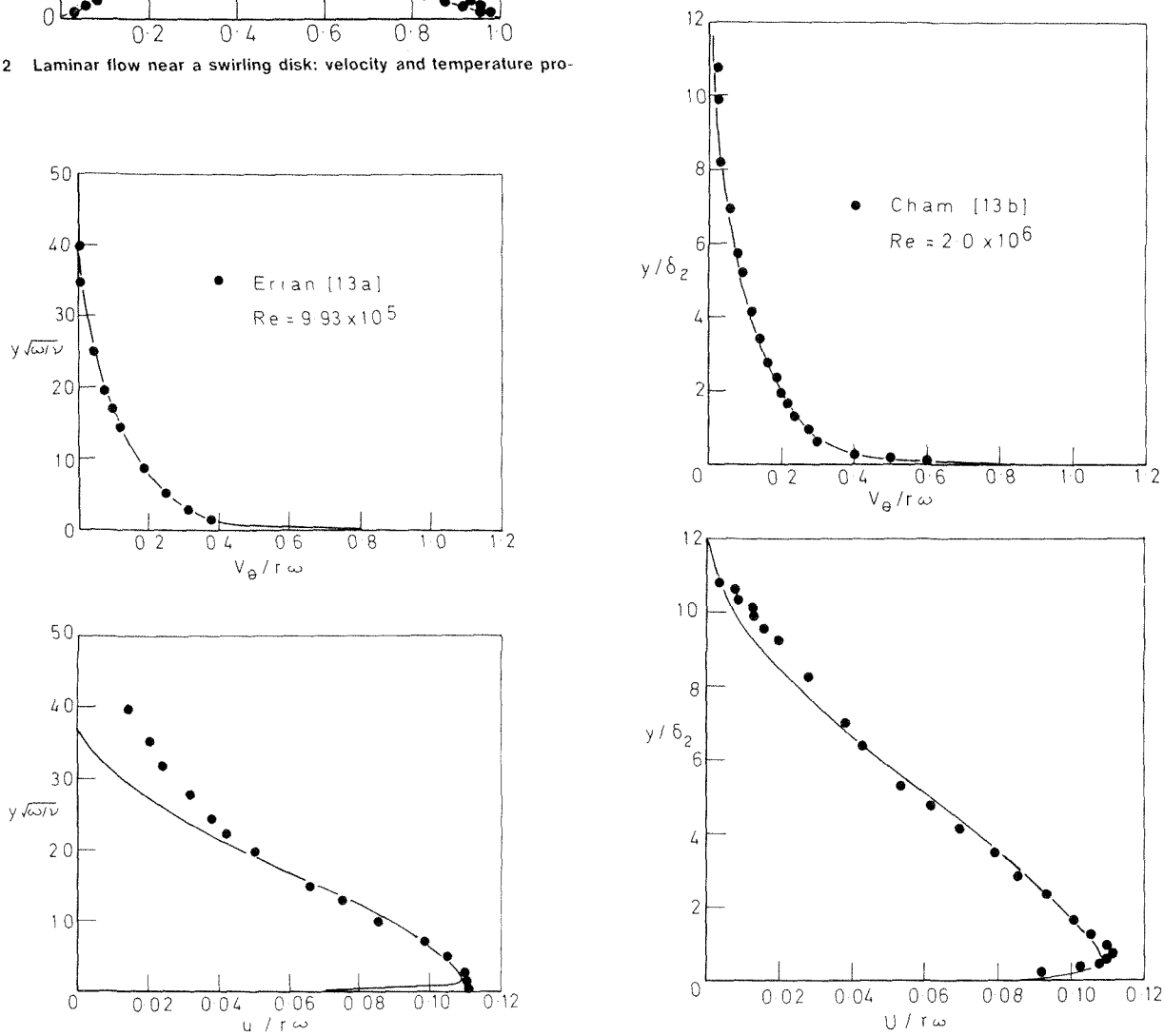

Fig. 3 Turbulent flow velocity profiles near a spinning disk

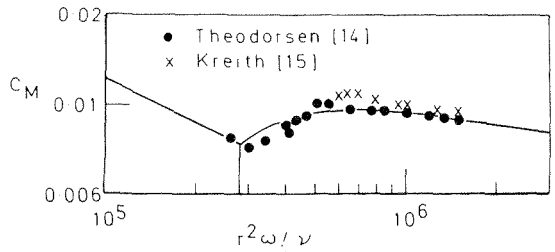

Fig. 4 Torque coefficient for spinning disk

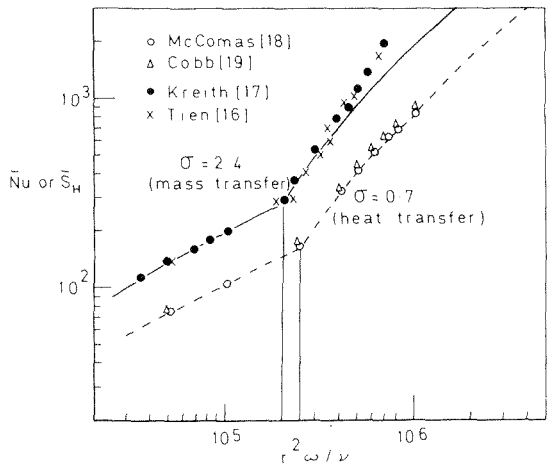

Fig. 5 Heat and mass transfer from a disk rotating in still air

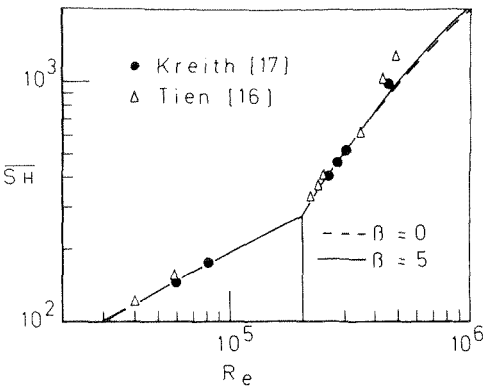

Fig. 6 Mass transfer from spinning 120 deg cone in still air

any particular apparatus. For this reason different values of R_t have sometimes been adopted for nominally the same geometry.

Predictions of torque coefficient for the rotating disk are shown in Fig. 4; R_t was taken as 2.8×10^5. Agreement with the measurements of Theodorsen and Regier [14] is within 5 percent over the whole range spanned by these data. The more recent measurements of Kreith, et al. [15] give values of C_M which are 5–10 percent higher than those of [14]. Thus it is probably the case that the predictions fall within the bounds of experimental uncertainty for this flow. Predictions of heat and mass transfer rates for the rotating disk geometry are shown in Fig. 5; the transition Reynolds number was taken as 2.4×10^5 and 2.0×10^5, respectively, i.e., a little lower than for the comparisons shown in Fig. 4. Agreement of predictions with the Nusselt number data is complete over the Reynolds number range explored. The mass transfer predictions are also satisfactory for Reynolds numbers below 5×10^5. Above this value, however, both the Tien and Campbell [16] data and those of Kreith, et al. [17] display a faster rate of increase with spin Reynolds number than do the predictions. We believe the relatively different behavior for the heat and mass transfer data is probably associated with the different molecular Prandtl/Schmidt numbers for the processes: 0.7 and 2.4, respectively.

Predictions of convective transport from spinning cones are shown in Figs. 6 to 9. No heat transfer or torque data appear to be available for the 120 deg cone. The naphthalene diffusion measurements of Kreith, et al. [17] and Tien and Campbell [16] display a very similar behavior to the disk data. With a transition Reynolds number of 2×10^5, agreement of predictions with measurements is very close for Reynolds numbers up to 4×10^5; thereafter the data display progressively higher levels of Sherwood number than the calculated values. For this cone angle there is scarcely any difference in the level of Sherwood number predicted with and without the swirl correction term.

All the 60 deg cone predictions were made with transition set at $Re = 10^5$, a value which seemed consistent with both the heat and mass transfer data. As with the disk, the heat transfer predictions shown in Fig. 7, are in almost perfect agreement with measurements while the mass transfer data deviate above the calculated values for Re 2×10^5. Slightly better overall agreement is obtained with $\beta = 5$.

Fig. 8 shows the predicted torque coefficient for the 60 deg cone compared with Kreith's [15b] high Reynolds number data. Here, for spin Reynolds number greater than about 3×10^5 the level of C_M for $\beta = 5$ is some 12 percent higher than in the absence of a swirl correction ($\beta = 0$). Kreith's data certainly support the higher values. At no point do the predicted values of C_M for $\beta = 5$ differ from the measured by more than 7 percent, a figure which lies well within the uncertainty limits of ±12 percent estimated by Kreith.

The only data known to us of velocity profiles near spinning cones are those of [20]. Predictions are compared in Fig. 9 with measurements on an 80 deg cone. For this flow, the choice of $\beta = 5$ leads to predictions much closer to the measured profiles than does $\beta = 0$. Although overall the agreement is probably satisfactory, the predicted axial velocity approaches zero in the outer region of the boundary layer considerably more quickly than the experimental data suggest. This pattern is the same observed for the disk flow data of Erian and Tong shown in Fig. 3(*a*) (but in con-

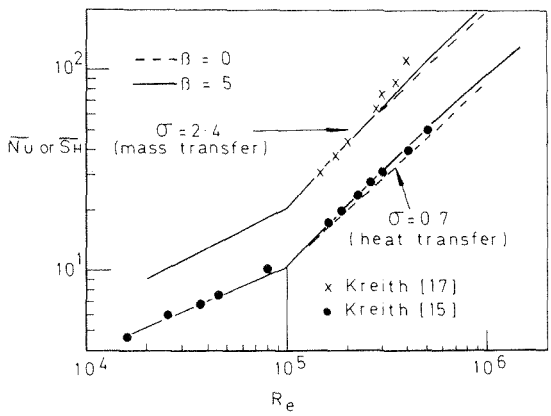

Fig. 7 Heat and mass transfer from spinning 60 deg cone in still air

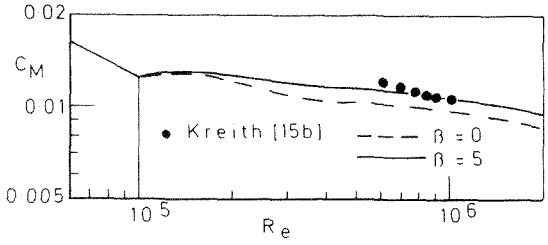

Fig. 8 Torque coefficient for spinning 60 deg cone in still air

trast to the Cham and Head data of Fig. 3(*b*)).

The final test case is the external flow along a cylinder in which the cylinder is rotating about its axis. Measured mean velocity profiles by Furuya, et al. [21] are shown in Fig. 10 for the case where the spin velocity at the surface of the cylinder is twice that of the axial free stream. Again the predicted solutions for $\beta = 5$ are in close agreement with the measured profiles over the whole of the fully turbulent region. We note, however, that the calculated profiles seem to exhibit a steeper slope in the immediate vicinity of the wall, especially the profile of circumferential velocity. This last feature is not entirely consistent with the variation of momentum thicknesses δ_{2x} and $\delta_{2\theta}$ along the cylinder shown in Fig. 11. Results at three levels of Reynolds numbers are shown, the lower two being those of Furuya, et al. [21] and at the highest Reynolds number, those of Parr [22]. The rate of growth of swirl momentum thickness is evidently predicted satisfactorily for the case where $\beta = 5$ (implying that the predicted velocity profile in fact has the correct slope in the neighborhood of the wall). Too large a rate of growth of *axial* momentum thickness is predicted, however, the discrepancy being especially large for Parr's high spin rate data. An implication of the foregoing result is that, to predict the correct rate of growth of both the axial and swirl boundary layers, a nonisotropic effective viscosity must be used.

Concluding Remarks

The present enquiry has shown that use of the Prandtl mixing length hypothesis leads to generally satisfactory predictions of flow near spinning surfaces provided the mixing length is made a linear function of the equivalent "swirling flow" Richardson number, a concept originally introduced by Bradshaw [9] for the prediction of nonswirling, plane flows over curved surfaces. Examination of the mean velocity profiles near a spinning 80 deg cone and a rotating cylinder in an external stream has shown that the swirling flow modification brings great improvement in predictive accuracy over the standard version.

There are nevertheless some shortcomings in the predictions at high swirling rates that should be noted. We have already mentioned that the present model predicts too fast a growth rate of axial momentum thickness along the spinning cylinder. Perhaps the underprediction of the rates of mass transfer from the spinning disks and cones finds its origin in a similar cause, i.e., the effective viscosity becoming highly nonisotropic as the level of swirl progressively increases. If this is the case, Figs. 5 and 7 suggest that it is in the immediate near-wall region where viscous damping is important that the turbulent transport coefficient is especially anisotropic. For, the heat transfer data are well predicted in each case while the mass transfer data are not. Now for present purposes the only significant difference between the heat and mass transport processes is that the near-wall region offers proportionately a much geater resistance to mass transfer than heat transfer. The different behavior could be explained if it is in the near-wall region that the effective viscosity model developed in this work breaks down. (In this connection it is relevant to

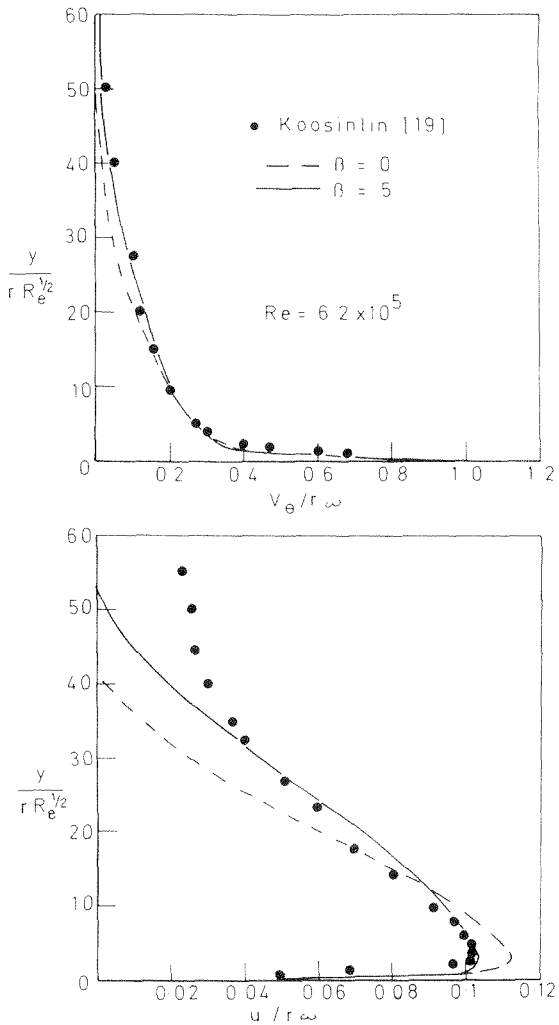

Fig. 9 Velocity profiles near an 80 deg spinning cone

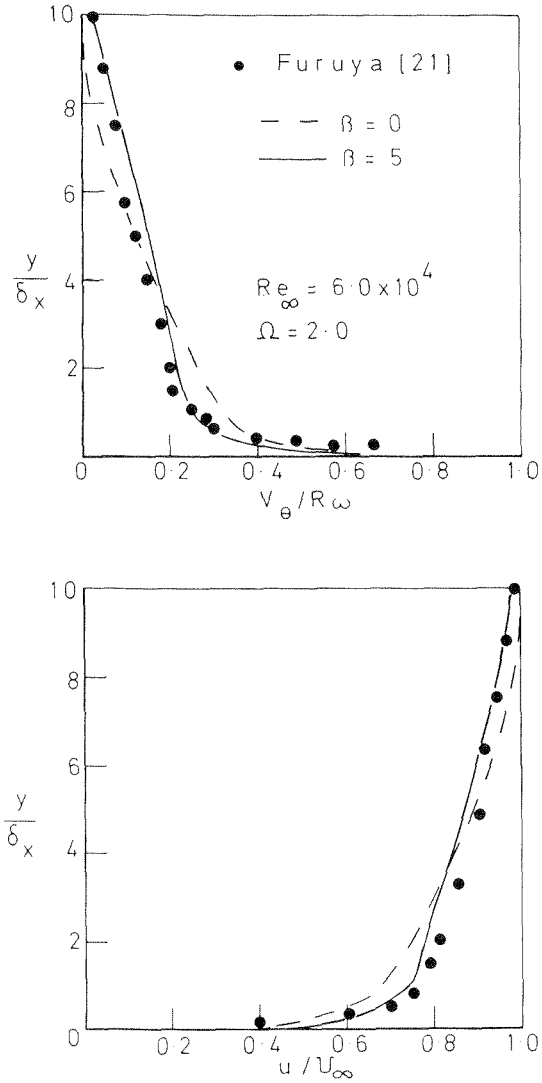

Fig. 10 Velocity profiles in flow past spinning cylinder

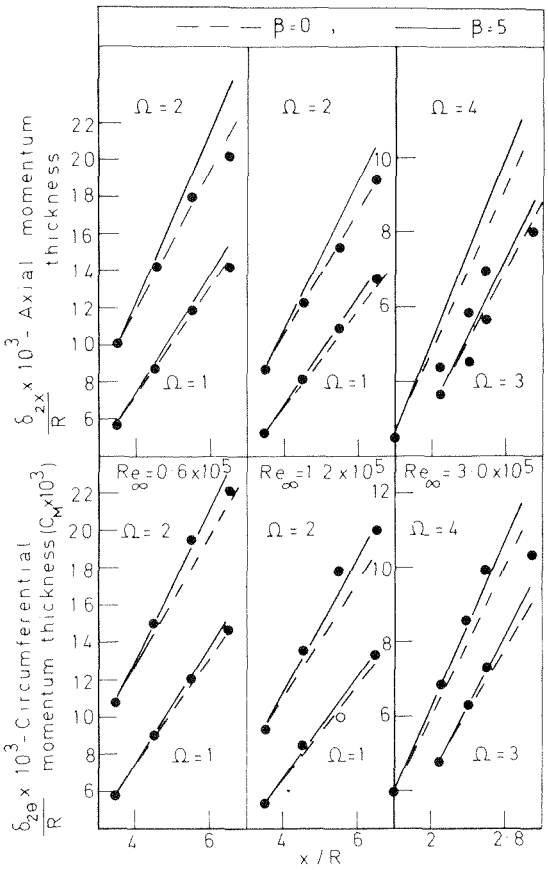

Fig. 11 Momentum thickness development for flow past spinning cylinder

mention that Johnston's three-dimensional boundary layer data [23] implied a strongly nonisotropic viscosity near the wall). It would be valuable to extend present experimental data in this area to higher Prandtl and Schmidt numbers to help resolve this question.

Finally, it may be concluded that to develop a model of turbulence for predicting swirling flows near walls which possess significantly greater universality than the present one will require the abandonment of the effective viscosity concept. The most promising route seems to be one in which transport equations are solved for each of the nonzero Reynolds stress components. Models of this kind have been presented in references [24 and 25] and by a few other workers. In principle, these models are capable of accounting for the nonisotropic features of swirling turbulent flows that have eluded the present model. Because of their much greater complexity, however, they have as yet been subject to little testing. Indeed, apart from the vortex-flow prediction of [24], there seems to have been no calculations made of swirling flow, an omission that ought soon to be remedied.

Acknowledgments

The work has been supported by the Science Research Council through contract B/RG/1863. We gratefully acknowledge advice by Dr. F. C. Lockwood concerning the adaption of GENMIX to the flow geometries considered in the present work.

References

1 Bradshaw, P., "Effects of Streamline Curvature on Turbulent Flow," AGARDograph No. 169, 1973.

2 Prandtl, L., "Bericht über Untersuchungen zur ausgebildeten Turbulenz," *ZAMM* Vol. 5, 1925, p. 136.

3 Jones, W. P., and Launder, B. E., "The Calculation of Low Reynolds Number Phenomena With a Two Equation Model of Turbulence," *International Journal of Heat and Mass Transfer*, Vol. 16, 1973, pp. 1119–1130.

4 Koosinlin, M. L., and Lockwood, F. C., "The Prediction of Boundary Layers on Rotating Axially Symmetrical Bodies," Imperial College, Mech. Eng. Dept., Rep. BL/TN/B/42, 1971.

5 Owen, J. M., "Flow Between a Rotating and a Stationary Disc," PhD thesis, University of Sussex, 1969.

6 Lilley, D. G., and Chigier, N. A., "Non-Isotropic Turbulent Stress Distribution in Swirling Flows From Mean Value Distributions," *International Journal of Heat and Mass Transfer*, Vol. 14, 1971, p. 573.

7 Launder, B. E., and Priddin, C. H., "A Comparison of Some Proposals for the Mixing Length Near a Wall," International Journal of Heat Mass Transfer, Vol. 16, 1972, pp. 700–702.

8 Van Driest, E. R., "On Turbulent Flow Near a Wall," *J. Aero. Sci.* Vol. 23, 1956, p. 1007.

9 Bradshaw, P., "The Analogy Between Stream Line Curvature and Buoyancy in Turbulent Shear Flow," *Journal of Fluid Mechanics*, Vol. 36, 1971, p. 177.

10 Patankar, S. V., and Spalding, D. B., *Heat and Mass Transfer in Boundary Layers*, Intertext Books, London, 1970.

11 Cochran, W. G., "The Flow Due to a Rotating Disc," *Proc. Camb. Phil. Soc.*, Vol. 30, 1934, p. 325.

12 Sparrow, E. M., and Gregg, J. L., "Heat Transfer From a Rotating Disc to Fluids of any Prandtl Number," JOURNAL OF HEAT TRANSFER, Vol. 81, 1959, p. 249.

13(*a*) Erian, F. F., and Tong, Y. H., "Turbulent Flow Due to a Rotating Disc," *The Physics of Fluids*, Vol. 14, No. 12, Dec. 1971, p. 2588.

13(*b*) Cham, T. S., and Head, M. R., "Turbulent Boundary Layer Flows on a Rotating Disc," *Journal of Fluid Mechanics*, Vol. 37, 1969, p. 429.

14 Theodorsen, T., and Regier, A., "Experiments on Drag of Revolving Discs, Cylinders and Stream Line Rods at High Speed," NACA Rep. 793, 1944.

15(*a*) Kreith, F., and Kneisel, K., "Convection From an Isothermal Cone Rotating in Air," *Heat Transfer, Thermodynamics and Education*, Boelter anniversary volume, H. A. Johnson, ed., McGraw-Hill, New York, 1964, pp. 247–254.

15(*b*) Kreith, F., "Frictional Drag and Convective Heat Transfer of Rotating Cones in Mixed and Turbulent Flow," *Process Heat Transfer and Fluid Mech. Inst.* Stanford, 1966.

16 Tien, C. L., and Campbell, D. T., "Heat and Mass Tranfer From Rotating Cones," *Journal of Fluid Mechanics*, Vol. 17, 1963, p. 105.

17 Kreith, F., Taylor, J. H., and Chong, J. P., "Heat and Mass Transfer From a Rotating Disc," JOURNAL OF HEAT TRANSFER, TRANS. ASME, 1959, p. 95.

18 McComas, S. T., and Hartnett, J. P., "Temperature Profiles and Heat Transfer Associated With a Single Disc Rotating in Still Air," 4th Int. Conference, Heat Transfer 1970, Vol. 3, FC 7.7, 1970.

19 Cobb, C., and Saunders, O. A., "Heat Transfer From a Rotating Disc," *Proc. Royal Soc.*, A236, 1956, p. 343.

20 Koosinlin, M. L., and Lockwood, F. C., "Turbulent Mean Velocity Measurements on a Rotating Cone," Imperial College, Mech. Eng. Rep. BL/TN/A/55, 1972.

21 Furuya, Y., Nakamura, I., and Kawachi, H., "The Experiments on the Skewed Boundary Layer on a Rotating Body," *JSME*, Vol. 9, No. 36 1966, p. 702.

22 Parr, V. O., "Untersuchungen der dreidimensionalen Grenzschicht an rotierenden Drehkorpern bei axialer Anstromung," *Ing. Arch.*, Vol. 32, 1963, p. 393.

23 Johnston, J. P., "Measurements in a Three-Dimensional Turbulent Boundary Layer Induced by a Swept Forward Facing Step," *Journal of Fluid Mechanics*, Vol. 42, 1970, p. 823.

24 Donaldson, C., du P., "Calculations of Turbulent Shear Flows for Atmospheric and Vortex Motions," *AIAA Journal* Vol. 10, 1972.

25 Launder, B. E., Reece, G. R., and Rodi, W., "Progress in the Development of a Reynolds Stress Turbulence Closure," Imperial College, Mech. Eng. Dept. Rep. HTS/73/31, 1973.

Kamal-Eldin Hassan[1]
Mohamed A. Hilal[2]

Mechanical Engineering Department,
Faculty of Engineering,
Cairo University,
Cairo, Egypt

Direct Contact Convection Between Liquid Jets and Air in Crossflow

Direct contact, or fluid-to-fluid heat convection in the absence of mass transfer is investigated experimentally. A large number of hot liquid jets were cooled by a cross stream of air. It was found that the heat flux thus exchanged is significantly less than that had the jets been enclosed in thin tubes of equal diameter, but larger than the heat flux due to pure conduction in the liquid jets. The results are presented in terms of the usual dimensionless criteria.

Introduction

In ordinary heat exchangers, the fluids involved do not come in direct contact with each other, being separated by a solid wall. In open heat exchangers, usually condensers or cooling towers, the fluids come in contact with each other to take advantage of the mass transfer effect. In the present work, heat is exchanged between two immiscible fluids in direct contact without mass transfer. This is a rather novel design that could be useful in certain practical applications.

The experiments reported here are a part of a rather extensive study planned for this general problem. In this extensive study the effects of geometry, liquid properties, flow characteristics, etc., would be determined. However, the results of the first experimental series seem to be interesting enough as to merit reporting at this time.

Measurements were taken on a "bank" of liquid jets cooled by air in crossflow. The liquid used was the light fuel oil used in high speed diesel engines. This oil was circulated for an extended period of time under the most severe conditions of the experiment before readings were taken. This circulation at high temperature evaporated the lighter constituents of the oil, and reduced the mass transfer to a minimum. The results obtained are correlated in terms of a Nusselt number as function of the two fluids Reynolds numbers.

Apparatus

The apparatus used is sketched in Fig. 1. Air is supplied by a variable speed centrifugal fan to a circular tunnel of the shown main dimensions. The air discharge is measured by a pitot tube A in a contracted cross section to improve the accuracy of the manometer readings. Inlet air temperature is measured by precision mercury-in-glass thermometer B.

The air enters the heat exchange section through flow transformer section C that changes the circular cross section to a rectangular cross section 47 cm (18½ in.) wide, and 40 cm (15¾ in.) high. The air leaves the heat exchange section through a second transformer, and leaves the duct through nozzle D.

The hot liquid is pumped to the top of the heat exchange section, and passes through a wire screen E to distribute it evenly on the orifice plate F. The liquid level above this plate is indicated by a glass tube indicator. The orifice plate is a 3 mm (⅛ in.) thick stiffened brass plate, it has 1410 orifices each 1 mm (0.04 in.) diameter arranged in 47 "lines" 10 mm (⅜ in.) apart with longitudinal pitches of 20 mm (0.8 in.) in the air flow direction. The liquid jets fall vertically on transverse horizontal V-shaped baffles G that define the air flow cross section.

The cooled liquid jets are collected in a conical "tray" and leave through syphon pipe H, where the exit liquid temperature is measured by a precision mercury-in-glass thermometer, to the collecting barrel I. The liquid is then pumped from the barrel by pump J through a 4 kW adjustable electric heater K that heats it to a temperature 20 to 25 C above the inlet air temperature. The liquid leaving the heater passes through a positive displacement flow meter L before entering the top of the heat exchanger to complete the circuit.

The heat exchange section is equipped with two large glass windows on opposite sides to observe the liquid jets. At the air exit of this section, vertical Z-shaped baffles M are placed to catch any liquid droplets that may be carried by the air, and drain them down to the collecting cone.

Measurements

The measurements are primarily those of flow rates, and inlet and exit temperatures of the two fluids.

The air flow is controlled by adjusting the fan speed and using orifice plates on its suction duct. The air velocity, practically uni-

[1] At present, Visiting Professor, School of Mechanical Engineering, Georgia Institute of Technology, Atlanta, Ga.

[2] At present Post Doctoral Fellow, Applied Superconductivity Group, Nuclear Engineering Department, University of Wisconsin, Madison, Wisc.

Contributed by the Heat Transfer Division for publication in the JOURNAL OF HEAT TRANSFER. Manuscript received by the Heat Transfer Division, August 24, 1974. Paper No. 74-HT-X.

form[3] in the contracted cross section, is measured by Pitot tube A in Fig. 1, and used in conjunction with a precision inclined manometer. The inlet air temperature was measured by mercury-in-glass thermometer B, it was in the range of 20 to 30 deg C during the experiments. The air temperature rise, which was in the order of 4 to 12 C, was measured by differential copper-constantan thermocouples for better accuracy. The cold junction was placed with thermometer B, and the hot junction in nozzle D.

The liquid flow was controlled by adjusting the pump speed, and by a gate valve on the pump delivery; it was measured by the positive displacement flow meter L in Fig. 1. The exit liquid temperature was measured by a mercury-in-glass thermometer in syphon tube H. The liquid temperature drop was in the order of 2 C and, therefore, very critical in the calculations of the liquid heat loss. For this reason, it was measured by a differential copper-constantan thermopile with five hot junctions just above the orifices plate F, and five cold junctions placed in the syphon tube H with the thermometer.

As mentioned before, the liquid used was light fuel oil, circulated in the apparatus at high temperatures to evaporate the lighter constituents. For this reason, its published properties were not used; they were measured [1][4] at 15 deg C (60 deg F) and found as follows:

Thermal conductivity	0.163 W/m C 0.094 Btu/h ft F
Density	860 kg/m^3 53.7 lb/ft^3
Specific heat	2.13 kJ/kg C 0.51 Btu/lb F
Dynamic viscosity	2.4×10^{-3} Pa.s or kg/m s 5.8 lb/h ft

The values of these properties at other temperatures were determined from relations recommended by the National Bureau of Standards [2]

Scope

As mentioned in the apparatus description, the experimental section is fitted with glass windows to observe the liquid jets. This was necessary to ensure that no nozzles were clogged, and that the jets and air velocities are not too high as to render the jets unstable or inclined to any considerable extent. Satisfaction of these conditions limited the velocities used to the ranges presented.

Calculations

The measurements taken on the apparatus were used to determine the heat flux exchanged. Analysis showed that heat losses from the hot liquid to the environment and conducted to the air through the orifice plate were within 0.3 percent of the measured heat fluxes [1]. Consequently, these heat fluxes were not corrected and were used directly to determine a mean heat transfer coefficient. The results thus obtained are presented in dimensionless form; viz. a Nusselt number as function of the two Reynolds numbers of the fluids. In this part, the methods used in calculations are outlined.

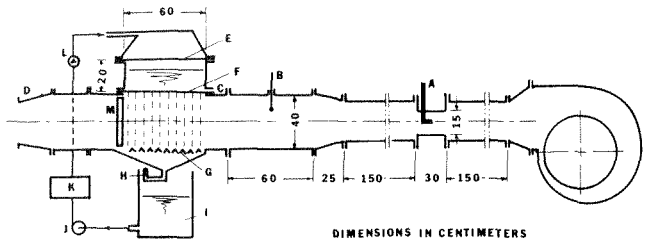

Fig. 1

The heat flux was calculated for each fluid from its rate of mass flow $\dot{m}$, specific heat c, and temperature drop or rise Δt. The heat exchanger was taken as a crossflow recuperator with one fluid (the air) mixed. From a measured value of the heat flux q, the corresponding inlet temperature of the liquid $t_{l,i}$, and that of the air $t_{a,i}$, the effectiveness of this heat exchanger was determined from

$$\eta_{Ex} = q/(\dot{m}c)_a(t_{l,i} - t_{a,i}) \tag{1}$$

The subscript a denotes the water equivalent rate for the air which was invariably lower than that of the liquid and, therefore, limits the highest possible heat flux.

With the heat exchanger effectiveness determined, a mean heat transfer coefficient h could be calculated from the following expression of η_{Ex} for crossflow heat exchangers with one fluid mixed

$$\eta_{Ex} = 1 - \exp\left\{-\frac{(\dot{m}c)_l}{(\dot{m}c)_a}\left[1 - \exp\frac{-hS}{(\dot{m}c)_l}\right]\right\} \tag{2}$$

In this relation, the subscript l denotes the liquid, and the surface S was taken nominally as $\pi N\delta L$. Here N is the number of jets (1410), L their length (40 cm), and δ the orifice diameter (1 mm). As a result, the average heat transfer coefficient h is also a nominal value.

For the correlation of the results in dimensionless form, a relation of the following form would be expected

$$N_{Nu} = N_{Nu}(N_{Re,l}, N_{Re,a}, N_{Pr,l}, N_{Pr,a}, l_l/l_a, k_l/k_a) \tag{3}$$

The inclusion of the last two ratios of length criteria and thermal conductivities as independent variables is due to the fact that only one length criterion, and one thermal conductivity can be used in the Nusselt number N_{Nu}. In the present experiments the two fluids did not change, neither did the geometry. For this reason, the foregoing relation reduces to the following form for the present study.

$$N_{Nu} = N_{Nu}(N_{Re,l}, N_{Re,a}) \tag{4}$$

[3] Previous tests on the same wind tunnel showed that the error involved in such a measurement is less than 1 percent for velocity and temperature.

[4] Numbers in brackets designate References at end of paper.

Nomenclature

c = specific heat, J/kg C
h = heat transfer coefficient, W/m^2 K
$K_1, K_2 \ldots$ = dimensionless constants
k = thermal conductivity, W/m K
L = jet length, m
l = length criterion, m
$\dot{m}$ = rate of mass flow, kg/s
N_{Bi} = Biot number, dimensionless
N_{Fo} = Fourier number, dimensionless
N_{Nu} = Nusselt number, dimensionless
N_{Pr} = Prandtl number, dimensionless
N_{Re} = Reynolds number, dimensionless
q = heat flux, W
S = heat transfer surface area, m^2
t = temperature, deg C
U = overall heat transfer coefficient, W/m^2 K
δ = orifice diameter, m
ϵ = fractional error in heat flux, dimensionless
η_{Ex} = effectiveness of heat exchange, dimensionless
θ = relative temperature drop, defined by equation (15), dimensionless

Subscripts

a = air
i = in
l = liquid
m = mean
o = out
U = overall value

This was further used in the more usual exponential form

$$N_{Nu} = K_1 N_{Re,l}{}^{m} N_{Re,a}{}^{n} \tag{5}$$

In the foregoing relation, the orifice diameter δ and the mean liquid velocity in it were used to determine the liquid Reynolds number. For the determination of the air Reynolds number, it seemed reasonable to use the nozzle diameter as the length criterion because of the large pitch-to-diameter ratio used for the jets. The air velocity used is the mean on the facial area of the experimental cross section. For the evaluation of Nusselt number, the length criterion is taken as the nozzle diameter, and the air thermal conductivity is used. The use of this property is due to the fact that at the air-liquid interface the air temperature rise was much larger than the liquid temperature drop [1].

Results

In the experiments, the heat flux q is measured for both the liquid side as q_l, and the air side as q_a. The accuracy of their determination is estimated to be within ±5 and 6 percent, respectively, [1]. Naturally, the two flux values obtained seldom coincided. For this reason a percentage difference was used as criterion, it is defined by

$$\epsilon = (q_l - q_a)/q_l \tag{6}$$

In 82.5 percent of the runs, ϵ is within ±10 percent. In 10 percent of the runs, this difference is larger than ±15 percent. These large differences, up to +40 percent in a few runs, are encountered with high Reynolds numbers for both the liquid and air, invariably with the heat flux measured for the air side the lower value. The large difference could, therefore, be explained as due to partial atomization of the liquid at the jets lower ends. With some droplets carried by the air, their partial evaporation would cool it resulting in the large discrepancies measured. An approximate analysis showed that this is a very probable cause [1]. For this reason, the heat loss from the oil is used in the calculations where the percentage difference ϵ is more than 15 percent. In the remaining, and by far the large majority of runs, a mean of the two fluxes is used [1].

The results obtained in the manner outlined in the foregoing and in the previous sections are presented as experimental points on logarithmic scales in Figs. 2 to 4. Fig. 2 gives the variation of Nusselt number with air Reynolds number, with liquid Reynolds number as parameter. Lines that correlate these experimental points were observed by using the method of least squares. It was found that a single relation could not be used for all the range of air Reynolds numbers. Consequently, two relations are used for each liquid Reynolds number that merge in the air Reynolds number range of 65 to 80.

Fig. 3 is the counterpart of Fig. 2. It represents a different series of experiments and gives Nusselt number as a function of the liquid Reynolds number with air Reynolds number as parameter.

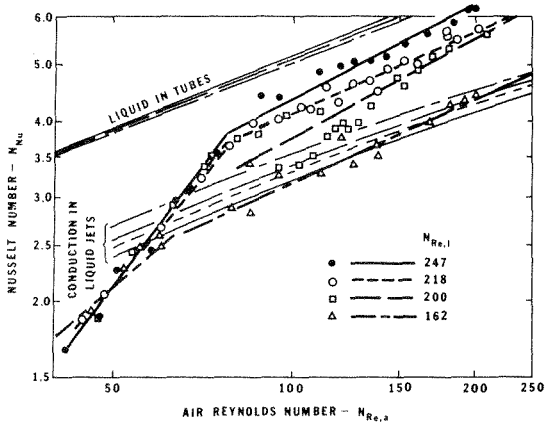

Fig. 2

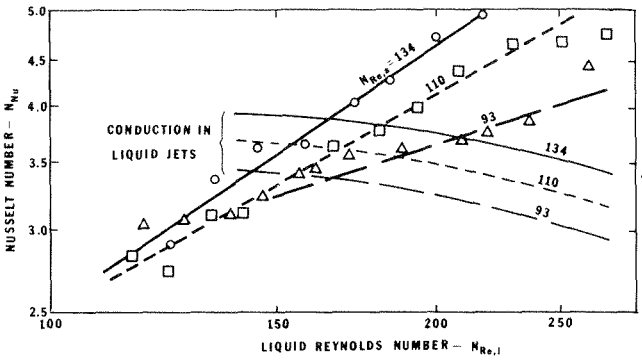

Fig. 3

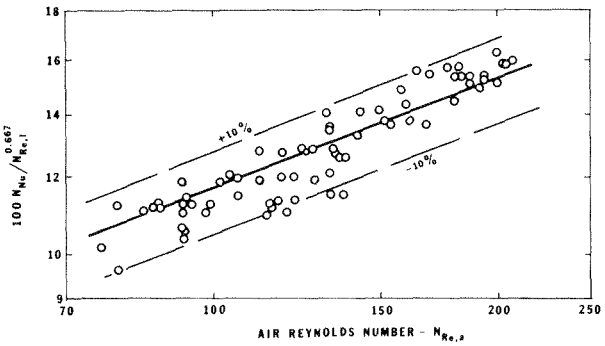

Fig. 4

Air Reynolds numbers in the higher range were used in this set of experiments.

All the results are correlated in the form of equation (5) using an extension of the method of least squares to three variables [1]. For air Reynolds number less than 80, equation (5) takes the following form

$$N_{Nu} = 0.0047\, N_{Re,l}{}^{0.2} N_{Re,a}{}^{1.29} \tag{7}$$

Of the data covered, more than 80 percent of the results fall within ±8 percent of this correlation.

For air Reynolds numbers more than 80, the following relation is applicable

$$N_{Nu} = 0.021\, N_{Re,l}{}^{0.667} N_{Re,a}{}^{0.367} \tag{8}$$

This relation is plotted in Fig. 4 with the corresponding experimental points.

Discussion

The present problem seems to be a novel one that has not been considered previously. Consequently, earlier results that could be compared with the present ones were not found. However, the heat transfer coefficient as determined in the present experiments could be compared with the overall heat transfer coefficient between a liquid in a tube bundle and a gas flowing across the bundle. As usual, this overall heat transfer coefficient U could be determined in terms of the liquid and air heat transfer coefficients h_l and h_a from

$$\frac{1}{U} = \frac{1}{h_l} + \frac{1}{h_a} \tag{9}$$

The liquid side heat transfer coefficient h_l could be determined from the following relation for laminar flow in pipes [3]

$$N_{Nu,l} = 2.38\,(N_{Re}\, N_{Pr}\, \frac{\delta}{L})^{1/3} \tag{10}$$

The air side heat transfer coefficient h_a for flow across a tube could be obtained from Hilpert's relation [3] for the air Reynolds number range of 40 to 4000, and based on the orifice diameter

$$N_{Nu,a} = 0.7 N_{Re,a}^{0.466} \quad (11)^5$$

In these relations, Nusselt number is corrected for the ratio of jet to orifice diameter (0.78). For the tube bundles, it is recommended [3] that the constant in equation (11) be increased by 50 percent. It was not increased, however, in order to use the least possible value for the heat transfer coefficient h_a. Both equations (10) and (11) use the pipe diameter as the length criterion so that they could be compared with the experimental results and, at the same time, give a least overall Nusselt number $N_{Nu,U}$[6] which could be obtained by combining these equations into equation (9) as

$$N_{Nu,U} = K_2 N_{Re,a}^{0.466} N_{Re,l}^{1/3} / (N_{Re,a}^{0.466} + K_3 N_{Re,l}^{1/3}) \quad (12)$$

The dimensionless constants K_2 and K_3 in this relation depend on the fluid properties, and in the present case have the values 5.51 and 7.85, respectively, using mean property values.

The form of equation (12) is different from that of equation (8) and, therefore, could not be plotted in Fig. 4. Instead, it is plotted as four separate curves that fall at the top of Fig. 2.[7] In spite of the fact that these curves are the lowest for flow across tube bundles, they are significantly higher than those realized in the experiments. However, the two curve groups tend to merge when extrapolated to high Reynolds numbers where the liquid jets loose their stability and the interfacial area between the two fluids increases. It is significant that the air Reynolds number at which merging occurs decreases with increasing liquid Reynolds number.

The degradation of the heat flux in direct contact, or fluid-to-fluid convection may seem strange. However, it might be explained through the accompanying decrease in the interfacial shear stress, being less than 5 percent of that on the liquid side, had a solid surface been present.

Calculations to check this effect were carried out as follows. If there is no shear stress, the liquid velocity would be uniform throughout the jet. The liquid would then "flow" as a moving solid cylinder through which heat would be transmitted by conduction only. In this case, the liquid temperature drop could be estimated from the mathematically equivalent transient case of a solid cylinder exposed to convection. "Temperature response" charts are available for this latter case. The "conductive Nusselt number" $N_{Nu,c}$ could be determined from the jet's Fourier and Biot numbers as outlined in the Appendix. Heisler charts of temperature distribution and thermal response [3] were used and the results plotted in Figs. 2 and 3 fall below the experimental curves as shown. It should be noted that this "conductive" group falls below the experimental group in spite of the fact that in the calculations of the former group, equation (11) was used based on the orifice diameter, and with the coefficient increased by 50 percent for tube bundles to give the highest conductive Nusselt number.

As could be seen, the effect of the liquid Reynolds number is reversed in the conductive group. An increase in the liquid Reynolds number is accompanied by a decrease in the "dwell period" of a liquid jet in the air stream; this decreases the liquid temperature drop and, therefore, the conductive Nusselt number. All the conductive curve group falls below the experimental group, except for the lower range of the liquid Reynolds number. This discrepancy in the lower range curve is, most probably, due to the use of too high values for the air side heat transfer coefficient in the determination of this conductive curve group. Apart from the 50 percent increase of the air side coefficient which might be too high, it is conceivable that the actual heat transfer coefficient on the air side would be considerably decreased due to the absence of a solid interface.

The intersection of the conductive and experimental curves at low air Reynolds numbers ($N_{Re,a} < 70$) is, most probably, due to the possibility that the lower limit for the applicability of equation (11), $N_{Re,a} = 40$, is too low. It seems that this lower limit should rather be in the order of $N_{Re,a} = 70$ to 80. This would obviate the intersection, and explains the discontinuity in the inclination of the experimental lines. This discontinuity may indicate a sharp change in the air flow mode at air Reynolds numbers in this range. It further indicates the dominance of the effect of air flow on the overall heat exchange, as could also be affirmed by a comparison of the indices in equations (7) and (8).

On the other hand, the effect of liquid Reynolds number as determined by experiments follows closely the pattern for the case of convection across a solid separating interface. This shows that convection, rather than pure conduction, is still the dominant factor on the liquid side in the experimental range reported.

Conclusions

An experimental study of direct contact convection between liquid jets and air in crossflow without mass transfer is reported. The heat fluxes measured are higher than those due to pure conduction into the jets, but lower than those between air and liquid in tube bundles of the same diameter as the orifices. This higher limit is approached, and probably surpassed as the liquid jets lose their stability at high liquid and air Reynolds numbers.

Acknowledgment

Dr. S. P. Kezios of Georgia Institute of Technology suggested the calculations of the "conductive" Nusselt number as a check on the velocity distribution in the liquid jets.

References

1 Mohamed A. Hilal, "Heat Transfer From Liquid Jets in a Moving Gas Stream," unpublished MSc thesis, Faculty of Engineering, Cairo University, 1969.

2 Gutherie, I. V. B., *Petroleum Products Handbook*, McGraw-Hill, New York, 1960, pp. 8-48.

3 Jakob, M., *Heat Transfer*, Wiley, New York, Vol. 1, 1958, pp. 544, 560, 284-288, 418.

4 Fand, R. M., and Keswani, K. K., "Recalculation of Hilpert's Constants," JOURNAL OF HEAT TRANSFER, TRANS. ASME, Series C, Vol. 95, 1973, pp. 224-226.

Determination of Conductive Nusselt Number

The conductive Nusselt number, as mentioned in the text, could be determined from the liquid jets Fourier and Biot numbers. It could be shown that these dimensionless numbers are given by

$$N_{Fo} = K_4 / N_{Re,l} \quad (13)$$

$$N_{Bi} = K_5 N_{Re,a}^{0.466} \quad (14)$$

The dimensionless constants K_4 and K_5 in the foregoing relations depend on the fluids properties and the jets dimensions. The values used here are $K_4 = 50.6$ and $K_5 = 0.058$.

With these dimensionless groups known, the relative temperature drop at the jet center could be obtained from appropriate charts. The mean relative temperature drop θ at the liquid jets lowest ends could then be determined from the temperature distribution curves. As mentioned in the text, Heisler's chart and curves are used [3]. This mean relative temperature drop θ is defined as

$$\theta = (t_{l,i} - t_{l,o}) / (t_{l,i} - t_{a,m}) \quad (15)$$

With θ determined, the conductive Nusselt number could be determined from

$$N_{Nu,c} = K_6 N_{Re,l} \theta \quad (16)$$

This dimensionless constant K_6 is, again, a function of the liquid properties and orifice diameter; it is taken as 0.12.

[5] A recent paper [4] shows that the use of modern property values with Hilpert's experimental data would reduce the constant in this equation by about 4 percent.

[6] It should be noted that the experimental Nusselt number is practically independent of the diameter used.

[7] The two upper curves for $N_{Re,l} = 247$ and 218, are very near to each other as to practically coincide.

S. H. Cho

Department of Mechanical Engineering,
Korea Military Academy,
Seoul, Korea

J. E. Sunderland

Department of Mechanical and
Aerospace Engineering,
University of Massachusetts,
Amherst, Mass.

Phase Change Problems With Temperature-Dependent Thermal Conductivity

An exact solution is presented for the temperature distribution and phase change position of a semi-infinite body which is initially at a constant temperature different from the fusion temperature. The temperature of the free surface is instantaneously changed and held constant at a value that will cause either melting or solidification of the body. The thermal conductivity is assumed to vary linearly with temperature. The convection in the liquid phase due to density change is also considered.

Introduction

Heat conduction problems involving melting or solidification have been studied by a large number of investigators. The reviews of Bankoff [1][1] and Muehlbauer and Sunderland [2] cover most of the papers that have been written on this subject. These problems are difficult to solve due to variable properties and moving boundaries.

To simplify the analysis, most investigators assume that the properties of any given phase are independent of temperature. It is this simplification that the current study avoids. In this analysis, the thermal conductivity varies linearly with temperature. New functions are defined; and an exact solution of the phase change problem is obtained in terms of these functions. The effect of the conductivity variation on phase change speed is also discussed.

Statement of the Problem and Assumptions

The one-dimensional temperature distribution in a homongenous and isotropic, semi-infinite body undergoing a phase change satisfies the following differential equations in the solid and liquid regions, respectively [3];

$$(\rho C_p)_1 \frac{\partial T_1}{\partial t} = \frac{\partial}{\partial x}(k_1 \frac{\partial T_1}{\partial x}), \quad 0 < x < S(t) \tag{1}$$

$$(\rho C_p)_2 \frac{\partial T_2}{\partial t} + (\rho_2 - \rho_1) C_{p_2} \frac{dS}{dt} \frac{\partial T_2}{\partial x} = \frac{\partial}{\partial x}(k_2 \frac{\partial T_2}{\partial x}), \quad x > S(t) \tag{2}$$

Solutions to these equations will be obtained subject to the following assumptions:

(a) All the physical properties (including density) except the thermal conductivity are constant for each phase, but might be different for different phases.

(b) The thermal conductivity, hence also the thermal diffusivity of each phase changes linearly with temperature.

(c) Phase change occurs at a fixed temperature, the fusion temperature.

(d) The initial temperature is uniform and at time $t = 0$, the surface temperature is suddenly changed and held constant.

(e) Convection within the liquid phase due to density change is considered, however boyancy effects are neglected.

The analysis in this paper applies both to melting and solidification of semi-infinite bodies. For clarity, however, solidification is considered. A typical temperature distribution during solidification is shown in Fig. 1. From assumptions *c* and *d*, thermal diffusivities of the solid and liquid phases can be given as

$$a_1 = a_{01}(1 + \beta_1 \frac{T_1 - T_0}{T_i - T_0}) \tag{3}$$

and

$$a_2 = a_{02}(1 + \beta_2 \frac{T_2 - T_0}{T_i - T_0}) \tag{4}$$

where a_{01} and a_{02} are the values of the thermal diffusivity of the solid and the liquid phases at T_0, respectively.[2]

The initial conditions at $t = 0$ are

$$T_2 = T_i \geq T_f, \quad x > 0 \tag{5}$$

and

$$S(0) = 0 \tag{6}$$

The boundary condition at the free surface, $x = 0$ is

$$T_1(0,t) = T_0 < T_f, \quad t > 0 \tag{7}$$

At the moving fusion front, $x = S(t)$, two additional conditions must be satisfied.

[1] Numbers in brackets designate References at end of paper.

Contributed by the Heat Transfer Division for publication in the JOURNAL OF HEAT TRANSFER. Manuscript received by the Heat Transfer Division, February 6, 1973. Paper No. 74-HT-Z.

[2] The liquid phase does not exist at T_0, and a_{02} is obtained by extrapolation.

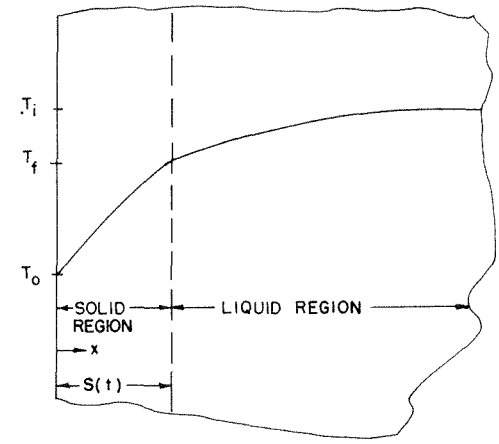

Fig. 1 Typical temperature distribution during solidification

$$T_1 = T_2 = T_f \quad \text{at} \quad x = S(t) \tag{8}$$

and

$$k_1 \frac{\partial T_1}{\partial x} - k_2 \frac{\partial T_2}{\partial x} = \rho_1 H \frac{dS}{dt} \text{ at } x = S(t) \tag{9}$$

The problem consists of two parts, finding the temperature distributions and the phase change thickness. Let

$$\theta_1 = \frac{T_1 - T_0}{T_i - T_0} \tag{10}$$

$$\theta_2 = \frac{T_2 - T_0}{T_i - T_0} \tag{11}$$

$$\theta_f = \frac{T_f - T_0}{T_i - T_0} \tag{12}$$

$$\eta = \frac{x}{2\sqrt{a_{01}t}} \tag{13}$$

$$a_{12} = a_{02}/a_{01} \tag{14}$$

$$k_{12} = k_2/k_1 \text{ at } T = T_f \tag{15}$$

and assume that

$$\theta_1(x,t) = \theta_1(\eta) \tag{16}$$

$$\theta_2(x,t) = \theta_2(\eta) \tag{17}$$

$$S(t) = 2\lambda\sqrt{a_{01}t} \tag{18}$$

where λ is a constant to be determined later. Then when the conductivity varies linearly equations (1 to 2) are transformed to

$$\frac{d}{d\eta}\{(1 + \beta_1\theta_1)\frac{d\theta_1}{d\eta}\} + 2\eta\frac{d\theta_1}{d\eta} = 0,\ 0 < \eta < \lambda \tag{19}$$

$$a_{12}\frac{d}{d\eta}\{(1 + \beta_2\theta_2)\frac{d\theta_2}{d\eta}\} + 2[\eta + (\frac{1}{\rho_{12}} - 1)\lambda]\frac{d\theta_2}{d\eta} = 0,\ \eta > \lambda \tag{20}$$

where $\rho_{12} = \rho_2/\rho_1$. Boundary conditions (5 to 9) become

$$\theta_1 = 0 \text{ at } \eta = 0 \tag{21}$$

$$\theta_2 = 1 \text{ as } \eta \to \infty \tag{22}$$

$$\theta_1 = \theta_2 = \theta_f \text{ at } \eta = \lambda \tag{23}$$

$$\frac{d\theta_1}{d\eta} - k_{12}\frac{d\theta_2}{d\eta} = 2h\lambda \text{ at } \eta = \lambda \tag{24}$$

where

$$h = \frac{\rho_1 H a_{01}}{k_{1f}(T_i - T_0)} \tag{25}$$

and k_{1f} is the value of the thermal conductivity of the solid phase at T_f.

Now the original phase change problem is equivalent to solving the dimensionless equations (19 to 25).

Definition of the Modified Error Function

Consider a second-order nonlinear ordinary differential equation

$$\frac{d}{d\eta}\{(1 + \beta\theta)\frac{d\theta}{d\eta}\} + 2\eta\frac{d\theta}{d\eta} = 0 \tag{26}$$

with the boundary conditions

$$\theta = 0 \quad \text{at} \quad \eta = 0 \tag{27}$$

and

$$\theta = 1 \quad \text{as} \quad \eta \to \infty \tag{28}$$

The solution of equations (26 to 28) can be obtained by a numerical method, e.g., the Runge-Kutta method. If the solution is designated as $\phi_\beta(\eta)$, which can be called the "modified error function," then by definition

$$\frac{d}{d\eta}\{(1 + \beta\phi_\beta)\frac{d\phi_\beta}{d\eta}\} + 2\eta\frac{d\phi_\beta}{d\eta} = 0 \tag{29}$$

$$\phi_\beta(0) = 0 \tag{30}$$

$$\phi_\beta(\infty) = 1 \tag{31}$$

Note that when $\beta = 0$ equation (26) becomes linear, and

$$\phi_0(\eta) = \text{erf}(\eta) = \frac{2}{\sqrt{\pi}}\int_0^\eta e^{-z^2}dZ \tag{32}$$

The following properties of $\phi_\beta(\eta)$ are useful for the analysis of the phase change problem.

Theorem 1. The following function

$$\theta = \theta_0 + (\theta_\infty - \theta_0)\phi_\delta(\eta/\sqrt{1 + \beta\theta_0}) \tag{33}$$

where

$$\delta = \frac{\beta(\theta_\infty - \theta_0)}{1 + \beta\theta_0} \geq -1 \tag{34}$$

Nomenclature

a = thermal diffusivity (m^2/hr)
a_{01} = thermal diffusivity of solid phase at T_0 (m^2/hr)
a_{02} = thermal diffusivity of liquid phase at T_0 (m^2/hr)
C_p = specific heat at constant pressure (J/kg deg K)
H = heat of solidification (J/kg)
h = dimensionless heat of solidification defined by equation (25) (dimensionless)
k = thermal conductivity (W/m deg K)
$S(t)$ = phase change thickness at time t (m)
T = temperature (deg C)
T_f = fusion temperature (deg C)
T_i = initial temperature (deg C)
T_0 = surface temperature (deg C)
t = time (hr)
x = space coordinate (m)
α = constant defined by equation (42) (dimensionless)
β = constant (dimensionless)
δ = constant defined by equation (40) (dimensionless)
ϵ = constant defined by equation (41) (dimensionless)
ζ = variable defined by equation (44) (dimensionless)
η = variable defined by equation (13) (dimensionless)
θ = temperature (dimensionless)
λ = constant defined by equation (18) (dimensionless)
ρ = density (kg/m^3)
$\phi_\beta(\eta)$ = modified error function defined by equations (26-28) (dimensionless)

Subscripts

f = property at fusion point
1 = property of the solid phase
2 = property of the liquid phase
12 = ratio of properties of the liquid phase to the solid phase

and

$$1 + \beta\theta_0 > 0 \tag{35}$$

is the solution of the differential equation (26) which satisfies the boundary conditions

$$\theta = \theta_0 \quad \text{at} \quad \eta = 0 \tag{36}$$

and

$$\theta = \theta_\infty \quad \text{as} \quad \eta \to \infty \tag{37}$$

This theorem can be easily proved by direct substitution. A more general theorem is given in the Appendix.

Solution of the Phase Change Problem

When the thermal conductivity varies linearly with temperature, using the property of the modified error function $\phi_\beta(\eta)$, the solutions of equations (19 to 24) are found to be

$$\theta_1 = \theta_f \frac{\phi_\delta(\eta)}{\phi_\delta(\lambda)}, \quad 0 < \eta < \lambda \tag{38}$$

and

$$\theta_2 = 1 - (1 - \theta_f)\left\{\frac{1 - \phi_\epsilon\left[\dfrac{\eta + (\dfrac{1}{\rho_{12}} - 1)\lambda}{\sqrt{a_{12}(1 + \beta_2\alpha)}}\right]}{1 - \phi_\epsilon(\zeta)}\right\}, \quad \lambda < \eta \tag{39}$$

where constants λ, δ, ϵ, and α are determined from

$$\delta\phi_\delta(\lambda) = \beta_1\theta_f \tag{40}$$

$$\epsilon = \frac{\beta_2(1 - \alpha)}{1 + \beta_2\alpha} \tag{41}$$

$$\phi_\epsilon(\zeta) = \frac{\theta_f - \alpha}{1 - \alpha} \tag{42}$$

and

$$\frac{\phi_\delta'(\lambda)}{\lambda\phi_\delta(\lambda)} - \frac{1 - \theta_f}{\theta_f}\frac{(C_p)_{12}}{1 + \beta_2\alpha}\frac{\phi_\epsilon'(\zeta)}{\zeta[1 - \phi_\epsilon(\zeta)]} = 2h/\theta_f \tag{43}$$

where

$$(C_p)_{12} = C_{p_2}/C_{p_1}$$

and

$$\zeta = \lambda/\rho_{12}\sqrt{(1 + \beta_2\alpha)a_{12}} \tag{44}$$

Equations (40) and (41) are obtained from the theorem, equation (42) from boundary condition (23), and equation (43) from boundary condition (24). The boundary conditions (21) and (22) are satisfied by the values of the modified error function at $\eta = 0$ and $\eta = \infty$.

Converting to the original physical variables, the temperature distributions in the solid and liquid regions are obtained from

$$T_1 = T_0 + (T_f - T_0)\frac{\phi_\delta(x/2\sqrt{a_{01}t})}{\phi_\delta(\lambda)} \tag{45}$$

and

$$T_2 = T_i - (T_i - T_f)\left\{\frac{1 - \phi_\epsilon\left[\dfrac{x}{2\sqrt{a_{02}t}(1 + \beta_2\alpha)} + \dfrac{(\dfrac{1}{\rho_{12}} - 1)\lambda}{\sqrt{a_{12}(1 + \beta\alpha)}}\right]}{1 - \phi_\epsilon(\zeta)}\right\} \tag{46}$$

The similarity between this solution and Neumann's solution [3] is obvious.

Discussion

Some values of the modified function $\phi_\beta(\eta)$ obtained by a Runge-Kutta method are given in Fig. 2. The numerical computations of $\phi_\beta(\eta)$ have been checked for $\beta = 0$ by comparing them with the error function equation (32).

Crank [4] considered diffusion problems when the diffusivity is a function of concentration, and presented graphs of $\phi_\beta(\eta)$ without relating to phase change problems. Wagner [5] considered the special case when diffusivity is directly proportional to the concentration. This case corresponds to the function $\phi_{-1}(\eta)$.

In order to compute the values of δ, ϵ, λ, α, and ζ, equations (40 to 44) must be solved by a trial and error procedure. A value of α, where $\alpha < \theta_f$, is assumed, then ϵ is obtained from equation (41), ζ from equation (42), λ from equation (44), and δ from equation (40). The values obtained for α, δ, ϵ, λ, and ζ are substituted into equation (43). If equation (43) is not satisfied, a new value of α is obtained and the foregoing procedure is repeated until equation (43) is satisfied. For this computation values of $\beta\phi_\beta(x)$, $\phi_\beta'(x)/[x\{\phi_\beta(x)\}]$, and $\phi_\beta'(x)/[x\{1 - \phi_\beta(x)\}]$ are given in Figs. 3 to 5.

When the initial temperature of the body is equal to the fusion temperature, $\theta_f = 1$, equation (43) reduces to

$$\frac{\phi_\delta'(\lambda)}{\lambda\phi_\delta(\lambda)} = 2h \tag{47}$$

and equation (39) becomes

$$\theta_2 = 1 \quad \text{for} \quad \eta > \lambda$$

If the conductivities are constant, $\beta_1 = \beta_2 = 0$, then from equations (40 to 41), $\delta = \epsilon = 0$, and the solution reduces to the classical Neumann solution [3].

When the initial temperature equals the fusion temperature and the linear variation of thermal conductivity is neglected, the mean values should be used. In this case the phase change thickness is obtained from

$$S_m = 2\lambda_a\sqrt{a_{01}t} \tag{48}$$

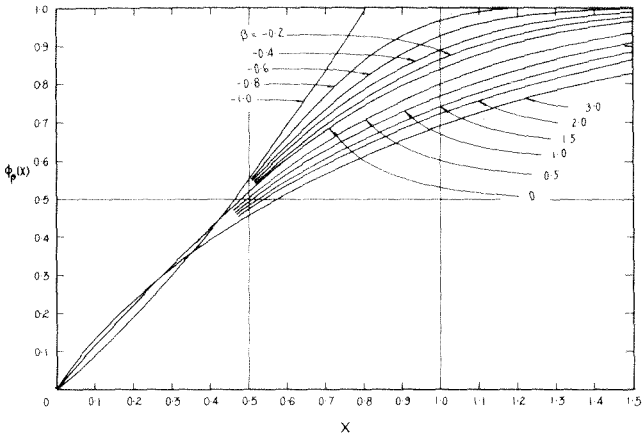

Fig. 2 Graph of $\phi_\beta(x)$

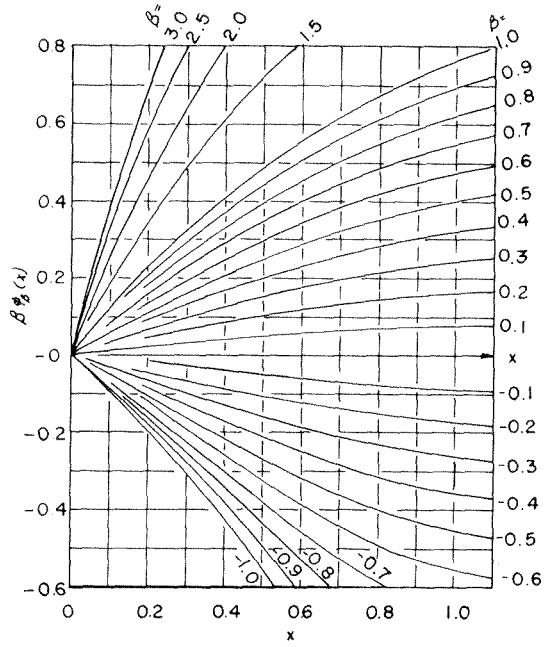

Fig. 3 Graph of $\phi_\beta(x)$

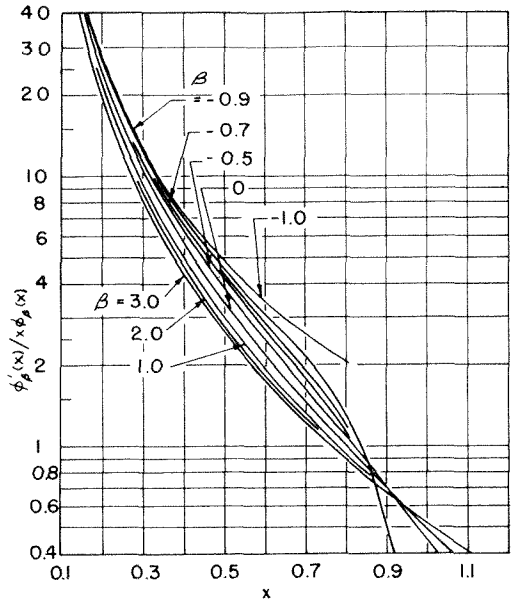

Fig. 4 Graph of $\phi_\beta'(x)/[x\{\phi_\beta(x)\}]$

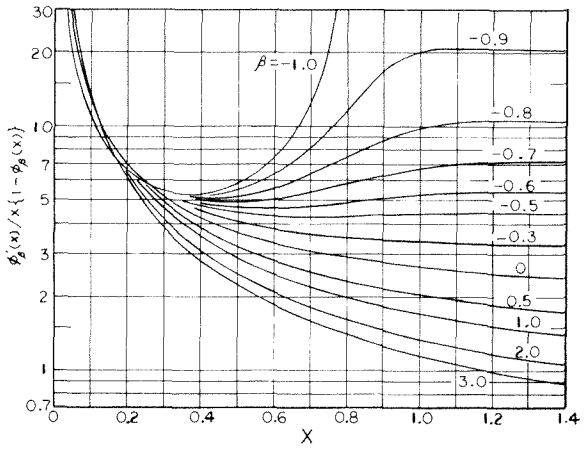

Fig. 5 Graph of $\phi_\beta'(x)/[x\{1-\phi_\beta(x)\}]$

where λ_a is obtained from the following equations:

$$\frac{\frac{2}{\sqrt{\pi}}e^{-\lambda_m^2}}{\lambda_m \operatorname{erf}(\lambda_m)} = 2h_m = 2h(1+\beta) \tag{49}$$

$$\lambda_a = 2\lambda_m\sqrt{1+\beta/2} \tag{50}$$

Comparing equations (18) and (48),

$$\frac{S_m}{S} = \frac{\lambda_a}{\lambda}$$

Some values of λ and λ_a are given in Table 1. For the range of λ and β of Table 1 it is seen that the effect of linear variation of the thermal conductivity on phase change speed is not significant when the mean value is used. However, the difference becomes larger for large $|\beta|$ and small h.

References

1 Bankoff, S. G., "Heat Conduction or Diffusion With Change of Phase," *Advances in Chemical Engineering*, T. B. Drew and J. W. Hoopes, Jr. eds., Academic Press, New York, Vol. 5, 1964, pp. 75–150.

2 Muehlbauer, J. C., and Sunderland, J. E., "Heat Conduction With Freezing or Melting," *Applied Mechanics Reviews*, Vol. 18, 1965, pp. 951–959.

3 Carslaw, H. S., and Jaeger, J. C., *Conduction of Heat in Solids*, Oxford University Press, London, Chapter 11, 1959.

4 Crank, J., *Mathematics of Diffusion*, Oxford University Press, London, Chapters 9 and 12, 1956.

Table 1 Effect of linear variation of conductivity on phase change speed

λ ↓	$\delta\rightarrow$	0.3	0.2	0.1	−0.1	−0.2	−0.3
	β	0.068	0.045	0.022	−0.022	−0.044	−0.065
	h	11.8	11.9	12.0	12.3	12.4	12.6
0.2	h_m	12.6	12.5	12.3	12.0	11.9	11.8
	λ_m	0.197	0.198	0.199	0.201	0.202	0.206
	λ_a	0.200	0.200	0.200	0.200	0.200	0.202
	β	0.128	0.085	0.043	−0.043	−0.086	−0.129
	h	2.67	2.71	2.76	2.86	2.92	2.98
0.4	h_m	3.01	2.94	2.88	2.74	2.66	2.59
	λ_m	0.388	0.392	0.396	0.406	0.409	0.415
	λ_a	0.400	0.400	0.400	0.401	0.400	0.401
	β	0.177	0.119	0.060	−0.061	−0.123	−0.186
	h	1.04	1.05	1.07	1.11	1.13	1.16
0.6	h_m	1.22	1.18	1.13	1.04	0.993	0.945
	λ_m	0.573	0.581	0.590	0.610	0.622	0.633
	λ_a	0.598	0.598	0.599	0.601	0.602	0.603
	β	0.216	0.145	0.073	−0.075	−0.152	−0.232
	h	0.488	0.492	0.496	0.506	0.513	0.520
0.8	h_m	0.594	0.564	0.533	0.468	0.435	0.399
	λ_m	0.753	0.767	0.785	0.819	0.843	0.863
	λ_a	0.793	0.794	0.799	0.803	0.810	0.811
	β	0.245	0.165	0.083	−0.085	−0.173	−0.263
	h	0.251	0.250	0.248	0.244	0.241	0.236
1.0	h_m	0.312	0.286	0.264	0.223	0.199	0.174
	λ_m	0.933	0.955	0.976	1.039	1.061	1.100
	λ_a	0.988	0.994	0.996	1.016	1.014	1.025
	β	0.265	0.179	0.090	−0.092	−0.186	−0.282
	h	0.134	0.130	0.127	0.117	0.111	0.103
1.2	h_m	0.169	0.154	0.138	0.106	0.090	0.074
	λ_m	1.108	1.136	1.165	1.239	1.286	1.342
	λ_a	1.180	1.185	1.191	1.210	1.225	1.244

5 Wagner, C., "Diffusion of Lead Chloride Dissolved in Solid Silver Chloride," *The J. of Chem. Phys.*, Vol. 18, 1950, pp. 1227–1230.

Appendix

A Generalization of Theorem No. 1

The following theorem is a generalization of theorem No. 1:

Theorem. Let the solution of the following boundary value problem

$$\frac{d}{d\eta}\{D(f)\frac{df}{d\eta}\} + 2\eta\frac{df}{d\eta} = 0 \tag{51}$$

$$f(0) = 0 \tag{52}$$

$$f(\infty) = 1 \tag{53}$$

where

$$D(f) = (1 + \beta f + \gamma f^2)^n \tag{54}$$

be designated as

$$f(\eta) = \phi_{\beta\gamma}{}^n(\eta) \tag{55}$$

then

$$\tilde{f}(\eta) = f_0 + (f_\infty - f_0)\phi_{\delta\epsilon}{}^n(c\eta) \tag{56}$$

where

$$\delta = \frac{(\beta + 2\gamma f_0)(f_\infty - f_0)}{1 + \beta f_0 + \gamma f_0{}^2} \tag{57}$$

$$\epsilon = \frac{\gamma(f_\infty - f_0)^2}{1 + \beta f_0 + \gamma f_0{}^2} \tag{58}$$

and

$$c = (1 + \beta f_0 + \gamma f_0{}^2)^{-n/2} \tag{59}$$

is the solution of equation (51) which satisfies the boundary conditions

$$\tilde{f}(0) = f_0 \tag{60}$$

and

$$\tilde{f}(\infty) = f_\infty \tag{61}$$

When $\gamma = 0$ and $n = 1$, this reduces to theorem 1. When $\gamma = 0$, it always results that $\epsilon = 0$; when $\beta = 0$ and $\gamma \neq 0$, however, δ may not be equal to zero. Fujita [4] obtained the solutions of diffusion problems which are special cases of equation (51).

D. M. Burch
B. A. Peavy
R. W. Allen

Department of Mechanical Engineering,
University of Maryland, College Park, Md.

Time-Dependent Transpiration Heat Transfer in Porous Cylinders

This paper investigates the transient temperature distribution within transpiration-heated and -cooled porous tubes that occur after a step increase in the rate of convective heat transfer at one of the tube surfaces. Analytic solutions are presented for transpiration cooling, catalytic chemical reactor, and tubular regenerator applications. These solutions include the effect of forced convective heat transfer at both tube surfaces where conventional heat-transfer coefficients are used to define the boundary conditions.

1 Introduction

Transient temperature distributions develop in hot startup of transpiration-cooled porous tubes of magneto-plasma-dynamic generators and rocket nozzles. They also develop in the hot startup of gas heated porous regenerator matrices and porous tubular chemical reactors. In the case of transpiration cooling, the porous tube is transmitting protective cooling gas unidirectionally at the time the coolant-discharge (blowing) surface is suddenly exposed to severe convective heating by a high-temperature gas stream. Regenerator hot startup, or single blow, occurs when the initially isothermal tubular regenerator matrix is suddenly exposed to a flow of a high-temperature gas through its interstices for the purpose of storing thermal energy. In the hot startup of the porous tube catalytic chemical reactor, a high-temperature catalyst gas is suddenly introduced on one side of the initially isothermal porous tube and is forced through the porous tube and into the reaction zone, in order to increase the rate of reaction of the species of a gas mixture flowing in the reaction zone.

After hot startup of a given matrix material, a transient temperature distribution develops in the matrix material. Interest focuses on the effect of matrix storage, the enthalpy transport action of the transpiring gas, and matrix heat conduction in the gas-flow direction. In many porous heat transfer matrices, heat is readily conducted perpendicular to the gas flow direction, and the internal wetted surface area and the interstitial convective heat transfer coefficient between the gas and matrix are large. There conditions cause the difference in temperature between the matrix and gas to be very nearly indistinguishable throughout the matrix. A direct consequence of this condition is that the gas and matrix temperature may be treated as being equal, affording a significant simplification in the mathematical analysis. Another consequence of this condition is that the conventional heat-transfer coefficient definition may be used to define convective boundary conditions at the bounding surfaces of the porous matrix.

Schneider and Brogan [1][1] developed an analytical solution for the transient temperature distribution in a transpiration-cooled porous flat plate. At the gas-entry surface, a nonconvective boundary condition was specified in which the rise in enthalpy of the gas from its upstream reservoir value was set equal to the rate of heat conduction from this face. That is, the gas flow was taken to be normal to the gas-entry face with no net lateral fluid motion at this face. Burch [2] extended the solution of Schneider and Brogan to include the effect of forced convective heat transfer at the gas-entry face.

Schneider [3] presented analytical solutions for the steady-state temperature distribution in a transpiration-cooled porous flat plate and tube for the case of high-temperature gas flowing inside the tube. Convective boundaries were specified at both boundary surfaces. At the gas-entry surface a convective heat-transfer coefficient was defined as the additive surface conductance resulting from the net lateral fluid motion. Koh, et al. [4] presented a steady-state analytical solution for the transpiration-cooled slab which takes into account a finite temperature difference between gas and matrix. Later Koh, et al. [5], presented similar solutions for transpiration-cooled cylinders and spheres.

Jiji [6] derived analytical solutions for the transient temperature distribution in a transpiration-cooled tube for the case of the outside tube surface suddenly exposed to high-temperature convective heat transfer and the case of the outside tube surface suddenly exposed to a high-intensity heat flux. At the gas-entry surface, the rate of convective heat transfer was set equal to the rise of enthalpy of the gas from its upstream reservoir value.

Schumann [7] presented analytical solutions for the transient temperature distribution of a gas and solid during the starting operation of a porous flat plate regenerator. Matrix conduction in the flow direction was neglected. Creswick [8] extended the Schumann analysis by the finite difference technique to include the effect of longitudinal conduction. Later, Howard [9] expanded the work of Creswick by compiling comprehensive numerical results into a chart from which the intersticial heat-transfer coefficient could be determined from a transient test. Moreland [10] obtained an alternate numerical solution to this problem utilizing numerical inversions of Laplace transforms.

This paper investigates the transient temperature distribution in transpiration-heated and -cooled porous tubes which are suddenly exposed to high-temperature convective heat-transfer at

[1] Numbers in brackets designate References at end of paper.

Contributed by the Heat Transfer Division for publication in the JOURNAL OF HEAT TRANSFER. Manuscript received by the Heat Transfer Division, July 31, 1973. Paper No. 74-HT-Q.

one of the tube surfaces. Analytical solutions are presented for the following transpiration heat-transfer applications:

1 Transpiration-cooling:
   (*a*) High-temperature gas flowing inside the tube, coolant transpiring radially inward.
   (*b*) High-temperature gas flowing at the outside tube surface, coolant transpiring radially outward.
2 Catalytic chemical reactors:
   (*a*) Reacting gas mixture flowing inside the tube, high-temperature catalyst gas injected radially inward.
   (*b*) Reacting gas mixture flowing at the outside tube surface, high-temperature catalyst gas injected radially outward.

These solutions include the effect of forced convective heat transfer at both tube surfaces where conventional convective heat-transfer coefficients are used to define the boundary conditions. Furthermore, the catalytic reactor solutions may be extended to tubular regenerators merely by allowing the convective heat-transfer coefficient at the gas-exit surface to vanish.

2 Analysis

An enlarged segment of a porous tube is shown in Fig. 1. The tube has an inner radius, a and outer radius, b and is initially at a temperature, T_g of a fluid transpiring through the porous matrix. The mass flow rate $\dot{m}$ of transpirant is assumed to be constant and is defined as a positive quantity for flow radially outward and as a negative quantity for flow radially inward. The thermal, physical, and transport properties of the matrix and the fluid are considered to be constant with respect to temperature and position. Consistent with the analysis of Weinbaum and Wheeler [11] on porous metal walls, it is assumed that at any radial position within the matrix, the flow and solid are at the same temperature. Within a narrow region at the gas-entry surface of an actual matrix the gas temperature will depart from the matrix temperature. The solutions of the present paper do not take this effect into account, and some departure from prediction and actual matrix behavior should be expected in this narrow region, depending on the coarseness of the pores.

With the foregoing assumptions and heat and mass flow only in a radial direction within the porous cylinder, a heat balance may be performed on the cylindrical element of unit length and thickness, dr shown in Fig. 1.

The sum of the net rate of heat conduction and the increase in fluid energy content is equal to the rate of energy storage in the cylindrical element, giving the partial differential equation

$$2\pi\lambda_m \frac{\partial}{\partial r}\left(r \frac{\partial T}{\partial r}\right) \mp \dot{m} C_g \frac{\partial T}{\partial r} = 2\pi r \rho_m C_m \frac{\partial T}{\partial t} \tag{1}$$

or

$$\frac{\partial^2 v}{\partial r^2} + \frac{(1 \mp 2\nu)}{r}\frac{\partial v}{\partial r} = \frac{1}{\alpha_m}\frac{\partial v}{\partial t} \tag{2}$$

where the dimensionless flow rate, matrix thermal diffusivity, and dimensionless temperature excess are defined by

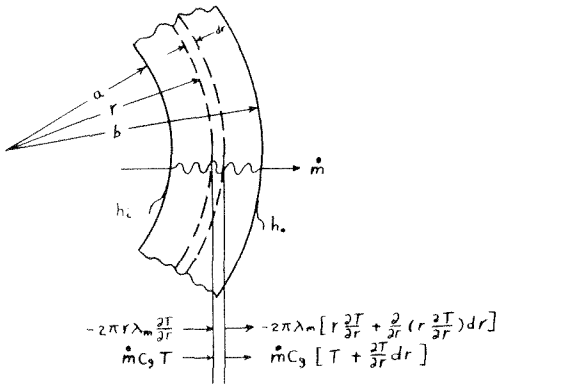

Fig. 1 Enlarged segment of a porous tube showing the heat balance on a cylindrical element

$$\nu = \frac{\dot{m} C_g}{4\pi\lambda_m}, \quad \alpha_m = \frac{\lambda_m}{\rho_m C_m}, \quad \text{and} \quad v = \frac{T - T_g}{T_f - T_g} \tag{3}$$

respectively. The factor $(1 - 2\nu)$ is applicable for the condition with a transpiring fluid flowing in a direction of increasing radius. For flow in the reverse direction, the factor $(1 + 2\nu)$ is applicable.

The porous cylinder is initially at the temperature of a fluid transpiring through it by means of an applied pressure difference. The initial condition is expressed by

$$v = 0, \quad T = T_g \text{ for } t \leq 0, \text{ and } a \leq r \leq b \tag{4}$$

When the temperature of the fluid flowing inside the cylinder, $r < a$, is suddenly elevated to and maintained at T_f, heat is transferred from the fluid to the inner surface. This condition may be expressed by the relation

$$-\lambda_m \frac{\partial T}{\partial r} = h_i(T_f - T) \text{ at } r = a \tag{5}$$

At the outside surface, $r = b$, heat that is conducted through the matrix is transferred by convection to the fluid in the plenum annulus at temperature, T_g. This condition may be expressed by the relation

$$-\lambda_m \frac{\partial T}{\partial r} = h_0(T - T_g) \text{ at } r = b \tag{6}$$

where h_i and h_0 are the heat-transfer coefficients at the inside and outside surfaces, respectively. Equations (5) and (6) may be expressed by the dimensionless relations

$$-a \frac{\partial v}{\partial r} = H_i(1 - v) \text{ at } r = a \tag{7}$$

$$-b \frac{\partial v}{\partial r} = H_0 v \text{ at } r = b \tag{8}$$

where v is defined (3) and $H_i = ah_i/\lambda_m$ and $H_0 = bh_0/\lambda_m$ are the

Nomenclature

a = inside radius of tube
b = outside radius of tube
C_g = specific heat of gas transpirant
C_m = specific heat of matrix
Fo = Fourier number, $\mathrm{Fo} = \alpha_m t/L^2$ where L is characteristic length
h_i = heat-transfer coefficient at inside tube surface
h_0 = heat-transfer coefficient at outside tube surface
H_i = Biot number at inside tube surface, $H_i = h_i a/\lambda_m$
H_0 = Biot number at outside tube surface, $H_0 = h_0 b/\lambda_m$
H_* = reference Biot number corresponding to $\nu = 0$
$\dot{m}$ = superficial radial mass flow rate of gas coolant per unit length
q_r = radial heat flow per unit length of tube
r = radius
t = time
T = temperature
T_g = initial temperature of porous tube
v = temperature excess, $v = (T - T_g)/(T_f - T_g)$
α_m = matrix thermal diffusivity, $\alpha_m = \lambda_m/\rho_m C_m$
β_n = roots of characteristic equations
λ_m = thermal conductivity of matrix
ν = dimensionless flow rate, $\nu = \dot{m}C_g/4\pi\lambda_m$
ρ_m = density of porous matrix

Subscripts

f = refers to hot gas stream
g = refers to gas
i = refers to inside tube surface
m = refers to matrix
0 = refers to outside tube surface
$*$ = reference corresponding to $\nu = 0$

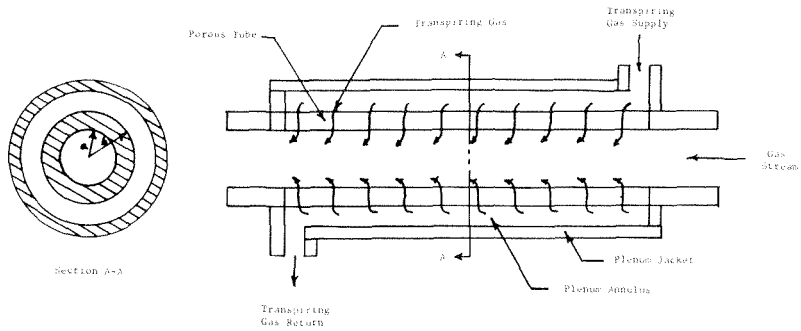

Fig. 2 Transpiration heat-transfer apparatus

dimensionless Biot numbers at the inside and outside surfaces, respectively.

When the temperature of the fluid flowing in the plenum annulus, $r > b$, is suddenly elevated to and maintained at T_f, the boundary conditions are defined similarly by the relations

$$a \frac{\partial v}{\partial r} = H_i v \text{ at } r = a \tag{9}$$

$$b \frac{\partial v}{\partial r} = H_0(1 - v) \text{ at } r = b \tag{10}$$

3 Transpiration Heat-Transfer Applications

The applications discussed in the introduction to this paper can, in general, be separated into three categories, namely: transpiration cooling, catalytic chemical reactor, and tubular regenerator applications. Each of these applications must consider the direction of transpiration fluid flow, the assumptions made in the previous section, and the values assigned to the thermal and physical properties, in particular the coefficients of heat-transfer h_0 and h_i as defined in (5) and (6).

For a practical application, the lateral flow of gas inside the cylinder and in the plenum annulus as shown in Fig. 2 will give a net lateral component of fluid motion at both surfaces of the tube. For this reason the coefficients of heat transfer at these surfaces must include a component due to forced convection in addition to a component that provides for a change in enthalpy of the transpiring fluid on entry to and exit from the surfaces. Correlations for predicting heat-transfer coefficients with boundary-layer suction (fluid entry) and blowing (fluid exit) may be found in [12, 13, 14].

A Transpiration Cooling. The first transpiration cooling solution was derived for the case of the inside surface of the transpiration-cooled tube of Fig. 2 suddenly exposed to a high-temperature gas stream. The tube is initially at the temperature of a cold gas which is transpiring radially inward. Suddenly, a high-temperature gas stream flows inside the tube, while the flow of transpirant is maintained constant. The temperature distribution within the tube is governed by differential equation (2) with a plus sign (flow radially inward). Furthermore, since the step increase in the rate of convective heat transfer occurs at the inside surface, boundary conditions (7) and (8) apply. The solutions, (A-2) and (A-3), which satisfy the foregoing conditions are derived in the Appendix.

The second transpiration cooling solution was derived for the case of the outside surface of the tube suddenly exposed to a high-temperature gas stream. Since the flow of transpirant for this case is radially outward, the temperature distribution within the tube is governed by differential equation (2) with a minus sign. Furthermore, since the step increase in the rate of convective heat transfer for this case is at the outside surface, boundary conditions (9) and (10) apply. The solutions, (A-6) and (A-7), which satisfy the foregoing conditions are derived in the Appendix.

Both of the foregoing transpiration cooling solutions are also applicable to transpiration heating applications, such as in deicing operations. In these applications, a high-temperature gas is forced to transpire through a porous tube to prevent ice formation at one of its surfaces which is exposed to a low-temperature convective environment.

The transient temperature distribution for the case of the inside surface of a transpiration-cooled tube suddenly exposed to a high-temperature gas stream is shown in Fig. 3. A radius ratio $b/a = 2$, an inside Biot number $H_i = 1$, an outside Biot number $H_0 = 1.5$, and a transpirant flow rate $\nu = 0.5$ were selected for the analysis. In the center plot radial temperature distributions within the tube are plotted for selected Fourier numbers (elapsed times). Initially ($F_0 = 0$), the tube is at the transpiring gas supply temperature T_g. High temperature gas flow is suddenly initiated inside the tube. After a small period of time ($F_0 = 0.01$), the temperature rises sharply in a narrow region at the hot inner surface, while the remainder of the tube is still unaffected. As time progresses, the temperature profiles rise in the tube until the steady-state distribution ($F_0 = \infty$) is reached. To the left of the center plot, the variation of temperature with time is plotted for the inside surface ($r = a$). To the right of the center plot, a similar plot is given for the outside surface ($r = b$). At both surfaces the temperature rises exponentially with time, but the response

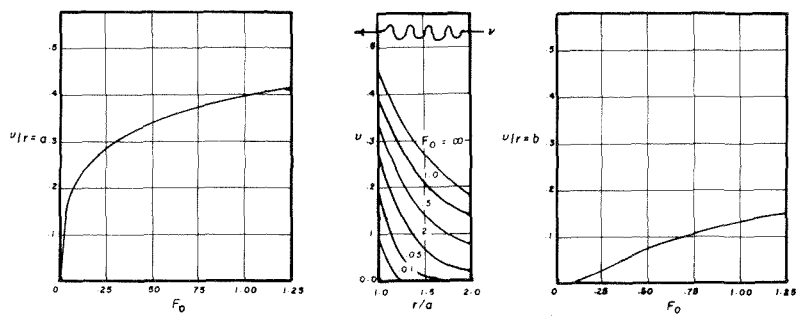

Fig. 3 Transient temperature distribution in a transpiration-cooled tube after sudden exposure to a hight-temperature gas stream at the inside surface ($\nu = 0.5$, $b/a = 2$, $H_0 = 1.5$, and $H_i = 1$)

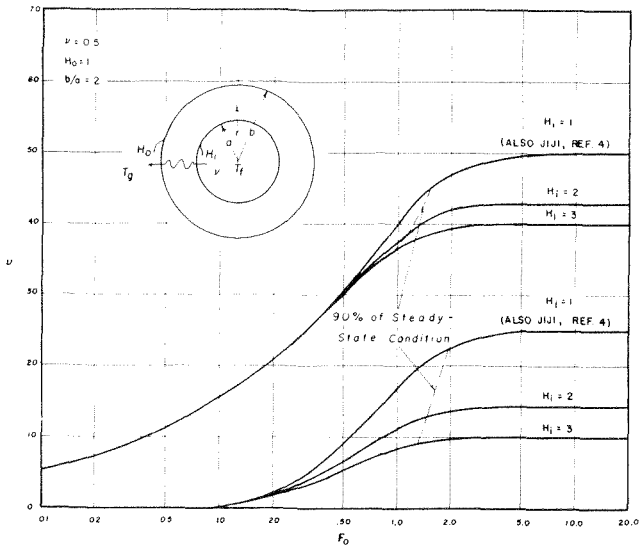

Fig. 4. The effect of forced convection at the gas-entry surface on the temperature response at the hot-side surface (upper set of curves) and cold-side surface (lower set of curves)

at the cooler outside surface is considerably slower, owing to the time required for the effect of the high-temperature convective environment at the inside surface to be propagated to the outside surface.

The presence of forced convection at the cold-side gas-entry-surface of a transpiration-cooled tube will have a significant influence on the previously described transient-temperature distributions. This effect is investigated for the case of the outside surface of a transpiration-cooled tube suddenly exposed to a high-temperature gas stream with the coolant transpiring radially outward. An outside Biot number $H_0 = 1$, a transpirant flow rate $\nu = 0.5$, and a radius ratio $b/a = 2$ were selected for the analysis. Fig. 4 shows the temperature response at the hot-side surface (upper set of curves) and cold-side surface (lower set of curves) for selected rates of convective heat transfer at the gas-entry surface. The condition $H_i = 2\nu$ corresponds to a condition of no forced convection at the gas-entry surface studied by Jiji [4]. Thus, the curves for $H_i = 1$ represent the condition of no forced convection at the gas-entry surface. It is seen that the present solution agrees with the solution of Jiji. The added effect of forced convection at the gas-entry surface is to lower the magnitude of the temperature response at both surfaces and reduce the time required to reach a steady condition. The reduction in temperature is most pronounced at the cold-side surface where the additional convective heat transfer corresponding to outside Biot numbers $H_i = 2$ and $H_i = 3$ lowered the steady-state temperature 43 and 60 percent, respectively. At the hot-side surface, the reduction in temperature was less and was not felt until nearly a steady condition was reached. A broken line is drawn through the points on the curves where the temperature reaches 90 percent of its steady-state value, showing that an increase in force convection reduces the time required to reach a steady-state condition.

The transpirant flow rate ν significantly effects the transient temperature distribution within a transpiration-cooled tube through its enthalpy transport action within the tube and at the boundary layers of the tube surfaces. Since variations in the transpirant flow rate ν will have a strong influence on the heat-transfer coefficients at the tube surfaces, the following experimental relation was used to adjust these heat-transfer coefficients for the enthalpy transport action of the suction and blowing:

$$H = \frac{-2\nu}{\mathrm{Exp}(-2\nu/H_*) - 1} \tag{11}$$

where H_* = Biot number without suction or blowing
ν = transpirant flow rate (defined positively for flow into the surface)

Mickley, et al. [12] developed this relation for predicting heat-transfer coefficients for flow along a flat plate with boundary-layer suction and blowing. The results of Kalny [13] and Aggarwal and Hollingsworth [14] indicate that this correlation is approximately valid for flow at the inside surface of a cylindrical annulus. For the present analysis equation (11) is applied to both the inside and outside surfaces. Note that it can be shown that for vanishing transpirant flow rates ($\nu \to 0$), H approaches H_*. When the transpirant flow rate becomes very large ($\nu \to \infty$), H approaches 2ν at the suction surface and vanishes at the blowing surface.

The effect of the flow rate ν on the temperature distribution was investigated for the case of the inside surface of a transpiration-cooled tube suddenly exposed to a high-temperature gas stream. For this analysis, a radius ratio $b/a = 2$, and Biot numbers without suction and blowing equal to unity were selected. The temperature response at the inside hot-side surface is plotted for selected transpirant flow rates ν in Fig. 5. The Biot numbers corresponding to the selected transpirant flow rates ν were calculated from equation (11) and these values were used to calculate the temperature curves. An increase in the transpirant flow rate ν significantly lowered the temperature and reduced the time required to reach a steady-state condition. The curve for $\nu = 0$ corresponds and agrees with the solution of Cawslaw and Jaeger [15]. As in the previous plot, a broken line is drawn through the points on the curves where the temperature reaches 90 percent of its steady-state value.

B Catalytic Chemical Reactors. *In a catalytic chemical reactor* the injection of a catalyst gas is used to control the rate of a chemical reaction taking place between the species of a gas mixture. The catalyst gas itself does not enter the chemical reaction and remains unaltered, but the rate of reaction is strongly dependent on the temperature of the injected catalyst gas.

The first solution was derived for the case of a chemical reactor tube inside of which a reacting gas mixture is flowing (see Fig. 2). The rate of the reaction is being initially controlled by a catalyst gas that is transpiring radially inward. The catalyst gas at the outside surface is suddenly elevated in temperature, so as to speed up the rate of reaction of the gas mixture flowing inside the tube. The temperature distribution within the tube for this case is governed by differential equation (2) with a plus sign (flow radially inward). Furthermore, since the step change in temperature occurs at the outside surface, boundary conditions (9) and (10) apply. The resulting solution is given by (A-9) and (A-10) of the Appendix.

The second solution is derived for the inverted case of a chemi-

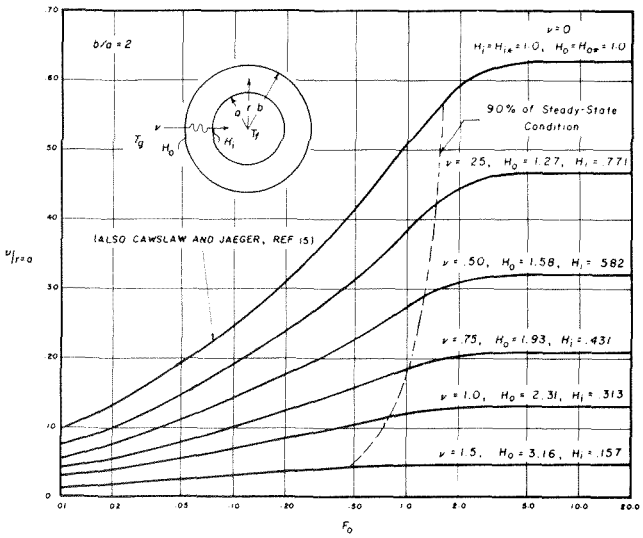

Fig. 5 The net effect of the transpirant flow rate ν on the transient temperature distribution within a transpiration-cooled tube

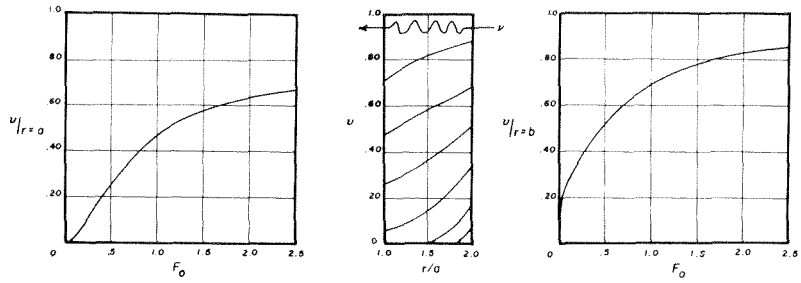

Fig. 6 Transient temperature distribution within a chemical reactor after the catalyst gas being injected at the outside surface is suddenly elevated in temperature ($\nu = 0.5$, $b/a = 2$, $H_0 = 1.5$, $H_i = 0.5$)

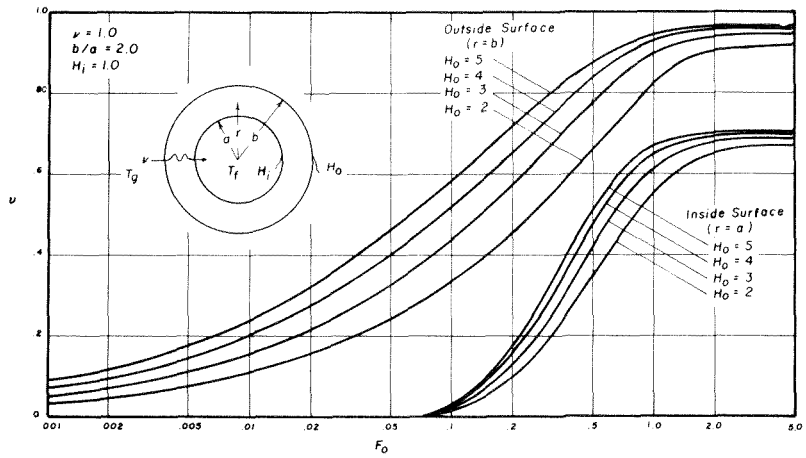

Fig. 7 The effect of forced convection at the gas-entry surface on the transient temperature response at the outside surface (upper set of curves) and inside surface (lower set of curves)

cally reacting gas mixture flowing in the plenum annulus of Fig. 2. The rate of reaction is being initially controlled by a catalyst that is transpiring radially outward. The temperature of the catalyst gas flowing inside the tube is suddenly elevated in temperature, so as to increase the rate of reaction of the gas mixture flowing in the annulus. The solution for the temperature distribution that satisfies differential equation (2) with a minus sign (flow radially outward) and boundary conditions (7) and (8) is given by (A-11) and (A-12) of the Appendix.

The transient temperature distribution within a chemical reactor tube for the case of a chemically reacting gas mixture flowing inside the tube is shown in Fig. 6. A radius ratio $b/a = 2$, an inside Biot number $H_i = 0.5$, an outside Biot number $H_0 = 1.5$, and a catalyst flow rate $\nu = 0.5$ were selected for the analysis. In the center graph, radial temperature distributions within the tube are plotted for selected Fourier numbers. The tube is initially at a uniform temperature T_g. High-temperature catalyst gas is suddenly forced to transpire radially inward. After a small period of time ($F_0 = 0.01$), the temperature rises sharply in a narrow region at the outside gas-entry surface, while the remainder of the tube is still unaffected. As time progresses, the temperature profiles rise until a steady condition ($F_0 = \infty$) is reached. Notice, the shape of the steady-state distribution is concave downward for a chemical reactor tube, whereas it is concave upward for a transpiration-cooled tube. To the left of the center graph, the temperature response of the inside surface is plotted. To the right of the center graph, a similar plot for the outside surface is given. The temperature at both surfaces is seen to vary exponentially with time but slightly more time is required for the inside surface to reach a steady-state condition.

Force convection at the gas-entry surface of a chemical reactor tube will have a significant effect on the previously described transient temperature distributions. This effect is investigated for the case of a reacting gas mixture flowing inside the reactor tube. A catalyst flow rate $\nu = 1$, a radius ratio $b/a = 2$, and an inside Biot number $H_i = 1$ were selected for the analysis. In Fig. 7 the temperature response at the outside surface (upper set of curves) and the inside surface (lower set of curves) is plotted for selected outside Biot number H_0. Previous solutions in the literature took $H_0 = 2\nu$ which corresponds to a condition of no forced convective heat transfer at the gas-entry surface. The condition $\nu = 1$ and $H_0 = 2$ represents this latter condition. The presence of forced convective heat transfer at the gas-entry surface ($H_0 > 2$) raises the temperature within the tube during the transient adjustment and decreases the time required for the temperature to reach a steady-state condition. Increasing the outside Biot number H_0 from 2 to 5 reduces by approximately 50 percent the time required for the temperature at the hot-side gas-entry surface to reach 90 percent of its steady-state, whereas at the cold-side gas exit surface the corresponding reduction in time was approximately 41 percent. Forced convection at the gas-entry surface has little effect on the magnitude of the steady-state temperature distribution which is contrary to the transpiration-cooled tube (see Fig. 4).

C Tubular Regenerators. A very efficient method of exchanging heat between two gases at substantially different temperatures is to alternately pass these gases through a porous cylindrical matrix, like the transpiration heat-transfer apparatus of Fig. 2. The catalytic reactor tube soultions derived in the Appendix represent approximate solutions for the starting operation of a transpiration-heated or -cooled regenerator. In most regenerators the gas flow rates are large causing the gas-exit surface to be very nearly adiabatic. Therefore, when using these solutions, the Biot number at the gas-exit surface should be set equal to zero. This is consistent with most regenerator solutions in the literature which take the gas-exit surface to be adiabatic. When using these solutions, it should be noted that the free stream temperature at the gas-exit surface is incorrectly maintained at the constant value

T_g. In an actual regenerator this temperature would rise throughout the transient adjustment period. However, since the heat transfer to this surface is negligible, the fact that the mathematics incorrectly maintains the bulk gas temperature at this surface equal to a constant value will not effect the solution for the temperature distribution within the tube.

In designing a transpiration-heated and -cooled regenerative heat exchanger tube, a foremost consideration is the time required for the temperature within the regenerator to be switched from one level to another. A parameter having much bearing on the response time (the time required for the temperature to be switched from one level to 90 percent of its new steady-state value) is the transpirant flow rate ν. This effect is investigated for a regenerator that is suddenly exposed to a high-temperature gas transpiring radially outward. A radius ratio $b/a = 2$ was selected for the analysis. From equation (11), the Biot number with high rates of blowing is seen to vanish, whereas the Biot number with high rates of suction is seen to approach 2ν. Since large transpirant flow rates are usually used in regenerator applications, an outside surface Biot number $H_0 = 0$ and an inside surface Biot number $H_i = 2\nu$ were used for the analysis. The temperature response at the gas-exit surface is of particular interest, since this surface is the last point in the tube to reach a steady-state value. The variation of temperature with time at the outside surface is plotted in Fig. 8 for selected transpirant flow rates ν. Changing the transpirant flow rate ν from 3 to 20 reduced the response time by a factor of 9.

APPENDIX

The partial differential equation

$$\frac{\partial^2 v}{\partial r^2} + \frac{1 \pm 2\nu}{r} = \frac{1}{\alpha}\frac{\partial v}{\partial t} \tag{2}$$

is satisfied by the following general solution

$$v = A + Br^{\pm 2\nu} + r^{\pm\nu} C_\nu(\beta r) e^{-\beta^2 \alpha t} \tag{A-1}$$

where the cylinder function $C_\nu(\beta r) = DJ_\nu(\beta r) + EY_\nu(\beta r)$ is a linear combination of the Bessel functions of order ν and of the first and second kind, respectively. By setting $\partial v/\partial t = 0$, the first and second terms of (A-1) are the time-independent or steady-state terms. The constants A, B, D, and E are to be determined from the initial condition (4) and the appropriate set of boundary conditions (7) and (8) or (9) and (10).

Relationships involving the cylinder function that are necessary for deriving the solutions found in the following sections are defined by the following:

$$\frac{d}{dr}[r^{-\nu} C_\nu(\beta r)] = -\beta r^{-\nu} C_{\nu+1}(\beta r)$$

$$\frac{d}{dr}[r^{\nu} C_\nu(\beta r)] = -\beta r^{\nu} C_{\nu+1}(\beta r) + 2\nu r^{\nu-1} C_\nu(\beta r)$$

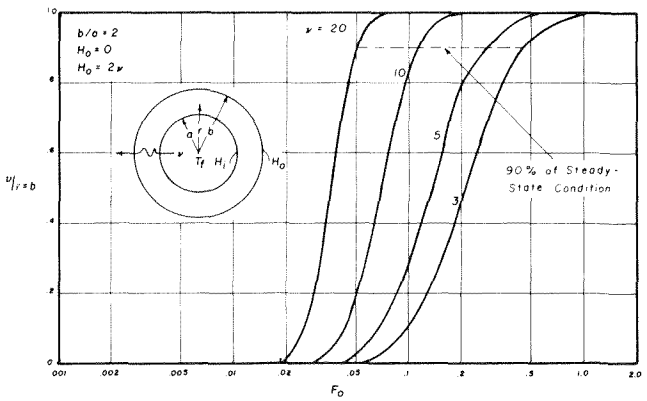

Fig. 8 The effect of the transpirant flow rate ν on the temperature response at the gas-exit surface of a tabular regenerator

$$\int r C_\nu^2(\beta r)dr = \frac{r^2}{2}\left[C_\nu^2(\beta r) + C_{\nu+1}^2(\beta r) - \frac{2\nu}{\beta r} C_\nu(\beta r) C_{\nu+1}(\beta r)\right]$$

$$\int r[Mr^{\nu} + Nr^{-\nu}] C_\nu(\beta r)dr = \frac{r}{\beta}[Mr^{\nu} + Nr^{-\nu}] C_{\nu+1}(\beta r) - \frac{2\nu N r^{-\nu}}{\beta^2} C_\nu(\beta r)$$

The various coefficients replacing D and E in the cylinder function are defined by the following:

$$P_n = H_0 Y_\nu(\beta_n b/a) - \beta_n b/a\, Y_{\nu+1}(\beta_n b/a)$$
$$Q_n = H_0 J_\nu(\beta_n b/a) - \beta_n b/a J_{\nu+1}(\beta_n b/a)$$
$$R_n = H_i Y_\nu(\beta_n) + \beta_n Y_{\nu+1}(\beta_n)$$
$$S_n = H_i J_\nu(\beta_n) + \beta_n J_{\nu+1}(\beta_n)$$
$$U_n = (H_i - 2\nu) Y_\nu(\beta_n) + \beta_n Y_{\nu+1}(\beta_n)$$
$$W_n = (H_i - 2\nu) J_\nu(\beta_n) + \beta_n J_{\nu+1}(\beta_n)$$
$$X_n = (H_0 + 2\nu) Y_\nu(\beta_n b/a) - \beta_n b/a\, Y_{\nu+1}(\beta_n b/a)$$
$$Z_n = (H_0 + 2\nu) J_\nu(\beta_n b/a) - \beta_n b/a J_{\nu+1}(\beta_n b/a)$$

1 Hot Gas Inside, Coolant Transpiring Radially Inward

For the case with hot gas flowing longitudinally in the inside of a cylindrical tube and with the transpiring coolant flowing radially inward (case with $(1 + 2\nu)$ of (3)), the general solution (A-1) must satisfy the boundary condition (7) and (8) and the initial condition (4). Setting $v = v_s + v_t$, where v_s and v_t are the steady-state and time-dependent portions, respectively, the solution becomes

$$v_s = \frac{H_i[(2\nu - H_0) + H_0(b/r)^{2\nu}]}{H_i(2\nu - H_0) + H_0(2\nu + H_i)(b/a)^{2\nu}} \tag{A-2}$$

where

$$v_t = H_i(a/r)^{\nu} \Sigma A_n C_\nu(\beta_n r/a) e^{-\beta_n^2 \alpha t/a^2}$$
$$C_\nu(\beta_n r/a) = P_n J_\nu(\beta_n r/a) - Q_n Y_\nu(\beta_n r/a) \tag{A-3}$$

and β_n are the positive roots of the characteristic equation $P_n S_n - Q_n R_n = 0$. From the definition for β_n let

$$\rho_n = \frac{P_n}{R_n} = \frac{Q_n}{S_n}$$

The discrete values for the cylinder function, using the Wronskian relation $J_{\nu+1}(Z)Y_\nu(Z) - J_\nu(Z)Y_{\nu+1}(Z) = 2/\pi Z$, are defined by

$$C_\nu(\beta_n) = -2\rho_n/\pi,\ C_\nu(\beta_n b/a) = 2/\pi,\ \beta_n C_{\nu+1}(\beta_n) = \frac{2H_i\rho_n}{\pi},\ \beta_n b/a\, C_{\nu+1}(\beta_n b/a) = \frac{2H_0}{\pi}$$

The constants A_n of (A-3) are determined using the orthogonality of the defined cylinder function and the initial condition (4), or $v_t = -v_s$ at time $t = 0$. This gives,

$$A_n \int_a^b r C_\nu^2(\beta_n r/a)dr = -\int_a^b r[Mr^{\nu} + Nr^{-\nu}] C_\nu(\beta_n r/a)dr \tag{A-4}$$

where M and N are the coefficients of the first and second terms of (A-2) multiplied by $(r/a)^{\nu}$. The integral on the left side of (A-4) was previously defined in indefinite form. Taking the limits and the discrete values given in the foregoing, its value is

$$\int_a^b r C_\nu^2(\beta_n r/a)dr = \frac{2a^2}{\pi^2\beta_n^2}[H_0^2 + (\beta_n b/a)^2 - 2\nu H_0 - \rho_n^2(H_i^2 + \beta_n^2 + 2\nu H_i)]$$

Also, the integral on the right gives zero at $r = b$, and at $r = a$ gives

$$-\int_a^b r[Mr^{\nu} + Nr^{-\nu}] C_\nu(\beta_n r/a)dr = \frac{2a^2\rho_n}{\pi\beta_n^2}$$

From (A-4), the value for A_n of (A-3) is

$$A_n = \frac{\pi\rho_n}{H_0^2 + (\beta_n b/a)^2 - 2\nu H_0 - \rho_n^2(H_i^2 + \beta_n^2 + 2\nu H_i)} \tag{A-5}$$

Substituting $H_0 = H_0' + 2\nu$ (where H_0' is the additive surface conductance due to forced convection at the coolant-entry face),

the steady-state solution of (A-2) reduces to Schneider's solution [3].

2 Hot Gas Outside, Coolant Transpiring Radially Outward

For the case with hot gas flowing longitudinally outside of a cylindrical tube and with the transpiring coolant flowing radially outward (case with $(1 - 2\nu)$ of (3)), the general solution (A-1) must satisfy the initial condition (4) and boundary conditions (9) and (10). As in the previous case, the solution is written in the same form, or

$$\theta_s = \frac{H_0[(2\nu - H_i) + H_i(r/a)^{2\nu}]}{H_0(2\nu - H_i) + H_i(2\nu + H_0)(b/a)^{2\nu}} \quad \text{(A-6)}$$

$$\theta_t = H_0(r/b)^{\nu}\Sigma B_n C_\nu(\beta_n r/a)e^{-\beta_n^2 \alpha t/a^2} \quad \text{(A-7)}$$

where $C_\nu(\beta_n r/a) = U_n J_\nu(\beta n r/a) - W_n Y_\nu(\beta n r/a)$, and β_n are the positive roots of $U_n Z_n - W_n X_n = 0$. The values of B_n are

$$B_n = \frac{\pi \rho_n}{H_i^2 + \beta_n^2 - 2\nu H_i - \rho_n^2[H_0^2 + (\beta_n b/a)^2 + 2\nu H_0]} \quad \text{(A-8)}$$

where $\rho_n = W_n/Z_n$

The substitution, $H_i = 2\nu$ in (A-6) and (A-7) gives the same solution as found in (12) of Jiji [6].

3 Hot Gas Transpiring Radially Outward

For the case of a hot gas transpiring radially outward (case $(1 - 2\nu)$ of (3)) which would approximate the heating portion of a transpiration-cooled regenerator cycle, the general solution (A-1) must satisfy (4) and the boundary conditions (7) and (8). The solution is given by

$$\theta_s = \frac{H_i[(2\nu + H_0) - H_0(r/b)^{2\nu}}{H_i(2\nu + H_0) + H_0(2\nu - H_i)(a/b)^{2\nu}} \quad \text{(A-9)}$$

$$\theta_t = H_i(r/a)^{\nu}\Sigma D_n C_\nu(\beta_n r/a)e^{-\beta_n^2 \alpha t/a^2} \quad \text{(A-10)}$$

where $C_\nu(\beta_n r/a) = X_n J_\nu(\beta_n r/a) - Z_n Y_\nu(\beta_n r/a)$, β_n are roots of $U_n Z_n - W_n X_n = 0$, and $D_n = -B_n$, (A-8). An application to the regenerator cycle is to set $H_i = 2\nu$ and $H_0 = 0$.

4 Hot Gas Transpiring Radially Inward

For the case of a hot gas transpiring radially inward (case $(1 + 2\nu)$ or (3)), the general solution (A-1) must satisfy the initial condition (4) and the boundary conditions (9) and (10). The solution is given by

$$\theta_s = \frac{H_0[(2\nu + H_i) - H_i(a/r)^{2\nu}]}{H_0(2\nu + H_i) + H_i(2\nu - H_0)(a/b)^{2\nu}} \quad \text{(A-11)}$$

$$\theta_t = H_0(b/r)^{\nu}\Sigma E_n C_\nu(\beta_n r/a)e^{-\beta_n^2 \alpha t/a^2} \quad \text{(A-12)}$$

where $C_\nu(\beta_n r/a) = R_n J_\nu(\beta_n r/a) - S_n Y_\nu(\beta_n r/a)$, β_n are roots of $P_n S_n - Q_n R_n = 0$, and $E_n = -A_n$, (A-5).

In all of the foregoing four cases, the steady-state solution for $\nu = 0$, may be found by setting $\nu = 0$ in (2) and are given by the equation,

$$\theta_s = \frac{H_i V_i[1 + H_0 \ln(b/r)] + H_0 V_2[1 + H_i \ln(r/a)]}{H_i + H_0 + H_i H_0 \ln(b/a)}$$

where the appropriate substitutions are $V_2 = 0$, $V_1 = 1$ or $V_1 = 0$, $V_2 = 1$. The time dependent solutions (A-3), (A-7), (A-10), and (A-12) for $\nu = 0$ are found to be identical to a general solution found in Carslaw and Jaeger [15] with the appropriate substitutions from (7) through (10).

References

1 Schneider, P. J., and Brogan, J. J., "Temperature Response of a Transpiration-Cooled Plate," *Journal of the A. R. S.*, Vol. 32, No. 1, Jan., 1962.

2 Burch, D., "Thermal Analysis for a Transpiration-Cooled Plate," Paper for Master Degree at University of Maryland, July, 1970.

3 Schneider, P. J., "Temperatures and Thermal Stresses in Transpiration-Cooled Power-Producing Plates and Tubes," *Jet Propulsion*, Vol. 27, Aug. 1957.

4 Koh, J. C. Y., and del Casal, E. R., "Heat and Mass Flow Through Porous Matrices for Transpiration Cooling," *Proceedings of the 1965 Heat Transfer and Fluid Mechanics Institute*, June, 1965.

5 Koh, J. C. Y., et al., "Investigation of Fluid Flow and Heat Transfer in Porous Matrices for Transpiration Cooling," AFFDL-TR-65-228, Jan. 1966.

6 Jiji, L., "Transient Response of a Transpiration-Cooled Cylindrical Surface," *AIAA Journal*, Vol. 3, No. 11, Dec. 1965.

7 Schumann, T. E. W., "Heat Transfer: A Liquid Flowing Through a Porous Prism," *Journal of Franklin Institute*, CCVIII, July-Dec. 1929, pp. 405-416.

8 Creswick, F. A., "A Digital Computer Solution of the Equations for Transient Heating of a Porous Solid Including the Effects of Longitudinal Condition," *Industrial Mathematics*, 1957, pp. 61-69.

9 Howard, C. P., "The Single-Blow Problem Including the Effects of Longitudinal Conduction," ASME Paper No. 64-GTP-11, Jan. 1964.

10 Moreland, F. E., "Solution of the Single Blow Problem With Longitudinal Conduction by Numerical Inversion of Laplace Transforms," MA thesis, United States Naval Post Graduate School, Monterey, Calif., 1964.

11 Weinbaum, L., and Wheeler, H. L., Jr., "Heat Transfer in Sweat Cooled Porous Metals," *Journal of Applied Physics*, Vol. 20, Jan., 1949.

12 Mickley, H. S., Ross, R. C., Squyers, A. L., and Steward, W. E., "Heat Mass, and Momentum Transfer for Flow Over a Flat Plate with Blowing or Suction," NACA TN 3208, July, 1954.

13 Kalny R., "Measurements of the Effect of Suction on Friction and Heat Transfer at the Outer Wall of an Annular Turbulent Flow," PhD thesis, Department of Mechanical Engineering, University of Maryland, 1970.

14 Aggarwal, J. K., and Hollingsworth, M. A., "Heat Transfer for Tubulent Blow With Suction in a Porous Tube," *International Journal of Heat and Mass Transfer*, Vol. 16, 1973, pp. 591-609.

15 Carslaw, H. S., and Jaeger, J. C., *Conduction of Heat in Solids*, Oxford Clarendon Press, 1959, pp. 332-334.

R. A. Schapery
Professor.
R. E. Martin
Assoc. Professor.

Texas A&M University,
College Station, Texas

The Thermal Diffusivity of Highly-Filled Rubber

The influence of strain and temperature on the thermal diffusivity of solid propellant is investigated. Starting with the classical heat conduction equation for constant thermal properties, a simple procedure for experimentally determining the diffusivity and checking the validity of this equation is described. Existing theoretical bounds on the conductivity of composites with voids are then reviewed. Following a description of the experimental program, transient temperatures in two different solid propellants, covering the temperature range −320 deg F to 140 deg F and strain range 0 to 20 percent, are given and compared with theory. The diffusivity is found to vary noticeably with both strain and temperature.

Introduction

The thermal diffusivity of a particulate-filled polymeric material may, in general, depend on both current and past values of strain and temperature as a result of two distinctly different mechanisms.

Strain-induced vacuoles affect the thermal conductivity and density; in turn, these properties cause changes in the diffusivity since it is equal to the ratio of conductivity to density and specific heat. Composite materials, such as solid propellant, consisting of soft elastomeric matrices highly-filled with hard particles may contain voids between the matrix and particles (dewetting) and within the matrix far below the point of gross failure [1].[1] For a given applied strain, vacuole dilatation usually increases with increasing strain rate and decreasing temperature [1].

The second mechanism is related to viscoelastic behavior of the polymeric matrix and its effect on the matrix's specific heat. This thermal property usually decreases with decreasing temperature, especially as the temperature passes through the glass-transition region; moreover, the specific heat within this region is strongly dependent on the rate of cooling as a result of slow molecular configuration rearrangements [2]. Thus, the diffusivity can be expected to increase as the material is cooled in the neighborhood of the glass-transition temperature since the conductivity does not normally decrease; see, e.g., [3].

It should be noted that the glass transition temperature, as normally defined for amorphous polymers, is the temperature at which the thermal expansion coefficient is nearly discontinuous [4]. This temperature is somewhat dependent on the experimental time scale over which the volume change is measured; a variation of approximately six deg (deg F) per decade change in time scale is typical [4]. Essentially, the same molecular processes are believed to produce this behavior and the dependence of specific heat on temperature history; a generally accepted molecular theory of volume viscoelasticity is based on the concept of free volume [4], just as that for specific heat is based on the related hole theory of liquids and glasses [2, 5]. Results of these two theories recently have been related in [6] by using a relationship between specific heat and thermal expansion derived in [7] from the theory of irreversible thermodynamics.

For the purpose of this paper, the term "glass transition range" will be defined as the temperature range over which the specific heat depends measurably on temperature history. The approximate lower limit of this range is the long-time glass transition temperature, T_g, as defined in the foregoing. In view of the unfilled polymer data in [2] and [5], for example, the range may be as broad as 50 deg F or more, depending on the different cooling and heating rates used. Furthermore, the greatest variation with respect to history in specific heat occurs when a sample is slowly cooled through the glass-transition range and then rapidly heated [2].

The present study was motivated by the foregoing considerations and the fact that significant discrepancies between measured and predicted transient temperature distributions (where the latter were based on the assumption of constant diffusivity) have been reported for solid propellant grain structures [8-10]. Although all of the sources of this error are not known there is evidence in [8, 9] that the thermal diffusivity varies appreciably with temperature. In [9], thermal data obtained in transient temperature tests were numerically differentiated which, together with the heat conduction equation, were used to derive local values of thermal diffusivity. It was concluded that the diffusivity is both time and temperature dependent; however, we do not believe these results necessarily imply diffusivity depends on variables other than temperature since the numerical procedure was based on the equation for constant conductivity and not that for temperature-dependent conductivity, equation (1).

The specific objective of this paper is to report on the accuracy of the classical heat conduction equation with constant diffusivity and reasons for deviations, if any, for strained solid propellant subjected to a wide range of strains and specified boundary tem-

[1] Numbers in brackets designate References at end of paper.

Contributed by the Heat Transfer Division for publication in the JOURNAL OF HEAT TRANSFER. Manuscript received by the Heat Transfer Division, July 30, 1973. Paper No. 74-HT-W.

peratures. The first three sections are concerned with theoretical aspects of thermal properties. Experimental work on the measurement of thermal diffusivity of two different solid propellants and a comparison of theoretical and experimental results for transient temperatures are discussed in the fourth and fifth sections. Some final remarks deal with the relative effects of temperature dependent specific heat and conductivity.

Finally, we should add that those thermal properties of composite materials which are discussed in this paper are assumed to be independent of specimen size and temperature gradients. These assumptions are valid as long as the dimensions of microstructural inhomogeneity are very small compared to (i) specimen dimensions and (ii) distances over which the temperature varies appreciably. Properties of composite materials which satisfy these assumptions are usually called "effective properties." Both conditions (i) and (ii) are met in many composite material applications; except at very short times under sudden boundary temperature changes, they are met in the experimental investigation described herein.

The Classical Heat Conduction Equation

The classical equation of heat conduction in nonhomogeneous orthotropic materials, assuming the principal material axes correspond to the fixed x, y, z axes, is [11]:

$$\frac{\partial}{\partial x}\left(k_1 \frac{\partial \theta}{\partial x}\right) + \frac{\partial}{\partial y}\left(k_2 \frac{\partial \theta}{\partial y}\right) + \frac{\partial}{\partial z}\left(k_3 \frac{\partial \theta}{\partial z}\right) = \rho c \frac{\partial \theta}{\partial t} \quad (1)$$

where (x, y, z) defines a fixed rectangular Cartesian coordinate system and

$\theta \equiv T - T_R$ = difference between local temperature, T, and a convenient reference temperature, T_R

k_1, k_2, k_3 = thermal conductivities in principal directions

ρ = density; c = specific heat (based on unit mass)

For isotropic materials set $k_1 = k_2 = k_3 \equiv k$.

This equation was derived under the assumption of constant strain [11] and, therefore, c is actually the specific heat for constant strain. However, with the condition that the strains are small, the effect of strain (or stress) state on the specific heat of monolithic elastic solids usually can be neglected [11]. Under this same condition, the form of the left-hand side of equation (1) remains valid with varying strains.

For later use, we will give the solution for two-dimensional heat conduction in the rectangle shown in Fig. 1. Assuming isotropy in the x-y plane and that ρc and the in-plane conductivity, k, are constant, equation (1) reduces to

$$\frac{\partial^2 \theta}{\partial x^2} + \frac{\partial^2 \theta}{\partial y^2} = \frac{1}{\kappa} \frac{\partial \theta}{\partial t} \quad (2)$$

where $\kappa \equiv k/\rho c$ = thermal diffusivity; the conductivity in the z direction is not necessarily equal to k. The temperature $\theta = \theta_0 h(t)$ is given along the entire boundary, where $h(t)$ = unit-step function ($h(t) = 0$ for $t < 0$ and $h(t) = 1$ for $t > 0$) and θ_0 = constant. The initial condition throughout the body is $\theta = 0$. We find by a standard method of analysis that

$$\frac{\theta}{\theta_0} = 1 - f_x f_y \quad (3)$$

where

$$f_x = \frac{4}{\pi} \sum_{m=1,3,\ldots}^{\infty} (-1)^{\frac{m+1}{2}} \frac{e}{m}^{-m^2 t/\tau_T} \cos\left(\frac{m\pi}{2}\frac{x}{a}\right) \quad (4)$$

$$f_y = \frac{4}{\pi} \sum_{m=1,3,\ldots}^{\infty} (-1)^{\frac{m+1}{2}} \frac{e}{m}^{-m^2 t/\lambda^2 \tau_T} \cos\left(\frac{m\pi}{2}\frac{y}{b}\right) \quad (5)$$

$$\lambda \equiv \frac{b}{a} = \text{aspect ratio} \quad (6)$$

$$\tau_T \equiv \frac{4a^2}{\pi^2 \kappa} = \text{thermal diffusion time constant} \quad (7)$$

Solution (3) at the center ($x = y = 0$) is plotted versus $\log t/\tau_T$ ($\log \equiv \log_{10}$) in Fig. 1 for several values of λ.

It is important to observe that the temperature depends on only one material property, namely the thermal diffusivity, and its only effect is seen in the time constant, τ_T. This fact, together with the semilogarithmic plots in Fig. 1, can be conveniently used to evaluate the accuracy of the heat conduction equation (2) for a given material and to obtain a numerical value for the diffusivity. In particular, for a given aspect ratio (b/a) the experimental data are plotted in the form of θ/θ_0 versus $\log t$. The amount of horizontal translation which is required to superpose the theoretical (Fig. 1) and experimental curves is equal to $\log v_T$, where $\log \tau_T > 0$ (<0) when the same abscissa is used and the experimental curve is to the right (left) of the theory; the diffusivity κ is then found from the relation

$$\log \kappa = \log \frac{4a^2}{\pi^2} - \log \tau_T \quad (8)$$

If the two curves differ in shape, so that complete superposition cannot be achieved, then equation (2) with constant κ is not valid. The discrepancy can arise from temperature-dependence and/or temperature history-dependence of the diffusivity.

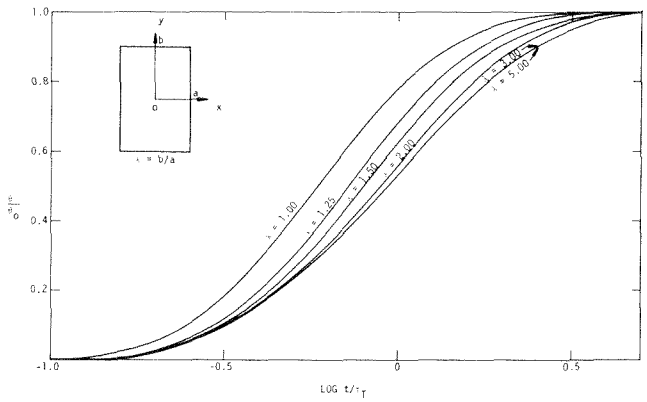

Fig. 1 Time-dependence of center temperature ($x = y = 0$)

Heat Conduction With Discontinuous Specific Heat

A heat conduction equation for viscoelastic media has been derived in [6], and is identical to equation (1) except c is replaced by the "secant specific heat," $c_s \equiv Q/\partial\theta/\partial t$; Q is the rate of heat addition per unit mass under constant mechanical stresses. Evaluation of c_s in terms of temperature history by means of nonequilibrium thermodynamic theory is reported in [6]. For the study at hand, it will be sufficient to note here that

$$c_s = \begin{cases} c_g & \text{if } T < T_g \\ c_e & \text{if } T >> T_g \end{cases} \quad (9)$$

where T_g is the long-time glass-transition temperature. Also, c_g and $c_e (c_g < c_e)$ are the glassy and equilibrium specific heats, respectively; both of these limiting values depend on temperature but not on temperature history.

Thermal Conductivity of Materials With Vacuoles

In the experimental program to be described later, long cylindrical bars of solid propellant were subjected to various amounts of axial tensile strain and then immersed in a bath. For this loading condition, even with vacuole formation, the material is thermally *isotropic* with respect to two-dimensional heat flow in the plane of the cross section. Therefore, except near the ends, equation (2) should apply if the conductivity is constant. Of course, the thermal conductivity in the cross section and in the axial direction are, in general, different.

We now turn to the brief review of some theoretical results on conductivity which later will be compared to measurements on solid propellants.

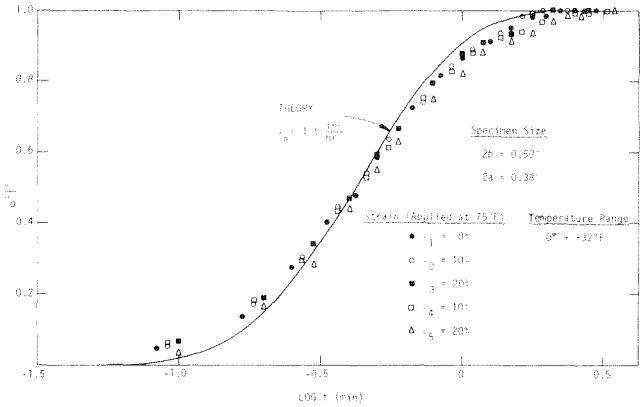

Fig. 2 Effect of strain on center temperature (CTPB sample No. 2)

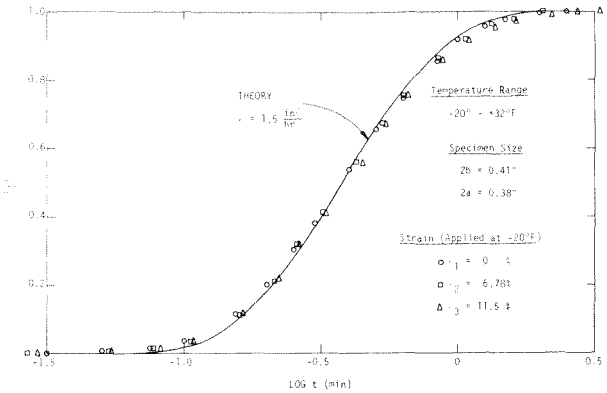

Fig. 3 Effect of strain on center temperature (CTPB sample No. 3)

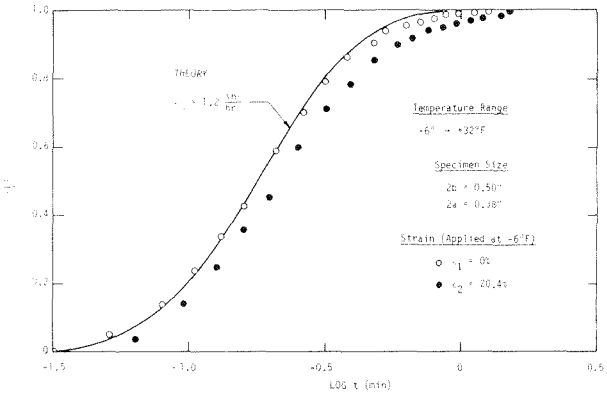

Fig. 4 Effect of strain on center temperature (PBAN propellant)

The thermal conductivity of monolithic or composite materials with vacuoles can be predicted by treating the voids as a distinct phase with zero conductivity and using existing theories for composites (see, for example, [13, 14, and 15] for isotropic composites and [16] and [17] for anisotropic composites).

Let us consider first the result for an isotropic monolithic material with a statistically uniform distribution (with respect to location and orientation) of voids. According to [14], the best possible upper and lower bounds on conductivity, k, in terms of void volume fraction, are given by the expression

$$0 \leq k \leq k_m \frac{1 - \alpha_v}{1 + (\alpha_v/2)} \tag{10}$$

where k_m = conductivity of the monolithic material without voids, and α_v = volume fraction of voids. The upper bound is also an exact result obtained by one of the so-called self-consistent schemes (SCS) [14], and can be shown to be the conductivity for the case in which the voids form a "composite spheres assemblage;" by definition, this is an arrangement in which the void distribution in size and space is such that the total volume can be considered to be entirely made up of hollow spheres, each having the same void fraction as the composite.

Another result of interest concerns the bounds on the transverse conductivity of a monolithic material having circular, cylindrical cavities; from [16 or 17]:

$$0 \leq k \leq k_m \frac{1 - \alpha_v}{1 + \alpha_v} \tag{11}$$

where k_m and α_v are defined in the foregoing. Just as for the sphere model, the upper bound is exact when the voids have varying diameters and are distributed in accordance with that described in the foregoing for spherical voids. The conductivity for the axial direction is given exactly as [16]:

$$k_a = (1 - \alpha_v)k_m \tag{12}$$

The foregoing results, equations (10) to (12), can also be used when the material is itself a composite having conductivity k_m, as long as the voids are large compared to the size and spacing of the constituents. When this latter condition is not satisfied, we can draw upon the more involved results in [15] as long as the total body, with voids, is thermally isotropic. Consider, for example, solid propellant. For this case, in the absence of voids, we can assume there are two phases: phase No. 1 consists of a large volume fraction of ammonium perchlorate particles (α_1 and k_1) and phase No. 2 is the matrix consisting of rubber with a small amount of very fine aluminum powder (α_2 and k_2). From [15], with voids as the third phase,

$$0 \leq k \leq k_1 + \frac{A_1}{1 - (A_1/3k_1)} \tag{13}$$

where

$$A_1 = -\frac{3}{2}\alpha_v k_1 + \frac{\alpha_2}{(k_2 - k_1)^{-1} + (3k_1)^{-1}} \tag{14}$$

Several available methods of predicting conductivities of heterogeneous materials and their agreement with experimental data are examined in [18].

Experimental Investigations

The experimental program was designed to ascertain the effects of strain level, heating and cooling rate, and temperature range on the thermal diffusivity of state-of-the-art composite solid propellants. The specimens were furnished by the Aerojet Solid Propulsion Company and the Air Force Rocket Propulsion Laboratory. A carboxy-terminated polybutadiene composite propellant (CTPB) containing approximately 76 volume percent solid particles (aluminum powder and ammonium perchlorate) was used as the primary test material because of its availability at the beginning of the program. The second material was a poly(butadiene-co-acrylonitrile) composite (PBAN) with approximately 73 volume percent solid particles. (The glass transition temperature for polybutadiene propellant is typically around −115 deg F.)

The experimental study of strain-level effects was conducted on both CTPB and PBAN propellants, while only the CTPB propellant was used in the investigation of time and temperature effects which is reported herein. Data on these latter effects for a fluorocarbon propellant are given in [6]; since the results are very similar to those for the CTPB propellant and the filler volume fraction is not known we have not included these data.

Nominal cross-sectional dimensions (prior to straining) and initial and final temperatures are given in Figs. 2 to 6; the axial length of all specimens was approximately two in. Imposed axial strains are listed in Figs. 2 to 4 in their order of application. (The specimens corresponding to Figs. 5 and 6 were not under load.) Failure occurred near the grips whenever a strain somewhat larger than 20 percent was applied.

For the thermal measurements copper-constantan (ISA Type T) thermocouple wire with Teflon® insulation was selected because of its excellent sensitivity over the temperature range of interest. Thermocouple placement for determination of center tem-

perature was accomplished by insertion through a hypodermic needle located along the specimen's axis. All samples were X-rayed in order to precisely determine the location of the thermocouple junction. Samples which exhibited gross misalignment of the thermocouple junction from the axial center line were rejected. In all cases, the location of the thermocouple was noted for later use in interpreting thermal data.

Generally, the test procedure consisted of allowing a specimen to reach thermal equilibrium at the desired initial temperature by using either an environmental chamber or dry ice (−105 deg F) and then immersing the specimen in heated or cooled water or liquid nitrogen (−320 deg F), depending on the temperature range of interest. Replicate samples were made for each configuration and the tests were normally run twice for each temperature excursion; no significant difference between excursions appeared and, except for some influence of thermocouple misalignment, the specimen-to-specimen variation in thermal response was very small. After completing some of the tests with and without imposed axial strain, thermal tests were rerun on unloaded specimens to spot-check for residual effects of water penetration and straining; none of significance were observed. For a more detailed description of specimen instrumentation and testing the reader is referred to [6].[2]

It should be recalled that the theoretical solution given earlier, equation (3), is based on a step change in the surface temperature. Three different techniques of mounting the surface thermocouples were checked, and all results indicated that the propellant surface reached 90 percent of the total change produced by the bath in less than one sec. Considering the fact that the total time required for thermal equilibrium was at least one min in all cases, the assumption of a step-temperature change is believed to be valid. Tests were also conducted to determine what effect, if any, heat conduction in the thermocouple lead wires had on the center thermocouple junction temperature. These tests consisted of running temperature versus time tests with and without the lead wires insulated by one-half inch thick rubber. A maximum relative error of only 1.8 percent due to lead wire heat conduction was observed. (That this effect is negligibly small was also confirmed analytically.)

Another possible source of error in measuring center temperature is the air gap between the thermocouple junction and the propellant. The maximum relative difference between the junction and propellant temperatures was estimated theoretically (assuming idealized geometries of concentric spheres and cylinders) to be no greater than 5 percent; this maximum error occurs during the early portion of the test. It should also be added that this error decreases with increasing axial tensile strain level because of lateral contraction of the hole surrounding the thermocouple junction.

[2] The PBAN propellant was not tested until after writing [6].

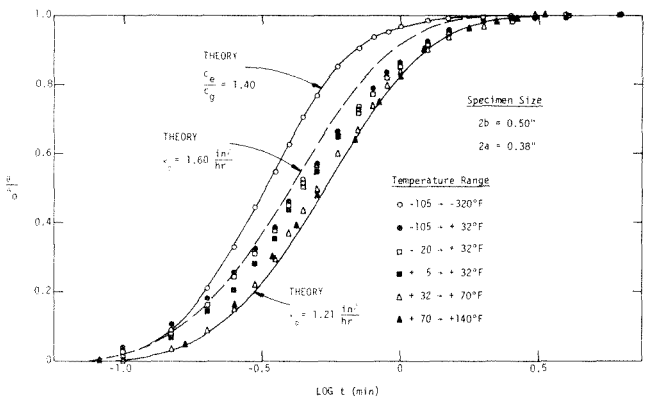

Fig. 5 Effect of temperature range on center temperature (CTPB propellant)

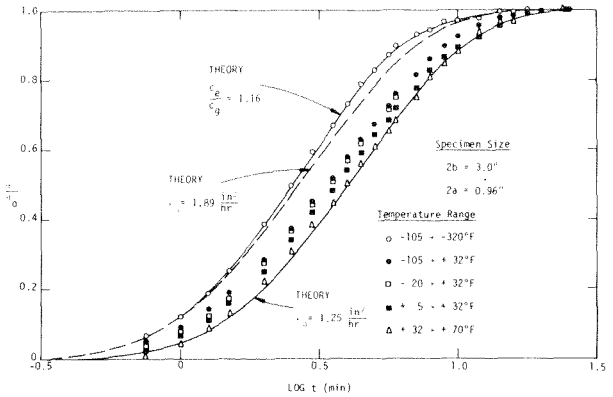

Fig. 6 Effect of temperature range on center temperature (CTPB propellant, large specimen)

Discussion of Results

Effect of Strain Level. The results for CTPB samples No. 2 and No. 3 are shown in Figs. 2 and 3, respectively. The data for the strained specimens in these figures have been corrected for the effect of strain on the cross-sectional dimensions. This correction consisted of horizontally translating the original data to the right an amount equal to log $(1 + \epsilon_l)^{-2}$, where $\epsilon_l (<0)$ is the lateral strain; in view of equation (7), this process reduces all data to the initial cross-sectional dimensions. The effect of thermal expansion, or contraction, on the dimensions was found to be negligible.

The solid line in each of the figures is the prediction obtained from equation (3) after horizontally translating the theoretical curve until it matched the zero strain data at $\theta/\theta_0 = 0.5$. The indicated value of κ was then calculated from equation (8).

The shapes of the theoretical curve and experimental data are somewhat different for both specimens, with the greatest discrepancy existing for sample No. 2. It is believed that this behavior is primarily due to the thermocouples being slightly off-center, and to a lesser extent due to the diffusivity being a weakly decreasing function of temperature (see the next subsection) in the ranges shown. The first conclusion has been verified by (i) using equation (3) to calculate the temperature versus time for locations away from the center ($x \neq 0$, $y = 0$) and finding that the experimentally observed shape of θ versus log t is predicted at slightly off-center points; and by (ii) X-raying all of the specimens to find that those specimens, including the ones discussed in the next subsection, which had the most closely centered thermocouples provided temperatures which were in the best agreement with equation (3) in the −20 and 32 deg F range.

An effect of strain level, although small, does exist; namely, the data at a given temperature tend to move to longer times with increasing strain. The largest horizontal difference between the strained and unstrained results is approximately 0.04 units in Fig. 2 and 0.02 units in Fig. 3; corresponding dilatations are approximately 3 percent (at ϵ_5) and 2 percent (at ϵ_3), respectively, which values were obtained using a gas dilatometer described in [19].[3] (Both specimens were very close to failure at these strains as they broke after being unloaded and reloaded to strains slightly above these values.) This horizontal difference implies the time constant τ_T (equation (7)) has increased or, equivalently, the diffusivity has decreased by 9.6 percent and 4.7 percent, respectively.

As a simple check on part of the foregoing theory, the diffusivity of CTPB propellant at room temperature will be predicted and compared with experimental results. The following properties will be used under the assumption that they are unaffected by chemical and physical interactions between phases:

[3] The dilatation did not change noticeably when the axial strain was held constant.

	Thermal conductivity Btu/hr-ft-deg F	Specific heat Btu/lb-deg F	Density lb/in.^{3}
Ammonium perchlorate [20]	0.29	0.27	0.070
Rubber binder [21, 22][4]	0.09	0.43	0.033
Aluminum [22]	117.00	0.22	0.098

First, however, it will be necessary to calculate several composite properties which are needed in the application of the theory. In the absence of dilatation the density is $\rho_0 = \alpha_{ap}\rho_{ap} + \alpha_r\rho_r + \alpha_{al}\rho_{al} = 0.064$ lb/in.^{3}, where ap $\equiv$ ammonium perchlorate (66.5 percent), $r \equiv$ rubber (23.5 percent), al $\equiv$ aluminum (10 percent) and, as before, the α are the volume fractions. With vacuole dilatation, the density is

$$\rho = \rho_0(1 - \alpha_v) \tag{15}$$

Specific heat in terms of mass fractions, w, is $c = w_{ap}c_{ap} + w_rc_r + w_{al}c_{al} = 0.28$ Btu/lb − deg F, which is essentially the same with or without voids (since the contribution from gas in the voids is negligible).

The thermal conductivity of the propellant is calculated in two steps. First, we find the conductivity, k_{ra}, of a rubber matrix with small aluminum particles using equation (3.31) in [14]:

$$k_{ra} = k_r\left[1 + \frac{\alpha_{al}'}{\left(\frac{k_r}{k_{al} - k_r}\right) + \frac{\alpha_r'}{3}}\right] \tag{16}$$

where the α' are volume fractions referred to the volume of rubber plus aluminum only. Because $k_{al} \gg k_r$,

$$k_{ra} \simeq k_r\left[1 + \frac{3\alpha_{al}'}{\alpha_r'}\right] = 0.20 \text{ Btu/hr-ft-deg F} \tag{17}$$

It should be noted that since the particles have a higher conductivity than the matrix, equation (16) is a lower bound to the actual conductivity, and is an exact result if the particles are spherical and distributed in accordance with the so-called composite spheres assemblage [14]. We now calculate the propellant's conductivity by considering it to be made up of relatively large ammonium perchlorate particles embedded in a matrix consisting of rubber plus aluminum powder. Equation (16) can be used again (since $k_{ap} > k_{ra}$) but with the following substitutions: $k_r \to k_{ra}$, $k_{al} \to k_{ap}$, $\alpha_{al}' \to \alpha_{ap}$, $\alpha_r' \to \alpha_{ra}$, and $k_{ra} \to k_0$, where k_0 is the propellant conductivity *without* voids. We find $k_0 = 0.26$ Btu/hr-ft-deg F. The diffusivity in the absence of voids is $\kappa_0 = k_0/\rho_0 c = 1.21$ in.^{2}/hr, which is approximately 20 percent less than the experimental value of 1.5 in.^{2}/hr in the range 0 deg −32 deg F. However, the prediction is based on properties at room temperature, and is close to the measured diffusivity of 1.25 in.^{2}/hr in the 32–70 deg F range (see Fig. 6).

We now return to the problem of predicting the effect of voids on the diffusivity. The very idealized conductivity model of a statistically homogeneous material with large voids, equation (10), together with equation (15) for density, yields for an isotropic body,

$$0 \le \kappa \le (1 + \alpha_v/2)^{-1}\kappa_0 \simeq (1 - 0.50\alpha_v)\kappa_0 \tag{18}$$

This void size in solid propellant is comparable to that of the AP particles, and therefore equation (18) is not strictly valid. However, it is to be noted that the conductivity of the AP particles given in the table and that of the rubber-aluminum matrix, equation (17), are relatively close; in fact, if they were the same, equation (18) would be rigorously valid. In order to demonstrate that this estimate is quite good for the case at hand, we will use equation (13) to obtain the bounds on conductivity and then diffusivity; this equation places no restriction on the relative size of the ammonium perchlorate and voids. In terms of the present notation, we have that $k_1 = k_{ap}$, $k_2 = k_{ra}$, and $\alpha_2 = \alpha_{ra}{}^0(1 - \alpha_v)$, where $\alpha_{ra}{}^0$ is the volume fraction of the rubber-aluminum matrix without voids. Use of equation (13) and the properties, along with the assumption $\alpha_v \ll 1$, yields

$$0 \le k \le 0.89(1 - 1.45\alpha_v)\frac{k_{ap}}{k_0}k_0 = (1 - 1.45\alpha_v)k_0 \tag{19}$$

In terms of diffusivity, $0 \le \kappa \le (1 - 0.45\ \alpha_v)\kappa_0$, which is very close to equation (18) as originally suggested in view of the closeness of the conductivities k_{ra} and k_{ap}.

The uniaxial state of stress in the specimens causes the voids to be ellipsoidal, rather than spherical, with the major axis parallel to the stress direction [1]. Since the voided composite is not actually isotropic it is of interest to evaluate the effect of voids using a model which accounts for this orthotropy. The cylindrical hole model, equations (11) and (12), provides a simple limit case for the orthotropic composite conductivity. In terms of diffusivity, equation (11) becomes

$$0 \le \kappa \le (1 + \alpha_v)^{-1}\kappa_0 \simeq (1 - \alpha_v)\kappa_0 \tag{20}$$

which may be compared with the result for spherical voids, equation (18).

For 3 percent void content (in sample No. 2), the sphere and cylinder models yield, respectively, a 1.5 percent and 3 percent decrease in the upper bound diffusivity. In contrast, the specimen's diffusivity decreased by 9.6 percent; similar results are found for sample No. 3, with the measured decrease in diffusivity being more than twice the predicted decrease. However, the upper bounds, in predicting a very small change, are certainly much better estimators than the lower bound of zero.

Let us now consider another limit case, which will provide a better lower bound on diffusivity than zero. Consider the propellant to be completely dewetted, with all the AP particles entirely inside the voids and not in contact with the rubber-aluminum binder. Furthermore, assume the cavities are cylindrical, of varying size, and randomly distributed in accordance with the composite cylinders assemblage model [17]; the upper bound on transverse conductivity, equation (11), with $k_m = k_{ra}$ is then the exact value [17]. Thus, for transverse heat flow

$$k = \frac{k_{ra}}{k_0}\frac{1 - \alpha_v}{1 + \alpha_v}k_0 = 0.77\frac{1 - \alpha_v}{1 + \alpha_v}k_0 \tag{21}$$

and for axial heat flow, $k_a = 0.77(1 - \alpha_v)\ k_0$. Translating these results into diffusivity, with $\alpha_v \simeq \alpha_{ap}$ since full dewetting is assumed, we find $\kappa \simeq 0.6$ in.^{2}/hr and $\kappa_a \simeq 1.0$ in.^{2}/hr, which provide idealized lower bounds on the actual transverse and axial diffusivities. It is important to observe that these lower bounds are very sensitive to the amount of aluminum in the binder (through its effect on k_{ra}), and they would be much smaller if there were no aluminum. On this basis, it is expected that the diffusivity of a composite with little or no aluminum, such as the PBAN propellant, would be more strongly affected by vacuole dilatation than CTPB propellant.

Predictions for the PBAN propellant (1 percent aluminum powder and 72 percent ammonium perchlorate) are summarized as follows: $\rho_0 = 0.06$ lb/in.^{3}, $c = 0.29$ Btu/lb-deg F, $k_{ra} = 0.10$ Btu/hr-ft-deg F, $k_0 = 0.22$ Btu/hr-ft-deg F, and $\kappa_0 = 1.0$ in.^{2}/hr. Equation (18) retains its present form and the remaining ones become, respectively, $0 \le k \le 1.22\ (1 - 1.45\ \alpha_v)k_0$, $k_a = 0.46\ (1 - \alpha_v)k_0$, $\kappa = 0.28$ in.^{2}/hr, and $\kappa_a = 0.49$ in.^{2}/hr, where the latter two values are idealized lower bounds.

Results for the PBAN propellant are shown in Fig. 4. The predicted κ_0 (1.0) is a little less than the observed value shown in the figure, probably due in part to the uncertainty in rubber conductivity. The propellant exhibited a 21 percent decrease in diffusivity under a strain of 20.4 percent; the corresponding dilatation is 4 percent [19]. This change in diffusivity is approximately 5 times the void content, whereas the average CTPB diffusivity change is 2.7 times the void content. This greater change in diffusivity for

[4] These properties vary somewhat from polymer to polymer, and therefore the values shown are, at best, only representative.

the PBAN propellant is as expected because of its lower aluminum content compared to the CTPB propellant.

Time-Temperature Effects. Figs. 5 and 6 show the center temperature in two different sizes of CTPB samples over a wide temperature range. The diffusivity of the CTPB propellant above T_g is estimated to vary from 1.89 to 1.21 in.^{2}/hr over the temperature range -105 to $+140$ deg F, as shown in these figures. Furthermore, a comparison of Figs. 5 and 6 shows that the nearly ten-fold difference in heating rate did not have any significant effect on diffusivity above -105 deg F.

All of the curves in Figs. 5 and 6 labeled "theory" with the diffusivity value shown were predicted using equation (3). The remaining curves, with a value for specific heat ratio shown, were calculated using constant values for k and ρ and the following discontinuous specific heat: $c = c_g$ for $T < T_g$ and $c = c_e$ for $T > T_g$, where c_g and c_e are constant; this special case is suggested by equation (9).

For the purposes of estimating T_g only the specific heat was assumed to change in the range -105 to -320 deg F; as another idealization, this change was assumed to be uniform over the sample, and occur when the center temperature reached T_g. The value of T_g was estimated by observing the point at which the measured temperature first departed from a constant diffusivity curve (the dashed line in each figure). The ratio c_e/c_g was then found by trial-and-error; the values of $c_e/c_g = 1.40$ and 1.16 indicated in the figures provide the best agreement between the theory and the measurements below T_g. The estimated values of T_g are -121 deg F and -148 deg F, corresponding to Figs. 5 and 6, respectively.

The estimated specific heat ratio in the first case seems high for the following reason. The specific heat ratio for the rubber itself is typically between two and three. Taking this ratio as three, we calculate the specific heat ratio for the CTPB propellant to be 1.12, which is close to the value of 1.16 found from Fig. 6. The discrepancy between the theoretical and experimental specific heat ratios is probably a result of the uncertainty in the magnitude of the horizontal shift needed to superpose the experimental and theoretical curves, both of which are relatively flat in the constant diffusivity region. A variation in estimated values of T_g and c_e/c_g is also to be expected because of the differences in sizes and resulting differences in temperature distribution and cooling rates. However, it is significant that both cooling curves are accurately predicted using piecewise-constant diffusivities, and that approximately the same value for glassy diffusivity ($\kappa_g \simeq 1.4 \times 1.6 \simeq 1.16 \times 1.89 \simeq 2.2$ in.^{2}/hr) is inferred from the two sizes of CTPB samples.

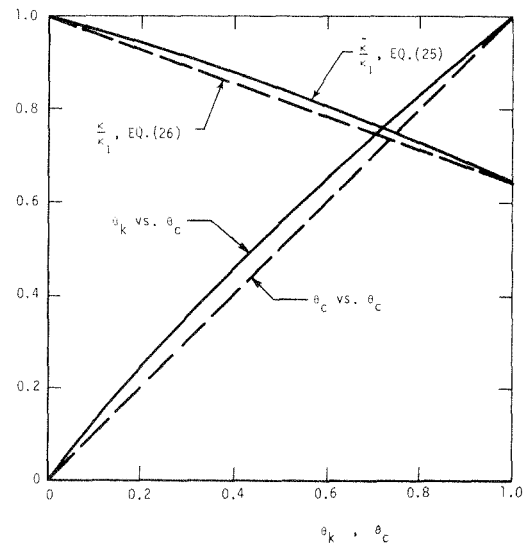

Fig. 7 Comparison of diffusivity and temperature functions for variable conductivity and specific heat

Temperature-Dependence of Thermal Diffusivity of CTPB Propellant. There are sufficient data in Figs. 5 and 6 to estimate the variation of diffusivity with temperature. Specifically, this may be accomplished by matching the theoretical curve for constant diffusivity to the early portion of each experimental curve; for this portion, the specimen's temperature is close to the initial temperature except at the boundary. It is found that the following linear function fits the data very well over the range $-105 \leq T \leq 76$ deg F:

$$\kappa = 1.50 - 0.0037T \text{ in.}^2/\text{hr}, \tag{22}$$

where T is in deg F; also, for $76 < T \leq 140$ deg F: $\kappa = 1.21$ in.^{2}/hr. With the exception of the diffusivity value for $T > 76$ deg F, the data for the large specimen in Fig. 6 were used to derive equation (22) because these experimental results are less sensitive to thermocouple misalignment than those in Fig. 5.

Without having separately measured values of specific heat or thermal conductivity, it cannot be determined if the temperature dependence of diffusivity is due to conductivity or specific heat or both. However, from a practical standpoint, this distinction is not important as we shall show that the transient temperature distribution is relatively insensitive to the source of the temperature dependence.

As one limit case which is consistent with equation (22) assume the conductivity is given by

$$k = k_1 - (k_1 - k_2)\left(\frac{T - T_1}{T_2 - T_1}\right) \tag{23}$$

over the temperature range $T_1 \leq T \leq T_2$, where k_1, k_2 = conductivity at temperature T_1 and T_2, respectively. Also, for this case ρc is assumed constant. Substitute conductivity equation (23) into the isotropic version of equation (1) and, after some manipulation, there results

$$\nabla^2\theta_k = \frac{1}{\tilde{\kappa}}\frac{\partial\theta_k}{\partial t} \tag{24}$$

where

$$\theta_k \equiv \frac{k^2 - k_1^2}{k_2^2 - k_1^2}, \quad \tilde{\kappa} \equiv \kappa_1\sqrt{1 - (1 - \frac{k_2^2}{k_1^2})\theta_k} \tag{25}$$

and $\nabla^2 \equiv \partial^2/\partial x^2 + \partial^2/\partial y^2 + \partial^2/\partial z^2$. Note also that $\kappa_1 = k_1/\rho c$.

As a second limit case, assume that conductivity is constant but that the diffusivity is given by

$$\kappa = \kappa_1 - (\kappa_1 - \kappa_2)\left(\frac{T - T_1}{T_2 - T_1}\right) = \kappa_1\left[1 - (1 - \frac{\kappa_2}{\kappa_1})\theta_c\right] \tag{26}$$

Thus, all temperature dependence of diffusivity is assumed to be due to the quantity ρc for this case. The governing equation for temperature is written in the form

$$\nabla^2\theta_c = \frac{1}{\kappa}\frac{\partial\theta_c}{\partial t} \tag{27}$$

where θ_c is a nondimensional temperature,

$$\theta_c \equiv \frac{T - T_1}{T_2 - T_1} \tag{28}$$

Let us now consider the following problem. A body is initially at a uniform temperature T_1, and is then suddenly subjected to a constant boundary temperature T_2. We are interested in the relative difference in temperature predicted by equation (24) for constant ρc and by equation (27) for constant k. Equations (25) and (28) show that the initial condition and boundary condition are the same for both cases; viz, $\theta_k = \theta_c = 0$ in the body at $t = 0$ and $\theta_k = \theta_c = 1$ on the boundary when $t > 0$. Thus, the solutions $\theta_k = \theta_k(x, y, z, t)$ and $\theta_c = \theta_c(x, y, z, t)$ would be identical if the diffusivity $\tilde{\kappa}$, equation (25), were the same as diffusivity κ, equation (26). These diffusivities are not exactly equal for equal values of θ_k and θ_c; but they are very close to one another for the CTPB propellant, where $k_2/k_1 = \kappa_2/\kappa_1 = 0.646$, as shown in Fig. 7. This figure shows that the maximum difference is approximately 0.02 κ_1. If, in order to estimate an upper bound on the difference $\theta_k - \theta_c$, we replace $\tilde{\kappa}$ in equation (25) by $\tilde{\kappa} = \kappa + 0.02\,\kappa_1 \simeq 1.02\,\kappa$, then

the solutions are equal except for a time-scale factor; viz. $\theta_k(x, y, z, 1.02t) = \theta_c(x, y, z, t)$.

Inasmuch as the temperature is a monotonically increasing function of time for this problem, we conclude $\theta_k \geq \theta_c$ for each set of variables (x, y, z, t). Moreover, assuming the maximum slope $d\theta_c/d(\log t)$ is approximately equal to or smaller than obtained for the constant diffusivity case (e.g., Fig. 1), we find $\text{MAX}(\theta_k - \theta_c) \simeq 0.015$. In order to relate this difference to relative temperature change, equation (28), we combine equations (23) and (25) to find

$$\theta_k = \theta_c[2 - (1 - \frac{k_2}{k_1})\theta_c]/(1 + \frac{k_2}{k_1}) \tag{29}$$

which is drawn in Fig. 7 for the CTPB propellant. Using $\text{MAX}(\theta_k - \theta_c) \simeq 0.015$ and the maximum difference from equation (29) yields $\text{MAX}[(T)_{c_p=\text{constant}} - (T)_{k=\text{constant}}] \simeq 0.04[T_2 - T_1] \simeq 7$ deg F, corresponding to a total temperature increase of 181 deg F. When the body is cooled instead of heated, in which T_2 is the initial temperature and T_1 is the boundary temperature, it is a simple matter to show that the maximum temperature difference is equal in magnitude (but of opposite sign) to the foregoing estimate (viz. 7 deg F).

Thus, we observe that the predicted temperature is relatively insensitive to the source of the temperature dependence of diffusivity since, for the extreme cases studied, the difference is at most 4 percent of the total temperature change. It should be emphasized, however, that this conclusion does *not* imply the solutions for the two variable diffusivity cases are close to the prediction for constant diffusivity. Indeed, the diffusivity itself exhibits a 56 percent change over the temperature range used in the analysis.

Conclusions

The diffusivity of solid propellant has been found to vary noticeably with respect to both temperature and applied strain. For temperatures above the glass transition value T_g, a maximum error of 20 percent of the total temperature change could result for the particular propellants and thermal conditions studied if the temperature dependence of diffusivity is not taken into account; this maximum error is larger if T_g lies between the minimum and maximum temperatures. The maximum error due to strain-induced vacuole formation is approximately 10 percent for strains up to 20 percent. (Had the diffusivity been found by matching theory and experiment at $\theta/\theta_0 = 0.1$ or 0.9, say, rather than at the 50 percent temperature-change point, $\theta/\theta_0 = 0.5$, the discrepancies caused by temperature and strain dependence of diffusivity could be greater.)

These errors in predicted temperature, which could occur if a constant diffusivity were used in the analysis, may lead to much larger percent errors in predicted stresses if the temperature is sufficiently low, as pointed out by San Miguel [9]; this sensitivity of stress to temperature is the result of the rapid increase in stiffness that occurs for a viscoelastic material as the temperature is reduced. With solid propellant structures, the strain distribution is generally nonuniform. Therefore, without further study, it is not apparent if it is actually necessary to account for strain-dependence of diffusivity when conducting a structural integrity analysis, especially when one considers the uncertainty in service environments and the fact that failure of a viscoelastic material is dependent on the entire stress-time history and not on just the instantaneous stress [23]. If failure predictions turn out to be sensitive to changes in thermal properties, then it may be necessary to determine them by conducting a much more extensive series of tests on strained specimens than described herein; e.g., determine diffusivity (or conductivity) and specific heat over a wide temperature range, in which the temperature gradient is kept small for each test.

Acknowledgment

The authors are indebted to Messrs. S. W. Beckwith, L. E. Lewis, and G. A. Walton for their very able assistance in conducting the experiments and reducing the data. They would also like to acknowledge helpful discussions on [6] with A. San Miguel, whose suggestions were incorporated into the present paper.

This work was sponsored by the Office of Naval Research under Contract No. N00014-68-A-0308-0003 with Texas A&M University.

References

1 Farris, R. J., "The Influence of Vacuole Formation on the Response and Failure of Filled Elastomers," *Trans. Soc. Rheol.*, Vol. 12, No. 2, 1968, pp. 315-334.

2 Wolpert, S. M., Weitz, A., and Wunderlich, B., "Time-Dependent Heat Capacity in the Glass Transition Region," *J. Polym. Sci. A-2*, Vol. 9, 1971, pp. 1887-1905.

3 Pasquino, Anne D., and Pilsworth, Malcolm N., "The Thermal Conductivity of Polystyrene, Oriented and Unoriented, With Measurements of the Glass-Transition Temperature," *J. Polymer Science B-2*, Vol. 3, 1964, pp. 253-255.

4 Ferry, J. D., *Viscoelastic Properties of Polymers*, Wiley, New York, Second ed., 1970.

5 Wunderlich, B., Bodily, D. M., and Kaplan, M. H., "Theory and Measurements of the Glass-Transformation Interval of Polystyrene," *J. Appl. Phys.*, Vol. 35, No. 1, 1964, pp. 95-102.

6 Schapery, R. A., and Martin, R. E., "On the Thermal Diffusivity of Filled Elastomers," Rept. No. MM 72-2, Mechanics and Materials Research Center, Texas A&M University, June 1972.

7 Schapery, R. A., "Application of Thermodynamics to Thermomechanical, Fracture, and Birefrigent Phenomena in Viscoelastic Media," *J. Appl. Phys.*, Vol. 35, No. 5, 1964, pp. 1451-1465.

8 San Miguel, Anthony, and McCarten, R. M., "Heat Transfer in Solid-Propellant Motors," *Journal of Spacecraft and Rockets*, Vol. 9, No. 3, Mar. 1972, pp. 129-130.

9 San Miguel, Anthony, "Prediction of Temperature Gradients in Solid Propellants," *Journal of Spacecraft and Rockets*, Vol. 7, No. 5, May 1970, pp. 533-538.

10 Leeming, H., et al., "Solid Propellant Structural Test Vehicle and Systems Analysis," Final Report, Air Force Rocket Propulsion Lab., AFRPL-TR-70-10, Mar. 1970.

11 Carslaw, H. S., and Jaeger, J. C., Conduction of Heat in Solids, Oxford Press, Second ed., 1959.

12 Schapery, R. A., "A Theory of Nonlinear Thermoviscoelasticity Based on Irreversible Thermodynamics," Fifth U. S. Nat. Cong. Appl. Mech., ASME, 1966, pp. 511-530.

13 Kerner, E. H., "The Electrical Conductivity of Composite Media," *Proc. Phys. Soc.*, Series B, Vol. 69, 1956, p. 802.

14 Hashin, Z., "Assessment of the Self Consistent Scheme Approximation: Conductivity of Particulate Composites," *J. Comp. Mat.* Vol. 2, No. 3, 1968, pp. 284-300.

15 Hashin, Z., and Shtrikman, S., "A Variational Approach to the Theory of the Effective Magnetic Permeability of Multiphase Materials," *J. Appl. Phys.*, Vol. 33, No. 10, 1962, pp. 3125-3131.

16 Hashin, Z., "Theory of Fiber Reinforced Materials," NASA, Langley Research Center, Contact NAS1-8818, Nov. 1970.

17 Donea, J., "Thermal Conductivities Based on Variational Principles," *J. Comp. Mat.*, Vol. 6, 1972, pp. 262-266.

18 Gorring, Robert L., and Churchhill, Stuart W., "Thermal Conductivity of Heterogeneous Materials," *Chemical Engineering Progress*, Vol. 57, No. 7, July 1961, pp. 53-59.

19 Schapery, R. A., "Studies on the Nonlinear Viscoelastic Behavior of Solid Propellant," Rept. No. MM 2803-73-2, Mechanics and Materials Research Center, Texas A&M University, May 1973.

20 Rosser, W. A., Jr., Inami, S. H., and Wise, H., "Thermal Diffusivity of Ammonium Perchlorate," *AIAA Journal*, Vol. 4, No. 4, 1966, pp. 663-666.

21 Furukawa, George T., McCoskey, Robert E., and King, Gerard J., "Thermal Properties of Some Butadiene-Styrene Copolymers," *Journal of Research of National Bureau of Standards*, Vol. 50, No. 6, June 1953, pp. 357-365.

22 Marks, L. S., *Mechanical Engineers'* Handbook, McGraw Hill, New York, Fifth ed., 1951.

23 Knauss, W. G., "The Mechanics of Polymer Fracture," *Appl. Mech. Rev.*, ASME, Vol. 26, No. 1, 1973, pp. 1-17.

H. J. Sneck
Professor,
Rensselaer Polytechnic Institute,
Troy, N. Y. Mem. ASME

D. H. Brown
Environmental Systems Engineer,
General Electric Co.,
Schenectady, N. Y. Mem. ASME

Plume Rise From Large Thermal Sources Such as Dry Cooling Towers

An experimental study of the dry buoyant plume rise from a finite size source into a stably stratified atmosphere has been performed. The test results are correlated with a recently published theory, which is shown to be applicable to a wide range of discharge conditions. Methods for predicting the height of the stratified plume accumulation, as well as the maximum rise height of the plume are presented.

Introduction

An increasing concern for the quality of the environment will undoubtedly cause the electric utility industry to seriously consider using more direct means of depositing power plant thermal discharge into its ultimate sink, the atmosphere. For this reason cooling towers, long used in Europe for this purpose are now receiving considerable attention in this country.

There is naturally some concern about the behavior of the plume emitted from the top of these towers since in many cases it is heavily laden with moisture evaporated from within the tower. The presence of an atmospheric inversion is known to have a particularly unfavorable influence on the plume's ability to rise for two reasons. First, an inverted atmosphere is a stable one which inhibits any vertical motion of itself, or anything injected into it. Second, ground based inversions usually occur in the absence of winds whose turbulence promotes the dispersion of the plume. If the rise height of a dry plume can be predicted under these limiting conditions, a conservative estimate of the plume's performance under general field conditions can be made.

There are relatively few large scale atmospheric phenomena which have so far lent themselves to laboratory size simulation. Plume rise, however, is the exception. Several investigators have produced buoyant plumes in the laboratory using liquids and very small sources. A very limited amount of data is available from these experiments, all of it for plumes with large ratios of rise height to source radius. Analytically these plumes may be treated as point sources if minor corrections are made to locate the virtual source.

Because cooling towers are usually large sources, the ratio of plume height to source radius for them is expected to be much smaller than those produced by previous experiments. Point source solutions, which do not take into account the size of the source, cannot be applied with accuracy to such plumes. From an analytical and experimental standpoint the investigation of the mechanics of a dry plume's rise from a finite size source in a statically inverted atmosphere is the logical first step toward remedying this deficiency.

Previous Work

There are a number of formulas which have been proposed to predict plume rise. Because of the highly complex phenomena involved all of them use empiricism in varying degrees. Briggs [1][1] has written an excellent review of plume rise theories and equations, comparing them with available data where possible.

Almost all of the studies of plume rise to date have been concerned with the efflux from stacks assuming that they can be treated mathematically as point sources. Very few of the plume rise formulations lend themselves readily to the modifications which are necessary to accommodate a finite size source. Among these, the most appealing is that suggested by Morton, Taylor, and Turner in their now classic paper [2]. Their semi-empirical model is probably the simplest possible mathematical description embodying all the essential phenomenological features. Its utility has been verified for buoyant liquid plumes rising in a static, density stratified environment [1], and for gaseous jets rising in unstratified ambient air [3]. Briggs [1] and Turner [4] have discussed the results of these experiments in light of the Morton theory, and they conclude that this simple model is satisfactory for the small size sources tested. Those few analytical papers which have dealt specifically with cooling tower plume's have used this model or some version of it, e.g., Hanna [5].

Turner notes in his survey that the empirical entrainment coefficient introduced by Morton has been found experimentally to vary considerably, contradicting Morton's assumption that it was a universal constant. Experimental results to be cited later in this paper also confirm the variability of this coefficient. Recently, Fox [6] has extended the analysis of Morton and shown that the entrainment coefficient varies along the plume's path. It is this

Contributed by the Heat Transfer Division for publication in the JOURNAL OF HEAT TRANSFER. Manuscript received by the Heat Transfer Division, March 3, 1973.

[1] Numbers in brackets designate References at end of paper.

improved version of the basic Morton theory which will be used in this paper to model the plume's behavior.

Statement of Problem

The analytical and experimental investigation which follows has the following objectives:

1 To determine the pertinent dimensionless modeling parameters for a dry plume's rise.

2 To adapt the Morton-Taylor-Turner-Fox analytical model to finite sources and solve the resulting equations in terms of the modeling parameters.

3 To design and construct an experimental facility which can be used to test the validity of the analytical model.

4 To compare the analytical predictions with results of experiments performed in the facility.

5 To investigate experimentally various methods of increasing plume rise.

Equations of Motion

Briggs [1] has rewritten the original Morton equations in a form such that dependent variables appear as integral averages over the plume cross section at any elevation. When written in this form it is not necessary to prescribe the velocity or temperature distribution within the plume except at the source.

The continuity equation using Briggs' notation takes the form

$$\frac{dV}{dZ} = -2bu_0 \tag{1}$$

where the vertical mass flux integral is defined by

$$V \equiv \frac{1}{\rho_0 \bar{\pi}} \int_0^b 2\pi r \rho w dr \tag{2}$$

and u_0 is the entrainment velocity of the "edge" of the plume, b.

The conservation of energy is expressed by the equation

$$\frac{dF}{dZ} = -GV \tag{3}$$

where

$$F \equiv \frac{1}{\rho_0 \bar{\pi}} \int_0^b 2\pi r \left(\frac{\theta - \theta_0}{\theta_0}\right) g \rho w dr \tag{4}$$

$$G \equiv \frac{g}{\theta_0} \frac{d\theta_0}{dZ} = \frac{g}{T_0}[\Gamma - \lambda] \tag{5}$$

In these relations θ is the potential temperature and G is defined according to Morton [2, 6].

The vertical momentum equation can be written as

$$\frac{d}{dZ}(WV) = \frac{F}{W} \tag{6}$$

using the integral definition for the flux of momentum

$$WV \equiv \frac{1}{\rho_0 \bar{\pi}} \int_0^b 2\pi r \rho w^2 dr \tag{7}$$

Equation (6) was obtained assuming that the potential temperature deficiency and the vertical velocity are controlled by the same turbulent diffusion process and are therefore similarly distributed over the plume cross section [7, 8].

The energy and momentum equations can be combined to eliminate explicit dependence on Z as follows

$$\frac{dF}{d(WV)} = -\frac{GWV}{F} \tag{8}$$

If G is constant, then

$$F^2 + G(WV)^2 = \text{constant}$$

where the constant on the right-hand side is most conveniently evaluated at the source, i.e., at the tower-top. This algebraic expression can be used in lieu of either the energy or momentum equation.

Entrainment Hypothesis

The set of three independent equations derived in the foregoing are not "closed" in the sense that there are more unknowns than equations. Inspection of the three equations suggests that the appropriate place to effect the closure is in the continuity equation, since only it contains the term bu_0. To this end, Morton [2] suggested that the entrainment velocity u_0 is proportional to a characteristic vertical velocity within the plume. Briggs phrased the same hypothesis somewhat differently stating that u_0 is proportional to $-W$, and b is proportional to the horizontal characteristic length $(V/W)^{1/2}$. These assumptions reduce the continuity equation to the form

$$\frac{dV}{dZ} = 2\alpha(WV)^{1/2} \tag{9}$$

where α is the empirical entrainment coefficient mentioned earlier.

Equation (9), along with the energy and momentum equations are formally equivalent to those given by Morton [2] for his "top-hat" profiles which are a special kind of "similar" distribution.

This particular entrainment hypothesis is actually the simplest possible representation of the highly complex process of the turbulent mixing of the ambient air with the plume gas. Some au-

Nomenclature

b = radius of plume
B = radius of plume at source
D = ΔZ vertical increment of height
$F = \frac{1}{\rho_0 \pi} \int_0^b 2\pi r \frac{\theta - \theta_0}{\theta_0} g\rho w dr$ vertical buoyancy flux integral
$F(0)$ = $g\,UB^2\Delta$ vertical buoyance flux integral at source
$\mathrm{Fr}^2 = \frac{W^{5/2}V^{1/2}}{F}$ squared local densimetric Froude number
G = stability parameter = $\frac{g}{\theta_0}\frac{d\theta_0}{dZ} = \frac{g}{T_0}[\Gamma - \lambda]$
p = absolute pressure
p_0 = atmospheric pressure
r = radial coordinate
T_0 = absolute atmospheric temperature
u_0 = horizontal plume entrainment velocity at b
U = plume velocity at source
$V = \frac{1}{\rho_0 \pi} \int_0^b 2\pi r \rho w dr$ vertical mass flux integral
w = temporal mean vertical velocity component
$WV = \frac{1}{\pi \rho_0} \int_0^b 2\pi r \rho w^2 dr$ vertical momentum flux integral
W = WV/V vertical momentum velocity
Z = vertical coordinate
ΔZ = incremental vertical height
Z_b = zero buoyancy height
Z_c = average height of stratified plume accumulation
Z_m = zero momentum height
Z_n = height at which entrainment becomes zero
$\alpha, \alpha_1, \alpha_2$ = dimensionless entrainment coefficients
Γ = adiabatic lapse-rate
$\Delta = \frac{\theta(0) - \theta_0}{\theta_0}$ dimensionless temperature increment at source
θ = plume potential temperature
θ_0 = potential temperature of ambient
$\theta(0)$ = plume potential temperature at source
λ = dry air lapse rate
ρ_0 = density of atmospheric air

thors have justified it on dimensional grounds and the fact that the plume's turbulence is self-generated by its own vertical motion. A number of other rationalizations are also possible [8]. The hypothesis' limitations have been investigated in [8], by Ricou and Spalding [3], and also by Abraham [9].

Morton's contention that α is a "universal constant" appears to be based on the fact that the entrainment coefficient for nonbuoyant jets has been found to be essentially constant. In fact, Morton's hypothesis is a localization of the jet entrainment equation. It envisions every cross section of the plume as the origin of a new plume with differential length dZ, each with an initial (local) value of entrainment proportional to $(WV)^{1/2}$. If all elemental length jets had the same entrainment coefficient, α would be a universal constant.

While a number of investigators have since recognized that the entrainment coefficient was in reality not a constant, Fox [6] appears to be the first to develop a rational extension of Morton's theory which allows for its variability. To do this he appended a higher order velocity-moment equation, a mechanical energy equation, to the set of equations used by Morton. This equation written in Briggs' notation is

$$C_1 \frac{d}{dZ}(W^2V) = 2F + C_2 W^3 \left(\frac{V}{W}\right)^{1/2} \tag{10}$$

where C_1 and C_2 are unknown constants. When this equation is combined with the momentum equation the result is

$$\frac{dV}{dZ} = \left[\frac{2F}{W^{5/2}V^{1/2}}\left(1 - \frac{1}{C_1}\right) - \frac{C_2}{C_1}\right](WV)^{1/2} \tag{11}$$

Comparing this with the mass conservation equation yields the entrainment coefficient:

$$\alpha = \alpha_1 + \frac{\alpha_2}{(F_r)^2} \tag{12}$$

where α_1 and α_2 are constants, where the local squared densimetric Froude number is defined by

$$F_r^2 = \frac{W^{5/2}V^{1/2}}{F} \frac{W^2}{F/(WV)^{1/2}} \tag{13}$$

Equation (11) can be considered to be an analytical verification of Morton's basic entrainment hypothesis that the entrainment rate is proportional to $(WV)^{1/2}$. The theory of Fox, however, replaces equation (9) with

$$\frac{dV}{dZ} = 2\left(\alpha_1 + \frac{\alpha_2 F}{W^{5/2}V^{1/2}}\right)(WV)^{1/2} \tag{14}$$

while retaining equations (3) and (6).

Characteristic Dimensionless Numbers

Two vertical plume dimensions are of interest. The first is the height to which the plume rises before the plume loses upward buoyancy as a result of ingesting ambient air. This will occur when $F = 0$. At this point the upward momentum will be a maximum. Thereafter the plume's inertia will carry it upward as its buoyancy turns negative. The plume will reach its zenith when its momentum vanishes. Two dimensionless numbers can be defined in terms of these characteristic heights,

$$\frac{Z_b}{B}, \text{ where } F = 0 \qquad \frac{Z_m}{B}, \text{ where } WV = 0$$

where B is the tower-top radius. It will be assumed that the velocity and temperature distributions at the source or tower-top are uniform, so that

$$U = \frac{\text{tower-top flow rate}}{\text{tower-top area}} = W(0)$$

$$B = \left(\frac{V(0)}{W(0)}\right)^{1/2} = b(0)$$

$$F(0) = gUB^2\Delta$$

The momentum equation (6) yields a dimensionless number known as the densimetric Froude number. At the tower-top this number squared is

$$F_r^2(0) = \frac{U^2}{gB\Delta}$$

The energy equation (3) yields a dimensionless number which measures the relative importance of the flux of buoyant energy to the rate of work done on the plume by the atmosphere. Again, at the tower-top this number is defined as

$$\frac{BG}{\Delta g}$$

The definition of the tower-top conditions permit the constant of the energy-momentum equation (8) to be evaluated with the result that

$$F^2 + G(WV)^2 = |F(0)|^2 + G(WV(0)|^2$$

$$= (gUB^2\Delta)^2 + G(B^2U^2)^2 \tag{15}$$

In the calculations to be described later it is somewhat more convenient to use a dimensionless number which does not contain the tower-top radius B, so $U^2/gB\Delta$ will be replaced with

$$G\left(\frac{U}{\Delta g}\right)^2 = \left(\frac{U^2}{gB\Delta}\right)\left(\frac{BG}{\Delta g}\right)$$

Plumes are expected to be geometrically similar when α_1, α_2, $GB/\Delta g$ and $G(U/\Delta g)^2$ are equal, i.e.,

$$\frac{Z}{B} = f\left[\alpha_1, \alpha_2, \frac{BG}{\Delta g}, G\left(\frac{U}{\Delta g}\right)^2\right]$$

This expression is the basis of experimental modeling of plumes in the laboratory and it also provides a compact means of presenting the analytical results.

Obviously, the ability to create relatively large values of λ in the laboratory is crucial to reducing the scale of the phenomena to laboratory sizes. Vertical temperature measurements in almost any room will show that gradients of the order of 1 deg F per ft are achieved naturally. Thus, it appears that a modest size chamber with a controlled vertical temperature gradient of reasonable size can be used to model the plume rise from a finite source in the expected operating range of large cooling towers.

Solutions of the Equations of Motion

For given values of α_1, α_2, G, and initial conditions at the tower-top, a very simple computer program can be written which will indicate the values of Z where F and WV go to zero. The three differential equations of motion are of the intial-value type and first order. The slopes of equations (14) and (3) were differentiated a second time to produce expressions for curvature along the

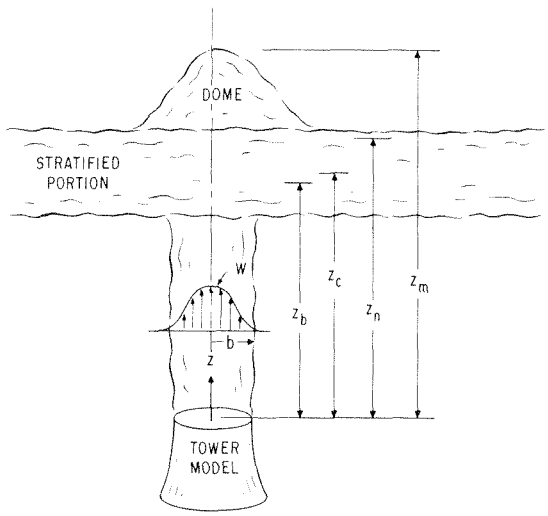

Fig. 1

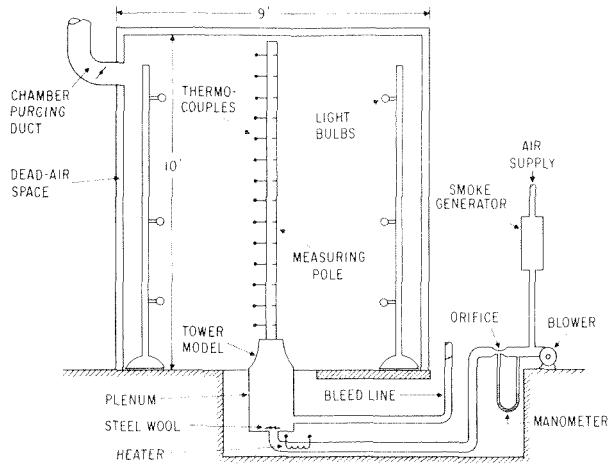

Fig. 2

path to further enhance the integration steps. At each increment V and F were evaluated by integration, and then WV was evaluated using equation (15). The height where F becomes zero was noted as Z_b, and thereafter when WV goes to zero the height Z_m is noted and the integration terminates.

Test Facilities and Procedures

The laboratory investigation of plume rise was done in an especially constructed wood-framed chamber approximately nine ft square horizontally and ten ft high (Fig. 2). The ceiling and three side walls were covered by polyethylene sheets on both the inside and outside. The fourth side wall was covered with wall board and painted flat-black to provide a background for observing the plume rise. A portion of the wall opposite the painted wall was covered with plexiglas.

Four poles were placed inside the chamber carrying light bulbs with wattages ranging from 150 to 25. By adjusting the number, wattage, and elevation of the bulbs on each of the four poles, relatively large temperature gradients were realized.

The tower itself was modeled using standard flow nozzles. Two different size nozzles were used with tower-top diameters of 7 and 10 in. The tops of these nozzles stood 11 and 15 in. above the floor level of the chamber.

Each tower was operated in the presence of two values of G equal to approximately 0.06 and 0.08 sec^{-2}. Two tower-top velocities were used with each size nozzle. The 7 in. dia nozzle velocities were approximately 1.4 and 1.9 ft per sec while the 10 in. tower was operated with velocities 0.75 and 0.95 ft per sec. For both towers Δ was varied over the range 0.005 to 0.03. With this range of variables the tower-top values of the dimensionless modeling numbers fell in the ranges

$$10^{-2} < G\left(\frac{U}{\Delta g}\right)^2 < 10, \quad 10^{-2} < \left(\frac{GB}{\Delta g}\right) < 10^{-1}$$

The air supplied to the tower was pumped by a radial flow blower through a calibrated metering orifice. On its way to the tower the air passed through an electrical heater and into a plenum beneath the floor of the chamber. Smoke, produced by rapidly burning grass-cuttings in a forced-draft combustor, was introduced into the supply system just before the metering orifice. By throttling the blower and heating the air, a warm, smoky discharge was delivered to the nozzle by the plenum at a known flow-rate.

A nearly uniform velocity and temperature distribution at the tower-top was obtained by placing screening or steel wool over the duct entrance to the plenum.

The temperature gradient within the chamber was determined by reading ten thermocouples spaced one ft apart on a vertical pole placed near the tower. This same pole was marked off in one inch increments so that the maximum and minimum smoke levels could be observed through the plexiglass panel.

Four thermocouples were placed in the throat of the nozzle (i.e., at the tower-top), one in the center and three in the form of a triad. These were used to determine the tower-top plume temperature and also its uniformity. A fifth thermocouple was attached to the outside of the tower at the tower-top level to read the ambient temperature in the chamber at this level. From these five thermocouples reading the value of Δ was evaluated.

Before each series of tests the position and wattage of the pole-supported light bulbs was adjusted by trial and error to achieve the desired straight line temperature increase from bottom to top within the chamber.

Comparison of the Experimental Results With the Theory of Morton

The visible portion of a smoke filled plume has three clearly discernable heights that are noted in Fig. 1. Directly over the source there is a dome-like region where the plume reaches its greatest height. The plume gas which spills out of this dome is negatively buoyant and so sinks to lower levels before reaching neutral buoyancy. As a result two other levels can be observed which are the upper and lower stratified boundaries or edges of the sidewise spreading plume. It is between these two levels that the effluent from the source is eventually stored in a stable environment.

The lower level is remarkably smooth and easily delineated from the clear ambient air below it. The upper level is somewhat more ragged. These levels, between which the plume stratifies horizontally, are well established very quickly after the flow from the source is initiated. All three heights were measured for each experiment.

All of the previous laboratory investigations of plume rise [2, 6, 9] have been primarily concerned with the height of the dome-like portion of the plume directly above the source. The recommended values of Morton's constant α based on measurements of this height range from 0.08 to 0.12 [4]. One of the initial objectives of this investigation was to determine whether these published values of Morton's α which had been obtained using liquids and small size sources were also valid for large size sources and gases. (Fox's work had not yet been published at this point). A program was written to evaluate α from the test data using the Morton theory i.e., equations (3), (6), and (9). Some seventy-five individual tests were processed. The results are shown in Fig. 3 for both the 7 in. and 10 in. towers.

Nonbuoyant jets with large initial velocities are known to possess a potential-core starting at the source. These cores persist to about 8 to 10 dia downstream. It was initially thought that the variation of α exhibited in Fig. 3 could be attributed to the influence of such a core. To test this conjecture a test was made with an array of thermocouples placed along the plume center line. A core would carry gas at the discharge temperature high into the chamber. The results of a typical test are shown in Fig. 4, where it is evident that the center-line temperature decreases monotonically along the plume's path. Apparently the large, vigorous turbulent eddies generated by the plume as it issues from the source prevent the persistence of the core usually associated with the finer grained turbulent structure of jets.

It is evident from the experimental results that the Morton entrainment coefficient is in reality an average over the length of the plume which unfortunately depends, at least implicitly, on the length of the plume.

Comparison of the Experimental Results With the Theory of Fox

The variation of α exhibited in Fig. 3 is not at all surprising when viewed in the light of Fox's analysis which was published midway through this study. His equations contain two coefficients which would appear to give the theory greater freedom to fit the experimental data. This is really not the case, however,

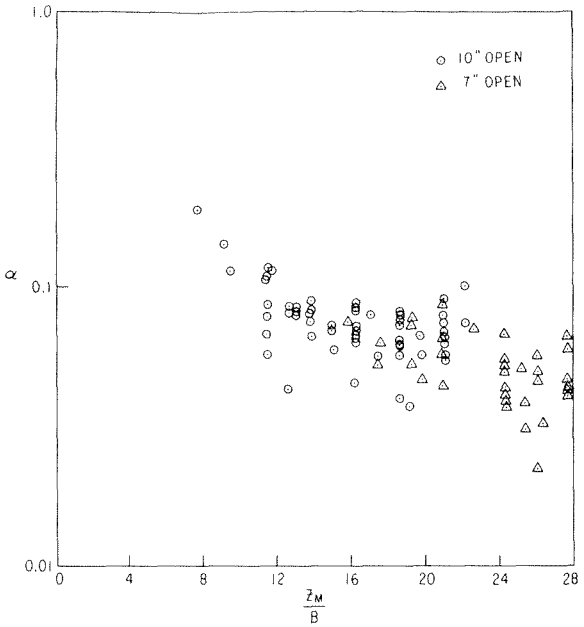

Fig. 3

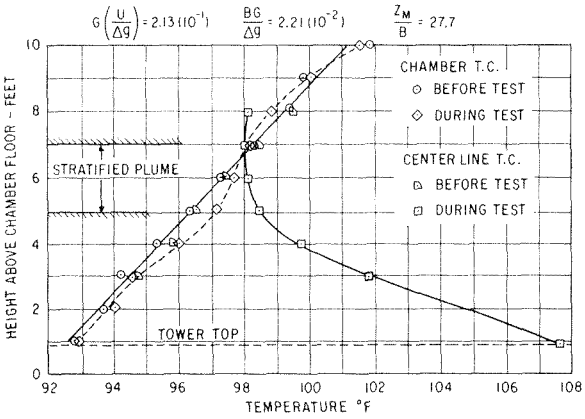

Fig. 4

since α_1 and α_2 are not arbitrarily introduced into the theory, but are intimately related to certain physical features of the plume.

The coefficient α_2 was calculated by Fox to be 0.5 assuming Gaussian velocity and density difference profiles. He found, however, that correlation between the theory and his experimental results were rather insensitive to the choice of α_2. The coefficient α_1 was not calculated by Fox since it requires accurate knowledge of the radial distribution of the turbulent shear stress. Based on experimental evidence he recommended a value for α_1 of 0.0378. Since his results are for Gaussian profiles, while the equations used here are akin to Morton's top-hat equations, these values require adjustment. If Fox's values for α_1 and α_2, as well as his local squared densimetric Froude number, are converted to top-hat notation via the same rules which transform Morton's Gaussian analysis into a top-hat analysis (references [4, 7]), then the entrainment equation becomes

$$\alpha \approx 0.0535 + \frac{0.25}{(F_r)^2}$$

Although these transformations are not strictly legitimate (since the kinetic energy fluxes are not matched), they do indicate the relative sizes of α_2 and α_2 for top-hat profiles.

With these initial estimates of α_1 and α_2, the computer program was used to compute Z_m/B, and then the value for α_1 was varied to bring the computed maximum rise and the experimental results into good agreement over the entire range of test values. The best fit occurs when $\alpha_1 = 0.044 \pm 0.002$ and $\alpha_2 = 0.25$. The fit is not particularly sensitive to small changes in these values.

The values of α_1 and α_2 recommended by Fox were obtained from experiments which he performed with initial densimetric Froude numbers of the order of 100, which resulted in Z_m/B of the order of 100. These test conditions would yield jet-like behavior, and the Froude number should have relatively little effect. As a result Fox concluded that the Morton theory was sufficiently accurate for predicting the maximum penetration of the plume. Fig. 3 indicates that this is not the case for buoyancy dominated plumes.

Fig. 5 shows that Fox's theory compares very well with the data obtained in air for modest Z_m/B. According to Fox's own experiments the theory is also applicable to liquid jets with very large Z_m/B. Further evidence of its general applicability is provided by the results of Abraham [11]. He performed tests using liquids in the same manner as Fox, obtaining Z_m/B of the order of 70 for $<G(U/\Delta g)^2 < 10$. His test points are also shown in Fig. 5, and they too correlate very well with the theory. Abraham's tests are for initial densimetric Froude numbers of the order of 10, which classifies them as much less jet-like than those of Fox.

Hirst [12] has performed a rather thorough investigation of the earlier stages of the plume's development, i.e., the zone of flow establishment. On the basis of his findings, he tentatively recommends an entrainment equation for a vertical plume of the form

$$\frac{-bU_0}{BV} = (0.0204 + 0.0284\,\frac{b}{B})[1.0 + \frac{34}{(F_r)^2}]$$

Considering the rather slow growth of the plume's radius, the right-hand side of this equation reduces to approximately the form of equation (12) with coefficients reasonably close to those found in the foregoing. The left-hand side of the Hirst equation, however, defines an entrainment coefficient based on the initial momentum rather than the local momentum. The local momentum generally first increases and then decreases to zero at the plume's zenith. For this reason, it is not possible to compare the two hypotheses directly except to say that on a gross basis they are roughly comparable. It would be worth noting again that the derivation of the Brigg's version of the Morton equations (1) to (6) requires only that the potential temperature deficiency and the vertical velocity be "locally similar," i.e., change in-step from top-hat to Gaussian.

Based on the experimental evidence obtained here, it appears that the entrainment theory of Fox accurately predicts the maximum rise height of a buoyant plume over a very wide range of operating conditions including plumes that would normally be considered to have relatively large development zones. The Fox theory thus exhibits a distinct advance over the earlier theory of Morton, which it modifies.

Maximum and Minimum Heights of the Stratified Portion of the Plume

Observations of many plumes, generated under widely different tower-top and chamber conditions, indicate that the plume's shape generally remains the same, varying only in size but not in proportion. If all plumes are indeed geometrically similar, the ratios of their characteristic dimensions must be consistent.

The roughly seventy-five open-tower data sets were processed to determine if geometric similarity actually exists. Two ratios were evaluated, both using the maximum rise height as a reference. It was found that the ratio of the top edge of the stratified portion of the plume to the maximum height of the dome were normally distributed with an average of 0.77 and a standard deviation of ±0.055. A similar computation of the ratio of the lower edge of the stratified portion of the plume to the maximum height of the dome also yielded a normal distribution with an average of 0.415 and a standard deviation of ±0.055.

These same heights can be scaled from the drawings and photographs in the papers by Fox and Abraham [6, 11]. Approxi-

mately the same ratios are obtained even for the jet-like plumes of Fox.

Based on the consistency of these ratios it is safe to assume that once the maximum height of a plume is known the height of the stratified portion can be estimated with reasonable accuracy using these simple proportions.

Significance of the Zero Entrainment Height

A rather remarkable feature of the Fox entrainment coefficient is that it may become negative if the value of $1/Fr^2$ becomes sufficiently negative. The height at which this occurs is above the zero buoyancy level.

Abraham [11] has also proposed a theory which allows for negative entrainment. His analysis predicts transition from positive to negative entrainment at a fixed value of 81 percent of the maximum plume height. Calculations using the Fox theory show that this ratio varies from 0.68 to 0.79 over the range of the test data. Over the entire range of computed values this ratio varies more with Z_m/B when $G(U/\Delta g)^2 < 1.0$ than when $G(U/\Delta g)^2 > 1.0$. For jet-like plumes $G(U/\Delta g)^2/BG/\Delta g \gg 1.0$, this ratio is very nearly independent of Z_m/B and is close to Abraham's predicted value.

The fact that the top edge of the stratified plume is approximately at the computed zero entrainment height suggests that gas is expelled from the plume in the upper dome portion, and then sinks due to its negative buoyancy and forms a stratified layer whose top is roughly at the zero entrainment level. Fox cautions against attaching too much physical significance to the theoretical predictions near the plume top. This is because the entrainment velocity approaches minus infinity as the vertical velocity approaches zero at Z_m. Obviously, the theory cannot describe the details of the very last stages of the plume's rise, but it may still be sufficiently correct to predict the gross behavior of the dome region.

If ingestion ceases and only outflow from the plume can occur, the temperature of the plume in the dome would be expected to remain more or less constant. Fig. 4 indicates that this is true of the center-line temperature, at least. Typically, the center-line temperature is found to be close to the local ambient temperature at the level of the top edge of the stratified portion of the plume, and remains almost constant at that value up into the dome portion. Consequently there can be very little mixing of the plume with the surroundings between these levels, even though there is still considerable turbulence associated with the motion.

Significance of the Zero Buoyancy Height for $G(U/\Delta g)^2 \leq 1.0$

The calculated values of the zero buoyancy height Z_b to maximum height Z_m ratio are very nearly constant for $G(U/\Delta g)^2 < 1.0$.

This ratio varies between 0.50 and 0.60 depending on the maximum height, which places the zero buoyancy level roughly mid-

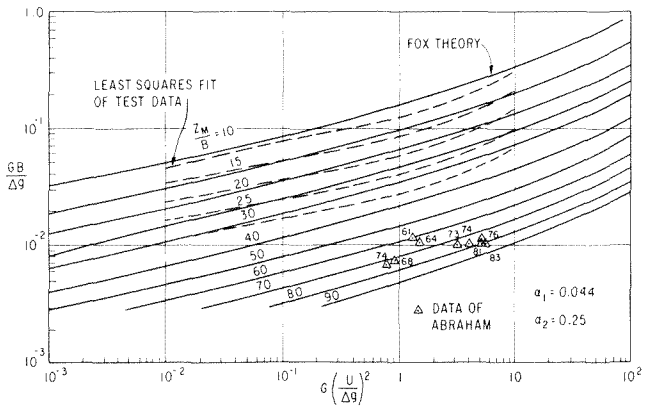

Fig. 5

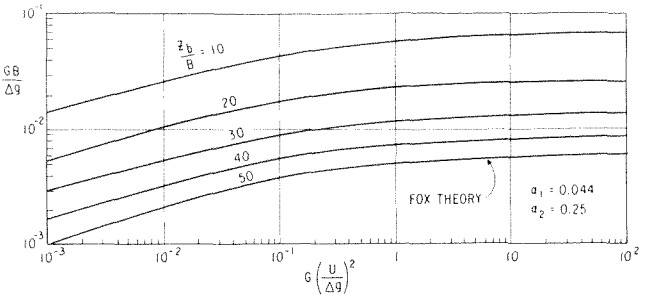

Fig. 6

way between the bottom edge and the top edge of the stratified portion of the plume.

Based on this information a simple model can be constructed for the formation of the stratified portion of the plume. Assume that negative entrainment in the dome portion maintains the average dome density at the value which it had at the zero entrainment level. Temperature measurements within the stratified portion of the plume indicate that it has a nearly linear vertical temperature distribution with a slightly smaller slope than the ambient as shown in Fig. 4. If the stratified plume and the ambient air are essentially isolated from each other, then the condition for vertical equilibrium in a global sense requires the density of the stratified portion to equal the density of the displaced ambient air. Presuming that the dome gas descends from the dome into the stratified portion while conserving its average density, the elevation of the midplane of the stratified portion is given by

$$Z_c = Z_n + \left.\frac{F}{VG}\right|_{Z_n} \tag{16}$$

where Z_n is the height at which the entrainment coefficient vanishes. Computations show that this height is almost exactly equal to Z_b.

Significance of the Zero Buoyancy Height for $G(U/\Delta g)^2 > 1.0$

When the plume is jet-like near the source and G is constant, the rate of entrainment is essentially constant between the source and the zero buoyancy level. This behavior can be demonstrated by normalizing equation (8) as follows:

$$\frac{1}{G}\left(\frac{F}{B^2U^2}\right) + \left(\frac{WV}{B^2U^2}\right)^2 = 1 + \frac{1}{G}\left(\frac{g\Delta}{U}\right)^2 - 1 \tag{17}$$

Since B^2U^2/F is initially very small and approaches zero as $Z \to Z_b$, then $WV \approx BU$ and $\alpha \to \alpha_1$. Equation (9) therefore reduces to

$$\frac{dV}{dZ} \approx 2\alpha_1 BU$$

or

$$V \cong 2\alpha BUZ + B^2U$$

Equation (3) becomes

$$\frac{dF}{dZ} = -GV \approx -G(2\alpha_1 BUZ + B^2U)$$

or

$$F = gU^2B\Delta - G(\alpha_1 BUZ^2 + B^2UZ)$$

At $Z = Z_b$, $F = 0$ so that

$$\frac{GB}{g\Delta} = \frac{1}{\alpha_1 \frac{Z_b}{B}\left[\frac{Z_b}{B} + \frac{1}{\alpha_1}\right]} \tag{18}$$

This solution for large $G(U/\Delta g)^2$ compliments that of Morton [2] for $G(U/g\Delta)^2 \to 0$. The asymptotic values of the Z_b/B curves in Fig. 6 can be checked using this formula.

Below the zero buoyancy level the plume is almost identical to a nonbuoyant jet. The height Z_b is generally well below the bottom edge of the stratified plume when $G(U/\Delta g)^2 > 1.0$, so that once again there is probably little re-entrainment of the stratified plume into the rising plume. In this instance, the center line between the upper and lower edge of the stratified plume lies above the calculated value of Z_c when the previous model describing the formation of the stratified plume is adopted here.

The stratified plume is obviously lighter than predicted by this model. The additional buoyancy could be achieved by mixing with the ambient air during the fall-out process, although this explanation is purely speculative.

Conclusions

1 Experiments performed in an environmental chamber in the presence of an inversion show that the entrainment coefficient for a dry plume is not a universal constant, but is a variable.

2 The experimental results are in good agreement with the variable entrainment coefficient theory proposed by Fox.

3 The characteristic plume rise-heights above a finite size source in a constant lapse rate inversion are functions of the two tower-top dimensionless numbers.

4 The ratio of the height of the upper edge of the stratified portion of the plume to the maximum (dome) height of the plume is found to be very nearly constant for all plumes.

5 The height at which the entrainment is predicted to become negative is almost coincident with the height of the upper edge of the stratified portion of the plume.

6 The ratio of the height of the lower edge of the stratified portion of the plume to the maximum (dome) height is found to be nearly constant.

7 For buoyancy dominated plumes the predicted zero buoyancy height is very nearly coincident with the average height of the stratified portion of the plume.

References

1 Briggs, G. A., *Plume Rise,* AEC Critical Review Series, TID-25075, Clearinghouse for Federal Scientific and Technical Info., N.B.S., U. S. Department of Commerce, 1969.

2 Morton, B. R., Taylor, G. I., and Turner, J. S., "Turbulent Gravitational Convection From Maintained and Instantaneous Sources," *Proceedings Royal Society,* (London), Series A., Vol. 234, 1956, p. 1.

3 Ricou, F. P., and Spalding, D. B., "Measurements of Entrainment by Axisymmetrical Turbulent Jets," *Journal of Fluid Mechanics,* Vol. 11, 1961, p. 21.

4 Turner, J. S., "Buoyant Plumes and Thermals," *Annual Review of Fluid Mechanics,* Vol. 1, 1969.

5 Hanna, S. R., "Rise and Condensation of Large Cooling Tower Plumes, *Journal of Applied Meteorology,* Vol. 11, Aug. 1972, p. 793.

6 Fox, D. G., "Forced Plume in a Stratified Fluid," *Journal of Geophysical Research,* Vol. 75, No. 33, 20 Nov. 1970, p. 6818.

7 Morton, B. R., "Buoyant Plumes in a Moist Atmosphere," *Journal of Fluid Mechanics,* Vol. 2, 1957, p. 127.

8 Sneck, H. J., and Brown, D. H., "Cooling Tower Discharge Buoyant Plume Rise Through Atmospheric Inversions," General Electric TIS Report 71-C-311, 1971.

9 Abraham, G., "Entrainment Principle and Its Restrictions to Solve Problems of Jets," *Journal of Hydraulic Research,* Vol. 3, No. 2, 1965, p. 1.

10 Daily, J. W., and Harleman, D. R. F., *Fluid Dynamics,* Addison Wesley, 1966, p. 422.

11 Hirst, E., "Analysis of Buoyant Jets Within the Zone of Flow Establishment," ORNL-TM-3470, Aug. 1971.

V. L. Eriksen
Assistant Director, Research and Development, Harrison Radiator Division, General Motors Corp., Lockport, N. Y.

R. J. Goldstein
School of Mechanical and Aerospace Engineering, University of Minnesota, Minneapolis, Minn.

Heat Transfer and Film Cooling Following Injection Through Inclined Circular Tubes

Film cooling effectiveness and heat transfer are measured downstream of injection through discrete holes into a turbulent mainstream boundary layer. Air is injected through both a single hole and a row of holes spaced at three-diameter intervals and inclined at an angle of 35 deg to the main flow. There is little difference between the heat transfer coefficient with blowing and without blowing at low blowing rates (mass flux ratios). In fact, at low blowing rates, injection is found to decrease somewhat the heat transfer coefficient from that measured without blowing. As the mass flux ratio increases past unity, the heat transfer coefficient increases especially with injection through a row of holes. The peak heat transfer is usually found at the edge of the spreading jets (i.e., between two holes). At a blowing rate near two, the lateral average of the heat transfer is as much as 27 percent higher than the heat transfer with no blowing. The increase in heat transfer is attributed to the interaction between the jets and the free stream, causing high levels of turbulence.

Introduction

With film cooling, a coolant is ejected locally through the wall of a structure in such a way that it creates a film along the surface, thereby protecting the structure from exposure to a hot gas stream. In a typical film cooling application, the problem is to predict or measure the relationship between the wall temperature distribution and the heat transfer. The geometry and mainstream and secondary flows may be fixed or may be permitted to vary. One may require the wall temperature for a given set of conditions or optimize the geometry, mainstream or coolant flow while maintaining the wall temperature below some critical value.

The heat transfer coefficient with film cooling is defined as

$$h = \frac{q}{T_w - T_{aw}} . \tag{1}$$

The adiabatic wall temperature is often presented in dimensionless form as the film cooling effectiveness. For low speed, constant property flow the film cooling effectiveness is given by

$$\eta = \frac{T_{aw} - T_r}{T_2 - T_r} . \tag{2}$$

The heat transfer coefficient, as defined by equation (1), is often relatively close to the value without injection. The adiabatic wall temperature, however, can vary considerably and is more difficult to predict. Most film cooling studies are therefore concerned with the determination of the film cooling effectiveness.

A large number of parameters are involved in film cooling. The shape of the channel through which the coolant flows and the angle of injection can be altered for both two-dimensional and three-dimensional film cooling. In addition, the spacing between holes and the number of rows of holes can be varied for the three-dimensional case. The film cooling process also depends on the dimensionless parameters describing the main flow as well as the coolant flow. The ratios of the velocities and densities of the flows are especially important. These quantities are often grouped into the parameters known as the blowing rate (mass flux ratio) and momentum flux ratio. The blowing rate is expressed as

$$M = \frac{\rho_2 U_2}{\rho_\infty U_\infty} \tag{3}$$

and the momentum flux ratio is given by

$$I = \frac{\rho_2 U_2^2}{\rho_\infty U_\infty^2} \tag{4}$$

The subscript 2 denotes the coolant flow; and the subscript ∞ represents the main flow. Other important parameters are the Reynolds number of the main flow, the turbulence in the main flow and the thickness of the mainstream boundary layer at the point of injection. If large temperature differences are employed, the variation of properties throughout the flow field is important.

Two-dimensional film cooling has been studied rather extensively [1],[1] the bulk of the work being concerned with the determination of the film cooling effectiveness. Heat transfer studies

Contributed by the Heat Transfer Division for Publication in the JOURNAL OF HEAT TRANSFER. Manuscript received by the Heat Transfer Division, July 19, 1973. Paper No. 74-HT-V.

[1] Numbers in brackets designate References at end of paper.

with two-dimensional film cooling indicate that injection has little effect on the heat transfer coefficient for blowing rates less than 0.5. At higher blowing rates, the heat transfer coefficient near the slot is usually observed to be somewhat higher than without injection. Its value in this region seems to be quite dependent on injection geometry. Further downstream, the heat transfer coefficient approaches the value without injection.

Three-dimensional film cooling has not been studied as extensively as two-dimensional film cooling. Most of the earlier research was concerned with determination of the film cooling effectiveness [2-13] and is reviewed in [1, 14, and 15].

Information concerning heat exchange between the wall and gas flow in a three-dimensional film cooling environment is sparse. Metzger and co-workers [16, 17] measured the average heat transfer for injection through a row of holes at angles of 20 and 60 deg and hole spacings of 1.55 and 1.71 diam. Results for injection at 20 deg do not differ significantly from results without injection. For 60-deg injection the average heat transfer coefficient was higher than that without injection in the region immediately downstream of the holes but soon decreased to the same value. Burggraf and Huffmeier [19] measured average heat transfer downstream of injection through single and staggered double rows of holes at an angle of 35 deg. For blowing rates less than 1.0, they did not find significant differences between results with and without injection. At blowing rates of 1.5 and 2.0, the heat transfer was greater than occurs without injection. The heat transfer near injection at these higher blowing rates is correlated by the equation for heat transfer without injection when the mass velocity is replaced with the coolant mass velocity.

In the present investigation local values of the heat transfer coefficient are determined for injection of heated and unheated jets of air through holes. Secondary injection is through a row of tubes spaced at three diameter intervals across the span and inclined at an angle of 35 deg to the main flow (Fig. 1). A few measurements are conducted using a single tube from the row. The outlets of the tubes are flush with the surface on which measurements are conducted. A constant heat flux is generated electrically at the test surface and local surface temperatures are measured. Experiments are conducted at moderate temperatures. Differences in the density ratio and variation of fluid properties throughout the flow field should be taken into consideration when using the results for high temperature applications.

Apparatus

The experiments are conducted in a subsonic, open-circuit wind tunnel. The air mainstream in the tunnel flows from the room through an entrance section, the test section, a diffuser, a blower, and finally through a silencer before being discharged outside the building. The secondary, or injected air, is supplied by the building air compressor. The flow rate is controlled by a pressure regulator and needle valve and is measured with a thin plate orifice meter. Temperature fluctuations introduced by the compressor are eliminated by passing the air through a long coiled copper tubing submerged in a large tank of water. The air is heated in a stainless steel tube around which heating tapes are wrapped. The heated air flows into a plenum chamber that provides uniform flow to the injection tubes. This system is described in greater detail elsewhere [5, 6, 9].

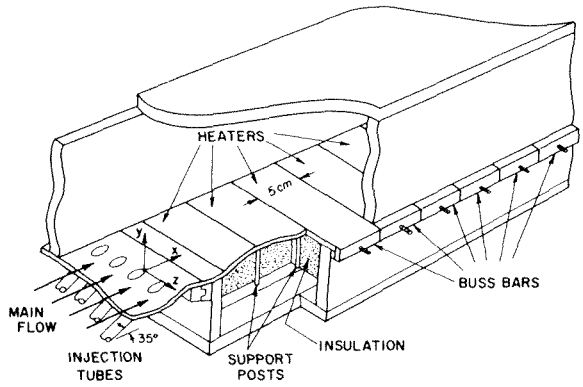

Fig. 1 Test section

The test section is 20.3 cm by 20.3 cm in cross section, and 153.8 cm long. The bottom wall is constructed of Textolite (linen based phenolic manufactured by General Electric) and the top and side walls are constructed of Plexiglas and Textolite. The test section consists of three segments.

The first segment of the test section contains an impact probe and wall pressure tap to determine the free stream velocity, a thermocouple probe to measure the temperature of the main flow, and two thermocouple junctions embedded in the bottom wall to determine the free stream recovery temperature. The bottom wall is thin (0.32 cm thick) to allow it to respond quickly to any temperature changes in the main flow. A 0.064 cm dia boundary layer trip wire is located on the bottom wall approximately 3.8 cm downstream of the contraction section. An additional sandpaper-type trip is located on the bottom surface on the contraction section about 24 cm upstream of its outlet. This additional trip is included to provide a thicker boundary layer than was used in previous studies [5-10].

The next segment contains a row of five tubes at an angle of 35 deg to the direction of main flow as shown on Fig. 1. The 1.18 cm ID tubes, spaced at three-dia intervals, are cemented into the

Nomenclature

D = diameter of injection tube
h = heat transfer coefficient defined using difference between wall and adiabatic wall temperature, see equation (1)
$\bar{h}$ = heat transfer coefficient defined using difference between laterally averaged wall and adiabatic wall temperature, see equation (5)
h_0 = heat transfer coefficient without injection
I = momentum flux or dynamic pressure ratio, $\rho_2 U_2^2/\rho_\infty U_\infty^2$
M = blowing rate, $\rho_2 U_2/\rho_\infty U_\infty$
q = wall heat flux
$\bar{q}$ = laterally averaged wall heat flux
Re_D = Reynolds number using free stream velocity and injection tube diameter ($\mathrm{Re}_D = \rho_\infty U_\infty D/\mu_\infty$)
S = slot width for two-dimensional film cooling and equivalent slot width for three-dimensional film cooling, $S = \pi D/(4$ times center-to-center hole spacing)
T_{aw} = adiabatic wall temperature
$\overline{T_{aw}}$ = laterally averaged adiabatic wall temperature
T_r = mainstream recovery temperature
T_w = wall temperature
$\overline{T_w}$ = laterally averaged wall temperature
T_2 = injection temperature
T = mainstream temperature
U_2 = mean velocity in injection tube
U_∞ = mainstream velocity
X = distance downstream of downstream edge of injection hole, see Fig. 1
Y = distance normal to test surface, see Fig. 1
Z = lateral distance from center of injection hole, see Fig. 1
δ^* = boundary layer displacement thickness
δ_0^* = boundary layer displacement thickness at the upstream edge of the injection hole
η = film cooling effectiveness, see equation (2)
μ_∞ = dynamic viscosity of mainstream gas
ρ_2 = density of injected gas
ρ_∞ = density of mainstream gas

bottom plate of the segment and ground flush to the tunnel surface. In order to reduce heat conduction from the tube to the plate, the injection plate is thinned from the back side to a thickness of 0.16 cm in the region surrounding the tubes. Thermocouples are soldered on the outside of the injection tubes. The inlet ends of the injection tubes join the plenum chamber mentioned in the foregoing. All tubes are surrounded with fiberglass and styrofoam insulation.

The assembly consisting of the bottom plate of the injection segment, the tubes, tunnel floor, and the plenum chamber is free to slide in the lateral direction. The holes through which the secondary gas flows can thus be located at any lateral position in the tunnel and a single row of thermocouples can be used to measure wall temperature distributions downstream of injection.

The third segment of the test section contains the test plate. Eighteen stainless steel electrical heaters are cemented to the Textolite plate as shown on Fig. 1. The test plate is designed to minimize heat losses out the back and conduction within the wall. Heat should then be transferred to the flow at the location where it is produced and the local heat transfer coefficient can be determined from the local wall temperature. In reality, there are heat losses due to conduction out the back and radiation from the test surface. There are also small errors in the measured local wall temperature due to heat loss through the thermocouple leads and conduction within the wall. Corrections that are applied to the measurements to take these factors into account are discussed in [15]. The 0.16 cm plate that the heaters are cemented to is backed by 5 cm of styrofoam insulation. The stainless steel heaters are 0.025 mm thick by 5.04 cm in the flow direction. They span the entire width of the test plate and are spaced 0.04 mm apart. Copper buss bars are soldered to the ends of the heater strips.

Power for the heaters is provided by two 900 w direct current power supplies wired in series. The current passes through a shunt and through each of the heaters that are all wired in series. Current flow is determined from the voltage drop across the calibrated shunt and the heat generated is calculated from the current flow and the resistance of the heaters. Wall temperatures are measured by 36 gage iron-constantan thermocouples that are embedded in the Textolite plate behind the heater. The thermocouple junction is electrically insulated from the heater.

Operating Conditions and Procedures

Steady-state conditions exist during all tests. For injection of heated jets, a temperature difference of approximately 55 deg C is used, resulting in a density ratio of approximately 0.85. When unheated jets are used, the density ratio is 1.0. The range of variables studied is as follows: free stream velocity U = 30.5 − 61.0 m/sec, Reynolds number based on free stream velocity and injection tube diameter Re_D = 0.22 × 10^5 − 0.44 × 10^5, displacement boundary layer thickness at the point of injection δ_0^* = 0.14 − 0.21 cm, blowing rate M = 0.1 − 1.95 and wall heat flux q = 0 − 0.20 W/cm^2, resulting in differences between the wall temperature and adiabatic wall temperature in the range 0 − 33 deg C. The wall heat flux is not varied as an independent variable, but only to provide approximately the same temperature difference between the wall and mainstream flow as the free stream velocity is varied.

The secondary air temperature, T_2, is taken as that measured by thermocouples six dia upstream of the tube outlet. The difference between this temperature and the mainstream temperature varies by approximately one percent across the row of holes, most of this variation being between the outside tubes and those adjacent to them. Variation in excess temperature across the inner three tubes is much less than one percent. Velocity at the outlet of the tubes varies by approximately one percent across the row.

Velocity profiles measured at locations both on and off the center line of the test surface and at different positions along the length of the test section without injection are found to be in good agreement with each other and with the fully developed turbulent profile reported by Klebanoff and Diehl [20]. At the point of injection, the boundary layer is approximately 45 percent thicker than in the previous 35 deg injection studies. Boundary layer growth on the walls of the test section causes the main flow velocity to increase by approximately six percent over the length of the test section.

The experimentally determined heat transfer coefficient without secondary injection is used as a reference for tests with injection. The injection holes are covered with thin tape to provide a smooth surface and the wind tunnel is operated at the same velocities as for tests with secondary injection. This heat transfer coefficient depends not only on the free stream velocity and position along the heated wall, but it is also a weak function of the hydrodynamic starting position from where the velocity boundary layer starts to grow to the location where heating of the wall begins. Comparison of the experimental results without injection with theory [21] shows that the theory and results agree quite well at downstream locations where the influence of hydrodynamic starting length is small [15].

The primary flow in the wind tunnel, the secondary flow through the injection tubes and the heat flux from the test surface can be changed to conduct the experiments under a variety of conditions. Adiabatic wall temperatures are determined by operating the tunnel with injection of heated secondary air and no heat flux from the test surface. Heat transfer coefficients are determined with a heated wall and with either heated or unheated injection air. In the former case, the heat transfer coefficient is defined using the difference between the heated wall temperature and the adiabatic wall temperature that was measured under the same flow conditions. With unheated injected air, the heat transfer coefficient is defined using the difference between the heated wall temperature and the free stream recovery temperature. Two separate sets of measurements are necessary to determine the heat transfer coefficient by the first method whereas only one set is necessary for the second. Because these two techniques yield essentially the same results [15], the second method is used for most of the measurements.

Results

Film Cooling Effectiveness. Adiabatic wall temperature measurements for injection through the row of holes display the same trends with X/D, Z/D, and blowing rate as found in previous studies [7, 8] so complete film cooling effectiveness distributions are not included here. Variation of the center-line film cooling effectiveness with Reynolds number and boundary layer thickness at the point of injection is shown on Fig. 2. Included on this figure are results for injection through both a single hole and a row of holes at an angle of 35 deg to the main flow [5–9]. No significant difference has been found between center-line results for injection through this single hole or the row of holes for $M \leq 1.0$ [7, 8]. Data from [5–9] does not permit independent consideration of the variation of film cooling effeviveness with Reynolds number and boundary layer thickness as these two quantities are related. Inclusion of data from the present investigation does permit such a comparison as an additional boundary layer trip is used here. The boundary layer is now thicker at free stream velocities equal to those in [5–9]. The center-line film cooling effectiveness is seen to increase as δ_0^*/D is decreased at a fixed value of the Reynolds number. When the boundary layer at the point of injection is thin, the jet encounters a greater "force" (due to the higher fluid momentum close to the wall) upon leaving the injection tube than for a thicker boundary layer and is turned more, remaining closer to the wall and increasing the film cooling effectiveness. The variation is not as great at the larger values of δ_0^*/D as for the smaller values of δ_0^*/D in [7 and 8]. Fig. 2 also indicates that the film cooling effectiveness seems to increase with the Reynolds number, Re_D, but it is difficult to determine the amount of the increase with the limited amount of data on the figure. If anything, one might expect the opposite effect because of greater mixing at higher Reynolds numbers.

Heat Transfer Coefficient. The heat transfer coefficient downstream of a single 35 deg hole is presented on Fig. 3 for M = 0.5, 0.97, 1.46, and 1.95. The heat transfer is within approximate-

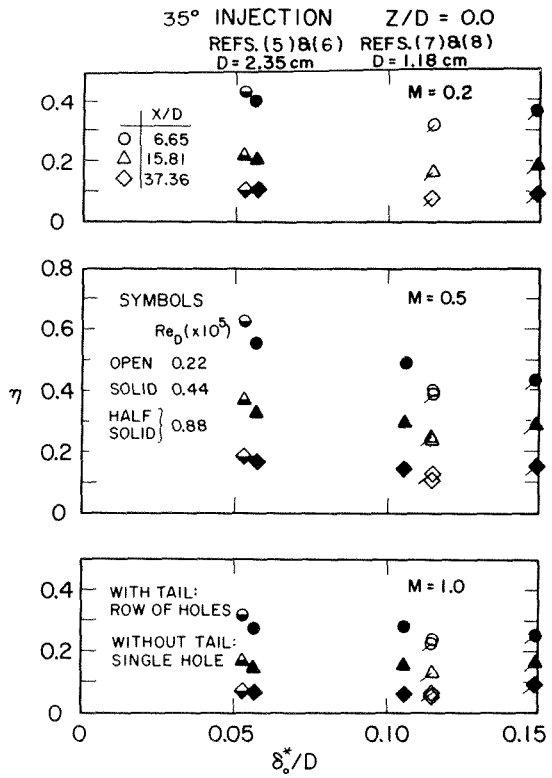

Fig. 2 Variation of center-line film cooling effectiveness with displacement boundary layer thickness

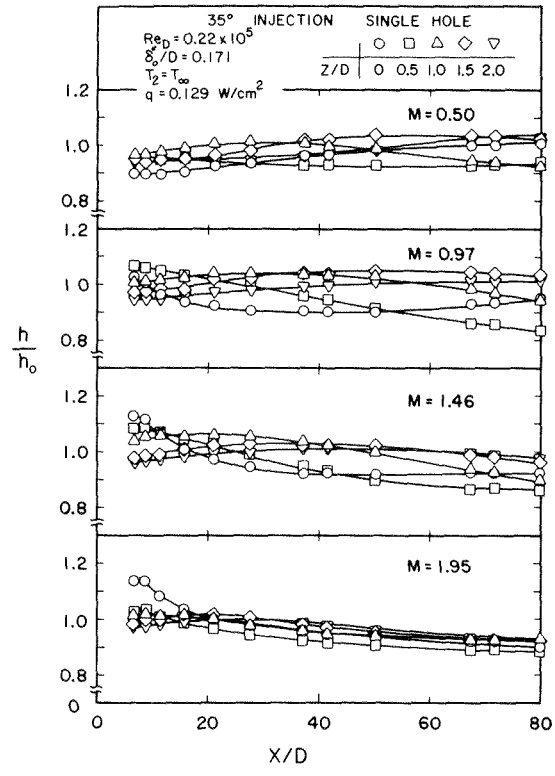

Fig. 3 Heat transfer coefficient downstream of injection through a single hole, $Re_D = 0.22 \times 10^5$

ly 15 percent of the value without injection for all of these blowing rates. It is often less than that found without injection, especially at the lower blowing rates and far downstream for the higher blowing rates. The injected mass apparently thickens the boundary layer, thus decreasing the heat transfer coefficient in these areas. This effect is countered by increased heat transfer due to turbulence at locations where the edge of the jet and the mainstream interact. The heat transfer coefficient is increased near the hole where the jet and mainflow interact strongly at the higher blowing rates. At the lower blowing rates, interaction between the jet and the mainstream cause the heat transfer coefficient to be higher near the edges of the jet than on the jet center line.

Results from [15] indicate that the heat transfer coefficient for injection through a hole at an angle of 90 deg to the mainflow is approximately 15–20 percent greater than the value without injection at $X/D = 7.33$ and still 10–15 percent greater at $X/D = 35.44$ for $M > 0.5$. Comparison of these values with Fig. 3 shows the heat transfer coefficient for normal injection to be considerably larger than for 35 deg injection. A jet injected at 35 deg has a velocity component in the direction of the main flow; a jet injected normal to the mainstream has no initial velocity component in the direction of main flow. For normal injection there is therefore more interaction between the jet and the mainstream, resulting in higher turbulence levels and a higher heat transfer coefficient than for 35 deg injection. This effect is in agreement with film cooling effectiveness results of [6] where lower effectiveness values and increased spreading of the jet for normal injection when compared to 35 deg injection are attributed to greater interaction between the jet and mainstream during normal injection.

The heat transfer coefficient downstream of injection through a row of 35 deg holes spaced at three dia intervals across the span is presented on Figs. 4 and 5 for Reynolds numbers of 0.44×10^5 and 0.22×10^5, respectively. Except for center-line values near the point of injection, the heat transfer coefficients for $M = 0.1$ and $M = 0.2$ (Fig. 4) fall within 5 percent of the value without injection. For $M = 0.2$, the center-line heat transfer coefficient is somewhat less than the value between holes where the jets interact with the mainstream and with each other. Results for a blowing rate of approximately 0.5 are included on both Fig. 4 and Fig. 5. The heat transfer coefficient is seen to vary from approximately 10 percent lower to 5 percent more than that measured without injection. The center-line heat transfer coefficient is again lower than the value near the edge of the jets. Results at $Re_D = 0.22 \times 10^5$ (Fig. 5) are approximately 3 percent lower than results for the higher Reynolds number.

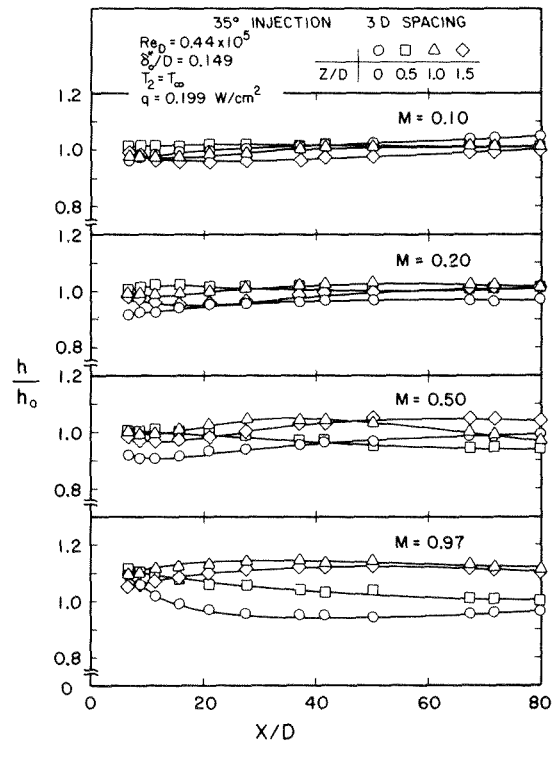

Fig. 4 Heat transfer coefficient downstream of injection through a row of holes, $Re_D = 0.44 \times 10^5$

Figs. 4 and 5 also include results for a blowing rate of approximately 1.0. For $Re_D = 0.44 \times 10^5$, the heat transfer coefficient on the center line decreases from a value that is approximately 10 percent greater than the flat plate value and nearly constant across the span to a value approximately 4–5 percent below the value without injection for $X/D > 30$. At downstream locations, the heat transfer coefficient between holes where the jets interact with each other and with the main flow is approximately 15–20 percent greater than the center-line value. The heat transfer coefficient at the lower Reynolds number (Fig. 5, $Re_D = 0.22 \times 10^5$) displays similar trends but is approximately 4 percent lower than the heat transfer coefficient for $Re_D = 0.44 \times 10^5$.

Fig. 5 also contains results for blowing rates of $M = 1.45$ and 1.94. The variation of center-line heat transfer coefficient is similar to that observed with $M = 0.99$, decreasing from a value that is nearly constant across the span. The heat transfer coefficient between holes increases rapidly in the downstream direction, apparently due to the jets interacting, reaching a maximum at $X/D = 20$–25 and then decreasing. The maximum value of the heat transfer coefficient (occurring at $Z/D \simeq 1$) is greater than the value without injection by approximately 22 percent for $M = 1.45$ and 37 percent for $M = 1.94$.

Comparison of results for the single hole (Fig. 3) and the row of holes (Fig. 5) shows little difference for $M = 0.5$. At $M = 1.0$, center-line results are similar for the single hole and the row, but heat transfer coefficients between holes are higher for the row than those at the same lateral distance from the single jet. At $M \simeq 1.5$ and 2.0, the heat transfer coefficients following the row of holes are much greater than those for injection through a single hole. Interaction between adjacent jets thus causes increased heat transfer even near the holes at blowing rates above $M = 0.5$.

In film cooling applications, where the surface to be cooled is a good heat conductor, conduction within the wall decreases lateral variations in the wall temperature. The film cooling effectiveness and heat transfer coefficient depend primarily on X/D. A heat transfer coefficient $\bar{h}$ that can be used in these applications is calculated by averaging the wall temperatures that are measured to determine local heat transfer coefficients

$$\bar{h}(X/D) = \frac{\bar{q}}{\bar{T}_w(X/D) - \bar{T}_{aw}(X/D)}. \quad (5)$$

The bar denotes an average in the lateral direction only. For three dia hole spacing,

$$\bar{T}_w(X/D) = \frac{1}{3}\int_{-1.5}^{+1.5} T_w(X/D, Z/D)d(Z/D). \quad (6)$$

The adiabatic wall temperature and approximately constant (variation is due to change of resistance of heaters with temperature) wall heat flux are averaged in the same way.

The heat transfer coefficient defined using laterally averaged wall temperatures is presented on Figs. 6(*a*) and 6(*b*) for $Re_D = 0.44 \times 10^5$ and $Re_D = 0.22 \times 10^5$, respectively. Fig. 7 contains a crossplot of this heat transfer coefficient against the blowing rate M. Fig. 6(*a*) shows that results for $M \leq 0.5$ do not differ from values without injection by more than 3 percent for $Re_D = 0.44 \times 10^5$. The heat transfer coefficient at the lower Reynolds number (Fig. 6(*b*)) varies from approximately 6 percent below the flat plate value near injection to approximately 3–5 percent below the value without injection at downstream locations for $M = 0.2$ and 0.5. The heat transfer coefficient for heated injection is smaller than for unheated injection by approximately 1 percent for $M = 0.2$ and 1.5 percent for $M = 0.5$. These differences are similar to those that are observed for normal injection through a single tube and are partly due to the higher uncertainties that are associated with heated injection [15].

At $M = 0.99$, the heat transfer coefficient decreases from approximately 10–12 percent above the value without injection near the hole to 5–6 percent above flat plate values at downstream locations for $Re_D = 0.44 \times 10^5$. Fig. 7 shows results for $Re_D = 0.22 \times 10^5$ to be approximately 5 percent lower than those at the higher Reynolds number for $M = 0.99$. The heat transfer coefficient determined with heated injection ($\rho_2/\rho_\infty = 0.85$) is approximately 2 percent higher than that found with unheated injection ($\rho_2/\rho = 1$) at this blowing rate. Since the jet is penetrating into the mainstream for $M = 1$, the increased heat transfer coefficient for heated injection at this blowing rate could be due to the differ-

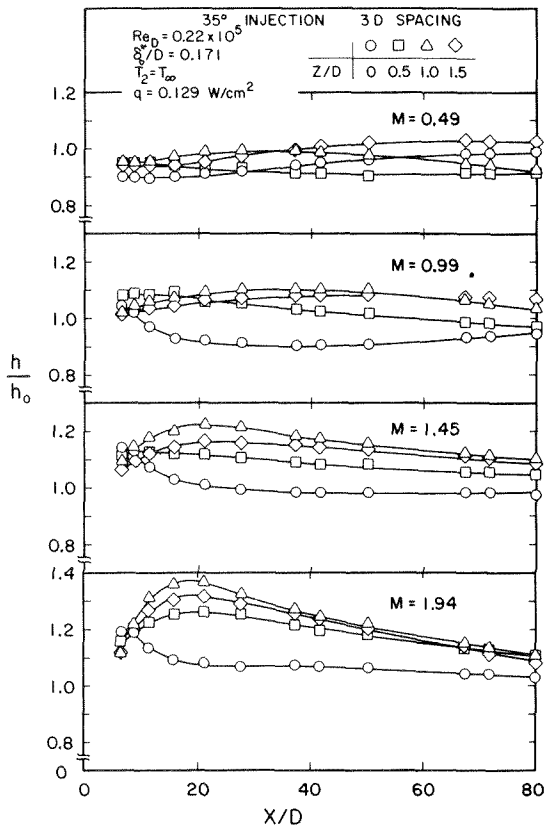

Fig. 5 Heat transfer coefficient downstream of injection through a row of holes, $Re_D = 0.22 \times 10^5$

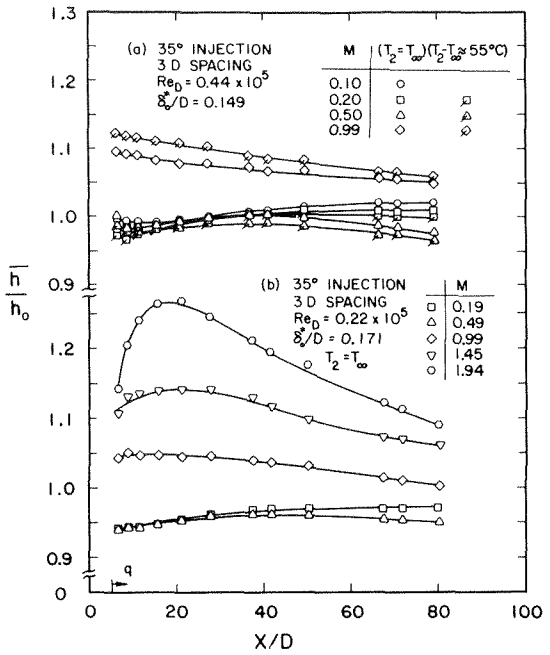

Fig. 6 (*a*) $RE_D = 0.44 \times 10^5$; (*b*) $Re_D = 0.22 \times 10^5$. Heat transfer coefficient based on laterally averaged wall temperatures downstream of injection through a row of holes.

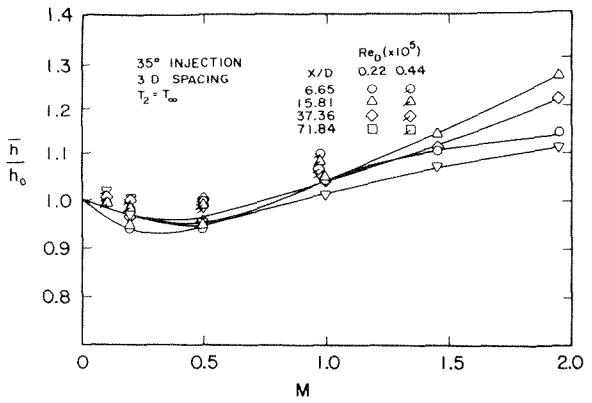

Fig. 7 Variation of heat transfer coefficient based on laterally averaged wall temperatures with blowing rate for injection through a row of holes

ence in the momentum flux ratio I between heated and unheated injection.

For $M = 1.45$ and $M = 1.94$, the laterally averaged heat transfer coefficient increases in the downstream direction, reaches a peak at $X/D \simeq 20$ and then decreases at larger values of X/D. The peak value is about 14 percent greater than the value without injection for $M = 1.45$ and about 27 percent higher for $M = 1.94$. References [7] and [8] show the film cooling effectiveness increasing with X/D for 35 deg injection through a row of holes at $M = 1.5$ and 2. The jets penetrate into the main flow at these blowing rates and the increase in effectiveness is explained as being the result of spreading of the jets. The increased values of the heat transfer coefficient can result from the high turbulence level near the edges of the jets that are spreading toward the wall.

Increased values of the heat transfer coefficient, especially near the point of injection and at the higher blowing rates, have been attributed to turbulence that results from interaction between the jets and the main flow. Turbulence measurements have been reported for normal injection of a single jet into the main flow. References [9 and 10] report the turbulence intensity to be as high as 60 percent in the region near injection for blowing rates greater than 1. Very large eddies have also been observed for normal injection in [15]. Although turbulence levels would not be expected to be as high for 35 deg injection as for normal injection, it is believed that they are still high enough to promote heat transfer.

The heat transfer coefficient based on the average (in both the lateral and downstream directions) wall temperature was determined by Metzger and co-workers [16, 17] for injection through a row of holes at an angle of 60 deg with the main flow. Hole spacings of 1.55 and 1.71 dia were used at blowing rates $M = 0.25$, 0.50, and 0.75. Although the wall temperatures used to calculate $\bar{h}$ in the present work are averaged only in the lateral direction, $\bar{h}$ can be compared with the results of [16 and 17] at low blowing rates where h does not vary much in the downstream direction. The heat transfer reported in [16 and 17] is a few percent above flat plate values at $M = 0.25$, while the results on Figs. 6*(a)* and 6*(b)* for $M = 0.2$ are 3–5 percent below flat plate values at $Re_D = 0.22 \times 10^5$ and approximately equal to the value without injection for $Re_D = 0.44 \times 10^5$. The small difference between the results could be due to the difference in blowing rates, different Reynolds numbers or the different injection geometries. For $M = 0.5$, the heat transfer coefficients of [16 and 17] decrease from approximately 25 percent above the flat plate value near the hole to approximately 10 percent above the value without injection at $X/S \simeq 65$ ($X/S = 65$ corresponds to $X/D = 29.8$ for 1.71 dia spacing and $X/D = 33$ for 1.55 dia spacing). The large difference between these results and the data in Figs. 6*(a)* and 6*(b)* which fall a few percent below the value without injection may be due to differences in geometry or increased mass flow in the mainstream due to secondary injection. The larger injection angle would increase interaction between the jet and mainstream and the smaller hole spacings should increase interaction between neighboring jets. Both of these effects would tend to increase the heat transfer coefficient. For $M = 0.5$, secondary injection apparently increases the mainstream flow rate in [16 and 17] by 5–10 percent [18]. This additional mass flow could increase the heat transfer coefficient by 4–8 percent.

Conclusions

Comparison of film cooling effectiveness for 35 deg injection through a row of holes with results from other investigations indicates that the film cooling effectiveness varies with Reynolds number and boundary layer thickness at the point of injection as well as X/D, Z/D, and M. Fig. 2 shows that the center-line film cooling effectiveness decreases as the boundary layer thickness at the point of injection is increased. When the boundary layer at the point of injection is thin, the jet encounters a greater "force" upon leaving the injection tube than in a thicker boundary layer and is turned faster, remaining closer to the wall and increasing the film cooling effectiveness. This effect, as would be expected, seems most important at $M \simeq 0.5$ which is the blowing rate where penetration of the jet begins to be important. The film cooling effectiveness appears to increase somewhat with Reynolds number Re_D.

The heat transfer coefficient for 35-deg injection through a single hole is observed to be smaller than has been observed for normal injection. The jet injected at 35 deg has a velocity component in the direction of main flow; the jet injected normal to the mainstream has no initial velocity component in the direction of main flow. There is therefore more interaction between the normally injected jet and the mainstream, resulting in higher turbulence levels and a higher heat transfer coefficient than for 35-deg injection. This is in agreement with film cooling results of [6] where lower effectiveness values and increased spreading of the jet for normal injection when compared to 35-deg injection are attributed to greater interaction between the jet and mainstream for normal injection.

There is little difference between the heat transfer coefficient for 35-deg injection through a single hole or through a row of holes spaced at three-diameter intervals across the span for $M = 0.5$. At $M = 1.0$, center-line heat transfer results are similar for the single hole and row, but heat transfer for the row is higher between holes than at the same lateral distance from the single jet. At $M = 1.5$ and 2, heat transfer results for a row of holes are much higher than for injection through a single hole at all lateral positions. Interaction between adjacent jets and between the jets and the mainstream increases heat transfer at blowing rates above $M = 0.5$. A similar effect was observed in [7 and 8] where interaction between jets increased the film cooling effectiveness at blowing rates greater than 1.

At blowing rates $M = 1$, 1.5, and 2, the heat transfer coefficient varies by as much as 20 percent in the lateral direction for 35-deg injection through the row of holes. The heat transfer coefficient is greatest between holes where the jets interact with the mainstream and with each other. At blowing rates $M = 1.5$ and 2, the heat transfer coefficient based on laterally averaged wall temperatures first increases in the downstream direction, reaches a maximum value at $X/D \simeq 20$ and then decreases with X/D. The jets penetrate into the free stream at these blowing rates and then spread toward the wall. The heat transfer coefficient increases with X/D for $X/D \leq 20$ because of the high turbulence level near the edges of the jets that are spreading toward the wall.

The heat transfer coefficient for 35-deg injection through the row of holes at $Re_D = 0.44 \times 10^5$ is approximately 3–5 percent higher than at $Re_D = 0.22 \times 10^5$. The higher heat transfer coefficient at the larger Reynolds number may be due to increased mixing of the secondary flow at the higher Reynolds number and thinner free stream boundary layer.

Acknowledgment

The work reported herein was conducted at the University of Minnesota Heat Transfer Laboratory with the support of NASA Lewis Research Center under Contract NAS 3-13200. Support

from the Office of Naval Research under Contract N00014-68-A-0141-0001 during the final stages of the work is also acknowledged. The assistance of Mr. P. R. Glamm in the laboratory is deeply appreciated.

References

1 Goldstein, R. J., "Film Cooling," *Advances in Heat Transfer,* Academic Press, New York and London, Vol. 7, 1971, pp. 321–379.

2 Wieghardt, K., "Hot-Air Discharge for De-Icing," AAF Translation, Report No. F-TS-919-Re, Wright Field, 1946.

3 Papell, S. J., "Effect on Gaseous Film Cooling of Coolant Injection Through Angled Slots and Normal Holes," NASA Technical Note D-299, 1960.

4 Chin, J. H., Skirvin, S. C., Hayes, L. E., and Burggraf, F., "Film Cooling With Multiple Slots and Louvers," JOURNAL OF HEAT TRANSFER, TRANS. ASME, Series C., Vol. 83, 1961, pp. 281–292.

5 Goldstein, R. J., Eckert, E. R. G., and Ramsey, J. W., "Film Cooling With Injection Through Holes: Adiabatic Wall Temperatures Downstream of a Circular Hole," *Journal of Engineering for Power,* TRANS. ASME, Series A, Vol. 90, 1968, pp. 383–395.

6 Goldstein, R. J., Eckert, E. R. G., and Ramsey, J. W., "Film Cooling With Injection Through a Circular Hole," NASA CR-54604, May 1968 (also University of Minnesota Heat Transfer Laboratory TR No. 82.

7 Goldstein, R. J., Eckert, E. R. G., Eriksen, V. L., and Ramsey, J. W., "Film Cooling Following Injection Through Inclined Circular Tubes," NASA CR-72612, Nov. 1969 (also University of Minnesota Heat Transfer Laboratory TR No. 91).

8 Goldstein, R. J., Eckert, E. R. G., Eriksen, V. L., and Ramsey, J. W., "Film Cooling Following Injection Through Inclined Circular Tubes," *Israel Journal of Technology,* Vol. 8, No. 1–2, 1970, pp. 145–154.

9 Ramsey, J. W., "The Interaction of a Heated Air Jet With a Deflecting Flow," PhD thesis, University of Minnesota, 1969.

10 Ramsey, J. W., and Goldstein, R. J., "Interaction of a Heated Jet With a Deflecting Flow," JOURNAL OF HEAT TRANSFER, TRANS. ASME, Series C, Vol. 93, 1971, pp. 365–372 (cf. NASA CR-72613 and University of Minnesota Heat Transfer Laboratory TR No. 92, Apr. 1970).

11 Ramsey, J. W., Goldstein, R. J., and Eckert, E. R. G., "A Model for Analysis of the Temperature Distribution With Injection of a Heated Jet Into an Isothermal Flow," Paper FC 8.5, *Heat Transfer 1970,* Vol. III, Elsevier Publishing Co., Amsterdam, 1970.

12 Eriksen, V. L., Eckert, E. R. G., and Goldstein, R. J., "A Model for Analysis of the Temperature Field Downstream of a Heated Jet Injected into an Isothermal Crossflow at an Angle of 90°," University of Minnesota Heat Transfer Laboratory TR No. 101).

13 Liess, C., and Carnel, J., "Application of Film Cooling to Gas-Turbine Blades," *High Temperature Turbines,* AGARD-CP 73-71, 1971, pp. 23-1–23-9.

14 Eckert, E. R. G., "Film Cooling With Injection Through Holes," *High Temperature Turbines,* AGARD-CP-73-71, pp. 17-1–17-17.

15 Eriksen, V. L., "Film Cooling Effectiveness and Heat Transfer With Injection Through Holes," PhD thesis, University of Minnesota, 1971 (also NASA CR-72991 and University of Minnesota HTL TR No. 102).

16 Metzger, D. E., and Fletcher, D. D., "Surface Heat Transfer Immediately Downstream of Flush, Non-Tangential Injection Holes and Slots," *Journal of Aircraft,* Vol. 8, 1971, p. 33.

17 Metzger, D. E., Biddle, J. R., and Warren, J. M., "Evaluation of Film Cooling Performance on Gas Turbine Surfaces," *High Temperature Turbines,* AGARD-CP-73-71, 1971, pp. 24-1–24-7.

18 Eckert, E. R. G., Goldstein, R. J. and Pedersen, D. R., "Comment on 'Evaluation of Heat Transfer for Film-Cooled Turbine Blades,'" *Journal of Aircraft,* Vol. 8, No. 1, 1971, pp. 63–64.

19 Burggraf, F., and Huffmeier, R. W., "Film Effectiveness and Heat Transfer Coefficients for Injection From One and Two Rows of Holes at 35° to the Surface," AEG-Technical Information Series Report No. R70AEG351, General Electric Co., Lynn, Mass., Cincinnati, Ohio, Aug. 1970.

20 Klebanoff, P. S., and Diehl, Z. W., "Some Features of Artificially Thickened Fully Developed Turbulent Boundary Layers With Zero Pressure Gradient," NACA Report 1110, 1952.

21 Reynolds, W. C., Kays, W. M., and Kline, S. J., "Heat Transfer in the Turbulent Incompressible Boundary Layer, III-Arbitrary Wall Temperature and Heat Flux," NASA Memorandum 12-3-58W, 1958.

journal of heat transfer

technical briefs

This section consists of contributions of 1500 words or less (about 5 double-spaced typewritten pages, including figures). Technical briefs will be reviewed and approved by the specific division's reviewing committee prior to publication. After approval such contributions will be published as soon as possible, normally in the next issue of the journal.

A Method for Improving the Efficiency of Monte Carlo Calculation of Heat Conduction Problems

G. E. Zinsmeister[1] and J. A. Sawyerr[2]

Introduction

Monte Carlo methods are generally inefficient for whole temperature field calculations in heat conduction problems. Presently, they can only be recommended for single point calculations since they possess the unique advantage of allowing calculation of a single point without calculating the whole field. They may also offer an advantage in surface heat flux calculations since a surface temperature gradient at a point can be obtained by calculating at most two points (i.e., the surface temperature if not specified and the temperature at a point just below the surface). For whole field calculations, however, Monte Carlo methods are simply too inefficient to be recommended. This note presents a method for improving the efficiency of whole field calculations using Monte Carlo.

Some improvements in the efficiency of Monte Carlo calculations for heat conduction problems were developed by Haji-Sheikh and Sparrow [1, 2][3] (who used a method previously suggested by both Brown [3] and Muller [4]) and Emery and Carson [5]. Both methods (the floating random walk and the exodus method) involve the concept that a walker leaving a point within an enclosed region must pass through an interposed boundary. If the probability of reaching a point on this interposed boundary is known, the walker can start from the interposed boundary. "Bookkeeping procedures" suggested by Curtiss [6] utilized this concept in yet a different way as early as 1949. The method presented here is an additional way of implementing this concept, and is called the "shrinking boundary" method.

The Shrinking Boundary Method

In the standard random walk method for heat conduction problems (i.e., the Laplace equation), the temperature at a point in the conduction region is obtained by dispatching a large number of walkers from the point and allowing them to walk randomly in the conduction region on a superimposed finite difference grid until they hit a boundary where they are absorbed or terminate.[4] The temperature at the point of dispatch is then calculated by multiplying the temperature at each boundary point times the number of particles absorbed at that boundary point, summing these results over the entire boundary, and, finally, dividing by the number of particles originally dispatched. The shrinking boundary concept involves exactly the same procedure except that once an internal point has been calculated it can be treated as a boundary point. That is, it can also absorb particles. This will decrease the calculation time for the next point since the walkers will have an additional point for terminating their walk. With subsequent calculations, the savings in calculation time become even greater. This note is directed to the question of how much of a saving in time is possible.

The choice of the name "shrinking boundary" to describe this concept should not mislead one into thinking that calculations must be performed from the boundary inward. One could start from an internal point and work outward or even choose the succession of points to be calculated in a random manner. The determination of the relative merits of various shrinking patterns is also discussed in this note.

The Computer Program

The detailed computer program which used the exodus method on a square grid is available in [8]. Here we present only unique concepts necessary to implement the method.

To implement the shrinking boundary method, it is necessary to keep track of nodes which have been already calculated. The method used in this research was to assign a code of one to non-calculated nodes which was then changed to zero when the node was calculated. The code had three functions: *(a)* to keep walkers at an absorbing node from being distributed to an adjacent node; *(b)* to guide the calculation of the total number of walkers which have been absorbed; and *(c)* to guide the scoring after a sufficient

[1] Assoc. Professor, Mechanical and Aerospace Engineering Department, University of Massachusetts, Amherst, Mass. Mem. ASME.

[2] Graduate Student, Mechanical and Aerospace Engineering Department, University of Massachusetts, Amherst, Mass.

[3] Numbers in brackets designate References at end of technical brief.

Contributed by the Heat Transfer Division of THE AMERICAN SOCIETY OF MECHANICAL ENGINEERS. Manuscript received by the Heat Transfer Division, October 11, 1973.

[4] The total absorption of particles on the boundary is true only for Dirichlet boundary conditions. For insulated or convective boundary conditions, walkers may be reflected back into the region. Only Dirichlet conditions are considered here though the method is applicable to other boundary conditions. For details see [6, 7].

Table 1 Normalized times for various methods and network sizes

NET-WORK SIZE	NO. OF INTER-NAL NODES	STANDARD EXODUS METHOD TIME (MILLISECONDS)	SHRINKING BOUNDARY EXODUS METHOD					GAUSS-SEIDEL METHOD
			ROW-BY-ROW	ALTERNATE COLUMN	CHECKER-BOARD	SPIRAL IN	SPIRAL OUT	
3x3	4	532	.91	.90	.83	.89	.91	.35
4x4	9	3173	.78	.65	.66	.78	.68	.15
5x5	16	12615	.69	.57	.52	.71	.54	.09
6x6	25	38799	.63	.46	.45	.67	.45	.07
7x7	36	98807	.59	.44	.40	.63	.39	.05

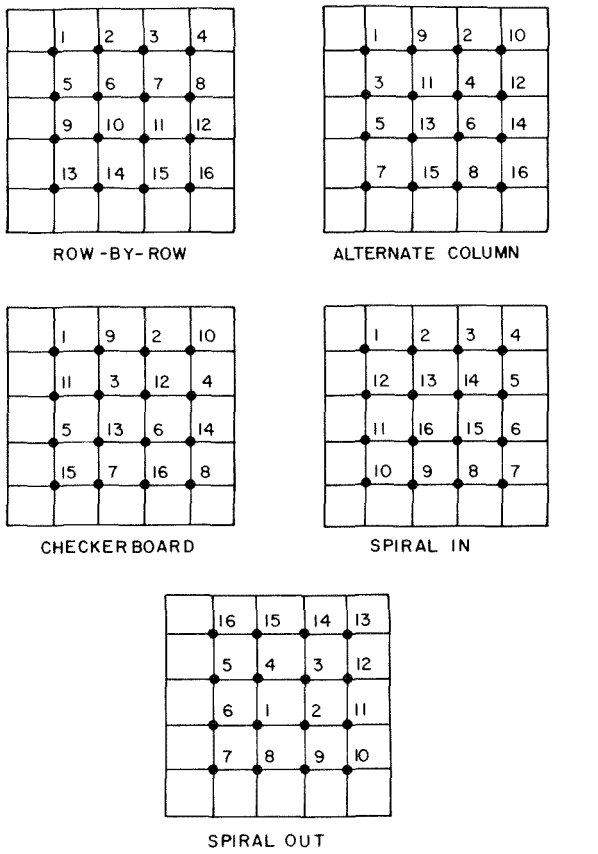

Fig. 1 Shrinking methods for a 5 × 5 network (numbers indicate the order of calculation)

fraction of the walkers are terminated.

The program was also designed to give the probability distribution with which a walker would terminate on the *original* boundary. These probability distributions are essentially Green's function for the region and are much more general than a specific temperature field [7, 9]. Since such distributions can be obtained with little extra calculation time (a distinct advantage of the Monte Carlo approach), the method used to obtain them is described here. To work with termination probability distributions using the shrinking boundary method requires a conditional probability calculation. That is, if the probability of a walker reaching an internal absorbing node j from node i is $P(i, j)$ and the probability of reaching a boundary node k from j is $P(j, k)$, then the probability of leaving i, passing through j before hitting any other internal absorbing node and finally reaching k is $P(i, j)\,P(j, k)$. The probability of leaving i and reaching k is then $\Sigma_j P(i, j)\,P(j, k) + P^*(i, k)$ where $P^*(i, k)$ is the probability of reaching k without passing through any internal absorbing nodes.

The master program was designed to accommodate various shrinking patterns by simply changing a few lines of the program. The program for the standard exodus method (i.e., with non-shrinking boundaries) was identical with the shrinking exodus program except for deletion of the portion which changed the code when a node was calculated and the portion which did the conditional probability calculation.

For comparison purposes, a separate program utilizing the Gauss-Seidel method to obtain Green's function was also written.

Results and Conclusions

The programs described in the foregoing were run to three significant figure accuracy on the UMASS time-sharing system for five square networks as indicated in Table 1. The CPU time for the complete calculation (excluding compilation and printout) were obtained and used to construct Table 1 where only the time for running the standard exodus method is given. All other results for five shrinking patterns (see Fig. 1) are normalized with respect to the standard exodus time. Fig. 2 presents some of the results graphically.

Several conclusions can be drawn from the results:

1 The shrinking boundary exodus method is more efficient than the standard exodus method for all shrinking patterns tested.

2 The spiral out and checkerboard patterns are the most efficient and are of comparable efficiency though the spiral out pattern seems to be getting better for larger networks.

3 The shrinking boundary exodus method becomes more efficient for larger networks in comparison with the standard exodus method.

4 No shrinking pattern tested made the shrinking boundary exodus method competitive with the Gauss-Seidel method.[5]

Summary

For whole field calculations, the shrinking boundary concept alone will not make Monte Carlo methods competitive with standard methods for solving heat conduction problems. Since it offers no advantage over the standard exodus method for single

[5] While an absolute comparison cannot be made because of possible programming inefficiencies, the Gauss-Seidel times were so much less that this conclusion seems valid. Also, remember that the Gauss-Seidel program calculated Green's function for which it is not well suited. Thus for a single temperature field calculation, the Gauss-Seidel method will be even more efficient in comparison with the shrinking boundary exodus method than Table 1 indicates.

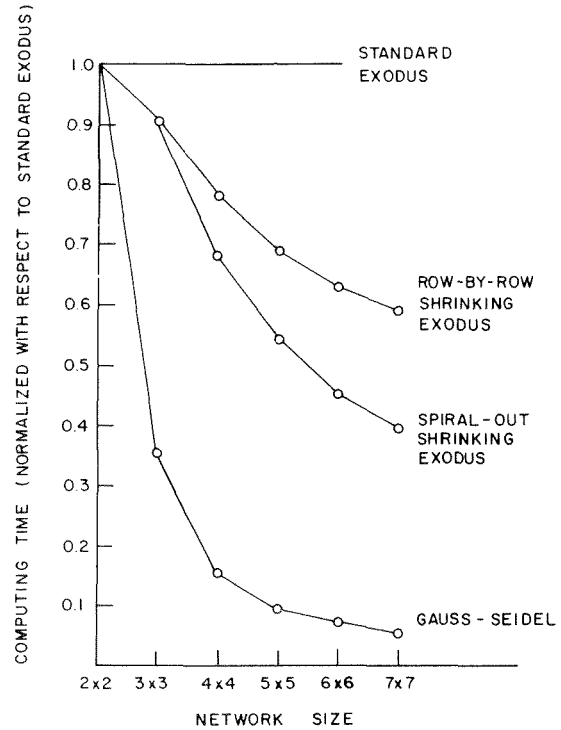

Fig. 2 Computing time versus network size for various methods

point calculations it cannot be recommended for this application. However, it may be competitive with standard methods for surface heat flux calculations where it is necessary to calculate the temperatures of a layer of nodes just below the surface. For the present, then, standard methods are to be recommended above Monte Carlo methods except for the above exceptional cases.

In spite of these negative recommendations, there is the strong possibility that the shrinking boundary concept will find useful application in conjunction with another method for improving the efficiency of Monte Carlo calculations which is presently under study. This additional method, called the "inscribed figure" method, uses the Monte Carlo method to split a heat conduction region into smaller regularly shaped regions which can then be handled by standard analytical methods. Both the splitting procedure and the calculation of temperatures in irregularly shaped subregions will be done by the shrinking boundary exodus method since it has proven to be significantly faster than the standard exodus method.

Finally, it should be pointed out that the shrinking boundary concept is not limited to conduction problems alone. It can be applied to both convection and radiation problems. Since some radiation problems are amenable only to Monte Carlo analysis [10], the use of this concept and other sampling processes is certainly warranted.

References

1 Haji-Sheikh, A., and Sparrow, E. M., "The Solution of Heat Conduction Problems by Probability Methods," JOURNAL OF HEAT TRANSFER, TRANS. ASME, Series C, Vol. 89, 1967, pp. 121-131.

2 Haji-Sheikh, A., and Sparrow, E. M., "The Floating Random Walk and Its Application to Monte Carlo Solutions of Heat Equations," *Journal of the Society for Industrial and Applied Mathematics*, Vol. 14, 1966, pp. 370-389.

3 Brown, G. W., "Monte Carlo Methods," in *Modern Mathematics for the Engineer*, E. F. Beckenbach, ed., McGraw-Hill, N. Y., 1958, pp. 279-303.

4 Muller, M. E., "Some Continuous Monte Carlo Methods for the Dirichlet Problem," *Annals of Mathematical Statistics*, Vol. 27, 1956, pp. 569-589.

5 Emery, A. F., and Carson, W. W., "A Modification to the Monte Carlo Method—The Exodus Method," JOURNAL OF HEAT TRANSFER, TRANS. ASME, Series C, Vol. 90, 1968, pp. 328-332.

6 Curtiss, J. H., "Sampling Methods Applied to Differential and Difference Equations," *Proc. Seminar on Scientific Computation*, IBM Corporation, N. Y., 1949.

7 Zinsmeister, G. E., "Monte Carlo Methods as an Aid in Teaching Heat Conduction," *Bulletin of Mechanical Engineering Education*, Vol. 7, 1968, pp. 77-86.

8 Sawyerr, J. A., M.S. Project Report, Mechanical and Aerospace Engineering Department, University of Massachusetts, Amherst, Mass., 1973.

9 Chandler, R. D., et al., "The Solution of Steady State Convection Problems by The Fixed Random Walk Method," JOURNAL OF HEAT TRANSFER, TRANS. ASME, Series C, Vol. 90, 1968, pp. 361-363.

10 Howell, J. R., "Application of Monte Carlo to Heat Transfer Problems," in *Advances in Heat Transfer*, Academic Press, N. Y., Vol. 5, 1968.

Heat Conduction in Bodies With Small Boundary Perturbations

W. A. Scheffler[1]

There are many methods of calculating the temperature distribution in bodies of irregular shape. This note describes another method which is simple in application and has the advantage that it employs known solutions to problems of bodies of regular shape. The method employs perturbation theory and can be used in any number of dimensions. A rigorous discussion of this technique is given in reference [1].[2]

A specific example that occurs in the simulation of a nuclear reactor control rod by an aluminum tube is undertaken. Consider two annular cylindrical surfaces, the inner surface is of irregular shape with a radius given by;

$$r_p = a\,[\,1 + \epsilon\, f(\theta)\,] \tag{1}$$

The assumption of steady-state conditions is made. In addition, the boundary condition on the inner surface is one of constant temperature, T_i. The ϵ appearing in equation (1) is the eccentricity of the perturbation from the boundary's circular form. Let the outer surface be regular of constant radius, r_0, and have a constant surface temperature T_b.

The standard assumption is that the temperature distribution in the above configuration is given by;

$$T(r, \theta, \epsilon) = T_0(r, \theta) + \epsilon T_1\,(r, \theta) + 0\,(\epsilon^2) \tag{2}$$

where only terms of order ϵ are kept. The temperature distribution, T_0, is given by the unperturbated distribution i.e., by setting ϵ equal to zero in (1) and (2). Therefore,

$$T_0\,(r, \theta) = A \ln r + B \tag{3}$$

where A and B are left as arbitrary constants to be determined later.

The temperature at the nonsymmetrical boundary is;

$$T(r_p, \theta) = T_i = T_0\,(r_p, \theta) + \epsilon T_1\,(r_p, \theta) \tag{4}$$

where again terms of order ϵ^2 have been dropped. Now expand the terms on the right-hand side of equation (4) in a Taylor series about the unperturbated radius, a, and keep only terms of order ϵ;

$$T_0(r_p, \theta) = T_0(a, \theta) + \frac{\partial T_0}{\partial r}\Big|_{r_p = a} (r_p - a) \tag{5}$$

$$T_1(r_p, \theta) = T_1(a, \theta) + \frac{\partial T_1}{\partial r}\Big|_{r_p = a} (r_p - a) \tag{6}$$

where from (1)

$$r_p - a = a\epsilon f(\theta) \tag{7}$$

Equations (4), (5), (6), and (7) may now be combined to give to order ϵ

$$T_i = T_0(a, \theta) + \epsilon[aT_0'(a, \theta)f(\theta) + T_1(a, \theta)] \tag{8}$$

Now equate coefficients of order ϵ in (8) to find

$$T_i = T_0(a, \theta) \tag{9}$$

and

$$aT_0'(a, \theta)f(\theta) + T_1(a, \theta) = 0 \tag{10}$$

Now equations (3) and (9) are used to obtain

$$T_i = A \ln a + B \tag{11}$$

Likewise, equations (3) and (10) are used to obtain

$$T_1(a, \theta) = -Af(\theta) \tag{12}$$

In a similar manner one evaluates the temperature distribution $T(r, \theta)$ at the outer surface, $r = r_0$

$$T(r_0, \theta) = T_b = T_0(r_0, \theta) + \epsilon T_1(r_0, \theta) \tag{13}$$

Again matching coefficients of order ϵ, one obtains

$$T_b = A \ln r_0 + B \tag{14}$$

and

$$T_1(r_0, \theta) = 0 \tag{15}$$

Now equations (11) and (14) are used to determine the con-

[1] Department of Mechanical and Chemical Engineering, Joint Center for Graduate Study, Richland, Wash.

[2] Numbers in brackets designate References at end of technical brief.

Contributed by the Heat Transfer Division of THE AMERICAN SOCIETY OF MECHANICAL ENGINEERS. Manuscript received by the Heat Transfer Division, July 27, 1973.

point calculations it cannot be recommended for this application. However, it may be competitive with standard methods for surface heat flux calculations where it is necessary to calculate the temperatures of a layer of nodes just below the surface. For the present, then, standard methods are to be recommended above Monte Carlo methods except for the above exceptional cases.

In spite of these negative recommendations, there is the strong possibility that the shrinking boundary concept will find useful application in conjunction with another method for improving the efficiency of Monte Carlo calculations which is presently under study. This additional method, called the "inscribed figure" method, uses the Monte Carlo method to split a heat conduction region into smaller regularly shaped regions which can then be handled by standard analytical methods. Both the splitting procedure and the calculation of temperatures in irregularly shaped subregions will be done by the shrinking boundary exodus method since it has proven to be significantly faster than the standard exodus method.

Finally, it should be pointed out that the shrinking boundary concept is not limited to conduction problems alone. It can be applied to both convection and radiation problems. Since some radiation problems are amenable only to Monte Carlo analysis [10], the use of this concept and other sampling processes is certainly warranted.

References

1 Haji-Sheikh, A., and Sparrow, E. M., "The Solution of Heat Conduction Problems by Probability Methods," JOURNAL OF HEAT TRANSFER, TRANS. ASME, Series C, Vol. 89, 1967, pp. 121-131.

2 Haji-Sheikh, A., and Sparrow, E. M., "The Floating Random Walk and Its Application to Monte Carlo Solutions of Heat Equations," *Journal of the Society for Industrial and Applied Mathematics*, Vol. 14, 1966, pp. 370-389.

3 Brown, G. W., "Monte Carlo Methods," in *Modern Mathematics for the Engineer*, E. F. Beckenbach, ed., McGraw-Hill, N. Y., 1958, pp. 279-303.

4 Muller, M. E., "Some Continuous Monte Carlo Methods for the Dirichlet Problem," *Annals of Mathematical Statistics*, Vol. 27, 1956, pp. 569-589.

5 Emery, A. F., and Carson, W. W., "A Modification to the Monte Carlo Method—The Exodus Method," JOURNAL OF HEAT TRANSFER, TRANS. ASME, Series C, Vol. 90, 1968, pp. 328-332.

6 Curtiss, J. H., "Sampling Methods Applied to Differential and Difference Equations," *Proc. Seminar on Scientific Computation*, IBM Corporation, N. Y., 1949.

7 Zinsmeister, G. E., "Monte Carlo Methods as an Aid in Teaching Heat Conduction," *Bulletin of Mechanical Engineering Education*, Vol. 7, 1968, pp. 77-86.

8 Sawyerr, J. A., M.S. Project Report, Mechanical and Aerospace Engineering Department, University of Massachusetts, Amherst, Mass., 1973.

9 Chandler, R. D., et al., "The Solution of Steady State Convection Problems by The Fixed Random Walk Method," JOURNAL OF HEAT TRANSFER, TRANS. ASME, Series C, Vol. 90, 1968, pp. 361-363.

10 Howell, J. R., "Application of Monte Carlo to Heat Transfer Problems," in *Advances in Heat Transfer*, Academic Press, N. Y., Vol. 5, 1968.

Heat Conduction in Bodies With Small Boundary Perturbations

W. A. Scheffler[1]

There are many methods of calculating the temperature distribution in bodies of irregular shape. This note describes another method which is simple in application and has the advantage that it employs known solutions to problems of bodies of regular shape. The method employs perturbation theory and can be used in any number of dimensions. A rigorous discussion of this technique is given in reference [1].[2]

A specific example that occurs in the simulation of a nuclear reactor control rod by an aluminum tube is undertaken. Consider two annular cylindrical surfaces, the inner surface is of irregular shape with a radius given by;

$$r_p = a\,[\,1 + \epsilon\, f(\theta)\,] \tag{1}$$

The assumption of steady-state conditions is made. In addition, the boundary condition on the inner surface is one of constant temperature, T_i. The ϵ appearing in equation (1) is the eccentricity of the perturbation from the boundary's circular form. Let the outer surface be regular of constant radius, r_0, and have a constant surface temperature T_b.

The standard assumption is that the temperature distribution in the above configuration is given by;

$$T(r, \theta, \epsilon) = T_0(r, \theta) + \epsilon T_1\,(r, \theta) + 0\,(\epsilon^2) \tag{2}$$

where only terms of order ϵ are kept. The temperature distribution, T_0, is given by the unperturbated distribution i.e., by setting ϵ equal to zero in (1) and (2). Therefore,

$$T_0\,(r, \theta) = A\,\ln\,r + B \tag{3}$$

where A and B are left as arbitrary constants to be determined later.

The temperature at the nonsymmetrical boundary is;

$$T(r_p, \theta) = T_i = T_0\,(r_p, \theta) + \epsilon T_1\,(r_p, \theta) \tag{4}$$

where again terms of order ϵ^2 have been dropped. Now expand the terms on the right-hand side of equation (4) in a Taylor series about the unperturbated radius, a, and keep only terms of order ϵ;

$$T_0(r_p, \theta) = T_0(a, \theta) + \frac{\partial T_0}{\partial r}\Big|_{r_p = a}(r_p - a) \tag{5}$$

$$T_1(r_p, \theta) = T_1(a, \theta) + \frac{\partial T_1}{\partial r}\Big|_{r_p = a}(r_p - a) \tag{6}$$

where from (1)

$$r_p - a = a\epsilon f(\theta) \tag{7}$$

Equations (4), (5), (6), and (7) may now be combined to give to order ϵ

$$T_i = T_0(a, \theta) + \epsilon[aT_0'(a, \theta)f(\theta) + T_1(a, \theta)] \tag{8}$$

Now equate coefficients of order ϵ in (8) to find

$$T_i = T_0(a, \theta) \tag{9}$$

and

$$aT_0'(a, \theta)f(\theta) + T_1(a, \theta) = 0 \tag{10}$$

Now equations (3) and (9) are used to obtain

$$T_i = A\,\ln\,a + B \tag{11}$$

Likewise, equations (3) and (10) are used to obtain

$$T_1(a, \theta) = -Af(\theta) \tag{12}$$

In a similar manner one evaluates the temperature distribution $T(r, \theta)$ at the outer surface, $r = r_0$

$$T(r_0, \theta) = T_b = T_0(r_0, \theta) + \epsilon T_1(r_0, \theta) \tag{13}$$

Again matching coefficients of order ϵ, one obtains

$$T_b = A\,\ln\,r_0 + B \tag{14}$$

and

$$T_1(r_0, \theta) = 0 \tag{15}$$

Now equations (11) and (14) are used to determine the con-

[1] Department of Mechanical and Chemical Engineering, Joint Center for Graduate Study, Richland, Wash.

[2] Numbers in brackets designate References at end of technical brief.

Contributed by the Heat Transfer Division of THE AMERICAN SOCIETY OF MECHANICAL ENGINEERS. Manuscript received by the Heat Transfer Division, July 27, 1973.

stants A and B. Equations (12) and (15) determine the boundary conditions on $T_1(r, \theta)$.

To determine $T_1(r, \theta)$, one notes that the form assumed for $T(r, \theta, \epsilon)$ is linear and so each term must satisfy the heat conduction equation. The problem now is one where $T_1(r, \theta)$ is the same as if the body were of regular shape with boundary conditions (12) and (15). The general solution to this problem is found by standard techniques to be

$$T_1(r,\theta) = \sum_{n=1}^{\infty} \left[\left(C_n r^n + \frac{D_n}{r^n}\right) \cos n\theta + \left(E_n r^n + \frac{F_n}{r^n}\right) \sin n\theta \right] + D_0 \ln r + C_0 \quad (16)$$

The constants appearing in (16) are determined from the boundary conditions as

$$C_n = \frac{a^n f_n^{(1)}}{r_0^{2n} - a^{2n}} \quad (17)$$

$$D_n = \frac{r_0^{2n} a^n f_n^{(1)}}{a^{2n} - r_0^{2n}} \quad (18)$$

$$C_0 = \frac{f_0^{(1)} \ln (r_0)}{\ln (a/r_0)} \quad (19)$$

$$E_n = \frac{a^n f_n^{(2)}}{a^{2n} - r_0^{2n}} \quad (20)$$

$$F_n = \frac{a^n r_0^{2n} f_n^{(2)}}{r_0^{2n} - a^{2n}} \quad (21)$$

$$D_0 = \frac{f_0^{(1)}}{\ln (r_0/a)} \quad (22)$$

where $f_n^{(1)}$ and $f_n^{(2)}$ are the Fourier coefficients

$$f_0^{(1)} = -\frac{A}{2\pi} \int_0^{2\pi} f(\theta) d\theta \quad (23)$$

$$f_n^{(1)} = -\frac{A}{\pi} \int_0^{2\pi} f(\theta) \cos n\theta d\theta (n = 1,2,\ldots) \quad (24)$$

and

$$f_n^{(2)} = -\frac{A}{\pi} \int_0^{2\pi} f(\theta) \sin n\theta d\theta \ (n = 1,2,\ldots) \quad (25)$$

The temperature perturbation, $T_1(r, \theta)$, is thus determined. It was determined by using the general solution for two concentric annular passages, but with boundary conditions generated from the perturbation scheme. If it happens that both boundaries are perturbated, a similar calculation can be pursued with two eccentricities, ϵ_1 and ϵ_2, entering the problem.

In order to give a rigorous discussion of convergence of the series given by equation (2), one would have to calculate the nth order term in the series. However, one can see that the convergence of the series (2) is strongly dependent on the choice of $f(\theta)$. Higher order terms in the series requires that higher order terms be kept in the expansions (5) and (6). These higher order terms are proportional to $f(\theta)$ raised to an appropriate power. In regions where $f(\theta)$ is greater than unity, more terms in the series (2) must be kept in order to obtain an accurate representation of the temperature distribution. A further discussion for series like equation (2) is found in reference [1].

References

1 Cole, J. D., *Perturbation Methods in Applied Mathematics*, Blaisdell Publishing Co., 1968.

Thermal Resistance of a Buried Cylinder With Constant Flux Boundary Condition

R. Thiyagarajan[1] and M. M. Yovanovich[2]

Nomenclature

- a = distance from ground surface to origin of bicylindrical
- g = metric coefficient
- k = thermal conductivity
- Q = total heat flow rate per unit length of pipe
- q = flux per unit area
- R = thermal resistance
- $R_{q=c}$ = constant flux resistance
- $R_{T=c}$ = constant temperature resistance
- r_0 = pipe radius
- T = temperature
- T_a = average surface temperature
- ψ = bicylindrical coordinate
- η = bicylindrical coordinate
- ω = distance from ground surface to pipe center

Introduction

The determination of the thermal resistance for heat transfer between the surface of a buried pipe or a buried cylinder and ground level is important and has been calculated for the constant temperature boundary condition at the pipe surface [1-4].[3] The method used most often is based upon the superposition of infinite line source and sink solutions [1-3]. A solution based upon bicylindrical coordinates is also available [4]. A buried cable or a heating wire with uniform joulean heating will have a constant flux condition. However, in real situations, the actual boundary condition is not known exactly. It is felt that in most cases, it will be between the constant temperature and the constant flux condition. It becomes necessary then, to have the thermal resistance values corresponding to these two extreme cases. The thermal resistance to the constant flux condition is not available in conduction heat transfer texts, except reference [5], where a solution based upon bicylindrical coordinates is given. This solution in reference [5] is in error because the temperature and the thermal resistance go to zero, for the same heat transfer, as the pipe is displaced farther below ground level. This is obviously incorrect. The purpose of this technical brief, therefore, is to fill this gap and to point out the error in reference [5], so that we will have the thermal resistance values corresponding to the extreme cases, namely constant temperature and constant flux conditions. This brief deals with the exact solution based upon bicylindrical coordinates. The thermal resistance with a constant flux boundary condition is compared with the well-known expression for the constant temperature boundary condition.

Analysis

The governing differential equation for steady heat transfer through a homogeneous and isotropic medium of thermal conductivity k in bicylindrical coordinates is [4, 6]

$$\frac{\partial^2 T}{\partial \eta^2} + \frac{\partial^2 T}{\partial \psi^2} = 0 \quad (1)$$

[1] Graduate Research Assistant, Thermal Engineering group, Department of Mechanical Engineering, University of Waterloo, Waterloo, Ont., Canada.

[2] Professor of Mechanical Engineering, Thermal Engineering group, Department of Mechanical Engineering, University of Waterloo, Waterloo, Ont., Canada. Mem. ASME.

[3] Number in brackets designate References at end of technical brief.

Contributed by the Heat Transfer Division of THE AMERICAN SOCIETY OF MECHANICAL ENGINEERS. Manuscripts received by the Heat Transfer Division July 3, 1973.

stants A and B. Equations (12) and (15) determine the boundary conditions on $T_1(r, \theta)$.

To determine $T_1(r, \theta)$, one notes that the form assumed for $T(r, \theta, \epsilon)$ is linear and so each term must satisfy the heat conduction equation. The problem now is one where $T_1(r, \theta)$ is the same as if the body were of regular shape with boundary conditions (12) and (15). The general solution to this problem is found by standard techniques to be

$$T_1(r,\theta) = \sum_{n=1}^{\infty} \left[\left(C_n r^n + \frac{D_n}{r^n}\right) \cos n\theta + \left(E_n r^n + \frac{F_n}{r^n}\right) \sin n\theta \right] + D_0 \ln r + C_0 \quad (16)$$

The constants appearing in (16) are determined from the boundary conditions as

$$C_n = \frac{a^n f_n^{(1)}}{r_0^{2n} - a^{2n}} \quad (17)$$

$$D_n = \frac{r_0^{2n} a^n f_n^{(1)}}{a^{2n} - r_0^{2n}} \quad (18)$$

$$C_0 = \frac{f_0^{(1)} \ln (r_0)}{\ln (a/r_0)} \quad (19)$$

$$E_n = \frac{a^n f_n^{(2)}}{a^{2n} - r_0^{2n}} \quad (20)$$

$$F_n = \frac{a^n r_0^{2n} f_n^{(2)}}{r_0^{2n} - a^{2n}} \quad (21)$$

$$D_0 = \frac{f_0^{(1)}}{\ln (r_0/a)} \quad (22)$$

where $f_n^{(1)}$ and $f_n^{(2)}$ are the Fourier coefficients

$$f_0^{(1)} = -\frac{A}{2\pi} \int_0^{2\pi} f(\theta) d\theta \quad (23)$$

$$f_n^{(1)} = -\frac{A}{\pi} \int_0^{2\pi} f(\theta) \cos n\theta d\theta (n = 1,2,\ldots) \quad (24)$$

and

$$f_n^{(2)} = -\frac{A}{\pi} \int_0^{2\pi} f(\theta) \sin n\theta d\theta \ (n = 1,2,\ldots) \quad (25)$$

The temperature perturbation, $T_1(r, \theta)$, is thus determined. It was determined by using the general solution for two concentric annular passages, but with boundary conditions generated from the perturbation scheme. If it happens that both boundaries are perturbated, a similar calculation can be pursued with two eccentricities, ϵ_1 and ϵ_2, entering the problem.

In order to give a rigorous discussion of convergence of the series given by equation (2), one would have to calculate the nth order term in the series. However, one can see that the convergence of the series (2) is strongly dependent on the choice of $f(\theta)$. Higher order terms in the series requires that higher order terms be kept in the expansions (5) and (6). These higher order terms are proportional to $f(\theta)$ raised to an appropriate power. In regions where $f(\theta)$ is greater than unity, more terms in the series (2) must be kept in order to obtain an accurate representation of the temperature distribution. A further discussion for series like equation (2) is found in reference [1].

References

1 Cole, J. D., *Perturbation Methods in Applied Mathematics*, Blaisdell Publishing Co., 1968.

Thermal Resistance of a Buried Cylinder With Constant Flux Boundary Condition

R. Thiyagarajan[1] and M. M. Yovanovich[2]

Nomenclature

- a = distance from ground surface to origin of bicylindrical
- g = metric coefficient
- k = thermal conductivity
- Q = total heat flow rate per unit length of pipe
- q = flux per unit area
- R = thermal resistance
- $R_{q=c}$ = constant flux resistance
- $R_{T=c}$ = constant temperature resistance
- r_0 = pipe radius
- T = temperature
- T_a = average surface temperature
- ψ = bicylindrical coordinate
- η = bicylindrical coordinate
- ω = distance from ground surface to pipe center

Introduction

The determination of the thermal resistance for heat transfer between the surface of a buried pipe or a buried cylinder and ground level is important and has been calculated for the constant temperature boundary condition at the pipe surface [1-4].[3] The method used most often is based upon the superposition of infinite line source and sink solutions [1-3]. A solution based upon bicylindrical coordinates is also available [4]. A buried cable or a heating wire with uniform joulean heating will have a constant flux condition. However, in real situations, the actual boundary condition is not known exactly. It is felt that in most cases, it will be between the constant temperature and the constant flux condition. It becomes necessary then, to have the thermal resistance values corresponding to these two extreme cases. The thermal resistance to the constant flux condition is not available in conduction heat transfer texts, except reference [5], where a solution based upon bicylindrical coordinates is given. This solution in reference [5] is in error because the temperature and the thermal resistance go to zero, for the same heat transfer, as the pipe is displaced farther below ground level. This is obviously incorrect. The purpose of this technical brief, therefore, is to fill this gap and to point out the error in reference [5], so that we will have the thermal resistance values corresponding to the extreme cases, namely constant temperature and constant flux conditions. This brief deals with the exact solution based upon bicylindrical coordinates. The thermal resistance with a constant flux boundary condition is compared with the well-known expression for the constant temperature boundary condition.

Analysis

The governing differential equation for steady heat transfer through a homogeneous and isotropic medium of thermal conductivity k in bicylindrical coordinates is [4, 6]

$$\frac{\partial^2 T}{\partial \eta^2} + \frac{\partial^2 T}{\partial \psi^2} = 0 \quad (1)$$

[1] Graduate Research Assistant, Thermal Engineering group, Department of Mechanical Engineering, University of Waterloo, Waterloo, Ont., Canada.

[2] Professor of Mechanical Engineering, Thermal Engineering group, Department of Mechanical Engineering, University of Waterloo, Waterloo, Ont., Canada. Mem. ASME.

[3] Number in brackets designate References at end of technical brief.

Contributed by the Heat Transfer Division of THE AMERICAN SOCIETY OF MECHANICAL ENGINEERS. Manuscripts received by the Heat Transfer Division July 3, 1973.

where η and ψ are the bicylindrical coordinates, Fig. 1. The surface of the ground is $\eta = 0$, and can have the temperature $T = 0$. The surface of the pipe $\eta = \eta_0$, has a constant flux boundary condition [4].

$$\left[\frac{k}{\sqrt{g_\eta}}\frac{\partial T}{\partial \eta}\right]_{\eta_0} = \frac{Q}{2\pi r_0} \tag{2}$$

The metric coefficient in the η-direction g_η, i.e., normal to the pipe surface, is given by the following expression [4, 6]:

$$g_\eta = \frac{a^2}{[\cos h\ \eta - \cos\ \psi]^2} \tag{3}$$

where a is the distance from the ground surface to the origin of the coordinate system, Fig. 1. By symmetry the other boundary conditions are $\partial T/\partial\psi = 0$ at $\psi = 0$ and π.

Equation (1) can be separated into two ordinary differential equations whose solutions depend upon trigonometric as well as hyperbolic functions. By the method of separation of variables, the solution to equation (1) satisfying the boundary conditions is

$$T(\eta, \psi) = \frac{Q}{\pi k}\left[\frac{\eta}{2} + \sum_{n=1}^{\infty}\frac{e^{-n\eta_0}}{n\cos h(n\eta_0)}\sin h\ (n\eta)\cos\ (n\psi)\right] \tag{4}$$

where η_0 is related to the pipe radius and the distance from ground surface to the pipe center line as follows [4]:

$$\omega = r_0 \cos h\ \eta_0 \tag{5}$$

Equation (4) differs from the solution given in reference [5], in that it does not contain the term $1/\sin h\eta_0$. The thermal resistance will be defined as the difference between the average pipe surface temperature and the ground surface temperature divided by the total heat flow rate. Therefore

$$R_{q=c} = \frac{T_a}{Q} \tag{6}$$

where

$$T_a = \frac{\int_0^\pi T\sqrt{[g_\psi]}_{\eta=\eta_0}\,d\psi}{\int_0^\pi [\sqrt{g_\psi}]_{\eta=\eta_0}\,d\psi} \tag{7}$$

with $g_\psi = g_\eta$ for the bicylindrical system [4, 6]. Upon substitution of equation (4) into (7) and evaluating, one obtains for the average pipe surface temperature

$$T_a = \frac{Q}{\pi k}\left[\frac{\eta_0}{2} + \sum_{n=1}^{\infty}\frac{e^{-2n\eta_0}}{n}\tan h\ (n\eta_0)\right] \tag{8}$$

According to our definition of thermal resistance, the constant flux resistance per unit length of pipe is therefore:

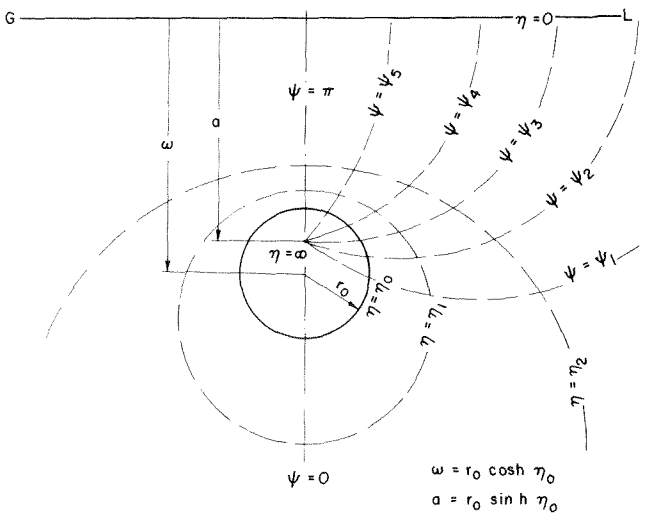

Fig. 1

Table 1

ω/r_0	η_0	$\frac{R_{q=c}}{R_{T=c}}$
1.001	0.04	20.21
1.005	0.10	9.07
1.010	0.14	6.44
1.050	0.31	2.97
1.1	0.44	2.18
1.2	0.62	1.66
1.3	0.76	1.44
1.4	0.87	1.32
1.5	0.96	1.25
1.6	1.05	1.20
1.7	1.12	1.16
1.8	1.19	1.14
1.9	1.26	1.11
2.0	1.32	1.10
3.0	1.76	1.03
4.0	2.06	1.015
5.0	2.29	1.009
10.0	2.99	1.002

$$R_{q=c} = \frac{\eta_0}{2\pi k} + \frac{1}{\pi k}\sum_{n=1}^{\infty}\frac{e^{-2n\eta_0}}{n}\tan h\ (n\eta_0) \tag{9}$$

This expression can now be compared with the constant temperature resistance expression [1–3]

$$R_{T=c} = \frac{1}{2\pi k}\ln\left[\frac{\omega}{r_0} + \sqrt{(\frac{\omega}{r_0})^2 - 1}\right] \tag{10}$$

which can also be written as

$$R_{T=c} = \frac{\eta_0}{2\pi k} \tag{11}$$

The ratio of the constant flux resistance to the constant temperature resistance is simply:

$$\frac{R_{q=c}}{R_{T=c}} = 1 + \frac{2}{\eta_0}\sum_{n=1}^{\infty}\frac{e^{-2n\eta_0}}{n}\tan h\ (n\eta_0) \tag{12}$$

The ratio is shown in Table 1 for typical values of ω/r_0 and corresponding values of η_0.

Conclusion

An exact solution for the constant flux boundary condition is presented and the thermal resistance expression is compared with the well-known constant temperature expression. It is seen in equation (12) and Table 1, that the resistance for the constant flux boundary condition is equal to the constant temperature resistance plus an additional resistance which is due to the fact that more heat leaves the bottom portion of the pipe under constant flux conditions than under constant temperature conditions. This effect is strongly dependent upon η_0. If the pipe is buried deeper than 5 pipe radii, the difference between the two resistances is less than one percent. It can be seen that for all practical purposes a pipe which is buried at a depth of 3 or more pipe radii, can be treated as a pipe having constant temperature boundary conditions. Also for a pipe which is buried 1.5 radii or more, the difference in the resistances corresponding to the two extreme boundary conditions is 25 percent or less. Where there is a possibility, that the actual boundary condition may lie in between the two extreme cases, we now have the opportunity to use a realistic value, since we have solutions available for both cases.

References

1 Eckert, E. R. G., and Drake, R. M., *Heat and Mass Transfer*, Second ed., McGraw-Hill, New York, pp. 60–64.

2 Boelter, L. M. K., Cherry, V. H., Johnson, H. A., and Martinelli, R. C., *Heat Transfer Notes*, McGraw-Hill, New York, 1965, pp. 297–299.

3 Schenck, H., *Heat Transfer Engineering*, Prentice-Hall, 1959, pp. 35–46.

4 Yovanovich, M. M., *Advanced Heat Conduction*, ME 751 Notes; to be published.

5 Lebedev, N. N., Skalskaya, I. P., and Uflyand, Ya. S., *Problems in Mathematical Physics*, (translated from Russian), Prentice Hall, 1965.

6 Magnus, W., and Oberhettinger, F., *Formulas and Theorems for the Functions of Mathematical Physics*, Chelsea Publishing Co., New York, 1949, pp. 153.

Turbulent Flow in a Tube With Wall Suction

M. R. Doshi[1] **and W. N. Gill**[1]

Nomenclature

A = constant in van Driest damping factor for impermeable tube, equation (5)
A_1 = constant in damping factor for permeable tube, equations (9), (10), and (11)
DF = damping factor, equations (5), (6), (8), and (9)
K = momentum flux factor, equation (3)
l^+ = dimensionless mixing length
r = radial coordinate
r_w = tube radius
r^+ = dimensionless radial coordinate, ru^*/ν
r_w^+ = dimensionless tube radius, $r_w u^*/\nu$
Re = Reynolds number, equation (2)
u = time averaged axial velocity
u_{max} = time averaged center-line velocity
u^* = friction velocity, $\sqrt{\tau_w/\rho}$
u^+ = u/u^*
$\bar{u}$ = mean axial velocity
v = times averaged transverse velocity
v_w = suction velocity at wall
v_w^+ = v_w/u^*
y = transverse coordinate, $r_w - r$
y^+ = yu^*/ν
μ = viscosity
ρ = density
ν = kinematic viscosity, μ/ρ
X = $v_w^+ y^+/2$
τ = shear stress
τ_w = shear stress at wall

Introduction

Recently Kinney and Sparrow [1][2] analyzed turbulent flow, heat transfer, and mass transfer in a tube with surface suction. The Reynolds stress was expressed in terms of the mixing length model. In the wall region, the van Driest damping factor was modified to account for the effect of wall suction. However, this model predicts an increase in the turbulence level due to suction which is contrary to the experimental observation of Weissberg and Berman [2, 3, 4]. Apparently this motivated Merkine, Solan, and Winograd [5] to take an empirical route for the modification of the van Driest damping factor and their results agree better with the experiments. The purpose of this paper is to show that by proper interpretation of the damping factor modification suggested by Kinney and Sparrow, their results can be improved significantly without additional empiricism. This is quite valuable in view of the fact that the damping factor concept originated by van Driest [6] is very useful in solving simple turbulent flow problems, and can be modified for solving some complicated problems [7, 8 among others].

Analysis

As shown by Kinney and Sparrow [1], continuity and momentum equations along with the assumption of local similarity can be reduced to the following integro-differential equation:

$$\frac{du^+}{dy^+} + l^{+2}\left(\frac{du^+}{dy^+}\right)^2 = \frac{r^+}{r_w^+} - \left(\frac{v_w}{\bar{u}}\right)\left\{\frac{\mathrm{Re}}{2} - \frac{2}{r_w^+}\int_0^{y^+} u^+ (r_w^+ - y^+)dy^+\right\}\frac{u^+}{r^+} + 4\left(\frac{v_w}{\bar{u}}\right)\frac{1}{r_w^+}\left\{\left[1 - \left(\frac{r^+}{r_w^+}\right)^2\right]\frac{\mathrm{Re}^2}{8}K - \int_0^{y^+} u^{+2}(r_w^+ - y^+)dy^+\right\}\frac{1}{r^+} \quad (1)$$

with the boundary condition $u^+ = 0$ at $y^+ = 0$. The Reynolds number Re and the momentum flux factor K are given by

$$\mathrm{Re} = \frac{2r_w\bar{u}}{\nu} = 2r_w^+\bar{u}^+ = \frac{4}{r_w^+}\int_0^{r_w^+} u^+(r_w^+ - y^+)dy^+ \quad (2)$$

and

$$K = \frac{8}{\mathrm{Re}^2}\int_0^{r_w^+} u^{+2}(r_w^+ - y^+)dy^+ \quad (3)$$

An expression for the mixing-length will complete the statement of the problem. For an impermeable tube, the mixing-length can be written as [9, p. 568]

$$\frac{l^+}{r_w^+} = DF\left\{0.4\frac{y^+}{r_w^+} - 0.44\left(\frac{y^+}{r_w^+}\right)^2 + 0.24\left(\frac{y^+}{r_w^+}\right)^3 - 0.06\left(\frac{y^+}{r_w^+}\right)^4\right\} \quad (4)$$

where the van Driest damping factor

$$DF = 1 - \exp(-y^+/A) \quad (5)$$

is obtained from the solution of Stokes' second problem, i.e., flow near an oscillating impermeable flat plate. Kinney and Sparrow [1] extended this concept by considering flow near an oscillating porous plate with suction at the wall. (This problem also has been studied by Nicoll, Strong, and Woolner [10].) They obtained the following expression for the damping factor:
For suction

$$DF = 1 - \exp\left\{-X - \frac{1}{\sqrt{2}}\left[\left(X^4 + 4\left(\frac{y^+}{A}\right)^4\right)^{1/2} + X^2\right]^{1/2}\right\} \quad (6)$$

where

$$X = v_w^+ y^+/2 \quad (7)$$

Note that for the case of an impermeable tube, $v_w^+ = 0$, equation (6) reduces to equation (5).

It is essential to recognize an important difference between the case of an oscillating porous plate, and that of turbulent flow in a tube or over a stationary plate with a porous wall. In the case of an oscillating plate, the plate generates the oscillations which are damped as the distance from the plate increases. Turbulent fluctuations in pipe flow (or over a stationary plate), on the other hand, are damped as the stationary pipe wall or plate is approached. Thus, the oscillating plate plays the role of the turbulent core in pipe flow and the turbulent free stream in flow over a flat plate. Consequently, the oscillating plate can be viewed as facing the stationary wall and therefore, transverse flow toward the stationary wall (suction) is accompanied by transverse flow away from the oscillating plate. Conversely, transverse flow away from the stationary wall (injection) is accompanied by transverse flow toward the oscillating plate. Thus, when developing the damping factor expression, by solving the oscillating porous plate problem, the transverse velocity should be reversed. This requires the sign of v_w in equation (6) to be changed. In this way, the damping direction is made compatible with the transverse flow direction. The corrected form of equation (6) is:

$$DF = 1 - \exp\left\{X - \frac{1}{\sqrt{2}}\left[\left(X^4 + 4\left(\frac{y^+}{A}\right)^4\right)^{1/2} + X^2\right]^{1/2}\right\} \quad (8)$$

where

$$X = v_w^+ y^+/2$$

and

$$v_w^+ > 0 \text{ for suction}$$

$$v_w^+ < 0 \text{ for injection}$$

Equation (8) also can be written as

[1] Faculty of Engineering and Applied Sciences, State University of New York at Buffalo, Buffalo, N. Y.

[2] Numbers in brackets designate References at end of technical brief.

Contributed by the Heat Transfer Division of THE AMERICAN SOCIETY OF MECHANICAL ENGINEERS. Manuscript received by the Heat Transfer Division, September 26, 1973.

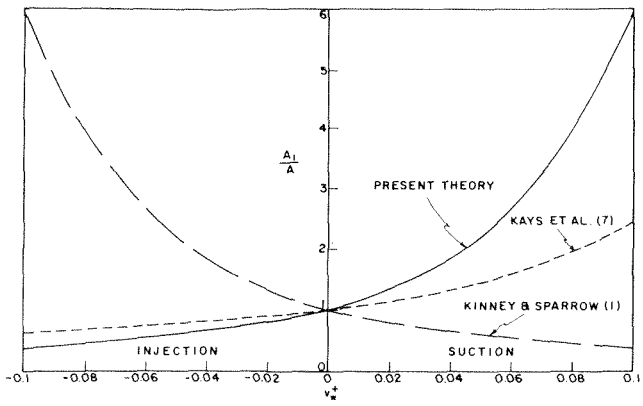

Fig. 1 Comparison of the damping factor constant

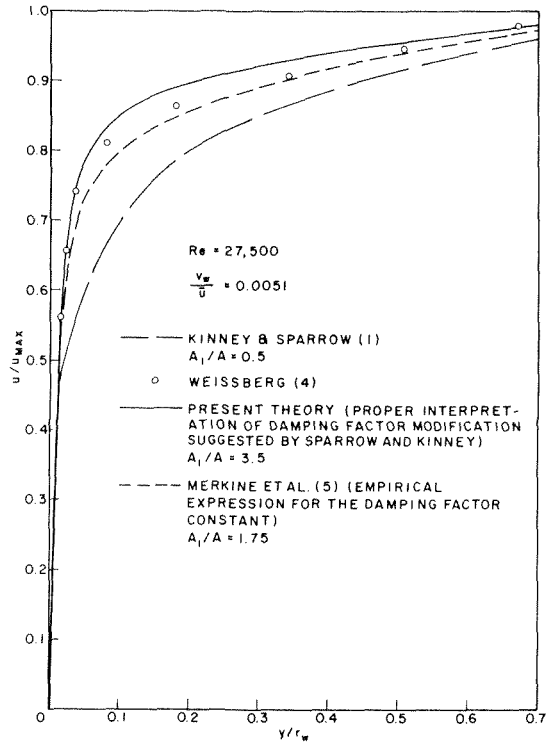

Fig. 2 Comparison of predicted and measured velocity profiles in turbulent pipe flow with uniform wall suction

$$DF = 1 - \exp\,(-y^+/A_1) \tag{9}$$

where

$$A_1 = \frac{1}{-\frac{v_w^+}{2} + \left[\frac{v_w^{+2}}{8} + \left(\frac{v_w^{+4}}{64} + \frac{1}{A^4}\right)^{1/2}\right]^{1/2}} \tag{10}$$

Merkine, Solan, and Winograd used an expression suggested by Kays, Moffat, and Thielbahr [7] on the basis of their experimental data for flat plates:

$$A_1 = \frac{4.42}{0.17 - v_w^+} \tag{11}$$

The damping factor constants obtained from equations (10) and (11) are compared in Fig. 1. The theoretical result, equation (10), and the empirical expression of Kays, et al. [7] indicate the same trend—A_1 increases for suction and decreases for injection. However, the expression of Kinney and Sparrow shows the reverse trend and in view of the arguments presented in the foregoing and the available experimental evidence, should be corrected by changing the sign of v_w^+ in the damping factor expression. The corrected velocity profiles, shown in Fig. 2, agree quite well with the experimental data of Weissberg and Berman.

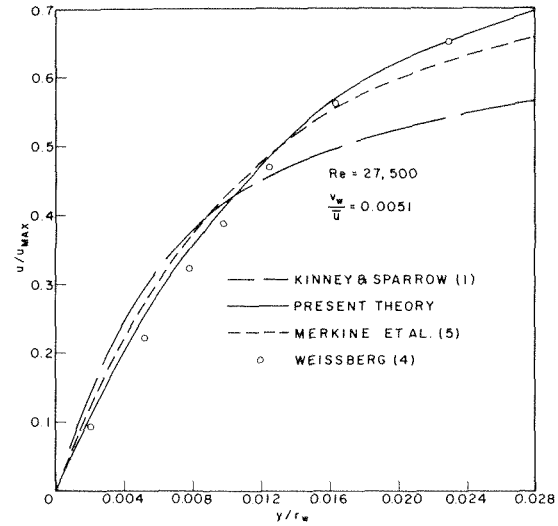

Fig. 3 Comparison of velocity profiles close to the wall of the porous pipe

The damping factor correction is more important in the region near the wall. Results for the wall region are shown in Fig. 3. It is encouraging to note that the results obtained from the present theory follow the experimental data very closely.

We conclude from this that the van Driest damping factor concept is quite useful and when modified properly to account for the transverse velocity at the wall, it can be used successfully to predict the velocity profiles and friction factors for turbulent flow in a porous tube. An important point is that by such a modification of the damping factor we are able to predict velocity profiles and friction factors for the turbulent flow in a porous tube by using information available for the flow in an impermeable tube.

Acknowledgment

The authors are grateful to Prof. R. B. Kinney, University of Arizona, for supplying a copy of his computer program which was of great help in obtaining numerical results reported herein. This work was supported in part by NSF grant KO34380.

References

1 Kinney, R. B., and Sparrow, E. M., "Turbulent Flow, Heat Transfer, and Mass Transfer in a Tube With Surface Suction," JOURNAL OF HEAT TRANSFER, TRANS. ASME, Series C, Vol. 92, No. 1, Feb. 1970, pp. 117–125.

2 Weissberg, H. L., and Berman, A. S., "Velocity and Pressure Distributions in Turbulent Pipe Flow With Uniform Wall Suction," *Proceedings of the Heat Transfer and Fluid Mechanics Institute*, Vol. 14, 1955, pp. 1–30.

3 Weissberg, H. L., "Velocity Profiles and Friction Factors for Turbulent Pipe Flow With Uniform Wall Suction," Report K-1264, Union Carbide Nuclear Company, Oak Ridge Gaseous Diffusion Plant, Oak Ridge, Tenn., 1956.

4 Weissberg, H. L., "Velocity and Pressure Distributions in Turbulent Pipe Flow With Uniform Wall Suction," Report K-1187 (Physics), K-25 Plant, Carbide and Carbon Chemicals Company, Oak Ridge, Tenn., 1954.

5 Merkine, L., Solan, A., and Winograd, Y., "Turbulent Flow in a Tube With Wall Suction," JOURNAL OF HEAT TRANSFER, TRANS. ASME, Series C, Vol. 93, No. 2, May 1971, pp. 242–244.

6 van Driest, E. R., "On Turbulent Flow Near a Wall," *Journal of the Aeronautical Sciences*, Vol. 23, 1956, p. 1007.

7 Kays, W. M., Moffat, R. J., and Thielbahr, W. H., "Heat Transfer to the Highly Accelerated Turbulent Boundary Layer With and Without Mass Addition," JOURNAL OF HEAT TRANSFER, TRANS. ASME, Series C, Vol. 92, No. 3, Aug. 1970, pp. 499–505.

8 Cebeci, T., "A Model for Eddy Conductivity and Turbulent Prandtl Number," JOURNAL OF HEAT TRANSFER, TRANS. ASME, Series C, Vol. 95, No. 2, May 1973, pp. 227–234.

9 Schlichting, H., *Boundary Layer Theory*, McGraw Hill, N. Y., 1968.

10 Nicoll, W. B., Strong, A. B., and Woolner, K. A., "On the Laminar Motion of a Fluid Near an Oscillating Porous, Infinite Plane," *Journal of Applied Mechanics*, TRANS. ASME, Series E, Vol. 35, No. 1, Mar. 1968, pp. 164–166.

Prediction of Heat Transfer in Turbulent Pipe Flow With Constant Wall Temperature

I. S. Habib[1] **and T. Y. Na**[1]

Nomenclature

- A^+ = damping factor for eddy viscosity
- B^+ = damping factor for eddy conductivity
- k = thermal conductivity
- l = mixing length, $l^+ = l\sqrt{\tau_w/\rho}/\nu$
- Nu = Nusselt number
- Pr, PR = Prandtl number, ν/α
- Pe = Peclet number, Pe = Re Pr
- p = static pressure
- q = heat flux
- Re, RE = Reynolds number, $u(2R)/\nu$
- r = radial coordinate, $r^+ = r\sqrt{\tau_w/\rho}/\nu$
- St = Stanton number = Nu/(Re Pr)
- u = axial velocity, $u^+ = u\sqrt{\tau_w/\rho}$
- v^* = shear velocity = $\sqrt{\tau_w/\rho}$
- x = axial coordinate, $x^+ = x\sqrt{\tau_w/\rho}/\nu$
- y = transverse coordinate normal to wall, $y^+ = y\sqrt{\tau_w/\rho}/\nu$
- α = thermal diffusivity
- ϵ_m, ϵ_h = kinematic eddy viscosity and eddy conductivity, respectively
- θ = nondimensional temperature = $(T_w - T)/(T_w - T_c)$; $\theta_b = (T_w - T_b)/(T_w - T_c)$
- ν = kinematic viscosity
- ρ = density
- τ = shear stress

Subscripts

- b = bulk
- c = center line
- w = at wall

Introduction

In the present note we employ a new mixing length model to analyze the turbulent heat transfer in pipes with constant wall temperature. The model was originally developed for boundary layer flows by Cebeci [1][2] and has been thoroughly described and employed before [2] in the analysis of the turbulent heat transfer in pipes with constant wall heat flux. The model was found to yield results for the Nusselt number and the temperature distribution that are in excellent agreement with the existing experimental data at low, medium, as well as at high values of the Prandtl number, and for Reynolds number exceeding 10^4. For the case of constant wall temperature, the model also yields results that are in excellent agreement with existing data over the same ranges of Prandtl number and Reynolds number.

Analysis

In the present analysis we study the problem of steady-state heating and cooling of an incompressible Newtonian fluid inside a smooth circular tube. The boundary condition is that of a constant wall temperature. The flow is considered to be turbulent with the temperature and velocity profiles fully developed. The fluid is assumed to have constant physical properties. Under these assumptions the momentum equation is written in the usual notations as follows:

$$\frac{-2r^+}{R^+} = \frac{d}{dr^+}\left[r^+\left(1 + \frac{\epsilon_m}{\nu}\right)\frac{du^+}{dr^+} \right] \tag{1}$$

subject to the conditions

$$r^+ = 0 \;:\; \frac{du^+}{dr^+} = 0 \tag{2a}$$

$$r^+ = R^+ \colon\; u^+ = 0 \tag{2b}$$

In equation (1) the expression for the shear stress at the wall, namely

$$-\frac{1}{\rho}\frac{dP}{dx} = \frac{2\tau_w}{\rho R} = \frac{2v^{*2}}{R} \tag{3}$$

has been used.

Introducing from Prandtl mixing length theory the relation

$$\frac{\epsilon_m}{\nu} = l^{+2}\frac{du^+}{dy^+} \tag{4}$$

where $y^+ = R^+ - r^+$, and integrating equation (1) once using boundary condition (2a), results in the following first-order differential equation for the velocity distribution

$$\frac{du^+}{dy^+} = \frac{2\left(1 - \dfrac{y^+}{R^+}\right)}{\left\{\sqrt{1 + 4l^{+2}\left(1 - \dfrac{y^+}{R^+}\right)} + 1\right\}} \tag{5}$$

subject to $y^+ = 0 : u^+ = 0$.

Following Seban and Shimazaki [3] where for fully developed turbulent flow we can write

$$\frac{\partial}{\partial x}\left(\frac{T_w - T}{T_w - T_b}\right) = 0 \tag{6}$$

the energy equation takes the form

$$u^+\frac{\theta}{\theta_b}\frac{d\theta_b}{dx^+} = \frac{1}{(R^+ - y^+)}\frac{d}{dy^+}\left\{(R^+ - y^+)\left(\frac{1}{Pr} + \epsilon_h^+\right)\frac{d\theta}{dy^+}\right\} \tag{7}$$

with the conditions

$$y^+ = 0 \;:\; \theta = 0 \tag{8a}$$

$$y^+ = R^+ \colon\; \theta = 1 \tag{8b}$$

The integration of equation (7)[3] using (8) results in the following equation for the temperature distribution.

$$\theta = \frac{\displaystyle\int_0^{y^+} \frac{1}{(R^+ - y'^+)\left(\frac{1}{Pr} + \epsilon_h^+\right)} \int_{R^+}^{y'^+} (R^+ - y''^+)u^+\theta\, dy''^+ \Big\} dy'^+}{\displaystyle\int_0^{R^+} \frac{1}{(R^+ - y'^+)\left(\frac{1}{Pr} + \epsilon_h^+\right)} \int_{R^+}^{y'^+} (R^+ - y''^+)u^+\theta\, dy''^+ \Big\} dy'^+} \tag{9}$$

The mixing length model used in this study is that presented and discussed in references [1, 2], and it is a modified form of that used previously by Kinney and Sparrow [4]. Using the form as presented in [1], and recalling equation (4), the expressions for ϵ_m and ϵ_h become

$$\frac{\epsilon_m}{\nu} = \epsilon_m^+ = (R^+)^2\left\{0.4\frac{y^+}{R^+} - 0.44\left(\frac{y^+}{R^+}\right)^2 + 0.24\left(\frac{y^+}{R^+}\right)^3 - 0.06\left(\frac{y^+}{R^+}\right)^4\right\}^2 \overline{DF_m}^2\frac{\partial u^+}{\partial y^+} \tag{10}$$

$$\text{where } \overline{DF_m} = \left[1 - \exp\left(-\frac{y^+}{A^+}\right)\right] \tag{11}$$

---

[1] Professor of Mechanical Engineering, The University of Michigan-Dearborn, Dearborn, Mich.

Contributed by the Heat Transfer Division of THE AMERICAN SOCIETY OF TECHNICAL ENGINEERS. Manuscript received by the Heat Transfer Division September 12, 1973.

[2] Numbers in brackets designate Reference at end of technical brief.

[3] We note that when equation (7) is divided by $u^+\theta$, the left-hand side, $(1/\theta_b)(d\theta_b/dx^+)$, becomes a function of x^+ only while the right-hand side is a function of y^+ alone. For this to be true each side should equal to the same constant C_1. This yields the variation of θ_b with x^+ as $\theta_b = C_2 e^{C_1 x^+}$, where C_2 is a constant of integration.

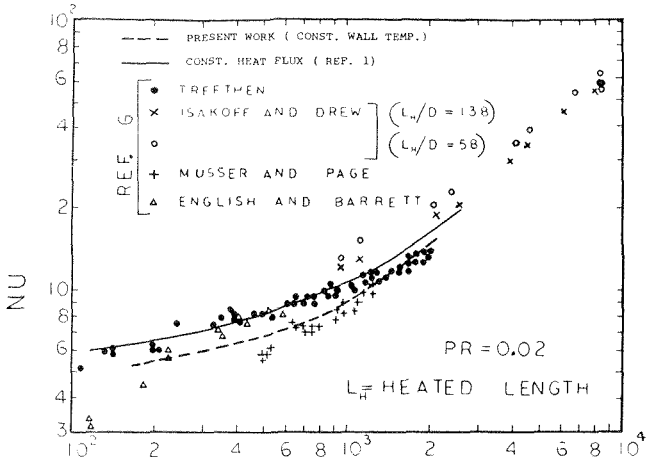

Fig. 1 Peclet number versus Nusselt number

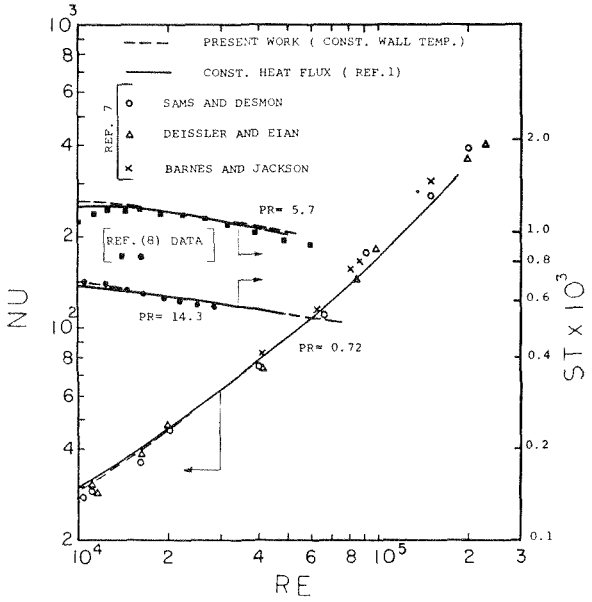

Fig. 2 Nusselt number and Stanton number versus Reynolds number

$$\text{and } \epsilon_h^+ = \frac{\epsilon_h}{\nu} = \epsilon_m^+ \frac{\overline{DF_h}}{\overline{DF_m}} \tag{12}$$

$$\text{Also, } \overline{DF_h} = \left[1 - \exp\left(-\frac{y^+\sqrt{Pr}}{B^+}\right)\right] \tag{13}$$

$$\text{and } A^+ = 26$$

$$B^+ = \sum_{i=1}^{5} C_i (\log_{10} Pr)^{i-1} \tag{14}$$

with $C_1 = 34.96$; $C_2 = 28.79$; $C_3 = 33.95$; $C_4 = 6.33$; $C_5 = -1.186$.

Employing this model and using the definition of Nusselt number along with equation (9), we obtain the following expression for Nusselt number

$$Nu = \frac{Pr\ \mathrm{Re}\ R^+}{2\phi(R^+)} \tag{15}$$

where

$$\phi(R^+) = \int_0^{R^+} \left\{ \frac{1}{(R^+ - y^+)\left(\frac{1}{Pr} + \epsilon_h^+\right)} \int_{R^+}^{y^+} (R^+ - y^{+\prime}) u^+ \theta dy^{+\prime} \right\} dy^+ \tag{16}$$

Results and Conclusions

The solution for the velocity distribution is obtained by numerically integrating equation (5) using the expression for the mixing length presented in reference [1]. The temperature distribution is obtained from equation (9) by the method of successive substitution. It was found that in most cases no more than three substitutions were needed for the solution to converge. With temperature and velocity distribution known, Nusselt number, then, was calculated from equation (15).

Representative results for Nusselt number and Stanton number are shown in Figs. 1 and 2 for Prandtl number equal to 0.02, 0.73, 5.7, and 14.3. We plotted the present results "constant wall temperature" along with the results of reference [2] "constant wall heat flux." The values of Nusselt numbers for Pr exceeding 0.72 for both boundary conditions are virtually identical. However for Pr = 0.02 the constant wall temperature solution resulted in lower values for Nusselt number than the constant heat flux. This is in agreement with the results presented in reference [5].

As a final conclusion, we would like to indicate that the present model for eddy conductivity and eddy viscosity results in good agreement with the experimental data over a wide range of Pr and Re and for both constant wall heat flux and constant wall temperature.

References

1 Cebeci, T., "A Model for Eddy Conductivity and Turbulent Prandtl Number," JOURNAL OF HEAT TRANSFER, TRANS. ASME, Series C, Vol. 95, 1973, pp. 227-236.

2 Na, T. Y., and Habib, I. S., "Heat Transfer in Turbulent Pipe Flow Based on a New Mixing Length Model," *Applied Scientific Research*, Vol. 28, Nov. 1973.

3 Seban, R. A., and Shimazaki, T. T., "Heat Transfer to a Fluid Flowing Turbulently in a Smooth Pipe With Walls at Constant Temperature," TRANS. ASME, Vol. 73, 1951, pp. 803-809.

4 Kinney, R. B., and Sparrow, E. M., "Turbulent Flow, Heat Transfer and Mass Transfer in a Tube With Surface Suction," JOURNAL OF HEAT TRANSFER, TRANS. ASME, Series C, Vol. 92, No. 1, 1970, pp. 117-125.

5 Kays, W. M., *Convective Heat and Mass Transfer*, McGraw-Hill, New York, 1966.

6 McAdams, W. H., *Heat Transmission*, Third ed., McGraw-Hill, New York, 1954.

7 Lawn, C. J., "Turbulent Heat Transfer at Low Reynolds Number," JOURNAL OF HEAT TRANSFER, TRANS. ASME, Series C, Vol. 91, No. 4, 1969, pp. 532-536.

8 Gowan, R. A., and Smith, J. W., "The Effect of the Prandtl Number on Temperature Profiles for Heat Transfer in Turbulent Pipe Flow," *Chem. Eng. Sci.*, Vol. 22, 1967, pp. 1701-1711.

Configuration Factors for Radiant Heat Exchange in Cavities Bounded at the Ends by Parallel Disks and Having Conical Centerbodies

J. Holchendler,[1] and W. F. Laverty,[2]

Nomenclature

A_i = surface area i
dA_i = differential element on surface i
F_{i-j} = configuration factor from surface i to j
l, m, n = directional cosines
L = axial distance from surface 1 to 3
R_i = radial dimension as specified in Fig. 1
r, θ, Z = cylindrical coordinates
X, Y, Z = cartesian coordinates

[1] Senior Engineer, Pratt & Whitney Aircraft, East Hartford, Conn.

[2] Project Engineer, Pratt & Whitney Aircraft, East Hartford, Conn.

Contributed by the Heat Transfer Division of THE AMERICAN SOCIETY OF MECHANICAL ENGINEERS. Manuscript received by the Heat Transfer Division August 31, 1973.

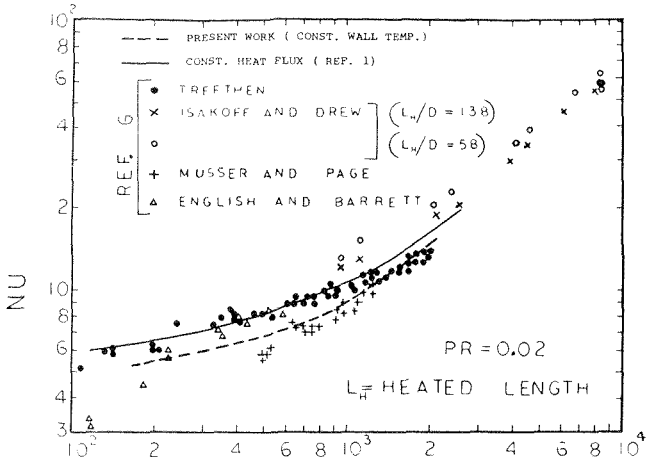

Fig. 1 Peclet number versus Nusselt number

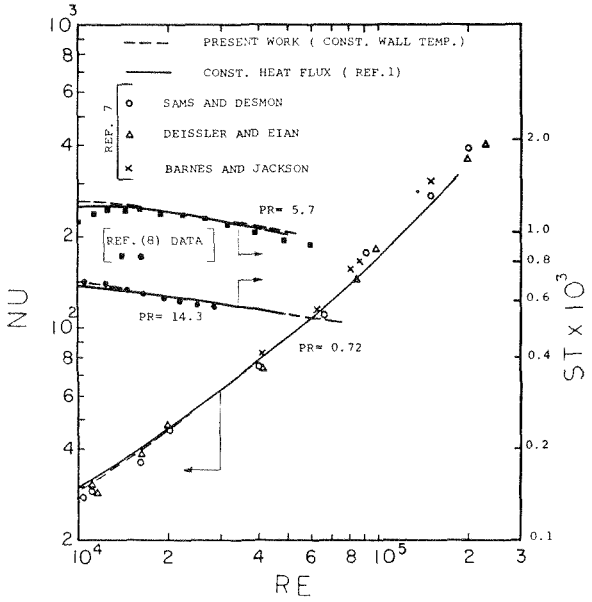

Fig. 2 Nusselt number and Stanton number versus Reynolds number

$$\text{and } \epsilon_h^+ = \frac{\epsilon_h}{\nu} = \epsilon_m^+ \frac{\overline{DF_h}}{\overline{DF_m}} \tag{12}$$

$$\text{Also, } \overline{DF_h} = \left[1 - \exp\left(-\frac{y^+\sqrt{Pr}}{B^+}\right)\right] \tag{13}$$

$$\text{and } A^+ = 26$$

$$B^+ = \sum_{i=1}^{5} C_i (\log_{10} Pr)^{i-1} \tag{14}$$

with $C_1 = 34.96$; $C_2 = 28.79$; $C_3 = 33.95$; $C_4 = 6.33$; $C_5 = -1.186$.

Employing this model and using the definition of Nusselt number along with equation (9), we obtain the following expression for Nusselt number

$$Nu = \frac{Pr\ \mathrm{Re}\ R^+}{2\phi(R^+)} \tag{15}$$

where

$$\phi(R^+) = \int_0^{R^+} \left\{ \frac{1}{(R^+ - y^+)\left(\frac{1}{Pr} + \epsilon_h^+\right)} \int_{R^+}^{y^+} (R^+ - y^{+\prime}) u^+ \theta dy^{+\prime} \right\} dy^+ \tag{16}$$

Results and Conclusions

The solution for the velocity distribution is obtained by numerically integrating equation (5) using the expression for the mixing length presented in reference [1]. The temperature distribution is obtained from equation (9) by the method of successive substitution. It was found that in most cases no more than three substitutions were needed for the solution to converge. With temperature and velocity distribution known, Nusselt number, then, was calculated from equation (15).

Representative results for Nusselt number and Stanton number are shown in Figs. 1 and 2 for Prandtl number equal to 0.02, 0.73, 5.7, and 14.3. We plotted the present results "constant wall temperature" along with the results of reference [2] "constant wall heat flux." The values of Nusselt numbers for Pr exceeding 0.72 for both boundary conditions are virtually identical. However for Pr = 0.02 the constant wall temperature solution resulted in lower values for Nusselt number than the constant heat flux. This is in agreement with the results presented in reference [5].

As a final conclusion, we would like to indicate that the present model for eddy conductivity and eddy viscosity results in good agreement with the experimental data over a wide range of Pr and Re and for both constant wall heat flux and constant wall temperature.

References

1 Cebeci, T., "A Model for Eddy Conductivity and Turbulent Prandtl Number," JOURNAL OF HEAT TRANSFER, TRANS. ASME, Series C, Vol. 95, 1973, pp. 227-236.

2 Na, T. Y., and Habib, I. S., "Heat Transfer in Turbulent Pipe Flow Based on a New Mixing Length Model," *Applied Scientific Research*, Vol. 28, Nov. 1973.

3 Seban, R. A., and Shimazaki, T. T., "Heat Transfer to a Fluid Flowing Turbulently in a Smooth Pipe With Walls at Constant Temperature," TRANS. ASME, Vol. 73, 1951, pp. 803-809.

4 Kinney, R. B., and Sparrow, E. M., "Turbulent Flow, Heat Transfer and Mass Transfer in a Tube With Surface Suction," JOURNAL OF HEAT TRANSFER, TRANS. ASME, Series C, Vol. 92, No. 1, 1970, pp. 117-125.

5 Kays, W. M., *Convective Heat and Mass Transfer*, McGraw-Hill, New York, 1966.

6 McAdams, W. H., *Heat Transmission*, Third ed., McGraw-Hill, New York, 1954.

7 Lawn, C. J., "Turbulent Heat Transfer at Low Reynolds Number," JOURNAL OF HEAT TRANSFER, TRANS. ASME, Series C, Vol. 91, No. 4, 1969, pp. 532-536.

8 Gowan, R. A., and Smith, J. W., "The Effect of the Prandtl Number on Temperature Profiles for Heat Transfer in Turbulent Pipe Flow," *Chem. Eng. Sci.*, Vol. 22, 1967, pp. 1701-1711.

Configuration Factors for Radiant Heat Exchange in Cavities Bounded at the Ends by Parallel Disks and Having Conical Centerbodies

J. Holchendler,[1] and W. F. Laverty,[2]

Nomenclature

A_i = surface area i
dA_i = differential element on surface i
F_{i-j} = configuration factor from surface i to j
l, m, n = directional cosines
L = axial distance from surface 1 to 3
R_i = radial dimension as specified in Fig. 1
r, θ, Z = cylindrical coordinates
X, Y, Z = cartesian coordinates

[1] Senior Engineer, Pratt & Whitney Aircraft, East Hartford, Conn.
[2] Project Engineer, Pratt & Whitney Aircraft, East Hartford, Conn.

Contributed by the Heat Transfer Division of THE AMERICAN SOCIETY OF MECHANICAL ENGINEERS. Manuscript received by the Heat Transfer Division August 31, 1973.

GEOMETRIC DESCRIPTION FOR CONFIGURATION FACTORS

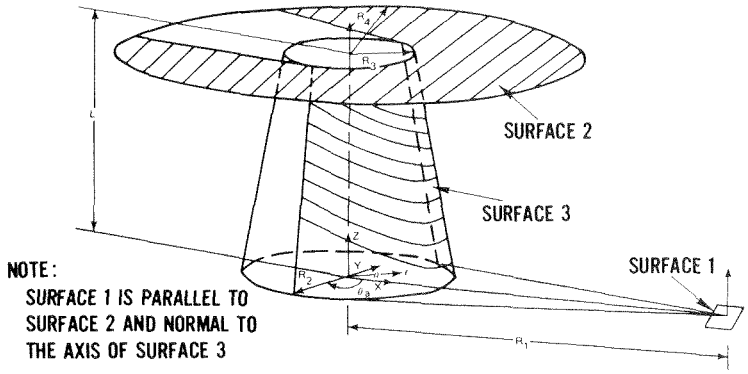

Fig. 1

ρ = length of vector from dA_i to dA_j
θ_i = angle formed by normal to surface i and vector between surfaces i and j

Using contour integration, radiation configuration factors are derived and presented in closed form solution for the case of a differential area to a parallel disk with conical blockage and for the case of the same differential element to the conical centerbody.

Introduction

With advancing technology, gas turbine cycle temperatures have risen to the degree that radiation has become a significant mode of heat transfer within internal engine cavities. Geometrically, most cavities of interest can be modeled as cylinders or truncated cones with or without cylindrical or conical centerbodies. Some of the configuration factors needed for analysis of such cavities are available in standard references such as the report of Hamilton and Morgan [1].[3] Two geometries important to the analysis which have not been treated in the open literature, are the element to disk with conical blockage, and the element to truncated cone, both of which are shown in Fig. 1.

The objective of this paper is to present the results of analysis done to evaluate the configuration factors for these two geometries. These results were used to generate, by means of numerical integration, computer subprograms to evaluate the configuration factors for use in cavities having axial symmetry.

Method of Analysis

Two methods of analysis were considered for evaluation of the configuration factors, direct integration and contour integration. Since contour integration of both geometries to be considered involves only circular arcs and straight lines, it is the better of the two.

The configuration factor between a surface area element dA_1 and a definite area A_2 is defined by the equation:

$$F_{dA_1\text{-}A_2} = \frac{1}{\pi}\int_{A_2} \frac{\cos\theta_1 \cos\theta_2}{\rho^2}\, dA_2 \tag{1}$$

where ρ is the length of a vector between dA_1 and dA_2, and θ and θ_2 are the angles between this vector and normals to dA_1 and dA_2, respectively. In the contour integration method the surface integral (1) is transformed to the line integral:

$$F_{dA\text{-}A_2} = \frac{1}{2\pi}\oint_c \Big\{ \frac{n_1(Y_2 - Y_1) - m_1(Z_2 - Z_1)}{\rho^2}\, dX_2 + \frac{l_1(Z_2 - Z_1) - n_1(X_2 - X_1)}{\rho^2}\, dY_2 + \frac{m_1(X_2 - X_1) - l_1(Y_2 - Y_1)}{\rho^2} dZ_2 \Big\} \tag{2}$$

where X_1, Y_1, and Z_1 are the coordinates of dA_1, l_1, m_1, and n_1 are direction cosines of the normal to dA_1, X_2, Y_2, and Z_2 are the coordinates of points on the periphery of dA_2 and ρ is the distance between dA_1 and the point (X_2, Y_2, Z_2).

For the coordinate system shown in Fig. 1, dA_1 is located on the X axis with its normal parallel to the Z axis, $X_1 = R_1$ and $Y_1 = 0$ so that equation (2) reduces to:

$$F_{dA_1\text{-}A_2} = \frac{1}{2\pi}\oint_c \frac{Y_2 dX_2 - (X_2 - R_1)dY_2}{(X_2 - R_1)^2 + Y_2^2 + Z_2^2} \tag{3a}$$

and in cylindrical coordinates:

$$F_{dA_1\text{-}A_2} = \frac{1}{2\pi}\oint_c \frac{R_1 \sin\theta_2 dr_2 + r_2(R_1\cos\theta_2 - r_2)d\theta_2}{r_2^2 + Z_2^2 + R_1^2 - 2r_2R_1\cos\theta_2} \tag{3b}$$

One final simplification can be made in view of the symmetry of the problems about the X axis. Referring to equation (3) it is observed that both the denominator and the variable X_2 have the same value at points of symmetry whereas the variable Y_2 reverse sign. Since the integration is carried out proceeding in one direction around the contour, dY_2 will have the same sign at points of symmetry whereas dX_2 will reverse sign. The net result is that the portion of the line integral on the negative side of the X axis is equal to that on the positive side so that only the integrals on one side of the X axis must be evaluated. The closed contour will be obtained by doubling the integral for the half space contour.

Solution

From Fig. 1 it is clear that in solving the two problems, integration will be carried out along the three circular arcs dimensioned as R_2, R_3, R_4. The four lines required to complete the contours are shadow lines which are generated by intercepts between the disk and cone surfaces with the two planes which pass through the element dA_1 and are tangent to the cone.

The tangent lines are seen to be lines of constant θ which would pass through the apex of the truncated cone if it were extended. Working in the plane $Z = 0$, the angle, θ_a, of these tangent lines is easily shown to be:

$$\theta_a = \cos^{-1}\left(\frac{R_2}{R_1}\right) \tag{4}$$

Referring to Fig. 2, the intercepts of the tangent planes with the plane $Z = L$ are seen to be straight lines which are tangent to the circle $r = R_3$, $Z = L$ at $\theta = \pm\theta_a$. These lines which complete the contour of surface 2 are readily shown to intersect the circle $r = R_4$, $Z = L$ at

$$\theta_b = \theta_a + \cos^{-1}\left(\frac{R_3}{R_4}\right) \tag{5}$$

Having defined the curves and break points needed for the con-

[3] Number in brackets designate References at end of technical brief.

tour integration, it remains to carry out the integration for each of the two problems.

Configuration Factor for the Element to Annular Disk With Conical Blockage. The contour to be integrated is shown in Fig. 2. Making use of the simplicity of the curves and the symmetry argument the complete integral is computed as twice the sum of the integrals from a to b, b to c, and c to d. The first of these, from a to b along the circular arc $r_2 = R_3$, $Z_2 = L$, is computed using equation (3b):

$$\oint_a^b = \frac{1}{2\pi}\int_0^{\theta_a} \frac{R_3(R_1 \cos\theta_2 - R_3)d\theta_2}{R_3^2 + L^2 + R_1^2 - 2R_3R_1\cos\theta_2} \tag{6}$$

Defining $\alpha_i = R_i^2 + R_1^2 + L^2$ and $\beta_i = 2R_i R_1$ and dividing the first term in the numerator by the denominator gives:

$$\int_a^b = \frac{1}{2\pi}\int_0^{\theta_a} \left[\frac{\frac{\alpha_3}{2} - R_3^2}{\alpha_3 - \beta_3\cos\theta_2} - \frac{1}{2} \right] d\theta_2 \tag{7}$$

Making use of standard integral tables and observing that $\alpha_3 > \beta_3$ because the denominator is the square of the radius vector gives:

$$\oint_a^b = \frac{1}{2\pi}\left\{ \frac{\alpha_3 - 2R_3^2}{\sqrt{\alpha_3^2 - \beta_3^2}} \tan^{-1}\left[\frac{\sqrt{\alpha_3^2 - \beta_3^2}\tan\frac{\theta_a}{2}}{\alpha_3 - \beta_3} \right] - \frac{\theta_a}{2} \right\} \tag{8}$$

Considering next the integral along the line b-c, it is readily shown that the equation of the line is given by:

$$Y_2 = \left(\frac{R_3}{\cos\theta_a} - X_2\right)\frac{1}{\tan\theta_a}, \quad Z_2 = L \tag{9}$$

Using equation (9) to eliminate the variable X from equation (3a) the integral along the line b-c is reduced to a quadratic in Y_2 which integrates to give:

$$\oint_b^c = \frac{R_3 - R_2}{2\pi\sqrt{(R_3 - R_2)^2 + L^2}}\left[\tan^{-1}\left\{\frac{\sqrt{R_1^2 - R_2^2}}{\sqrt{(R_3 - R_2)^2 + L^2}}\right\} - \tan^{-1}\left\{\frac{\sqrt{R_4^2 - R_3^2} + \sqrt{R_1^2 - R_2^2}}{\sqrt{(R_3 - R_2)^2 + L^2}}\right\}\right] \tag{10}$$

The final integral to be solved, from c to d along the circular arc $r_2 = R_4$, $Z_2 = L$, is again computed using the equation (3b).

$$\oint_c^d = \frac{1}{2\pi}\int_{\theta_b}^{0} \frac{R_4(R_1\cos\theta_2 - R_4)d\theta_2}{R_4^2 + L^2 + R_1^2 - 2R_4R_1\cos\theta_2} \tag{11}$$

Comparing equation (11) with equation (6) and making use of the definitions of α and β and equation (8) leads directly to the solution:

$$\oint_c^d = -\frac{1}{2\pi}\left\{ \frac{\alpha_4 - 2R_4^2}{\sqrt{\alpha_4^2 - \beta_4^2}} \tan^{-1}\left[\frac{\sqrt{\alpha_4^2 - \beta_4^2}\tan\left(\frac{\theta_b}{2}\right)}{\alpha_4 - \beta_4} \right] - \frac{\theta_b}{2} \right\} \tag{12}$$

Summing the terms (equations (8), (10), and (12)) and making use of equations (4) and (5), plus basic trogonometric relationships to reduce the solution to the basic variables yields the final result:

$$F_{dA_1\text{-}A_2} = \frac{1}{2\pi}\cos^{-1}\left(\frac{R_3}{R_4}\right) + \frac{R_1^2 - R_3^2 + L^2}{\pi\sqrt{[(R_1 + R_3)^2 + L^2][(R_1 - R_3)^2 + L^2]}} \times \tan^{-1}\sqrt{\frac{[(R_1 + R_3)^2 + L^2](R_1 - R_2)}{[(R_1 - R_3)^2 + L^2](R_1 + R_2)}} - \frac{R_1^2 - R_4^2 + L^2}{\pi\sqrt{[(R_1 + R_4)^2 + L^2][(R_1 - R_4)^2 + L^2]}} \tan^{-1}\sqrt{\frac{[(R_1 + R_4)^2 + L^2][R_1R_4 - R_2R_3 + \sqrt{(R_1^2 - R_2^2)(R_4^2 - R_3^2)}]}{[(R_1 - R_4)^2 + L^2][R_1R_4 + R_2R_3 - \sqrt{(R_1^2 - R_2^2)(R_4^2 - R_3^2)}]}} \tag{13}$$

CONTOUR FOR DISK WITH BLOCKAGE

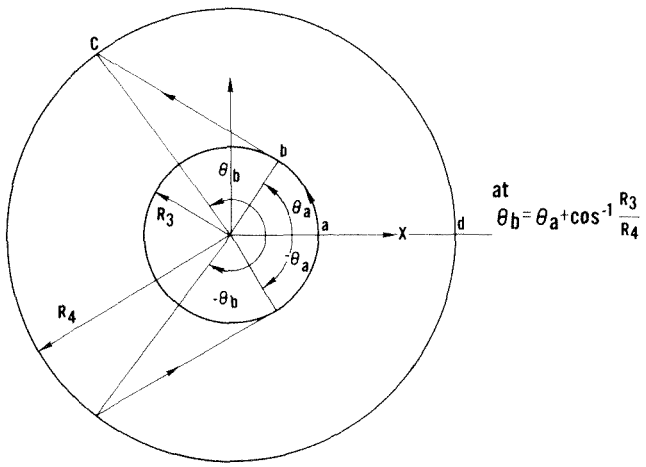

Fig. 2

$$- \frac{R_3 - R_2}{\pi\sqrt{(R_3 - R_2)^2 + L^2}}\left\{\tan^{-1}\left[\frac{\sqrt{R_1^2 - R_2^2} + \sqrt{R_4^2 - R_3^2}}{\sqrt{(R_3 - R_2)^2 + L^2}}\right] - \tan^{-1}\left[\frac{\sqrt{R_1^2 - R_2^2}}{\sqrt{(R_3 - R_2)^2 + L^2}}\right]\right\} \tag{13}$$

Configuration Factor for the Element to Truncated Cone. The contour to be integrated for the element to truncated cone configuration factor is shown in Fig. 3. As in the solution of the first problem the symmetry of the contour permits the configuration factor to be computed as twice the sum of the integrals from e to f, f to g, and g to h.

The first integral, from e to f along the circular arc $r_2 = R_2$, $Z_2 = 0$ is obtained from equation (3b).

$$\oint_e^f = \frac{1}{2\pi}\int_0^{\theta_a} \frac{R_2(R_1\cos\theta_2 - R_2)d\theta_2}{R_2^2 + R_1^2 - 2R_2R_1\cos\theta_2} \tag{14}$$

Integration of equation (14), similar to the integration of equation (6), yields:

$$\oint_e^f = \frac{1}{2\pi}\left\{-\frac{\theta_a}{2} + \tan^{-1}\left[\frac{R_1 + R_2}{R_1 - R_2}\tan\left(\frac{\theta_a}{2}\right)\right]\right\} \tag{15}$$

The second integral is along the line f to g which is given by the equation:

$$Z = \left(\frac{r_2 - R_2}{R_3 - R_2}\right)L, \quad \theta_2 = \theta_a \tag{16}$$

CONTOUR FOR TRUNCATED CONE

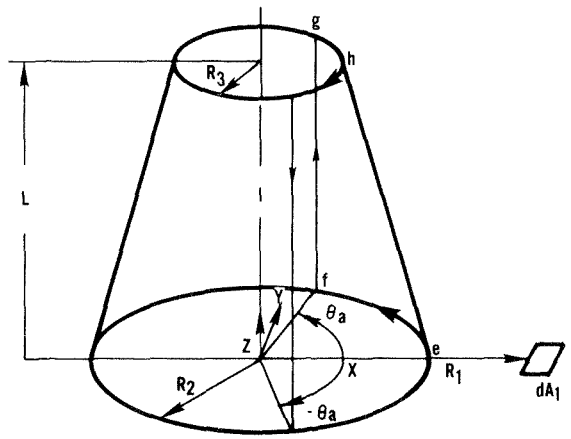

Fig. 3

Again using equation (3*b*) the integral is a quadratic form which is readily evaluated and reduced using equation (4) to yield:

$$\oint_f^g = \frac{1}{2\pi} \frac{R_3 - R_2}{\sqrt{(R_3 - R_2)^2 + L^2}} \tan^{-1} \sqrt{\frac{(R_3 - R_2)^2 + L^2}{R_1^2 - R_2^2}} \quad (17)$$

The third integral, from g to h along circular arc $r_2 = R_3$, $Z_2 = L$ was evaluated in the previous problem with the direction of integration reversed. Therefore using equation (8) gives:

$$\oint_g^h = -\frac{1}{2\pi} \left\{ \frac{\alpha_3 - 2R_3^2}{\sqrt{\alpha_3^2 - \beta_3^2}} \tan^{-1} \left[\frac{\sqrt{\alpha_3^2 - \beta_3^2}}{\alpha_3 - \beta_3} \tan\left(\frac{\theta_a}{2}\right) \right] - \frac{\theta_a}{2} \right\} \quad (18)$$

The final solution is now obtained by summing the terms (equations (15), (17), and (18)) which, after reduction to basic variables yields the result:

$$F_{dA_1\text{-}A_3} = \frac{1}{\pi} \left\{ \tan^{-1} \sqrt{\frac{R_1 + R_2}{R_1 - R_2}} + \frac{R_3 - R_2}{\sqrt{(R_3 - R_2)^2 + L^2}} \tan^{-1} \sqrt{\frac{(R_3 - R_2)^2 + L^2}{R_1^2 - R_2^2}} - \frac{R_1^2 - R_3^2 + L^2}{\sqrt{[(R_1 - R_3)^2 + L^2][(R_1 + R_3)^2 + L^2]}} \tan^{-1} \sqrt{\frac{[(R_1 + R_3)^2 + L^2](R_1 - R_2)}{[(R_1 - R_3)^2 + L^2](R_1 + R_2)}} \right\} \quad (19)$$

Integrated Forms

To complete the solution of the cavity problem it is desirable to extend the element, dA_1, to an annular ring concentric with the centerbody. This is accomplished in a straight-forward manner using the equation:

$$F_{A_1\text{-}A_i} = \frac{2}{R_{1_0}^2 - R_{1_i}^2} \int_{R_{1_i}}^{R_{1_0}} F_{dA_1\text{-}A_i} R_1 \, dR_1 \quad (20)$$

where $R_{1(i)}$ and $R_{1(0)}$ are, respectively, the inner and outer radii of the annular ring. Because of the complexity of the differential configuration factor terms, $F_{dA(1)\,-\,A(i)}$ as given by equations (13) and (19), numerical integration was used, to solve equation (20) for the two cases. Listings of the two Fortran computer programs which were written for this purpose for the ring to disk, $F_{A(1)\,-\,A(2)}$, and for the ring to centerbody, $F_{A(1)\,-\,A(3)}$, are available upon request.

In closing it should be noted that, within the limitations of axial symmetry, the centerbody may be divided into several axial subareas and the opposing disk may be divided into annular rings by standard view factor algebra techniques. View factor algebra is also used to determine the configuration factors to a fourth surface which encloses the cavity.

References

1 Hamilton, D. C., and Morgan, W. R., "Radiant-Interchange Configuration Factors," NACA Technical Note 2836, 1952.

2 Leuenberger, H., and Person, R. A., "Compilation of Radiation Shape Factors for Cylindrical Assemblies," ASME Paper No. 56-A-144.

3 Sparrow, E. M., and Cess, R. D., *Radiation Heat Transfer*, Brooks/Cole Publishing Co., 1970.

The Effect of an Electric Field in the Presence of Noncondensable Gas on Film Condensation Heat Transfer

A. K. Seth[1] **and L. Lee**[2]

Introduction

This study describes the effect of a uniform electric field in the presence of noncondensable gas on film condensation heat transfer to the outside of a horizontal tube.

The effects of electric fields on film condensation have been studied by Choi [1],[3] Velkoff and Miller [2], and, more recently, Holmes and Chapman [3]. They have found that the condensation heat transfer rate of Freon 113 or Freon 114 can be increased markedly by the application of an electric field.

Choi condensed Freon 113 on the inside of a vertical tube with an electrode at the axis of the tube. By applying a uniform electric field, Choi found that the heat transfer coefficient could be increased by 100 percent. Velkoff and Miller condensed Freon 113 on a flat plate which was parallel to electrodes with d-c potential applied. They found that the heat transfer coefficient could be increased by 200 percent. More recently, Holmes and Chapman condensed Freon 114 on a grounded, inclined flat plate, with a nonuniform electric field produced by applying a voltage to a second plate placed above the first at various angles. They found that the heat transfer coefficients could be increased by as much as ten times as with no electric field applied when a voltage above 40 KV was imposed.

Othmer [5] has conducted a systematic experimental study of the effects of noncondensable gases on the condensation of steam when mixed with air. Empirical relationships between variables have been derived from the experiments and trial and error solutions of heat transfer for several situations are given by [5, 6, 7]. Sparrow and Lin [8], and Minkowycz and Sparrow [9] obtained boundary layer solutions of film condensation with the presence of noncondensable gases for a variety of physical conditions. Their findings indicate that even with a small fraction of noncondensable gases, the heat transfer rate in film condensation may be reduced by 50 percent or more.

Since it is difficult and expensive to eliminate all noncondensable gases in a bulk vapor, the ability to overcome their poisoning affect on heat transfer in film condensation with suitable electric fields appears to be significant. This paper reports the effect of electric fields on the film condensation of vapor Freon in the presence of air on the outside of a horizontal tube.

Experimental Apparatus and Procedures

The experimental investigation was carried out in a condenser loop using Freon 113 as the test fluid. The experimental equipment is shown in Fig. 1.

During testing, Freon 113 was heated by a water bath with the temperature controlled by a 500 W heater, stirrer, and thermostat. Freon 113 flowed from the boiler to the inlet chamber through a ⅜ in. ID copper tubing, around which heating tapes were wound to prevent Freon from condensing in the tubing. Inside the condenser, Freon condensed on the outer surface of a 1 in. ID horizontal copper tube, which was inside and concentric with a 2 in. OD glass tube, which makes up the condenser. Six copper constantan insulated thermocouples were embedded in the condensing surface to measure the surface temperature. The condensing surface was cooled by counterflowing cooling water. The condensation heat transfer rate was determined by accurate measurement of the coolant flow rate and the coolant temperature increase.

[1] Project Engineer, Balco Inc., Medford, Mass.

[2] Assoc. Professor, Department of Mechanical Engineering, University of Maine, Orono, Me.

[3] Numbers in brackets designate References at end of technical brief.

Contributed by the Heat Transfer Division of THE AMERICAN SOCIETY OF MECHANICAL ENGINEERS. Manuscript received by the Heat Transfer Division October 29, 1973.

Again using equation (3*b*) the integral is a quadratic form which is readily evaluated and reduced using equation (4) to yield:

$$\oint_f^g = \frac{1}{2\pi} \frac{R_3 - R_2}{\sqrt{(R_3 - R_2)^2 + L^2}} \tan^{-1} \sqrt{\frac{(R_3 - R_2)^2 + L^2}{R_1^2 - R_2^2}} \quad (17)$$

The third integral, from g to h along circular arc $r_2 = R_3$, $Z_2 = L$ was evaluated in the previous problem with the direction of integration reversed. Therefore using equation (8) gives:

$$\oint_g^h = -\frac{1}{2\pi} \left\{ \frac{\alpha_3 - 2R_3^2}{\sqrt{\alpha_3^2 - \beta_3^2}} \tan^{-1} \left[\frac{\sqrt{\alpha_3^2 - \beta_3^2}}{\alpha_3 - \beta_3} \tan\left(\frac{\theta_a}{2}\right) \right] - \frac{\theta_a}{2} \right\} \quad (18)$$

The final solution is now obtained by summing the terms (equations (15), (17), and (18)) which, after reduction to basic variables yields the result:

$$F_{dA_1\text{-}A_3} = \frac{1}{\pi} \left\{ \tan^{-1} \sqrt{\frac{R_1 + R_2}{R_1 - R_2}} + \frac{R_3 - R_2}{\sqrt{(R_3 - R_2)^2 + L^2}} \tan^{-1} \sqrt{\frac{(R_3 - R_2)^2 + L^2}{R_1^2 - R_2^2}} - \frac{R_1^2 - R_3^2 + L^2}{\sqrt{[(R_1 - R_3)^2 + L^2][(R_1 + R_3)^2 + L^2]}} \tan^{-1} \sqrt{\frac{[(R_1 + R_3)^2 + L^2](R_1 - R_2)}{[(R_1 - R_3)^2 + L^2](R_1 + R_2)}} \right\} \quad (19)$$

Integrated Forms

To complete the solution of the cavity problem it is desirable to extend the element, dA_1, to an annular ring concentric with the centerbody. This is accomplished in a straight-forward manner using the equation:

$$F_{A_1\text{-}A_i} = \frac{2}{R_{1_0}^2 - R_{1_i}^2} \int_{R_{1_i}}^{R_{1_0}} F_{dA_1\text{-}A_i} R_1 \, dR_1 \quad (20)$$

where $R_{1(i)}$ and $R_{1(0)}$ are, respectively, the inner and outer radii of the annular ring. Because of the complexity of the differential configuration factor terms, $F_{dA(1)\,-\,A(i)}$ as given by equations (13) and (19), numerical integration was used, to solve equation (20) for the two cases. Listings of the two Fortran computer programs which were written for this purpose for the ring to disk, $F_{A(1)\,-\,A(2)}$, and for the ring to centerbody, $F_{A(1)\,-\,A(3)}$, are available upon request.

In closing it should be noted that, within the limitations of axial symmetry, the centerbody may be divided into several axial subareas and the opposing disk may be divided into annular rings by standard view factor algebra techniques. View factor algebra is also used to determine the configuration factors to a fourth surface which encloses the cavity.

References

1 Hamilton, D. C., and Morgan, W. R., "Radiant-Interchange Configuration Factors," NACA Technical Note 2836, 1952.

2 Leuenberger, H., and Person, R. A., "Compilation of Radiation Shape Factors for Cylindrical Assemblies," ASME Paper No. 56-A-144.

3 Sparrow, E. M., and Cess, R. D., *Radiation Heat Transfer*, Brooks/Cole Publishing Co., 1970.

The Effect of an Electric Field in the Presence of Noncondensable Gas on Film Condensation Heat Transfer

A. K. Seth[1] **and L. Lee**[2]

Introduction

This study describes the effect of a uniform electric field in the presence of noncondensable gas on film condensation heat transfer to the outside of a horizontal tube.

The effects of electric fields on film condensation have been studied by Choi [1],[3] Velkoff and Miller [2], and, more recently, Holmes and Chapman [3]. They have found that the condensation heat transfer rate of Freon 113 or Freon 114 can be increased markedly by the application of an electric field.

Choi condensed Freon 113 on the inside of a vertical tube with an electrode at the axis of the tube. By applying a uniform electric field, Choi found that the heat transfer coefficient could be increased by 100 percent. Velkoff and Miller condensed Freon 113 on a flat plate which was parallel to electrodes with d-c potential applied. They found that the heat transfer coefficient could be increased by 200 percent. More recently, Holmes and Chapman condensed Freon 114 on a grounded, inclined flat plate, with a nonuniform electric field produced by applying a voltage to a second plate placed above the first at various angles. They found that the heat transfer coefficients could be increased by as much as ten times as with no electric field applied when a voltage above 40 KV was imposed.

Othmer [5] has conducted a systematic experimental study of the effects of noncondensable gases on the condensation of steam when mixed with air. Empirical relationships between variables have been derived from the experiments and trial and error solutions of heat transfer for several situations are given by [5, 6, 7]. Sparrow and Lin [8], and Minkowycz and Sparrow [9] obtained boundary layer solutions of film condensation with the presence of noncondensable gases for a variety of physical conditions. Their findings indicate that even with a small fraction of noncondensable gases, the heat transfer rate in film condensation may be reduced by 50 percent or more.

Since it is difficult and expensive to eliminate all noncondensable gases in a bulk vapor, the ability to overcome their poisoning affect on heat transfer in film condensation with suitable electric fields appears to be significant. This paper reports the effect of electric fields on the film condensation of vapor Freon in the presence of air on the outside of a horizontal tube.

Experimental Apparatus and Procedures

The experimental investigation was carried out in a condenser loop using Freon 113 as the test fluid. The experimental equipment is shown in Fig. 1.

During testing, Freon 113 was heated by a water bath with the temperature controlled by a 500 W heater, stirrer, and thermostat. Freon 113 flowed from the boiler to the inlet chamber through a ⅜ in. ID copper tubing, around which heating tapes were wound to prevent Freon from condensing in the tubing. Inside the condenser, Freon condensed on the outer surface of a 1 in. ID horizontal copper tube, which was inside and concentric with a 2 in. OD glass tube, which makes up the condenser. Six copper constantan insulated thermocouples were embedded in the condensing surface to measure the surface temperature. The condensing surface was cooled by counterflowing cooling water. The condensation heat transfer rate was determined by accurate measurement of the coolant flow rate and the coolant temperature increase.

[1] Project Engineer, Balco Inc., Medford, Mass.

[2] Assoc. Professor, Department of Mechanical Engineering, University of Maine, Orono, Me.

[3] Numbers in brackets designate References at end of technical brief.

Contributed by the Heat Transfer Division of THE AMERICAN SOCIETY OF MECHANICAL ENGINEERS. Manuscript received by the Heat Transfer Division October 29, 1973.

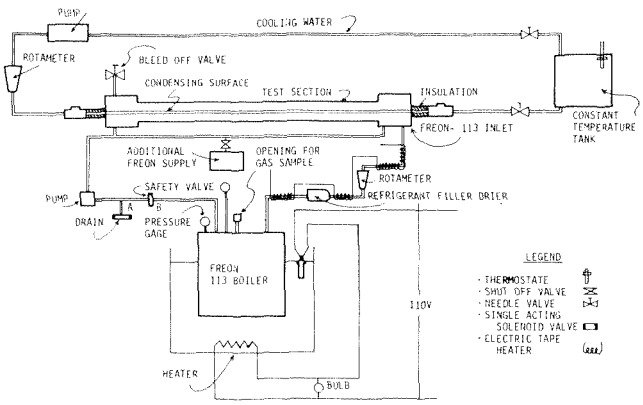

Fig. 1 Schematic diagram of experimental apparatus

To apply a uniform, radial electric field to the condensing Freon, a wire gage was wrapped around the glass tube of the condenser. The wire gage was connected to a high voltage source and the condensing surface was grounded. This arrangement eliminated any effect of the electric field on the condensing surface thermocouples. The condensed Freon 113 from the condenser was pumped back to the boiler.

To change the fraction of air in the bulk Freon 113 vapor, a method of weight displacement was used. Since Freon vapor is heavier than air, at the same temperature and pressure, a bleed valve (see Fig. 1) at a higher elevation is an efficient way of removing air. A gas chromatograph was used to determine the amount of air in the Freon vapor. A 1000 microlitre, gas tight, hypodermic syringe was used to collect samples. The needle was used to penetrate into the boiler through an opening covered by a rubber cup. At least two samples of gas were taken for each run.

Results and Discussion

Visual Observation. Before applying the electric field, the film was allowed to become very quiet and streamlined. The condensated Freon formed drops on the bottom of the condensing tube which separated from the tube after they grew to a certain size. By the application of an electric field, the separation rate of a drop became less while the number of drops increased. The shape of drops changed from spherical to ellipsoidal. Also, a wave like pattern of condensate was observed on the condensing surface with ridges of condensate flowing downward. Choi [1] observed the film breaking into drops on a vertical tube in the presence of an electric field, and predicted that at extremely high field intensities, the fluid would break away from the condensing surface in fine jets. In this study, no such phenomenon was observed. Differences in the geometry of the condensing surface between this study and Choi's or an insufficiently high field intensity may be the cause of the departure from his prediction.

Experimental Results. Fig. 2 shows that a high percentage of air in the bulk Freon vapor causes a reduction of heat transfer to the tube surface that far outweighs the increase of heat transfer to be expected from the thinning of the film caused by the electric field. For example, ratio of measured heat transfer coefficient and theoretical Nusselt's prediction (h/h_0) at 10 percent of air only varies from 0.14 with OKV to 0.26 with 25 KV. This compares with an increase of h/h_0 from 1 to 1.6 with no air present and the same change of field voltage. A 15 KV field causes about the same increase of heat transfer as the decrease that is caused by 1.8 percent air since h/h_0 remains 1.0. At around 3 percent air with 25 KV, the effect of the electric field and air concentration at the interface are again of the same magnitude since h/h_0 equals 1.0.

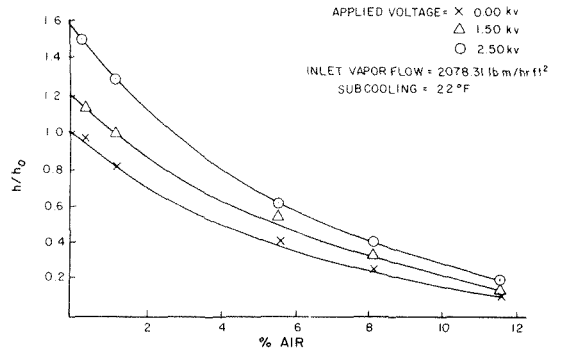

Fig. 2 Ratio of measured heat transfer coefficient and theoretical Nusselt's prediction (h/h_0) versus percentage air content

From the experiment results, we may conclude that though the presence of noncondensable gases in the bulk Freon vapor with or without an electric field decreases the film condensation heat transfer, the electric field may be used as a means to overcome the poisoning effect of noncondensable gases when only a small fraction of noncondensable gases are present and to substantially increase heat transfer when no noncondensable gas is present.

References

1 Choi, H. Y., "Electrodynamic Condensation Heat Transfer," JOURNAL OF HEAT TRANSFER, TRANS. ASME, Series C, Vol. 90, No. 1, Feb. 1968, pp. 98–102.

2 Velkoff, H. R., and Miller, J. H., "Condensation of Vapor on a Vertical Plate With a Transverse Electric Field," JOURNAL OF HEAT TRANSFER, TRANS. ASME, Series C, Vol. 87, May, 1965, pp. 197–201.

3 Holmes, R. E., and Chapman, A. J., "Condensation of Freon 114 In the Presence of Strong Nonuniform, Alternating Electric Field," JOURNAL OF HEAT TRANSFER, TRANS. ASME, Series C, Vol. 92, No. 4, Nov. 1970, pp. 616–620.

4 Othmer, D. F., "The Condensation of Steam," *Industrial and Engineering Chemistry*, Vol. 21, 1929, pp. 577–583.

5 Colburn, A. D., and Drew, T. B., "The Condensation of Mixed Vapors," *Trans. AIChE*, Vol. 33, 1937, pp. 197–208.

6 Kern, D. A., *Process Heat Transfer*, McGraw Hill, 1950, pp. 339–351.

7 Henderson, C. L., and Marchello, J. M., "Film Condensation in the Presence of a Noncondensable Gas," JOURNAL OF HEAT TRANSFER, TRANS. ASME, Series C, Vol. 91, No. 3, Aug. 1969, pp. 447–450.

8 Sparrow, E. M., and Lin, S. H., "Condensation Heat Transfer in the Presence of a Noncondensable Gas," JOURNAL OF HEAT TRANSFER, TRANS. ASME, Series C, Vol. 86, No. 2, Aug. 1964, pp. 430–436.

9 Minkowycz, W. J., and Sparrow, E. M., "Condensation Heat Transfer in the Presence of Noncondensable," *International Journal of Heat and Mass Transfer*, Vol. 9, 1966, pp. 1125–1124.

Predicting Heat Transfer Coefficients With Film Cooling From a Row of Holes

D. J. Wilson,[1] V. L. Eriksen,[2] and R. J. Goldstein[3]

Nomenclature

D = diameter of injection holes measured normal to the coolant flow

H = center to center transverse spacing of injection holes

$\bar{h}/\bar{h}_0$ = ratio of heat transfer coefficients for the equivalent two-dimensional slot with and without film cooling at the same location and mainstream conditions

L = distance from injection to origin of wall heating

[1] Associate Professor, Department of Mechanical Engineering, University of Alberta. Assoc. Mem. ASME.

[2] Assistant Director, Research and Development, Harrison Radiator Division, General Motors Corporation. Assoc. Mem. ASME.

[3] Professor, Department of Mechanical Engineering, University of Minnesota, Minneapolis, Minn. Mem. ASME.

Contributed by the Heat Transfer Division of THE AMERICAN SOCIETY OF MECHANICAL ENGINEERS. Manuscript received by the Heat Transfer Division November 26, 1973.

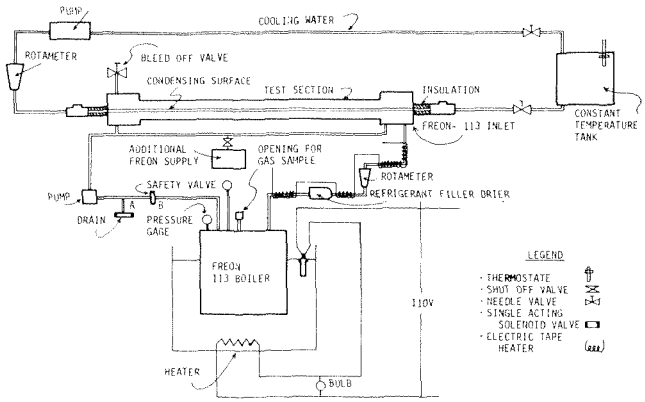

Fig. 1 Schematic diagram of experimental apparatus

To apply a uniform, radial electric field to the condensing Freon, a wire gage was wrapped around the glass tube of the condenser. The wire gage was connected to a high voltage source and the condensing surface was grounded. This arrangement eliminated any effect of the electric field on the condensing surface thermocouples. The condensed Freon 113 from the condenser was pumped back to the boiler.

To change the fraction of air in the bulk Freon 113 vapor, a method of weight displacement was used. Since Freon vapor is heavier than air, at the same temperature and pressure, a bleed valve (see Fig. 1) at a higher elevation is an efficient way of removing air. A gas chromatograph was used to determine the amount of air in the Freon vapor. A 1000 microlitre, gas tight, hypodermic syringe was used to collect samples. The needle was used to penetrate into the boiler through an opening covered by a rubber cup. At least two samples of gas were taken for each run.

Results and Discussion

Visual Observation. Before applying the electric field, the film was allowed to become very quiet and streamlined. The condensated Freon formed drops on the bottom of the condensing tube which separated from the tube after they grew to a certain size. By the application of an electric field, the separation rate of a drop became less while the number of drops increased. The shape of drops changed from spherical to ellipsoidal. Also, a wave like pattern of condensate was observed on the condensing surface with ridges of condensate flowing downward. Choi [1] observed the film breaking into drops on a vertical tube in the presence of an electric field, and predicted that at extremely high field intensities, the fluid would break away from the condensing surface in fine jets. In this study, no such phenomenon was observed. Differences in the geometry of the condensing surface between this study and Choi's or an insufficiently high field intensity may be the cause of the departure from his prediction.

Experimental Results. Fig. 2 shows that a high percentage of air in the bulk Freon vapor causes a reduction of heat transfer to the tube surface that far outweighs the increase of heat transfer to be expected from the thinning of the film caused by the electric field. For example, ratio of measured heat transfer coefficient and theoretical Nusselt's prediction (h/h_0) at 10 percent of air only varies from 0.14 with OKV to 0.26 with 25 KV. This compares with an increase of h/h_0 from 1 to 1.6 with no air present and the same change of field voltage. A 15 KV field causes about the same increase of heat transfer as the decrease that is caused by 1.8 percent air since h/h_0 remains 1.0. At around 3 percent air with 25 KV, the effect of the electric field and air concentration at the interface are again of the same magnitude since h/h_0 equals 1.0.

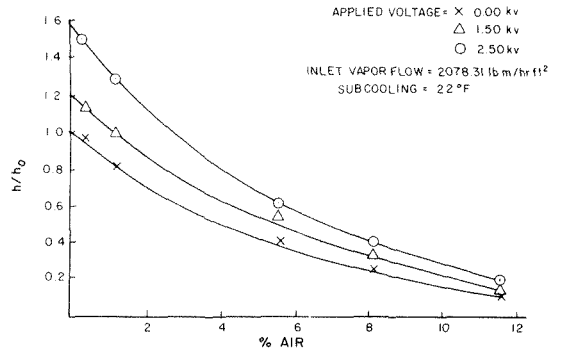

Fig. 2 Ratio of measured heat transfer coefficient and theoretical Nusselt's prediction (h/h_0) versus percentage air content

From the experiment results, we may conclude that though the presence of noncondensable gases in the bulk Freon vapor with or without an electric field decreases the film condensation heat transfer, the electric field may be used as a means to overcome the poisoning effect of noncondensable gases when only a small fraction of noncondensable gases are present and to substantially increase heat transfer when no noncondensable gas is present.

References

1 Choi, H. Y., "Electrodynamic Condensation Heat Transfer," JOURNAL OF HEAT TRANSFER, TRANS. ASME, Series C, Vol. 90, No. 1, Feb. 1968, pp. 98–102.

2 Velkoff, H. R., and Miller, J. H., "Condensation of Vapor on a Vertical Plate With a Transverse Electric Field," JOURNAL OF HEAT TRANSFER, TRANS. ASME, Series C, Vol. 87, May, 1965, pp. 197–201.

3 Holmes, R. E., and Chapman, A. J., "Condensation of Freon 114 In the Presence of Strong Nonuniform, Alternating Electric Field," JOURNAL OF HEAT TRANSFER, TRANS. ASME, Series C, Vol. 92, No. 4, Nov. 1970, pp. 616–620.

4 Othmer, D. F., "The Condensation of Steam," *Industrial and Engineering Chemistry*, Vol. 21, 1929, pp. 577–583.

5 Colburn, A. D., and Drew, T. B., "The Condensation of Mixed Vapors," *Trans. AIChE*, Vol. 33, 1937, pp. 197–208.

6 Kern, D. A., *Process Heat Transfer*, McGraw Hill, 1950, pp. 339–351.

7 Henderson, C. L., and Marchello, J. M., "Film Condensation in the Presence of a Noncondensable Gas," JOURNAL OF HEAT TRANSFER, TRANS. ASME, Series C, Vol. 91, No. 3, Aug. 1969, pp. 447–450.

8 Sparrow, E. M., and Lin, S. H., "Condensation Heat Transfer in the Presence of a Noncondensable Gas," JOURNAL OF HEAT TRANSFER, TRANS. ASME, Series C, Vol. 86, No. 2, Aug. 1964, pp. 430–436.

9 Minkowycz, W. J., and Sparrow, E. M., "Condensation Heat Transfer in the Presence of Noncondensable," *International Journal of Heat and Mass Transfer*, Vol. 9, 1966, pp. 1125–1124.

Predicting Heat Transfer Coefficients With Film Cooling From a Row of Holes

D. J. Wilson,[1] V. L. Eriksen,[2] and R. J. Goldstein[3]

Nomenclature

D = diameter of injection holes measured normal to the coolant flow

H = center to center transverse spacing of injection holes

$\bar{h}/\bar{h}_0$ = ratio of heat transfer coefficients for the equivalent two-dimensional slot with and without film cooling at the same location and mainstream conditions

L = distance from injection to origin of wall heating

[1] Associate Professor, Department of Mechanical Engineering, University of Alberta. Assoc. Mem. ASME.

[2] Assistant Director, Research and Development, Harrison Radiator Division, General Motors Corporation. Assoc. Mem. ASME.

[3] Professor, Department of Mechanical Engineering, University of Minnesota, Minneapolis, Minn. Mem. ASME.

Contributed by the Heat Transfer Division of THE AMERICAN SOCIETY OF MECHANICAL ENGINEERS. Manuscript received by the Heat Transfer Division November 26, 1973.

M = $\rho_2 u_2/\rho_\infty u_\infty$, injection parameter
n = power law coefficient in $u/u_\infty = (y/\delta)^{1/n}$ where θ is the boundary layer thickness
Re_∞ = $\rho_\infty u_\infty D/\mu_\infty$, mainstream Reynolds number
S = width normal to the coolant flow of equivalent slot
T = absolute temperature
u = velocity
x = distance downstream from point of injection
x_{0i}, x_0 = distance upstream of injection point to apparent boundary layer origin with, and without film cooling, respectively
α = angle of injection
η_c = effectiveness of adiabatic film cooling on a hole center line
μ = dynamic viscosity
ρ = fluid density

Subscripts

0 = without film cooling injection
i = with film cooling injection
2 = at the exit of a coolant injection hole
∞ = of the mainstream
$*$ = at the reference state, P_∞, T^*

Gas film cooling is presently being employed to protect combustion chambers and gas turbine blades from the high temperature gases passing over their surfaces. In these and other practical situations where the film cooled surface is not adiabatic it is necessary to assess the effect of the injected coolant on the convective heat transfer coefficient in order to predict the surface temperature. A simple model is presented here which predicts the effect of injection from a row of holes on the downstream heat transfer coefficient.

With film cooling from a transverse row of inclined circular holes, the flow disturbances generated by the jets of injected fluid give rise to lateral variations in surface heat transfer coefficients. In practical situations, heat conduction within the cooled surface will reduce any lateral variations in surface temperature which are induced by the laterally varying heat transfer, and the use of laterally averaged values will be adopted here, thus effecting a considerable simplification by reducing the problem to its two-dimensional equivalent. This equivalent system is assumed to be a flush slot, inclined at the same angle to the surface as the row of holes, from which coolant is ejected with the same mass and momentum fluxes as the laterally averaged values from the row of holes. The temperature and density of the coolant, and the mainstream conditions, are taken to be the same for both the row of holes and the slot. Equality of mass and momentum fluxes for the row of holes and the equivalent slot requires the injection parameter M to be the same for the slot as for a coolant hole. With this constraint the width S of the equivalent slot is $\pi D^2/4H$. The heat transfer coefficients can be predicted using the theory of Wilson and Goldstein [1],[4] which assumes that the effect of injection on heat transfer can be accounted for by a shift in the virtual origin of the turbulent boundary layer. For air, fluid property variations are approximated by assuming $\mu \propto T^{0.76}$ and $\rho \propto T^{-1}$, and by employing the reference temperature of Eckert [2]. Using this,

$$\frac{\bar{h}}{\bar{h}_0} = \left(\frac{T_{*_0}}{T_{*_i}}\right)^{0.63} \left[\frac{x + x_0}{x + x_{0i}}\right]^{0.21} \left[\frac{1 - \left[\frac{x_0 + L}{x + x_0}\right]^{0.79\left(\frac{n+2}{n+1}\right)}}{1 - \left[\frac{x_{0i} + L}{x + x_0}\right]^{0.79\left(\frac{n+2}{n+1}\right)}}\right]^{\frac{1}{n+2}} \tag{1}$$

The magnitude of x_{0i} is determined by examining the coolant's mass and momentum addition to the boundary layer, and the subsequent alteration of momentum thickness at the slot. Averaging the mass and momentum injection rates in the transverse direction, the theory in [1] reduces to

$$\left(\frac{x_{0i}}{D}\right)^{0.79} = \left(\frac{x_0}{D}\right)^{0.79} + C_1 M \,\mathrm{Re}_\infty^{0.21} \left[\frac{T_{*_0}}{T_\infty}\right]^{0.63} \left(\frac{\pi D}{4H}\right)\left[1 - M\frac{T_2}{T_\infty}\cos\alpha\right]$$

where

$$C_1 = 4.35(10)^{0.535\left(\frac{n+2}{n}\right)} \tag{2}$$

The prediction of equations (1) and (2) are compared at two different locations in Figs. 1 and 2 with the laterally averaged measurements of Eriksen and Goldstein [3], who injected coolant from a row of circular tubes inclined at 35 deg to the main stream and spaced three dia between centers. The measured center-line adiabatic film cooling effectiveness η_c from [3] is also shown, and it is apparent that when M exceeds a critical value of about 0.5, the effectiveness decreases abruptly, and the heat transfer coefficient shows a sharp rise, possibly due to increased boundary layer mixing induced by the coolant flow. For values of the injection rate less than this critical value, the theoretical predictions for $\bar{h}/\bar{h}_0$ are in good agreement with experiment, while at higher injection rates the theory underestimates the effect of film cooling on heat transfer. At rates of coolant injection near and above this critical blow-off condition the boundary layer model employed here is probably no longer valid and its prediction of the minimum in $\bar{h}/\bar{h}_0$ may be fortuitous.

In a situation involving a film cooled turbine blade, the small

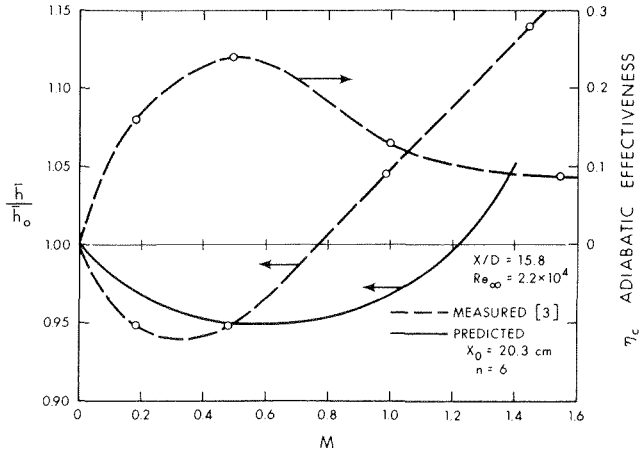

Fig. 1 Effect of injection rate on heat transfer and effectiveness at 15.8 hole diameters downstream

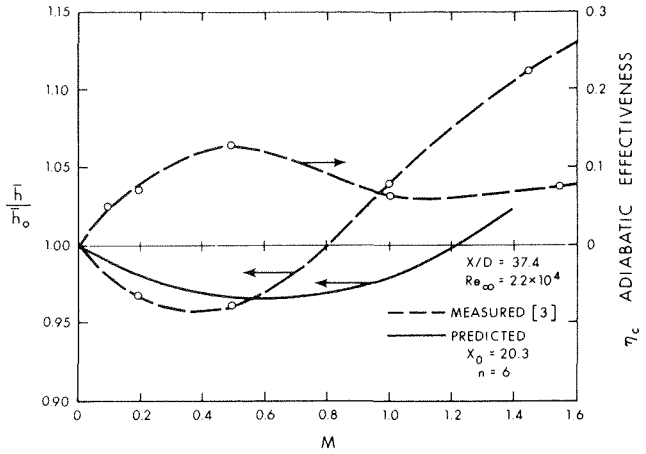

Fig. 2 Effect of injection rate on heat transfer and effectiveness at 37.4 hole diameters downstream

[4] Numbers in brackets designate References at end of technical brief.

decrease in h/h_0 below unity observed in the experiments of Eriksen and Goldstein may be considerably augmented by fluid property variations. Using (1) and (2) to estimate the effect of fluid property variations on a typical film cooled turbine blade, predicted a decrease in h/h_0 several times that observed in Eriksen and Goldstein's experiments. Because the theory outlined here employs only a simple reference temperature model for variable property effects, further refinements are necessary to accurately determine the importance of these effects.

References

1 Wilson, D. J., and Goldstein, R. J., "Effect of Film Cooling Injection on Downstream Heat Transfer Coefficients in High Speed Flow," JOURNAL OF HEAT TRANSFER, TRANS. ASME, Series C, Vol. 95, No. 4, Nov. 1973, pp. 505–509.

2 Eckert, E. R. G., "Survey of Heat Transfer at High Speeds," Wright Aero. Development Center Tech. Rept. 54-70, 1954; see also Eckert, E. R. G., and Drake, R. M., *Heat and Mass Transfer*, McGraw-Hill, 1959, p. 270.

3 Eriksen, V. L., and Goldstein, R. J., "Heat Transfer and Film Cooling Following Injection Through Inclined Circular Tubes," JOURNAL OF HEAT TRANSFER, TRANS. ASME, Series C, Vol. 96, No. 2, May, 1974, pp. 239–245.

Comparison of Nusselt Number and Drag Coefficient of Screen-Covered and Smooth Cylinders in Crossflow

R. L. Gorton[1] and J. T. Ratcliffe[2]

Nomenclature

A = smooth cylinder surface area, ft^2

C_D = drag coefficient, $\dfrac{F}{LD(1/2\,\rho V^2)}$

D = smooth cylinder diameter, ft.

F = drag force on cylinder, lb

k = thermal conductivity, Btu/hr-ft-F deg

L = cylinder length, ft

Nu = Nusselt number, $\dfrac{(q/A)D}{k(T_s - T_f)}$

q = heat transfer rate from cylinder, btu/hr

Re = Reynolds number, $\dfrac{VD}{\mu}$

ρ = air density, lb/ft^3

T_f = air stream temperature, deg F

T_s = average temperature of cylinder surface, deg F

V = air stream velocity, ft/sec

Introduction

The work reported here is an initial evaluation of an easily constructed heat transfer enhancement surface: screen wire roughness attached to a smooth surface. In this use screen wire apparently provides both turbulence promotion and surface extension by the wire. Additionally, design flexibility is easily achieved because screen wire is readily obtainable in a wide variety of materials, wire sizes, mesh sizes, and weave patterns.

This study had as its purpose comparison of heat transfer and drag results obtained from a variety of screened surfaces to those obtained from a smooth surface. The configuration chosen was a horizontal cylinder in air crossflow. This is a commonly occurring practical geometry, and well established smooth cylinder results are available for comparison to experimental results obtained here.

Copper tube and copper screen were chosen because these are easily joined to provide good thermal contact. The screen mesh sizes were rather arbitrarily chosen on the basis of practicality and availability.

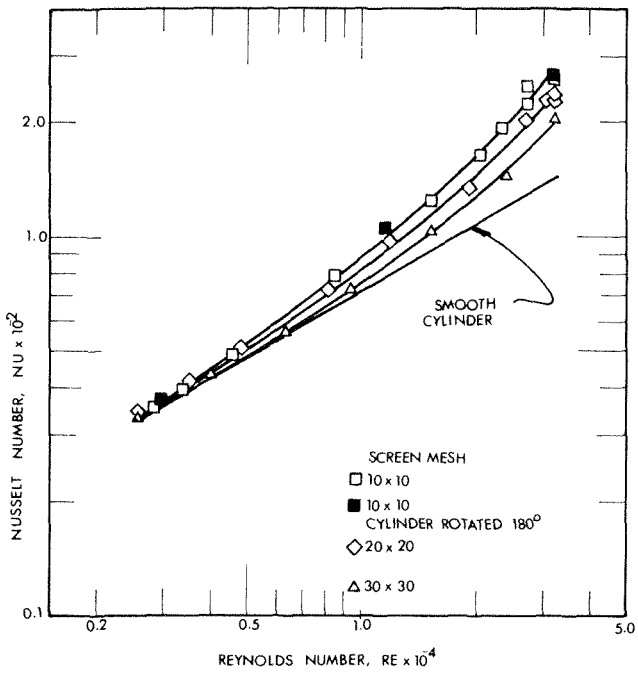

Fig. 1 Screened cylinder heat transfer results

Experimental Apparatus and Procedure

For this initial evaluation, square weave copper wire screen of 10, 20, and 30 meshes per in. (0.025, 0.016, and 0.013 in. wire dia, respectively) were selected. These were attached by soldering uniformly to 5⅜ in. lengths of 1⅛ in. OD copper tube.

Three tubes were constructed for heating by electric cartridge heaters. Five thermocouples were used for surface temperature measurement.

The test cylinders were mounted in a 12-ft section of 6 × 12 in. flat oval duct. Mounting was by attachment of insulating end plugs to support arms extending from a plate above the duct.

Power input to the cartridge heater was determined from voltage and current measurements, and power level was adjusted with a variable transformer.

The test cylinders were mounted on a calibrated spring balance arrangement and inserted into a 6-in. round duct for drag determination.

More complete description of the experimental apparatus is contained in reference [1].[3]

To provide reference information, heat transfer results were obtained for all three of the test cylinders before screen was applied. The cylinders then had screen attached and were tested to provide screened cylinder results.

From the measured results, Reynolds number, Nusselt number, and Drag coefficient were determined.

Results and Discussion

Experimental heat transfer results are shown in Fig. 1. The smooth cylinder results represent the average of the results from the three separate unscreened cylinder tests. Only minimal varia-

[1] Associate Professor, Mechanical Engineering Department, Kansas State University, Manhattan, Kan. Mem. ASME.

[2] Charmin Paper Company, Mehoopany, Pennsylvania. Assoc. Mem. ASME.

Contributed by the Heat Transfer Division of THE AMERICAN SOCIETY OF MECHANICAL ENGINEERS. Manuscript received by the Heat Transfer Division March 15, 1973.

[3] Numbers in brackets designate References at end of technical brief.

decrease in h/h_0 below unity observed in the experiments of Eriksen and Goldstein may be considerably augmented by fluid property variations. Using (1) and (2) to estimate the effect of fluid property variations on a typical film cooled turbine blade, predicted a decrease in h/h_0 several times that observed in Eriksen and Goldstein's experiments. Because the theory outlined here employs only a simple reference temperature model for variable property effects, further refinements are necessary to accurately determine the importance of these effects.

References

1 Wilson, D. J., and Goldstein, R. J., "Effect of Film Cooling Injection on Downstream Heat Transfer Coefficients in High Speed Flow," JOURNAL OF HEAT TRANSFER, TRANS. ASME, Series C, Vol. 95, No. 4, Nov. 1973, pp. 505–509.

2 Eckert, E. R. G., "Survey of Heat Transfer at High Speeds," Wright Aero. Development Center Tech. Rept. 54-70, 1954; see also Eckert, E. R. G., and Drake, R. M., *Heat and Mass Transfer*, McGraw-Hill, 1959, p. 270.

3 Eriksen, V. L., and Goldstein, R. J., "Heat Transfer and Film Cooling Following Injection Through Inclined Circular Tubes," JOURNAL OF HEAT TRANSFER, TRANS. ASME, Series C, Vol. 96, No. 2, May, 1974, pp. 239–245.

Comparison of Nusselt Number and Drag Coefficient of Screen-Covered and Smooth Cylinders in Crossflow

R. L. Gorton[1] and J. T. Ratcliffe[2]

Nomenclature

A = smooth cylinder surface area, ft^2

C_D = drag coefficient, $\dfrac{F}{LD(1/2\,\rho V^2)}$

D = smooth cylinder diameter, ft.

F = drag force on cylinder, lb

k = thermal conductivity, Btu/hr-ft-F deg

L = cylinder length, ft

Nu = Nusselt number, $\dfrac{(q/A)D}{k(T_s - T_f)}$

q = heat transfer rate from cylinder, btu/hr

Re = Reynolds number, $\dfrac{VD}{\mu}$

ρ = air density, lb/ft^3

T_f = air stream temperature, deg F

T_s = average temperature of cylinder surface, deg F

V = air stream velocity, ft/sec

Introduction

The work reported here is an initial evaluation of an easily constructed heat transfer enhancement surface: screen wire roughness attached to a smooth surface. In this use screen wire apparently provides both turbulence promotion and surface extension by the wire. Additionally, design flexibility is easily achieved because screen wire is readily obtainable in a wide variety of materials, wire sizes, mesh sizes, and weave patterns.

This study had as its purpose comparison of heat transfer and drag results obtained from a variety of screened surfaces to those obtained from a smooth surface. The configuration chosen was a horizontal cylinder in air crossflow. This is a commonly occurring practical geometry, and well established smooth cylinder results are available for comparison to experimental results obtained here.

Copper tube and copper screen were chosen because these are easily joined to provide good thermal contact. The screen mesh sizes were rather arbitrarily chosen on the basis of practicality and availability.

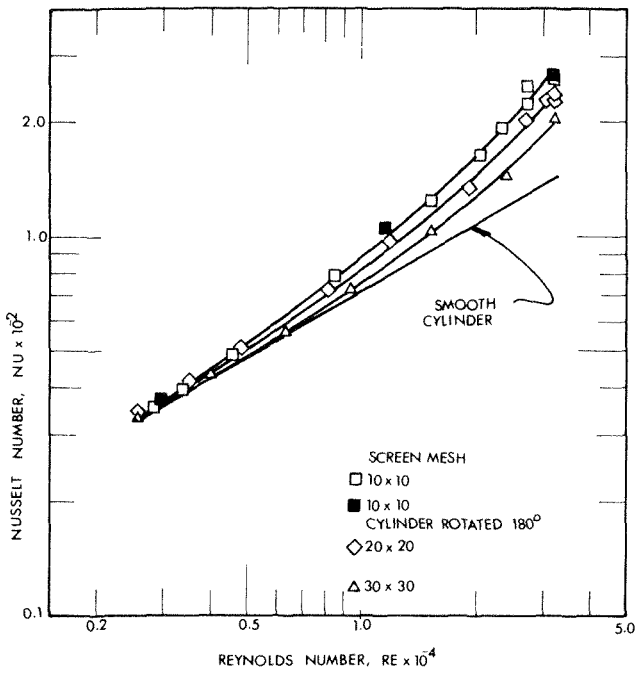

Fig. 1 Screened cylinder heat transfer results

Experimental Apparatus and Procedure

For this initial evaluation, square weave copper wire screen of 10, 20, and 30 meshes per in. (0.025, 0.016, and 0.013 in. wire dia, respectively) were selected. These were attached by soldering uniformly to 5⅜ in. lengths of 1⅛ in. OD copper tube.

Three tubes were constructed for heating by electric cartridge heaters. Five thermocouples were used for surface temperature measurement.

The test cylinders were mounted in a 12-ft section of 6 × 12 in. flat oval duct. Mounting was by attachment of insulating end plugs to support arms extending from a plate above the duct.

Power input to the cartridge heater was determined from voltage and current measurements, and power level was adjusted with a variable transformer.

The test cylinders were mounted on a calibrated spring balance arrangement and inserted into a 6-in. round duct for drag determination.

More complete description of the experimental apparatus is contained in reference [1].[3]

To provide reference information, heat transfer results were obtained for all three of the test cylinders before screen was applied. The cylinders then had screen attached and were tested to provide screened cylinder results.

From the measured results, Reynolds number, Nusselt number, and Drag coefficient were determined.

Results and Discussion

Experimental heat transfer results are shown in Fig. 1. The smooth cylinder results represent the average of the results from the three separate unscreened cylinder tests. Only minimal varia-

[1] Associate Professor, Mechanical Engineering Department, Kansas State University, Manhattan, Kan. Mem. ASME.

[2] Charmin Paper Company, Mehoopany, Pennsylvania. Assoc. Mem. ASME.

Contributed by the Heat Transfer Division of THE AMERICAN SOCIETY OF MECHANICAL ENGINEERS. Manuscript received by the Heat Transfer Division March 15, 1973.

[3] Numbers in brackets designate References at end of technical brief.

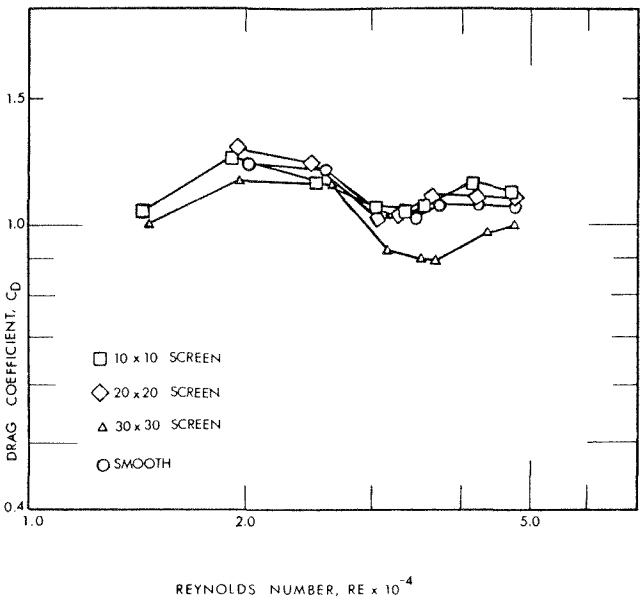

Fig. 2 Drag results

tion among heat transfer results was obtained from the individual smooth cylinders. This lack of variation demonstrated that the bare cylinders were free of any thermal dissimilarity due to construction differences.

The average smooth cylinder results were approximately 22 percent higher than the low turbulence Hilpert correlation (2 percent turbulence), but were below the higher turbulence (7–18 percent) results of Comings, et al. [2].

The remaining three curves of Fig. 1 are results of the screened cylinder test and can be compared to the smooth cylinder curve for determination of Nusselt number increases due to screen application.

The Nusselt number for all cylinders were nearly equal at low values of Reynolds number. With increasing Reynolds number, the Nusselt numbers increased at different rates, the greatest rate of increase being obtained with the coarsest mesh (10 × 10) screened cylinder. At the highest Reynolds number the increases were 84 percent for the 10 mesh, 68 percent for the 20 mesh and 44 percent for the 30 mesh screened cylinders.

The curves are seen to deviate from the straight line relationship shown for the smooth tube results. The straight line result may be represented by an expression of the form

$$\mathrm{Nu} = C\,\mathrm{Re}^{a}$$

for constant Prandtl number. The deviation indicates that the exponent, a, is not a constant, but is itself a function of Reynolds number for the screen roughened tubes.

Results from the drag experiment are presented in Fig. 2. The difference among the curves lies roughly within the uncertainty level of the experiment. The dominant point is that large increases in drag due to screening of the smooth cylinders were not measured. The probable explanation is that in the Reynolds number range of the experiments, pressure drag is the major component of total drag on cylinders. Surface roughening had an apparent effect on total drag at less than the 10 percent level due to the dominance of pressure drag and the rather minor influence of skin friction. This result is similar to that of Achenbach [3, 4] who reported measurement of friction contribution to total drag on roughened cylinders in the 2–6 percent range.

Summary and Conclusions

The results of this experiment show that significant increases in Nusselt number can be realized by employing screen type roughness elements on cylinders in crossflow. Increases up to 84 percent were achieved with the 10 × 10 screen at the highest Reynolds number.

Nusselt number increases were found to be a function of screen mesh size, the coarsest mesh producing the greatest increase. Attempts to find an effective diameter or equivalent roughness which would allow correlation of the results were not successful. Additionally, it was not possible to separate the portion of the heat transfer increase due to surface extension from that due to increased turbulence. The effect of the added surface appears to be of secondary importance since the smallest heat transfer increases were realized with the 30 mesh screen, which provided the greatest area increase of the three screens used.

The Nusselt number of gains were achieved with only minimal increase in drag coefficient.

References

1 Gorton, R. L., and Ratcliffe, J. T., "Heat Transfer Effectiveness of Screen Wire Roughness Elements on Cylinders in Cross Flow," ASME Paper No. 72-WA/HT-51.

2 Knudsen, J. G., and Katz, D. L., *Fluid Dynamics and Heat Transfer*, McGraw-Hill, New York, 1958, p. 505.

3 Achenbach, E., "Influence of Surface Roughness on the Cross-Flow Around A Circular Cylinder," *Journal of Fluid Mechanics*, Vol. 46, Part 2, 1971, pp. 321–335.

4 Achenbach, E., "Influence of Surface Roughness on the Flow Through a Staggered Tube Bank," *Warme und Stoffubertragung*, Vol. 4, 1971, pp. 120–126.

Conductance of Packed Spheres in Vacuum[1]

M. M. Yovanovich[2] The authors have made an important contribution to a very important and complex mechanical-thermal problem. The mechanical problem is the major obstacle, because it depends upon mechanical forces acting upon the contact areas and the stress distribution due to these forces. The mechanical forces are functions of the sphere diameter distribution and the packing of the spheres. The stress distribution is a complex function of the physical properties of the spheres, and certain geometric parameters: sphere diameter, wall thickness, contact radius to sphere diameter ratio, and, very important, the contact radius to wall thickness ratio.

Equation (1), therefore, is valid for solid spheres, and may be a good approximation for "thick" wall spheres, but it is, no doubt, inappropriate for "thin" wall spheres. The demarcation between thick and thin walls is, at present, not available. Thus equation (1) should be used with caution to predict the contact radius whenever mechanical forces are small, i.e., contact radius much smaller than sphere diameter, and smaller than the wall thickness. For large mechanical forces, i.e., contact radius comparable or greater than the wall thickness, equation (1) cannot be used. These statements apply to uncoated spheres. The mechanical interaction of coated spheres is even more complex, and the use of equation (1) of the previously published paper is questionable for all mechanical loads.

The thermal analysis of the constriction resistance of a single solid sphere presented by the authors is identical to that of Kaganer [9],[3] and must be considered to be an approximate solution limited to uncoated solid spheres under very light loading. The author's parameter S_R, defined by equation (20) and its values shown in Table 1, exhibit a peculiar behavior as (r_c/r_0) increases for all values of (t/r_0). Can the authors give a physical explanation for this odd phenomenon?

Kaganer [9] proposed an alternate method for predicting the effect of packing upon the apparent conductivity. Have the authors compared the two methods?

In this paper the following expression is given:

$$R = (1/\pi t k_s) \ln [1/\tan (\theta_0/2)] \qquad (55)$$

for the total resistance "for the special case of a thin-shell sphere, the heat flow being considered to be one-dimensional, having two isothermal contact regions diametrically opposite each other." Equation (55), as used by the authors, is not the exact solution for the thermal problem they have considered. The actual problem, and the derivation of equation (55) can be found in reference [10].

It is, however, interesting to note that equation (55) with θ_0 as defined by the authors is in very good agreement with their constant heat flux solution for $(t/r_0) = 10^{-3}$ and (r_c/r_0) ranging from 10^{-3} to 10^{-2}.

In my correspondence with Cunnington [11] and Tien [12], I proposed as an approximate solution for the apparent conductivity of hollow microscpheres the following expression:

$$(k_a/k_s) = (r_c/r_0)/[1 + (2/\pi)(r_c/t) \ln [1/\tan (\alpha/2)] \qquad (56)$$

where $\alpha \equiv \eta (r_c/r_0)$, and η is an empirical parameter depending upon the ratio (t/r_0) and it ranges between 20 and 40. It is obvious that (r_c/t) can be written as the product of (r_c/r_0) and (r_0/t), so that (k_a/k_s) depends upon (r_c/r_0), (t/r_0) and η only.

Equation (56) is based upon a thermal model which considers the constriction resistance due to the contact areas as well as the resistance of the walls. Thus, equation (56) includes the resistance given by equation (55). Equation (56) shows explicitly the importance of the geometric parameters upon the apparent conductivity. It agrees remarkably well with the test data of reference [4] of the previously published paper. Table 3 shows the comparison between equation (56) and the values given by Chan and Tien in Fig. 4. The comparison is made at (r_c/r_0) equal to 10^{-3} and 10^{-2} with $\eta = 40$. The agreement between equation (56) and the results of the analysis presented in this paper is very good considering the assumptions which were used. Equation (56) underpredicts the apparent conductivity because it is based upon the simple cubic packing. Face-centered cubic and body-centered cubic packings will increase the values predicted by equation (56), and the agreement will be better than shown in Table 3.

It is recommended that fundamental analytical and experimental studies be undertaken to resolve the complex mechanical problem. Having solved the mechanical problem, the thermal problem should then be reexamined to see whether the solutions presented in this paper are valid for the entire range of (r_c/r_0) and (t/r_0). Until that time the results of this paper and equation (56) should be considered to be approximations, valid for small (r_c/r_0), and equation (1) of the previously published paper can only be used for predicting (r_c/r_0) when (t/r_0) is large.

Table 3 Comparison of equation (56) and values given in Fig. 4

$r_c/r_0 = 10^{-3}$				
t/r_0	1	0.1	0.01	0.001
$(k_a/k_s) \times 10^4$ equation (56)	9.95	9.52	6.64	1.65
(Fig. 4) $\times 10^4$ Chan-Tien	10	~9.9	~8.6	~1.9
$r_c/r_0 = 10^{-2}$				
$(k_a/k_s) \times 10^3$ equation (56)	9.65	7.35	2.17	0.27
(Fig. 4) $\times 10^4$ Chan-Tien	10	~8.5	~2.5	~0.32

Additional References

9 Kaganer, M. G., "Contact Heat Transfer in Granular Material Under Vacuum," *Journal of Engineering Physics*, Vol. 11, No. 1, 1966, pp. 30-36.

10 Yovanovich, M. M., "A General Expression for Predicting Conduction Shape Factors," AIAA Paper No. 73-121, AIAA 11th Aerospace Sciences Meeting, Washington, D. C., Jan. 10-12, 1972.

11 Cunnington, G. R., personal communication.

12 Tien, C. L., personal communication.

Authors' Closure

Professor Yovanovich's comments constitute an excellent addition to the paper. The authors are indebted to him for his interest and contributions.

The microsphere insulation is seldom subjected to extremely

[1] By C. K. Chan and C. L. Tien, published in the Aug. 1973 issue of JOURNAL OF HEAT TRANSFER, TRANS. ASME, Series C, Vol. 95, No. 3, pp. 302-308.

[2] Professor, University of Waterloo, Waterloo, Ontario, Canada.

[3] Numbers in brackets designate Additional References at end of Discussion.

Table 4 Comparison between equations (57) and (50)

Numerical factor	Simple cubic	Body centered cubic	Face centered cubic
$3.12\delta_s^{4/3}$ (equation 57)	1.32	1.87	2.09
$S_p(1-\mu^2)^{1/3}$ (equation 50)	1.34	1.93	2.68

high compressive loads. For moderate loading pressure (say $P \sim 10^4 N/M^2$), the contact radius ($r_c/r_0 \sim 10^{-2}$) is still much smaller than the normal wall thickness ($t/r_0 \sim 10^{-1}$) of hollow microspheres. On this basis, the Hertz formula as given in equation (1) is a legitimate approximation for the hollow microspheres. As indicated in the paper, as well as Professor Yovanovich's comment, an exact stress analysis for hollow spheres in contact is not available at present.

The parameter S_R shown in Table 1 was obtained by taking the ratio of R_2/R_2'. Both R_2 and R_2' are computed to an accuracy of three significant figures in the series summation of equations (23) and (24). Thus S_R is accurate only to two significant figures and not four significant figures as given in the table. The numerical fluctuation of S_R for increasing values of (t/r_0) is caused by different truncation errors in summing up both series. The authors wish to apologize for the misleading figures shown in Table 1.

The expression in reference [9] for the apparent conductivity of granular material is

$$k = 3.12\ \delta_s^{4/3} k_s P^{1/3} E^{-1/3} \tag{3}$$

This expression indicates the same dependence of k on k_s, P, and E as equation (50) in the paper. The only difference between the two expressions is the numerical factor which is a function of porosity. As a matter of interest, the numerical factors of these two expressions are computed for the three regular packing patterns and for $\mu = 0.22$. The comparison is shown in Table 4.

It is interesting to note that the present analysis compares very well with Kaganer's results except for the face centered cubic arrangement. The discrepancy is probably due to the different physical models employed.

Local Free Convection to Non-Newtonian Fluids From a Horizontal, Isothermal Cylinder[1]

T. Y. Na[2] The authors have contributed greatly in investigating, both analytically and experimentally, the problem of natural convection of power-law fluids over external surfaces. I would like to bring to the attention of the authors an analysis of the existence of similarity solutions of the same problem[3] which the authors seem to have overlooked in their literature survey.

Author's Closure

The authors are gratified at the interest shown in this paper by Professor Na.

[1] By C. C. Gentry and D. E. Wollersheim, published in the Feb. 1973 issue of JOURNAL OF HEAT TRANSFER, TRANS. ASME, Series C Vol. 96, No. 1, pp. 3–8.

[2] Professor, School of Engineering, University of Michigan, Dearborn, Mich.

[3] Na, T. Y. and Hansen, A. G., "Possible Similarity Solutions of Laminar Natural Convection Flow of Non-Newtonian Fluids," *International Journal of Heat and Mass Transfer*, Vol. 9, 1966, pp. 261–262.

The excellent reference cited by Professor Na, which deals with similar solution existence criteria for free convection from vertical, isothermal flat plates to non-Newtonian fluids, confirms the findings by Acrivos [7] for the case in which the inertial terms appearing in the momentum equation are not neglected. In the present paper, experimental data are compared with similar and integral solution results under the restrictive condition that $N_{Pr(ar)} \to \infty$, which is tantamount to neglecting the momentum equation inertial terms.

Vapor Flow in Cylindrical Heat Pipes[1]

L. S. Galowin,[2] L. S. Fletcher,[3] and M. J. DeSantis[4] The authors have presented an interesting theoretical analysis for flow properties within a cylindrical heat pipe utilizing finite difference techniques for solution of the governing differential equations. Transformation of the dependent variables to the stream function and the vorticity, results in an elliptic partial differential equation for analysis of confined flow within a heat pipe. Solutions of such equations almost always appear to be wholly dependent upon the stipulation of the initial velocity profiles, and therefore the results are sometimes quite arbitrary. It would be instructive if the authors would compare their results with other methods of solution for pipe flows with mass addition/removal at the walls.

The Bankston and Smith analysis differs from the results of a recent experimental investigation of laminar flow in a porous pipe with uniform wall suction, and a recent theoretical analysis of laminar flow in a porous pipe with variable wall suction. The significant differences are the assumption of a uniform velocity at the wall as compared to nonuniform wall velocities in the condenser section of the heat pipe, and the numerical results indicating that the pressures fall rather than rise in the condenser section of the pipe.

An experimental investigation of the pressure variations occurring in incompressible laminar flow in a closed end porous tube with uniform wall suction as a model for the condenser of a heat pipe has been conducted by Quaile and Levy [21].[5] In addition to the presentation of experimental data for pressure variations, theoretical "similarity" and "inlet" solutions were shown for comparison. Both the experimental data and the reported theoretical solutions over a small range of radial Reynolds numbers indicated an increasing pressure in the condenser region.

The analysis of Galowin and DeSantis [12] for laminar pipe flow in a porous wall cylinder has been extended for the heat pipe condenser section to incorporate the boundary condition of variable wall suction as a model for vapor condensation [22]. This analysis shows excellent agreement with the experimental data of Quaile and Levy [21] and further substantiates the rise in pressure in the porous tube. This excellent comparison between experiment and theory indicates that the assumption of variable wall suction provides the representative boundary condition at the porous tube wall. Separation and reverse flows were not mentioned in the report of the experimental investigation nor in the recent theoretical analysis. Perhaps the experimental technique adopted [21] suppressed the development of the separation regions exhibited in the Bankston and Smith analysis. The choice

[1] By C. A. Bankston and H. J. Smith, published in the Aug. 1973 issue of JOURNAL OF HEAT TRANSFER, TRANS. ASME, Series C, Vol. 95, No. 3, pp. 371-376.

[2] Engineering Consultant, ENER-G Associates, Clifton, N. J. Mem. ASME.

[3] Assoc. Professor, Mechanical, Industrial & Aerospace Engineering, Rutgers University, New Brunswick, N. J. Mem. ASME.

[4] Scientific Consultant, Lyndhurst, N. J.

[5] Numbers in Brackets designate Additional References at end of Discussion.

Table 4 Comparison between equations (57) and (50)

Numerical factor	Simple cubic	Body centered cubic	Face centered cubic
$3.12\delta_s^{4/3}$ (equation 57)	1.32	1.87	2.09
$S_p(1-\mu^2)^{1/3}$ (equation 50)	1.34	1.93	2.68

high compressive loads. For moderate loading pressure (say $P \sim 10^4 N/M^2$), the contact radius ($r_c/r_0 \sim 10^{-2}$) is still much smaller than the normal wall thickness ($t/r_0 \sim 10^{-1}$) of hollow microspheres. On this basis, the Hertz formula as given in equation (1) is a legitimate approximation for the hollow microspheres. As indicated in the paper, as well as Professor Yovanovich's comment, an exact stress analysis for hollow spheres in contact is not available at present.

The parameter S_R shown in Table 1 was obtained by taking the ratio of R_2/R_2'. Both R_2 and R_2' are computed to an accuracy of three significant figures in the series summation of equations (23) and (24). Thus S_R is accurate only to two significant figures and not four significant figures as given in the table. The numerical fluctuation of S_R for increasing values of (t/r_0) is caused by different truncation errors in summing up both series. The authors wish to apologize for the misleading figures shown in Table 1.

The expression in reference [9] for the apparent conductivity of granular material is

$$k = 3.12\,\delta_s^{4/3} k_s P^{1/3} E^{-1/3} \tag{3}$$

This expression indicates the same dependence of k on k_s, P, and E as equation (50) in the paper. The only difference between the two expressions is the numerical factor which is a function of porosity. As a matter of interest, the numerical factors of these two expressions are computed for the three regular packing patterns and for $\mu = 0.22$. The comparison is shown in Table 4.

It is interesting to note that the present analysis compares very well with Kaganer's results except for the face centered cubic arrangement. The discrepancy is probably due to the different physical models employed.

Local Free Convection to Non-Newtonian Fluids From a Horizontal, Isothermal Cylinder[1]

T. Y. Na[2] The authors have contributed greatly in investigating, both analytically and experimentally, the problem of natural convection of power-law fluids over external surfaces. I would like to bring to the attention of the authors an analysis of the existence of similarity solutions of the same problem[3] which the authors seem to have overlooked in their literature survey.

Author's Closure

The authors are gratified at the interest shown in this paper by Professor Na.

The excellent reference cited by Professor Na, which deals with similar solution existence criteria for free convection from vertical, isothermal flat plates to non-Newtonian fluids, confirms the findings by Acrivos [7] for the case in which the inertial terms appearing in the momentum equation are not neglected. In the present paper, experimental data are compared with similar and integral solution results under the restrictive condition that $N_{Pr(ar)} \to \infty$, which is tantamount to neglecting the momentum equation inertial terms.

Vapor Flow in Cylindrical Heat Pipes[1]

L. S. Galowin,[2] L. S. Fletcher,[3] and M. J. DeSantis[4] The authors have presented an interesting theoretical analysis for flow properties within a cylindrical heat pipe utilizing finite difference techniques for solution of the governing differential equations. Transformation of the dependent variables to the stream function and the vorticity, results in an elliptic partial differential equation for analysis of confined flow within a heat pipe. Solutions of such equations almost always appear to be wholly dependent upon the stipulation of the initial velocity profiles, and therefore the results are sometimes quite arbitrary. It would be instructive if the authors would compare their results with other methods of solution for pipe flows with mass addition/removal at the walls.

The Bankston and Smith analysis differs from the results of a recent experimental investigation of laminar flow in a porous pipe with uniform wall suction, and a recent theoretical analysis of laminar flow in a porous pipe with variable wall suction. The significant differences are the assumption of a uniform velocity at the wall as compared to nonuniform wall velocities in the condenser section of the heat pipe, and the numerical results indicating that the pressures fall rather than rise in the condenser section of the pipe.

An experimental investigation of the pressure variations occurring in incompressible laminar flow in a closed end porous tube with uniform wall suction as a model for the condenser of a heat pipe has been conducted by Quaile and Levy [21].[5] In addition to the presentation of experimental data for pressure variations, theoretical "similarity" and "inlet" solutions were shown for comparison. Both the experimental data and the reported theoretical solutions over a small range of radial Reynolds numbers indicated an increasing pressure in the condenser region.

The analysis of Galowin and DeSantis [12] for laminar pipe flow in a porous wall cylinder has been extended for the heat pipe condenser section to incorporate the boundary condition of variable wall suction as a model for vapor condensation [22]. This analysis shows excellent agreement with the experimental data of Quaile and Levy [21] and further substantiates the rise in pressure in the porous tube. This excellent comparison between experiment and theory indicates that the assumption of variable wall suction provides the representative boundary condition at the porous tube wall. Separation and reverse flows were not mentioned in the report of the experimental investigation nor in the recent theoretical analysis. Perhaps the experimental technique adopted [21] suppressed the development of the separation regions exhibited in the Bankston and Smith analysis. The choice

[1] By C. C. Gentry and D. E. Wollersheim, published in the Feb. 1973 issue of JOURNAL OF HEAT TRANSFER, TRANS. ASME, Series C Vol. 96, No. 1, pp. 3–8.

[2] Professor, School of Engineering, University of Michigan, Dearborn, Mich.

[3] Na, T. Y. and Hansen, A. G., "Possible Similarity Solutions of Laminar Natural Convection Flow of Non-Newtonian Fluids," *International Journal of Heat and Mass Transfer*, Vol. 9, 1966, pp. 261–262.

[1] By C. A. Bankston and H. J. Smith, published in the Aug. 1973 issue of JOURNAL OF HEAT TRANSFER, TRANS. ASME, Series C, Vol. 95, No. 3, pp. 371-376.

[2] Engineering Consultant, ENER-G Associates, Clifton, N. J. Mem. ASME.

[3] Assoc. Professor, Mechanical, Industrial & Aerospace Engineering, Rutgers University, New Brunswick, N. J. Mem. ASME.

[4] Scientific Consultant, Lyndhurst, N. J.

[5] Numbers in Brackets designate Additional References at end of Discussion.

ERRATA

An errata on D. J. Wilson and R. J. Goldstein, "Effect of Film Cooling Injection on Downstream Heat Transfer Coefficients in High Speed Flow," published in the November, 1973, issue of the JOURNAL OF HEAT TRANSFER pp. 505–509.

Equation (4) has been stated incorrectly. It should be written

$$\frac{C_f}{2} = \frac{0.123}{(10)^{0.678(\frac{n+2}{n})}} \left(\frac{\rho u_\infty \theta}{\mu}\right)^{-0.268} \tag{4a}$$

where C_f is the skin friction coefficient for a constant property flow.

To avoid the problem of having to evaluate θ at the reference state equation (4*a*) is combined with the constant property integral momentum equation, integrated and then evaluated at the reference state to yield

$$\frac{C_{f*}}{2} = \frac{0.182}{10^{0.535(\frac{n+2}{n})}} \left(\frac{\rho_* u_\infty X}{\mu_*}\right)^{-0.21} \tag{4b}$$

Combining (4*b*) with the integral momentum equation for a compressible boundary layer,

$$\frac{d\theta}{dX} = \frac{C_{f*}}{2} \left(\frac{\rho_*}{\rho_\infty}\right) \tag{4c}$$

equation (5) in the paper can be obtained.

The authors regret that in condensing the derivation of equation (5), that (4) was incorrectly stated.